GEOPHYSICAL MONOGRAPH SERIES

AGU
ADVANCING EARTH AND SPACE SCIENCE

Distributed Acoustic Sensing in Geophysics

Methods and Applications

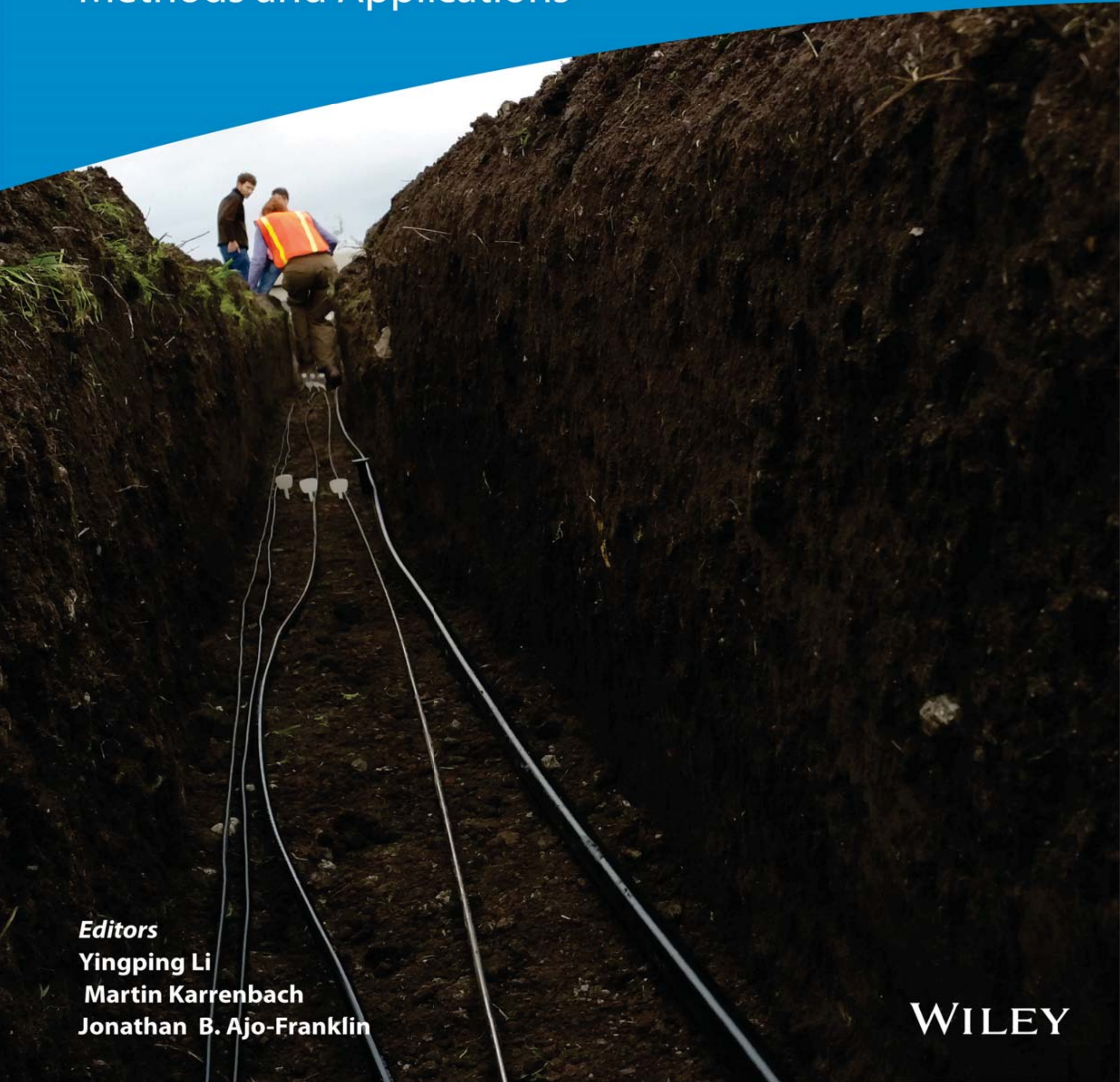

Editors
Yingping Li
Martin Karrenbach
Jonathan B. Ajo-Franklin

WILEY

GEOPHYSICAL MONOGRAPH SERIES

Distributed Acoustic Sensing in Geophysics

Methods and Applications

Yingping Li, BlueSkyDas, USA
Martin Karrenbach, OptaSense Inc., USA
Jonathan B. Ajo-Franklin, Rice University and Lawrence Berkeley National Laboratory, USA

Distributed Acoustic Sensing (DAS) is a technology that records sound and vibration signals along a fiber optic cable. Its advantages of high resolution, continuous, and real-time measurements mean that DAS systems have been rapidly adopted for a range of applications, including hazard mitigation, energy industries, geohydrology, environmental monitoring, and civil engineering.

Distributed Acoustic Sensing in Geophysics: Methods and Applications presents experiences from both industry and academia on using DAS in a range of geophysical applications.

Volume highlights include:

- DAS concepts, principles, and measurements
- Comprehensive review of the historical development of DAS and related technologies
- DAS applications in hydrocarbon, geothermal, and mining industries
- DAS applications in seismology
- DAS applications in environmental and shallow geophysics

The American Geophysical Union promotes discovery in Earth and space science for the benefit of humanity. Its publications disseminate scientific knowledge and provide resources for researchers, students, and professionals.

Cover Design: Wiley
Cover Image: © Jonathan Ajo-Franklin

www.wiley.com

WILEY

Also available as an e-book

AGU ADVANCING EARTH AND SPACE SCIENCE

ISBN 978-1-119-52179-2

Geophysical Monograph Series

Geophysical Monograph Series

212 **The Early Earth: Accretion and Differentiation** *James Badro and Michael Walter (Eds.)*
213 **Global Vegetation Dynamics: Concepts and Applications in the MC1 Model** *Dominique Bachelet and David Turner (Eds.)*
214 **Extreme Events: Observations, Modeling and Economics** *Mario Chavez, Michael Ghil, and Jaime Urrutia-Fucugauchi (Eds.)*
215 **Auroral Dynamics and Space Weather** *Yongliang Zhang and Larry Paxton (Eds.)*
216 **Low-Frequency Waves in Space Plasmas** *Andreas Keiling, Dong-Hun Lee, and Valery Nakariakov (Eds.)*
217 **Deep Earth: Physics and Chemistry of the Lower Mantle and Core** *Hidenori Terasaki and Rebecca A. Fischer (Eds.)*
218 **Integrated Imaging of the Earth: Theory and Applications** *Max Moorkamp, Peter G. Lelievre, Niklas Linde, and Amir Khan (Eds.)*
219 **Plate Boundaries and Natural Hazards** *Joao Duarte and Wouter Schellart (Eds.)*
220 **Ionospheric Space Weather: Longitude and Hemispheric Dependences and Lower Atmosphere Forcing** *Timothy Fuller-Rowell, Endawoke Yizengaw, Patricia H. Doherty, and Sunanda Basu (Eds.)*
221 **Terrestrial Water Cycle and Climate Change Natural and Human-Induced Impacts** *Qiuhong Tang and Taikan Oki (Eds.)*
222 **Magnetosphere-Ionosphere Coupling in the Solar System** *Charles R. Chappell, Robert W. Schunk, Peter M. Banks, James L. Burch, and Richard M. Thorne (Eds.)*
223 **Natural Hazard Uncertainty Assessment: Modeling and Decision Support** *Karin Riley, Peter Webley, and Matthew Thompson (Eds.)*
224 **Hydrodynamics of Time-Periodic Groundwater Flow: Diffusion Waves in Porous Media** *Joe S. Depner and Todd C. Rasmussen (Auth.)*
225 **Active Global Seismology** *Ibrahim Cemen and Yucel Yilmaz (Eds.)*
226 **Climate Extremes** *Simon Wang (Ed.)*
227 **Fault Zone Dynamic Processes** *Marion Thomas (Ed.)*
228 **Flood Damage Survey and Assessment: New Insights from Research and Practice** *Daniela Molinari, Scira Menoni, and Francesco Ballio (Eds.)*
229 **Water-Energy-Food Nexus – Principles and Practices** *P. Abdul Salam, Sangam Shrestha, Vishnu Prasad Pandey, and Anil K Anal (Eds.)*
230 **Dawn–Dusk Asymmetries in Planetary Plasma Environments** *Stein Haaland, Andrei Rounov, and Colin Forsyth (Eds.)*
231 **Bioenergy and Land Use Change** *Zhangcai Qin, Umakant Mishra, and Astley Hastings (Eds.)*
232 **Microstructural Geochronology: Planetary Records Down to Atom Scale** *Desmond Moser, Fernando Corfu, James Darling, Steven Reddy, and Kimberly Tait (Eds.)*
233 **Global Flood Hazard: Applications in Modeling, Mapping and Forecasting** *Guy Schumann, Paul D. Bates, Giuseppe T. Aronica, and Heiko Apel (Eds.)*
234 **Pre-Earthquake Processes: A Multidisciplinary Approach to Earthquake Prediction Studies** *Dimitar Ouzounov, Sergey Pulinets, Katsumi Hattori, and Patrick Taylor (Eds.)*
235 **Electric Currents in Geospace and Beyond** *Andreas Keiling, Octav Marghitu, and Michael Wheatland (Eds.)*
236 **Quantifying Uncertainty in Subsurface Systems** *Celine Scheidt, Lewis Li, and Jef Caers (Eds.)*
237 **Petroleum Engineering** *Moshood Sanni (Ed.)*
238 **Geological Carbon Storage: Subsurface Seals and Caprock Integrity** *Stephanie Vialle, Jonathan Ajo-Franklin, and J. William Carey (Eds.)*
239 **Lithospheric Discontinuities** *Huaiyu Yuan and Barbara Romanowicz (Eds.)*
240 **Chemostratigraphy Across Major Chronological Eras** *Alcides N. Sial, Claudio Gaucher, Muthuvairavasamy Ramkumar, and Valderez Pinto Ferreira (Eds.)*
241 **Mathematical Geoenergy:Discovery, Depletion, and Renewal** *Paul Pukite, Dennis Coyne, and Daniel Challou (Eds.)*
242 **Ore Deposits: Origin, Exploration, and Exploitation** *Sophie Decree and Laurence Robb (Eds.)*
243 **Kuroshio Current: Physical, Biogeochemical and Ecosystem Dynamics** *Takeyoshi Nagai, Hiroaki Saito, Koji Suzuki, and Motomitsu Takahashi (Eds.)*
244 **Geomagnetically Induced Currents from the Sun to the Power Grid** *Jennifer L. Gannon, Andrei Swidinsky, and Zhonghua Xu (Eds.)*
245 **Shale: Subsurface Science and Engineering** *Thomas Dewers, Jason Heath, and Marcelo Sánchez (Eds.)*
246 **Submarine Landslides: Subaqueous Mass Transport Deposits From Outcrops to Seismic Profiles** *Kei Ogata, Andrea Festa, and Gian Andrea Pini (Eds.)*
247 **Iceland: Tectonics, Volcanics, and Glacial Features** *Tamie J. Jovanelly*
248 **Dayside Magnetosphere Interactions** *Qiugang Zong, Philippe Escoubet, David Sibeck, Guan Le, and Hui Zhang (Eds.)*
249 **Carbon in Earth's Interior** *Craig E. Manning, Jung-Fu Lin, and Wendy L. Mao (Eds.)*
250 **Nitrogen Overload: Environmental Degradation, Ramifications, and Economic Costs** *Brian G. Katz*
251 **Biogeochemical Cycles: Ecological Drivers and Environmental Impact** *Katerina Dontsova, Zsuzsanna Balogh-Brunstad, and Gaël Le Roux (Eds.)*
252 **Seismoelectric Exploration: Theory, Experiments, and Applications** *Niels Grobbe, André Revil, Zhenya Zhu, and Evert Slob (Eds.)*
253 **El Niño Southern Oscillation in a Changing Climate** *Michael J. McPhaden, Agus Santoso, and Wenju Cai (Eds.)*
254 **Dynamic Magma Evolution** *Francesco Vetere (Ed.)*
255 **Large Igneous Provinces: A Driver of Global Environmental and Biotic Changes** *Richard. E. Ernst, Alexander J. Dickson, and Andrey Bekker (Eds.)*
256 **Coastal Ecosystems in Transition: A Comparative Analysis of the Northern Adriatic and Chesapeake Bay** *Thomas C. Malone, Alenka Malej, and Jadran Faganeli (Eds.)*
257 **Hydrogeology, Chemical Weathering, and Soil Formation** *Allen Hunt, Markus Egli, and Boris Faybishenko (Eds.)*
258 **Solar Physics and Solar Wind** *Nour E. Raouafi and Angelos Vourlidas (Eds.)*
259 **Magnetospheres in the Solar System** *Romain Maggiolo, Nicolas André, Hiroshi Hasegawa, and Daniel T. Welling (Eds.)*
260 **Ionosphere Dynamics and Applications** *Chaosong Huang and Gang Lu (Eds.)*
261 **Upper Atmosphere Dynamics and Energetics** *Wenbin Wang and Yongliang Zhang (Eds.)*
262 **Space Weather Effects and Applications** *Anthea J. Coster, Philip J. Erickson, and Louis J. Lanzerotti (Eds.)*
263 **Mantle Convection and Surface Expressions** *Hauke Marquardt, Maxim Ballmer, Sanne Cottaar, and Jasper Konter (Eds.)*
264 **Crustal Magmatic System Evolution: Anatomy, Architecture, and Physico-Chemical Processes** *Matteo Masotta, Christoph Beier, and Silvio Mollo (Eds.)*
265 **Global Drought and Flood: Observation, Modeling, and Prediction** *Huan Wu, Dennis P.Lettenmaier, Qiuhong Tang, and Philip J Ward (Eds.)*
266 **Magma Redox Geochemistry** *Roberto Moretti and Daniel R. Neuville (Eds.)*
267 **Wetland Carbon and Environmental Management** *Ken W. Krauss, Zhiliang Zhu, and Camille L. Stagg (Eds.)*
268 **Distributed Acoustic Sensing in Geophysics: Methods and Applications** *Yingping Li, Martin Karrenbach, and Jonathan B. Ajo-Franklin (Eds.)*

Geophysical Monograph 268

Distributed Acoustic Sensing in Geophysics

Methods and Applications

Yingping Li
Martin Karrenbach
Jonathan B. Ajo-Franklin
Editors

This work is a co-publication of the American Geophysical Union and John Wiley & Sons, Inc.

AGU
ADVANCING EARTH AND SPACE SCIENCE

WILEY

This edition first published 2022

Published under the aegis of the AGU Publications Committee

Registered Office
John Wiley & Sons, Inc., 111 River Street, Hoboken, NJ 07030, USA

Editorial Office
111 River Street, Hoboken, NJ 07030, USA

For details of our global editorial offices, customer services, and more information about Wiley products, visit us at www.wiley.com.

Wiley also publishes its books in a variety of electronic formats and by print on demand. Some content that appears in standard print versions of this book may not be available in other formats.

Library of Congress Cataloging-in-Publication Data
Names: Li, Yingping, editor. | Karrenbach, Martin, editor. | Ajo-Franklin, Jonathan, editor.
Title: Distributed acoustic sensing in geophysics : methods and applications / Yingping Li, Martin Karrenbach, Jonathan Ajo-Franklin, editor.
Description: First edition. | Hoboken, NJ : Wiley-American Geophysical Union, [2021] | Series: Geophysical monograph series | Includes bibliographical references.
Identifiers: LCCN 2021015330 (print) | LCCN 2021015331 (ebook) | ISBN 9781119521792 (cloth) | ISBN 9781119521822 (adobe pdf) | ISBN 9781119521778 (epub)
Subjects: LCSH: Geophysics–Methodology. | Optical fiber detectors. | Imaging systems in geophysics. | Microseisms. | Tomography.
Classification: LCC QC808.5 .D57 2021 (print) | LCC QC808.5 (ebook) | DDC 681/.25–dc23
LC record available at https://lccn.loc.gov/2021015330
LC ebook record available at https://lccn.loc.gov/2021015331

Cover Design: Wiley
Cover Image: © Jonathan Ajo-Franklin

Set in 10/12pt Times New Roman by Straive, Pondicherry, India

10 9 8 7 6 5 4 3 2 1

CONTENTS

LIST OF CONTRIBUTORS

Fan Ai
School of Optical and Electronic Information
National Engineering Laboratory for Next Generation Internet Access System
Huazhong University of Science and Technology
Wuhan, China

Jonathan B. Ajo-Franklin
Department of Earth, Environmental and Planetary Sciences
Rice University
Houston, Texas, USA
and
Energy Geosciences Division
Lawrence Berkeley National Laboratory
Berkeley, California, USA

Jonathan A. Baldwin
U.S. Army Corps of Engineers
Washington, District of Columbia, USA

Biondo L. Biondi
Department of Geophysics
Stanford University
Stanford, California, USA
and
Institute for Computational and Mathematical Engineering
Stanford, California, USA

Joel Le Calvez
Schlumberger
Houston, Texas, USA

Timothy Robert Carr
Department of Geology and Geography
West Virginia University
Morgantown, West Virginia, USA

Athena Chalari
Silixa Ltd.
Elstree, UK

Yuan-Zhong Chen
School of Information and Communication Engineering
University of Electronic Science and Technology of China
Chengdu, China
and
BGP Inc.
China National Petroleum Corporation
Zhuozhou, China

Robert G. Clapp
Department of Geophysics
Stanford University
Stanford, California, USA

Thomas Coleman
Silixa LLC.,
Missoula, Montana, USA

Julia Correa
Energy Geosciences Division
Lawrence Berkeley National Laboratory
Berkeley, California, USA
and
Centre for Exploration Geophysics
Curtin University
Perth, Australia
and
CO2CRC Limited
Melbourne, Australia

Thomas M. Daley
Energy Geosciences Division
Lawrence Berkeley National Laboratory
Berkeley, California, USA

Shan Dou
Visier Inc.
Vancouver, British Columbia, Canada

Yuting Duan
Shell Technology Center
Houston, Texas, USA

Andreas Ellmauthaler
Halliburton
Houston, Texas, USA

Cunzheng Fan
School of Optical and Electronic Information
National Engineering Laboratory for Next Generation Internet Access System
Huazhong University of Science and Technology
Wuhan, China

Mahmoud Farhadiroushan
Silixa Ltd.
Elstree, UK

Kurt L. Feigl
Department of Geoscience
University of Wisconsin–Madison
Madison, Wisconsin, USA

Shengwen Feng
Key Laboratories of Transducer Technology
Institute of Semiconductors
Chinese Academy of Sciences
Beijing, China
and
College of Materials Science and Opto-Electronic Technology
University of Chinese Academy of Sciences
Beijing, China

Dante Fratta
Department of Civil and Environmental Engineering
University of Wisconsin–Madison
Madison, Wisconsin, USA

Barry M. Freifeld
Class VI Solutions Inc.
Oakland, California, USA

Stanislav Glubokovskikh
Centre for Exploration Geophysics
Curtin University
Perth, Australia
and
CO2CRC Limited
Melbourne, Australia

Guang-Min Hu
School of Information and Communication Engineering
University of Electronic Science and Technology of China
Chengdu, China

Jian-Hua Huang
BGP Inc.
China National Petroleum Corporation
Zhuozhou, China

Fantine Huot
Department of Geophysics
Stanford University
Stanford, California, USA

Payam Kavousi Ghahfarokhi
Department of Geology and Geography
West Virginia University
Morgantown, West Virginia, USA

Martin Karrenbach
OptaSense Inc. (A LUNA Company)
Brea, California, USA

Denis Kiyashchenko
Shell Technology Center
Houston, Texas, USA

Chelsea E. Lancelle
Department of Civil and Environmental Engineering
University of Wisconsin–Platteville
Platteville, Wisconsin, USA

Michel J. LeBlanc
Halliburton
Houston, Texas, USA

Fang Li
Key Laboratories of Transducer Technology
Institute of Semiconductors
Chinese Academy of Sciences
Beijing, China
and
College of Materials Science and Opto-Electronic Technology
University of Chinese Academy of Sciences
Beijing, China

Fei Li
BGP Inc.
China National Petroleum Corporation
Zhuozhou, China

Hao Li
School of Optical and Electronic Information
National Engineering Laboratory for Next Generation Internet Access System
Huazhong University of Science and Technology
Wuhan, China

Xiaolei Li
OVLINK Inc.
Wuhan, China

Yan-Peng Li
BGP Inc.
China National Petroleum Corporation
Zhuozhou, China

Yingping Li
BlueSkyDas (formerly Shell)
Houston, Texas, USA

Nathaniel J. Lindsey
FiberSense
Sydney, Australia

Deming Liu
School of Optical and Electronic Information
National Engineering Laboratory for Next Generation Internet Access System
Huazhong University of Science and Technology
Wuhan, China

Jorge Lopez
Shell Brasil Petróleo Ltda.
Rio de Janeiro, Brazil

Neal Lord
Department of Geoscience
University of Wisconsin–Madison
Madison, Wisconsin, USA

Lilong Ma
Key Laboratories of Transducer Technology
Institute of Semiconductors
Chinese Academy of Sciences
Beijing, China
and
College of Materials Science and Opto-Electronic Technology
University of Chinese Academy of Sciences
Beijing, China

Eileen R. Martin
Department of Mathematics
Virginia Polytechnic Institute and State University
Blacksburg, Virginia, USA

Keithan Martin
Department of Geology and Geography
West Virginia University
Morgantown, West Virginia, USA

Albena Mateeva
Shell Technology Center
Houston, Texas, USA

Takashi Mizuno
Schlumberger
Houston, Texas, USA

Inder Monga
Energy Sciences Network
Lawrence Berkeley National Laboratory
Berkeley, California, USA

Tom Parker
Silixa Ltd.
Elstree, UK

Roman Pevzner
Centre for Exploration Geophysics
Curtin University
Perth, Australia
and
CO2CRC Limited
Melbourne, Australia

Daniel Raymer
Schlumberger
Houston, Texas, USA

Michelle Robertson
Energy Geosciences Division
Lawrence Berkeley National Laboratory
Berkeley, California, USA

Verónica Rodríguez Tribaldos
Energy Geosciences Division
Lawrence Berkeley National Laboratory
Berkeley, California, USA

Sergey Shatalin
Silixa Ltd.
Elstree, UK

Qizhen Sun
School of Optical and Electronic Information
National Engineering Laboratory for Next Generation Internet Access System
Huazhong University of Science and Technology
Wuhan, China

Konstantin Tertyshnikov
Centre for Exploration Geophysics
Curtin University
Perth, Australia
and
CO2CRC Limited
Melbourne, Australia

Clifford H. Thurber
Department of Geoscience
University of Wisconsin–Madison
Madison, Wisconsin, USA

Chris Tracy
Energy Sciences Network
Lawrence Berkeley National Laboratory
Berkeley, California, USA

Whitney Trainor-Guitton
Department of Geophysics
Colorado School of Mines
Golden, Colorado, USA
and
W Team Geosolutions
Twin Falls, Idaho, USA

Craig Ulrich
Energy Geosciences Division
Lawrence Berkeley National Laboratory
Berkeley, California, USA

Herbert F. Wang
Department of Geoscience
University of Wisconsin–Madison
Madison, Wisconsin, USA

Shi-Ze Wang
BGP Inc.
China National Petroleum Corporation
Zhuozhou, China

Mark E. Willis
Halliburton
Houston, Texas, USA

Cody Wilson
Department of Geology and Geography
West Virginia University
Morgantown, West Virginia, USA

Todd Wood
Energy Geosciences Division
Lawrence Berkeley National Laboratory
Berkeley, California, USA

Jun-Jun Wu
BGP Inc.
China National Petroleum Corporation
Zhuozhou, China

Xiang Wu
Halliburton Far East Pte. Ltd.
Singapore

Tuanwei Xu
Key Laboratories of Transducer Technology
Institute of Semiconductors
Chinese Academy of Sciences
Beijing, China
and
College of Materials Science and Opto-Electronic Technology
University of Chinese Academy of Sciences
Beijing, China

Zhijun Yan
School of Optical and Electronic Information
National Engineering Laboratory for Next Generation Internet Access System
Huazhong University of Science and Technology
Wuhan, China

Kaiheng Yang
Key Laboratories of Transducer Technology
Institute of Semiconductors
Chinese Academy of Sciences
Beijing, China
and
College of Materials Science and Opto-Electronic Technology
University of Chinese Academy of Sciences
Beijing, China

Sinem Yavuz
Centre for Exploration Geophysics
Curtin University
Perth, Australia
and
CO2CRC Limited
Melbourne, Australia

Gang Yu
BGP Inc.
China National Petroleum Corporation
Zhuozhou, China
and
School of Information and Communication Engineering
University of Electronic Science and Technology of China
Chengdu, China

Siyuan Yuan
Department of Geophysics
Stanford University
Stanford, California, USA

Xiangfang Zeng
State Key Laboratory of Geodesy and Earth's Dynamics
Innovation Academy for Precision Measurement Science and Technology
Chinese Academy of Sciences
Wuhan, China
and
Department of Geoscience
University of Wisconsin–Madison
Madison, Wisconsin, USA

Wei Zhang
School of Optical and Electronic Information
National Engineering Laboratory for Next Generation Internet Access System
Huazhong University of Science and Technology
Wuhan, China

LIST OF REVIEWERS

Reza Barati
Matt Becker
Gary Binder
Biondo L. Biondi
Stefan Buske
Dongjie Cheng
Feng Cheng
Steve Cole
Julia Correa
Thomas M. Daley
Timothy Dean
Yuting Duan
Mahmoud Farhadiroushan
Barry M. Freifeld
Andrew Greenwood
Alireza Haghighat
Ge Jin
John Michael Kendall
Hunter Knox
Ivan Lim Chen Ning
Nathaniel J. Lindsey
Min Lou
Linquing Luo
Stefan Lüth
Eileen R. Martin
Robert Mellors
Khalid Miah
Douglas Miller
Takashi Mizuno
Gerrit Olivier
Roman Pevzner
Michelle Robertson
Verónica Rodríguez Tribaldos
Bill Roggenthen
Baishali Roy
Ali Sayed
Alireza Shahkarami
Robert Stewart
Aleksei Titov
Whitney Trainor-Guitton
Milovan Urosevic
Guchang Wang
Herbert F. Wang
Erik Westman
Ethan Williams
Mark E. Willis
Xiangfang Zeng
Ge Zhan
Zhongwen Zhan
Haijiang Zhang
Ran Zhou
Ding Zhu
Tieyuan Zhu

PREFACE

Distributed acoustic sensing (DAS) systems are optoelectronic instruments that measure acoustic interactions (distributed strain or strain rate) along the length of a fiber-optic sensing cable. DAS observation systems can record sound and vibration signals along several tens of kilometers of sensing optical fiber with fine spatial resolution (1–10 m) and over a wide frequency range (from millihertz to tens of kilohertz). DAS provides a large sensing aperture for acquiring high-resolution acoustic data in both time and space domains. The advantages of DAS technology have enabled its rapid adoption across a range of applications, including geophysics geohydrology, environmental monitoring, geotechnical and civil engineering (railroad, tunnel, and bridge monitoring), hazard mitigation and prevention, and safety and security fields.

This monograph focuses on various DAS applications in geophysics. The use of DAS in the oil, gas, geothermal, and mining industries for high-resolution borehole and surface seismic imaging, and microseismic monitoring for hydraulic fractures has accelerated with improvements in the sensitivity of DAS instruments, advances in real-time big data processing, and flexible and economic deployment of fiber-optic sensing cables. There is also growing interest in using DAS for critical geophysical infrastructure applications, such as earthquake and near-surface passive seismic analysis, including the development of tailored or novel numerical techniques. This book aims to engage both the scientific and industrial communities to share their knowledge and experiences of using DAS for novel geophysical applications.

The origin of this book was the 2017 American Geophysical Union (AGU) Fall Meeting, when scientists and engineers from both industry and academia gathered in New Orleans to present their fantastic research outcomes on DAS instrumentations and applications in geophysics and seismology. As DAS technologies have continued to advance, more and more successful geophysical DAS applications have been reported and published in different geophysical and seismological journals, abstracts, and proceedings of technical conferences, such as the AGU, the Society of Exploration Geophysicists (SEG), the European Association of Geoscientists and Engineers (EAGE), the Society of Petroleum Engineers (SPE), and the Seismological Society of America (SSA). However, few DAS books are available on DAS principles, instrumentation, and geophysical applications. Many attendees at the DAS sessions at the 2017 AGU Fall Meeting expressed that there was a need for a book on DAS geophysical applications. We had interesting discussions with many scientists and engineers working on the frontier of DAS geophysical applications about the potential for a book. We specially recognize Biondo L. Biondi, Thomas M. Daley, William Ellsworth, Mahmoud Farhadiroushan, Barry M. Freifeld, Albena Mateeva, Robert Mellors, Clifford H. Thurber, Herbert Wang, and Mark E. Willis, as well as many others for their encouragement.

During the 2017 AGU Fall Meeting in New Orleans, we fortunately got an opportunity to meet with the AGU Books Editor, Dr. Bose, who was already aware of this rapidly growing scientific field. We discussed a potential book on DAS geophysical applications, and she was very supportive and invited us to submit a book proposal for an AGU monograph. With no surprise, this DAS book proposal received very positive comments and constructive suggestions from all reviewers. Several reviewers also asked for an opportunity to submit their own contributions to this monograph. We are grateful to those anonymous reviewers of the book proposal for their positive comments and constructive suggestions that led this book to be initiated.

This monograph is organized into four parts. Part I starts with principles of DAS measurements and instruments. DAS interrogation units transmit a pulse of laser light into the fiber. As this pulse of light travels down the fiber, interactions within the fiber result in light reflections known as backscatter (Rayleigh scattering). Backscatters are determined by tiny strain events within the fiber, which in turn are caused by localized acoustic energy. This backscattered light travels back up the fiber toward the interrogation unit where it is sampled. Part II introduces various DAS applications in the oil and gas, geothermal, and mining industries. Part III looks at DAS applications in seismic monitoring. DAS microseismic monitoring of hydraulic fracturing is an industry application but with passive seismic sources. The microseismic DAS method has been shown to have sufficient sensitivity to record very small magnitude microearthquakes with DAS deployed in boreholes. Microseismic DAS systems can be naturally extended to monitoring larger earthquake activity, and slow deformation of Earth's structure with large-scale fiber-optic networks. Part IV discusses DAS environmental and shallow geophysical applications such as geological carbon dioxide sequestration. The final chapter presents a review of fiber optical sensing applications in geophysics including historical developments and recent advances. The list of over 900 literature references of DAS and related technologies will benefit readers, especially newcomers who have just stepped into this fast-growing field.

We would like to thank the AGU Books Editorial Board for supporting this monograph. Without the efforts from contributing authors it would not have been possible to accomplish this project. We would also like to thank the many volunteer reviewers who spent tremendous amounts of time and effort to ensure that each chapter is of the highest quality. We appreciate Jonathan B. Ajo-Franklin, Biondo L. Biondi, Mahmoud Farhadiroushan, Albena Mateeva, and Siyuan Yuan for providing their pictures as candidates for the book cover design. Thanks are also extended to the AGU Books editorial team at Wiley, especially Dr. Rituparna Bose, Layla Harden, Noel McGlinchey, Vaishali Rajasekar, Sangaprabha Mohan, Bobby Kilshaw, Nithya Sechin, and Emily Bae, for their organization, management, and cover design.

This monograph will be the first comprehensive handbook for anyone interested in learning DAS principles and applications. We hope that the book will have a wide spectrum of readers – such as geophysicists, seismologists, geologists, and geoscientists; environmental scientists; and graduate and undergraduate students in geophysics and geoscience – with a common interest in DAS geophysical applications. This book also provides a common platform to the scientific and industry communities to share state-of-the-art DAS technology.

Yingping Li
BlueSkyDas (formerly Shell), USA

Martin Karrenbach
OptaSense Inc. (A LUNA Company), USA

Jonathan B. Ajo-Franklin
Rice University and Lawrence Berkeley National Laboratory, USA

Part I

Distributed Acoustic Sensing (DAS) Concept, Principle, and Measurements

1

High Definition Seismic and Microseismic Data Acquisition Using Distributed and Engineered Fiber Optic Acoustic Sensors

Sergey Shatalin, Tom Parker, and Mahmoud Farhadiroushan

ABSTRACT

The distributed acoustic sensor (DAS) offers a new versatile tool for geophysical applications. The system allows seismic signals to be recorded along tens of kilometers of optical fiber and over a wide frequency range. In this chapter we introduce the concept of DAS and derive an expression for the system response by modeling the superposition of the coherent backscatter fields along the fiber. Expressions are derived for converting the optical phase to strain rate and equivalent particle motion. We discuss DAS signal processing and denoising methods to deal with the random nature of the Rayleigh scatter signal and to further improve dynamic range and sensitivity. Next we consider DAS parameters such as spatial resolution, gauge length and directionality in comparison with geophones. We present some field trial results that demonstrate the benefits of the DAS for vertical seismic profiling and microseismic detection. Finally we discuss the fundamental sensitivity limit of DAS. We consider how the scattering properties of conventional fiber can be engineered to deliver a step-change DAS performance, beyond that of conventional geophones and seismometers. Theoretical findings are illustrated by the field data examples, including low-frequency strain monitoring and microseismic detection.

1.1. DISTRIBUTED ACOUSTIC SENSOR (DAS) PRINCIPLES AND MEASUREMENTS

In this chapter, we consider the principles and performance of distributed and precision engineered fiber optic acoustic sensors for geophysical applications (Hartog et al., 2013; Parker et al., 2014). In particular, system parameters such as spatial resolution, dynamic range, sensitivity, and directionality are examined for seismic and microseismic measurements.

In this first section, we consider the measurement principle of DAS, which uses naturally occurring random scatter centers along the fiber. We use the term *acoustics* in a broad physical sense here, like any propagation of mechanical disturbances (Lewis, 1985). We review different DAS systems, including direct-intensity-detection and phase-detection schemes, where we derive a mathematical relationship for optical phase recovery. Our aim is to explain the nature of the distributed acoustic signal and describe the natural limitations for DAS measurements. Such information is needed to optimize DAS recording parameters for geophysical applications. Examples of DAS parameter optimization for seismic applications can be found in Section 1.2. We also present some examples of active and passive seismic field data in Sections 1.2 and 1.3.

Silixa Ltd. Elstree, UK

Distributed Acoustic Sensing in Geophysics: Methods and Applications, Geophysical Monograph 268, First Edition.
Edited by Yingping Li, Martin Karrenbach, and Jonathan B. Ajo-Franklin.

DOI:10.1002/9781119521808.ch01

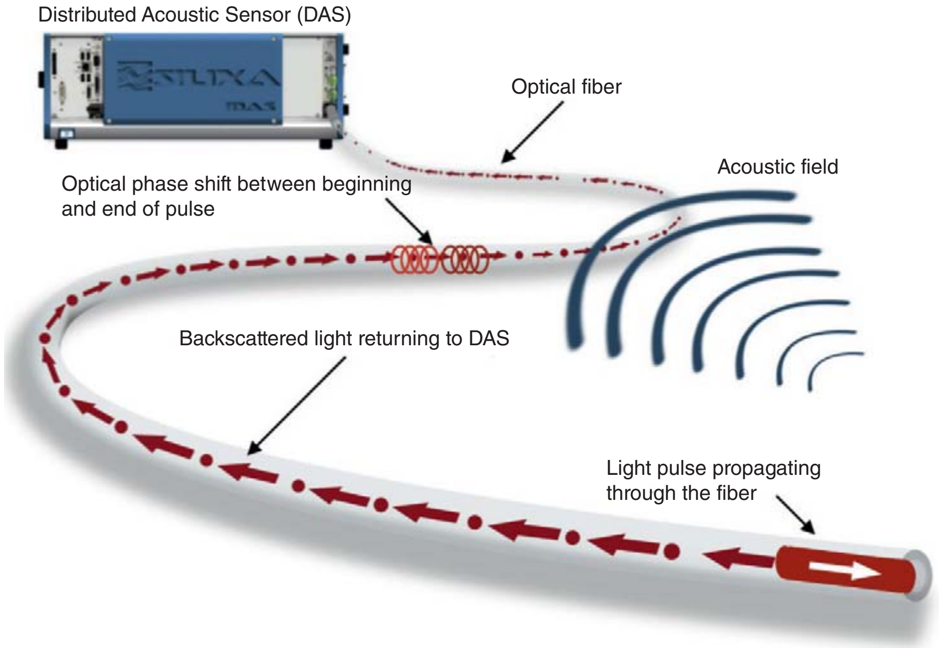

Figure 1.1 Operation principle of distributed acoustic sensing.

1.1.1. DAS Concept

The principle of distributed sensing is based on *optical time domain reflectometry* (OTDR), as indicated in Figure 1.1. When a laser pulse travels down an optical fiber, a tiny portion of the light is naturally scattered through Rayleigh, Raman (Dakin & Culshaw, 1989), and Brillouin (Parker et al., 1998) interactions and returns to the optoelectronic sensor unit. The measurement location can be determined from the time taken for the laser pulse to travel down the sensing fiber, and the backscatter light to return to the optoelectronic sensor unit.

Figure 1.1 shows the basic principle of DAS, where the sensing fiber is excited with a coherent laser pulse and the Rayleigh backscattered interference along the fiber is detected and digitized. An acoustic wave elongates the fiber and so changes the optical phase shift between backscatter components from the leading and trailing parts of the optical pulse. As a result of interference, the intensity of the returning light changes from pulse to pulse. It is also possible to determine the optical phase to recover acoustic phase so there are two classes of DAS, based on the detection of: (i) optical intensity and (ii) optical phase. With the intensity DAS technique, also referred to as *coherent optical time domain reflectometry* (COTDR), a perturbation along the fiber is detected by measuring the changes in the backscatter intensity from pulse to pulse, as indicated in Figure 1.2. COTDR has been used for the detection of temperature changes (Rathod et al., 1994; Shatalin et al., 1991) and acoustic vibration (Juškaitis et al., 1992; Posey et al., 2000), along multi-kilometer fiber cables (Juarez et al., 2005; Shatalin et al., 1998).

The principle of the COTDR system can be understood by analyzing the radiation generated by localized scatter centers (Taylor & Lee, 1993). Here, the coherent scattered light can be represented as the result of two reflections with random amplitude and phase. When the fiber is strained, the backscatter intensity varies in accordance with the strain rate (Figure 1.2), but with an unpredictable amplitude and phase, which changes along the fiber (Shatalin et al., 1998). As a result, the signal cannot be effectively accumulated for multiple seismic pulses: the fiber response to strain is highly nonlinear, and therefore the changes in amplitude and phase cannot be directly matched to the original strain affecting the fiber. The next section discusses ways of addressing this. Therefore, COTDR systems are not that useful for seismic applications.

With the phase DAS technique, the method for optical phase analysis is a key feature of system design. All techniques rely on phase modulation between the beginning and end of a pulse, which can be considered as a double pulse. Such modulation can be performed before or after light propagation over optical fiber, as indicated in Figure 1.3. We have limited our discussion to schemas that have been patented and implemented in practice. In one scheme, which is similar to that used for multiplexed interferometer sensors (Dakin, 1990), two laser pulses with different frequencies may be sent down the fiber (Figure 1.3a). In this case, the acoustic phase shift

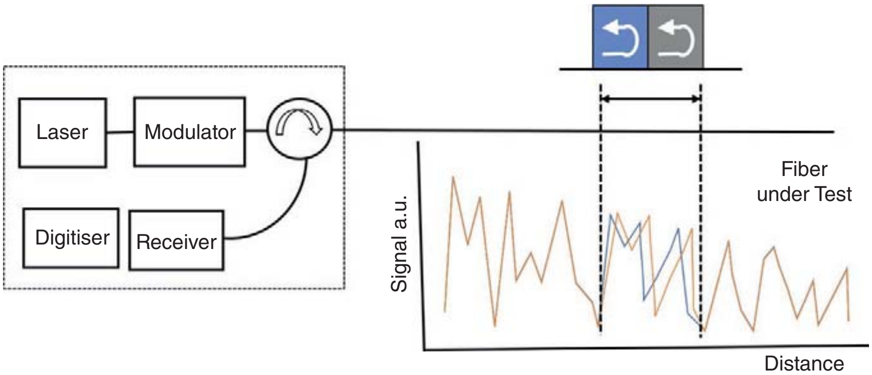

Figure 1.2 COTDR.

	Method	Adapted schematic diagram	Reference
a	Two pulses with shifted frequencies and embedded delay	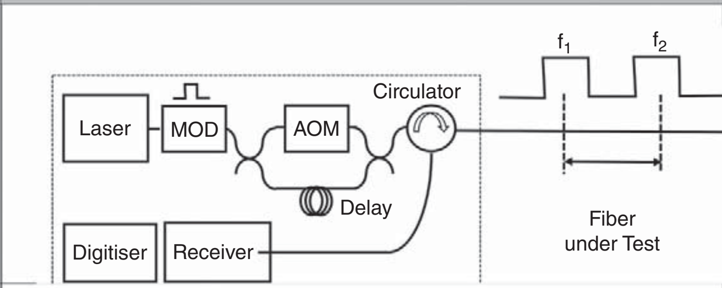	Crickmore & Hill, 2010
b	Interferometer with 3x3 coupler and embedded delay	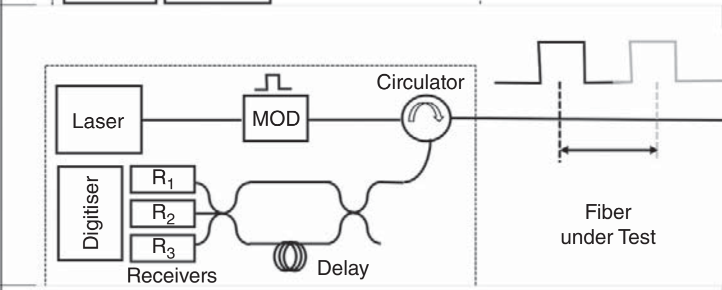	Farhadiroushan et al., 2010
c	Heterodyne	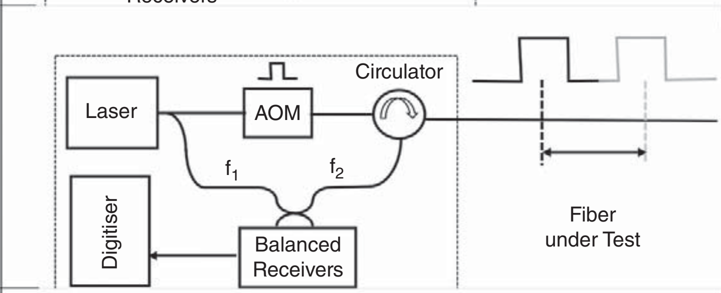	Hartog & Kader 2012
d	Different frequency comparator	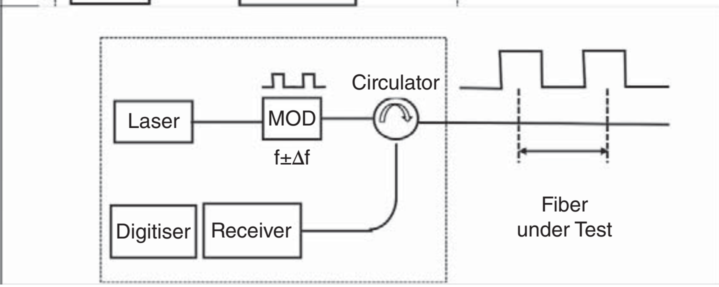	Farhadiroushan et al., 2010 Handerek, 2016 Crickmore & Ku, 2017

Figure 1.3 DAS schemas: MOD—intensity and frequency modulator; AOM—acousto-optic modulator.

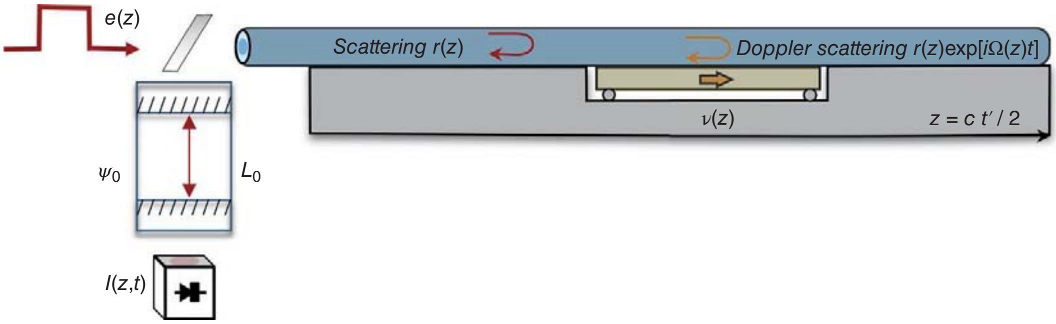

Figure 1.4 DAS optical setup. Distance is proportional to flytime.

will be transferred to a frequency difference and can be measured in the photocurrent radio frequency domain.

Other solutions, such as that shown in Figure 1.3b, contain an embedded delay line that defines the spatial resolution. We will focus our analysis on this class of systems. Another configuration uses optical heterodyne, as shown in Figure 1.3c, where the backscatter signal is continuously mixed with a slightly frequency shifted local oscillator laser. In this case, the elongation along the fiber is measured by computing the difference of the accumulated optical phase between two sections of fiber, and the measurement is carried out at differential frequency $f_1 - f_2$. Although this technique offers a flexible spatial resolution, it requires a laser source with extremely high coherence to achieve reasonable signal-to-noise ratio (SNR) performance over several tens of kilometers of fiber. The details of the heterodyne concept are thoroughly covered elsewhere (Hartog, 2017). Another method involves sending multiple pulses of different frequencies, either in series or from pulse to pulse, and then computing the phase of the backscatter signal, as indicated in Figure 1.3d. The phase calculation in this case is similar to first case (Figure 1.3a).

1.1.2. DAS Interferometric Optical Response

The theoretical concept of DAS is based on the assumption that the Rayleigh centers have no microscopic motion, but they are "frozen" inside glass during manufacture. In this case, the positions of the centers depend on the macroscopic motion of fiber and can coincide with the ground speed around a buried fiber (v). There are two time scales of relevance to DAS: (1) as optical pulse travels with speed c, significantly faster than ground motion, this dictates the spatial resolution; (2) seismic motion is responsible for interference changes pulse to pulse, which can be used to recover the seismic signal. All parameters for both fast and slow motions are summarized in the table of variables at the end of the chapter.

Let us calculate how the intensity of backscattered light changes when a section of fiber is moving with speed $v(z)$ under a seismic wave (Figure 1.4). The Rayleigh centers will move with the fiber, so the frequency of the backscattered light will experience a Doppler shift $\Omega(z)$ proportional to its speed, like for Brillouin scattering (Hartog, 2017). The aim of DAS can be considered as the measurement of Doppler shift for Rayleigh scattering derived from the detected photocurrent. The phase shift can be measured between two separate points in space, and then the resultant Doppler shift can be recovered with spatial integration, as will be shown later in the text. The first step is to analyze changes in intensity between different optical pulses to derive the fiber speed information, which will be equal to the ground speed in a seismic wave.

Consider a coherent optical pulse $e(t')$ that is launched into a single-mode optical fiber. The backscattered optical field $E(t')$ at time t' for light reemerging from the launch end can be expressed as a superimposition of delayed partial fields backscattered with a reflection coefficient $r_0(z)$ along the fiber axis z (Shatalin et al., 1998). This amplitude coefficient represents coupling between the forward and backward modes. For a speed of light in the fiber $c \approx 2\ \ 10^8 m/c$, and wave propagation constant β, we can use group and phase delays $2z/c$ and $2\int_0^z \beta(x)dx$, respectively. So, the emerging field will depend on interferometer optical delay, or gauge length, L_0 as:

$$E(t') = \int_0^L \left[e\left(t' - \frac{2z}{c}\right) + e\left(t' - \frac{2z}{c} - \frac{2L_0}{c}\right)\right] \cdot r_0(z) \cdot \exp\left[2i\int_0^z \beta(x)dx\right] dz \tag{1.1}$$

For a regular fiber, the phase shift term in Equation 1.1 can be separated into a constant part and a part changing with "slow" time t, representing pulse-to-pulse parameter variation with Doppler shift frequency $\Omega(z)$, which is proportional to scattering particle velocity $v(z)$ and wavelength frequency ω.

$$\int_0^z \beta(x,t)dx = \beta_0 z + \Omega(z)t \tag{1.2}$$

$$\Omega(z) = \omega \ v(z)/c = \frac{4\pi \ n_{eff} K_\varepsilon}{\lambda} v(z) \tag{1.3}$$

Here the strain coefficient K_ε relates the physical and optical length of fiber, n_{eff} is fiber effective refractive index, and λ is the laser wavelength. Equations 1.2–1.3 represent a well-known dualism, when a change in interference can be considered not only as a result of a change in phase, but also as a beating of a frequency due to a Doppler shift. The concept finds application in Doppler lidars, where Rayleigh scattering light contains wind speed information, so the height distribution of the speed can be detected using OTDR (Garnier & Chanin, 1992). The DAS conception is somewhat different: we do not measure the absolute velocity of Rayleigh scatterers, but the difference in such velocity along the gauge length. Another difference is that Rayleigh centers are frozen in a glass of fiber at a melting point of about 800°. Their movement follows the movement of the fiber, and hence very low Doppler frequencies (down to mHz) can be measured.

For simplicity of further calculations, the reflective coefficient $r_0(z)$ can be redefined as the effective reflective coefficient $r(z)$:

$$r(z) = r_0(z) \exp(\beta_0 z) \tag{1.4}$$

Then, to extract the Doppler shift from the intensity equation, we need to control the phase shift ψ_0 between delayed optical fields in the interferometer. So Equation 1.1 can be rearranged using Equations 1.2–1.4 to:

$$E(z,t) = [e(z) + e(z - L_0) \cdot \exp i\psi_0] \otimes r(z) \exp i[\Omega(z)t] \tag{1.5}$$

Here the convolution symbol $\otimes$ is used to simplify the expression, and the OTDR scale $z = 2ct'$ for the "fast" time t' is used. The convolution commutes with translations (Goodman, 2005), meaning that Equation 1.5 can be converted using $a(z_1 - z_2) \otimes b(z_1) = a(z_1) \otimes b(z_1 - z_2)$ to:

$$E(z,t) = e(z) \otimes \{r(z) \exp i[\Omega(z)t] + r(z - L_0) \exp i[\Omega(z - L_0)t + \psi_0]\} \tag{1.6}$$

Let us consider first the simple case of short pulse $e(z) = \delta(z)$ when δ is the Dirac delta function. Then convolution can be removed from Equation 1.5 because $\delta(z) \otimes a(z) = a(z)$, and the distance variation of Doppler shift $\Delta\Omega(z) = \Omega(z) - \Omega(z - L_0)$ can be represented via variation of intensity $I(z,t) = E(z,t)E(z,t)^*$. The expression in braces in Equation 1.6 represents a two-beam interference, so the intensity will vary harmonically depending on the phase. As we are interested in the intensity change, only the interference term needs be taken into consideration, which can be reshaped using the intensity derivative:

$$\frac{\partial I}{\partial t} = \frac{\partial E(z,t)}{\partial t} E(z,t)^* + E(z,t) \frac{\partial E(z,t)^*}{\partial t} \tag{1.7}$$

Then using convolution properties $\partial[a \otimes b(t)]/\partial t = a \otimes \partial b(t)/\partial t$, we can find intensity variation via phase shift Φ of backscattered light where there is argument of backscattering complex function:

$$\frac{\partial I}{\partial t} = 2\Delta\Omega(z)|r(z)r(z - L_0)^*| \sin(\psi_0 + \Phi) \tag{1.8}$$

$$\Phi = \Delta\Omega(z)t + Arg[r(z)r(z - L_0)^*] \tag{1.9}$$

The COTDR signal can be deduced from Equation 1.8 if we set $L_0 = 0 \quad and \quad \psi_0 = 0$. Even such a simple setup can deliver information on the Doppler shift and hence the ground speed $v(z)$ through the intensity variation $\partial I/\partial t \propto \Delta v$ in accordance with Equations 1.3, 1.8. Unfortunately, the proportionality factor contains an oscillation term, so we cannot distinguish positive speed from negative.

The result of computer modeling of a COTDR response on a differential Ricker wavelet for ground speed (Hartog, 2017) is presented in Figure 1.5. The right side shows 1D seismic wave moving in the z direction (in m) with a reflection from an interface with a positive reflection coefficient. Below the image is a time series of apparent velocity, when units are normalized to the expected optical phase shift in radians between points separated by gauge length 10 m. The left side of the figure corresponds to the relative pulse-to-pulse variation of the COTDR signal calculated in accordance with Equations 1.8–1.9. The sign of response changes randomly in accordance with an optical pulsewidth of 50 ns or 5 m. As a result, the signal cannot be effectively accumulated for multiple seismic pulselosityes because of the temperature drift between seismic shots. Temperature drift changes the phase constant of the fiber β_0 and, in accordance with Equation 1.4, the effective reflection coefficient $r(z)$ also changes. As a result of such drift, every seismic shot will have a unique, random, alternating, speckle-like signature that cancels the averaging sum. Fortunately, this problem can be overcome by optical phase recovery, when, after similar averaging, average values appear. Thus, the actual DAS output will be a combination of fiber speed information and the unaveraged portion of the random COTDR signal.

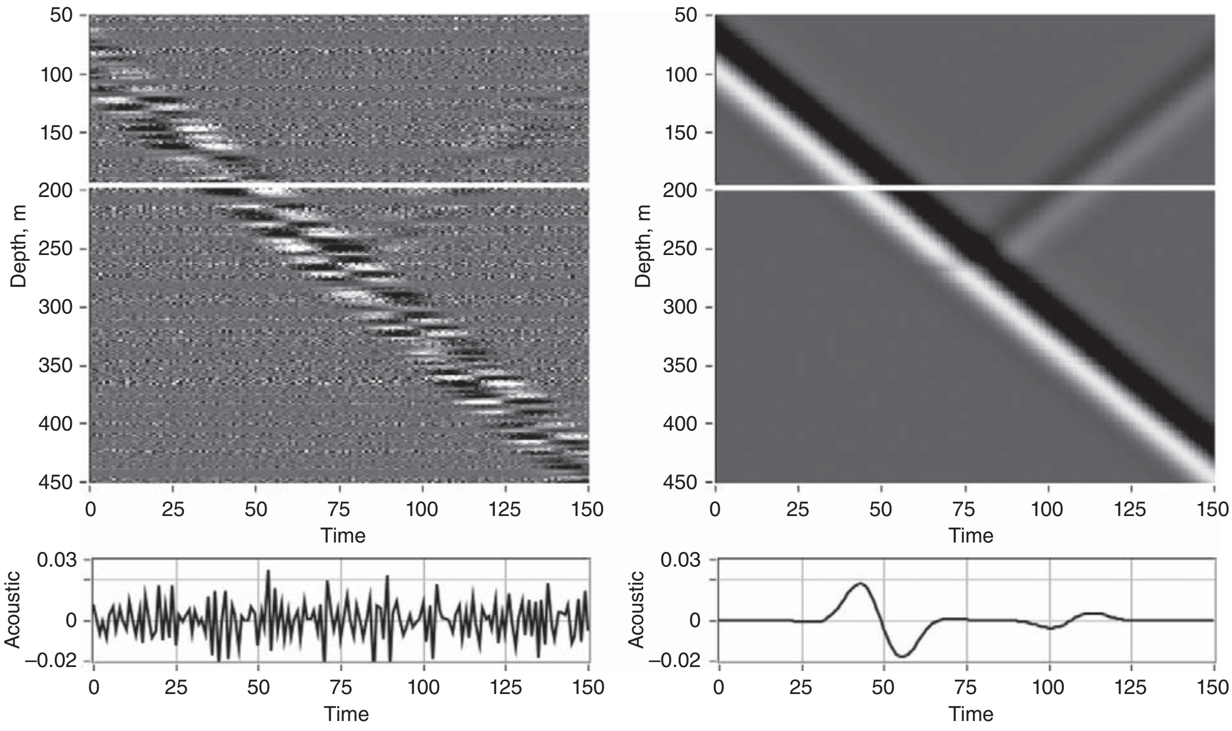

Figure 1.5 COTDR response (Equation 1.6) shown in the left panel of the simulated signal of a ground velocity wavelet shown in the right panel. The signals' cross-section along the white line is shown in the bottom panels in radians. Source: Based on Correa et al. (2017).

1.1.3. DAS Optical Phase Recovery

The randomness of the COTDR signal can be reduced through proper control of the external interferometer phase shift ψ_0, which can be achieved in many ways. All these methods are based on the fact that COTDR intensity is random in distance but will vary harmonically depending on the phase, as follows from Equation 1.1 (see Figure 1.6). So, phase control can reveal phase information regardless of the random nature of the signal.

We will start our phase analysis with a simple, although not very practical, approach, where the phase shift ψ_0 is locked onto a fringe $\sin(\psi_0 + \Phi) \equiv 1$. Such an approach was used earlier to analyze the spatial resolution in phase microscopy (Rea et al., 1996). Then Equations 1.8 and 1.9 can be averaged over an ensemble of delta correlated backscattering coefficients $\langle r(u)r(w)\rangle = \rho^2\delta(u - w)$ as:

$$\left\langle \frac{\partial I(z,t)}{\partial t} \right\rangle = 2\rho^2 \Delta\Omega(z) \tag{1.10}$$

$$\left\langle \frac{\partial \Phi(z,t)}{\partial t} \right\rangle = \frac{1}{2\rho^2} \left\langle \frac{\partial I(z,t)}{\partial t} \right\rangle \tag{1.11}$$

Equation 1.10 demonstrates that the sign of Doppler shift can be measured by DAS with proper phase control. The same data can be extracted directly from phase information, as is clear from Equation 1.11.

So far, we have analyzed the short pulse case, where the pulsewidth is significantly smaller than the external interferometer delay. In reality, such pulses cannot deliver significant optical power, which is necessary for precise measurements. Fortunately, Equations 1.10–1.11 can be generalized for a nonzero length optical pulse $e(z)$ directly from Equation 1.5 in the same way that an optical incoherent image was obtained in Goodman (2005) using correlation averaging $\langle (a \otimes r_1)(a \otimes r_2)\rangle = \langle a^2 \rangle \otimes \langle r_1 r_2 \rangle$. This expression is valid for an uncorrelated field, generated by random reflection points $\langle r_1(z_1) r_2(z_2)\rangle = \delta(z_1 - z_2)$. This calculation confirms that Equation 1.11 remains the same, as it represents averaging over different harmonic signals, but Equation 1.10 will be reshaped to:

$$\left\langle \frac{\partial I(z,t)}{\partial t} \right\rangle = 2\rho^2 e(z)^2 \otimes \Delta\Omega(z) \tag{1.12}$$

Equation 1.11 gives us the possibility to introduce a dimensionless signal as a phase change over a repetition or sampling frequency F_S period $A(z) = F_S \cdot \partial\Phi/\partial t$, and so the DAS output $A(z)$ can be represented for pulsewidth $\tau(z) = e(z)^2$ from Equations 1.3, 1.10, and 1.11 as:

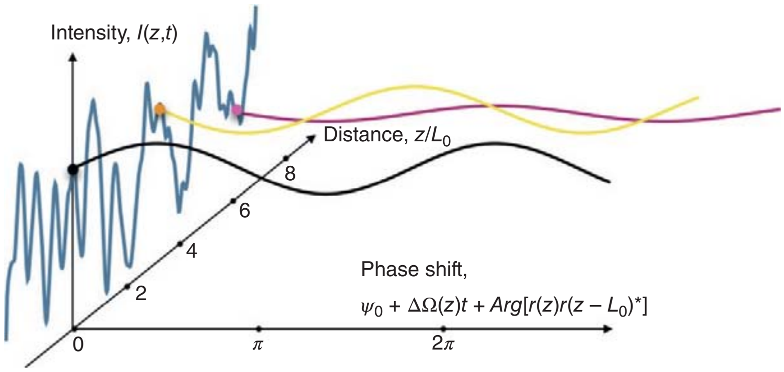

Figure 1.6 Intensity changes are irregular along distance but harmonic along phase shift axis.

$$\langle A(z)\rangle = \frac{1}{A_0 F_S}\cdot\tau(z)\otimes[v(z)-v(z-L_0)] \tag{1.13}$$

$$A_0 = \frac{\lambda}{4\pi n_{eff} K_\varepsilon} = 115nm \tag{1.14}$$

In Equation 1.14, the elongation corresponding to $\Delta\Phi = 1\,rad$ is $A_0 = 115nm$, calculated for $\lambda = 1550$, $n_{eff} = 1.468$ and $K_\varepsilon = 0.73$, which has been measured for conventional fiber (Kreger et al., 2006). The DAS signal is a convolution of pulse shape (as is typical for OTDR-type distributed sensors) with a measured field, which is the spatial difference in fiber elongation speed of points separated by a gauge length.

Phase measurements can be made in a more practical way than locking the interferometer onto a fringe by using intensity trace $I_j(z, t)$ $j = 1, 2, ..P$ from P multiple interferometers with different phase shifts. Such data can be collected consequentially in P optical pulses, but it reduces sensor bandwidth by P times. Alternatively, the information can be collected for one pulse using a multi-output optical component, such as a 3×3 coupler. In the general case, the phase shift $\Phi(z, t)$ can be represented (Todd, 2011) via the arctangent function ATAN of the ratio of imaginary Im Z to real part Re Z of linear combinations of intensities:

$$\Phi(z,t) = \mathrm{ATAN}\left(\frac{\mathrm{Im}\ Z}{\mathrm{Re}\,Z}\right) = \mathrm{ATAN}\frac{\sum_{j=1}^{P}\alpha_j I_j(z,t)}{\sum_{j=1}^{P}\gamma_j I_j(z,t)} \tag{1.15}$$

$$V = \sqrt{\mathrm{Im}\ Z^2 + \mathrm{Re}\,Z^2} \tag{1.16}$$

where V is the visibility given by the ratio of peak-to-peak intensity variation to average intensity of the interference signal. In particular, for a symmetrical 3×3 coupler, Im $Z = \sqrt{3}I_1 - \sqrt{3}I_3$ and Re $Z = I_1 - 2I_2 + I_3$. An additional modification of Equation 1.15 including phase unwrapping will be discussed in the next section. It is interesting to mention that a heterodyne approach (Hartog et al., 2013) can also use quadrature measurements similar to Equation 1.15, but in that case phase diversity is realized in the OTDR time/distance scale, which can affect spatial resolution. Also, we can mention that the interferometer approach does not need a highly coherent laser, as the optical lengths of interfering rays are nearly compensated (Posey et al., 2000).

The theoretical expression for DAS resolution (Equation 1.13) was obtained from analysis of an interferometer locked onto a fringe, and it is necessary to test how this is applicable to practical phase measurement algorithms. Also, Equation 1.13 contains averaging over a statistical ensemble, and it is important to understand what it means in a real application. To answer the questions, we have compared theoretical values with a simulation based on a 3×3 coupler setup for 100 different random Rayleigh scattering patterns for a wide variety of parameters and found good comparison after averaging. To illustrate this analysis, three optical pulsewidth settings were used for interferometer delay (gauge length) of $L_0 = 10m$ and a ground velocity zone of 40 m (Figure 1.7a–c).

All traces (Figure 1.7a–c) correspond to strain measurements rather than to ground velocity profile measurements. If the pulsewidth is small, $\tau = 10ns$, then averaging is not important, and the correspondence between different phase recovery algorithms are clear (Figure 1.7a). For a reasonable pulsewidth, $\tau = 50ns$, only averaged simulation results correspond to theory (Figure 1.7b). If pulsewidth $\tau = 100ns$ becomes equal to $L_0 = 10m$ in the OTDR scale, then averaging is critical, but after it 100 times averaging correspondence is good (Figure 1.7c). It is important to mention that this simulation did not include photodetector noise, and noise-like performance in Figure 1.7c can be explained by the

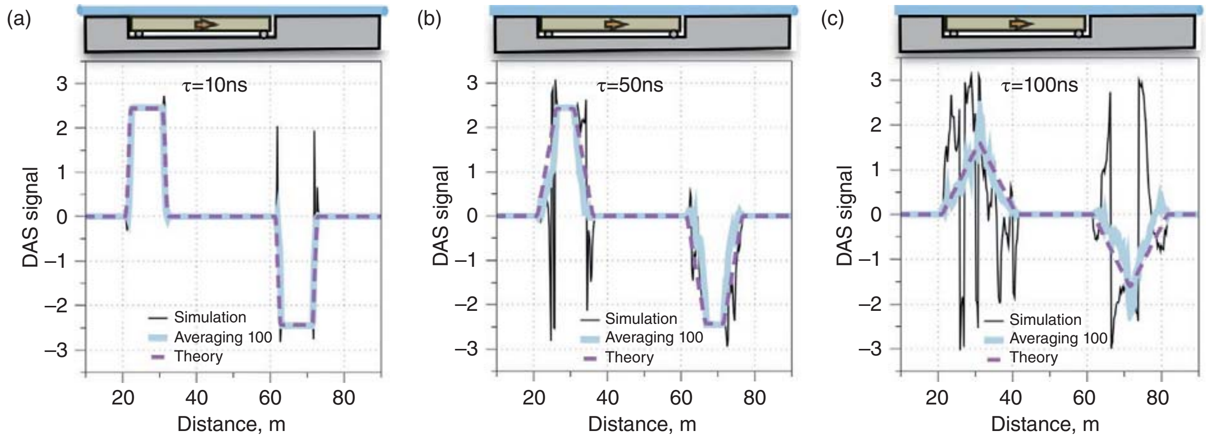

Figure 1.7 Comparison of DAS theoretical response (Equation 1.13) with simulation for a 3 × 3 coupler.

COTDR signal, which will be overlaid on the DAS signal with nonzero pulsewidth. This is a natural limit for increasing SNR by extending pulsewidth; we have a compromise between SNR and signal quality at around $L_0 = 2\tau$. Finally, we can expect that the theoretical expression (Equation 1.13) can be used for spatial resolution analysis for different phase recovery algorithms after a proper averaging.

1.1.4. DAS Dynamic Range Algorithms

An acoustic algorithm (Equation 1.15) transforms the DAS intensity signal into a phase shift proportional to fiber elongation value; a question then is how large can this phase shift be? An algorithm based on such ambiguous function as ATAN(x) can give a result only inside a limited region. The classic approach to recover large phase changes is unwrapping: stitching together two consecutive points t and $t + \Delta t$ from different branches of signal (Itoh, 1982):

$$A_1(z,t) = F_S \frac{\partial}{\partial t}\mathrm{UNWRAP}[\Phi(z,t)] \tag{1.17}$$

This unwrapping, or phase tracking, concept works only if the phase difference is inside two quadrants:

$$-\pi \le \Phi(t + \Delta t) - \Phi(t) < \pi \tag{1.18}$$

Equation 1.17 makes it possible to measure significant fiber elongation, much longer than the wavelength. If the sampling rate $F_S = 1/\Delta t$ is higher than the acoustic frequency F, a larger acoustic amplitude can be integrated $A_0F_S/2F \approx 68\mu$ over time for $F = 50Hz$ and $F_S = 50kHz$. Moreover, even this value has improved, and Equation 1.18 gives an idea of this. If the phase is a smooth function, we can differentiate in time $\Phi(t)$ before unwrapping. Then, the first differential linear term is removed, and condition becomes more relaxed:

$$-\pi \le \Phi(t + 2\Delta t) - 2\Phi(t + \Delta t) + \Phi(t) < \pi \tag{1.19}$$

So, the second order tracking algorithm can be obtained by differentiating the signal before unwrapping:

$$A_2(z,t) = F_S\ \mathrm{UNWRAP}\frac{\partial}{\partial t}[\Phi(z,t)] \tag{1.20}$$

Equation 1.20 has an analog in classical optics, where, instead of the wavefront phase gradient, the wrapped curvature of the wavefront can be unwrapped to increase the dynamic range (Servin et al., 2017). A comparison of these algorithms is presented in Figure 1.8 using modeling for a harmonic signal with a linearly increasing amplitude. It is visible that both algorithms can recover a significant phase range, but the second order tracking algorithm can deliver in excess of a 10 times larger dynamic range.

Theoretically, even higher order algorithms can be designed by repeating this process using higher order derivatives, but they are noisier as more points are involved in the calculation—as can be seen by comparing Equations 1.18 and 1.19. From a practical point of view, the proposed 1D (in time) unwrapping algorithms are error-free and simple enough to be implemented in real time. Potentially, noise immunity can be improved by transition to 2D (in time and distance) unwrapping, similar to that used in a synthetic aperture radar system (Ghiglia & Pritt, 1998). This solution can extract as much information about the phase as possible, but it is difficult to implement without post-processing.

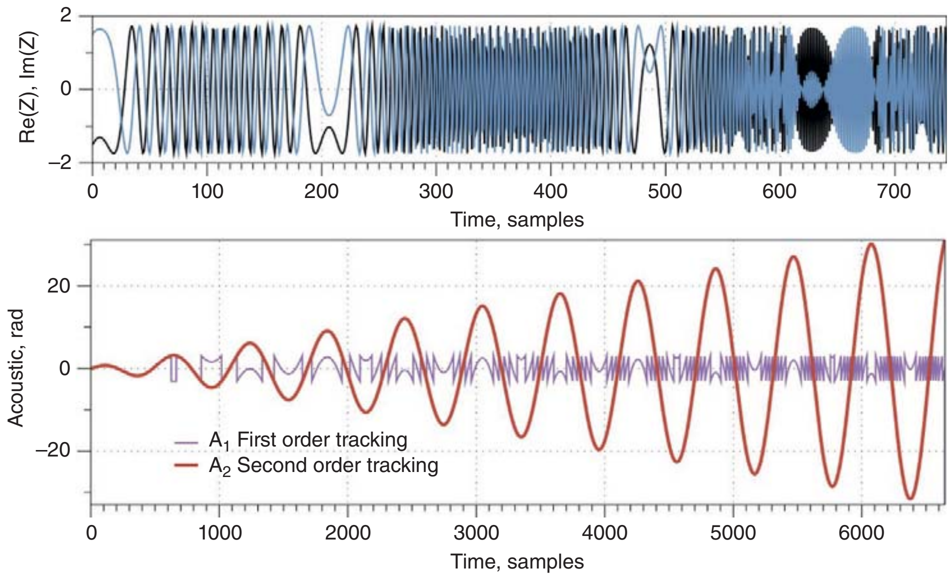

Figure 1.8 Comparison of first and second order tracking algorithms for DAS.

1.1.5. DAS Signal Processing and Denoising

In all phase-detection schemes, the change in optical phase between the light scattered in two fiber segments is determined, meaning we are measuring the deterministic phase change between two random signals. The randomness of the amplitude of the scattered radiation imposes certain limitations on the accuracy of the sensor, through the introduction of phase flicker noise. The source of flicker noise is an ambiguity: when the fiber is stretched, the scattering coefficient varies, and can become zero. In this case, the differential phase detector generates a noise burst regardless of which optical setup is used. The amplitude of such noise increases with decreasing frequency (as is expected for flicker noise) when the phase difference is integrated into the displacement signal.

From a quantum point of view, we need, for successive phase measurements, a number of interfering photon pairs scattered from points separated by the gauge length distance. In some "bad" points, there are no such pairs, as one point of scattering is faded. A natural way to handle this problem is to reject "bad" unpaired photons by controlling the visibility of the interference pattern. As a result, the shot noise can increase slightly as the price for the dramatic reduction of flicker noise. The rejection of fading points can be practically implemented by assigning a weighting factor to each measurement result and performing a weighted averaging.

This averaging can be done over wavelength if a multiwavelength source is used. Alternatively, we can slightly sacrifice spatial resolution and solve the problem by denoising using weighted spatial averaging (Farhadiroushan et al., 2010). The maximum SNR is realized when the weighting factor of each channel is chosen to be inversely proportional to the mean square noise in that channel (Brennan, 1959), meaning the squared interference visibility, V^2, can be used for the weighting factor as:

$$\langle A(z)\rangle \approx \frac{A(z)\cdot V^2(z)\otimes p(z)}{V^2(z)\otimes p(z)} \tag{1.21}$$

The averaging function $p(z) = 5m$ should optimally be chosen to be compatible with the pulsewidth $\tau(z) = 50ns$, which should be around half the interferometer length $L_0 = 10m$. With this width of the averaging function, it has no significant effect on the spatial resolution of the DAS. Modeling with and without weighted averaging is presented in Figure 1.9, which demonstrates that significant noise reduction can be achieved. It should be noted that this noise reduction is particularly marked in comparison with the coherent OTDR response, by contrasting with Figure 1.5. Nevertheless, weighted averaging suppresses rather than completely removes the effect of flicker noise, and some channels still demonstrate excessive noise (in addition to shot noise). Hence, the response over all depths at a given time for Figure 1.9 will contain spikes for faded channels.

As is explored in Section 1.3, the problem of flicker noise can be overcome by introducing engineered bright scatter zones along the fiber with constant spatial separation and uniform amplitude. Such scatter zones also reflect more photons, and so improve the shot noise detection limitation. In addition, the use of such engineered

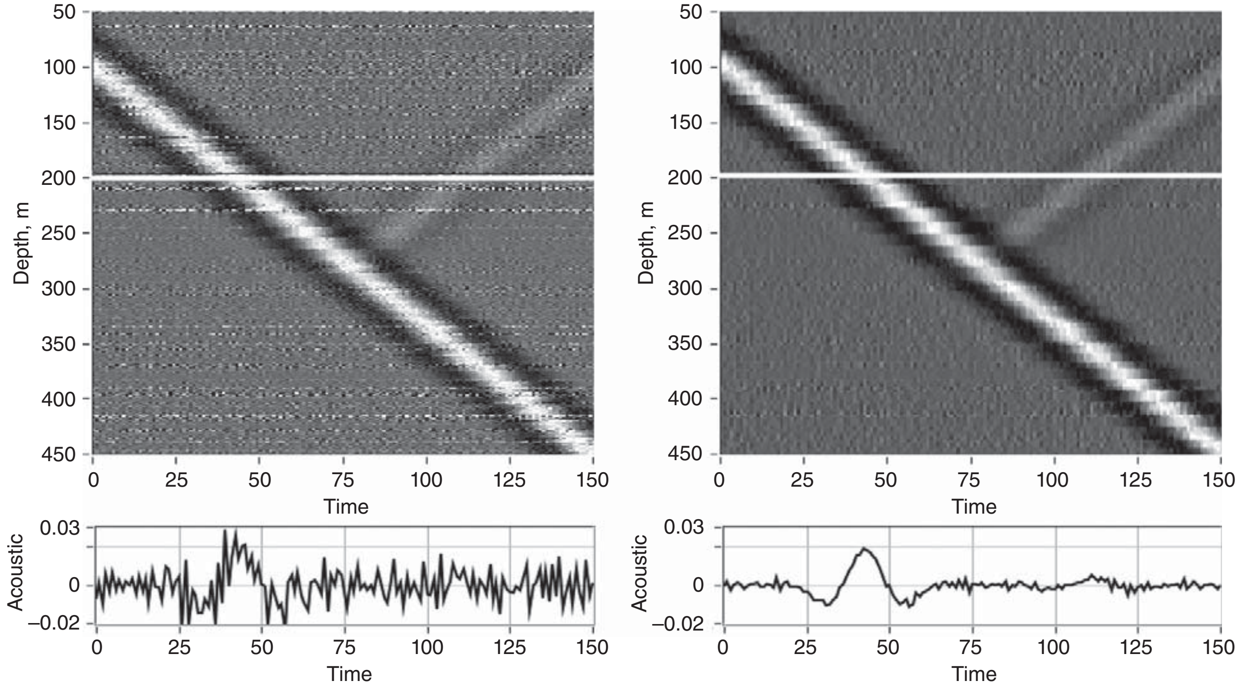

Figure 1.9 The left-hand panel shows modeling of raw DAS acoustic data (Equation 1.12); the right-hand panel shows the same shot with weighted averaging denoising (Equation 1.13) applied. The signals' cross-section along the white line is shown in the bottom panels in radians. The modeled source is shown in the right panel of Figure 1.5.

fiber allows the use of phase-detection algorithms with improved sensitivity and extended dynamic range.

1.1.6. Time Integration of DAS Signal

A DAS interrogator measures, in accordance with Equation 1.13, the speed difference between two sections of fiber that are separated by interferometer length L_0 (referred to also as the *gauge length*), as presented in Figure 1.10. In pulse-to-pulse consideration, the DAS response is linearly proportional to the fiber elongation averaged over the gauge length in the nanometer scale, or strain rate in the nanostrain per second scale. The consideration can also be extended to multiple pulses by time integration of the DAS signal. So, if fiber rests initially and ground displacement equals to zero $u(z, t_1) = 0$, then:

$$\int_{t_1}^{t_2} \langle A(z,t) \rangle dt = \frac{1}{A_0} \tau(z) \otimes [u(z,t_2) - u(z - L_0, t_2)] \quad (1.22)$$

meaning a time integrated DAS signal can be considered as an output of a huge caliper that is measuring fiber elongation between two points with sub-nanometer precision. This measuring principle is different from that of a geophone but is similar to an electromagnetic linear strain seismograph that can measure changes in distance between two points on the ground (Benioff, 1935).

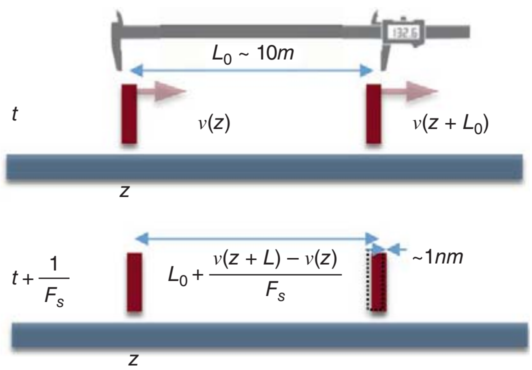

Figure 1.10 Illustration of two time-consecutive measurements when DAS output is proportional to fiber elongation between two probe pulses.

1.2. DAS SYSTEM PARAMETERS AND COMPARISON WITH GEOPHONES

In this section, we consider how DAS parameters (such as spatial resolution), gauge length, frequency response, and SNR enable DAS to become an effective tool for seismic measurements. Field data are also presented, with DAS output compared to geophone data.

1.2.1. DAS Optimization for Seismic Applications

Distributed fiber sensors measure physical parameters of an external environment continuously through the integration properties of light traveling along a lengthy optical path. This is quite different from point sensors, such as geophones, which make an inertial measurement of ground speed at fixed positions (SEAFOM, 2018). The DAS records a local strain rate, which can be converted into particle velocity to allow direct comparison with geophone data. Following Jousset et al. (2018), we can approximately represent DAS signal $A(z,t)$ via ground displacement $u(z,t)$, where F_S is the DAS sampling frequency and L_0 is the gauge length.

$$A(z,t) \propto [u(z,t+1/F_S) - u(z,t)] - [u(z-L_0, t+1/F_S) - u(z-L_0,t)] \quad (1.23)$$

If $F_S \to \infty$, $L_0 \to 0$, then the DAS signal can be presented in a double differential form:

$$A(z,t) \propto \frac{\partial}{\partial z}\frac{\partial}{\partial t}\; u(z,t) = \frac{\partial}{\partial z}\; v(z,t) \quad (1.24)$$

These simplified expressions (Equations 1.23–1.24) give us a qualitative sense of the DAS algorithm output. For a subsequent quantitative analysis, we shall need the detailed expression that was obtained in the previous section. Namely, for a nonzero interferometer gauge length L_0 and optical pulsewidth τ, averaged over random scattering DAS output, $A(z)$ can be represented by Equation 1.15 in expanded form:

$$\langle A(z)\rangle = \frac{1}{A_0 F_S}\cdot \tau(z)\otimes[\delta(z) - \delta(z-L_0)]\otimes v(z) \quad (1.25)$$

where F_S is sampling frequency and $A_0 = 115nm$ is a scale constant (Equation 1.14). So, the velocity field can be recovered by spatial integration starting from a motionless point as:

$$\overline{A(z)} = \int_0^z A(u)du = A(z)\otimes\theta(z) \quad (1.26)$$

Then DAS signal (Equation 1.25) can be transformed using shift invariant $a(z_1) \otimes b(z_1 + z_2) = a(z_1 + z_2) \otimes b(z_1)$ to:

$$\overline{\langle A(z)\rangle} = \frac{1}{A_0 F_S}\cdot \tau(z)\otimes[\theta(z+L_0) - \theta(z)]\otimes v(z) \quad (1.27)$$

where $\theta(z)$ is the Heaviside step function, whose value is zero for a negative argument. As expected, the DAS signal is represented (Equation 1.5) as a convolution of a point spread function with $v(z)$.

Spatially integrated signal (Equation 1.27) was modeled for 10 m gauge length and 50 ns pulsewidth, as shown in Figure 1.5 (right panel). The results of modeling (Equation 1.25) are presented in Figure 1.11 (left panel), and the result is converted to geophone-style data (Equation 1.26) in the right panel. From a practical point of view, low temporal frequencies, out of the range of interest, can be filtered out, and also spatial antialiasing filtering can be used. It is worth mentioning that the right panel of Figure 1.11 demonstrates the real change in polarity of the reflected seismic pulse. Also, spatial integration (Equation 1.26) acts as statistical averaging, which eliminates the randomness of the "staircasing" in Figure 1.5 left panel.

The most valuable geophysical information is delivered by sound waves with frequencies below $F_{MAX} = 150Hz$, as higher frequencies are attenuated by the ground. For a speed of sound $C = 3000m/s$, this corresponds to an acoustic wavelength $C/F_{MAX} = 20m$, so Nyquist's limit dictates that $L_G \le C/2F_{MAX} = 10m$ is the maximum spacing of conventional sensors. Formally, the linear spline approximation $G(z)$ of conventional antenna velocity $v(z)$ output can be represented using expressions from (Unser, 1999), as:

$$G(z) = \{[\theta(z+L_G) - \theta(z)]\otimes[\theta(z+L_G) - \theta(z)]\} \otimes[\mathrm{comb}(z/L_G)\cdot v(z)] \quad (1.28)$$

The spatial spectral response of DAS in acoustic angular wavenumber K_z can be represented by Fourier transform $\mathfrak{F}(K_z)$ following Goodman (2005):

$$|\mathfrak{F}_G(K_z)| = |\mathrm{sinc}(K_z L_G/2)\cdot[\mathrm{comb}(K_z L_G/2\pi)\otimes\mathfrak{F}(K_z)]| \quad (1.29)$$

Such spectral responses can be normalized for a constant signal $\mathfrak{F}(K) = 1$ (see black line in Figure 1.12). The comb function in (Equation 1.29) is responsible for the repeating of the spatial spectrum with a shift of $2\pi/\Lambda$, as is shown by the dotted line. To prevent aliasing, the signal spectrum should be inside Nyquist's limit, which is shown by the gray vertical line.

Let us compare the conventional velocity sensor with the DAS spectrum, calculated from the spatial resolution expression (Equation 1.25), by Fourier transform as:

$$\left|\mathfrak{F}_{(A)}(K_z)\right| = |\mathrm{sinc}(K_z\tau/2)\sin(K_z L_0/2)\cdot\mathfrak{F}(K_z)| \quad (1.30)$$

Two cases are presented in Figure 1.12: when the optical pulse length is almost equal to the interferometer gauge length $\tau = L_0$, and when it is half the interferometer gauge length $\tau = L_0/2$ (see dashed and solid blue lines, respectively). The absolute value is presented in the figure to aid comparison between curves. In the second case, we

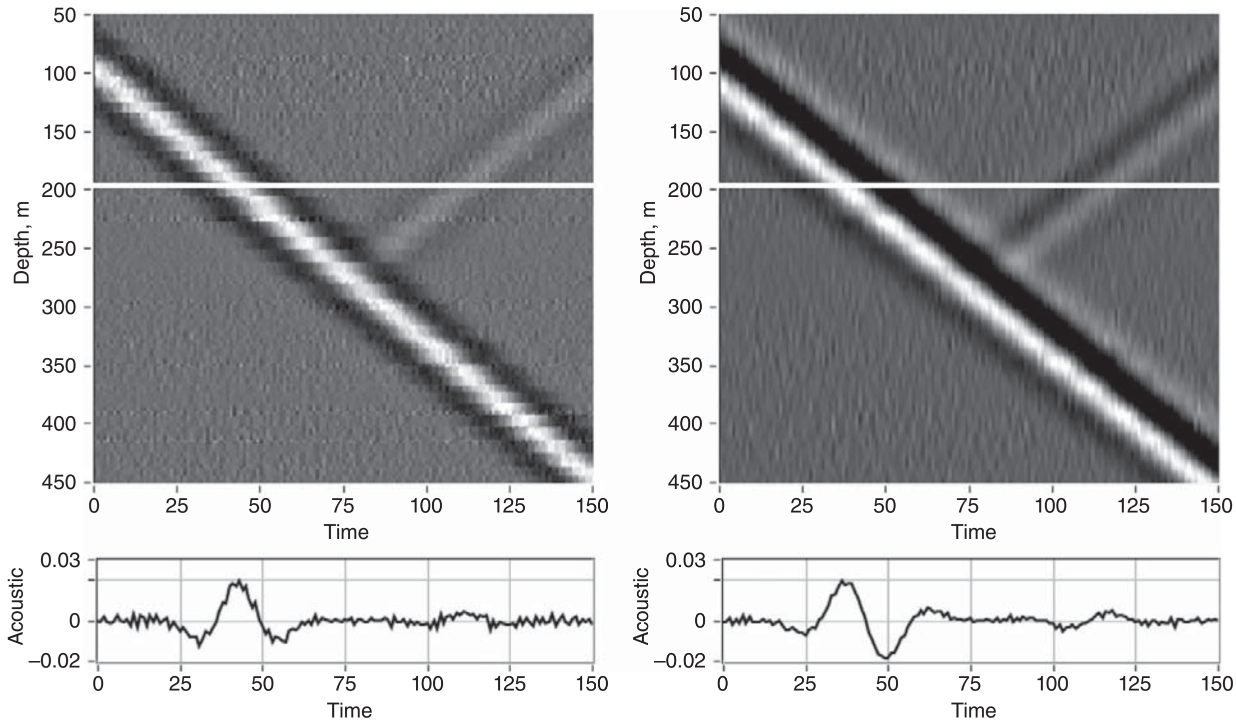

Figure 1.11 Acoustic measurements using DAS: The left panel represents strain rate measurement and the right panel displays ground speed measurement, the transform to which comprises filtering and integration. The signals' cross-section along the white line is shown in the bottom panels in radians. The modeled source is shown in the right panel of Figure 1.5.

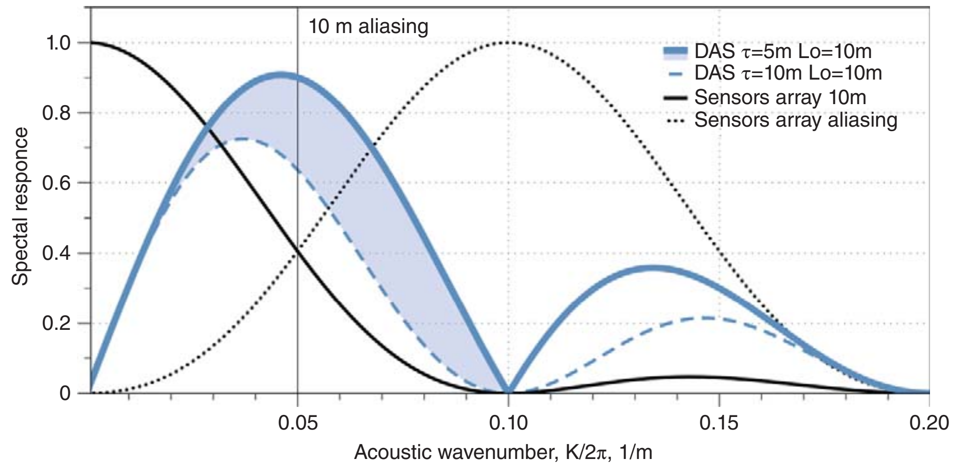

Figure 1.12 Comparison of DAS spectral response with that from a 10 m sensor antenna array.

have a gain, which is highlighted by the blue filling. This gain can be explained by signal smearing over a long pulse.

It seems from Figure 1.12 that DAS low frequency sensitivity is significantly lower than that of a geophone. Practically, however, this is not the case, as the geophone noise rises at low frequencies, and this can be characterized by some high-pass (HP) filters that limit the range to frequencies around 10 Hz (see dotted line in Figure 1.13). However, DAS has the potential to increase

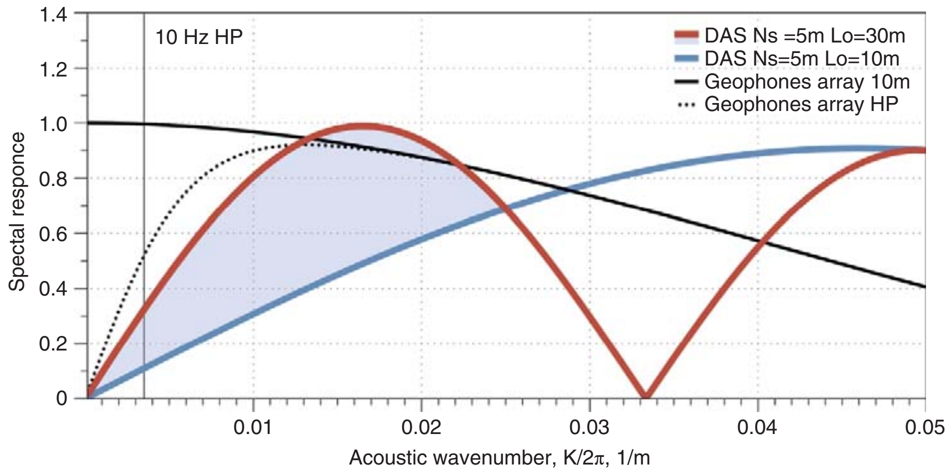

Figure 1.13 Low spatial frequency gain in DAS by using long interferometer.

the spectral response at low frequencies by increasing interferometer length—for example, from $L_0 = 10m$ to $L_0 = 30m$ (see Figure 1.13). So, potentially, the DAS response can be synthesized from two measurements: with a short interferometer gauge length to deliver high spatial frequency bandwidth, and a long one to deliver low frequency. As the result, full-frequency coverage can be as good as from a geophone antenna, or possibly even better, as will be shown in a later SNR comparison. An additional advantage over geophones is the large dynamic range of DAS at low frequencies, which will be discussed later.

1.2.2. DAS Directionality in Seismic Measurements

In the previous section, we analyzed the correspondence between DAS and geophones in the one-dimensional case and found that "geophone-style" velocity data can be extracted from DAS signals by spatial integration. However, in 3D analysis, we should consider that DAS is not a velocity sensor but a differential strain sensor. This is a fundamental difference: DAS can measure a component of 3D tensor (strain) but not 3D vector (velocity).

Directionality of the DAS response depends on the fiber optic cable configuration and the cable design, as the device itself is sensitive only to fiber elongation. We will start our consideration where the fiber is placed linearly inside a cable, with no slippage between fiber and cable, nor between the cable and the ground. In this case, fiber displacement will follow ground displacement, and sensitivity will depend on the relative position of fiber and seismic source. A similar mechanical principle was used for the electromagnetic linear strain seismograph to measure variations in the distance between two points of the ground (Benioff, 1935). DAS directional response with respect to incident angle Γ can be found by transformation of the strain tensor components with rotation using geometrical consideration. For a longitudinal (P) apparent wave, it will be $\cos^2\Gamma$, and for transversal (S) wave $\sin\Gamma \cos\Gamma$, similar to Benioff (1935) (see Figure 1.14). Detailed analysis and diagrams for Rayleigh and Love waves can be found in Martin et al. (2018).

In vertical seismic profiling (VSP), in the vertical part of the well, both cable and seismic waves are in the same direction for near-offsets, so the DAS is more sensitive to P-waves, in which the acoustic displacement vector coincides with the fiber direction. In other applications, such as fracking, the microseismic source is usually on a side of the cable, so shear waves can be effectively detected.

Cable orientation is responsible not only for acoustic amplitude but also for acoustic spatial resolution, even for the same acoustic wavelength. The cable acts as an acoustic antenna where the signal varies rapidly in space if the P-wave and cable direction coincide, but the signal remains the same over distance if the acoustic wave front is parallel to the cable. To take this effect into consideration, we need to expand the expression for acoustic wavelength K_z along the cable for Equations 1.29–1.30 as:

$$K_z = K\cos\Gamma = \frac{2\pi F}{C}\cos\Gamma \tag{1.31}$$

For a harmonic wave, directionality will directly affect not only the spatial resolution but also the temporal frequency. After Fourier transfer in the time domain, Equation 1.30, in the absence of aliasing, can be presented as:

$$|\mathfrak{I}_A(K_z, F)| = |\mathrm{sinc}(K_z L_0/4)\sin(K_z L_0/2)\cdot\mathfrak{I}(K_z, F)| \tag{1.32}$$

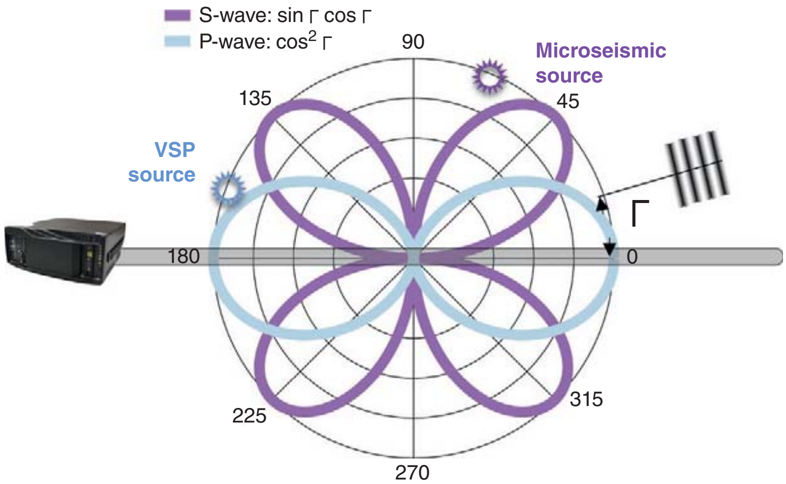

Figure 1.14 DAS with linear optical cable is more sensitive to *P*-wave in VSP configuration and to *S*-wave in microseismic events.

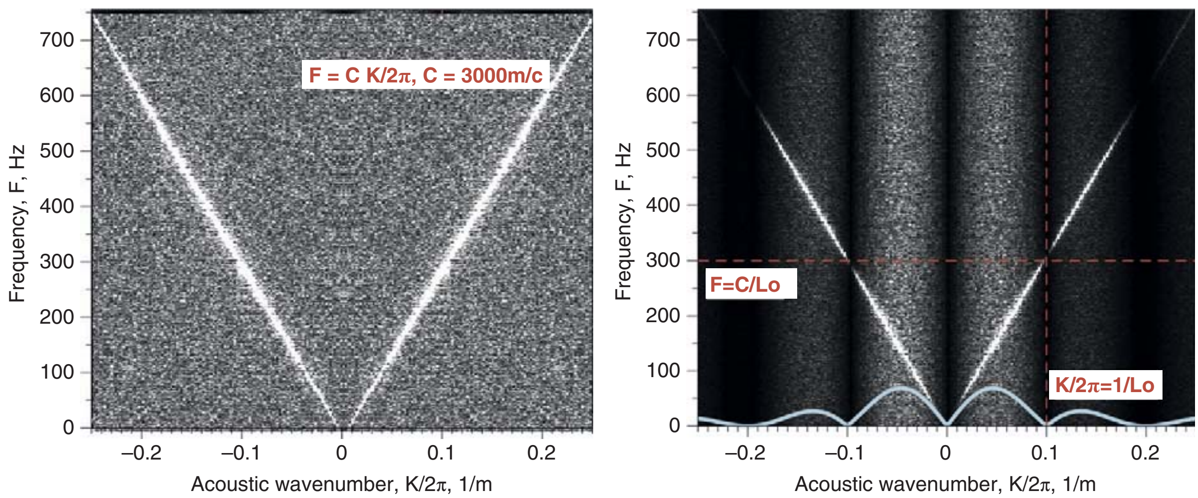

Figure 1.15 2D spectral representation on upgoing and downgoing acoustic waves: The left panel represents original signal and the right panel represents filtered signal, where the spatial filter shape is shown by a blue wavy line.

This expression (Equation 1.32) represents spatial filtering in the 2D Fourier domain as shown in Figure 1.15 for $L_0 = 10m$ for upgoing and downgoing waves, together with white phase noise. As far as harmonic waves can be represented as single lines, the result of spatial filtering is an intensity modulation of these lines. Such modulation is equivalent to temporal frequency modulation, so we can combine Equation 1.31 and Equation 1.32 to get:

$$|\mathfrak{F}_A(F)| = \left|\text{sinc}\left(\pi F \frac{\cos\Gamma L_0}{2C}\right) \sin\left(\pi F \frac{\cos\Gamma L_0}{C}\right) \cdot \mathfrak{F}(F)\right| \tag{1.33}$$

It is interesting to mention that, for uniform strain, where $C \to \infty$, we have $|\mathfrak{F}_A(F)| \propto \cos^2\Gamma$ as expected from Benioff (1935). The result of modeling of Equation 1.33 is presented in Figure 1.16 for different incident angles. An increase in angle expands the measurement frequency range but reduces low-frequency SNR at the same time.

DAS directivity can be significantly modified through appropriate cable design, which is currently a developing area. For example, field tests have shown that the helical placement of fiber within a squeezable material can deliver omnidirectional sensitivity (Hornman et al., 2013) for P-waves. The angular dependence will be

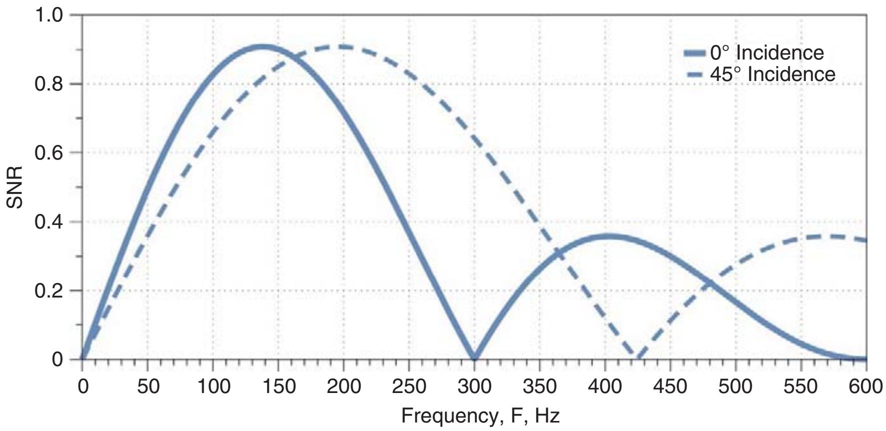

Figure 1.16 Normalized SNR curve (SNR vs. frequency) for a 3000 m/s wave speed of *P*-wave at 0° and 45° incident angles.

different for S-waves (Abbott et al., 2019), and a different helix pitch can be useful to optimize performance for different wave types (Baird, 2020). Additional complexity comes from cable construction, and the Poisson's ratio of the cable itself can affect the angular signature (Wuestefeld & Wilks, 2019). An even more sophisticated approach can be used to measure inertial acceleration—by using a dedicated non-isotropic cable, where a dense mass compresses the fiber along the cable (Farhadiroushan et al., 2017). Such a solution can be used for multi-component seismic acquisition, including for analysis of microseismic events.

This analysis demonstrates that the DAS broad spectral response can potentially correspond to conventional geophones and seismometers. In the next section, we will provide some examples of how such promises can be fulfilled in field measurements.

1.2.3. DAS Field Data Examples

DAS seismic services were introduced to deliver better characterization of geophysical properties by dramatically increasing the spatial density of acquired data. DAS technology enables the collection of seismic data with a wide range of source types. For in-well measurements, the optical fibers are embedded within ruggedized downhole cables that can be conveyed loosely in the well (wireline), or clamped to tubing and/or cemented with the completion, thereby offering a permanent sensor array (Figure 1.17). The usual assumption is that the stretching of the optical cable coincides with the deformation of the ground in the acoustic wave. In turn, the length of the optical fiber tracks the length of the optical cable due to internal friction. When the cable is attached to a pipe, the pipe deformation coincides with the ground deformation. If the cable is poorly connected to the pipe between the clamps, then lines on the VSP has a staircase-like shape. The period of the steps equals the distance between the clamps, which is about 10 m. Fortunately, this value does not significantly exceed the DAS resolution and practically does not degrade the quality of the VSP pattern.

A typical VSP seismic shot response for permanently installed fiber optic cable behind the casing is shown in Figure 1.18 for both the raw acoustic data and with the denoising algorithm applied.

An important practical question is the ability of the DAS to perform measurements on both single-mode (SM) and multi-mode (MM) optical fiber, since MM fiber has been deployed in many legacy installations. It was found experimentally that seismic data can be recorded equally well on both SM and MM fiber. This is achieved as the fundamental mode LP_{01} size diameter in MM fiber (14 μm) is nearly matched to SM fiber (10 μm), and, therefore, the DAS performance using MM fiber is similar to that from SM fiber. Strictly speaking, the SNR in MM fiber can be slightly worse at the near end of the fiber because of the optical coupling loss, and slightly better at the far end of the fiber because its larger core diameter allows higher optical power transmission along the fiber. Similar performance for SM and MM fiber was observed in field experiments (see Figure 1.19) when two fibers were placed side by side in an optical cable. These results show the feasibility of retrofitting DAS to existing MM fiber installations and so utilizing distributed temperature sensing infrastructure to perform the full scope of DAS services, which include not only seismic measurements but also well diagnostics and flow monitoring (Finfer et al., 2014).

For VSP applications in vertical wells, the direction of the well and fiber optic cable coincides for near-offsets with the seismic wave propagation, and so DAS is mostly

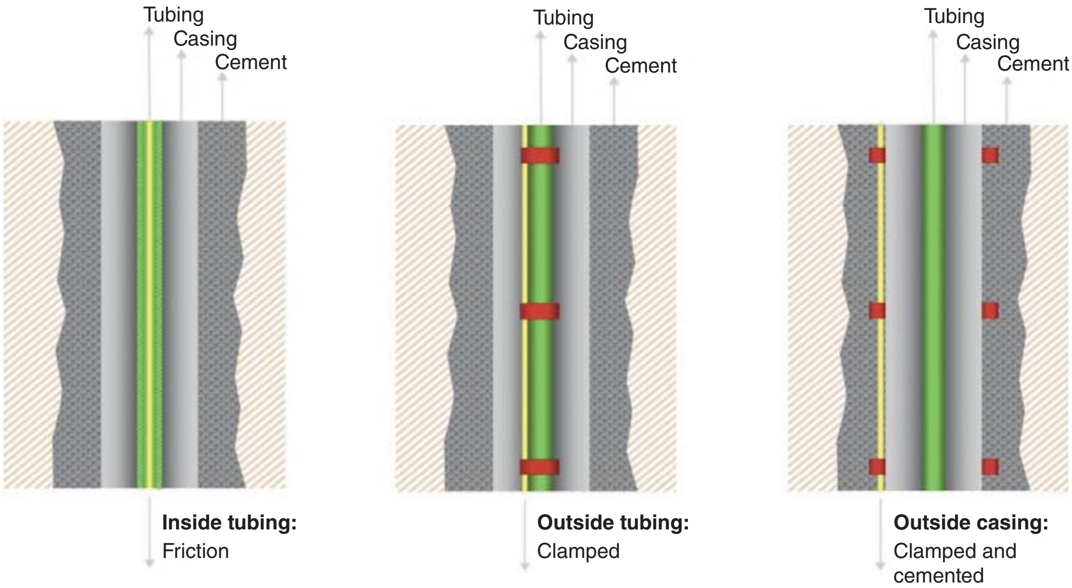

Figure 1.17 Sensing optical fiber cable deployments.

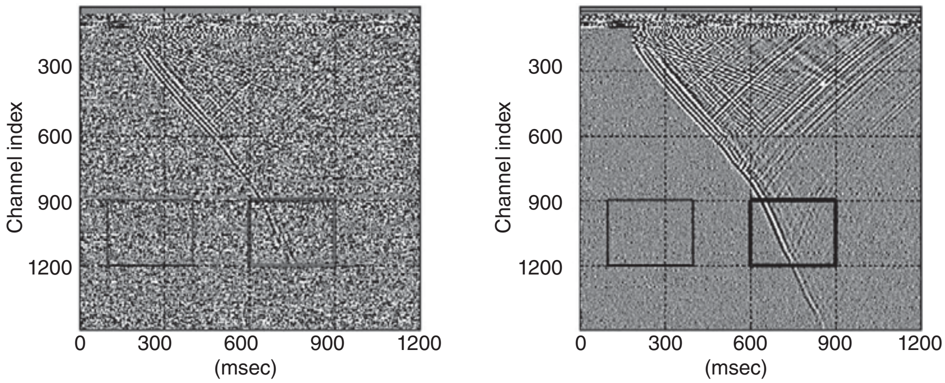

Figure 1.18 The left-hand panel shows a single shot of raw acoustic data; the right-hand panel shows the same shot with denoising applied from Miller et al. (2016).

sensitive to P-waves. This effect was tested by comparison with transverse and vertical geophones (see Figure 1.20). The geophone with transverse orientation (left panel) has not detected the P-wave, whereas the geophone with vertical orientation (central panel) has. The DAS (right panel) also has detected the P-wave as expected. It is worth noting that the case for far offsets is more complicated (Mateeva et al., 2014).

A comparison of DAS data (converted from strain rate to particle velocity) to co-located geophones indicates that the DAS data is consistent with geophone response. As a result, a 3D VSP image can be collected from multiple dynamite shots in a similar manner as for conventional geophones (Miller et al., 2016). The DAS records the seismic signal at every point along the optical fiber with each source activation, leading to much greater receiver coverage than is achievable with conventional borehole seismic methods. A typical result of DAS 3D VSP is presented in Figure 1.21.

Fine spatial resolution, in combination with good sensitivity and dynamic range, gives DAS a significant advantage for hydraulic fracture monitoring and the detection of microseismic events, particularly where a geophone chain cannot be readily positioned, such as in a treatment well. Figure 1.22 shows a waterfall plot (depth vs time), recording strong acoustic signals, corresponding to fluid placement across individual clusters, while, at the same time, detecting small microseismic events.

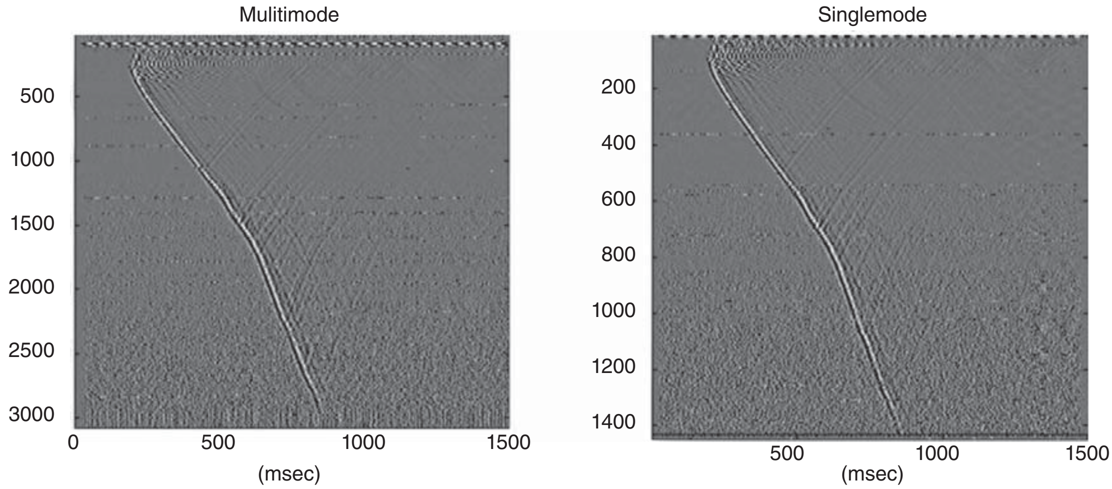

Figure 1.19 Comparison of DAS performance with SM and MM optical fiber.

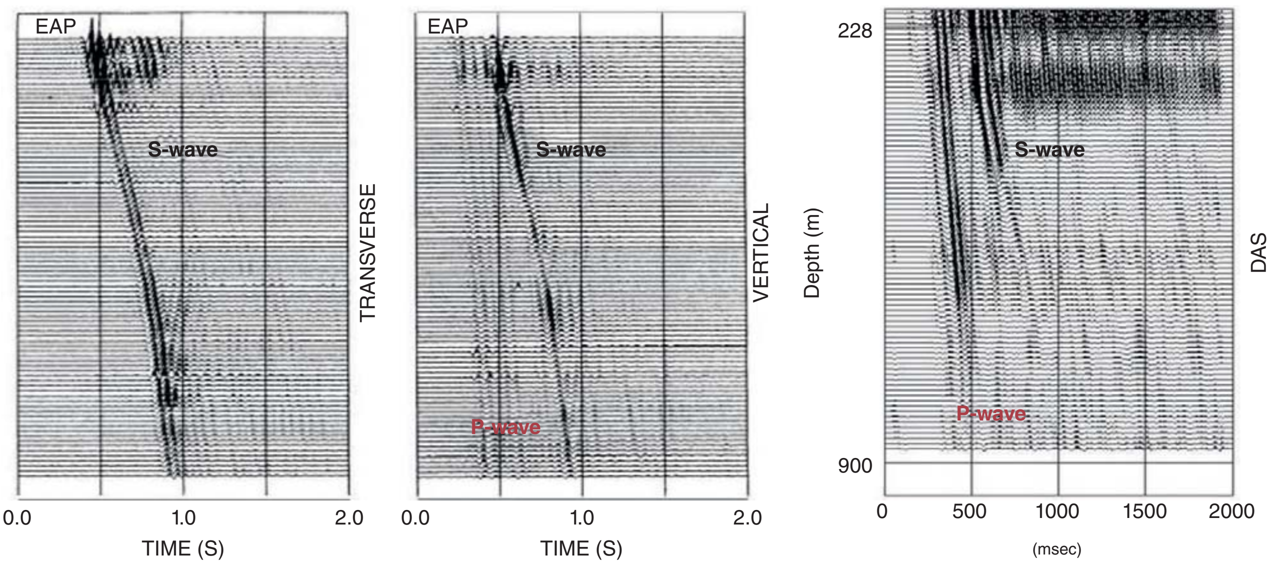

Figure 1.20 Directionality of DAS response: The left and central panels represent geophones with transverse and vertical orientation, and the right panel represents the DAS signal for VSP.

Optical fiber can also be used for offset well monitoring, as indicated in Figure 1.23. Here, the optical fiber cable, cemented behind the casing in the originally treated well, is used to monitor microseismic events and strain while an offset well is being treated. The shape and arrival time of P- and S-waves can be used for microseismic event picking and localization. The data can be used for optimizing the well spacing, cluster spacing, and stimulation parameters.

In summary, DAS is a new, versatile technology that can be deployed in many different configurations along boreholes where geophones cannot readily be deployed. The frequency response of DAS is comparable with geophones and can offer the benefits of wide aperture monitoring along the entire borehole with broad frequency response. Improvements in optical fibers and cable designs offer new possibilities for the DAS monitoring of geophysical properties.

1.3. DAS WITH PRECISION ENGINEERED FIBER

In this chapter, we consider how the scattering properties of conventional fiber can be engineered to deliver better DAS performance (Figure 1.24). We will show how an

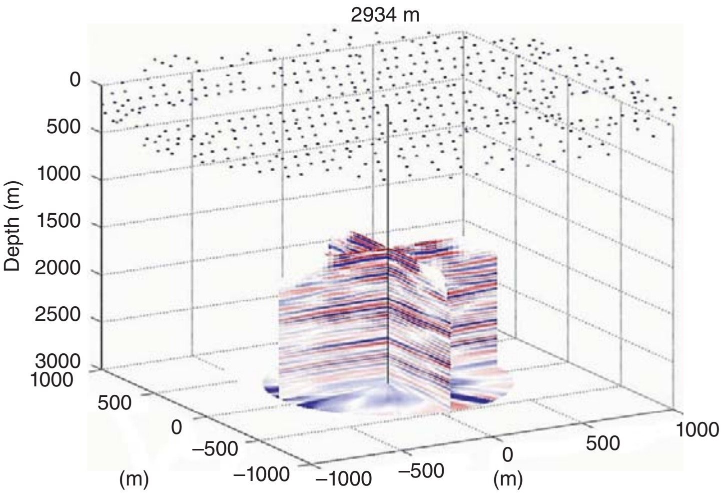

Figure 1.21 3D VSP: Two intersecting images processed from DAS seismic data acquired with the dynamite shot positions indicated from Miller et al. (2016).

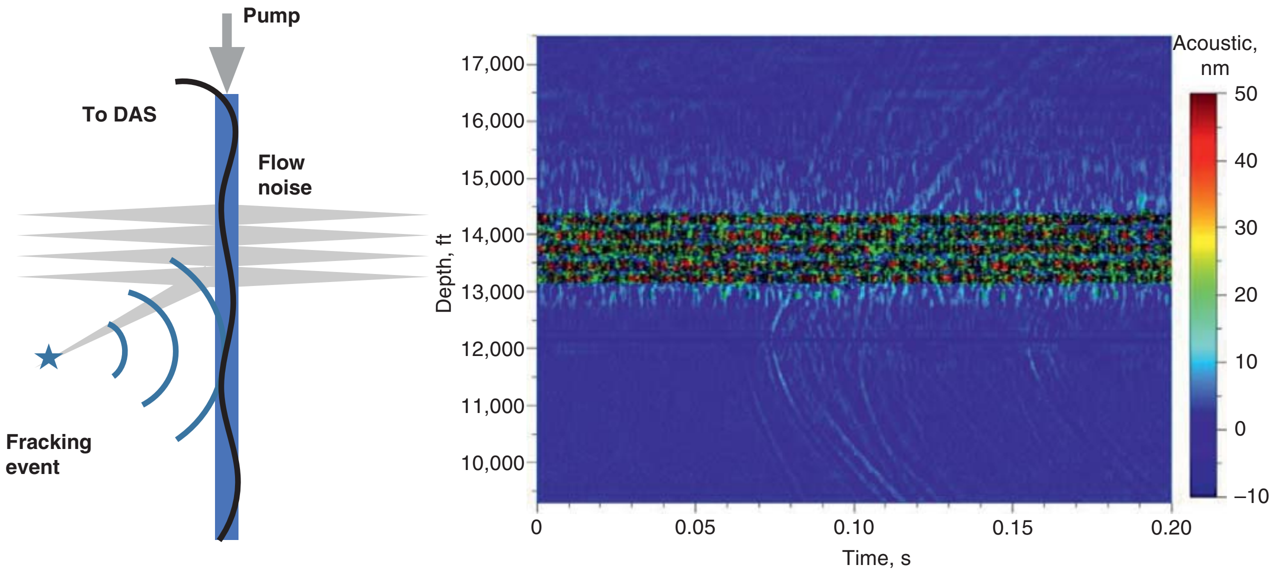

Figure 1.22 DAS hydraulic fracture monitoring in the treatment well with a fine spatial resolution and wide dynamic range for simultaneous cluster fluid allocation and microseismic monitoring.

SNR improvement can be achieved, along with a wider dynamic range, using engineered fiber with precisely uniform scattering centers. This approach differs from a simple increase in irregular backscattering intensity (Westbrook et al., 2017). We also consider the trade-offs between spatial resolution, signal-to-noise performance and frequency response, and present data acquired from several different seismic and microseismic surveys.

DAS performance is largely governed by how much light can be usefully collected from the optical fiber. In general, we require low-loss fiber for long range sensing, but higher scattering fiber to generate more light. These two apparently contradictory requirements can be balanced by engineering bright scatter centers in the fiber, without introducing significant excess loss for the forward propagating light. This can be achieved, for example, by using fiber Bragg grating technology.

For long fiber lengths, 100 times more light than Rayleigh level can be safely used (Farhadiroushan et al., 2021). That gives 20 dB reduction of acoustic noise caused by quantum shot noise at frequencies of around 1 kHz. This improvement can be even more at low frequencies

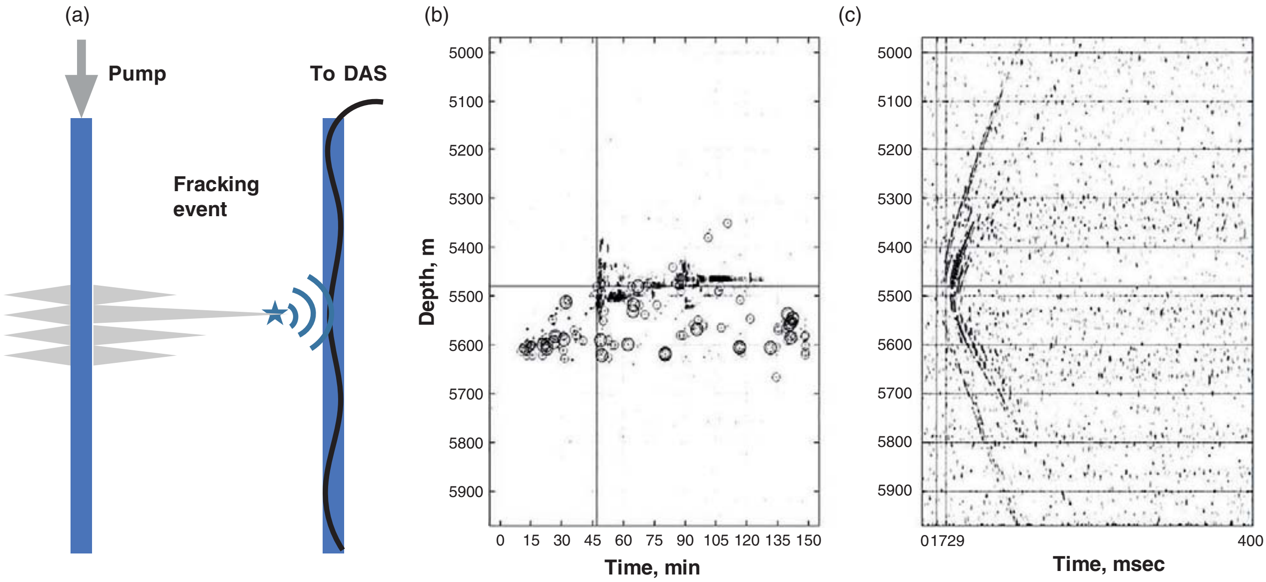

Figure 1.23 DAS hydraulic fracture monitoring in the offset (a) with a fine spatial resolution for microseismic monitoring (c), and localizing of microseismic events in time and space (b).

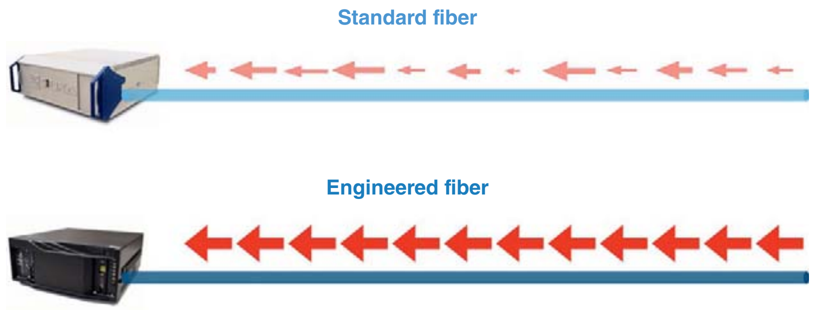

Figure 1.24 DAS with standard fiber and engineered fiber with precision bright scatter center zones.

as pink noise is suppressed by the regular structure of scattering. So, noise reduction can be more than 30 dB at around 1 Hz. This prediction was successfully confirmed in field surveys and are presented at the end of the chapter.

1.3.1. Precision engineered fiber concept

We will start our consideration from Equation 1.6 in Section 1.1 (titled 'Distributed Acoustic Sensor (DAS) Principles and Measurements'), which represents the scattered $E(z, t)$ field as a convolution of input optical field with scattering coefficient $r(z)$, for a gauge length L_0.

$$E(z,t) = e(z)\otimes\{r(z)\exp i[\Omega(z)t] + r(z-L_0) \exp i[\Omega(z-L_0)t + \psi_0]\} \tag{1.34}$$

where $e(z)$ is a coherent optical pulse and $\Omega(z) \propto v(z)$ is the Doppler shifted angular frequency, which is proportional to the local acoustic speed—see Figure 1.25.

The scattering coefficient for engineered fiber can be represented by a spatially periodic function (Farhadiroushan et al., 2021), meaning a reflection coefficient $r(z)$ can be represented by a set of defined scatter center zones separated by sampling distance L_S.

$$r(z) = R\sum_{j=0}^{M}\delta(z-jL_S) = R\ \ \mathrm{comb}(z/L_S) \tag{1.35}$$

where $comb(z)$ is the Dirac comb function, or sampling operator. If the gauge length is s times larger than sampling distance, $L_0 = sL_S$, $s = 1, 2\ldots$, then $r(z) = r(z - L_0)$, and the reflectivity function $r(z)$can be taken out of the brackets:

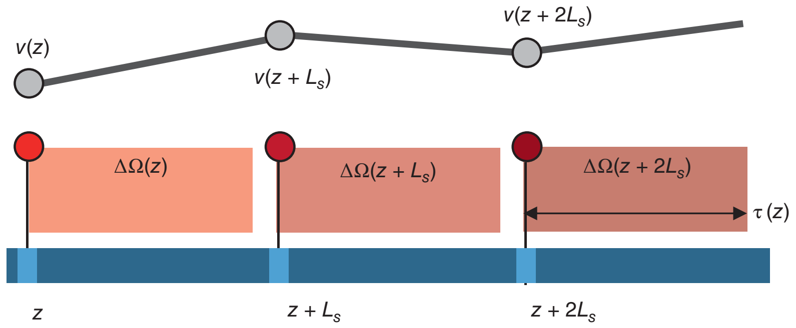

Figure 1.25 Optical fiber with defined scatter center zones and the corresponding Doppler shifted angular frequency sampled between the zones. The length occupied by optical pulse is less than the distance between the zones. The gray line corresponds to spatially integrated DAS output, following a linear spline approximation.

$$E(z,t) = R \cdot e(z) \otimes \{ \exp i[\Omega(z)t] + \exp i[\Omega(z-L_0)t + \psi_0]\} \text{comb}(z/L_S) \tag{1.36}$$

To prevent cross-interference and fading, the spatial length of the optical pulse should be smaller or equal to the distance between scatter center zones, so the spatial sampling of the optical field (Equation 1.35) can be represented by a train of pulses:

$$E(z,t) = R \cdot \sum_{j=0}^{M} e(z-jL_S) \cdot \{ \exp i[\Omega(jL_S)t] + \exp i[\Omega(jL_S - L_0)t + \psi_0]\} \tag{1.37}$$

The optical pulses from each zone are separated (see Figure 1.25), so the maximum signal intensity and maximum SNR can be delivered if the pulsewidth is equal to the sampling distance, or $\tau(z) = \theta(z + L_S) - \theta(z)$, where $\theta(z)$ is the Heaviside step function whose value is 0 for negative argument and 1 for positive argument. In this case, intensity can be calculated from the interference between pulses with the same index j, and, for each pulse, an acoustic signal $A(z) = F \cdot \partial\Phi/\partial t$, where $\Phi = \Delta\Omega(z)t$ can be recovered from Equation 1.34 using A_0 from Equation 1.14 as:

$$A(z) = \frac{1}{A_0 F_S} \cdot \sum_{j=0}^{M} [\theta(z - kL_S + L_S) - \theta(z - kL_S)] \cdot [v(kL_S) - v(kL_S - L_0)] \tag{1.38}$$

where $A_0 = 115nm$. Equation 1.38 can also be represented in convolution as:

$$A(z) = \frac{1}{A_0 F_S} \cdot [\theta(z + L_S) - \theta(z)] \otimes \{(v(z) - v(z - L_0)) \cdot \text{comb}(z/L_S)\} \tag{1.39}$$

The main parameter for spatial resolution is still the gauge length L_0, and the sampling distance can be chosen to have two points per gauge length $L_S = L_0/2$. We are considering here the physical spatial sampling, which is defined by the optical configuration, keeping in mind that the photocurrent sampling can have a higher rate. The difference from conventional fiber is an absence of averaging, as the detected signal is deterministic for engineered fiber, and excessive noise from non-averaged components will hence disappear. Also, the generated optical field can be significantly larger than with conventional Rayleigh backscattering, so the shot noise limitation can be reduced significantly.

The velocity field can be recovered by spatial integration starting from a motionless point as:

$$\overline{A(z)} = \int_0^z A(u)du = A(z) \otimes \theta(z) \tag{1.40}$$

So Equation 1.39 can be transformed to:

$$\overline{A(z)} = \frac{1}{A_0 F_S} \{[\theta(z + L_S) - \theta(z)] \otimes [\theta(z + L_0) - \theta(z)]\} \otimes comb(z/L_S) \cdot v(z) \tag{1.41}$$

Formally, the engineered fiber DAS signal expression (Equation 1.41) looks similar to that for standard fiber signal (Equation 1.27). If, say, $L_0 = L_S$, then, in Equation 1.41, the curly expression { } represents a chapeau function for linear spline interpolation (Unser, 1999), In other words, $v(z)$ is sampled and linearly interpolated with L_S period in Equation 1.41 without any smearing, as it was for the case of conventional fiber (Equation 1.27).

The results of modeling (Equation 1.39) are presented in Figure 1.26, left panel. The spatially integrated version of this signal (Equation 1.41) was modeled for $L_0 = 2L_S$, and is shown in Figure 1.26, right panel. Low temporal frequencies out of the range of interest can be filtered

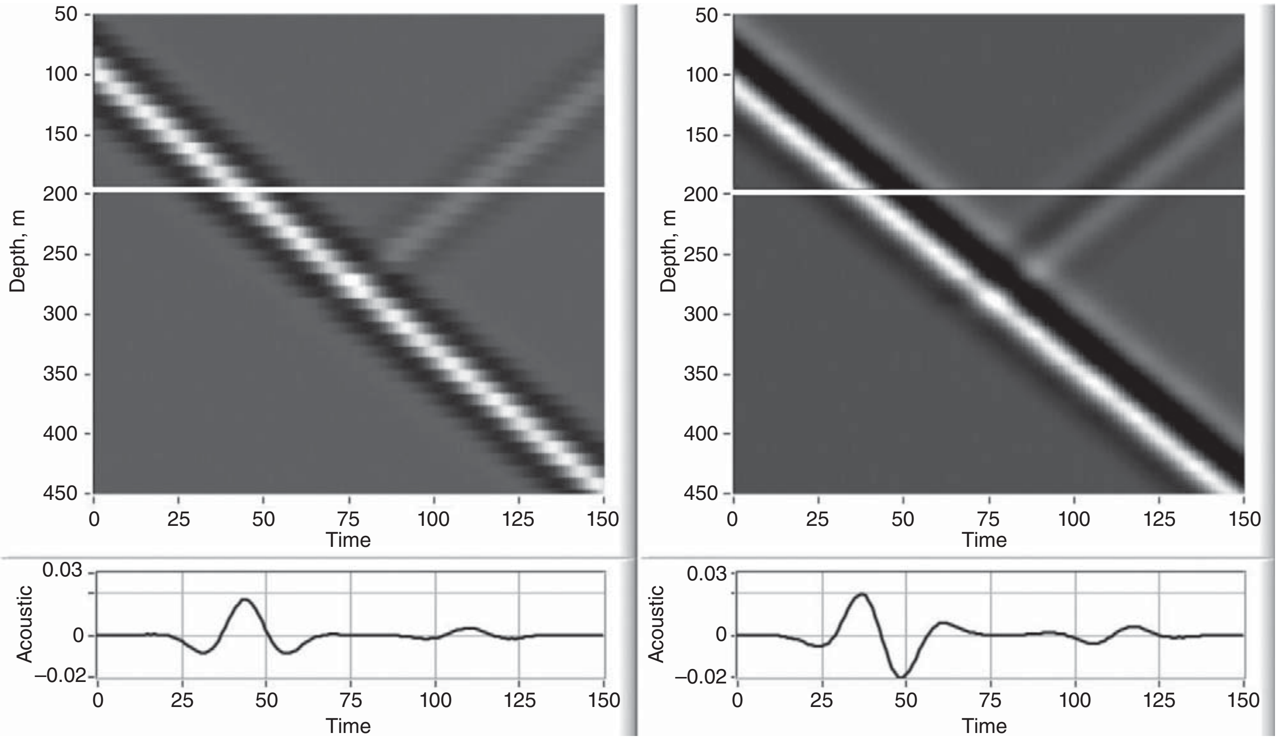

Figure 1.26 Acoustic measurements using DAS with precision engineered fiber: The left panel represents strain rate measurement (Equation 1.39) and the right panel displays ground speed measurement (Equation 1.41) after filtering and integration. The signals' cross-section along the white line is shown in the bottom panels in radians. The modeled source is shown in the right panel of Figure 1.5.

out, and also spatial antialiasing filtering can be used. It is worth mentioning that the right panel of Figure 1.26 is very similar to the original pulse (Figure 1.5), which demonstrates the real change of polarity of the reflected seismic pulse. Compared with Figure 1.10 (conventional fiber), Figure 1.26 shows better SNR and signal amplitude stability than with conventional fiber, and a more uniform size of the step in the "staircase" in the left panel, which can be easily filtered out.

The spatial spectral response in the wavenumber domain K_z can be represented by Fourier transform $\mathfrak{I}$:

$$|\mathfrak{I}_G(K_z)| = |\text{sinc}(K_z L_S/2)\sin(K_z L_0/2) \cdot [\text{comb}(K_z L_S/2\pi) \otimes \mathfrak{I}(K_z)]| \tag{1.42}$$

where $\mathfrak{I}(K_z)$ is the spatial spectral response of the seismic wave. Comparisons of DAS with engineered fiber spectral response for spatial sampling equal to the gauge length and half of gauge length are presented in Figure 1.27 based on Equation 1.41. For the high spatial sampling, we have a gain in the frequency range, which is highlighted by the gray filling. Moreover, it is easy to filter out the aliased component for high sampling as the spectral density is zero for maximum frequency, seen by comparing the position of the black and gray vertical lines in Figure 1.27. This advantage can explain the absence of "staircasing" and the smooth output in Figure 1.26 right panel. An additional advantage of high sampling is that, for a typical $L_0 = L_G = 5m$, the sampling is twice or even three times smaller than the sensor separation in a geophone array. This spatial frequency margin is useful because DAS timing is different from analog geophones. For a geophone antenna, we can filter out high-frequency space-time components in the time domain by electrically filtering individual channels before sampling to prevent spatial aliasing. This approach is ineffective for DAS when the time sampling acts directly on the rapidly changing photocurrent. The problem can be solved for DAS by mechanical filtering in the acoustic area using a special design of the sensing cable, as in Carroll & Huber (1986). An alternative approach involves some oversampling in the spatial domain, and the result is not completely independent. Subsequent filtering then removes high spatial frequencies and prevents aliasing.

Finally, we can neglect the comb function in Equation 1.42, following which Equation 1.42 is exactly

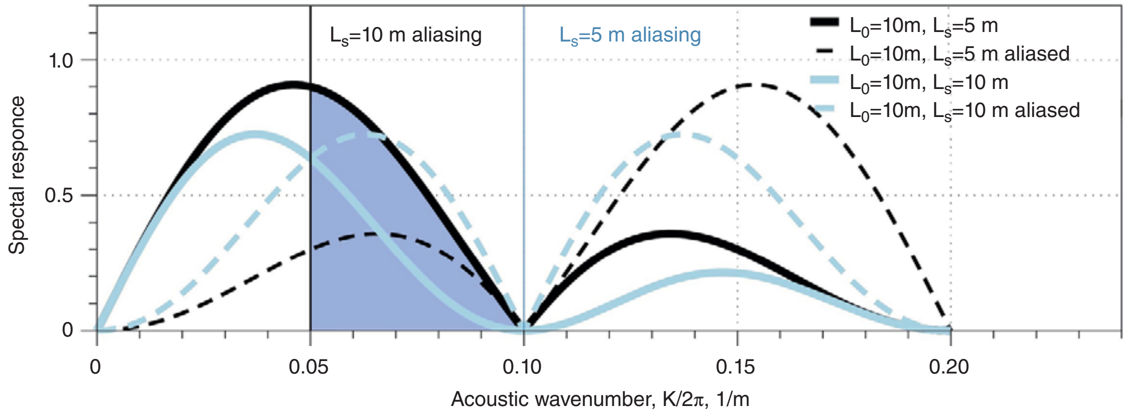

Figure 1.27 Comparison of DAS with engineered fiber spectral response for special sampling equal to gauge length (black) and half of gauge length (gray).

equivalent to the expression for a conventional fiber (Equation 1.30) with pulsewidth equal to the scattering period $L_S = \tau = 5m$.

DAS with engineered fiber combines the benefits of a distributed sensor, giving full coverage, with the high sensitivity of point sensors such as geophones. The scatter centers are precisely engineered along the length of the fiber and not distributed randomly as for standard fiber (see Figure 1.28). This allows the backscattered signal to be downsampled precisely and optimum spectral response to be obtained.

The DAS signal with engineered fiber, as expressed in Equation 1.39, can be considered as a staircase function with differential velocity sampling L_S: when sampled over each staircase distance L_S, the expression in the square brackets will be eliminated from Equation 1.39, and, therefore, the corresponding sinc function in Equation 1.43 will also be eliminated. As a result, the DAS signal with engineered fiber will be defined by $(v(z) - v(z - L_0))$, or comb filters in the spectral domain:

$$Specral\ Responce = \underset{j}{MAX} \frac{|\sin(jK_z L_0/2)|}{\sqrt{j}} \tag{1.43}$$

Equation 1.43 also includes a gain that can be obtained from synthetic gauge length optimization. With this approach, low spectral frequencies can be measured by adding a few consecutive downsampled signals. From a physical point of view, it means that the combination of multiple gauge lengths L_0 can be used to form a single long gauge length. The SNR for the resultant gauge length jL_0 will decrease proportionally to $\sqrt{j}$ in a shot noise limited DAS—see denominator in Equation 1.43. High spatial frequencies can still be measured with original gauge length L_0 without any loss of spatial resolution. Potentially, we can maximize the spectral response by choosing a proper averaging factor j for any spectral band, as is expressed in Equation 1.43. A simple practical implementation for optimizing both low and high spatial frequency can be realized by sliding a leaky distance integration of DAS signal similar to how it was done for velocity recovery (Equation 1.41).

The ultimate spectral response of DAS with standard (Equation 1.30) and engineered (Equation 1.43) fiber compared to that from a geophone array is shown in Figure 1.28. The pulsewidth of the DAS is the same as distance between scatter centers in engineered fiber $\tau = L_S = 5m$, and the gauge length is the same as the distance between geophones $L_G = L_0 = 10m$. In summary, downsampling of the DAS signal with engineered fiber can improve the spectral response as compared to standard fiber with the same gauge length. However, DAS with standard fiber can provide a wide spectral response without aliasing, as is shown in Figure 1.28.

1.3.2. Sensitivity and Dynamic Range

DAS sensitivity can be calculated for a fundamental limit—the shot noise generated by the number of photons detected. Let us estimate the photon number N per second based on input peak power $P_0 = 1\ W$, which is near to the maximum optical connector power damage threshold (De Rosa, 2002). The backscattered intensity can be found from the typical scattering coefficient for SM fiber $R_{BS} = 82dB$ for a 1 ns pulse (Ellis, 2007). For an optical pulsewidth $\tau = 50ns$, the energy quant for $\lambda = 1550nm$ is $h\nu = 1.28 \cdot 10^{-19}\ J$. We consider a relatively short fiber length, $L = 2000m$, to neglect nonlinear effects (Martins et al., 2013) and suppose that light is collected over an integration length $L_P = 5m$:

$$N = \frac{P_0 \tau R_{BS}}{h\nu}\left(\frac{L_P}{L}\right) = 6 \cdot 10^9 s^{-1} \tag{1.44}$$

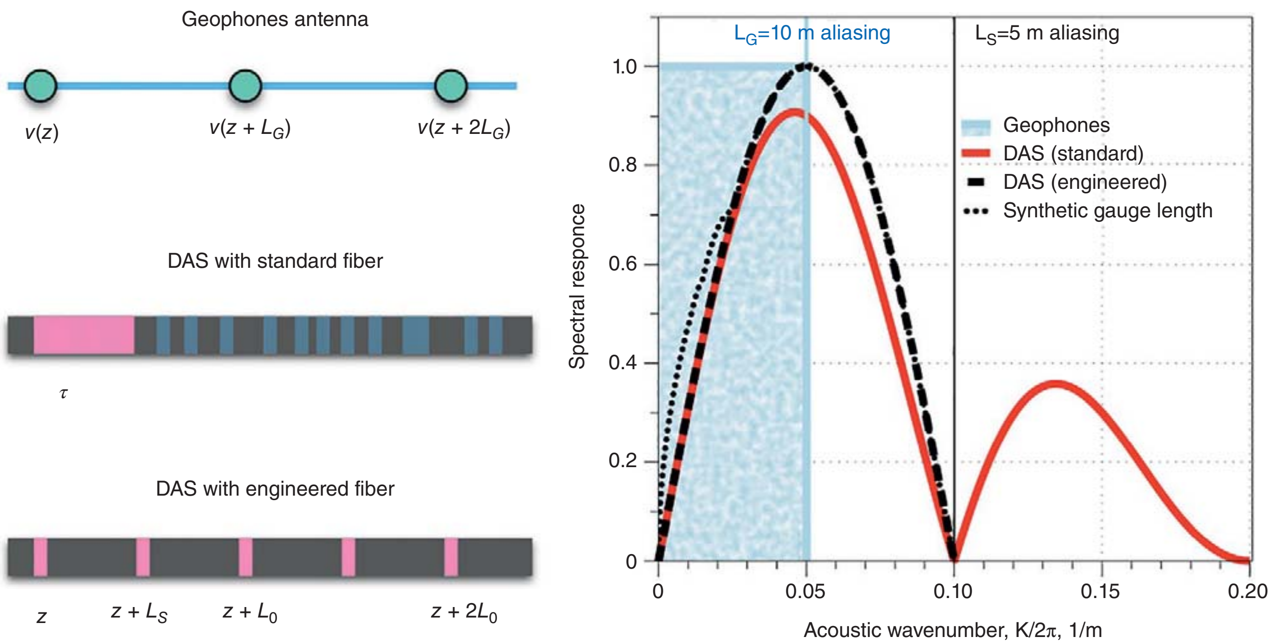

Figure 1.28 Ultimate SNR spectral response of DAS with standard and engineered fiber and geophone antenna. Pulse width of DAS is the same as distance between scatter centers along engineered fiber—5 m, and gauge length of DAS is the same as distance between geophones—10 m.

The shot or Poisson noise limit for phase measurement $\Phi_{\min}$ is proportional to $\sqrt{1/N}$, where the coefficient depends on the phase-detection approach. For a classical phase-locked homodyne, only half of the photons reach the photodetector when the interferometer operates in quadrature, and so the noise is $\sqrt{2/N}$. For both heterodyne and/or homodyne phase detection, the photons number halves again (Kazovsky, 1989), as sine and cosine signal components should be measured independently, and so the noise rises to $\sqrt{4/N}$. Direct photodetection at $\lambda = 1550nm$ is not sufficiently sensitive, so DAS usually uses an erbium doped fiber amplifier (EDFA) to boost the signal, which introduces additional noise. This noise can be simply represented by a noise figure $N_F \approx 3$, which can be reached with appropriate optical filtering as explained in Kirkendall & Dandridge (2004). In this case, the shot noise limit is then given by:

$$\Phi_{\min} = \frac{1}{V}\sqrt{\frac{4N_F}{N}} \sim 10^{-4} rad/\sqrt{Hz} \tag{1.45}$$

where visibility, $V = 0.5$, includes all other system imperfections such as polarization mismatch. Equation 1.45 represents the white noise level for 1 second time integration of the DAS signal. For engineered fiber, the number of photons can be up to 100 times larger than for conventional Rayleigh backscattering, so the noise will be 10 times smaller.

Another advantage of DAS with engineered fiber is a wider dynamic range that is defined as the ratio of the maximum detectable signal to the noise level. The typical geophone bandwidth is $\Delta F = 100Hz$, so the minimum strain level $\varepsilon_{\min}$ detectable for DAS for gauge length $L_0 = 10m$ within the same detection bandwidth is:

$$\varepsilon_{\min} = \frac{\Phi_{\min} A_0 \sqrt{\Delta F}}{L_0} \sim 0.01 nanostrain \tag{1.46}$$

where $A_0 = 115nm$ is the elongation corresponding to one radian phase shift (Equation 1.14).

Experimental measurements with conventional fiber DAS found a value three times higher, at $0.03 nanostrain$ (Miller et al., 2016). In this case, there was some extra flicker noise, as discussed earlier (see Figure 1.11). Here, a spiky noise structure corresponds to algorithm discontinuities that amplify photodetector noise, with a spectrum after DAS signal time integration, which is $\propto F^{-1}$. The typical low frequency limit when excessive noise starts to dominate over shot noise is between 10 and 100 Hz, depending on the fiber conditions.

For engineered fiber (Farhadiroushan et al., 2021), reflectivity can be engineered to be hundreds of times higher than the normal Rayleigh level, without any significant problems with crosstalk, such that $R = 100 \cdot R_{BS} \cdot \tau = -45dB$.

As a result, sensitivity is ten times higher, at around 1*pico-strain*, which corresponds to a 100x (20 dB) improvement in acoustic signal sensitivity.

It is important to compare the shot noise level of DAS with the noise level of high-sensitivity geophones and seismometers. The DAS white noise value should be added to flicker noise with coefficient μ and corrected for spatial filtering (Equation 1.46) as:

$$z_{\min} = \frac{\Phi_{\min} A_0 + \mu F^{-1}}{\left|\text{sinc}\left(\frac{\pi F L_0}{2C}\right) \sin\left(\frac{\pi F L_0}{C}\right)\right|} \tag{1.47}$$

The comparison in Figure 1.28 demonstrates that DAS sensitivity is compatible with geophones. The noise spectrum data for Sercel SG5-SG10 was adapted from Fougerat et al. (2018), and the seismometer Streckeisen STS-2 data from Ringler & Hutt (2010) and Wielandt & Widmer-Schnidrig (2002).

The sensitivity of DAS can even be improved at low frequencies by extending the gauge length from $L_0 = 10m$ to $L_0 = 30m$, but at the cost of increased noise at frequencies of more than 70 Hz. Also, 30 m data for DAS with engineered fiber is presented with synthetic gauge length optimization (Equation 1.44). It is worth mentioning that this optimization can be effectively applied to DAS with engineered fiber only, as it has no significant pink noise and can be effectively spatially averaged. As is clear from Figure 1.29, the performance of DAS with engineered fiber can reach seismometers, and it is deep below Peterson's low noise model level (Peterson, 1993). So, the engineered fiber antenna is an equivalent of a set of multiple seismic stations and can be used for passive seismic applications. Moreover, DAS with engineered fiber has unique sensing capability below 1 Hz, where gravitational wave detectors have limited environmental isolation (Matichard et al., 2015); DAS can be potentially used for such applications.

We now turn our attention to the increase in dynamic range achievable using DAS with an engineered fiber. The acoustic algorithm transforms DAS intensity signals into a phase shift proportional to the fiber elongation value. The algorithm is based on an ambiguous function such as ATAN(x), which give a valid result only inside a limited region (Itoh, 1982). As was analyzed in Section 1.1 (titled 'Distributed Acoustic Sensor (DAS) Principles and Measurements'), a set of different algorithms can be used, depending on the order of phase tracking. For the first and second order, we have:

$$-\pi \leq A_1(t) < \pi \tag{1.48}$$

$$-\pi \leq A_2\left(t + \frac{1}{F_s}\right) - A_2(t) < \pi \tag{1.49}$$

For limits (Equations 1.48–1.49), it is clear that the maximum recoverable strain $\varepsilon_{1,2}$ will depend on the algorithm order 1 or 2, and can also be increased using a higher sampling frequency F_s. For a harmonic signal $\cos(2\pi Ft)$, we can normalize strain results as:

$$\varepsilon_1 \leq \frac{A_0}{2L_0} \frac{F_S}{F} \tag{1.50}$$

$$\varepsilon_2 \leq \frac{A_0}{4\pi L_0} \left(\frac{F_S}{F}\right)^2 \tag{1.51}$$

The maximum strain comparison for the first and second order tracking algorithm ε_1 *and* ε_2 (Equations 1.50–1.51) is presented in Figure 1.30 for $F_S = 50kHz$ *and* $L_0 = 10m$. The second order algorithm can deliver

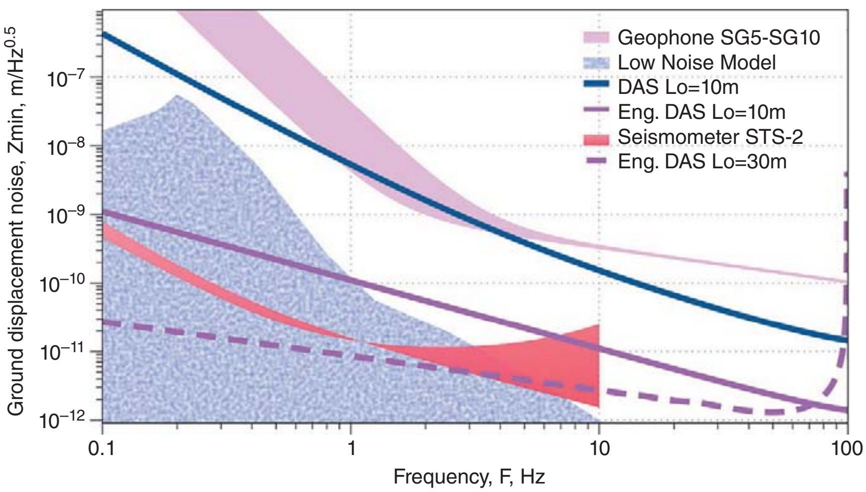

Figure 1.29 Displacement noise comparison of DAS (with and without engineered fiber) with seismometer and geophone. 30 m DAS data are for synthetic gauge length.

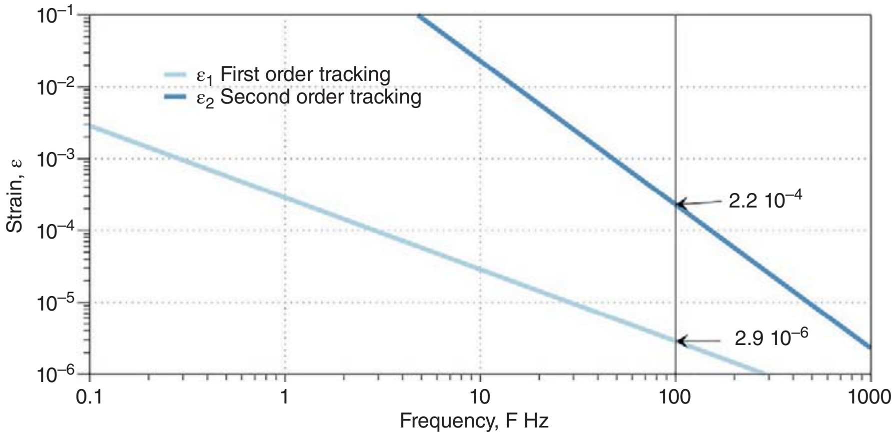

Figure 1.30 Maximum strain comparison of first and second order algorithms for DAS.

measurements of fiber strain up to fiber breakage point (~10%) at frequencies of around 10 Hz.

We can now estimate the maximum DAS dynamic range D as:

$$D = 20 \log_{10} \frac{\varepsilon_{1,2}}{\varepsilon_{\min}} \tag{1.52}$$

Using the real noise level $\varepsilon_{\min} = 0.03 nanostrain$ from Miller et al. (2016), we can estimate $D = 99dB$ for a maximum value $\varepsilon_1 = 2.9\mu strain$. This estimation gives the practical upper limit for seismic DAS at 100 Hz using Rayleigh scattering. Generally speaking, the second order tracking algorithm has limited applicability for a conventional DAS because flicker noise pulses can reach π and destroy measurements in accordance with Equation 1.49. Nevertheless, $120dB$ was achieved in Parker et al. (2014) when the fiber elongation zone was significantly smaller than the gauge length and pulsewidth, such that the flicker noise was suppressed. However, when a continuous seismic signal expands the reflectivity zone, then the reflection can disappear, and the signal has ambiguity. Fortunately, in engineered fibers, the scatter center zones are well defined, and so the reflectivity change is negligible. As a result, we can optimistically estimate a maximum $D = 167dB$ for engineered fiber using $\varepsilon_{\min} = 1 picostrain$ and maximum $\varepsilon_2 = 220\mu strain$—see Figure 1.30.

The dynamic range of DAS with engineering fiber was tested during a dry alluvium geology series of chemical explosions, including 50,000 kg TNT-equivalent at 300-m depth-of-burial (Abbott et al., 2019). "Two orders of magnitude more data relative to traditional geophones/accelerometers" was successfully recorded.

Summarizing, we can conclude that theoretical estimations demonstrate that the performance of DAS with engineered fiber can potentially exceed that of conventional geophones and seismometers. In general, given that the overall sensitivity of a DAS system is a function of the coupling, cable, fiber, electronics, and digital signal processing, field data is most convincing, and, in the next section, we will discuss some examples of high definition seismic and microseismic data that demonstrate the benefits of the engineered fiber DAS solution as compared to conventional DAS and geophones.

1.3.3. Field Trial Results

A comparison of DAS with standard and engineered fiber for a seismic sweep signal is presented in Figure 1.31. This measurement was provided using two different fibers placed side by side in the same optical cable, so the elongation of both fibers was identical. The top graphs (a) and (c) demonstrate the difference between the time-distance representation; the right panel (c), which represents engineered fiber, is visibly cleaner than the left panel (a). The detected seismic signal has the same shape (around 10 nm peak to peak for a channel 898) for engineered (d) and standard (b) fiber, except noise. Some change in amplitude (20%) can be explained by incomplete averaging of the DAS signal over distance, as is shown in Figure 1.7. There was less variation in the amplitude level for engineered fiber, and this stability can be important for 3D VSP, as was shown in Figure 1.21.

A comparison of DAS acoustic noise with standard and engineered fiber is presented in Figure 1.32. Noise spectral density versus distance is practically constant for engineered fiber (b) but varies significantly for standard fiber from channel to channel along distance (a). In other words, we can conclude that standard DAS noise depends on fiber randomness and can be far from the average value, but engineered fiber DAS noise is predictable. The SNR difference is emphasized by the signal Fourier transform in the bottom chart (c): the noise reduction

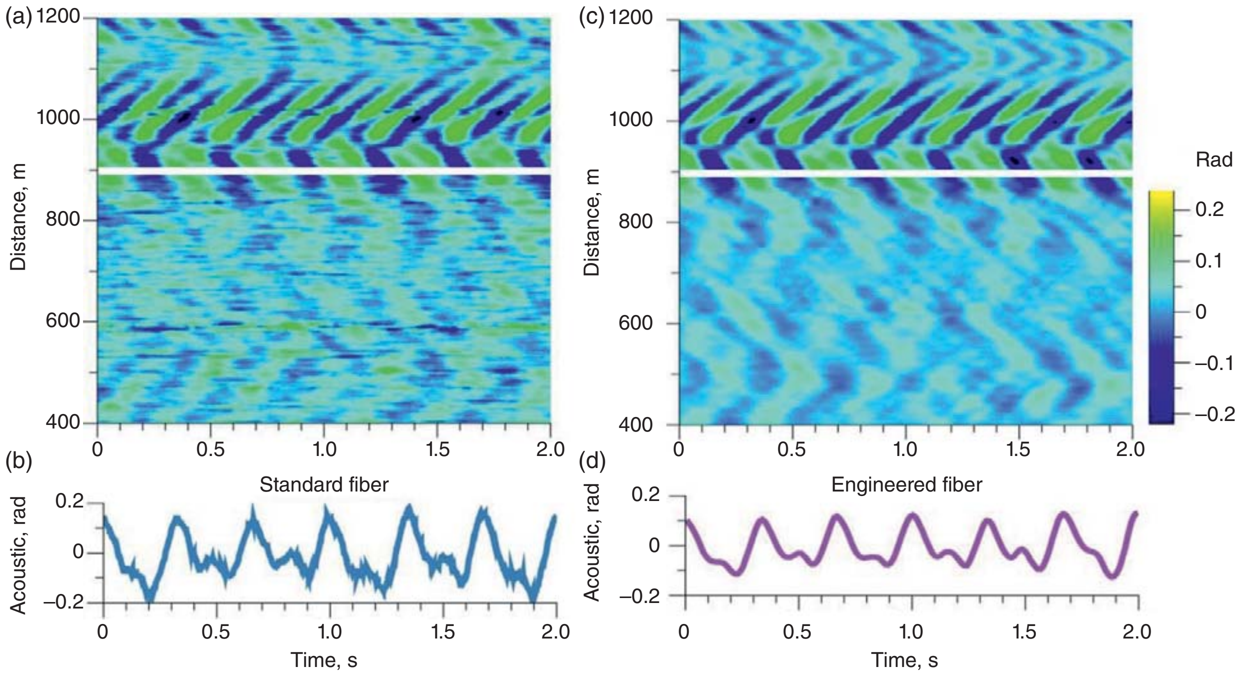

Figure 1.31 Comparison of DAS with Rayleigh scattering [(a) and (b)] and engineered fiber [(c) and (d)] for a seismic sweep signal. Acoustic signals are measured in optical phase radians.

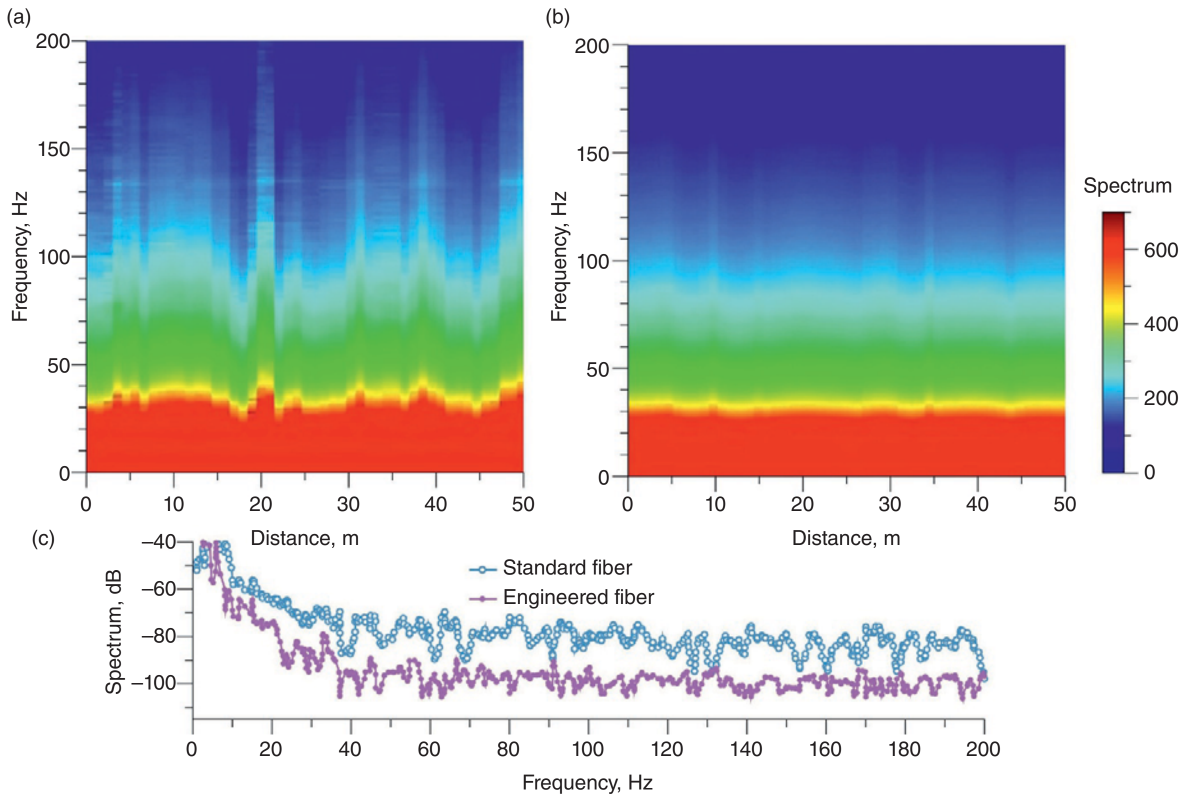

Figure 1.32 Comparison of DAS noise spectrums with Rayleigh scattering (a) and engineered fiber (b). Panel (c) represents acoustic noise spectrum density with respect to 1 rad/Hz0.5. Source: Based on Richter et al. (2019).

for engineered fiber is nearly 20 dB as was expected from shot noise estimation (Equation 1.46).

Fine spatial resolution in combination with good sensitivity gives DAS a significant advantage for detection of microseismic events, particularly where a geophone chain cannot be readily positioned. Such measurements are used in fracking jobs, where a wireline fiber optic cable is pumped down into an already completed observation well (Richter et al., 2019). This gives the possibility to determine the frack height and well interference with unprecedented clarity.

A typical microseismic event is presented in Figure 1.33, where both S- and P-waves are clearly visible, such that the distance from observation well to fracking event can be easily detected. Figure 1.34 shows how the same installation can be used to detect a "frac hit," where a fracking zone and strain extends slowly from the well undergoing treatment to the observation well. This new data allows completion engineers to map the depth, azimuth, and speed of the fractures and feed that information back into the fracture models to validate and optimize the designs for the next operation.

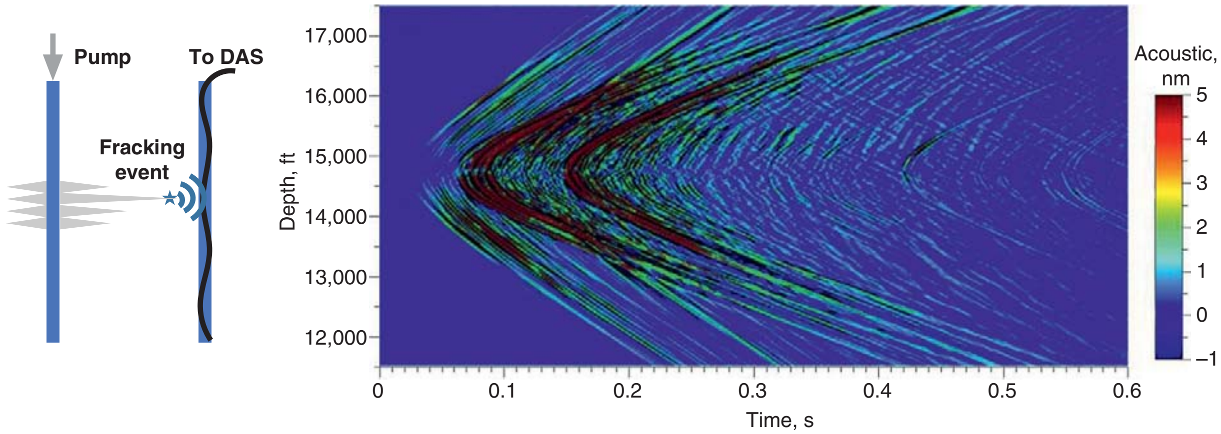

Figure 1.33 Microseismic event in observation well detected by DAS with engineered fiber.

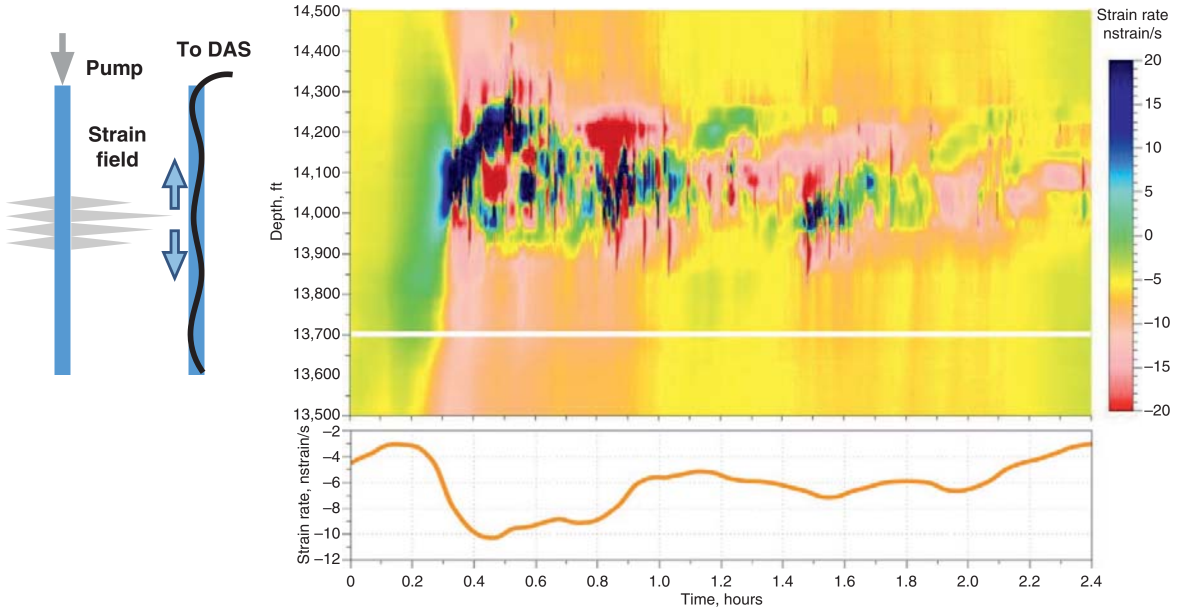

Figure 1.34 Example of low frequency (down to millihertz level) "slow strain" data, showing a fracking hit on an observation well from a well undergoing treatment. The time-averaged signal cross-section along the white line is shown in the bottom panel.

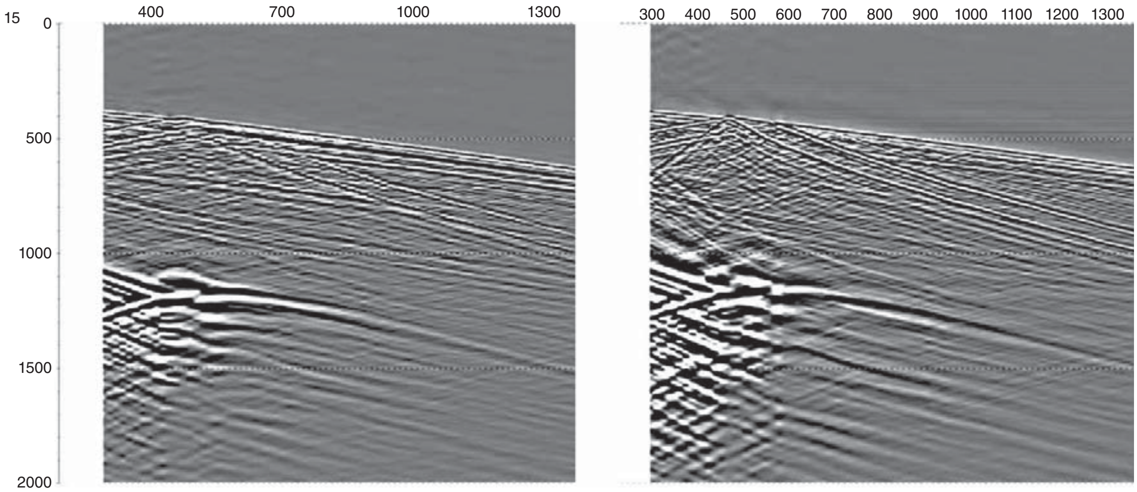

Figure 1.35 Comparison of geophones (left panel) and DAS with engineered fiber (right panel).

The results from a VSP survey in a carbon sequestration well (Correa et al., 2017) demonstrate that DAS with engineered fiber has the potential to provide similar, or even superior, quality data sets as compared to conventional geophones. An important aspect is that, due to the higher spatial sampling, DAS data has the capability to provide more detailed velocity information as compared to geophones. This conclusion was expected from the preceding theory and is illustrated in Figure 1.35, which demonstrates even a finer reflection structure from DAS than from geophones.

In summary, we have estimated the main DAS performance parameters for standard and engineered fiber and provided field data that correspond to the theoretical predictions of improved sensitivity and dynamic range.

ACKNOWLEDGMENTS

The authors would like to thank Roman Pevzner and Valeriya Shulakova (of CO2CRC, Curtin University) and Thomas M. Daley, Barry M. Freifeld, Jonathan Ajo-Franklin, and Shan Dou (of the Lawrence Berkeley National Laboratory) for the use of raw and processed surface seismic data and the presented field geometry. The authors would also like to acknowledge the significant help and support from their colleagues at Silixa. In addition, the authors thank the reviewers for their helpful comments in preparing this manuscript.

REFERENCES

Abbott, R. E., Mellors, R. E., & Pitarka, A. E. (2019). *Distributed acoustic sensing observations and modeling of the DAG series of chemical explosions*. Paper presented in CTBT Science & Technology 2019 Conference, T2.3-P12. https://ctnw.ctbto.org/ctnw/abstract/32643

Baird, A. (2020). *Modelling the response of helically wound DAS cables to microseismic arrivals*. Paper presented in First EAGE Workshop on Fibre Optic Sensing (Vol. 2020, No. 1, pp. 1–5). European Association of Geoscientists & Engineers.

Benioff, H. (1935). A linear strain Seismograph. *Bulletin of the Seismological Society of America*, *25*(4), 283–309.

Brennan, D. G. (1959). Linear diversity combining techniques. *Proceedings of the IRE*, *47*(6), 1075–1102. doi: 10.1109/JRPROC.1959.287136

Carroll, J., & Huber, D. (1986). A fiber-optic hydrophone with a mechanical anti-aliasing filter. *Journal of Lightwave Technology*, *4*(1), 83–86.

Correa, J., Egorov, A., Tertyshnikov, K., Bona, A., Pevzner, R., Dean, T., et al. (2017). Analysis of signal to noise and directivity characteristics of DAS VSP at near and far offsets—A CO2CRC Otway Project data example. *The Leading Edge*, *36*(12), 994a1–994a7. doi: 10.1190/tle36120994a1.1

Crickmore, R. I., & Hill, D. J. (2010). *U.S. Patent No. 7,652,245*. Washington, DC: U.S. Patent and Trademark Office.

Crickmore, R., & Ku, E. (2017). *U.S. Patent Application No. 15/309,076*.

Dakin, J. P. (1990). Distributed fibre optic sensor system. *UK Patent, GB2222247A*.

Dakin, J., & Culshaw, B. (Eds.). (1989). *Optical fiber sensors: Systems and applications* (Vol. 2, Chap. 15). Artech House Optoelectronics. Norwood, Massachusetts.

De Rosa, M., Carberry, J., Bhagavatula, V., Wagner, K., & Saravanos, C. (2002). High-power performance of single-mode fiber-optic connectors. *Journal of Lightwave Technology*, *20* (5), 851.

Ellis, R. (2007). Explanation of reflection features in optical fiber as sometimes observed in OTDR measurement traces. *Corning White Paper*.

Farhadiroushan, M., Finfer, D., Strusevich, D., Shatalin, S., & Parker, T. (2021). Non-isotropic acoustic cable. *U.S. Patent Application No. 15/804,657*.

Farhadiroushan, M., Parker, T. R., & Shatalin, S. (2010). Method and apparatus for optical sensing. *WO2010136810A2*.

Farhadiroushan, M., Parker, T., & Shatalin, S. (2021). U.S. Patent No. 10,883,861. Washington, DC: U.S. Patent and Trademark Office.

Finfer, D. C., Mahue, V., Shatalin, S., Parker, T., & Farhadiroushan, M. (2014, October). *Borehole flow monitoring using a non-intrusive passive distributed acoustic sensing (DAS)*. Paper presented in SPE Annual Technical Conference and Exhibition. Society of Petroleum Engineers. doi: 10.2118/170844-MS

Fougerat, A., Guérineau, L., & Tellier, N. (2018). *High-quality signal recording down to 0.001 Hz with standard MEMS accelerometers*. Paper presented in SEG Technical Program Expanded Abstracts 2018 (pp. 196–200). Society of Exploration Geophysicists.

Garnier, A., & Chanin, M. L. (1992). Description of a Doppler Rayleigh lidar for measuring winds in the middle atmosphere. *Applied Physics B*, *55*(1), 35–40.

Ghiglia, D. C., & Pritt, M. D. (1998). *Two-dimensional phase unwrapping. Theory, algorithms, and software*. New York, USA: A Wiley-Interscience Publication.

Goodman, J. W. (2005). *Introduction to Fourier optics* (Chap. 2, 6). Roberts and Company Publishers. Englewood, Colorado.

Handerek, V. (2016). *U.S. Patent No. 9,304,017*. Washington, DC: U.S. Patent and Trademark Office.

Hartog, A. H. (2017). *An introduction to distributed optical fibre sensors*. CRC press. Boca Raton, Florida.

Hartog, A. H., Kotov, O. I., & Liokumovich, L. B. (2013, July). *The optics of distributed vibration sensing*. Paper presented in Second EAGE Workshop on Permanent Reservoir Monitoring 2013–Current and Future Trends. doi: 10.3997/2214-4609.20131301

Hartog, A., & Kader, K. (2012). *U.S. Patent Application No. 13/221,280*.

Hornman, K., Kuvshinov, B., Zwartjes, P., & Franzen, A. (2013, June). *Field trial of a broadside-sensitive distributed acoustic sensing cable for surface seismic*. Paper presented in 75th EAGE Conference & Exhibition incorporating SPE EUROPEC 2013. doi: 10.3997/2214-4609.20130383

Itoh, K. (1982). Analysis of the phase unwrapping algorithm. *Applied Optics*, *21*(14), 2470–2470. doi: 10.1364/AO.21.002470

Jousset, P., Reinsch, T., Ryberg, T., Blanck, H., Clarke, A., Aghayev, R., et al. (2018). Dynamic strain determination using fibre-optic cables allows imaging of seismological and structural features. *Nature Communications*, *9*(1), 2509. doi: 10.1038/s41467-018-04860-y

Juarez, J. C., Maier, E. W., Choi, K. N., & Taylor, H. F. (2005). Distributed fiber-optic intrusion sensor system. *Journal of Lightwave Technology*, *23*(6), 2081–2087. doi: 10.1109/JLT.2005.849924

Juškaitis, R., Mamedov, A. M., Potapov, V. T., & Shatalin, S. V. (1992). Distributed interferometric fiber sensor system. *Optics Letters*, *17*(22), 1623–1625. doi: 10.1364/OL.17.001623

Kazovsky, L. G. (1989). Phase-and polarization-diversity coherent optical techniques. *Journal of Lightwave Technology*, *7*(2), 279–292. doi: 10.1109/50.17768

Kirkendall, C. K., & Dandridge, A. (2004). Overview of high performance fibre-optic sensing. *Journal of Physics D: Applied Physics*, *37*(18), R197. doi: 10.1088/0022-3727/37/18/R01

Kreger, S. T., Gifford, D. K., Froggatt, M. E., Soller, B. J., & Wolfe, M. S. (2006, October). *High resolution distributed strain or temperature measurements in single-and multi-mode fiber using swept-wavelength interferometry*. In Optical Fiber Sensors (p. ThE42). Optical Society of America. doi: 10.1364/OFS.2006.ThE42

Lewis, M. F. (1985). On Rayleigh waves and related propagating acoustic waves. In *Rayleigh-wave theory and application* (pp. 37–58). Springer, Berlin, Heidelberg.

Martin, E. R., Lindsey, N., Ajo-Franklin, J., & Biondi, B. (2018). EarthArXiv, *Introduction to interferometry of fiber optic strain measurements* (pp. 1–33).

Martins, H. F., Martin-Lopez, S., Corredera, P., Salgado, P., Frazão, O., & González-Herráez, M. (2013). Modulation instability-induced fading in phase-sensitive optical time-domain reflectometry. *Optics Letters*, *38*(6), 872–874. doi: 10.1364/OL.38.000872

Mateeva, A., Lopez, J., Potters, H., Mestayer, J., Cox, B., Kiyashchenko, D., et al. (2014). Distributed acoustic sensing for reservoir monitoring with vertical seismic profiling. *Geophysical Prospecting*, *62*(4), 679–692.

Miller, D. E., Daley, T. M., White, D., Freifeld, B. M., Robertson, M., Cocker, J., et al. (2016). Simultaneous acquisition of distributed acoustic sensing VSP with multi-mode and single-mode fibre-optic cables and 3C-geophones at the Aquistore CO2 storage site. *CSEG Recorder*, *41*(6).

Matichard, F., Lantz, B., Mittleman, R., Mason, K., Kissel, J., Abbott, B., et al. (2015). Seismic isolation of Advanced LIGO: Review of strategy, instrumentation and performance. *Classical and Quantum Gravity*, *32*(18), 185003.

Parker, T. R., Farhadiroushan, M., Feced, R., Handerek, V. A., & Rogers, A. J. (1998). Simultaneous distributed measurement of strain and temperature from noise-initiated Brillouin scattering in optical fibers. *IEEE Journal of Quantum Electronics*, *34*(4), 645–659. doi: 10.1109/3.663443

Parker, T., Shatalin, S., & Farhadiroushan, M. (2014). Distributed acoustic sensing—a new tool for seismic applications. *First Break*, *32*(2), 61–69. doi: 10.3997/1365-2397.2013034

Peterson, J. R. (1993). Observations and modeling of seismic background noise (No. 93-322). US Geological Survey.

Posey, R., Johnson, G. A., & Vohra, S. T. (2000). Strain sensing based on coherent Rayleigh scattering in an optical fibre. *Electronics Letters*, *36*(20), 1688–1689. doi: 10.1049/el:20001200

Rathod, R., Pechstedt, R. D., Jackson, D. A., & Webb, D. J. (1994). Distributed temperature-change sensor based on Rayleigh backscattering in an optical fiber. *Optics Letters*, *19*(8), 593–595. doi: 10.1364/OL.19.000593

Ringler, A. T., & Hutt, C. R. (2010). Self-noise models of seismic instruments. *Seismological Research Letters*, *81*(6), 972–983.

Rea, N. P., Wilson, T., & Juškaitis, R. (1996). Semiconductor laser confocal and interference microscopy. *Optics Communications*, *125*(1–3), 158–167. doi: 10.1016/0030-4018(95)00701-6

Richter, P., Parker, T., Woerpel, C., Wu, Y., Rufino, R., & Farhadiroushan, M. (2019). Hydraulic fracture monitoring and optimization in unconventional completions using a high resolution engineered fiber optic distributed acoustic sensor. *First Break, 37*(4), 66–68.

Servin, M., Kujawinska, M., & Padilla, J. M. (2017). Modern fringe pattern analysis in interferometry. In *Advanced Optical Instruments and Techniques* (pp. 101–152). CRC Press.
Shatalin, S. V., Treschikov, V. N., & Rogers, A. J. (1998). Interferometric optical time-domain reflectometry for distributed optical-fiber sensing. *Applied Optics*, *37*(24), 5600–5604. doi: 10.1364/AO.37.005600
Shatalin, S., Mamedov, A., Potapov, V., & Sedykh, D. (1991). *Optical frequency domain multiplexing of fiber-optic sensors*. The First International Soviet Fibre Optics Conference, ISFOC ′91 (pp. 307–308).
Subsea Fiber Optic Monitoring (SEAFOM) working group (2018). Measuring Sensor Performance—DAS Parameter Definitions and Tests SEAFOM-MSP-02. Retrieved from https://seafom.com/published-documents/
Taylor, H. F., & Lee, C. E. (1993). *U.S. Patent No. 5,194,847*. Washington, DC: U.S. Patent and Trademark Office.
Todd, M. (2011, April). *Noise propagation in a 3×3 optical demodulation scheme used for fiber Bragg grating interrogation*. Paper presented in Smart Sensor Phenomena, Technology, Networks, and Systems 2011 (Vol. 7982, p. 79820A). International Society for Optics and Photonics. doi: 10.1117/12.878694
Unser, M. (1999). Splines: A perfect fit for signal and image processing. *IEEE Signal Processing Magazine*, *16*(6), 22–38. doi: 10.1117/12.467162
Wielandt, E., & Widmer-Schnidrig, R. (2002). *Seismic sensing and data acquisition in the GRSN*. Ten Years of German Regional Seismic Network (GRSN) (pp. 73–83).
Westbrook, P. S., Feder, K. S., Ortiz, R. M., Kremp, T., Monberg, E. M., Wu, H., et al. (2017, April). *Kilometer length, low loss enhanced back scattering fiber for distributed sensing*. Paper presented in 2017 25th Optical Fiber Sensors Conference (OFS) (pp. 1–5). IEEE.
Wuestefeld, A., & Wilks, M. (2019). How to twist and turn a fiber: Performance modeling for optimal DAS acquisitions. *The Leading Edge*, *38*(3), 226–231.

TABLE OF VARIABLES

$a(z)$	arbitrary function
A_0	fiber elongation corresponding to 1 rad of phase shift
$A(z, t)$	output of DAS
$A_1(z)$	output of DAS with first order algorithm
$A_2(z)$	output of DAS with second order algorithm
$b(z)$	arbitrary function
c	optical speed of light in fiber
C	speed of sound
D	DAS dynamic range
$e(t')$	optical field of coherent input pulse
$E(t')$	optical field on photodetector
$\mathfrak{I}(K, F)$	Fourier transforms of seismic signal
$\mathfrak{I}$	Fourier transform symbol
F	frequency of sound
F_{MAX}	maximum frequency of sound
F_S	pulse repetition rate or sampling frequency
$G(z)$	geophone antenna response
$h\upsilon$	energy quant
$\mathrm{Im}\ Z$	imaginary part of interference output
$I_j(z, t)$	intensity trace for different interferometric output
$I(z, t)$	photodetector intensity trace
j	integer number
K	acoustic angular wavenumber
K_z	acoustic angular wavenumber along fiber
K_e	ratio of optical to physical length of fiber
L	fiber length
L_P	integration length
L_0	interferometer length also known as *gauge length*
L_S	scattering zones spacing
M	number of scattering zones
n_{eff}	fiber effective refractive index
N_F	noise figure of amplifier
N	number of photons per second
$p(z)$	averaging function
P_0	input peak power
P	number of different interferometric ports or pulses
R_{BS}	backscattering coefficient of fiber
$r_0(z)$	distribution of reflection/scattering coefficient along fiber axis
$r(z)$	distribution of reflection/scattering coefficient along fiber axis with optical phase shift included
$\mathrm{Re}\ Z$	real part of interference output
t'	"fast" optical time scale
t	"slow" acoustic time scale
$u(z, t)$	ground displacement
u	parameter of function
$v(z)$	fiber local speed along its axis and also ground speed
$V(z)$	interference visibility along fiber
x	parameter of integration: coordinate along fiber axis
z	coordinate along fiber axis
z_1	parameter of function
z_2	parameter of function
β	optical wave propagation constant of fiber
β_0	unperturbed optical wave propagation constant of fiber
$\Delta\Omega(z)$	distance variation of Doppler shift along fiber
Δv	distance variation of ground speed
ΔF	geophone bandwidth
δ	the Dirac delta function
ε_1	maximum recoverable strain for first order algorithm
ε_2	maximum recoverable strain for second order algorithm
$\varepsilon_{\min}$	minimum strain level
$\Phi_{\min}$	phase noise
Γ	incident angle of seismic wave
λ	laser wavelength
Λ	spacing of geophones
μ	flicker noise coefficient
ω	circular frequency of light
$\Omega(z)$	Doppler frequency shift of light
ψ_0	phase shift between delayed optical fields in interferometer
Φ	shift of backscattered light
ρ	backscattering intensity coefficient
$\theta(z)$	Heaviside step function
$\tau(z)$	input pulse
τ	optical pulsewidth

2

Important Aspects of Acquiring Distributed Acoustic Sensing (DAS) Data for Geoscientists

Mark E. Willis[1], Andreas Ellmauthaler[1], Xiang Wu[2], and Michel J. LeBlanc[1]

ABSTRACT

Fiber-optic distributed acoustic sensing (DAS) is a technology used for many strain measurement applications, including seismic monitoring. Because it is relatively new to the market, most geoscientists are unfamiliar with the details of the technology, but nevertheless are required to make important acquisition parameter decisions such as the type of fiber-optic glass to use, the deployment method for the fiber-optic cable, the gauge length, and how to diminish the effect of optical noise. This chapter provides a non-theoretical, practical approach to making these decisions in order to obtain high-quality DAS data sets.

2.1. INTRODUCTION

The exciting and rapidly evolving technology of DAS, which uses optical fibers to sense local changes in strain, acquires seismic data for many applications, such as vertical seismic profiling (VSP) (Barfoot, 2013; Mestrayer et al., 2011; Mateeva et al., 2017), earthquake monitoring (Martin et al., 2017), hydraulic-fracture geometry characterization (Jin & Roy, 2017), and microseismic monitoring (Hull et al., 2017). Improvements in the interrogator design (Hartog, 2017) and deployment methods (Ellmauthaler et al., 2020) have increased the signal-to-noise ratio (SNR) of the raw measurements, while processing improvements (Ellmauthaler et al., 2017; Chen et al., 2019; Willis et al., 2020) have allowed the removal of specific fiber-optic noise patterns in the data.

Acquiring seismic data using accelerometers, geophones, and seismometers is a well-developed and understood practice. Ironically, because it is so common, we rarely stop to question the actual field hardware used to acquire data or the software to process it; thus, it is frequently treated as a trusted commodity. In contrast, DAS technology is not as widely understood by the geophysics community, just as the requirements and applications of seismic data might not be generally grasped by fiber-optic engineers and physicists who build and maintain DAS hardware and software. This situation creates the potential for degradations in the quality of seismic data acquired by DAS. This chapter describes the practical aspects for obtaining quality borehole seismic data using DAS to bridge the gap between fiber-optic technologists and the geophysics community.

2.2. FIBER-OPTIC SENSOR

2.2.1. Sensing from Backscattered Light

At the center of DAS technology is the fiber-optic cable deployed in one of several ways as the seismic sensor. Unlike seismometers that are thought of as point sensors, a fiber-optic cable senses strain along the entire fiber, which can be thousands of kilometers long. Because

[1]*Halliburton, Houston, Texas, USA*
[2]*Halliburton Far East Pte. Ltd., Singapore*

Distributed Acoustic Sensing in Geophysics: Methods and Applications, Geophysical Monograph 268, First Edition.
Edited by Yingping Li, Martin Karrenbach, and Jonathan B. Ajo-Franklin.

DOI:10.1002/9781119521808.ch02

individual sensors do not make the measurement, it is referred to as a “distributed sensor measurement.” For ordinary telecommunication applications, a laser generates encoded light signals that pass information along the fiber to a distant receiver. Small defects or changes in the optical properties of the fiber along its length cause the light to be backscattered toward the laser source. The fiber is designed to minimize, by five to seven orders of magnitude as compared to the illuminating light, the amount of attenuation and backscattered light, so that data can be transmitted over large distances. However, this same unwanted backscattered light in telecommunications is used for DAS applications to detect and characterize local changes in the strain of the optical fiber from acoustic and seismic signals as well as from temperature changes.

When seismic waves or small temperature transients mechanically deform an optical fiber, the optical propagation properties of the fiber change, causing extremely small time delays during the travel path of the backscattered light. When a pulse of laser light is introduced into one end of the fiber, these small changes in the optical properties of the fiber create a continuous “shower” of scattered light emanating from virtually all points along the fiber as the pulse passes through. The timing change of the backscattered light forms the basis by which the strain, or deformation, of the fiber can be measured using an optical interrogation system.

2.2.2. Single vs. Multi-mode Fiber

One of the first features to determine is the type of fiber to use as the seismic sensor. Practically all older fiber installations use multi-mode fiber to enable the acquisition of temperature measurements using distributed temperature sensing (DTS). Most newer installations use a cable with two or more single-mode and two or more multimode fibers inside. For DAS applications, single-mode fiber currently provides the best SNR properties as compared to multi-mode fiber. Single-mode fiber has a small inner glass core diameter of 9 microns, which only allows a single, virtually direct path for the light to propagate; the light is totally internally reflected within the glass. On the contrary, multi-mode fiber has a larger glass core diameter of 50 or more microns. While the light is still completely internally reflected, the wider glass core thickness allows for multiple paths, or modes, to be transmitted through the fiber. More light energy can be pumped into the multi-mode fiber; however, the interference of the light pulse from the multiple paths can interfere with the quality of the DAS strain measurement. Thus, it is advisable to use single-mode fiber for DAS measurements whenever possible. Multi-mode fiber can be used for DAS measurements, but it usually requires additional optical hardware and does not normally provide an SNR as effective as single mode.

2.2.3. Deploying Fiber

The next determination is how the fiber will be deployed as the seismic sensor. Figure 2.1 shows three different deployment methods for DAS acquisition in a well. The retrievable fiber option uses an optical glass fiber installed inside either a wireline cable or coiled tubing. This option is by far the easiest to deploy, because it can be inserted

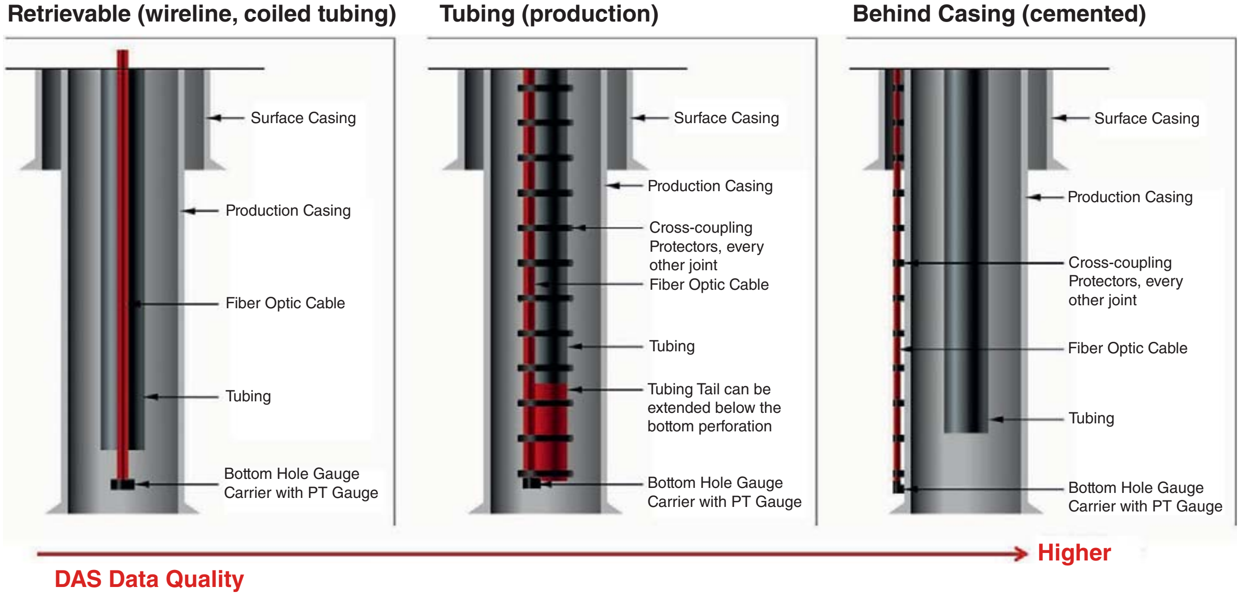

Figure 2.1 Options for acquiring DAS VSP data in a well.

into and removed from a well at any time. However, it is likely to have the lowest quality of strain measurement because the fiber is not directly coupled to the formation. A new method involves deploying a simple, disposable fiber-optic glass line into the well (Higginson et al., 2017). In addition to the coupling issue, this method could encounter depthing problems, because there is no control of the tension (thus, placement) of the fiber in the well. Another option is to strap the fiber-optic cable to production tubing; however, the highest quality comes from attaching the fiber-optic cable to the outside of the casing, and cementing the casing. For this option, the fiber-optic cable is directly coupled to the formation and has the best SNR of seismic signals propagating in the surrounding rock.

To monitor teleseismic events, existing fiber-optic telecommunication cables deployed in shallow-buried conduits could be used (Martin et al., 2017). Described in the following section, the potential issue is that the broadside response of the fiber to strain is controlled by a cosine-squared sensitivity to the angle of incidence for P waves, putting a null in the sensitivity for events arriving normal to the fiber. For yet another application, fiber-optic cables buried in shallow trenches can be used to monitor surface waves, and then interferometric means can characterize the shallow earth properties (Martin et al., 2016).

2.2.4. Handling Fiber-Optic Cables

Fiber-optic cables typically contain multiple strands of fiber-optic glass and can be included during the manufacturing of other cable types, such as wireline cables that have multiple electrical wires. Unlike conventional electrical cables, fiber-optic cables require a different handling strategy. Bends in fiber-optic cables must be minimized because a tight radius of curvature will allow the laser light trapped in the fiber to leak out of the glass core, thereby reducing the sensitivity of the strain measurements. Another important aspect is that fiber-optic connections must be made under clean conditions. Making fiber-optic connections under unclean conditions—where junction boxes are exposed to the wind, sand, dirt, and even oils from the skin—will generate significant optical losses; therefore, it is important to plan for clean areas and facilities where the optical connections can be made.

2.3. INTERROGATOR UNIT

2.3.1. Types of Interrogators

The laser that emits light pulses and the hardware measuring system to convert the backscattered light to a strain measurement are housed in the interrogator unit (IU). The dotted black line in Figure 2.2, left, shows a conceptual diagram of an IU. A pulse of light is emitted from the laser into a fiber-optic cable inside the IU. The light then encounters several optical elements inside the IU and exits using a surface cable connected to the length of fiber being used as a strain detector (e.g., in a well or shallow trench near the surface of the earth). The backscattered laser light returns from the sensing fiber and reenters the IU, where the light is routed through more optical devices, eventually encountering a receiver that converts the light into analog electrical signals that are then converted to a

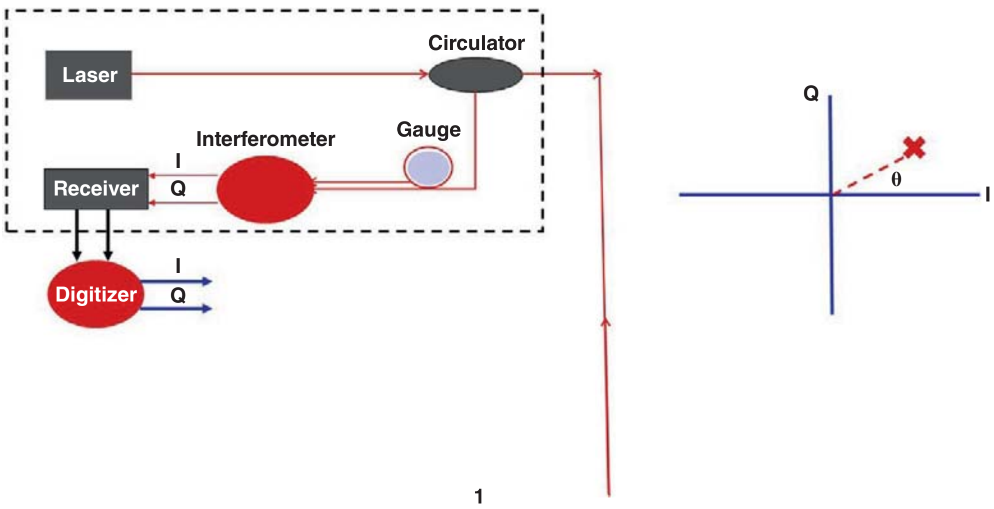

Figure 2.2 (Left) Conceptual diagram of an IU (inside the dotted black line); (right) relationship between the measurements of I and Q and the resulting extracted phase value Θ. The dotted red line represents the modulus (or length) of the I/Q vector.

digital data stream using digitizers, typically in a supporting computer system.

IUs might use several different optical designs to emit laser light into the optical fiber that converts the backscattered signals into a measurement of strain (Hartog, 2017). Practically all current hardware on the market use a differential phase method to obtain a high-fidelity and linear measurement of strain. Note that earlier technology, based only on the amplitude of the backscattered signal, did not provide a reliable measurement of strain, because the amplitude of the backscattered light was not linear with strain.

Essential to the reliable measurement of strain is the concept of a dual-pulse optical system. This methodology creates two pulses of backscattered light combined in an interferometric process to construct the phase difference between these pulses. These two pulses of light are delayed in time from each other, either at the launch path of the IU or by a time-delay loop of fiber in the receiver path of the IU. This time delay corresponds to what is called the "gauge length," the corresponding length of fiber it takes to create (half of) this time delay. Independent of the design, the effect of this time delay is to allow the system to compare the phase of the backscattered light at all points of the sensing fiber, each separated by gauge length. Figure 2.2 shows an example where the gauge is a physical loop of fiber creating a time delay of the backscattered light at the receiver path of the IU.

Figure 2.2 shows that the IU outputs are two signals—I and Q. The I signal is the interference of the direct optical path and the long optical path through the gauge, and the Q signal is created from the quadrature of the I signal. The phase of the vector spanned by the I and Q signals provides the differential phase measurement related to the strain in the fiber. Figure 2.2, right, shows how the phase is computed from the I and Q signals using:

$$\theta = arctan\left[\frac{\mathrm{Q}}{\mathrm{I}}\right] \tag{2.1}$$

The arctangent function returns a value within the phase range of $-\pi/2$ to $+\pi/2$. To obtain a continuous function of phase as a function of time, the computed phase values must be unwrapped by adding or subtracting integer multiples of π to the time series (Tribolet, 1977). The relative strain $\varepsilon(z, t)$ at each point z on the fiber at time t can be computed from this phase difference by (Equation 10, SEAFOM, 2018):

$$\varepsilon(z, t) = \theta(z, t)\frac{\lambda}{4\pi n\gamma G} \tag{2.2}$$

where λ is the wavelength of the laser light in vacuum used by the DAS interrogator, n is the refractive index of the glass, γ is the photoelastic scaling factor ($\gamma \approx 0.78$) for axial strain on silica fiber (Giallorenzi et al., 1982), and G is the gauge length. Strain rate can be computed from Equation 2.2 by taking the time derivative.

2.3.2. Synchronizing Source Information and Time Stamps

Data acquisition can generally be separated into either passive or active systems. For active systems, such as VSP and surface seismic acquisition, the firing of seismic sources is under control of the operator. In passive systems, data acquisition starts, and the desired signals (e.g., earthquakes or ambient noise) are not under our control. Regardless of the application, a reference time signal is necessary; thus, it is important for a global positioning system (GPS) time to be incorporated into the acquired data sets. For active sources, additional information is necessary, such as the origin time of the source, source signature, etc. Some systems directly record this information into the DAS data set in real time, while other systems record this information separately and combine it with DAS data later by comparing the GPS timestamps from DAS and source recording systems.

2.4. ACQUISITION PARAMETER SELECTION

2.4.1. Gauge Length

For DAS data acquisition, gauge length is among the most important choices to make. Gauge length imparts a wavenumber spectrum response that acts like an array of closely spaced single sensors. A longer gauge length decreases the usable frequency spectrum of the seismic signal; however, a long gauge length provides a better SNR because of the cancellation of random noise over the length of the gauge. Actually, the SNR, with respect to ambient (white) noise, increases as the square root of the gauge length.

Gauge length imparts notches (i.e., zeros) in the wavenumber domain according to sinc(kG), where k is the wavenumber and G is the gauge length; notch locations are at $k = n/G$, where n is the (integer) order of the notch. Because $k = 2\pi f/c$, where f is frequency and c is the apparent wave velocity, the effect of these notches depends on both frequency and apparent velocity of each wave in the seismic data.

The solid black lines in Figure 2.3 (top) show the locations of the first notch as a function of gauge length (horizontal axis) and frequency (vertical axis). Each line is associated with a specific apparent velocity that is labeled next to it, and the corresponding −20 dB point for each apparent velocity is represented by the dotted line. The area between the notch and the −20 dB point is grayed out. Looking at a 15 m gauge length, for a 500 m/s wave,

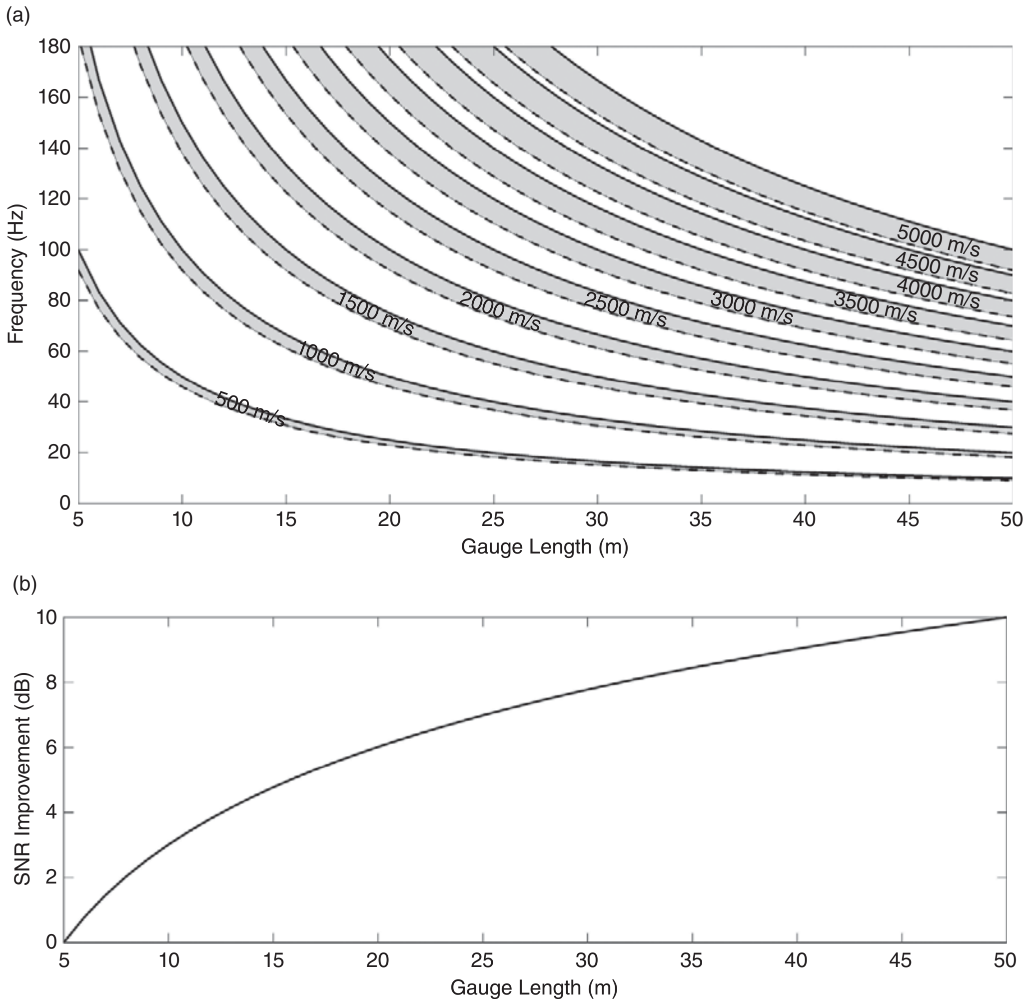

Figure 2.3 (Top) Location of first spectral notch for a range of gauge lengths; solid black line represents the spectral notch associated with the labeled velocity, and the dotted line represents the corresponding −20 dB point. (Bottom) Relative signal-to-noise improvement using different gauge lengths compared to a 5 m gauge.

the first spectral notch is located at 33 Hz, and the −20 dB point is located at 30.7 Hz. This means that, for all practical purposes, if a 15 m gauge is used, we can only effectively record waves traveling 500 m/s below 30.7 Hz; likewise, looking at a wave traveling 1000 m/s, we can only effectively record frequencies below 61.4 Hz. For waves traveling at the speed of water (1500 m/s), we are limited to frequencies under 92 Hz; however, if a 40 m gauge is used, the high frequency limits for waves traveling 500, 1000, 1500, 2000, and 2500 m/s are 11.5, 23.0, 34.5, 46.0, and 57.5 Hz, respectively.

Two trends are easily observed: (1) larger gauge lengths can be used if the apparent velocities of interest are large, and (2) spectral notches are not as limiting on the upper frequencies for small gauges. It might appear that the conclusion should be to always use a small gauge length; but, as previously mentioned, the SNR improves as the gauge length increases (Figure 2.3, bottom). The vertical axis shows the SNR improvement as compared to a 5 m gauge, in dB; thus, the improvement using a 15 m gauge is 4.8 dB, while the 40 m gauge provides 9 dB improvement. Therefore, the goal is to use as large a gauge length as possible without damaging the desired frequency content of the seismic waves being recorded.

For earthquake-monitoring applications where the frequency content is typically much less than 2 Hz, the notches will not affect the recorded spectrum, and thus a long gauge is appropriate. For a Gulf of Mexico deepwater VSP, it could be that seismic energy reflecting from the reservoir has a maximum frequency content of 20 Hz because of the earth's attenuation. Figure 2.3 (top) shows that any gauge length from 5 to 50 m can capture all seismic waves faster than 1000 m/s; thus, it might be worth the added SNR benefits to use a long gauge. However, if, instead, the application is shallow and unconsolidated formations with extremely slow P- and S-waves, and a high-frequency source is used, then an extremely short gauge should be used at the expense of SNR.

2.4.2. Sampling Rate

The IU sends a pulse of light into the fiber with a sampling rate of 10 kHz or higher. The time between these pulses are set so that the light has time to reach the end of the fiber and return as backscattered energy to the photodetector in the IU. The longer the sensing fiber, the slower this sampling rate should be, so that the pulse of light has the necessary time to return to the IU without interfering with another pulse.

2.4.3. Pulse Width

Pulse width is another important parameter to choose. The pulse of light sent by the IU into the fiber should be limited in time duration so that it does not impede the functionality of the interferometer. Strain measurement is created from the interference of the pulse of light going through both the direct (short) path and the long path through the gauge length delay coil. The time duration of the pulse should be chosen so that backscattered energy from the short path does not interfere or overlap with the time window containing the backscatter energy traveling along the long path. Figure 2.4 shows the suggested pulse widths associated with gauge lengths. The value of using a long pulse width as compared to a short one is that more light enters the fiber, and an improved SNR is obtained; however, if the pulse width used is too long so that the time footprint of the pulse is longer than the gauge length, the quality of the strain measurement drops.

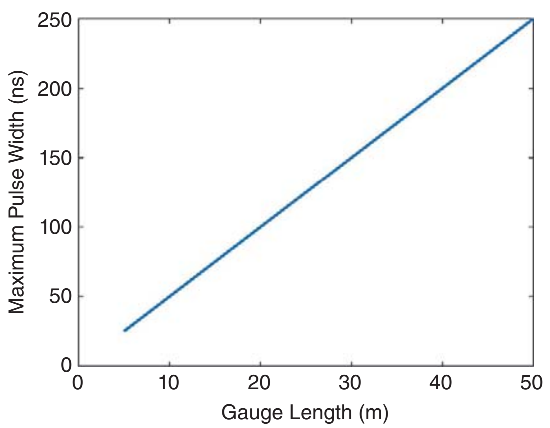

Figure 2.4 Recommended pulse width as a function of gauge length.

2.5. PREPROCESSING ISSUES

2.5.1. Fading

One unique property of all DAS data, compared to conventional seismic data, is the occurrence of channel fading, which is also called "vertical noise" because it appears as vertical stripes on a record where time is plotted on the vertical axis and channel number (or depth) on the horizontal axis. As discussed in the IU section, relative strain data are computed from the I and Q traces. The stability of extracting the phase term using Equation 2.1 depends upon the signal fidelity of both the I and Q traces. Because of the interaction of the backscattered light created from the distribution of random scattering sites in the fiber, there are occasions when the intensity of the backscattered light is low, causing the length (modulus) of the I/Q vector to be comparatively small in numerical value (Figure 2.2, right) and thus more subject to noise. This, in turn, makes taking the arctangent of Q/I to become extremely noisy. While the computation of the arctangent is stable, the phase-unwrapping algorithm is unable to determine the appropriate value of π to add to the phase to create a continuous signal, creating unexpected jumps in phase at these times on the trace.

The occurrence of fading changes in both time and distance along the fiber; for example, extremely small changes in the fiber's temperature move the scattering sites and cause temporary dimming of the backscattered signal at new locations. It has been observed (Ellmauthaler et al., 2016) that approximately 3% of the fiber is faded at any given moment; for example, if the sensing fiber has 5,000 channels, that translates to as many as 150 channels exhibiting some form of fading. However, even during small time intervals of approximately 1 min, the fading on the affected channels will move. Thus, if it is possible to repeat the source and take multiple measurements, it is easy to obtain reliable data eventually without fading.

Figure 2.5 shows simulated fading on a single channel. The top panel shows the I trace (blue) and Q trace (orange). In addition to the desired seismic signal, a temperature drift was simulated by a long period trend. Notice that, between 2 and 2.25 sec, the amplitudes of both I and Q traces diminish toward zero. The middle panel shows the resulting relative strain trace computed from the I and Q traces. The relative strain trace is continuous and smooth before and after this time interval. However, during the dimmed interval, it is evident that the phase-unwrapping algorithm has failed to unwrap the

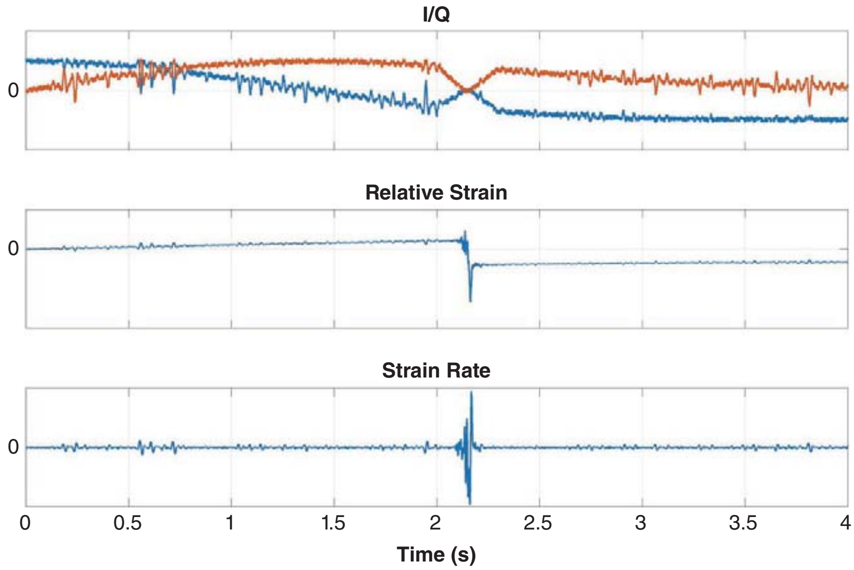

Figure 2.5 (Top) I (blue) and Q (orange) traces; (middle) corresponding relative strain; (bottom) strain rate.

phase properly, and multiple non-physical jumps in the strain trace occur. Notice that the temperature drift shows up as a background "ramp" on the relative strain data. The bottom panel shows the strain rate trace, which is simply the time derivative of the relative strain trace. Jumps in the relative strain trace become negative and positive spikes in the strain rate trace. The strain rate data is not as sensitive to the temperature drift since the time derivative is similar to a low-cut filter and has greatly reduced the long period temperature ramp.

It is difficult to perform conventional processing and analysis of the resulting seismic data without addressing these faded channels in either the relative strain or strain rate data. Figure 2.6 shows an example of strain rate DAS VSP data collected using a vibrator source with a 12 sec sweep and 4 sec listen time. The top two panels for Figure 2.6 show an uncorrelated trace without and with fading, respectively. Notice the spikes between 10 and 12 sec on the faded trace. The bottom two panels on Figure 2.6 show the corresponding correlated traces; it is evident that the spikes in the faded trace have affected the entire trace because of the correlation process. For land data, where it is possible to acquire multiple sweeps at the same shot point, the spikes caused by fading can be mitigated using a weighted stacking of the sweeps, which minimizes large amplitude spikes. For marine data, where typically only one "pop" is acquired at each shot point, a despiking algorithm can be used to remove the faded portions of the trace before further processing and analysis.

In addition to weighted stacking of the sweeps, another approach can be used when acquiring data. The response of the fiber to fading depends on the frequency of the laser light used. If two or more different frequencies of light are used to simultaneously acquire the same strain measurements in the fiber, the locations of the fading will most likely be different because of the disparate frequency sensitivities of the light to the scattering points in the fiber. Figure 2.7 shows the VSP strain rate data sets acquired using two frequencies. Figures 2.7a and 2.7b show the records using frequencies 1 and 2, respectively—notice that the locations of the fading are different between the two records. Figure 2.7c shows the result of the weighted stacking of data from two frequencies. A significant reduction in the number of faded channels can be observed by combining data acquired with more than one frequency of light. For clarity, Figure 2.7d shows the three traces (frequency 1, frequency 2, and weighted stack) for each of two channel locations (109 and 221). For channel 109, the frequency 1 data (in red) is faded; and, for channel 221, the frequency 2 data (in red) is faded. Thus, the weighted stack (in black) favors the non-faded trace (in blue).

2.5.2. Common-Mode Noise

The entire length of fiber from the IU to the end of the sensing fiber responds to any sound-imparting strain on the optical fiber; further, the IU is sensitive to sound. All sounds hitting the IU impose an unwanted signal simultaneously on all data channels. This unwanted signal is called "common-mode noise" or "horizontal noise," because it appears as horizontal streaks on the data record. Therefore, it is important to consider keeping the area surrounding the IU quiet and, ideally, isolated from

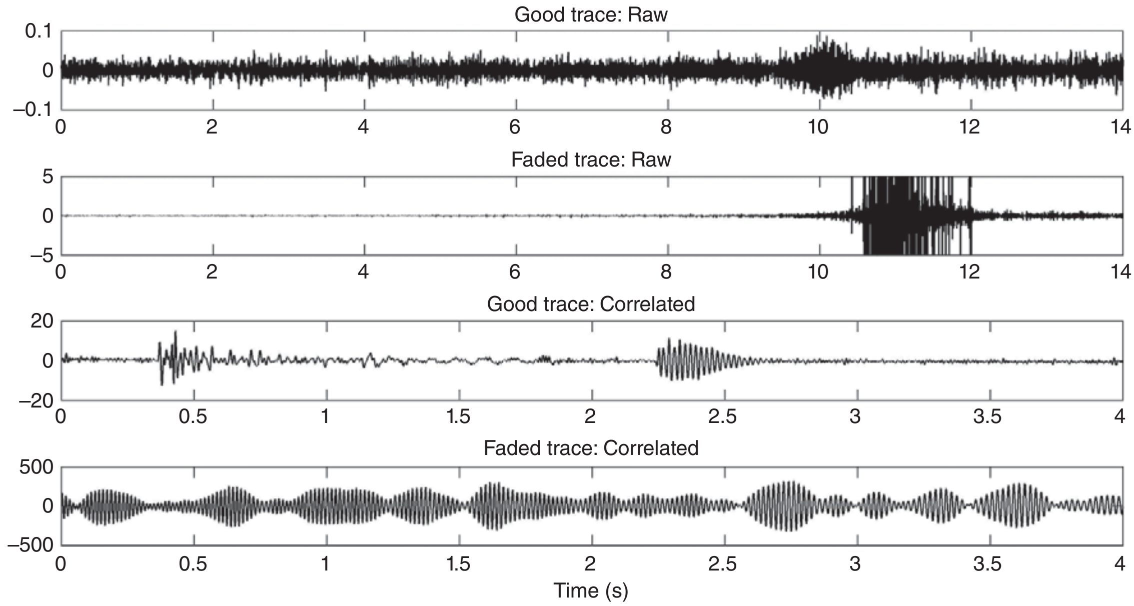

Figure 2.6 Strain rate VSP data collected with a vibrator – (top row) uncorrelated trace without fading; (second row) uncorrelated trace with fading between 10 and 12 s; (third row) corresponding correlated trace without fading; and (fourth row) corresponding correlated trace with fading.

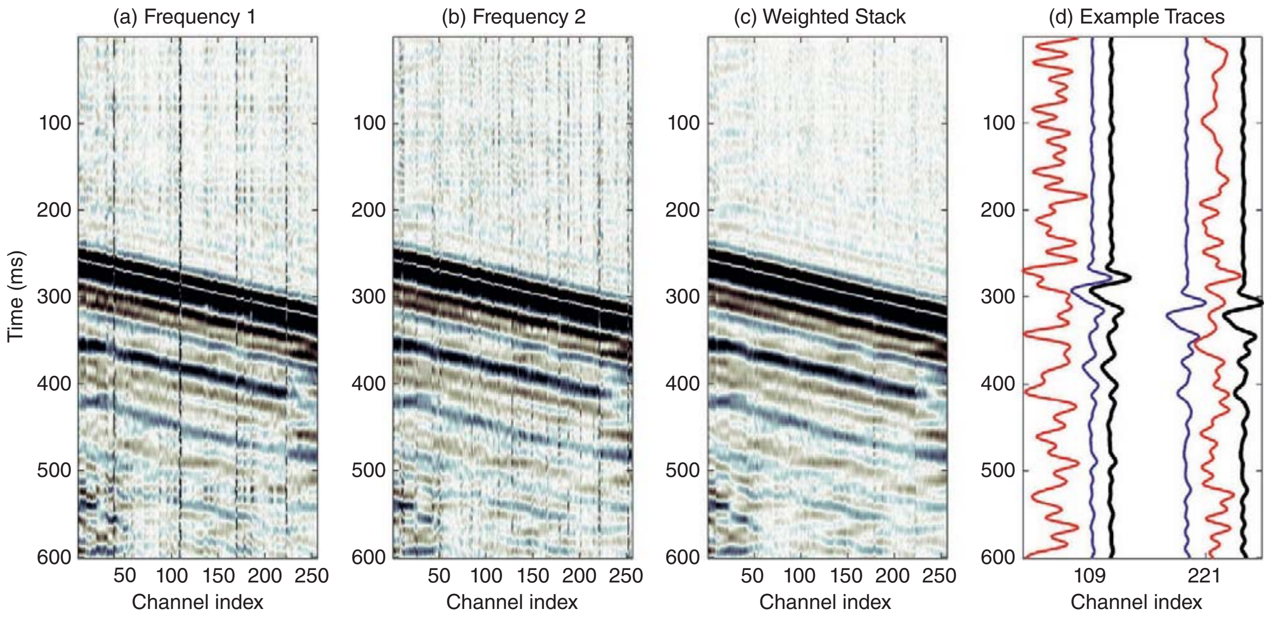

Figure 2.7 (a) single sweep using Frequency 1 – note the prominent fading at channels 38, 109, 169, and 223; (b) single sweep using Frequency 2 – note the prominent fading at channels 9, 128, 221, and 252; (c) weighted stack of data from both frequencies – note the strong reduction in fading; and (d) corresponding traces for channels 109 and 221, where the red trace is the faded trace, the blue is not faded, and the black trace is the weighted stack.

ground motion using a vibration-isolation table. Even with sound isolation, it is still likely that the derived strain rate data will exhibit common-mode noise.

Figure 2.8 (left) shows a record exhibiting common-mode noise, which is the horizontal noise that stripes across all channels. Figure 2.8 (right) shows the same record after signal processing has been applied to remove the common-mode noise. An estimate of the noise can be created by stacking together all the traces in the record. As long as the actual desired seismic signal is changing

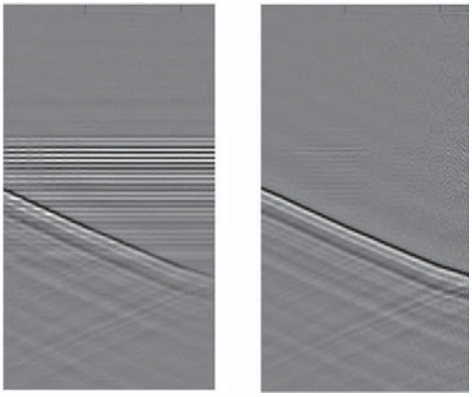

Figure 2.8 (Left) Strain rate record showing common-mode noise; (right) same record following common-mode noise removal.

significantly across the traces, the seismic signal will cancel itself, and only the common-mode noise will remain in the stack. This stacked trace, normalized by the number of traces in the record, is then subtracted from each trace in the record to obtain the denoised record.

2.5.3. Spatial Calibration of Channels

For conventional seismic acquisition methodologies using geophones, accelerometers, or seismometers, the location of each sensor is determined by conventional surveying techniques for surface instruments or wireline depth measurement technology for instruments deployed in wells. Fiber-optic cables pose a new challenge because the glass is distributed continuously over the entire cable, and the location of each measured channel is not specifically recorded, even though the trajectory of the cable might be surveyed accurately. A feature of fiber-optic cables is that a longer length of glass fiber is deliberately overly stuffed into its protective outer cable, so the glass fiber does not break when the cable is put under tension and stretched.

To first order, the location of each channel of DAS data can be estimated by the time of flight of the laser light. The velocity v of light for each type of fiber is fairly accurately known. The delay between the time the laser light is pulsed into the fiber and the time the backscattered light reaches the detector is known as the "time of flight" τ. This is the two-way time it takes the light to leave the laser, backscatter off a point in the fiber, and return to the detector; thus, the distance z along the fiber where the backscattering point is located is given by:

$$z = \tau \, v/2 \tag{2.3}$$

Other factors to consider are the lengths of optical cabling inside the IU and the surface cables connecting the IU to the beginning of the optical cable meant as the sensing cable, either in a well or buried in a trench or conduit. Additionally, it is possible the sensing cable might have been cut and spliced with extra cable inserted but not accounted for. These factors, including the potential uncertainty of the velocity of light in the fiber, make Equation 2.3 only an approximate solution to determining the depth or location of each DAS channel of data.

A practical solution to the spatial calibration of each channel issue is to use control points along the fiber where the location and/or depth of that point is known; for example, the location of the end of the fiber is recorded by the cable installer. Optically, it is easy to detect the end of the fiber from the lack of backscattered energy returning to the detector after a light pulse is emitted into the cable. By looking at the recorded DAS strain or strain rate data, the last channel after which there is no coherent data is easy to select as the end of the fiber and therefore can be mapped to the known location of the end of the fiber. The beginning of the sensing fiber can be located by a "tap" test at, for example, the wellhead for well-based applications, or at the location where the surface cable connects to the sensing fiber in a buried trench or telecommunications conduit. For shallow-buried fiber cables, additional tap tests can be combined with GPS measurements to obtain an accurate calibration of location of the channels.

Alternatively, an optical time domain reflectometer (OTDR) can be used to detect the end of the fiber and points along the fiber where it has been spliced. An OTDR detects the overall health of a fiber by estimating the light attenuation in the fiber, and it detect points where there are large losses, such as at splice points and cable terminations. If the cable installer recorded splice point locations (e.g., at the wellhead or at locations of pressure or temperature sensors), then they can be used as additional known locations along the fiber associated with the corresponding channels in DAS data. The depth or location along the fiber of each intermediate channel can then be interpolated between the known control points.

2.6. PROCESSING ISSUES

2.6.1. Angle of Incidence

The fiber's response to P-waves is somewhat similar to a single-component geophone. Bakku (2015) compared the far-field P-wave response for geophones ($\cos\Theta$) to optical fiber ($\cos^2\Theta$), where Θ is the angle of incidence of the wave hitting the fiber; 90° indicates normal to the fiber, and 0° is along the axial direction of the fiber. The solid line in Figure 2.9 (left) shows the response for a geophone

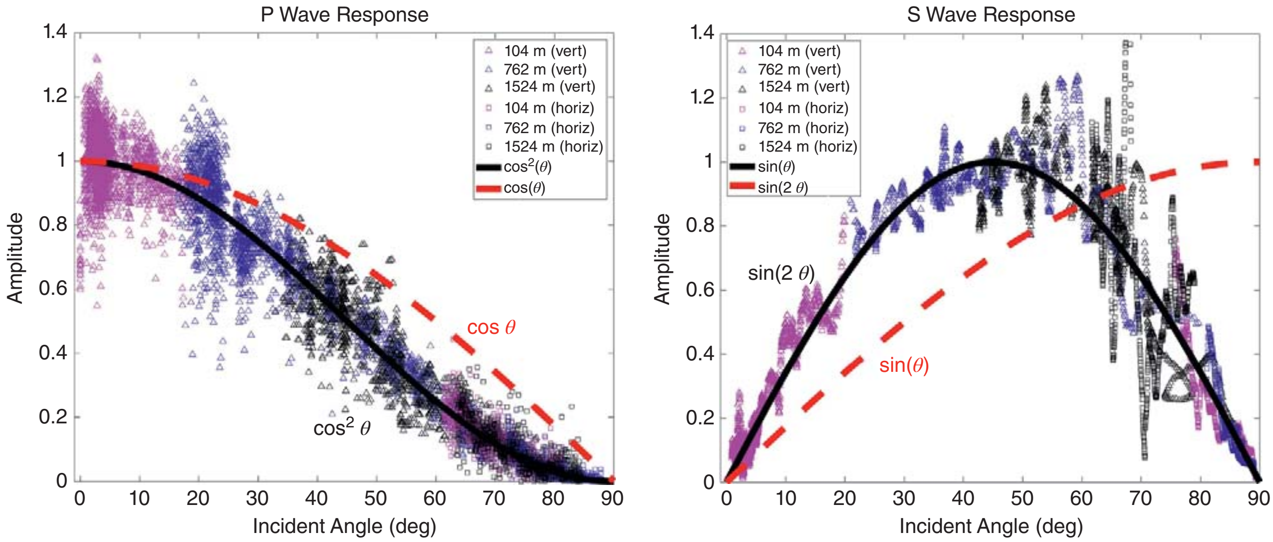

Figure 2.9 Angular response of the fiber to *P* waves (left) and *S* waves (right). The lines show the theoretical response for DAS (solid) and geophones (dotted), and the symbols show the extracted amplitude response from a field VSP data set. Source: Wu et al. (2017).

oriented in the axial direction of the fiber, and the dashed line shows the fiber response for P-waves. They are identical for normal and perpendicular angles but differ at intermediate angles, with the largest difference at 45°. Figure 2.9 (right) shows the far-field S-wave response ($\sin 2\Theta$) of the fiber by the solid line and the S-wave response ($\sin\Theta$) of a geophone oriented along the axial direction of the fiber by the dotted line. The response for S-waves is extremely different because the maximum response for the fiber occurs at 45°, as compared to 90° for the geophone. At 90° the DAS S-wave response is zero. This is because the S wave is merely translating the cable up and down and does not extend or compress the fiber at the normal (90°) angle to the fiber. Individual data points in Figure 2.9 come from a field example of a VSP that matches the theory.

2.6.2. Single Component vs. Three Components

A challenge with DAS data sets is that there is only a single component detecting strain along the axial length of the fiber. Conventional VSP and earthquake seismic recordings are typically acquired with three components (3C): one vertical and two orthogonal horizontal components. (Exploration surface seismic is normally acquired with only vertical component geophones.) While there are 3C optical sensors available that can be spliced into a fiber-optic cable, they are point sensors not directly related to DAS measurements. Research is ongoing to create 3C measurements using sets of helically wound fibers in a single cable; currently, they are not commercially available (Ning & Sava, 2018). However, this limitation restricts the ability of DAS data sets to locate the azimuthal direction of seismic waves hitting the fiber; in this way, it is quite similar to single-component geophone data sets.

2.7. DATA QUALITY: DAS VS. GEOPHONE COMPARISONS

2.7.1. Lower Intrinsic SNR and Higher Channel Density

The intrinsic SNR level of DAS data sets is lower than the corresponding geophone data sets because of, in part, the noise sources previously listed. However, in addition to those noise sources, there is an ambient noise floor present in the DAS recording system. One method to help improve this is to make repeated measurements and stack them together to increase the SNR. Another option is to use the increased number of data channels, which are typically every meter (although some systems record channels at less than a meter and others record every few meters). In contrast with conventional recording using widely spaced sensors, DAS data sets allow the ability to use neighboring channels to help improve the SNR by use of the redundancy of this information (Cheng et al., 2019). Typically, DAS channel spacing is considerably smaller than the seismic wavelengths to be measured; therefore, we do not expect rapid changes for the signal from channel to channel, allowing multi-trace filters (e.g., median filters, running mean filters, etc.) to help improve the SNR. In addition, wave types (e.g. tube waves and ground roll) typically aliased in widely spaced sensor data can be more easily filtered with tools such as f-k filtering acquired using DAS.

2.7.2. Strain, Strain Rate, and Particle Velocity

Geoscientists are accustomed to working with geophone and seismometer data where the measurement is displacement, velocity, and acceleration—while strain and strain rate data not as commonly used. Daley et al. (2016) described one method to convert from strain rate to an equivalent geophone response. Here, we generalize the process. Figure 2.10 shows the relationship between the various products that can be produced from a DAS data set. The native measurement from an IU is the phase from Equation 2.1. From a simple scalar multiplication, the relative strain from Equation 2.2 can be obtained. Converting the relative strain to strain rate requires a simple time derivative to be applied; to convert the strain rate data to velocity requires a spatial integration. One might think that velocity is the final destination for our processing, but, if it is necessary to compare it to geophone data, then the instrument response of the geophone should be included as the last step to simulate geophone data. Further, it is possible to go backward from the simulated geophone response, or actual geophone data, to any of the previous products using the inverse operation.

There have been many published comparisons of DAS and geophone data sets (Mestrayer et al., 2011; Willis et al., 2016; Olofsson & Martinez 2017; Wu et al., 2017). Favorable geophone data comparisons were published using both strain rate and strain rate converted to geophone response. Using relative strain data appears quite attractive because it is much richer in low frequencies. Recall that the time derivative to convert relative strain to strain rate is a linear ramp function in the frequency domain, significantly reducing low frequencies and boosting high frequencies. However, as observed in Figure 2.5, relative strain data are quite sensitive to the temperature drift that often swamps in amplitude the desired seismic signal. From a practical point of view, if the goal of acquiring DAS data is to obtain geophone-like data, then using strain rate or strain rate converted to geophone response is attractive. However, if the goal is low-frequency deformation or earthquake measurements, then it is possible that, with careful filtering of the relative strain data, it would be the best option.

2.8. SUMMARY

This chapter discussed many unique aspects of acquiring DAS data. If possible, it is preferable to acquire data using single-mode instead of multi-mode fiber. Better SNR data are obtained with permanently cemented fiber cable, but it is still possible to obtain fit-for-purpose data using retrievable fiber deployment methods. Field engineers need to be trained to keep the fiber-optic connections clean and the cable unbent. To obtain reliable DAS data, the IU should employ a differential phase scheme—nearly all current commercial systems use this method. It is important to ensure the timing information is preserved with DAS data; thus, GPS timing units will require appropriate access to an external antenna.

Gauge length continues to be an important decision. As discussed, a short gauge allows full fidelity of the resulting seismic signal, but a long gauge increases the SNR. As such, it is necessary to review the gauge length for the required data bandwidth. Pulse width can be easily chosen to match the gauge length to obtain the best illumination of the fiber. Fading is a natural feature of DAS acquisition and should always be addressed with both hardware and software. IUs using more than one light frequency are intrinsically better at reducing fading. Post-acquisition processing can address fading, particularly for land data sets where multiple vibrator sweeps are collected. Common-mode noise is caused by ambient sounds around the IU; therefore, keeping this area quiet helps prevent it. Further, simple post-acquisition processing will remove most of it.

Determining the appropriate depth or location of each DAS channel is important for the accuracy of the resulting DAS products. One improved method is to use known locations as calibration points with the interleaving channels interpolated from them. The angle-of-incidence response of the fiber is different from that of geophones. It is important to first determine its effect, and then, where appropriate, remove it. DAS data quality is intrinsically lower than that from geophones; however, because there

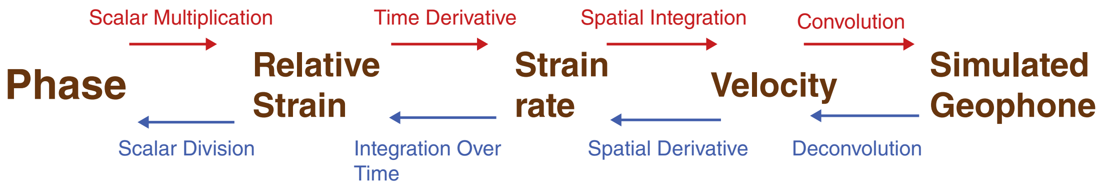

Figure 2.10 Relationship among the various products created from a DAS data set.

is frequently one or two orders of magnitude more density of information, the signal quality can be greatly improved. Finally, while the native measurement of a DAS system is phase, it can be converted to relative strain, strain rate, particle velocity, and an equivalent geophone response.

REFERENCES

Bakku, S. K. (2015). Fracture characterization from seismic measurements in a borehole (PhD thesis). Cambridge, MA: MIT.

Barfoot, D. A. (2013). *Efficient vertical seismic profiling using fiber-optic distributed acoustic sensing and real-time processing*. Paper presented at EAGE Borehole Seismic Workshop II, Malta. doi: 10.3997/2214-4609.20142554

Chen, J., Ning, J., Chen, W., Wang, X., Wang, W., & Zhang, G. (2019). Distributed acoustic sensing coupling noise removal based on sparse optimization. *Interpretation*, *7*(2). doi: 10.1190/INT-2018-0080.1

Cheng, D., Zhao, X., Willis, M.E., Zhou, R., & Quinn, D. (2019). *Receiver decimation and impact on DAS VSP processing quality*. Paper presented at EAGE Workshop on Borehole Geophysics, The Hague. doi.org/10.3997/2214-4609.2019X604020

Daley, T. M., Miller, D. E., Dodds, K., Cook, P., & Freifield, B. M. (2016). Field testing of modular borehole monitoring with simultaneous distributed acoustic sensing and geophone vertical seismic profiles at Citronelle, Alabama. *Geophysical Prospecting*, *64*(5), 1318–1334. doi: 10.1111/1365-2478.12324.

Ellmauthaler, A., Willis, M., Wu, X., & Barfoot, D. (2016). *Factors affecting the quality of DAS VSP data*. Paper presented at SEG Distributed Acoustic Sensing Workshop.

Ellmauthaler, A., Willis, M., Wu, X., & LeBlanc, M. (2017). *Noise sources in fiber-optic distributed acoustic sensing VSP data*. Paper presented at 79th EAGE Conference and Exhibition, Paris, France. doi: 10.3997/2214-4609.201700515

Ellmauthaler, A., Seabrook, B. C., Wilson, G. A., Maida, J., Bush, J., LeBlanc, M., et al. (2020) Distributed acoustic sensing in subsea wells. *The Leading Edge (Nov)*, *39*(11), 801. doi.org/10.1190/tle39110801.1

Giallorenzi, T. G., Bucaro, J. A., Dandridge, A., Sigel, G. H., Cole, J. H., Rashleigh, S. C., & Priest R. G. (1982). Optical fiber sensor technology. *IEEE Transactions on Microwave Theory and Techniques*, *30*(4), 472–511. doi: 10.1109/TMTT.1982.1131089

Hartog, A. H. (2017). *An introduction to distributed optical fibre sensors*. Boca Raton, FL: CRC Press.

Higginson, P., Purkis, D., & Webster, M. (2017). *Advancing the application of downhole fiber optics with a novel low cost disposable deployment method*. Paper presented at SPE Offshore Europe Conference & Exhibition. SPE-186124-MS. doi: 10.2118/186124-MS

Hull, R., Meek, R., Bello, H., & Miller, D. (2017). *Case history of DAS fiber-based microseismic and strain data, monitoring horizontal hydraulic stimulations using various tools to highlight physical deformation processes*. Paper presented at Unconventional Resources Technology Conference, Austin, Texas. URTEC-2695282-MS. doi: 10.15530/URTEC-2017-2695282

Jin, G., & Roy, B. (2017). Hydraulic-fracture geometry characterization using low-frequency DAS signal. *The Leading Edge*, *36*(12): 975–980. doi: 10.1190/tle36120975.1

Martin, E. R., Castillo, C. M., Cole, S., Sawasdee, P. S., Yuan, S., Clapp, R., et al. (2017). Seismic monitoring leveraging existing telecom infrastructure at the SDASA: Active, passive, and ambient-noise analysis. *The Leading Edge*, *36*(12): 1025–1031. doi: 10.1190/tle36121025.1

Martin, E. R., Lindsey, N. J., Dou, S., Ajo-Franklin, J. B., Wagner, A., Bjella, K., et al. (2016). *Interferometry of a roadside DAS array in Fairbanks, AK*. Paper presented at SEG International Exposition and 86th Annual Meeting. doi: 10.1190/segam2016-13963708.1

Mateeva, A., Lopez, J., Chalenski, D., Tatanova, M., Zwartjes, P., Yang, Z., et al. (2017). 4D DAS VSP as a tool for frequent seismic monitoring in deep water. *The Leading Edge*, *36*(12). doi: 10.1190/tle36120995.1

Mestrayer, J., Cox, B., Wills, P., Kiyashchenko, D., Lopez, J., Costello, M., et al. (2011). *Field trials of distributed acoustic sensing for geophysical monitoring*. Paper presented at 2011 SEG Annual Meeting. SEG-2011-4253. doi: 10.1190/1.3628095

Ning, I. L. C., & Sava, P. (2018). High-resolution multicomponent distributed acoustic sensing, *Geophysical Prospecting*, *66*(6), 1111–1122. doi: 10.1111/1365-2478.12634

Olofsson, B., & Martinez, A. (2017). Validation of DAS data integrity against standard geophones – DAS field test at Aquistore site. *The Leading Edge*, *36*(12). doi: 10.1190/tle.36120981.1

SEAFOM. (2018). DAS Parameter Definitions and Tests, Measuring Sensor Performance Document – 02 (SEAFOM MSP-02).

Tribolet, J. (1977). A new phase unwrapping algorithm. *IEEE Transactions on Acoustics, Speech, and Signal Processing*, *25* (2), 170–177. doi: 10.1109/TASSP.1977.1162923.

Willis, M. E., Barfoot, D., Ellmauthaler, A., Wu, X., Barrios, O., Erdemir, C., et al. (2016). Quantitative quality of distributed acoustic sensing vertical seismic profile data. *The Leading Edge*, *35*(7). doi: 10.1190/tle35070605.1

Willis, M. E., Palacios, W., Ellmauthaler, A., & Zhao, X. (2020). *Mitigation of zigzag noise on DAS VSP records acquired in vertical wells*. Paper presented at 2020 EAGE Annual Conference & Exhibition Online. doi.org/10.3997/2214-4609.202011089

Wu, X., Willis, M. E., Palacios, W., Ellmauthaler, A., Barrios, O., Shaw, S., & Quinn, D. (2017). Compressional- and shear-wave studies of distributed acoustic sensing acquired vertical seismic profile data. *The Leading Edge*, *36*(12), 987–993. doi: 10.1190/tle36120987.1

3

Distributed Microstructured Optical Fiber (DMOF) Based Ultrahigh Sensitive Distributed Acoustic Sensing (DAS) for Borehole Seismic Surveys

Qizhen Sun[1], Zhijun Yan[1], Hao Li[1], Cunzheng Fan[1], Fan Ai[1], Wei Zhang[1], Xiaolei Li[2], Deming Liu[1], Fei Li[3], and Gang Yu[3]

ABSTRACT

Distributed acoustic sensing (DAS) can record acoustic or seismic waves along the optical fiber with advantages of long distance, short operation time, full well coverage, and cost saving, which has important significance in borehole seismic surveys. By designing and fabricating a distributed microstructured optical fiber (DMOF) with successive longitudinal microstructures, the signal-to-noise ratio (SNR) of the Rayleigh backscattering light is enhanced and random interference fading is greatly eliminated, which are beneficial to improve the sensing performance of the system. Combined with coherent detection and phase demodulation, a DMOF-based fiber optic DAS system with a wide frequency bandwidth from 0.01 Hz to 60 kHz and an ultrahigh strain resolution of 3.4 $p\varepsilon/\sqrt{Hz}$ around 10 Hz was explored and demonstrated. By employing the DMOF-DAS system as data acquisition (DAQ) equipment (interrogator), zero-offset vertical seismic profile (VSP), offset VSP, and walkaway VSP test surveys were conducted in two oil fields in China, respectively, with DMOF cables deployed inside a water-filled borehole and cemented outside the casing, respectively. The good quality VSP data with a high SNR, correct amplitude, and clear upgoing/downgoing waves proved that the DMOF-DAS system could be a competitive alternative to geophone arrays for the acquisition of borehole seismic data.

3.1. INTRODUCTION

Various fields, including seismic recording (Ni et al., 2002; Ni et al., 2005), resource exploration (Jagannathan et al., 2009), hydrocarbon production (Yamate et al., 2017), security surveillance (Harma et al., 2005), and subsurface structure imaging (Michaels et al., 2005), greatly rely on acoustic sensing or seismic survey techniques. These applications have promoted the development of long-distance DAS technology. Specifically, a full well coverage downhole seismic array can be used to provide enhanced VSP imaging and monitor fluid and pressure changes in hydrocarbon production fields. High-resolution reservoir structure imaging and time-lapse reservoir monitoring provide us with critical information to guide the placement of production and water-injection wells in high-value

[1]*School of Optical and Electronic Information, National Engineering Laboratory for Next Generation Internet Access System, Huazhong University of Science and Technology, Wuhan, China*

[2]*OVLINK Inc., Wuhan, China*

[3]*BGP Inc., China National Petroleum Corporation, Zhuozhou, China*

Distributed Acoustic Sensing in Geophysics: Methods and Applications, Geophysical Monograph 268, First Edition.
Edited by Yingping Li, Martin Karrenbach, and Jonathan B. Ajo-Franklin.

DOI:10.1002/9781119521808.ch03

reservoirs. However, the active and electrical characteristics of traditional downhole seismic sensors (geophones) limit the practical applications in harsh environments, such as high pressure and high temperature.

Compared to a traditional VSP survey using a downhole three-component (3C) geophone array, the fiber optic DAS system (Jousset et al., 2018) uses only one single-mode optical fiber to achieve the same objective as a downhole geophone array, which demodulates the acoustic signal acting on the long-distance sensing fiber, through detecting the phase changes of the Rayleigh backscattering light from different positions along the fiber (Masoudi et al., 2013), to map the seismic signal distribution along the fiber. Because of the benefits of the passive sensing property, simple single-mode fiber (SMF) configuration, light weight, and high adaptability to harsh environments, the fiber optic DAS system achieves signal "transferring" and "sensing" simultaneously in one fiber and then provides much more convenience for downhole deployment and operation. Particularly, massive information along the full borehole without any dead zone can be acquired by using the fiber optic DAS system.

Recently, the fiber optic DAS system is increasingly being recognized as an alternative to geophone arrays for the acquisition of borehole seismic data. Recording seismic data using the fiber optic DAS system instead of a downhole geophone array has distinct advantages, especially for VSP surveys. The fiber optic cable covers the entire well, and a full well VSP data can be recorded with a single shot. Wells can be retrofitted with fiber optic cables by clamping them on tubing (Follett et al., 2014), pumping them inside tubing (Mateeva et al., 2014), using hybrid fiber optic wireline cables inside the casing (Frignet & Hartog, 2014), or cementing outside the casing. Specifically, in wells with preexisting optical cables for temperature or pressure measurements, DAS on demand or time-lapse VSPs can be acquired without well intervention (Mateeva et al., 2012, 2014). For practical applications, several researchers adopted the fiber optic DAS to realize an in-well and geophysical monitoring. VSP data in two field trials in Canada and the United States were recorded from the entire length of wellhead to tubing design (TD) (up to 4 km) (Mestayer et al., 2011). Molenaar et al. (2012) reported an exploration and production downhole field trial of fiber optic DAS in a tight gas well. Daley et al. (2013) also utilized fiber optic DAS to realize subsurface seismic monitoring.

Most fiber optic DAS systems measure the phase change of Rayleigh backscattering light in the fiber to record the acoustic or seismic wave. Assisted with demodulation techniques, including optical coherent detection, 3×3 coupler detection, and phase-generated carrier (PGC) detection, DAS systems based on optical time domain reflectometry (OTDR) and optical frequency domain reflectometry (OFDR) are constructed. Wang et al. (2015) proposed a novel fiber optic DAS technique based on phase extraction from a time-gated fiber OFDR. The sensing distance reaches 40 km with a resolution of 3.5 m, and the dynamic signal with a frequency of up to 600 Hz is detectable. In 2017, He et al. (2017) realized a DAS with a multievent waveform recovery ability from 20 Hz to 25 kHz with a dual-pulse phase OTDR. While the sensing distance is only about 400 m with a resolution of 20 m, the strain resolution is about 20 nε. Then, Chen et al. (2017) proposed a polarization-independent fiber optic DAS along the 10-km-long fiber with a spatial resolution of 5 m, and specifically the strain resolution reaches 245 pε over 100 Hz. However, the noise floor in infrasonic range is much higher, which is ascribed to the weak and random Rayleigh backscattering light in the SMF (Martins et al., 2013). To enhance the SNR of the backscattering sensing light, a highly Ge-doped fiber (Loranger et al., 2015), ultraviolet (UV) exposure of a hydrogen-loaded fiber (Loranger et al., 2015), the lumped Rayleigh reflectors (Gabai et al., 2017), and FC/PC connectors (Loranger et al., 2015) inserted in the fiber have been demonstrated to be effective. However, these methods also increase transmission loss, obviously working against the long-distance DAS. Hence, a novel sensing fiber with a high backscattering SNR and low transmission loss is desirable for the fiber optic DAS system. Moreover, the measurement resolution, response bandwidth, and long-term stability still need to be further improved.

In this chapter, we propose and demonstrate a DMOF-based ultrahigh sensitive DAS system and its applications in a borehole seismic survey. By introducing longitudinal microstructures as the local scatters along the fiber, the SNR of the backscattering light is greatly enhanced. Theoretical analysis proves that the sensing signal can keep stable both in time and spatial domains, ensuring high-resolution and high-stability measurement. Assisted by a coherent detection and differential sensing mechanism, a prototype of the DMOF-DAS system is assembled. Experimental results with a wide frequency range from 0.01 Hz to 60 kHz and an ultrahigh strain resolution of 3.4 pε/$\sqrt{\text{Hz}}$ around 10 Hz are achieved. Moreover, the field tests for VSP surveys demonstrate the excellent performance of the DMOF-DAS system and great potential applications for borehole seismic surveys.

3.2. PRINCIPLES AND METHODS OF DMOF-DAS

3.2.1. Principles of DAS Using Optical Fiber

Fiber optic DAS is an optoelectronic system that records the true acoustic or seismic signal continuously along the sensing fiber that can be tens of kilometers long. As described in Figure 3.1, when a pulse of light travels down an optical fiber, the backscattering light generates and then returns to the sensor unit. The optical fiber, affected by the localized acoustic or seismic signal along the fiber axis, will deform due to the photoelastic effect. The fiber length changes from L to $L \pm \Delta L$, resulting in the phase change of the scattering light transmitted in the optical fiber, which is essentially a sensing of the strain change along the optical fiber. Then the acoustic or seismic signal along the wave-affected optical fiber could be retrieved from the phase demodulation. Further, by recording the returning backscattering signal against time, a measurement of the acoustic or seismic wave field all along the fiber can be determined.

In general, although the fiber optic DAS system has achieved good performance and wide practical applications, most techniques utilize the SMF as the sensing element, which is mainly based on various spontaneous scattering effects in the fiber. However, the intensity of backscattering light is very low. For example, the Rayleigh backscattering light makes up 98% of the backscattering light while its scattering coefficient is only −55 dB, and the Brillion scattering coefficient is about 30 dB less than Rayleigh scattering. The weak Rayleigh light greatly lowers the SNR, and the interference between different scatters induces fading points randomly along the optical fiber, which prevents the ultrahigh precision and accuracy of fiber optic DAS measurement. And also, the distance-dependent SNR degradation leads to nonuniform performance along the long-distance fiber. Hence, high SNR and high stability are two important issues in the fiber optic DAS system.

3.2.2. Concept and Characteristics of DMOF

To enhance the SNR of the sensing signal light and ensure low transmission loss within the optical fiber, we propose a special sensing fiber named as DMOF for DAS. The design schematic of the sensing fiber is shown in Figure 3.2, which introduces successive microstructures with refractive index modulations in the fiber core through UV laser light exposure. The microstructures can be treated as small and strong scatters and distributed along the optical fiber with the same interval. Ultraweak fiber Bragg grating (UWFBG) inscribed on the fiber is one type of microstructure that has been recently employed to enhance the SNR for fiber optic DAS (Ai et al., 2017; Zhu et al., 2015). However, the spectra of UWFBG will shift with temperature and strain change (Yang et al., 2016), and consequently the uniformity of the SNR enhancing effect along the optical fiber is difficult to control. To overcome the effect of environmental change along the optical fiber, Rayleigh backscatters with only an increase in the SNR, but colorless, are desirable, which can be created by continuous UV laser light exposure alone without periodic refractive index modulation.

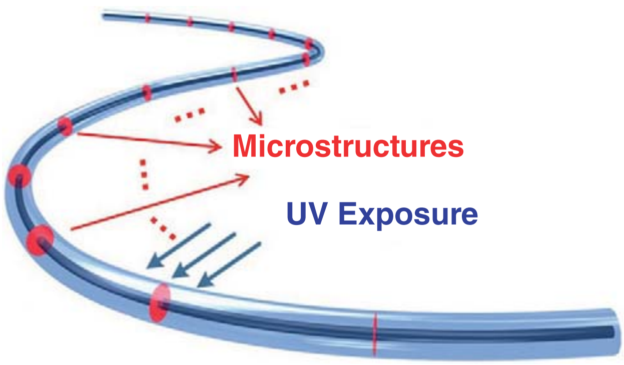

Figure 3.2 Schematic of DMOF.

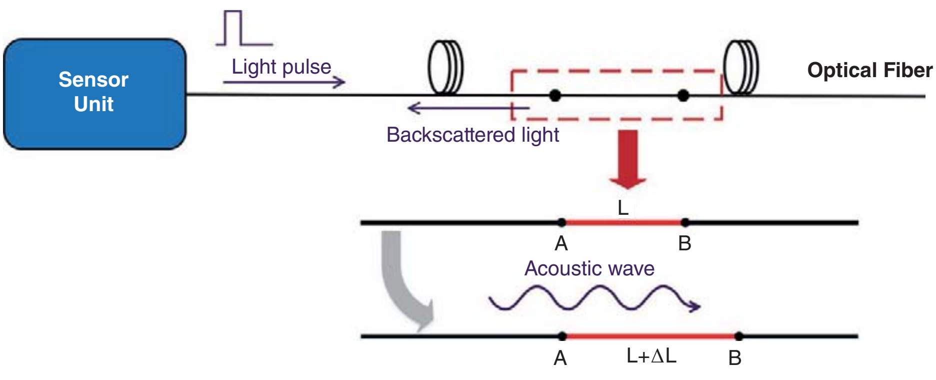

Figure 3.1 Schematic principle of the fiber optic DAS system.

Then, the stabilization effect of DMOF is systematically investigated through numerical simulation. To analyze the influence of the scattering light amplitude on the intensity distribution along the fiber, one microstructure is assumed to be inserted at the center of a 2-m-long SMF corresponding to the injected pulse width of 20 ns, serving as a stronger scatter. Random temperature fluctuation or strain effect is applied on the fiber section, resulting in the random phase change. When the intensity of the backscattering light from the microstructure is set to 0 dB, 3 dB, 7 dB, and 10 dB higher than the intensity from the SMF without microstructures, the dynamic intensity distributions around the scatter over 1,000 traces appear to be more and more stable, which are shown in Figures 3.3a–3d, respectively. Figure 3.3a shows that, when the scatter is weak, the intensity at any position is not stable, and the fading points along the fiber randomly move for different traces, which is a fatal defect for low-frequency acoustic sensing. The intensity distribution, especially the intensity at the scatter marked by the black dotted line, becomes more stable and grows stronger with the enhancement degree of the scatter. Hence, the intensity fading is gradually eliminated, and the SNR and long-term stability are improved step by step.

3.2.3. Fabrication and Performance Test of DMOF

The microstructured optical fiber is fabricated by a continuous online UV-inscription system, which consists of a fiber winding module, UV laser source, laser collimation module, and computer control unit; see Figure 3.4 for details. The fiber winding system is based on the reel-to-reel process of fiber with large winding velocity control (from 1 mm/min to 10 m/min) and uniform stress control

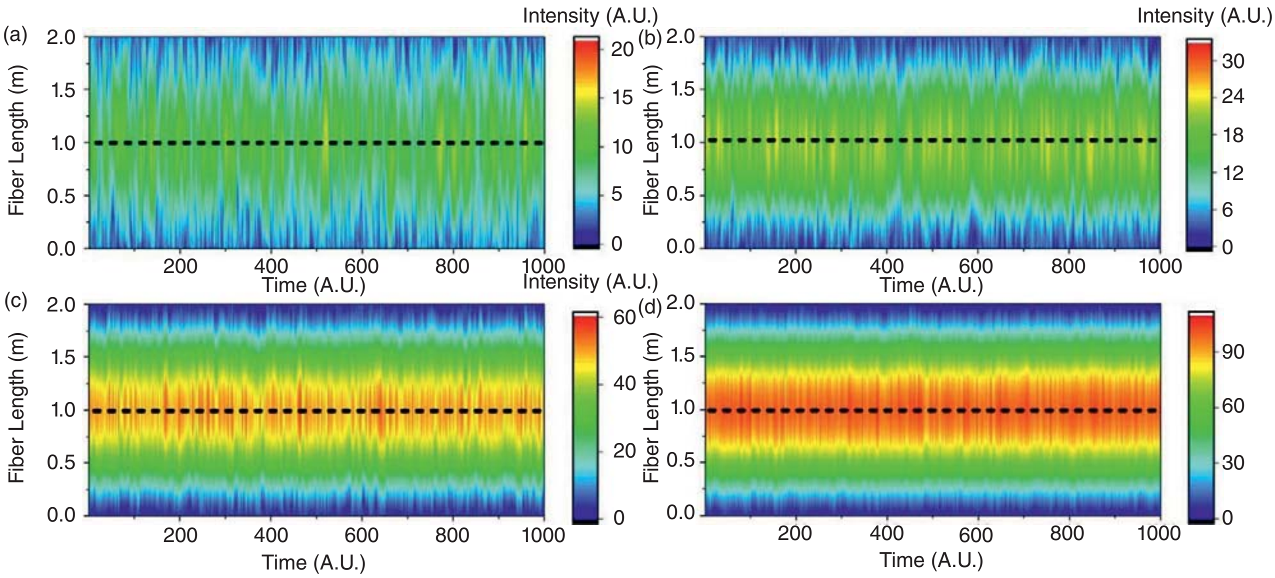

Figure 3.3 Simulated intensity distribution along fiber when the intensity of the backscattering light from the microstructure is, respectively, enhanced by (a) 0 dB, (b) 3 dB, (c) 7 dB, and (d) 10 dB higher than that from standard SMF.

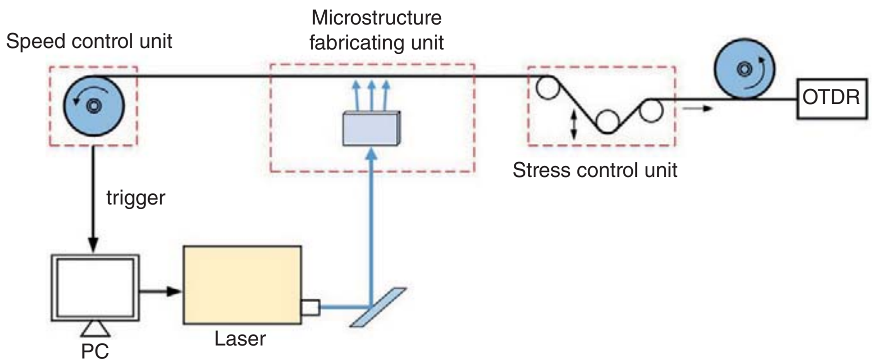

Figure 3.4 The block diagram of the continuous online DMOF fabrication system.

(from 0 to 100 N). The fiber used during the fabrication process is coated with a UV transparent silicone layer, which allows the microstructure fabrication process without removal of the fiber coating. The laser system we used was a conventional 248 nm pulsed excimer laser with a maximum pulse energy of 300 mJ and a large beam size of 26 mm × 12 mm, which can ensure highly effective UV exposure in the fiber core with only a single pulse of radiation, and acceptable fiber vibration during the winding process. Moreover, scattering intensity of the microstructure point over a large range of intensities could be controlled by the UV pulse energy. Finally, a microstructure with arbitrarily spatial distribution along the fiber could be designed by a computer control unit. The scattering intensity of each microstructure can be monitored by an OTDR system with an ultrashort pulsed tunable laser.

To test the optical characteristics of the DMOF, the light of an amplified spontaneous emission (ASE) source is injected into the fiber. The spectra of backscattering light in the SMF and DMOF are, respectively, observed through an optical spectrum analyzer and illustrated in Figure 3.5a. It is clear that the spectrum of backscattering light from the DMOF is colorless across the C band (1525–1656 nm), and its intensity has been improved by more than 10 dB from that of the SMF. Since the microstructures are weakly reflective and just located at local points, the total insertion loss is as low as to be neglected. Moreover, the intensity stability at certain points in the fiber without and with microstructures is, respectively, monitored during 100 s and presented in Figures 3.5b and 3.5c. Compared with the random fluctuation of the intensity distribution in the SMF, the DMOF keeps a much higher SNR and stability, both in spatial and time domains, which are in consistent with the simulation results.

3.2.4. System Configuration and Working Principle of the DMOF-DAS

The experimental setup is illustrated in Figure 3.6a. A typical coherent OTDR structure is adopted and the DMOF is used as the functional unit test (FUT) for sensing, both of which can improve the SNR of the acoustic sensing signals. A 40-mW laser source with a narrow linewidth of less than 1 kHz is split into two parts by the coupler with a splitting ratio of 1:99. One part serves as the local oscillate signal, and the other part is modulated into pulse with a duration time of 20 ns and frequency shifted with 200 MHz by the acoustical optical modulator (AOM). The erbium-doped fiber amplifier (EDFA) amplifies the average power of the pulse and pours the pulse into the FUT through the circulator. The backscattering light from the DMOF, which carries external acoustic information, is mixed with the local light and detected by the balanced photodetector (BPD) to generate the heterodyne beat frequency signal. It should be noted that, owing to the high SNR of backscattering light from the DMOF, only one amplifier is needed and inserted between the AOM and optical circulator, which is simpler than the SMF-based DAS interrogator. Then the electrical signal from the BPD is collected by a DAQ card. In order to sample the coherent signal of 200 MHz precisely, the acquisition speed of the DAQ is set as high as 2 GS/s. Then the acquired data are multiplied with the reference signal as the in-phase and quadrature (IQ) demodulation scheme to extract the phase information along the fiber.

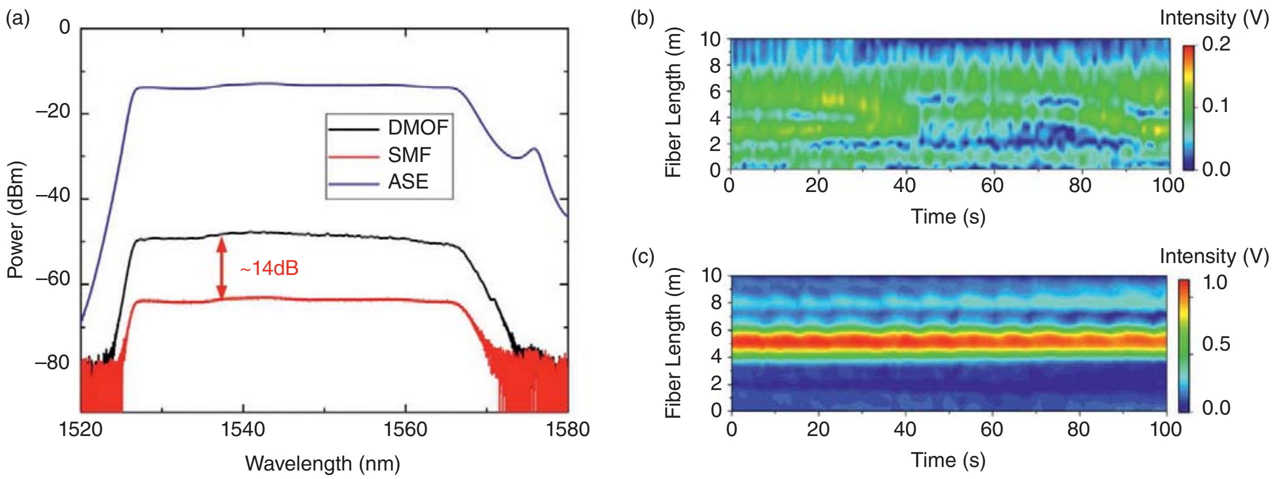

Figure 3.5 Comparison between the DMOF and the SMF: (a) Spectra of the backscattering light in the SMF and DMOF; the 100 s intensity distribution records of a 10-m-long section of SMF (b) and DMOF (c).

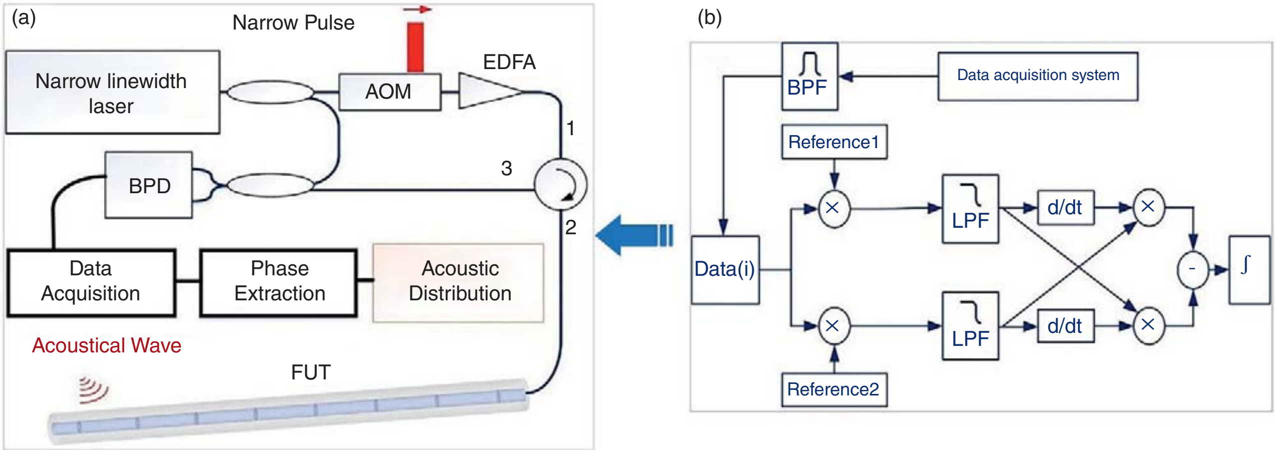

Figure 3.6 Working principle of DMOF-DAS: (a) System configuration and (b) phase extraction workflow.

The phase extraction process is described in detail as follows. The reflected light generated by the *i*th backscattering enhanced point can be expressed as:

$$E_{si}(t) = a_{si}\sin(2\pi f_s t + \varphi_{si}) \tag{3.1}$$

While the electric field intensity of the local oscillator can be described as:

$$E_L(t) = a_L\sin(2\pi f_L t + \varphi_L) \tag{3.2}$$

Therefore, the signal received by the BPD can be represented as:

$$I_{ri}(t) = Sa_{si}a_L\cos(2\pi\Delta f t + \varphi_i) \tag{3.3}$$

Where a_{si} and a_L are the amplitudes of the pulse signal from the *i*th microstructure and the local oscillator, respectively, S is the responsibility of the BPD, $\Delta f = f_S - f_L = 200$ MHz is the frequency shift of the probe pulse, and $\varphi_i = \varphi_{si} - \varphi_L$ is the phase difference between the signal light from the *i*th microstructure and the local oscillator. The frequency shift of 200 MHz could move the sensing signal to a high-frequency band, which is beneficial in eliminating the low-frequency noise. As shown in Figure 3.6b, a band-pass filter (BPF) with center frequency at 200 MHz is used for signal denoising. After band-pass filtering, the relatively pure beat frequency signal *Data(i)* can be obtained. In addition, a reference function is developed for phase extraction, as well as its orthogonal function that is generated by the Hilbert transform, which can be expressed as:

$$I_{ref1} = a_0\cos(2\pi\Delta f t + \varphi_0) \tag{3.4}$$

$$I_{ref2} = a_0\sin(2\pi\Delta f t + \varphi_0) \tag{3.5}$$

Multiply $I_{ri}(t)$ by I_{ref1} and I_{ref2}, respectively, and then a pair of the orthogonal functions about φ_i can be obtained after the low-pass filter (LPF). Furthermore, the differential cross-multiplying algorithm is employed to calculate the φ_i, and the following result is obtained:

$$\Phi_i = \varphi_i - \varphi_0 \tag{3.6}$$

Then, the phase change of the sensing fiber between *i*th and (*i+1*)th backscattering enhanced point can be described as:

$$\Delta\varphi_i = \Phi_{i+1} - \Phi_i = \varphi_{i+1} - \varphi_i \tag{3.7}$$

Consequently, the amplitude, frequency, and phase of the acoustic wave are represented by the optical phase change $\Delta\varphi_i$. Notably, here the spatial resolution is decided by the spatial interval of the backscattering enhanced scatters in the DMOF, and $\Delta\varphi_i$ is directly served as the output of each channel without additional moving average algorithm.

3.2.5. Performance of the DMOF-DAS

Based on the preceding key techniques, we developed the DMOF-DAS system as presented in Figure 3.7a, and the DMOF with a microstructure spatial interval of 5 m and a length of 1.44 km was deployed as the sensing fiber for the field test. Intrinsically speaking, the acoustic signal acted as the dynamic strain change on the sensing fiber. To test the acoustic sensitivity and linearity of the DMOF-DAS system response, a section of 1-m-long sensing fiber was wrapped on a cylindrical piezoelectric transducer (PZT), and a strain change with the step of 19.23 nε was applied on the fiber through the PZT. As illustrated in Figure 3.7b, the system exhibited high sensitivities of 0.0153 rad/nε for strain increasing and 0.0152 rad/nε for strain decreasing, as well as an ultrahigh linearity of 1. The slight phase difference between the two curves was only 0.0286 rad, which demonstrated an extremely low hysteresis error. It should be noted that the actual

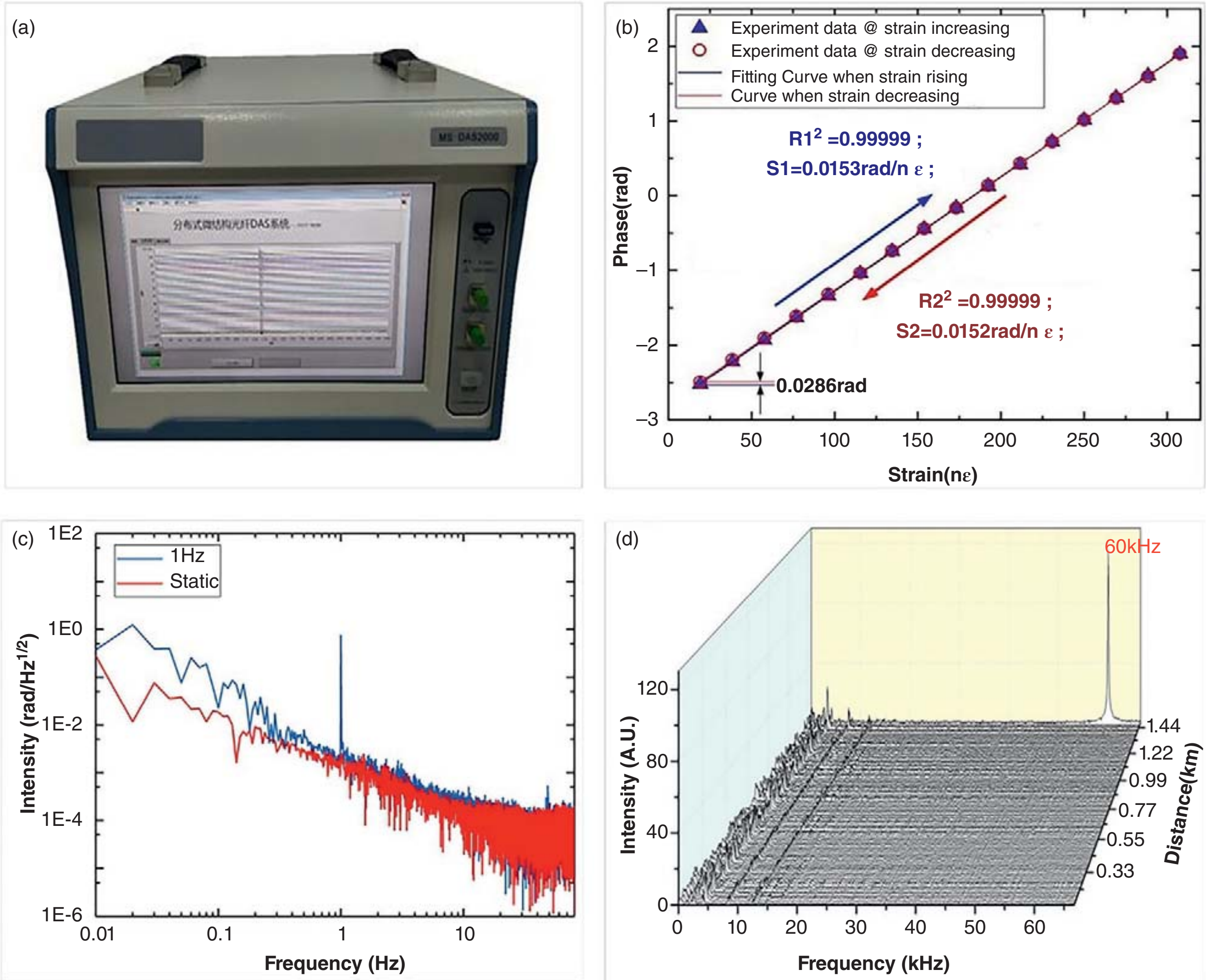

Figure 3.7 Sensing performance of the DMOF-DAS system: (a) Photograph of the equipment; (b) strain sensitivities and hysteresis for the strain increasing and decreasing processes; (c) noise PSD of phase change on two sections of the fiber with 1 Hz dynamic strain change and static strain change, respectively; and (d) frequency spectrum along the 1.44-km-long fiber when the dynamic strain change at a frequency of 60 kHz is applied on the fiber.

sensitivity of the DMOF-DAS system with 5 m spatial resolution will be five times that of the tested 1-m-long fiber, reaching 0.076 rad/nε. Figure 3.7c shows the power spectral density (PSD) of 1 Hz acoustic signal and the noise floor in static condition for estimating the strain measurement accuracy. It can be deduced that the minimum detectable strain change could be 4 nε/√Hz at 0.01 Hz and 3.4 pε/√Hz at 10 Hz, corresponding to the noise floor of 0.3 rad/√Hz and 2.7×10^{-4} rad/ √ Hz, respectively. These test results demonstrate the ultrahigh sensitivity, especially at the low-frequency band. Moreover, obvious peak locating at 1440 m, 60 kHz in Figure 3.7d, indicates that the maximum frequency of the acoustic signal can reach up to 60 kHz.

3.3. BOREHOLE SEISMIC SURVEY TESTS AND RESULTS

3.3.1. Zero-Offset VSP Survey in Fushan Oil Field

A field test using the DMOF-based fiber optic DAS system was conducted in the Fushan oil field of China National Petroleum Corporation (CNPC) in China. A zero-offset VSP survey was performed; its schematic is depicted in Figure 3.8a. A water-filled source pit for the electrical spark seismic source was used to generate seismic energy on the surface near the wellhead. A 524-m-long sensing DMOF optical fiber cable with a tight buffer, strength member, and outer jacket was deployed

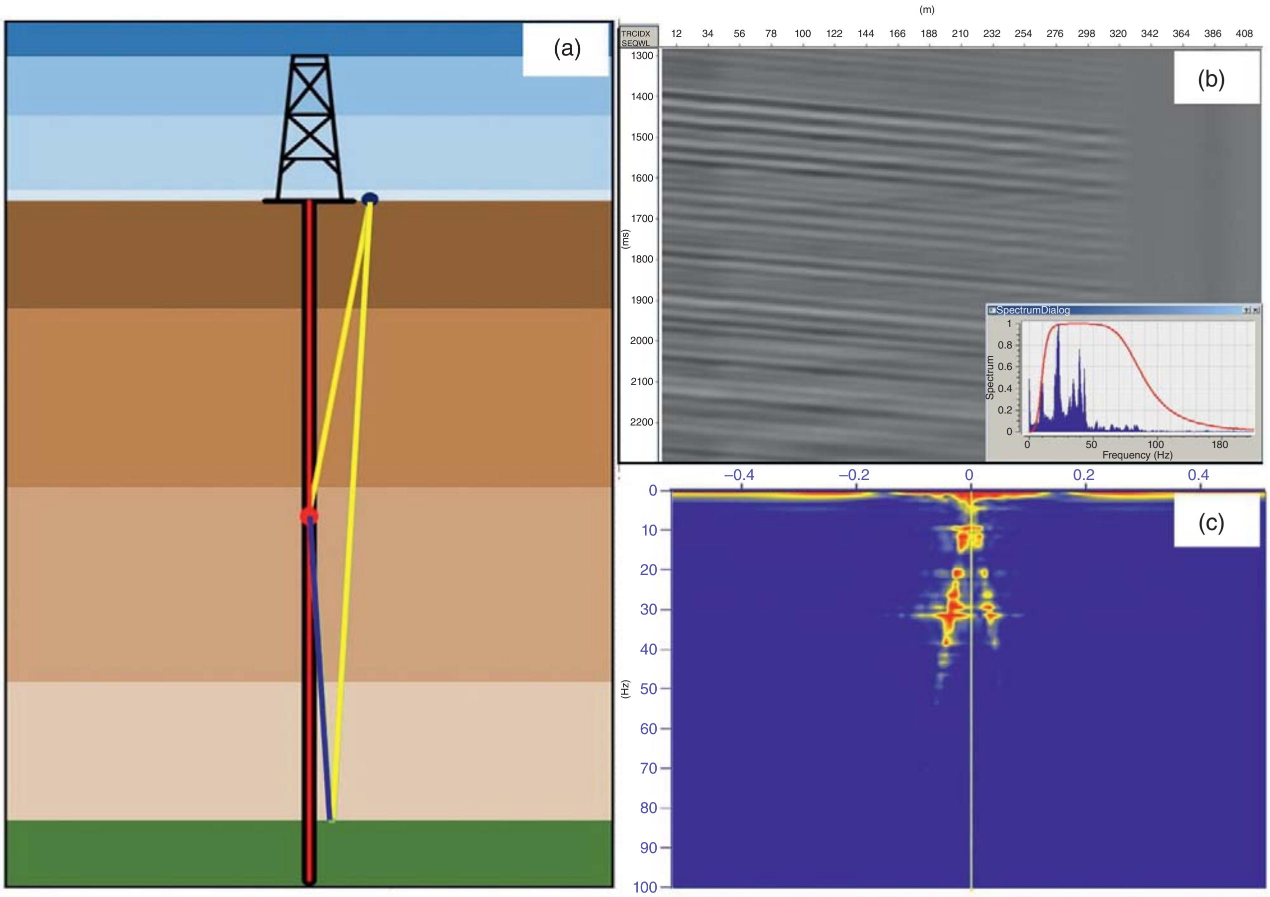

Figure 3.8 Field test in the Fushan oil field: (a) Schematic of the zero-offset VSP; (b) the DMOF-based fiber optic DAS system recorded borehole seismic data (inset: amplitude spectra of the seismic data); and (c) Frequency-wavenumber (F-K) domain spectra of the recorded borehole seismic data using the DMOF-based fiber optic DAS system.

into a cased borehole with a weight bar at the bottom to pull the fiber cable down in the borehole. The fiber cable was freely floated in the water-injection-filled borehole without any clamping, and the coupling between the fiber cable and the wellbore was realized by water.

From Figure 3.8b, it can be seen that the DMOF-based fiber optic DAS system recorded the borehole seismic data with a good SNR and correct amplitude, as well as a clear downgoing tube wave. The output receiving data spacing is 2 m. The tube wave is the dominant component in the water-filled shallow borehole, and the first arrival of the tube wave has an SNR of about 10 dB. In addition, Figure 3.8c presents the F-K domain spectra of the recorded DMOF-DAS borehole seismic data, where the linear event clearly indicates the strong downgoing tube wave and weak upgoing tube wave.

3.3.2. Walkaway VSP Survey in Suning Oil Field

A walkaway VSP survey using the DMOF-DAS system was conducted in the Suning oil field of CNPC in China. A 1.4-km-long armored DMOF cable was permanently cemented behind the casing, which resulted in an excellent coupling between the formation and the sensing fiber cable. Both vibrator (28 ton) and dynamite (16 kg charge) sources were used to generate seismic energy on the surface with different offset distance to the wellhead. The spacing of seismic sources was 40 m, and the farthest source was 8 km away from the wellhead. The DMOF-DAS VSP data with 2 m spacing were recorded by the DMOF-DAS system and are presented in Figures 3.9a and 3.9b. It can be seen that high-quality raw DMOF-DAS VSP data are obtained, which include clear upgoing

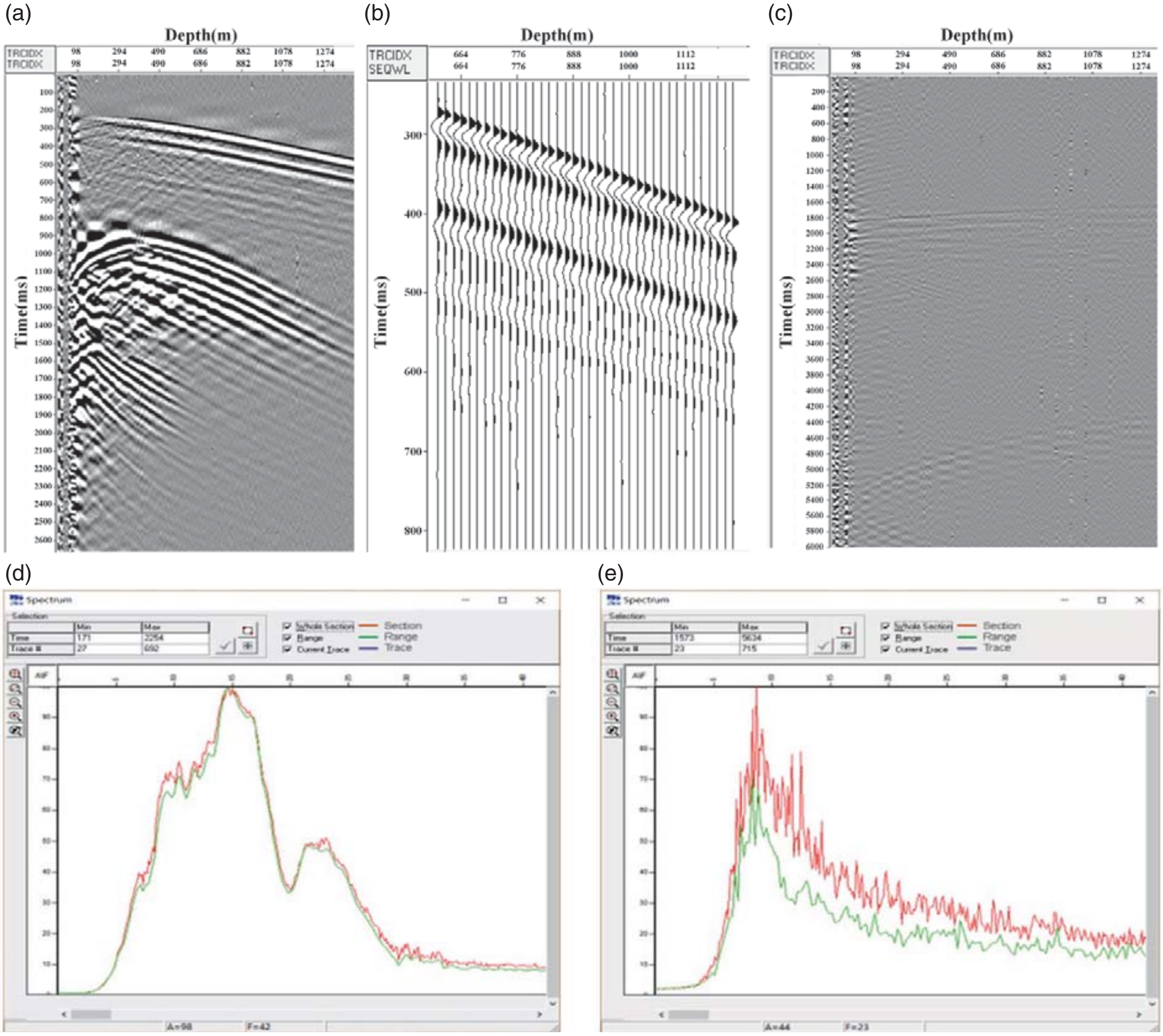

Figure 3.9 Recorded seismic data in well using DMOF-DAS: (a) DMOF-DAS VSP data at zero offset with stronger reflector and direct *P*-wave and *S*-wave arrivals; (b) zoomed-in view on part of the downgoing wave of (a); (c) VSP raw data display at the offset of 2.5 km; (d) the amplitude spectra of (a); and (e) the amplitude spectra of (c).

and downgoing waves with a very high SNR. The estimated SNR of direct arrival for the zero-offset DAS VSP data recorded from the armored optical cable cemented behind the casing is about 25 dB. A strong seismic reflector is presented, along with direct shear wave arrivals. Figure 3.9b is the zoomed-in view on part of raw DMOF-DAS VSP data and proves the high consistency of polarity and seismic energy attenuated in each channel with depth as expected.

Moreover, we measured the raw DMOF-DAS VSP data for different offset source locations. Figures 3.9a and 3.9c illustrate the raw DMOF-DAS VSP data when the source locations were near the wellhead and 2.5 km away from the wellhead, respectively. The raw zero-offset DMOF-DAS VSP data show a very high SNR (25 dB). While even the source was far away from the well, the direct *P*-wave and the direct *S*-wave were also observed with lower signal strength. The corresponding amplitude spectra of Figures 3.9a and 3.9c are plotted in Figures 3.9d and 3.9e, respectively, where the red curves represent the spectra of all the fiber section, and the green curves depict the spectra of the effective signal regions. It can be seen that the recorded signals have a wide frequency spectrum and correct amplitude.

3.4. DISCUSSIONS

The field test data have proved that the DMOF-based fiber optic DAS system can successfully acquire borehole seismic data with good quality. Through the deployment of the DMOF cable in a well as the sensing device, which is connected to the interrogator of the DAS system at surface, the seismic signals can be recorded along the full length of the well for each shot. A longer duration is not required for rigging up and down the conventional borehole geophone array; hence, the survey efficiency is significantly improved. Moreover, the DMOF-DAS system offers the opportunity to achieve a much higher spatial resolution (typically of 2 m) and lower cost than current technologies. In addition, the coupling method is very important for the VSP survey. For the water-injection coupling scheme, the tube wave will be the main noise. The cementation method will provide the strongest coupling, resulting in better VSP data with a higher SNR.

3.5. CONCLUSIONS

The general benefits of fiber optic DAS, such as a large number of channels and being free of power supply in the sensing area, make it more suitable for long-distance detection (sensing) at shortest time, significant cost saving, and without a need to interrupt other activities. Thus, fiber optic DAS is increasingly being recognized as a viable alternative to downhole geophone arrays for the acquisition of borehole seismic data. To increase the SNR and eliminate the random fading of the sensing fiber, DMOF was proposed as the sensing fiber and fabricated through the UV laser light exposure. By employing the coherent detection and IQ demodulation scheme, a DMOF-based fiber optic DAS system with a wide frequency range from 0.01 Hz to 60 kHz and an ultrahigh strain resolution of 3.4 $p\varepsilon/\sqrt{Hz}$ around 10 Hz was explored and demonstrated. The field zero-offset VSP, offset VSP, and walkaway VSP tests proved that the DMOF-DAS system can acquire borehole seismic data with good quality. Because of the benefits of the long-distance sensing and distributed monitoring capabilities, the fiber optic DAS system can dramatically reduce the operating time required to complete a normal borehole seismic survey and can achieve much higher full well spatial sampling than current technologies. The ability to acquire borehole seismic data in a producing well without the need to disrupt production also offers significant benefits to the operators.

ACKNOWLEDGMENTS

The authors would like to acknowledge the National Natural Science Foundation of China (NSFC) (Nos. 61922033 and 61775072), the Project of Economic Development of Guangdong in China (No. GDNRC 2020-045),the Science Fund for Creative Research Groups of the Natural Science Foundation of Hubei in China (No. 2018CFA004), the Major Projects of Technical Innovation of Hubei in China (No. 2018AAA040), and the Innovation Fund of Wuhan National Laboratory for Optoelectronics (WNLO).

The authors also thank BGP Inc. for its support in the discussion and field test.

The authors declare no competing financial interests.

Most of the material in this chapter has neither been published nor is under consideration for publication elsewhere.

REFERENCES

Ai, F., Sun, Q., Zhang, W., Liu, T., Yan, Z., & Liu, D. (2017). *Wideband fully-distributed vibration sensing by using UWFBG based coherent OTDR*. Paper presented at Optical Fiber Communication Conference, San Diego, CA.

Chen, D., Liu, Q., & He, Z. (2017). *Distributed fiber-optic acoustic sensor with sub-nano strain resolution based on time-gated digital OFDR*. Paper presented at Asia Communications and Photonics Conference, Optical Society of America.

Daley, T. M., Freifeld, B. M., Ajo-Franklin, J., Dou, S., Pevzner, R., Shulakova, V., et al. (2013). Field testing of fiber-optic distributed acoustic sensing (DAS) for subsurface seismic monitoring. *The Leading Edge*, *32*(6), 699–706. doi: 10.1190/tle32060699.1

Follett, J. L., Wyker, B., Hemink, G., Hornman, K., & Lumens, P. (2014). *Evaluation of fiber-optic cables for use in distributed acoustic sensing: Commercially available cables and novel cable designs*. Paper presented at SEG Annual Meeting. Society of Exploration Geophysicists.

Frignet, B. G., & Hartog, A. H. (2014). *Optical vertical seismic profile on wireline cable*. Paper presented at SPWLA 55th Annual Logging Symposium, Abu Dhabi, UAE.

Gabai, H., Shpatz, I., & Eyal, A. (2017). Lumped Rayleigh reflectors. *Optics Letters*, *42*(21), 4529–4531. doi:10.1364/OL.42.004529

Harma, A., McKinney, M. F., & Skowronek, J. (2005). *Automatic surveillance of the acoustic activity in our living environment*. Paper presented at 2005 IEEE International Conference on Multimedia and Expo, Amsterdam, Netherlands.

He, X., Xie, S., Liu, F., Cao, S., Gu, L., Zheng, X., & Zhang, M. (2017). Multi-event waveform-retrieved distributed optical fiber acoustic sensor using dual-pulse heterodyne phase-sensitive OTDR. *Optics Letters*, *42*(3), 442–445. doi: 10.1364/OL.42.000442

Jagannathan, S., Bertsatos, I., Symonds, D., Chen, T., Nia, H., Jain, A. D., et al. (2009). Ocean acoustic waveguide remote sensing (OAWRS) of marine ecosystems. *Marine Ecology Progress Series*, *395*, 137–160. doi:10.3354/meps08266

Jousset, P., Reinsch, T., Ryberg, T., Blanck, H., Clarke A., Aghayev R., et al. (2018). Dynamic strain determination using fibre-optic cables allows imaging of seismological and structural features. *Nature Communications*, *9*(1), 2509. doi:10.1038/s41467-018-04860-y

Loranger, S., Gagné, M., Lambin-Iezzi, V., & Kashyap, R. (2015). Rayleigh scatter based order of magnitude increase in distributed temperature and strain sensing by simple UV exposure of optical fibre. *Scientific Reports*, *5*, 11177. doi: 10.1038/srep11177

Martins, H. F., Martin-Lopez, S., Corredera, P., Filograno, M. L., Frazão, O., & Gonzalez-Herraez, M. (2013). Coherent noise reduction in high visibility phase-sensitive optical time domain reflectometer for distributed sensing of ultrasonic waves. *Journal of Lightwave Technology*, *31*(23), 3631–3637. doi:10.1109/JLT.2013.2286223

Masoudi, A., Belal, M., & Newson, T. P. (2013). A distributed optical fibre dynamic strain sensor based on phase-OTDR. *Measurement Science and Technology*, *24*(8), 085204. doi:10.1088/0957-0233/24/8/085204

Mateeva, A., Lopez, J., Potters, H., Mestayer, J., Cox, B., Kiyashchenko, D., et al. (2014). Distributed acoustic sensing for reservoir monitoring with vertical seismic profiling. *Geophysical Prospecting*, *62*(4), 679–692. doi: 10.1111/1365-2478.12116

Mateeva, A., Mestayer, J., Cox, B., Kiyashchenko, D., Wills, P., Lopez, J., et al. (2012). *Advances in Distributed Acoustic Sensing (DAS) for VSP*. Paper presented at SEG Annual Meeting, Society of Exploration Geophysicists.

Mestayer, J., Cox, B., Wills, P., Kiyashchenko, D., Lopez, J., Costello, M., et al. (2011). *Field trials of distributed acoustic sensing for geophysical monitoring*. Paper presented at SEG Annual Meeting, Society of Exploration Geophysicists.

Michaels, T. E., Michaels, J. E., Mi, B., & Ruzzene, M. (2005). Damage detection in plate structures using sparse ultrasonic transducer arrays and acoustic wavefield imaging. *AIP Conference Proceedings, 760*, 938–945. https:// doi.org/10.1063/1.1916774

Molenaar, M. M., Hill, D., Webster, P., Fidan, E., & Birch, B. (2012). First downhole application of distributed acoustic sensing for hydraulic-fracturing monitoring and diagnostics. *SPE Drilling & Completion*, *27*(01), 32–38. doi:10.2118/140561-MS.7

Ni, S., Kanamori, H., & Helmberger, D. (2005). Seismology: Energy radiation from the Sumatra earthquake. *Nature, 434* (7033), 582. doi: 10.1038/434582a

Ni, S., Tan, E., Gurnis, M., & Helmberger, D. (2002). Sharp sides to the African superplume. *Science*, *296*(5574), 1850–1852. doi: 10.1126/science.1070698

Wang, S., Fan, X., Liu, Q., & He, Z. (2015). Distributed fiber-optic vibration sensing based on phase extraction from time-gated digital OFDR. *Optics Express*, 2015, *23*(26), 33301–33309. doi: 10.1364/OE.23.033301

Yamate, T., Fujisawa, G., & Ikegami, T. (2017). Optical sensors for the exploration of oil and gas. *Journal of Lightwave Technology, 35*(16), 3538–3545. doi: 10.1109/JLT.2016.2614544

Yang, M., Bai, W., Guo, H., Wen, H., Yu, H., & Jiang, D. (2016). Huge capacity fiber-optic sensing network based on ultra-weak draw tower gratings. *Photonic Sensors*, *6*(1), 26–41. doi:10.1007/s13320-015-0298-0

Zhu, F., Zhang, Y., Xia, L., Wu, X., & Zhang, X. (2015). Improved Φ-OTDR sensing system for high-precision dynamic strain measurement based on ultra-weak fiber Bragg grating array. *Journal of Lightwave Technology*, *33*(23), 4775–4780. doi: 10.1109/JLT.2015.2477243

4

Distributed Acoustic Sensing System Based on Phase-Generated Carrier Demodulation Algorithm

Tuanwei Xu, Shengwen Feng, Fang Li, Lilong Ma, and Kaiheng Yang

ABSTRACT

We demonstrate a real-time distributed acoustic sensing (DAS) system based on phase-sensitive optical time domain reflectometry (Φ-OTDR) and phase-generated carrier (PGC) demodulation algorithm. An unbalanced Michelson interferometer (MI) with specific phase modulation is introduced to overcome phase fading caused by initial phase shift in fiber optic interferometer sensing. Owing to its relatively low data requirement and polarization-independent structure, PGC-DAS system exhibits the superiorities of real-time signal processing and Rayleigh polarization-induced fading suppression. A proof-of-concept system is constructed to demonstrate feasibility and sensing performance. Corresponding to the average phase noise of ~5×10^{-4} rad/√Hz, a strain sensitivity of 8.5 pε/√Hz is achieved with a spatial resolution of 10 m, as well as a frequency response range of 2 Hz to 1 kHz over 10 km sensing distance. Further, a field trial of this system is presented to validate it in qualitative seismic monitoring on land.

4.1. INTRODUCTION

DAS is an advanced technique developed in recent years to accurately measure ground vibration via fiber optic cables. DAS presents a possible new frontier for recording earthquake waves and other seismic signals in a wide range of research and public safety arenas (Juarez et al., 2005; Parker et al., 2014; Tanimola & Hill, 2009). It repurposes standard telecommunication fiber optic cables as a long series of single-component, in-line strain, or strain-rate sensors, which is a completely different way from conventional deployments of nodal devices. DAS can sample passing seismic waves at locations every few meters or closer along paths stretching for tens of kilometers. Therefore, DAS has many advantages, such as passivity, resistance to electromagnetic interference, and cost-effectiveness.

φ-OTDR is one of the most widely used schemes to achieve distributed strain or strain-rate sensing. In the early stage, research focused on detecting the interfering Rayleigh backscattering (RB) amplitude in the sensing fiber. In 1993, Taylor and Lee first monitored intrusion events by detecting RB intensity changes with Φ-OTDR technology (Taylor & Lee, 1993). However, the nonlinearity between RB amplitude and vibration could not satisfy the need for quantitative seismic measurement in local and regional seismology. Then, researchers began to investigate phase term (Feng et al., 2018;

Key Laboratories of Transducer Technology, Institute of Semiconductors, Chinese Academy of Sciences, Beijing, China; and

College of Materials Science and Opto-Electronic Technology, University of Chinese Academy of Sciences, Beijing, China

Distributed Acoustic Sensing in Geophysics: Methods and Applications, Geophysical Monograph 268, First Edition.
Edited by Yingping Li, Martin Karrenbach, and Jonathan B. Ajo-Franklin.

DOI:10.1002/9781119521808.ch04

Sha et al., 2017; Yan et al., 2017; Yang et al., 2018; Zinsou et al., 2019), which is almost linear to strain. Currently available DAS systems have characteristics in common that they use pulsed lasers to interrogate optical fibers and process RB phase to provide a nearly continuous estimate of fiber dynamic strain along the fiber. In general, they differ in the method to process RB light and may be separated into coherent detection, dual-pulse detection, and interferometer detection (Hartog, 2017). Coherent detection represents the fact that the phase is extracted by mixing RB signal and local oscillator (He et al., 2017; Lu et al., 2010; Wang et al., 2016). Dual-pulse detection uses two separate RBs with different probe frequencies or phases (Alekseev et al., 2014a, 2014b; Alekseev et al., 2015). Interferometer detection processes RB phase by mixing with itself with a time delay (Masoudi et al., 2013; Wang, Wang, et al., 2015; Wang, Shang, et al., 2015). A coherent heterodyne demodulation DAS system was proposed by Lu et al. (2010). The phase information of heterodyne signal was obtained by mixing the electrical driving signal of acoustic optical modulator (AOM); a spatial resolution of 5 m and a frequency response range of 1 kHz were achieved; and signal-to-noise ratio (SNR) was increased to 6.5 dB with 100 averaging times. To overcome polarization-induced signal fading, an improved polarization-maintaining scheme was presented (Qin et al., 2011). Further, a kind of double-pulse approach was proposed by Alekseev et al. (2014b), which used phase-modulated probe signals with predefined different phase shift sequences of 0, $-2/3\pi$, and $2/3\pi$. The system demonstrated a distributed phase monitoring capability over 2 km range with 100 Hz sinusoidal strain from piezoceramic modulator. Another dual-pulse DAS system with different frequency shifts was investigated by He et al. (2017). Combined with heterodyne demodulation, the strain frequency response was in the range of 50 Hz to 25 kHz, with a 0.9-73 rad amplitude on a 470 m long optical fiber. There are two kinds of interferometer DAS systems based on 3×3 coupler or PGC demodulation algorithm. For the former, a symmetric 3×3 coupler is adopted to eliminate slow phase shift of the interferometer (Sheem, 1981); the interference phase formed by self-delay of RB in a single pulse is recovered by using the feature of coupler with a phase difference of $\pm 120^\circ$ between output ports. Such an alternative approach was demonstrated by Masoudi et al. (2013); the demonstrated setup has a spatial resolution of 2 m with a frequency range of 500-5000 Hz along 1 km optical fiber (Masoudi et al., 2013). Because of three detectors and a sampling rate of 300 MSa/s per channel, the total data size would reach around 900 MSa/s, which leads to a huge challenge to realize real-time data processing. For PGC-DAS system (Fang et al., 2015), a PGC was introduced to overcome the initial phase shift problem (Dandridge et al., 1982), and an unbalanced MI with Faraday rotator mirrors (FRMs) was implemented to eliminate the influence of polarization fading (Huang et al., 1996). Compared with 3×3 demodulation, only one detector is needed, and a relatively low data stream helps to online recover phase information.

Here, we present a real-time PGC-DAS system. Combined with characteristics of large dynamic range and high sensitivity of PGC demodulation algorithm (Wang et al., 2015), the proposed system provides an effective technical solution to distributed fiber acoustic sensing. The sensing distance could reach 10 km with the minimum sample interval of 0.4 m. Corresponding to the average phase noise of 5×10^{-4} rad/$\sqrt{\text{Hz}}$, a strain sensitivity of 8.5 p$\varepsilon/\sqrt{\text{Hz}}$ was achieved with a spatial resolution of 10 m, as well as a frequency response range of 2 Hz to 1 kHz over 10 km sensing distance. A field trial of this PGC-DAS system was performed to compare nodal geophones. Results show that seismic records have a high consistency between them, proving the feasibility of PGC-DAS system in seismology.

4.2. PRINCIPLE

The principle of PGC-DAS system is shown in Figure 4.1. A coherent input light pulse passes through a circulator into the sensing optical fiber. RB light enters into an unbalanced MI with FRMs at the ends. There is a phase modulator on one arm of MI and an optical delay L_{MI} on the other arm. RB signal mixes with itself and is detected by one photoelectric detector (PD).

Intensity distribution of RB light is a type of Fourier transform of random permittivity fluctuations (Bao et al., 2016). Assume that the sensing fiber is composed of successive slices with a length of ΔL. Each slice contains M scattering centers, and polarization states between each scattering center are consistent. The interference field of backscattered light at distance $L_m = m\Delta L$ can be expressed by (Park et al., 1998):

$$\begin{aligned} E_{L_m}(t) &= E_0 P_m \exp(-\alpha L_m) \cdot \exp(-j2\beta L_m) \\ &\quad \cdot \sum_{k=1}^{M} r_k^i \exp\left(j\phi_k^j\right) \\ &= E_0 P_m \exp(-\alpha L_m) \cdot \exp(-j2\beta L_m) \cdot a_i \exp[j\phi_i(t)] \end{aligned} \tag{4.1}$$

where E_0 is electric field intensity of the incident light; P_m is polarization-dependent coefficient ranging from 0 to 1; α is optical power attenuation coefficient; r_k and φ_k are

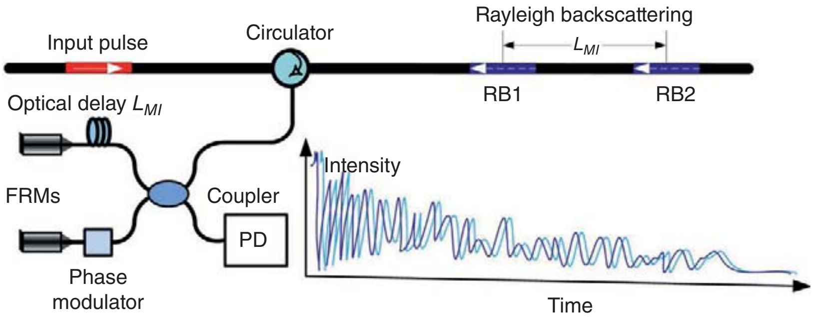

Figure 4.1 Principle of PGC-DAS system with an unbalanced MI.

scattering coefficient and phase of the kth scattering center, respectively; a_i and φ_i are reflectivity and phase of scattering unit, respectively; and β is propagation constant.

Then, scattering light enters into MI, and RB1 and RB2 separated by L_{MI} interference due to the same optical path. The interference electrical field $E(t)$ is written as:

$$\begin{aligned} E(t) &= E_L(t) + E_{L-L_{\mathrm{MI}}}(t) \\ &= E_0 P_L a_L \exp(-\alpha L)\cdot \exp(-j2\beta L)\cdot \exp[j\phi_L(t)] \\ &\quad + E_0 P_{L-L_{\mathrm{MI}}} a_{L-L_{\mathrm{MI}}} \exp[-\alpha(L-L_{\mathrm{MI}})] \\ &\quad \cdot \exp(-j2\beta L)\cdot \exp[j\phi_L(t)] \\ &\quad \cdot \exp(j2\beta L_{\mathrm{MI}})\cdot \exp\left[j\phi_{L-L_{\mathrm{MI}}}(t) - j\phi_L(t)\right] \\ &= A + B\exp[j\beta L_{\mathrm{MI}} + \Delta\phi(t)] \end{aligned} \tag{4.2}$$

With simplified coefficients A and B, the interference intensity is given by:

$$\begin{aligned} I(t) &= |E(t)|^2 = A^2 + B^2 + 2AB\cos[\beta L_{\mathrm{MI}} + \Delta\phi(t)] \\ &= I_D + I_C\cos[\beta L_{\mathrm{MI}} + \Delta\phi(t)] \end{aligned} \tag{4.3}$$

For PGC demodulation algorithm, a sinusoidal signal with a modulation frequency of ω_c is loaded on one arm of MI. Therefore, an additional phase modulation $C\cdot\cos(\omega_c t)$ is introduced in Equation 4.3 with $C = m\Delta L_{\mathrm{MI}}$, where m is the modulation index and ΔL_{MI} is the maximum length difference variation. Hence, the total phase of the interference light is:

$$\begin{aligned} \phi(t) &= C\cdot\cos(\omega_c t) + \beta L_{\mathrm{MI}} + \Delta\phi(t) \\ &= C\cdot\cos(\omega_c t) + \phi(t) \end{aligned} \tag{4.4}$$

And the interference intensity is rewritten as:

$$I(t) = I_D + I_C\cos[C\cdot\cos(\omega_c t) + \phi(t)] \tag{4.5}$$

After being multiplied separately with fundamental and second harmonic carriers $\cos(\omega_c t)$ and$\cos(2\omega_c t)$, and later with low-pass filtering, the in-phase and quadrature components $I_I(t)$ and $I_Q(t)$ are represented as (Dandridge et al., 1982):

$$\begin{aligned} I(t) &= -I_c J_1(C)\cdot\sin\phi(t) \\ Q(t) &= -I_c J_2(C)\cdot\cos\phi(t) \end{aligned} \tag{4.6}$$

where $J_1(C)$ and $J_2(C)$ are the first-order and the second-order Bessel function, respectively, of the first kind. When C is equal to 2.63, it satisfies $J_1(C) = J_2(C)$. Thus, the phase $\varphi(t)$ is calculated by:

$$\phi(t) = \arctan[I(t)/Q(t)]. \tag{4.7}$$

4.3. EXPERIMENTS AND RESULTS

The PGC-DAS system setup is illustrated in Figure 4.2. A 1550.15 nm coherent laser with a bandwidth of 3 kHz is modulated by AOM with an extinction ratio of 50 dB to an optical pulse. The pulse width and repetition rate are 50 ns and 8 kHz, respectively. The pulse light travels through an optical isolator (ISO) and is amplified by an erbium-doped fiber amplifier (EDFA). A fiber Bragg grating is utilized to filter redundancy in amplified spontaneous emission (ASE). The filtered pulse light is launched into the sensing fiber through a circulator. After that, RB light is injected into an unbalanced MI with a one-way optical path difference of 10 m, i.e., $L_{\mathrm{MI}} = 10$ m. FRMs are used to eliminate the influence of polarization fading. The mixed interference RB light is modulated by a sinusoidal signal with a modulation amplitude of 2.63 rad and arrives at the high-sensitivity optical detector (PD) with a bandwidth of 80 MHz. After analog-to-digital conversion at the analog digital converter (ADC), the obtained RB signal is sampled with a sampling rate of 250 MS/s, corresponding to the minimum sampling interval of 0.4 m. PGC demodulation scheme is implemented on a digital processing unit consisting of field programmable gate array/digital signal processor (FPGA/DSP)

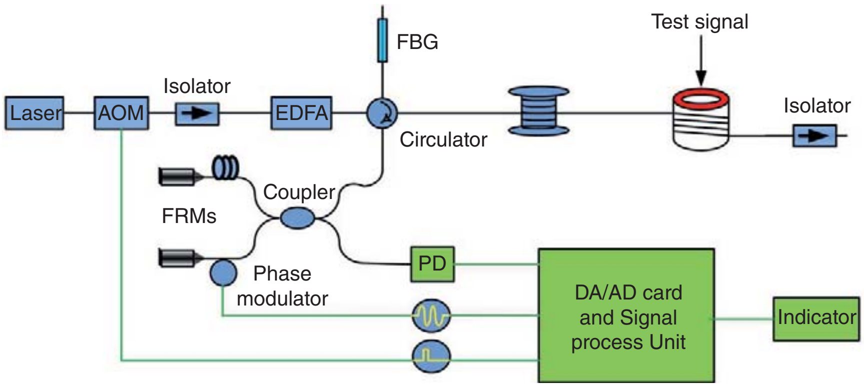

Figure 4.2 Setup of PGC-DAS system.

circuits and a real-time controller, which could realize more than 10,000 channels' real-time phase calculation. The sensing fiber is a 10 km standard single-mode fiber, and a fiber stretcher with a 6 m single-mode fiber wound on a piezoelectric ceramic tube is inserted in the sensing fiber as a unit under test. An isolator is placed at the end of the sensing fiber to remove unwanted end reflection.

The time series in Figure 4.3a contains 9,995 data points of Channel #4750. These data points are sampled with a time increment of 0.5 ms, which conceivably allows the time series to contain frequency content up to a Nyquist frequency of 1 kHz (Figure 4.3b). To remove quasi-static phase drift caused by environmental effects, a high-pass filter with a cutoff frequency of 2 Hz is adopted in the procedure. Thus, the frequency response range is limited to 2 Hz to 1 kHz.

Under the equation $\delta\varepsilon = \delta\varphi/(2\pi n L_{MI}/\lambda)$, the strain sensitivity is mainly determined by the phase noise $\delta\varphi$ and the spatial resolution L_{MI} (defined as the gauge length [Masoudi et al., 2013]). The phase noise is shown in Figure 4.3b, and the average value is around 5×10^{-4}rad/√Hz. With the designed spatial resolution L_{MI} = 10 m, the minimum detected strain of this PGC-DAS system is as small as 8.5 pε/√Hz.

Figure 4.4a displays a waterfall plot of the magnitude response of each channel in the sensing fiber around the fiber stretcher with a sinusoidal signal of 100 Hz. The *y*-axis is proportional to distance along the cable, with a distance increment of 0.4 m, and the color of each cell is proportional to the waveform amplitude. Figure 4.4b shows the superposition result of absolute amplitude of each channel. The signal boundary is defined by the channel of 10% of the absolute peak amplitude. Results show

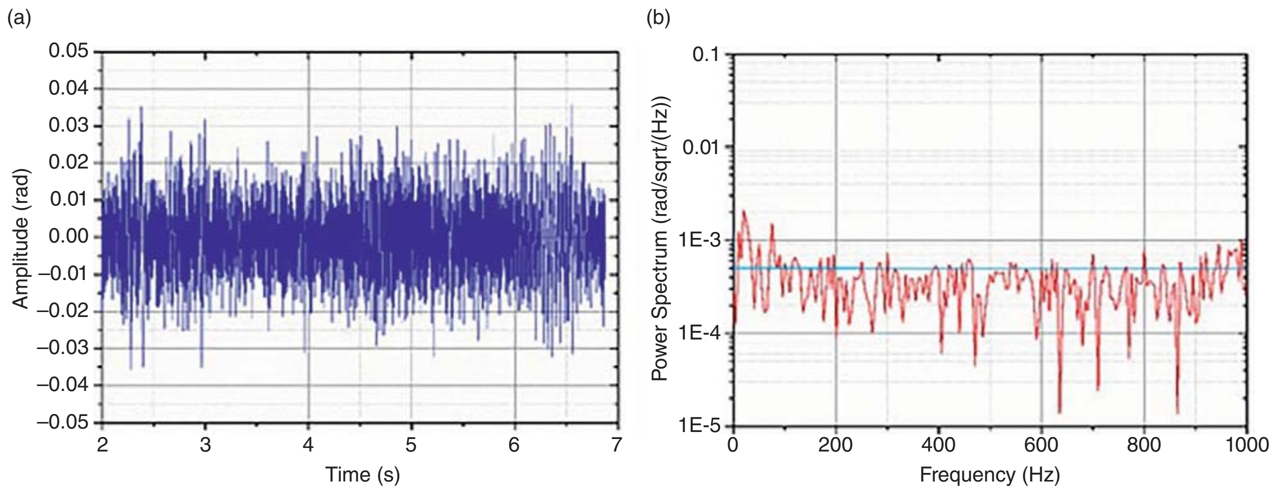

Figure 4.3 Phase noise of PGC-DAS system on Channel #4750: (a) Time series and (b) power spectrum.

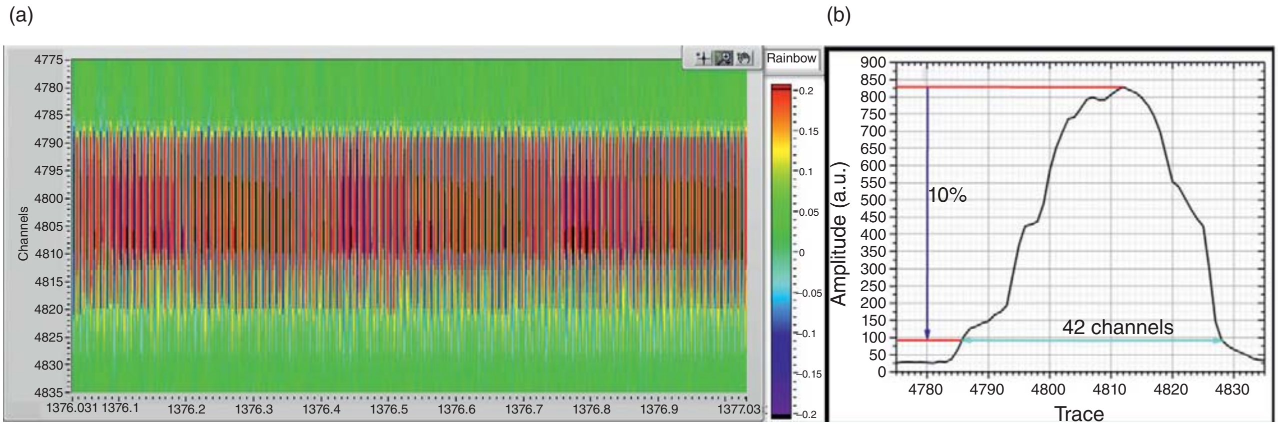

Figure 4.4 Intensity map of demodulation magnitude of each channel: (a) Waterfall plot and (b) superposition absolute magnitude.

that the sinusoidal signal ranges from Channel #4786 to Channel #4828, and the range is up to 16.8 m. By subtracting the coiled fiber length, the spatial resolution of PGC-DAS system is about 10.8 m, which is nearly consistent with the optical path difference L_{MI} = 10 m.

Figure 4.5 depicts the measurement of frequency response with a linear sweeping frequency signal from 2 Hz to 1 kHz. Each sweeping signal with a constant voltage amplitude of 0.5 Vpp lasts 2 s. Short-time Fourier transform (STFT) is used to indicate the relative linear and flat frequency response of PGC-DAS system.

The linearity of PGC-DAS system is an essential characteristic of quantitative seismic measurement. A sinusoidal strain signal of the fiber stretcher with sweeping voltage from 0.01 Vpp to 1.6 Vpp is used to inspect the amplitude response. The linearity of the strain response is shown in Figure 4.6. From the fitting result, the linear coefficient R^2 is 0.99941. An expected linear response capability is presented, and it proves the feasibility of the PGC-DAS system for the microseismic signal detection.

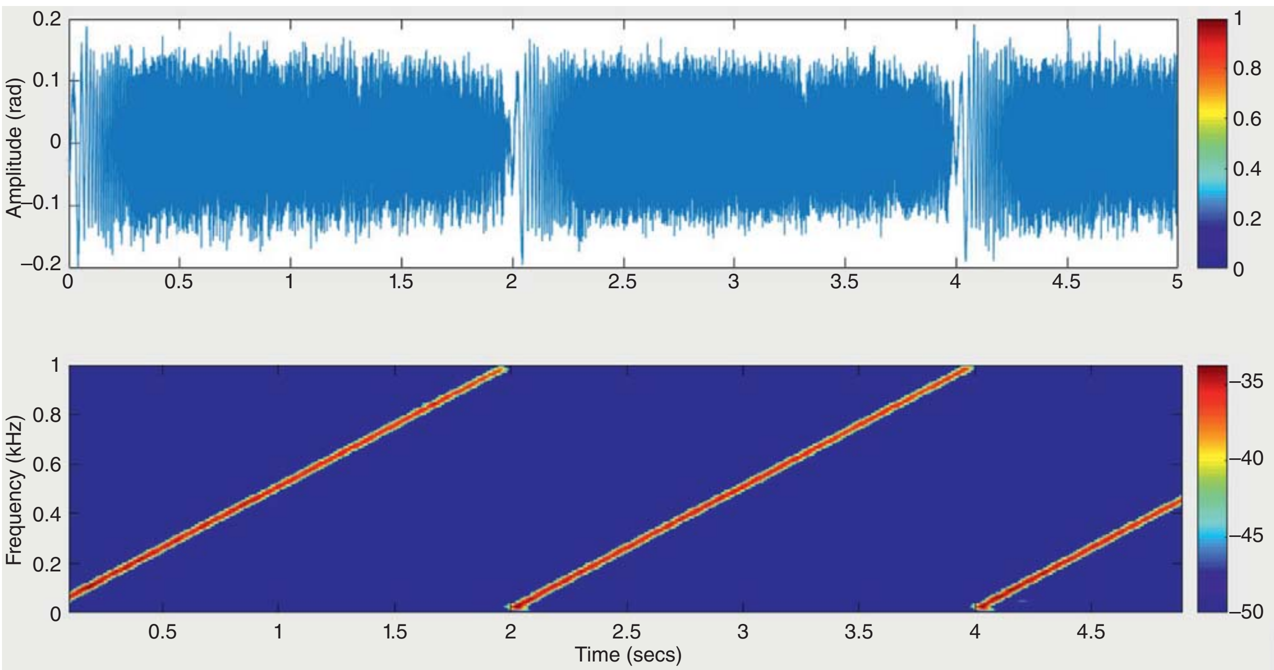

Figure 4.5 Time domain and STFT spectrogram of sweeping frequency signal.

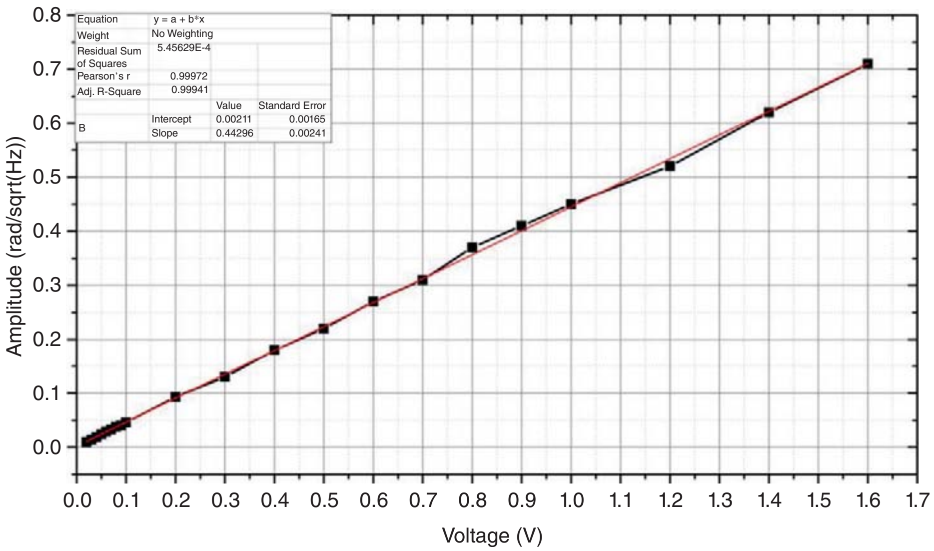

Figure 4.6 Amplitude response curve of PGC-DAS system.

4.4. FIELD TRIAL OF NEAR-SURFACE SEISMIC EXPERIMENT WITH PGC-DAS SYSTEM

A near-surface seismic experiment based on fiber optic cables and PGC-DAS system was conducted in Hebei Province, China. On the site, a 7 mm diameter fiber optic cable (Figure 4.7d) of about 430 m was buried in an approximate L shape at 0.4 m depth with a 230 m cable in Line 1 and a 200 m cable in Line 2 (Figures 4.7a and 4.7b). PGC-DAS system was connected at one end of the fiber optic cable to record multichannel seismic data at a sampling rate of 2 kHz with a spatial sampling interval of 1 m. For comparison, 80 conventional three-component (3C) geophones (Figure 4.7c) were buried along the cable with an interval of around 5 m. A vibroseis truck was employed as an active source at seven designed positions (P1, P2, P3, P4, P5, P6, and P7) around the fiber optic cable to investigate directivity, since optical fiber is mostly sensitive to axial strain along the fiber and lacks broadside sensitivity due to its silica glass nature.

Figure 4.8 shows multichannel seismic recordings of PGC-DAS system and geophone array in Line 1 at active source position #1. Since axial is the most sensitive direction of the fiber, the data of a 3C geophone for x-component were used. Both 40 channels' recordings for DAS system and geophones' array with the same interval of 5 m at similar positions were selected. Difference of seismic first arrivals' time between those two systems is due to trigger unsynchronization. DAS data were qualitatively similar to the signals observed on the geophones. Both direct wave and surface were clearly presented. However, there was apparently isolated noise in DAS data before the first arrivals (e.g., in Channels of 11, 151, and 161) due to interference fading. Simple contrast shows that this PGC-DAS system can provide reliable information to image and explore the shallow subsurface under this fiber cable.

4.5. CONCLUSIONS

We propose a real-time DAS system based on PGC demodulation algorithm. Compared with the previous work (Fang et al., 2015), it brings a 15.6 dB improvement in phase noise. The average noise could reach ~5×10^{-4} rad/√Hz, and the strain sensitivity is as small as 8.5 pε/√Hz for a 10 m spatial resolution. This PGC-DAS system could measure the dynamic vibration signal from 2 Hz to 1 kHz over a 10 km long optical fiber, with a linear coefficient R^2 of 0.99941 and a minimum spatial interval of 0.4 m. The near-surface seismic experimental results show that DAS data are qualitatively similar to the signals observed on the geophones. These facts suggest that DAS technology provides a novel and highly valuable tool for geophysical science in a wider sense. Moreover, PGC-DAS system has potential advantages in reducing size and power consumption due to simple structure and efficient phase demodulation algorithm, and a mini-PGC-DAS module is under development, with a size of 150 mm × 300 mm × 110 mm (width × depth × height) and a power consumption of 25 W, which could work at the bottom for submarine application.

Figure 4.7 Field trial of near-surface seismic experiment. (a) Plan view of experimental layout, (b) photo of the buried fiber optic cable, (c) photo of a 3C geophone, and (d) structure of the fiber optic cable.

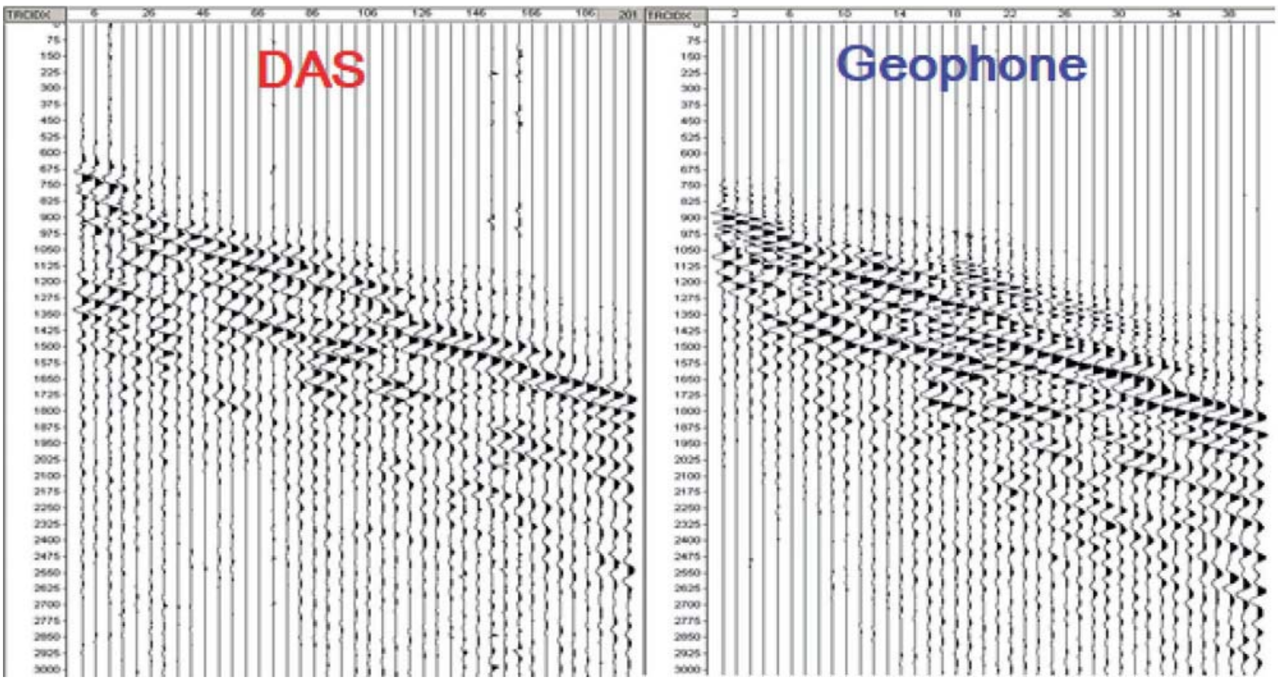

Figure 4.8 Initial data of DAS system and geophone array for *x*-component at P1 in Line 1.

ACKNOWLEDGMENTS

This work was funded by the National Natural Science Foundation of China (Grant Nos. 61875184 and 61775210), the National Key Research and Development Program of China (Grant No. 2017YFB0405500), the Strategic Priority Research Program of the Chinese Academy of Sciences (Grant Nos. XDC02040500 and XDA22040105), and State Key Laboratory of Geodesy and Earth's Dynamics, Institute of Geodesy and Geophysics, Chinese Academy of Sciences (Grant No. SKLGED2019-5-4-E).

REFERENCES

Alekseev, A. E., Vdovenko, V. S., Gorshkov, B. G., Potapov, V. T., & Sergachev, I. A. (2014a). A phase-sensitive optical time-domain reflectometer with dual-pulse phase modulated probe signal. *Laser Physics*, *24*(5).

Alekseev, A. E., Vdovenko, V. S., Gorshkov, B. G., Potapov, V. T., & Sergachev, I. A. (2014b). Phase-sensitive optical coherence reflectometer with differential phase-shift keying of probe pulses. *Quantum Electronics*, *44*(10), 965–969.

Alekseev, A. E., Vdovenko, V. S., Gorshkov, B. G., Potapov, V. T., & Simikin, D. E. (2015). A phase-sensitive optical time-domain reflectometer with dual-pulse diverse frequency probe signal. *Laser Physics*, *25*(6), 065101.

Bao, X., Zhou, D., Baker, C., & Chen L. (2017). Recent development in the distributed fiber optic acoustic and ultrasonic detection. *Journal of Lightwave Technology*, *35*(16), 3256–3267.

Dandridge, A., Tveten, A. B., & Giallorenzi, T. G. (1982). Homodyne demodulation scheme for fiber optic sensors using phase generated carrier. *IEEE Journal of Quantum Electronics*, *18*(10), 1647–1653.

Fang, G., Xu, T. W., Feng, S. W., & Li, F. (2015). Phase-sensitive optical time domain reflectometer based on phase generated carrier algorithm. *Journal of Lightwave Technology*, *33*(13), 2811–2816.

Feng, S., Xu, T., Huang, J., Yang, Y., Ma, L., & Li, F. (2018). Sub-meter spatial resolution phase-sensitive optical time-domain reflectometry system using double interferometers. *Applied Sciences*, *8*(10), 1899.

Hartog, A. (2017). *An introduction to distributed optical fiber sensors*. CRC Press, Taylor & Francis Group.

He, X., Liu, F., Qin, M., Cao, S., Gu, L., Zheng, X., & Zhang, M. (2017). Phase-sensitive optical time-domain reflectometry with heterodyne demodulation. 2017 25th Optical Fiber Sensors Conference (OFS) (pp. 1–4).

Huang, S., Lin, W., Chen M., Hung, S., & Chao, H. (1996). Crosstalk analysis and system design of time-division multiplexing of polarization-insensitive fiber optic Michelson interferometric sensors. *Journal of Lightwave Technology*, *14*(6), 1488–1500.

Juarez, J. C., Maier, E. W., Choi, K. N., & Taylor, H. F. (2005). Distributed fiber-optic intrusion sensor system. *Journal of Lightwave Technology*, *23*(6), 2081–2087.

Lu, Y., Zhu, T., Chen, L., & Bao, X. (2010). Distributed vibration sensor based on coherent detection of phase-OTDR. *Journal of Lightwave Technology*, *28*(22), 3243–3249.

Masoudi, A., Belal, M., & Newson, T. P. (2013). A distributed optical fibre dynamic strain sensor based on phase-OTDR. *Measurement Science and Technology*, *24*(8), 085204.

Park, J., Lee, W., & Taylor, H. F. (1998). *Fiber optic intrusion sensor with the configuration of an optical time-domain reflectometer using coherent interference of Rayleigh backscattering*. Proceedings of SPIE 3555, Optical and Fiber Optic Sensor Systems.

Parker, T., Shatalin, S., Farhadiroushan, M., Kamil, Y., Gillies, A., Finfer. D., & Estathopoulos, G. (2012). *Distributed Acoustic Sensing—a new tool for seismic applications*. *74th EAGE Conference & Exhibition incorporating SPE EUROPEC* 2012.

Qin, Z., Zhu, T., Chen, L., & Bao, X. (2011). High sensitivity distributed vibration sensor based on polarization-maintaining configurations of phase-OTDR. *IEEE Photonics Technology Letters*, *23*(15), 1091–1093.

Sha, Z., Feng, H., & Zeng, Z. (2017). Phase demodulation method in phase-sensitive OTDR without coherent detection. *Optics Express*, *25*(5), 4831–4844.

Sheem, S. K. (1981). Optical fiber interferometers with [3x3] directional-couplers—analysis. *Journal of Applied Physics*, *52*(6), 3865–3872.

Tanimola, F., & Hill, D. (2009). Distributed fibre optic sensors for pipeline protection. *Journal of Natural Gas Science and Engineering*, *1*(4), 134–143.

Taylor, H. F., & Lee, C. E. (1993). Apparatus and method for fiber optic intrusion sensing. Patent US5194847 A.

Wang, C., Shang, Y., Liu, X. H., Wang, C., Yu, H. H., Jiang, D. S., & Peng, G. D. (2015). Distributed OTDR-interferometric sensing network with identical ultra-weak fiber Bragg gratings. *Optics Express*, *23*(22), 29038–29046.

Wang, C., Wang, C., Shang, Y., Liu, X., & Peng, G. (2015). Distributed acoustic mapping based on interferometry of phase optical time-domain reflectometry. *Optics Communications*, *346*, 172–177.

Wang, Z. N., Zhang, L., Wang, S., Xue, N. T., Peng, F., Fan, M. Q., et al. (2016). Coherent Phi-OTDR based on I/Q demodulation and homodyne detection. *Optics Express*, *24*(2), 853–858.

Yang, G., Fan, X., Liu, Q., & He, Z. (2018). Frequency response enhancement of direct-detection phase-sensitive OTDR by using frequency division multiplexing. *Journal of Lightwave Technology*, *36*(4), 1197–1203.

Yan, Q., Tian, M., Li, X., Yang, Q., & Xu, Y. (2017). *Coherent Phi-OTDR based on polarization-diversity integrated coherent receiver and heterodyne detection*. 2017 25th Optical Fiber Sensors Conference (OFS) (pp. 1–4).

Zinsou, R., Liu, X., Wang, Y., Zhang, J., & Wang, Y. (2019). Recent progress in the performance enhancement of phase-sensitive OTDR vibration sensing systems. *Sensors (Basel)*, *19*(7), 1709.

Part II

Distributed Acoustic Sensing (DAS) Applications in Oil and Gas, Geothermal, and Mining Industries

5

Field Trial of Distributed Acoustic Sensing in an Active Room-and-Pillar Mine

Xiangfang Zeng[1,2], Herbert F. Wang[2], Neal Lord[2], Dante Fratta[3], and Thomas Coleman[4]

ABSTRACT

A distributed acoustic sensing (DAS) array consisting of three overlapping loops of cable was deployed in an active limestone and dolomite mine to sense ground vibration and examine the potential of DAS for seismic monitoring in active mine environments. The three cable loops were coupled to the mine floor in different ways: The first one was cemented into a shallow groove; the second one was covered with 2 cm of fine sand; and the third one was just loosely laid on the floor. The cemented cable loop provided the highest fidelity signal, and the cable loop loosely laid on the floor suffered from stronger noise and signal distortion. The maximum detectable distance for a 208 J weight-drop source was approximately 100 m, which was comparable to that for the horizontal component of a geophone. Two blasts were also recorded and located with this small array. Tomographic methods utilizing surface wave arrivals from the weight-drop source and differential *P*-wave travel times from the two mine blasts were applied to demonstrate the feasibility of imaging seismic structures with DAS observations. Uncertainty in picking arrivals, insufficient ray coverage, and strong directivity response of the DAS cable limited the resolution. Nonetheless, it appears that use of a properly installed and designed DAS array is practical for monitoring seismicity and seismic velocity changes in an active mine.

5.1. INTRODUCTION

The concepts of structural health monitoring using fiber-optic sensors (Glišić & Inaudi, 2007) to measure load, deformation, and temperature over both long and short time periods can be applied to underground mines (Wang & Gage, 2015). For example, distributed temperature sensing has been proposed to monitor temperature distribution in mines (Dubaniewicz et al., 1996) and its capabilities for monitoring temperature anomalies in an experimental mine have been demonstrated at Queensland University (Aminossadati et al., 2010). Similarly, mine-wide distributed fiber-optic sensing of deformation would enhance mine safety and design. Seismic monitoring, both active and passive, can provide information on changing stress conditions in an underground mine. DAS is especially promising for enhancing mine safety because of its seismometer-like recordings, its capacity to extend monitoring over great distances throughout a mine, and its dense receiver spacing. These attributes also provide

[1]State Key Laboratory of Geodesy and Earth's Dynamics, Innovation Academy for Precision Measurement Science and Technology, Chinese Academy of Sciences, Wuhan, China

[2]Department of Geoscience, University of Wisconsin–Madison, Madison, Wisconsin, USA

[3]Department of Civil and Environmental Engineering, University of Wisconsin-Madison, Madison, Wisconsin, USA

[4]Silixa LLC., Missoula, Montana, USA

Distributed Acoustic Sensing in Geophysics: Methods and Applications, Geophysical Monograph 268, First Edition.
Edited by Yingping Li, Martin Karrenbach, and Jonathan B. Ajo-Franklin.

DOI:10.1002/9781119521808.ch05

new opportunities for microseismic source location and seismic tomography.

DAS technology records the strain or strain rate, which can be converted into velocity/displacement, at meter-scale intervals everywhere along a fiber-optic cable (Parker et al., 2014). Near-infrared laser pulses are coupled into the optical fiber, and backscattered signals from impurities in the fiber-optic cable are analyzed at a sampling rate of tens of kilohertz. The phase of the backscattered signal is obtained by an unwrapping procedure. Interferometric analysis of the phase difference of the Rayleigh backscattered signal from two successive incident pulses generates a dynamic strain recording at meter-scale spacings. The phase difference is measured over a short section of cable that is called the gauge length, which typically ranges between 2 and 10 m (Wang et al., 2018). The phase response is proportional to the strain rate induced in the cable.

A DAS array was deployed on 27 and 28 July 2017 in the Lafarge-Conco mine in North Aurora, IL. In this chapter, we describe the installation of the fiber-optic cable, the data recorded during this two-day experiment, and the results for event location and tomographic imaging. We conclude with a discussion of how these methods can be used for mine monitoring.

5.2. EXPERIMENTAL METHODS

5.2.1. Cable Layout and Source Locations

The 1500 m long × 500 m wide wedge-shaped footprint of the Lafarge-Conco mine is divided into north and south sections by underground passageways beneath Interstate Highway I-88 (Figure 5.1a). The room-and-pillar mine (Figure 5.1a) has four levels down to a depth of approximately 80 m. It produces limestone and dolomite for aggregate (Meulemans et al., 2015; Wang et al., 2017). The rock is blasted in benches and hauled out of the mine by trucks and conveyor belts. The pillars supporting the roof are approximately 20 m on each side.

An approximately 1120 m of tactical fiber-optic cable was used in this study. First, an irregularly L-shaped groove of ~250 m long was cut in the floor between the pillars with a pavement saw (Figure 5.1b). The groove was approximately 1 cm wide and its depth ranged between 2 and 7 cm. The cable was installed in three loops that overlie one another. The first cable loop (Loop 1) was secured in the groove with self-leveling concrete, the mid-level loop (Loop 2) was covered by sand and silt-sized cuttings, and the top loop (Loop 3) was simply laid over Loop 2 (Figure 5.2a). This design provided an

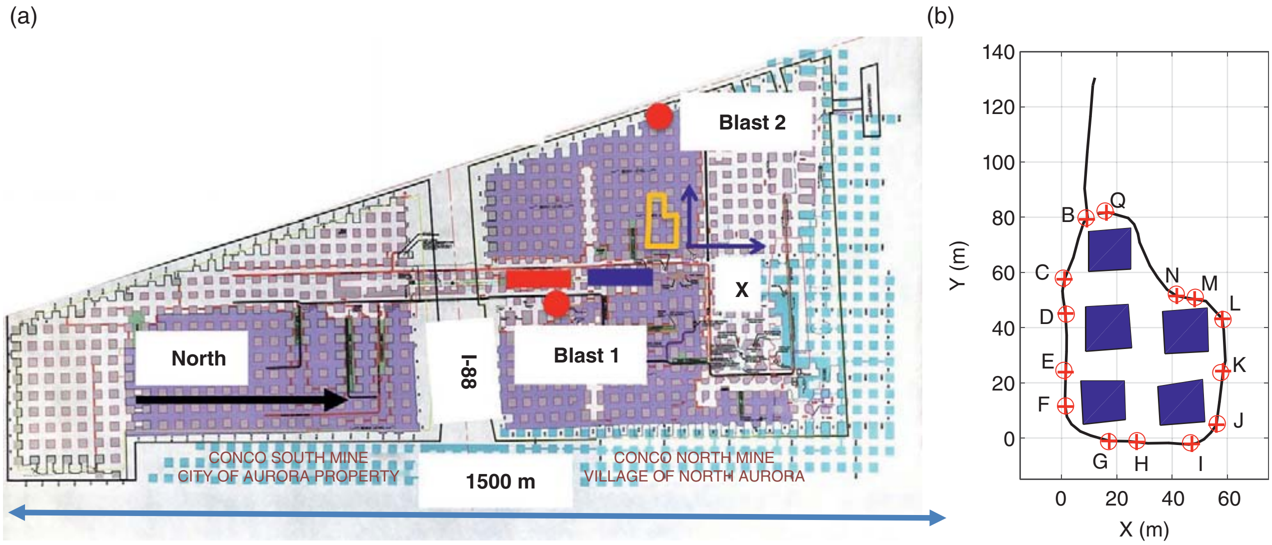

Figure 5.1 (a) Map of the Lafarge-Conco mine (presented with permission of Lafarge-Conco). Red solid circles denote the locations of the mine blasts executed during this experiment. The ramp and conveyor are represented by a red and a blue box, respectively. (b) Layout of the DAS array. The blue squares are pillars, and the solid line denotes the three loops of the DAS cable. The “weight-drop” and “tap-test” source locations (letters B through Q) are shown by red open circles.

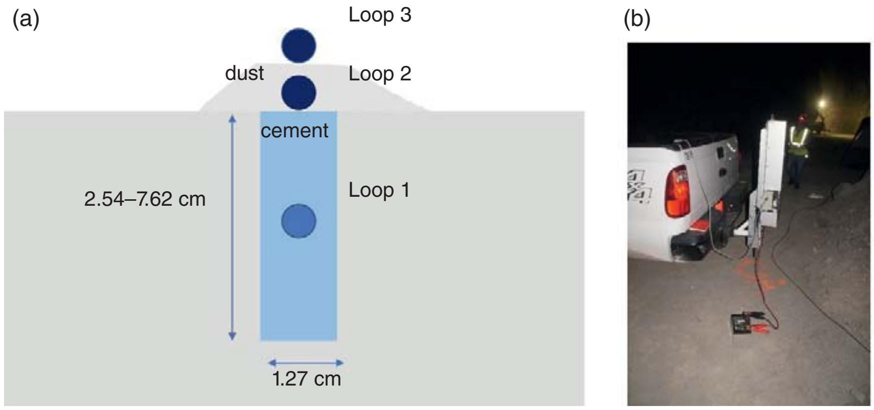

Figure 5.2 (a) Sketch of a cross-section showing the emplacement of co-located cables in the three loops. (b) View of the 23 kg ESS of GISCO company.

opportunity to compare the coupling efficiency associated with different levels of effort in cable installation.

A local coordinate system was set up by locating 50 points along the cable in a total-station survey. A series of hammer "tap-tests" were then performed at 14 points (letters B through Q shown in Figure 5.1b) to register surface positions with DAS channel numbers. These locations were also pointed where the bumper-mounted weight-drop device (a 23 kg electronic seismic source (ESS) of GISCO company; Figure 5.2b) was operated. Other sources included two daily mine blasts located outside of the DAS array (Figure 5.1a). Approximately 1,000 pounds of dynamite was used for each blast. The signals of the three sources were analyzed for different purposes.

5.2.2. Data Acquisition

A Silixa iDAS^{TM} interrogator (Silixa Ltd., Elstree, United Kingdom) was used to capture the strain-rate data sensed by the fiber-optic cable. A high-precision clock on the iDAS interrogator was synchronized with Global Positioning System (GPS) at the mine surface before going underground. A generator supplied electricity; however, deep-cycle batteries and an inverter were used during blasting when evacuation of mine personnel took place. The interrogator was affected by vibrations caused by trucks passing by on a nearby ramp, which generated high-coherency, common-mode noise across the array. The system's gauge length was set at 10 m, but the spatial sampling interval was 1 m. The data were acquired at a sampling rate of 1000 Hz in two modes: Trigger mode and continuous mode. The trigger mode recorded 30 s long waveforms when the active sources (hammer source and weight-drop source) were employed. During the daily blasts on 27 and 28 July 2017, the interrogator worked unattended in continuous mode and recorded up to 21 min of data.

In addition to the DAS array, two three-component short-period geophones (SENSOR Nederland PE-6/B) were used to provide comparisons and source timing. Omnirecs DATA-CUBE recorders, whose clocks were synchronized with GPS before going in and after leaving the mine, were used to continuously record ambient noise and active source signals. The recorder used for comparison with DAS records was installed at Location D shown in Figure 5.1b, and the second recorder was placed next to each ESS source in turn.

5.3. CABLE COUPLING COMPARISONS

The three co-located DAS channels at Location D were chosen to analyze how the cable installation affected the ground coupling. The traces from the hammer source excited at Location E are shown in Figures 5.3a and 5.3b. The waveforms of the first arrival (0.06–0.09 s) correlate well with each other, but the amplitude is the largest for Loop 3 and decreases from top to bottom. The amplitude of the top cable (Loop 3) for the later-arriving signal (0.10–0.16 s) is much greater than that for the first arrival, as well as those of the two lower cables. One explanation is that cable shaking was much greater because it was not buried/constrained. A similar pattern is also observed in the records for ESS sources. The similarity of waveforms among co-located channels is better for weaker signals from ESS sources farther away (Figure 5.3e). For a

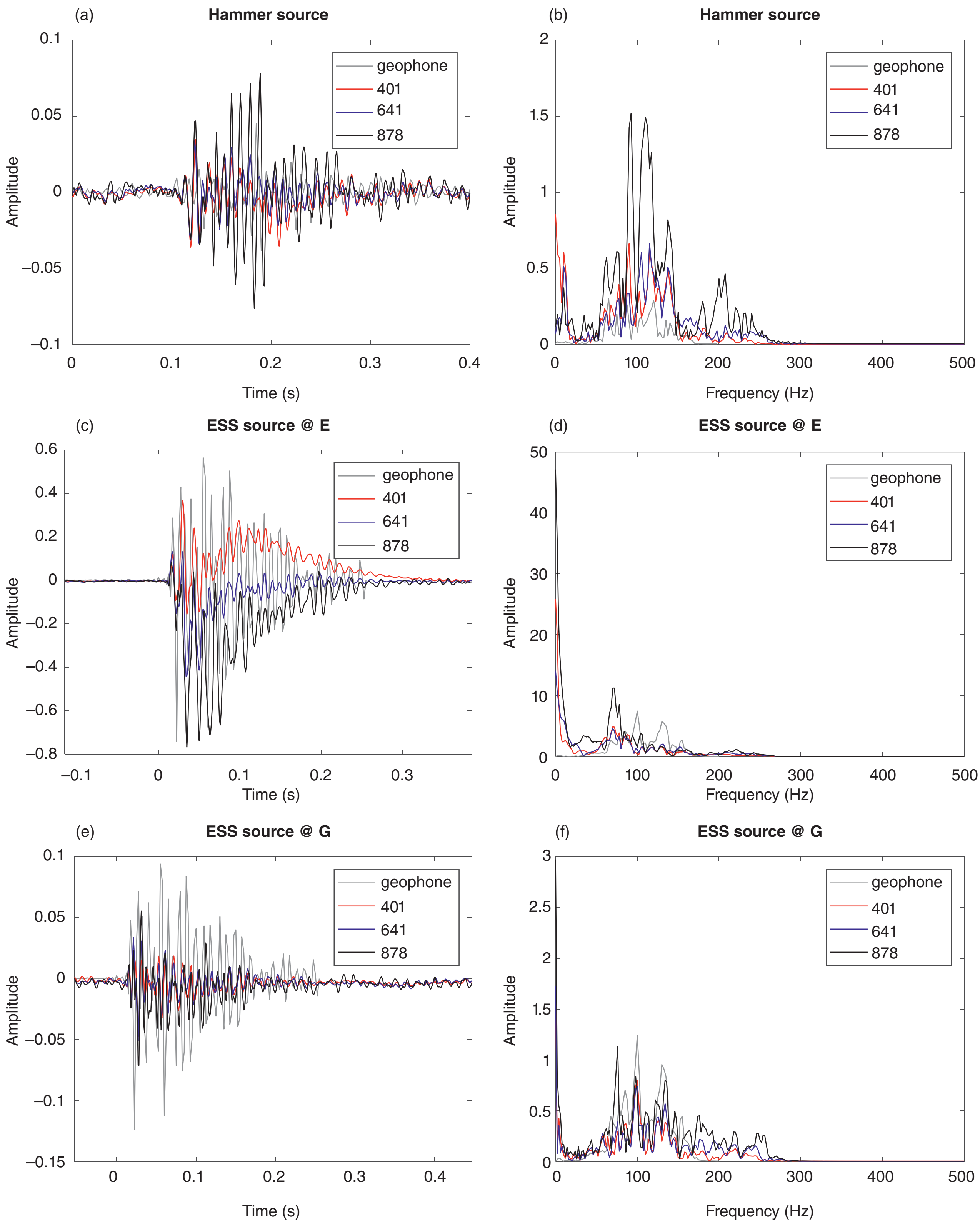

Figure 5.3 Waveforms and spectra for different source locations recorded on three DAS channels and a geophone co-located at Location D. Channels 401, 641, and 878 are in Loop 1, Loop 2, and Loop 3, respectively. (a) and (b) Hammer source at Location E. (c) and (d) ESS source at Location E. (e) and (f) ESS source at Location G. Traces of the east component of the geophone were normalized by a factor of 1.5×10^6 in (a) and (b), 3×10^5 in (c) and (d), and 18×10^5 in (e) and (f).

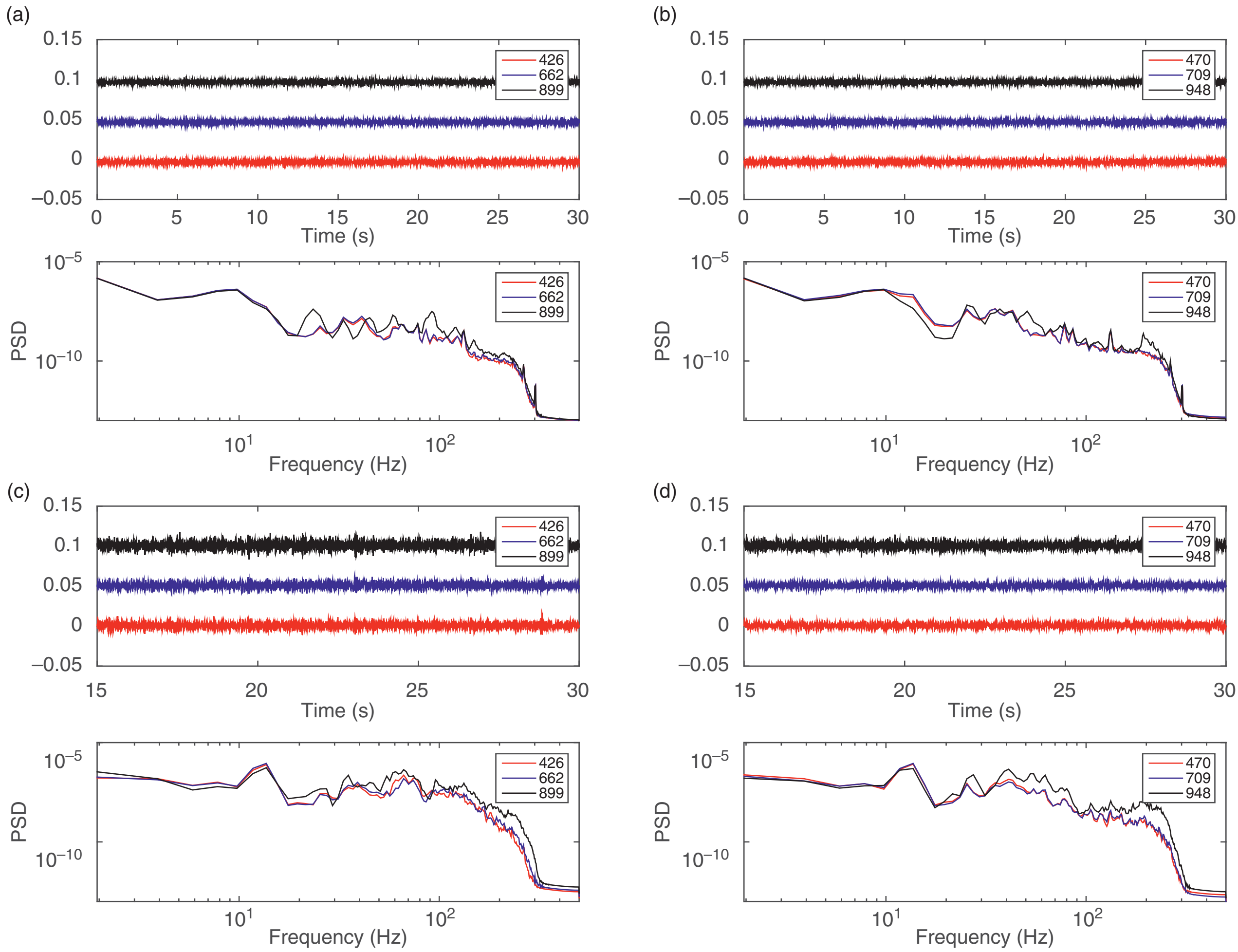

Figure 5.4 Ambient noise records at Location E (left column) and Location H (right column). Traces and spectra for a 30 s time window without mine activity before Blast 2 are shown in (a), and their spectra are shown in (b). Traces and spectra for a 15 s time window during normal mining operations are shown in (c) and (d). Red, blue, and black denote channels in Loop 1, Loop 2, and Loop 3, respectively.

nearby ESS source location, a strong 60–90 Hz signal is observed after the first arrival and its amplitude also deceases from top to bottom for co-located channels. This signal is not observed on the waveform and spectrum of the co-located geophone. Since the natural frequency of the PE-6/B geophone is 4.5 Hz and the typical spurious frequency is 140 Hz, the signal in the 60–90 Hz band is expected to be accurately recorded. The traces of co-located channels farther from the source (Figure 5.3e) are more consistent with each other than the traces of those close to the source. Therefore, the 60–90 Hz frequency signal may have been introduced during the phase unwrapping of large strains.

During the period of quiescence before the daily mine blast, Loop 3 channel also shows slightly stronger noise from Interstate Highway I-88 traffic at frequencies above 20 Hz, whereas power spectral densities of channels in Loop 1 and Loop 2 are stronger (e.g., 9% and 8%, respectively, for the channels at Location E at 9.8 Hz) in the traffic noise frequency band (4–20 Hz), especially for channels perpendicular to the highway (Figures 5.4a and 5.4b). During ordinary mining operations, the noise level of channels in Loop 3 is stronger than that of channels in Loop 1 and Loop 2 (Figures 5.4c and 5.4d).

5.4. DAS SENSITIVITY

A key characteristic for using DAS to monitor mine safety is its sensitivity. Because the DAS strain-rate sensitivity is primarily in the axial direction of the cable (Mateeva et al., 2014), its response depends on the angle between the incident strain signal and the cable direction, in addition to factors such as distance and ground coupling. To examine the sensitivity, the wavefield recorded by all DAS channels is shown in Figure 5.5a for the low-energy ESS source at Location D. The seismic signal was observed over the entire array for offsets between 0 and 91 m. The array can identify two phases. The first arrival is the body wave with a higher frequency content and the later, stronger arrival is the lower frequency surface wave (Figure 5.5b). The apparent velocity of the surface wave is approximately 2300 m/s, whereas the body wave travels much faster (~5000 m/s). It is difficult to manually track and pick the onset of the body wave. Automatic picking methods, such as the short-term average/long-term average (STA/LTA) method, are computed with a short time window; however, in our case, the interval between the body wave and the surface wave is too small for automatic pickers.

Arrivals are also difficult to identify because the amplitude decays with offset due to geometrical spreading and inelastic attenuation. To analyze the sensitivity of this DAS array, we investigated the amplitude decay curve for the ESS source signal. The signal amplitude is defined as the maximum amplitude in a 0.3 s time window starting from 0.15 s before the ESS origin time, and the noise level is the root-mean-square amplitude in a 0.2 s time window starting from 0.3 s before the ESS origin time. A high-pass filter (>50 Hz) is applied to the raw waveform to remove noise from truck traffic. Figure 5.6 shows the amplitudes of every fifth channel in each loop. The amplitude decays faster than the normal geometrical spreading of the surface wave and body wave, $1/r^{1/2}$ and $1/r$, respectively, where r is the offset. The observations are fit by an exponential decay function ($\log_{10}(\text{Amplitude}) = a_r + b)$), where the first term (a_r) reflects decay with offset and the second term (b) is a constant. Generally, the amplitude of the uncovered loop (Loop 3) is stronger and the decay constant $a = -0.0166$ is slightly smaller than those of the dust-covered loop (Loop 2) ($a = -0.0184$) and the cemented loop (Loop 1) ($a = -0.0191$). The crossover point of the amplitude curve and noise level is the point where the signal-to-noise ratio (SNR) equals 1 and can be considered as the maximum distance of detectability for a given magnitude (Mendecki et al., 1999). For the east component of the geophone at Location D, the decay term a is -0.0271, which means a faster decay (Figure 5.6d). In contrast, the maximum distance of detectability of the vertical component is approximately 150 m, which is approximately 50% larger than that of the east component and DAS Loop 1 and Loop 2 (~100 m). This result is also comparable to that of a typical accelerometer network in a gold mine (100 m for a Magnitude-3 event) (Mendecki et al., 1999).

5.5. LOCATING A SEISMIC SOURCE

The onsets of the first arrivals (P-wave) from the two daily blasts during this experiment are much clearer than those from the ESS source (Figure 5.7a). This data set provided an opportunity to better demonstrate the usage of DAS for seismic source location. In this study, we utilized

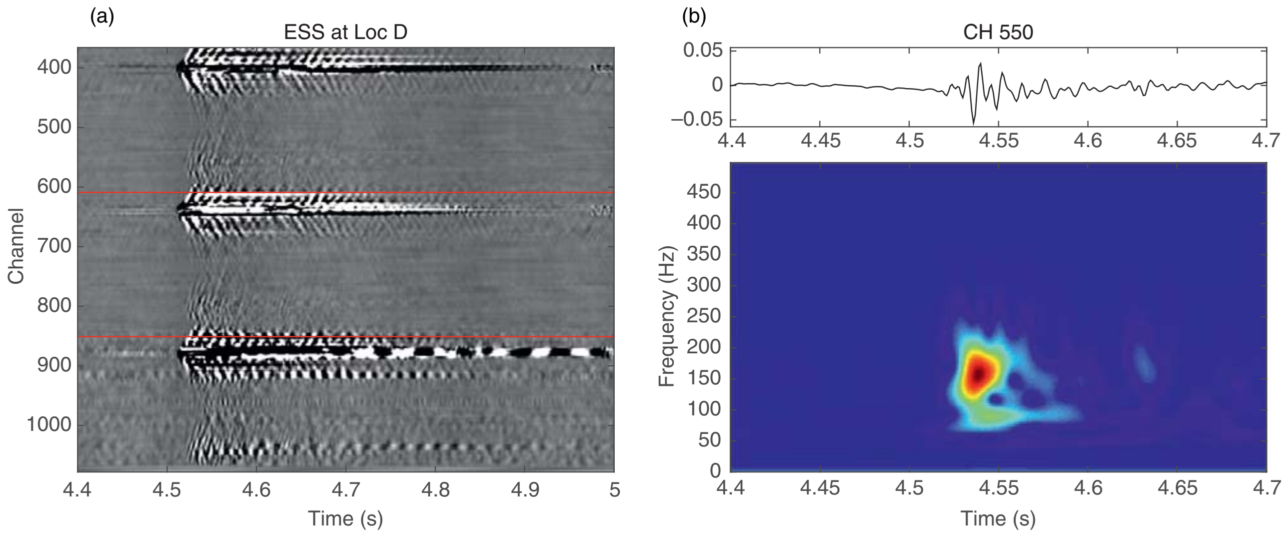

Figure 5.5 (a) Wavefield for all three cable loops for the source at Location D. Red lines indicate the beginning channels of Loop 2 and Loop 3. (b) Trace of Channel 550 and its spectrogram. Color represents spectral amplitude. The dashed lines denote arrivals for wave speeds of 5000 m/s, 4000 m/s, and 3000 m/s.

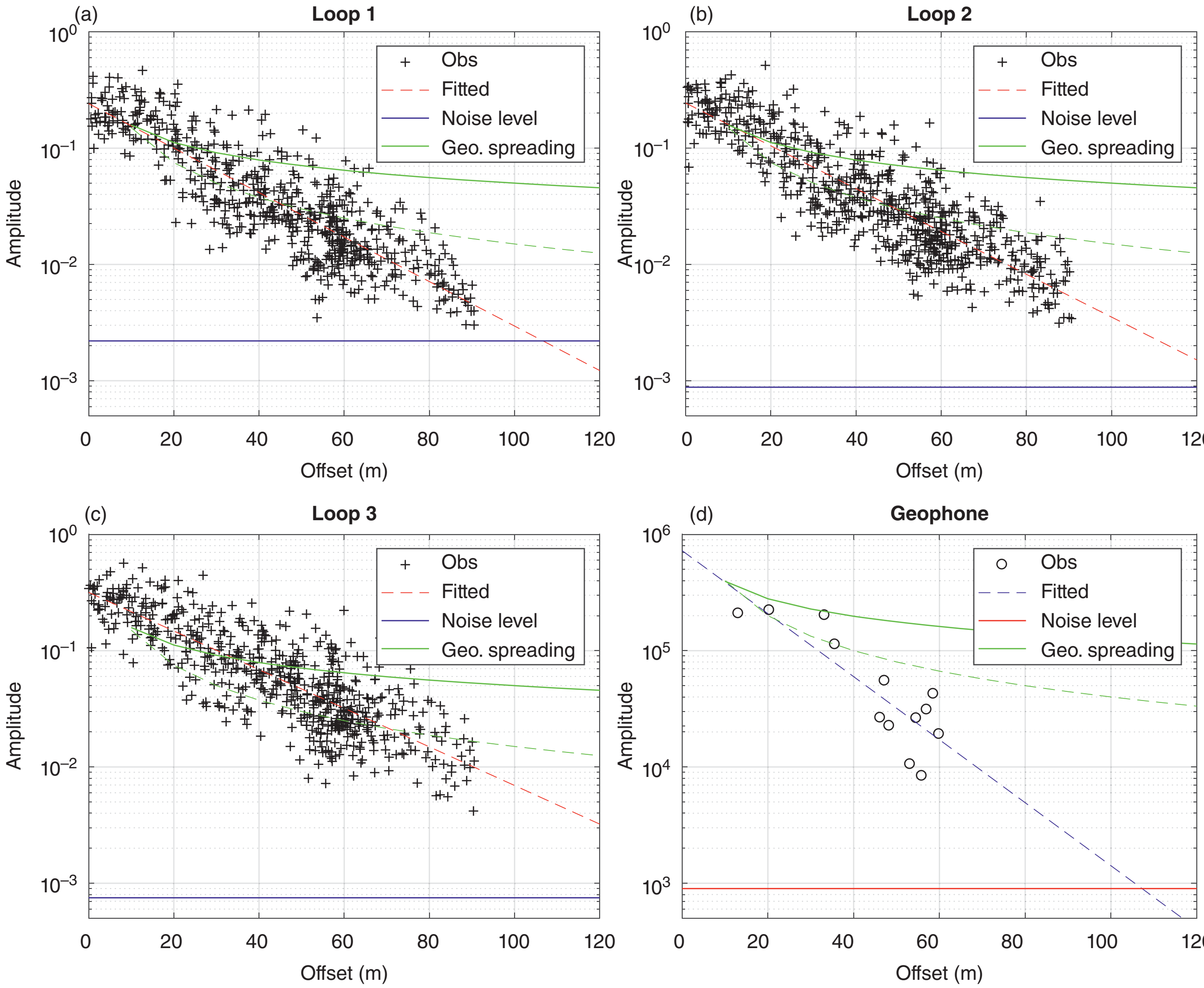

Figure 5.6 (a) Amplitude decay curves for Loop 1. Crosses show the amplitudes for 14 sources and the red dashed line denotes the best fit. The blue line represents the median noise level over all three loops. (b) Same as the preceding statement, but for Loop 2. (c) Same as the preceding statement, but for Loop 3. (d) Same as the preceding statement, but for the east component of the geophone at Location D. Geometrical spreading curves for surface waves and body waves are represented by green solid and dashed lines, respectively.

the records of Blast 2 executed on 28 July 2017. An automatic picker based on the Akaike information criterion (AIC) (Kitagawa & Akaike, 1978) method was employed to pick the onsets (Figure 5.7a). The velocity used for source location is the average velocity (5842 m/s) obtained from our picks. The source location was obtained using a grid-search method. All three loops recorded consistent arrivals. Since Loop 1 had the best coupling, its arrivals were used in the analysis. The predicted travel time from a given source location is computed with average *P*-wave velocity and the residual is computed as the RMS difference between observation and prediction. The optimal location is the point with the minimum residual. Because the blast occurred outside of the DAS array, the optimal location is not well constrained and contours of the residual are strongly elongated in an approximately 45° direction, as a result of the source-array geometry. The location accuracy would be significantly improved if a larger array were deployed. A larger array would also provide larger separation between later phases (e.g., the shear wave and surface wave) and the first arrival. Such a separation would make it easier to pick their onsets and obtain a more accurate differential time to reduce the trade-off between the origin time and location. However, the directional sensitivity of DAS would also need to be considered.

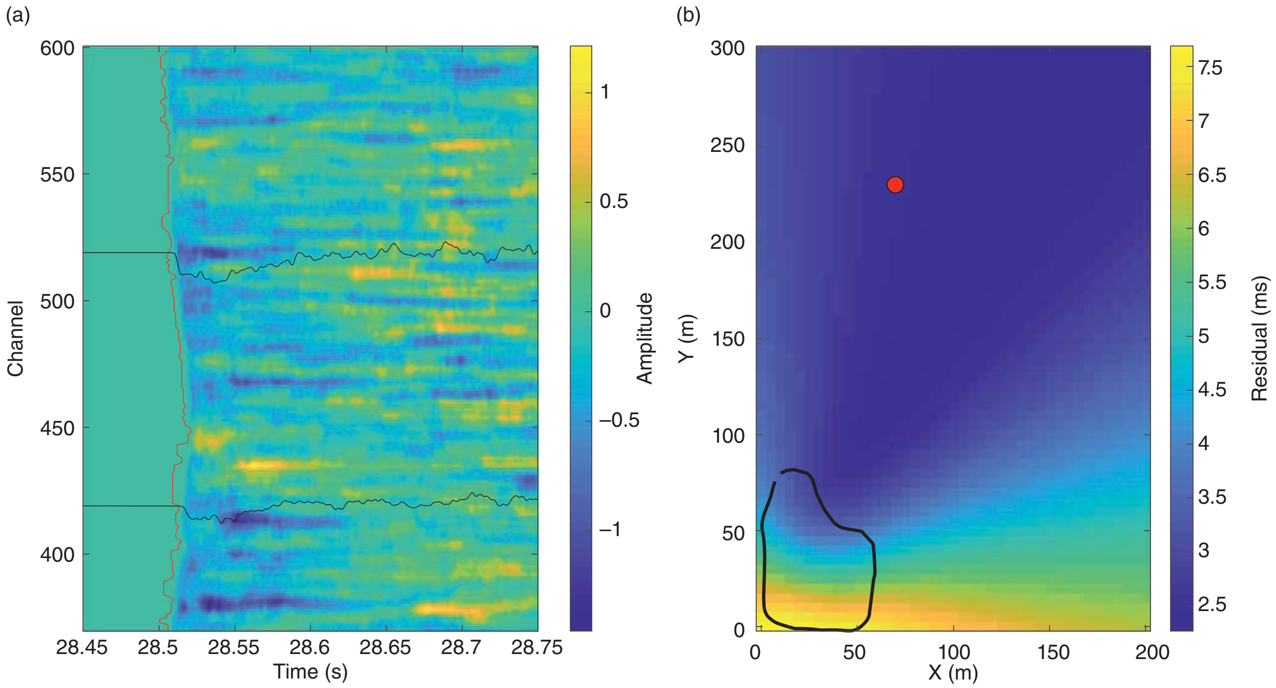

Figure 5.7 (a) Time vs. channel number plot for Loop 1 for the blast executed on 28 July. The first arrival is marked with the red line, and two sample traces are shown by black lines. (b) RMS of residuals from the grid-search location method. The red circle denotes the true location.

5.6. SURFACE WAVE TRAVEL-TIME TOMOGRAPHY

Stresses in underground mines are redistributed as new openings are excavated, which may cause pillar failures and loss of life (Esterhuizen et al., 2006). Monitoring the stress on pillars and its change can improve mine design and reduce failure risk. Since previous studies suggest that seismic tomography can be used to monitor stress changes in a mine (e.g., Scott et al., 1997), an attempt was made to determine if velocity differences could be associated with pillars within this DAS array. The surface wave arrivals at Loop 1 from the ESS source at different locations along the perimeter were utilized in this analysis.

To enhance the SNR, the records of all shots at one location were first stacked (Figure 5.8a). Then, the arrivals on every second channel were automatically picked by a classic STA/LTA picker (e.g., Allen, 1978). The length of the short time window was chosen to be 0.02 s, whereas that of the long-time window was 0.06 s. The arrival was picked at the peak of the STA/LTA curve, which corresponds to the surface wave on most channels. Quality control (QC) was introduced to remove outliers (Figure 5.8b). The first QC step is based on the SNR, which is defined as the ratio of the RMS amplitudes of the waveform before and after the pick. The second QC step requires that the STA/LTA peak value should be larger than 20. After removing low-quality picks, the arrival times were fit with a straight line that defines an average velocity and origin time. The picks that exceeded the specified upper and lower bounds of ±5 ms were considered outliers, likely corresponding to the *P*-wave or noise. More than 1,000 picks were obtained and most of them were picked on records for which the source and receiver were in-line (Figure 5.9a) because the particle motion of the surface wave excited by the in-line source was parallel to the cable direction, for which DAS is most sensitive. Therefore, the ray coverage in the center of the DAS array was sparse, which lowered the quality of the resulting tomographic image.

Because the sources and receivers were at the same level, seismic tomography was performed with a two-dimensional (2D) model, using a grid spacing of 10 m. We used the well-known simultaneous iterative reconstruction technique (SIRT) back projection method (e.g., Hole, 1992), which averages the model perturbation over rays hitting one cell. This method was also used by Friedel et al. (1996) to perform seismic tomography in the Homestake Mine. After four iterations, the RMS of residuals was reduced to 0.85 ms. A checkerboard test suggests that the resolution of our data set is

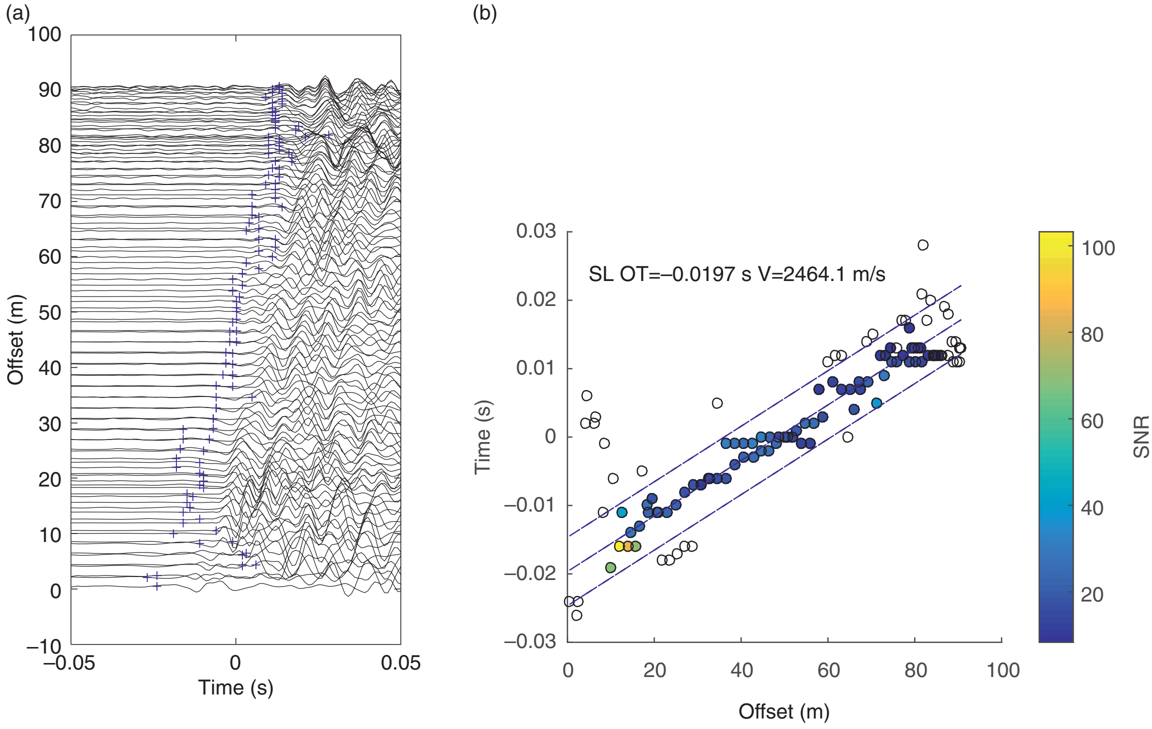

Figure 5.8 (a) Stacked traces for Loop 1 for the ESS source at Location B. Blue crosses denote picked arrivals. (b) Travel time vs. distance plot. Solid circles show picks used in the fitting. Its color represents SNR. Open circles denote outliers, which were removed from the fit. The blue lines are the fit to the arrivals and the upper (+5 ms) and lower bounds (−5 ms).

approximately 10 m × 10 m. The final model, with an average velocity of 2613 m/s, is shown in Figure 5.9. The typical *S*-wave velocity of dolomite ranges between 1900 and 3600 m/s (Bourbie et al., 1987). Considering the surface wave velocity to be ~0.92 V_s (e.g., Shearer, 1999), the inverted velocities readily fall into this broad range. Strong lateral velocity variations appear in the tomogram. The largest velocity anomalies are observed on edge cells and in the northeastern area (40 m < X < 50 m, 0 m < Y < 30 m), whereas velocities in the western cells (30 m < Y < 60 m) are relatively slower. Such large velocity variations were also reported in previous studies (e.g., Meulemans et al., 2015; Scott et al., 1997). We note that the lack of ray paths needs to be considered when interpreting velocity anomalies in edge cells.

Numerous studies suggest that the velocity in underground mines correlates well with stress distribution (e.g., Young & Maxwell, 1992). Higher stressed areas are imaged as high-velocity anomalies, whereas damage zones appear as low-velocity anomalies (e.g., Friedel et al., 1996). Meulemans et al. (2015) conducted 2D ultrasonic *P*-wave tomography in a single pillar near our DAS array. The tomographic plane was at a height of 1.25 m from the floor with source and receivers separated about 2 m along all sides of the pillar. Velocity changes between two surveys 6 months apart were interpreted as changes in stress associated with new excavation, which is expected for a room-and-pillar mine (Esterhuizen et al., 2006). However, no clear correlation of velocity with pillars emerges on the tomogram even in the densely sampled area (Figure 5.9b). Meulemans et al. (2015) reported the velocity anomaly area is less than 50% of the pillar. The picking uncertainty of 5 ms as the QC bound makes it difficult to image such small-scale features.

5.7. *P*-WAVE DIFFERENTIAL TRAVEL-TIME TOMOGRAPHY

Because of the difficulty in picking the weak *P*-wave arrivals for the low-energy weight-drop source records, we attempted an inversion based on the high-quality *P*-waveforms excited by two daily mine blasts. The 27 July blast was shot at approximately 15:48 local time near the conveyor and the 28 July blast was shot at approximately 15:46 to the west of the DAS array (Figure 5.1a). The ray paths formed an angle of approximately 135° relative to the DAS array (Figure 5.1a). The *P*-wave arrivals were picked on Loop 1 by a standard AIC picker (Figure 5.7a).

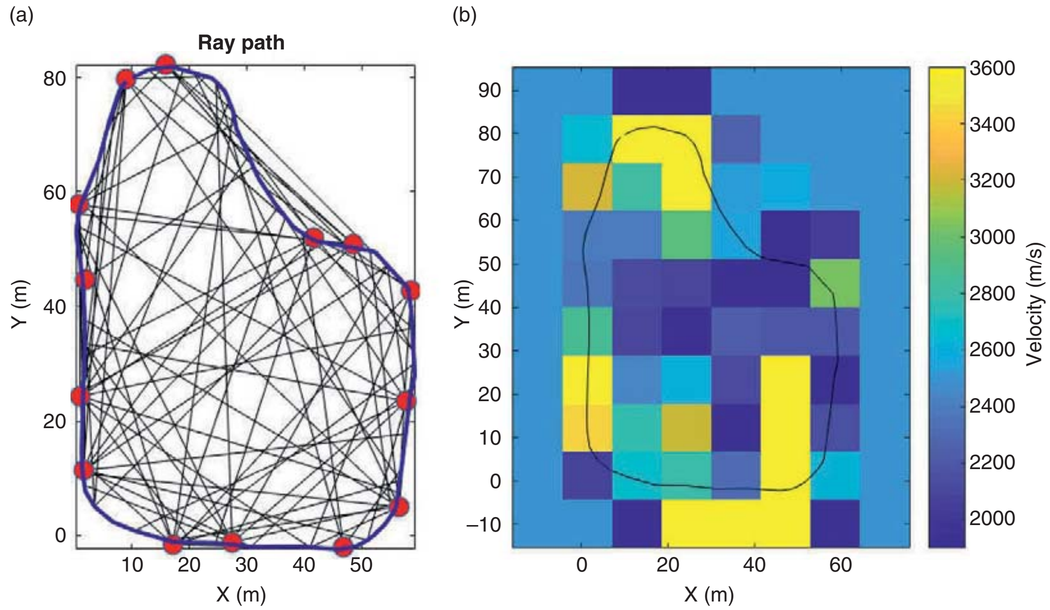

Figure 5.9 (a) Sample ray paths for surface wave tomography using the ESS source data set. Only 10% of the ray paths are shown for clarity. Red solid circles denote source locations. (b) Surface wave velocity tomogram.

To conduct standard travel-time tomography, the shot time of the blast is required to compute the absolute travel time, but time synchronization was not available. Therefore, we attempted to use differential travel time to overcome uncertainty in the origin time.

Differential travel times are widely used to reduce the common uncertainty (origin time, common ray path, etc.) shared by two or multiple observations and have been used in earthquake location and tomography (e.g., Waldhauser & Ellsworth, 2000; Zhang & Thurber, 2003). Two types of differential time are used in practice: The catalog differential time and cross-correlation differential time. The catalog differential time is the travel-time difference between two manually or automatically picked arrivals from two sources or stations that share most of their ray paths. Waveform cross-correlation is implemented in the time domain or in the frequency domain (e.g., cross-spectral analysis). The frequency-domain methods can be more accurate, but these require almost identical waveforms.

Because the blasts are on opposite sides of the DAS array and are far away, only a few rays cross within the DAS array. The setting is similar to teleseismic surface wave tomography, for which the source is outside of the array and differential travel times are used to image the structure beneath the array (e.g., Yang & Ritzwoller, 2008). Only channel pairs for which the difference in ray path azimuth is less than 2° were employed in the inversion to reduce additional time differences due to ray path differences outside of the array (Figure 5.10a). Even so, the paired waveforms were quite different (e.g., Figure 5.10a) and the cross-correlation method could not be used. The complicating factors were that the fiber-optic cable was not perfectly straight and that the cable sections were on opposite sides of any given DAS channel (Figure 5.10b). Therefore, the differential travel time was computed as the difference in arrivals picked by the AIC picker (Figure 5.10a). Because the differential travel time must be larger than the picking error, only channel pairs greater than 10 m apart were included. In total, 288 observations satisfied these criteria.

The average *P*-wave velocity from all observations was 5842 m/s, which falls into the dolomite range (3500–6500 m/s) measured in the laboratory (Bourbie et al., 1987) and is also consistent with the values obtained by Meulemans et al. (2015). The average velocity was adopted to construct a homogenous initial model. Because the number of observations was limited, the model space was again divided into 10 m × 10 m cells. Lateral variations in velocity clearly emerge on the tomogram obtained with the SIRT back projection method (Figure 5.11). The western part (30 m < Y < 80 m) shows relatively low velocities, whereas the northeastern part is relatively fast. Both anomalies are sampled by rays from the two blasts coming from different directions, which increases the reliability of this pattern. This finding also correlates well with the surface wave tomography result. Another higher velocity anomaly is seen in the cells on the western edge. However, the rays sampling the western-edge cells mostly come from Blast 2. The lack of intersecting rays in those cells

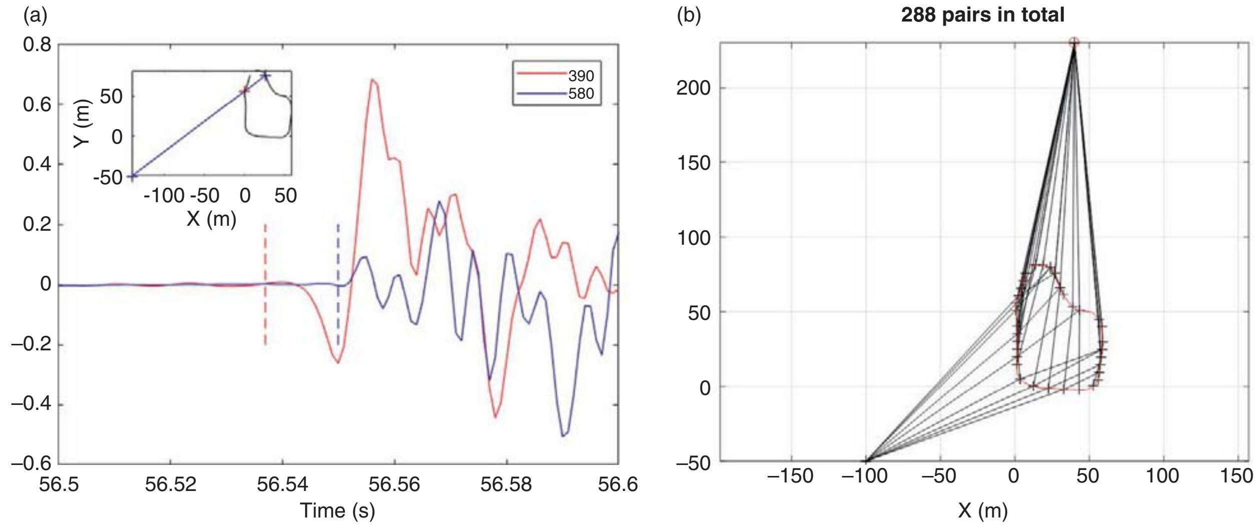

Figure 5.10 (a) Example waveforms and first arrivals from channel pair 390 and 580 in Loop 1 used for *P*-wave differential travel-time tomography. The inset shows the locations of Blast 1 (the cross in the lower left), Channel 390 (red), and Channel 580 (blue). (b) Sample ray paths for *P*-wave tomography using the 27 and 28 July mine blasts located outside the DAS array. Only 10% of the ray paths are shown for clarity.

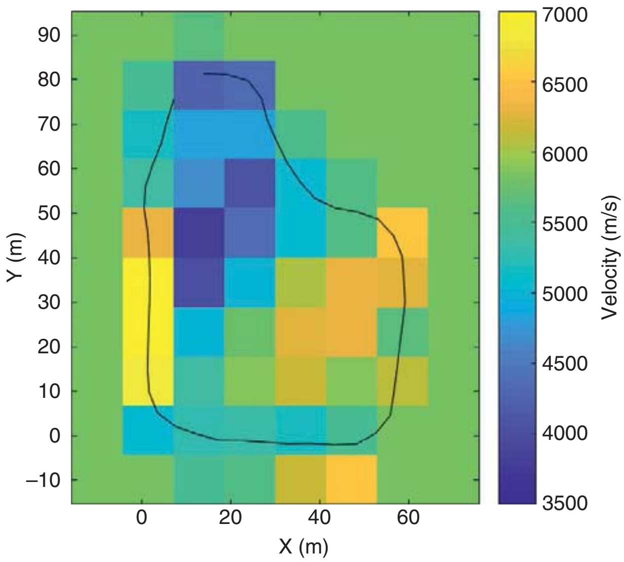

Figure 5.11 *P*-wave differential travel-time tomogram.

adds uncertainty to those results. No correlation between the pillar geometry and velocity is observed in our tomogram. One reason is that the resolution of our model is not sufficient to resolve such a small-scale feature. Having additional data from blasts in different directions would provide an improved tomogram and reveal more details to analyze stress distribution and redistribution.

5.8. DISCUSSION AND CONCLUSIONS

Although limited in scope, our DAS field trial in an active underground mine demonstrates the strong potential of DAS for mine monitoring. The most important gains that would occur in an array upscaled to encompass much larger volumes are that events can be located with much greater accuracy, and three-dimensional velocity models can be obtained. DAS also has potential application in locating a trapped miner. Hanafy et al. (2009) demonstrated that a hammer source signal recorded by a surface array could be utilized to locate a trapped miner. Mine-scale DAS can monitor and locate very weak signals even in a deep mine when other monitoring systems are not available. Redundant fiber-optic pathways would provide robustness against cable damage due to rock bursts and drift collapse.

An important practical consideration is the most cost-effective method for installing the cable. Our three-loop array allowed a comparison of the waveforms recorded by co-located channels. The cemented loop (Loop 1) provided a higher fidelity signal than the other two loops. Although the SNR is acceptable, the cable exposed to the air (Loop 3) can vibrate freely and produce signal distortion when a strong event occurs. Therefore, although it is desirable to secure DAS cables, a trade-off between the installation effort and fidelity can be considered. Another example of installing fiber-optic cables for DAS was reported by Nesladek (2017), who used various installation methods in the Montana Tech Orphan Boy Mine.

The most effective solution is to use preexisting telecommunications infrastructure fiber-optic cables in the mines. For example, DAS experiments on the 2.5 km long telecommunications infrastructure fiber-optic cable beneath the Stanford campus recorded earthquakes, as well as a variety of other events, such as construction noise, traffic, a garbage truck dropping a dumpster, and a quarry blast (Martin et al., 2018).

One drawback of DAS is the "broadside effect" or directional sensitivity. Since DAS measures strain along the cable, its azimuthal response is more complicated than that of a geophone because the variation in amplitude with the azimuth θ of an incident *P*-wave is $\cos^2\theta$ rather than $\cos\theta$. To better capture signals from various directions, two solutions have been proposed. The first solution is a special geometry of the cable layout. For example, a zigzag pattern was used in the PoroTomo project (Feigl & PoroTomo Team, 2018). The second solution is a specially designed cable. Helically wrapped/wound cables (e.g., Kuvshinov, 2016) or other engineered cables may lessen this problem in the future.

Because seismic tomography is an important application in mine monitoring, improvements in the picking precision and timing accuracy are needed. The picking precision is highly dependent on the SNR, and the easiest solution is to use larger energy sources. The gauge length is another important factor affecting the SNR (Dean et al., 2016; Willis et al., this volume). A better SNR can be achieved with larger gauge length, but this leads to averaging strain over longer cable segments. Such spatial smoothing also reduces the waveform difference between two nearby channels, which may increase the uncertainty of differential travel-time measurements.

Time-lapse tomography could be used to monitor mine development, which will be helpful in mine safety and efficiency. In addition to repeated active source tomography (Meulemans et al., 2015), several previous studies used travel-time tomography method (Westmann et al., 2012) and coda-wave interferometry method (Olivier & Brenguier, 2016) to reveal velocity changes interpreted in terms of mine development and atmospheric air pressure changes. It should also be feasible to utilize ambient noise tomography to monitor velocity changes in a future mine experiment as this method has been successfully applied to image near-surface structure with a surface DAS array (e.g., Zeng et al., 2017).

In summary, a DAS array installed in an active mine successfully recorded signals from sources with different energies. The maximum distance a 208 J source on a single channel can detect is approximately 100 m, which is comparable to the result for a traditional geophone. With a small channel spacing and simple installation, it is possible to build a highly capable seismic monitoring network. A dense DAS array throughout a mine can also help obtain a high-resolution seismic velocity model with the potential to monitor the stress state and help guide mine operations.

ACKNOWLEDGMENTS

This study was partly supported by the National Institute for Occupational Safety and Health (NIOSH) Office of Mine Safety and Health Research under Contract Number 211-2014-59580 led by Dr. Mary MacLaughlin at Montana Tech. X. Zeng thanks the Natural Science Foundation of China (41974067) and the LU JIAXI International Team Program supported by the K.C. Wong Education Foundation and the Chinese Academy of Sciences (GJTD-2018-12) for their support.

The authors also thank Lafarge-Conco personnel for mine access, logistical support, and assistance with cable installation in the mine floor. Kate Condon and Susan Richmond also participated in the installation of fiber-optic cable in the mine. The authors thank two anonymous reviewers, Dr. Clifford Thurber and Dr. Yingping Li, for their constructive comments that substantially improved the manuscript.

REFERENCES

Allen, R. V. (1978). Automatic earthquake recognition and timing from single traces. *Bulletin of the Seismological Society of America*, *68*(5), 1521–1532.

Aminossadati, S. M., Nayeemuddin, M. M., & Shemshad, J. (2010). Distributed temperature measurements using optical fibre technology in an underground mine environment. *Tunneling and Underground Space Technology*, *25*, 220–229.

Bourbie, T., Coussy, O., & Zinszner, B. (1987). *Acoustics of porous media*. Houston, TX, USA: Gulf Publishing Company.

Dean, T., Cuny, T., & Hartog, A. H. (2017). The effect of gauge length on axially incident P-waves measured using fibre optic distributed vibration sensing. *Geophysical Prospecting*, *65*(1), 184–193.

Dubaniewicz, T. H., Kovalchik, P. G., Scott, L. W., & Fuller, M. A. (1996). *Distributed measurement of conductor temperatures in mine trailing cables using fiber-optic technology*. Proceedings of the 1996 IEEE Industry Applications Conference Thirty-First IAS Annual Meeting. doi: 10.1109/IAS.1996.563918.

Esterhuizen, G. S., Iannacchione, A. T., Ellenberger, J. L., & Dolinar, D. R. (2006). *Pillar stability issues based on a survey of pillar performance in underground limestone mines*. In S. S. Peng, C. Mark, G. Finfinger, S. Tadolini, A.W. Khair, K. Heasley, & Y. Luo (Eds.), Proceedings of the 25th International Conference on Ground Control in Mining, August 1–3, 2006, Morgantown, West Virginia.

Feigl, K. L., & PoroTomo Team. (2018). *Overview and preliminary results from the PoroTomo project at Brady Hot Springs, Nevada: Poroelastic Tomography by adjoint inverse modeling of data from Seismology, Geodesy, and Hydrology*. Proceedings: 43rd Workshop on Geothermal Reservoir Engineering.

Stanford University, Stanford, California, 12–14 February 2018.

Friedel, M. J., Scott, D. F., Jackson, M. J., Williams, T. J., & Killen, S. M. (1996). 3-D tomographic imaging of anomalous stress conditions in a deep US gold mine. *Journal of Applied Geophysics*, *36*(1), 1–17.

Glišić, B., & Inaudi, D. (2007). *Fibre optic methods for structural health monitoring (1st ed.)*. Sussex, Chichester, UK.

Hanafy, S. M., Cao, W., McCarter, K., & Schuster, G. T. (2009). Using super-stacking and super-resolution properties of time-reversal mirrors to locate trapped miners. *The Leading Edge*, *28*(3), 302–307.

Hole, J. A. (1992). Nonlinear high-resolution three-dimensional seismic travel time tomography. *Journal of Geophysical Research: Solid Earth*, *97*(B5), 6553–6562.

Kitagawa, G., & Akaike, H. (1978). A procedure for the modeling of non-stationary time series. *Annals of the Institute of Statistical Mathematics*, *30*(1), 351–363.

Kuvshinov, B. N. (2016). Interaction of helically wound fibre-optic cables with plane seismic waves. *Geophysical Prospecting*, *64*(3), 671–688.

Martin, E. R., Huot, F., Ma, Y., Cieplicki, R., Cole, S., Karrenbach, M., & Biondi, B. (2018). A seismic shift in scalable acquisition demands new processing: Fiber-optic seismic signal retrieval in urban areas with unsupervised learning for coherent noise removal. *IEEE Signal Processing Magazine*, *35*(2), 31–40.

Mateeva, A., Lopez, J., Potters, H., Mestayer, J., Cox, B., Kiyashchenko, D., et al. (2014). Distributed acoustic sensing for reservoir monitoring with vertical seismic profiling. *Geophysical Prospecting*, *62*, 679–692.

Mendecki, A. J., Aswegen, G. V., & Mountfort, P. I. (1999). A guide to routine seismic monitoring in mines. In A. J. Jager, & J. A. Ryder (Eds.), *A handbook on rock engineering practice for tabular hard rock mines* (pp. 287–309). The Safety in Mines Research Advisory Committee, Johannesburg.

Meulemans, A., Wang, H., & Fratta, D. (2015). *Imaging the redistribution of stresses in a pillar during mining production*. In Integrating Innovations of Rock Mechanics: Proceedings of the 8th South American Congress on Rock Mechanics (p. 237), 15–18 November 2015, Buenos Aires, Argentina. IOS Press.

Nesladek, N. (2017). Comparing distributed acoustic sensing to three-component geophones in an underground mine (Master thesis). Montana Tech, Butte, MT.

Olivier, G., & Brenguier, F. (2016). Interpreting seismic velocity changes observed with ambient seismic noise correlations. *Interpretation*, *4*(3), SJ77–SJ85.

Parker, T., Shatalin, S., & Farhadiroushan, M. (2014). Distributed acoustic sensing; A new tool for seismic applications. *First Break*, *32*(2). doi:10.3997/1365-2397.2013034.

Scott, D. F., Williams, T. J., Friedel, M. J., & Denton, D. K. (1997). Relative stress conditions in an underground pillar, Homestake Mine, Lead, SD. *International Journal of Rock Mechanics and Mining Sciences*, *34*(3–4), 278-e1.

Shearer, P. (1999). *Introduction to seismology*. Cambridge: Cambridge University Press.

Waldhauser, F., & Ellsworth, W. L. (2000). A double-difference earthquake location algorithm: Method and application to the northern Hayward fault, California. *Bulletin of the Seismological Society of America*, *90*(6), 1353–1368.

Wang, H., & Gage, J. (2015). Fiber-optic monitoring in underground rock engineering. In Xia-Ting Feng (Ed.), *Rock Mechanics and Engineering (v. 4, pp. 529–560, Chap. 17)*. London: CRC Press.

Wang, H., Zeng, X., Lord, N., Fratta, D., & Coleman, T. (2017). University of Wisconsin-Madison final report of distributed acoustic sensing (DAS) field trial at the Lafarge-Conco mine in N. Aurora, IL in July 2017. Report submitted to Montana Tech.

Wang, H., Zeng, X., Miller, D., Fratta, D., Feigl, K., Thurber, C., & PoroTomo Team (2018). Ground motion response to a ML 4.3 earthquake using co-located distributed acoustic sensing and seismometer arrays. *Geophysical Journal International*, *213*, 2020–2036. doi: 10.1093/gji/ggy102.

Westman, E., Luxbacher, K., & Schafrik, S. (2012). Passive seismic tomography for three-dimensional time-lapse imaging of mining-induced rock mass changes. *The Leading Edge*, *31*(3), 338–345.

Yang, Y., & Ritzwoller, M. H. (2008). Teleseismic surface wave tomography in the western US using the Transportable Array component of US Array. *Geophysical Research Letters*, *35*(4), L04308.

Young, R. P., & Maxwell, S. C. (1992). Seismic characterization of a highly stressed rock mass using tomographic imaging and induced seismicity. *Journal of Geophysical Research: Solid Earth*, *97*(B9), 12361–12373.

Zeng, X., Lancelle, C., Thurber, C., Fratta, D., Wang, H., Lord, N., et al. (2017). Properties of noise cross-correlation functions obtained from a distributed acoustic sensing array at Garner Valley, California. *Bulletin of the Seismological Society of America*, *107*(2), 603–610.

Zhang, H., & Thurber, C. H. (2003). Double-difference tomography: The method and its application to the Hayward fault, California. *Bulletin of the Seismological Society of America*, *93*(5), 1875–1889.

6

On the Surmountable Limitations of Distributed Acoustic Sensing (DAS) Vertical Seismic Profiling (VSP) – Depth Calibration, Directionality, and Noise: Learnings From Field Trials

Albena Mateeva[1], Yuting Duan[1], Denis Kiyashchenko[1], and Jorge Lopez[2]

ABSTRACT

In this chapter, we comment on the most noted weaknesses of distributed acoustic sensing (DAS) – which are depth uncertainty, directionality, and noise – and their practical impact. We argue that, despite all shortcomings, DAS vertical seismic profiling (VSP) is already a very useable tool, able to unlock diverse new applications. By way of an example, we show that time-lapse (4D) DAS VSP performance is remarkably robust against adverse conditions in deep water, which, alongside affordability and nonintrusiveness, makes it suitable for frequent time-lapse monitoring.

6.1. INTRODUCTION

"DAS is not a poor-man's geophone. It is a powerful enabler of new seismic applications". This was Shell's vision that motivated intense pioneering efforts on DAS when this new seismic technology first emerged a decade ago. Our early efforts were on two fronts: Quickly maturing the ability of DAS to deliver basic VSP products, such as check shots, images, and time-lapse images, and identifying key advantages and disadvantages of DAS vs. geophone recordings (Mateeva et al., 2012; Mateeva, Lopez, et al., 2013). Our assessment was that the advantages of DAS were fundamental as they enabled novel applications that were unfeasible with geophones, while its disadvantages were manageable. This realization led us to prolifically field-test diverse seismic applications in conventional and unconventional settings, both active source (Table 6.1) and passive source (Webster, Cox, et al., 2013; Webster, Wall, et al., 2013; Webster et al., 2016).

While those field tests were all very instructive and proved the technical feasibility of assorted applications, business considerations, such as foreseeable impact and applicable base, guided the prioritization of which of them to mature. We have previously discussed and showcased some high-impact novel applications, e.g., three-dimensional (3D) VSP imaging from wells inaccessible with geophones (Mateeva, Mestayer, et al., 2013; Wu et al., 2015); full-field onshore monitoring via 3D VSP in many wells simultaneously, low-footprint refraction monitoring in geologically suitable areas with restricted surface access, and frequent time-lapse monitoring in deep water (Mateeva et al., 2014); and in situ VSP monitoring between hydraulic fracturing stages (Bakku et al., 2014), which is now known as "rapid" 4D DAS VSP (e.g., Binder et al., 2019; Zhou et al., 2019). As business priorities shifted between onshore and offshore over

[1]*Shell Technology Center, Houston, Texas, USA*
[2]*Shell Brasil Petróleo Ltda., Rio de Janeiro, Brazil*

Distributed Acoustic Sensing in Geophysics: Methods and Applications, Geophysical Monograph 268, First Edition.
Edited by Yingping Li, Martin Karrenbach, and Jonathan B. Ajo-Franklin.

DOI:10.1002/9781119521808.ch06

Table 6.1 Fields Trials of Active-Source DAS Seismic Applications by Shell from 2010 to 2015.

Field-tested application	Where	Does it work? Remarks
Better Velocity Models – 1D, 3D, and 4D	USA onshore, USA offshore, the Netherlands, Oman, and Brunei	Yes, mind depth calibration.
Wider/Higher Resolution VSP Images	USA, New Zealand, Canada, Brunei, and Malaysia	Yes, but is case dependent.
3D VSP in Otherwise Inaccessible Wells	U.S. deep water and Brunei	Yes
In Situ Hydraulic Fracturing Monitoring with VSP	U.S. unconventionals	Yes, formation changes detectable between stages (including transient effects), but interpretation and actionable responses need more work.
Low-Footprint Refraction Monitoring	Canada heavy oil	Yes, but need a reference sensor to account for source nonrepeatability.
Buried Surface Seismic for Permanent Reservoir Monitoring Onshore	USA and the Netherlands	Cables with helically wrapped fiber detect broadside arrivals. Need source maturation for a buried cross-spread. Want better interrogator.
Full-Field Coverage by Multiwell 3D VSP	Oman onshore, U.S. deep water, and Brunei	Yes, if fiber sufficiently available. Onshore wells drilled in patterns offer the best geometry for areal uplift, but congested infrastructure is a challenge for source access. In deep water, use multiples, too.
CO_2 Injection Monitoring	Canada onshore	Yes
4D VSP for Frequent Monitoring	U.S. deep water	Yes

the years, so did our focus on certain DAS applications. Currently, we employ DAS VSP onshore mainly for CO_2 storage and containment monitoring (Bacci et al., 2017; Cox et al., 2012) as it is among the few affordable methods for tracking time-lapse changes under the heterogeneous and time-varying overburden typical for onshore (Mateeva et al., 2016). Offshore, which has been our focus area in recent years, we have been maturing DAS as a tool for frequent monitoring in deep water for the purposes of production optimization in waterflood fields (Chalenski et al., 2016; Kiyashchenko et al., 2019; Mateeva et al., 2017; Zwartjes et al., 2018).

The success of any DAS VSP application requires the ability to deal with DAS shortcomings, such as depth uncertainty, directionality, and noise. Over the years, we have not only honed that ability but also evolved in our understanding of how each issue impacts us in practice. Undoubtedly, we have a lot more to learn, but we share some of our current understanding in the pages that follow. We devote a section to each of the main challenges mentioned, namely, depth calibration, lack of broadside sensitivity, and multitude of noises. While we draw on broad past experience, we examine these challenges mainly in the context of our current pursuit, i.e., 4D DAS VSP for frequent monitoring in deep water. We show that even when these challenges are profoundly and simultaneously present and compounded by cost-reduction measures, such as reduced source effort, DAS VSP is still able to provide useful information in 3D and 4D.

6.2. DEPTH CALIBRATION

In DAS measurements, the "depth" of a receiver is determined from the time of flight of a light signal in the fiber, from the interrogator to a certain sensing location and back. Knowing the refraction index of a fiber (which is not always trivial, e.g., due to changing temperature conditions or insufficient fiber documentation), that time of flight can be converted into distance along the fiber. Thus, the position of DAS channels *along the fiber* is relatively well known. However, the position of the fiber *with respect to the formation* can be uncertain for a number of reasons, e.g., redundant fiber length at completion features, such as the wellhead and packers, uncertain surface cable length, cable slack, cable tortuosity in the borehole, fiber overstuffing in the cable, etc. This uncertainty has been long recognized (e.g., Ellmauthaler et al., 2016; Lumens, 2014 – chapter 9; Wu et al., 2015). Typically, it requires efforts by both vendors and end users to minimize it. Vendors are expected to populate seismic trace headers with a reasonable estimate of DAS channel depths, based on measurements they take in the field and some limited input from the client (e.g., a completion diagram). Occasionally, the DAS vendor may be able to get additional calibrations by eavesdropping to concurrent in-well operations by another vendor (e.g., listening to perforation shots or the descent/ascent of wireline tools). That is most feasible in unconventional wells; however, it is not logistically easy as it requires significant planning and coordination.

After DAS seismic is delivered to the client, the end user may attempt to get additional calibrations by using a more detailed analysis of DAS and completion data (Madsen et al., 2016; Wu et al., 2015), comparison to geophones (e.g., Gordon et al., 2018), or correlations to well logs (Mateeva & Zwartjes, 2017). Being dependent on supplemental information, such refinements are not always possible. Thus, it is very important that the initial depth assignments by the DAS vendor be as good as the circumstances allow. That calls for utilizing jointly different types of information available in the field, including:

- DAS interrogator settings that define how far from the interrogator the first live channel is, output channel spacing, the total number of live channels, etc.
- Additional DAS interrogator settings that define how far from the presumably known fiber end the deepest live channel is (the availability of such information is vendor dependent) and zones of compromised vs. uncompromised optical quality related to the optical mitigation of fiber installation defects (e.g., shuttering of high optical reflections at fiber end or splices).
- Optical time domain reflectometry (OTDR)[1] traces showing the optical position of assorted splices along the fiber that can be related to known physical locations and help establish a piecewise correspondence between fiber length and well measured depth.
- Tap-tests at the wellhead that help find a correspondence between channel number and wellhead position.
- Physical measurement of lead-in cable length between interrogator and wellhead, when possible.

Each of these sources of information allows estimating certain fiber-segment lengths – some in terms of optical length and others in terms of physical length. None provides a complete or very accurate picture of where the DAS channels are. But putting findings from all of these together gives a decent initial understanding of the receiver layout, catches errors early, and raises awareness of potential complications (e.g., extra fiber somewhere in the well). Good communication between vendor and client is very important at this stage, as is diligent documentation. Note that none of the above-mentioned methods entails looking at seismic shots; all are things that the DAS vendor can and should do before the start of active acquisition.

When some DAS seismic becomes available at the early stages of acquisition, additional depth calibrations may be sought by correlating seismic features with well completion schematics, e.g., change in noise character across casing shoes, tube wave reflections at crossovers and packers, seafloor/earth surface reflections, etc. Those provide additional reference points that, in principle, could allow assigning variable channel spacing along the well, in case the fiber is nonuniformly distributed along the well. In practice, though, the resolution of picking seismic features is limited, especially for DAS surveys with a large gauge length. Thus, these additional reference points are useful mainly as quality control of the initial depth calibrations mentioned above rather than as refinement. Moreover, referencing to completion features is only indirectly related to what we want to know, i.e., DAS channel locations with respect to the rock formation, without any restrictive assumptions about cable behavior along the well (such as straightness along the well).

This is where methods, such as that developed by Mateeva and Zwartjes (2017), can help: they propose leveraging the dependence of DAS seismic amplitudes (proportional to strain or strain rate in the formation) on the local elastic modulus of the formation around the well. To establish depth correspondence between DAS data and geological formation, they correlate DAS receiver-consistent scalars (derived in the course of routine seismic processing) with well logs (Figure 6.1) – preferably, a combination of sonic (c) and density (ρ) logs. Mateeva and Zwartjes (2017) suggested correlating with ρc^2 under the assumption that neighboring receivers see roughly the same incident pressure wave. More recently, Pevzner et al. (2018) proposed using a constant energy flux assumption, under which DAS scalars would be proportional to $(\rho c^3)^{1/2}$. The exact choice of proportionality would be important if one were to invert DAS amplitude changes for medium parameter changes as proposed in patent application WO2018084984 and Pevzner et al. (2018) – that needs to be further investigated. However, for the purposes of depth calibration, the exact combination of sonic and density logs is of little consequence since the only requirement is to be able to correlate features on the DAS scalars' curve with features on the upscaled logs (determine the correlation lag between the two curves after each of them has had its mean removed and standard

[1] OTDR is a common tool for assessing losses along the optical path (i.e., along the fiber, at fiber connections, and fiber end).

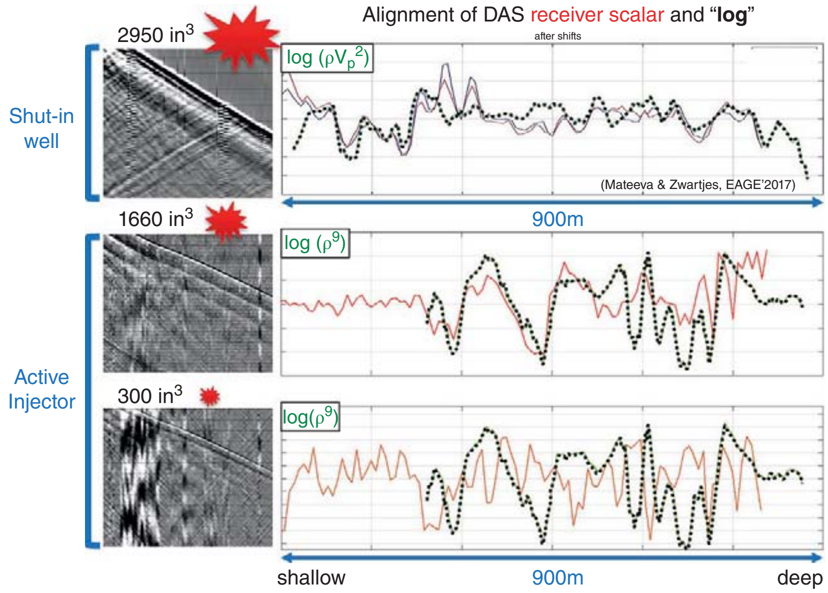

Figure 6.1 Absolute depth calibration using DAS receiver scalars (red and blue thin lines) and upscaled well logs (thick black/green dotted line), plotted as a function of depth (right), with representative near-offset shot gathers shown on the left: (Top) In a shut-in well with a typical OBN source – after Mateeva & Zwartjes (2017); (middle) in an active injector with a smaller source, typical for stand-alone DAS VSP – correlation between DAS scalars and upscaled logs is still possible despite lower SNR in input data; (bottom) in the same active well but with a very small source – correlation is hardly possible, since DAS scalars are dominated by well noise conditions instead of local geology.

deviation normalized over a selected depth range). In most rocks $c \sim \rho^4$ (Al Ismail, 2017). Therefore, $\rho c^2 \sim \rho^9$ while $(\rho c^3)^{1/2} \sim \rho^{6.5}$. Thus, the former quantity would exhibit stronger variability, which might be helpful for visual correlation in media with weak contrasts. If sonic or density logs are unavailable, correlation to gamma ray or other logs could be used.

The success of such absolute depth calibration depends on the availability of sufficiently long logs of suitable age and quality, and on the signal-to-noise ratio (SNR) of DAS VSP. If well logs are too short, correlation may be ambiguous; if they are too old, reservoir compaction may cause depth mismatch with recent DAS. Other depth uncertainties also exist in well logs, but logs are still the most direct reference to geology that a geophysicist has.

If DAS SNR is too low, even after denoising, DAS amplitude variations with depth may be more correlated with local well conditions than medium properties (Figure 6.1 (bottom)). In that case, absolute depth calibration may be difficult, but time-lapse calibration between different DAS VSP vintages may still be doable (i.e., correlate receiver scalars between two vintages rather than scalars with well logs). Figure 6.2 shows the 4D relative depth alignment of DAS receiver scalars from two vintages. Such relative depth calibration is easier to do because DAS seismic is available over most of the well, and thus, DAS scalar curves are long and equally affected by local geological complications and certain well noises. Correlating different vintages of DAS scalars is easier when the seismic sources for the two vintages are of similar strength (Figure 6.2).

For fields in which 4D interpretation is based on time-shifts, the importance of 4D depth calibration is obvious as nonrepeatable depth errors would lead to erroneous 4D time-shifts. Interestingly, for fields in which 4D interpretation is based only on amplitudes, 4D depth calibration is still important, but more so for deviated wells. For vertical wells in flat geology, nonrepeatable depth errors can be largely compensated by the vertical time alignment between vintages, normally done before 4D amplitude extraction. That is not the case for complicated geology or deviated wells as nonrepeatable depth errors in those cases lead to lateral shifts in the images that cannot be compensated by classical time alignment of images. Thus, 4D DAS depth calibration in deviated wells is particularly important (Figure 6.3).

6.3. DIRECTIONALITY

A conventional fiber-optic cable with a straight fiber allows DAS to measure strain or strain rate only along

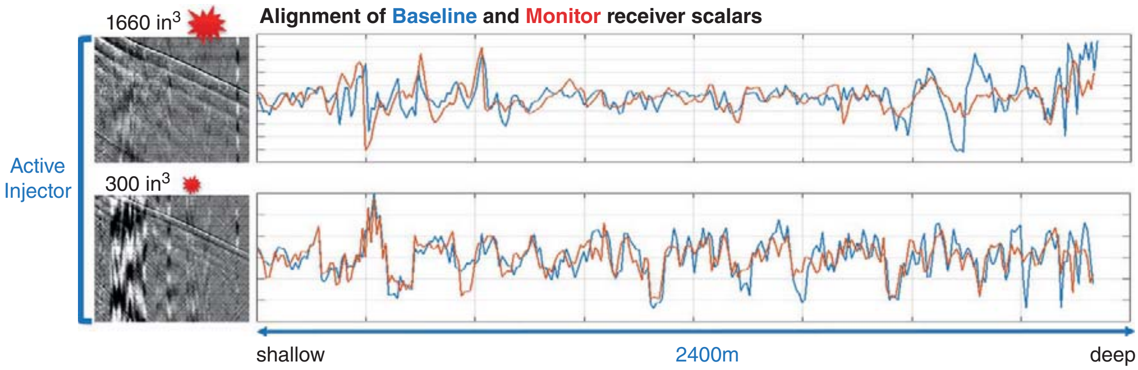

Figure 6.2 Relative depth calibration between time-lapse DAS VSP vintages (in the same active well as in Figure 6.1). DAS scalars between two vintages with a very small source (bottom) can be now confidently correlated thanks to long scalar curve and repeatable acquisition conditions. (Top) Correlation between DAS scalar vintages is harder, despite bigger sources, due to baseline and monitor having been acquired with different sources (5110 in.^{3} in baseline vs. 1660 in.^{3} in monitor, with different signatures and slightly different preprocessing before scalar derivation).

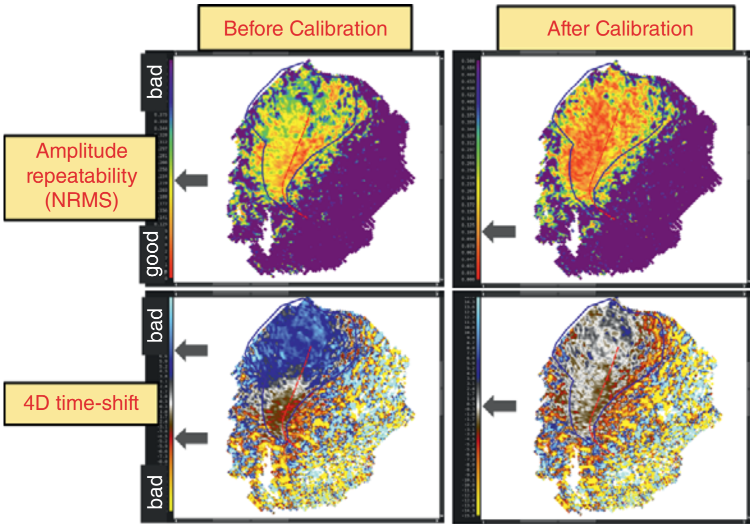

Figure 6.3 The impact (before/after) of relative depth calibration on 4D attributes from a deviated DAS well (well described in the example section) over a horizon that is not expected to change: Within the polygon of VSP illumination (outlined in blue), 4D amplitude noise drops from 23% to 11% (at an intermediate stage of processing), while 4D time-shifts that exhibited spurious positive (blue) and negative (red) values before depth calibration are nearly zero (white) after the calibration. For ease of comparison before/after, arrows point to representative values on the color scale of each map.

the fiber; i.e., the DAS sensor is a strongly directional one-component sensor (Kuvshinov, 2016). Special cables that are broadside sensitive have been proposed, developed, and field-tested mainly for surface seismic applications (Daley et al. 2013; Den Boer et al., 2013; Hornman, 2017; Hornman et al., 2015; Innanen, 2017; Lumens et al., 2013; Lumens, 2014; Ning & Sava, 2016). Those broadside-sensitive cables would be typically installed in trenches or shallow horizontal boreholes. While some are also being trialed in shallow vertical observation boreholes (Lawton et al., 2018), current cable versions are not suitable for deep deployment in active injectors and producers – the main type of wells in which fiber is wanted for various fiber-optic applications (distributed temperature sensing [DTS], DAS for flow profiling, well-integrity diagnostics, DAS VSP, etc.). Thus, in current VSP practice, we have only simple straight fibers.

For *P*-wave imaging from a vertical well in a horizontally layered medium, the main effect of DAS directionality is to down-weight contributions from large-offset shots, and thus, reduce the width of the image compared to what could have been obtained from an equally long array of less-directional sensors. This is largely a hypothetical comparison as it is seldom feasible to instrument an entire well with geophones or hydrophones; in practice, DAS images are wider than what is feasible to achieve with geophones (e.g., Zwartjes & Mateeva, 2015).

For a deviated well in a horizontally layered medium, DAS directionality leads to a characteristic image shape – the *P*-wave image is concentrated near the well below the deviated leg and, at depth, it is better toward the toe (Figure 6.4 and Figure 6.5c); the contributing shot patch is skewed toward the toe of the well.

For more complicated geometries, the impact of directionality needs to be modeled. A simple approach, useful for both illumination studies and acquisition design, is to do one-point raytracing from a subset of receiver locations in the borehole to a target reflector, and up to the surface. For every receiver location, the cone of outgoing rays must be along the borehole (unlike in 3C geophone VSP modeling, where the cone is often pointed toward the reflector as geophone components can be rotated to a direction of interest). The opening angle of the cone around the DAS well reflects expectations for the useable angle range, which, in turn, would depend on signal strength (source size, target depth, and reflectivity), background noise (well activities, fiber installation, and DAS interrogator), and the intended use of the data. Since it is hard to put an exact number on the maximum useable angle, we utilize some rules of thumb. For example, one could consider 45° as a conservative limit (*P*-wave amplitude halved by $\cos^2 45° = 0.5$) and 60° as a more liberal limit (amplitude quartered: $\cos^2 60° = 0.25$); opening the cone further is rarely advisable as the drop in amplitude beyond that is steep ($\cos^2 70° \approx 0.1$).

Note that while raytracing gives very useful qualitative indication of general image location, it is not enough to assess the boundaries of the reliably imaged area as those depend on additional factors, e.g., fold, migration rim, and subsurface complications. If a field has several wells with fiber (some have dozens), the DAS VSP image from one representative well can be used to calibrate raytracing for others. For example, as suggested in the paper of Zwartjes et al. (2018), one can determine the minimum ray hit count on a reflector (proxy for fold) for which the reflector is properly migrated (not yet "smiling" at the edges), based on structural comparison to surface seismic. Such calibration is most feasible in development settings, where high-quality 3D surface seismic is typically available. Alternatively, if reliable surface seismic is not available, one can put a threshold on the necessary hit count by examining the quality of common-image-point gathers in the existing VSP image. Once a hit count threshold is chosen, it can be applied to raytracing results from other wells (under similar conditions) to better predict the reliable image extent for future VSPs in those wells. In this way, one can create a "catalog of DAS VSP illumination" for a given field and use that for proactive planning of

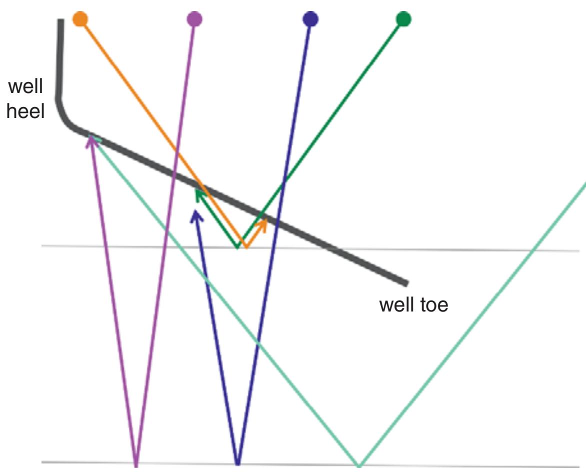

Figure 6.4 Ray contributions in deviated well – directionality considerations: (1) Reflectors near the well are better imaged than deep ones because rays are less broadside to the well (green ray 1 vs. blue ray 2). (2) For the same image point, shots on the toe side of the well contribute more than heel-side shots (orange ray 3 vs. green ray 1; orange arrival is more broadside to the well). (3) Deep reflectors are best imaged below the toe because the available receiver aperture for capturing along-well reflections is largest there (cyan ray 4 vs. magenta ray 5).

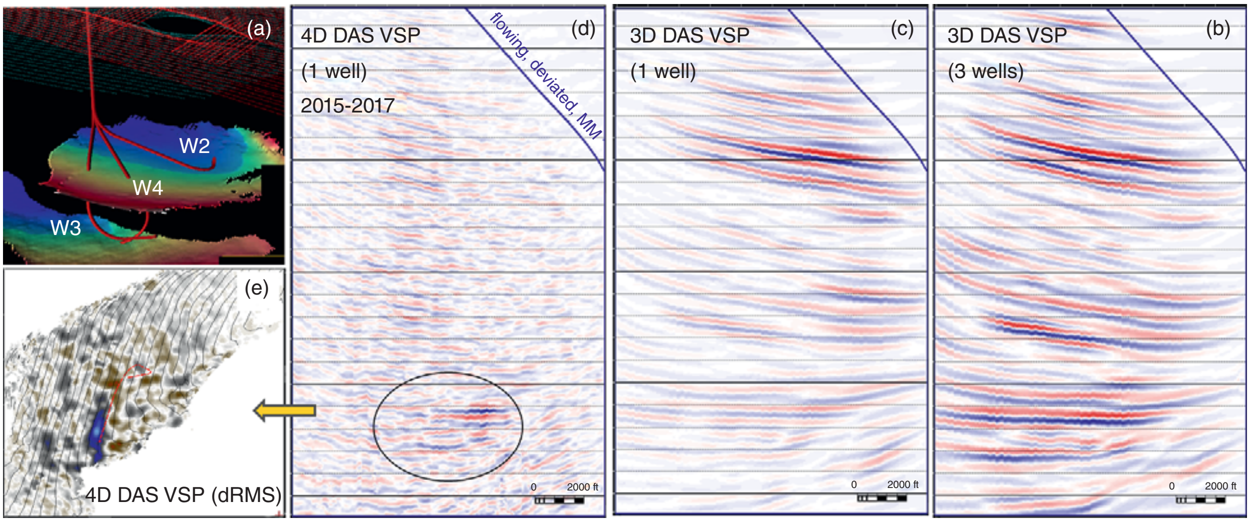

Figure 6.5 3D/4D DAS VSP from flowing wells: (a) Geometry of 2017 simultaneous DAS acquisition in three active injectors, W2 being the most deviated and the only one with a prior vintage, in 2015; (b) at far right, image from the three wells combined – excellent match to OBN (not shown here); (c) image from W2 alone – amplitudes fade away from well; at depth, amplitude holds better under the toe; (d) time-lapse image 2015–2017 from Well W2 alone – 4D signals at target depths (ellipse) stand out despite being in the sub-optimally illuminated area; and (e) map of 4D signal in a deep reservoir obtained from Well W2.

fiber-based surveillance, as discussed in the work of Zwartjes et al. (2018).

In addition to studying the image extent of VSP data (which is always a must for a VSP, regardless of sensor type), one could also attempt to correct DAS amplitudes for directionality. This can be done during shot processing in the τ–p domain. If medium P-wave velocity is known and constant, each slowness value, p, can be translated into an angle of incidence to the fiber (or rather, cosine of it) and thus, a correction for $\cos^2$ can be applied, up to a user-specified angle limit, before transforming the data back into the time-space domain. The successful application of such an approach to real 3D DAS VSP data was shown by Dy (2018), but the impact on the final 3D image was modest. Such directionality corrections are not routine in DAS VSP processing yet – either for pragmatic reasons (cost-benefit analysis) or concerns about ultimate impact (noise boost vs. signal amplitude gain, especially in 4D).

6.4. NOISE

One of the most attractive features of DAS is that it can be recorded in wells inaccessible by geophones, such as flowing production and injection wells. That makes the typical deployment environment of a DAS VSP much noisier than that of a geophone VSP. In addition, elements of the fiber-optic system can introduce noise in DAS seismic: the interrogator itself, trade-offs in its settings, cable deployment method, fiber type, fiber installation quality, etc. Over the years, interrogators and fibers have been improving, but DAS is still a “noisy measurement”. That reputation has stigmatized the method and slowed down its adoption by industry. The mistrust in a noisy measurement is understandable, but to avoid excessive stalling, one must consider the shift in dominant VSP use brought upon by DAS. While classical VSPs with geophones have been around for many decades, their typical application has been to exploration settings, with heavy emphasis on shot gather analysis as in check shots, corridor stacks for well correlation and look ahead, salt proximity surveys, walk-arounds for anisotropy estimation, etc. Such applications demand good SNR in the raw data, especially when receiver count is low. Imaging with 2D walk-away and 3D VSP has also been around for decades, but due to cost, intrusiveness, and receiver tool limitations, the number, size, and geometry of such surveys have been limited. For VSP with DAS, applications have shifted heavily toward development settings and permanent fibers, and 3D/4D VSP imaging has become the main product (although other products, such as velocity models, are still important, e.g., Li et al., 2015). A typical offshore VSP acquisition with DAS is 3D, multiwell, with tens of thousands of shots and hundreds of receivers per well. That means VSPs, at least offshore, are not small data sets anymore; each survey contains millions of traces, with the corresponding stacking power. This brute-force gain is one reason why we can get away with a noisier input. Before resorting to stacking power, of course, we can also make efforts to filter out noises. Aside from occasional optical noise bursts (spikes, striping, etc.), the strongest noises are typically related to well conditions: active injection/production (mainly at low frequencies, sometimes in isolated receiver ranges), tube waves, and tubing ringing (narrow band for an individual receiver, but its frequency varying across receivers). We can significantly suppress most DAS noises in processing. Given the abundance of DAS channels, we can also be selective in which ones to use. We routinely discard noisy channels from the shallow multicasing section instead of denoising them, but more surgical rejections deeper in the well are also possible. Most importantly, the main threat to VSP image quality is not random noise, but the processing methodology itself. Migration artifacts around the borehole and near the image edges (hot amplitudes, migration smiles, etc.) and improperly deconvolved overburden multiples can be far more detrimental to the image than random noise. Those processing challenges are also present in geophone VSP imaging and exacerbated by the shorter receiver array. That is why, despite the noisiness of raw data, DAS performs very competitively for 3D and 4D VSP imaging (besides being much easier to acquire from the perspective of cost and logistics).

This is not to say that further noise reductions and other improvements in DAS are not warranted as those would enhance reliability and widen the range of DAS applicability. But the point is that fit-for-purpose business-beneficial products are already obtainable. An example is given in the pages that follow.

6.5. OVERCOMING THE FULL SUITE OF CHALLENGES – EXAMPLE FROM DEEP WATER

In recent years, our focus has been on maturing DAS VSP as a tool for frequent monitoring in deep water (Mateeva et al., 2017). The goal is to supplement the time schedule of traditional 4D ocean bottom node (OBN) surveys with more frequent fit-for-purpose surveys so that fast reservoir processes related to injection and production can be better observed, understood, and managed. This is a challenging goal that requires extensive field testing. Our recent progress with DAS in that regard has been outlined in the papers of Zwartjes et al. (2018) and Kiyashchenko et al. (2019). Here, we briefly show just one challenging example to demonstrate 4D DAS VSP capabilities.

It is from an active injector, well W2 (Figure 6.5a), with a long (≈18 kft) multimode fiber installed on tubing – an assortment of factors that lead to high-noise conditions. The challenge of high noise is compounded by low signal due to significant well deviation (≈45°; broadside insensitivity) and reduced source effort in the monitor survey. The baseline DAS survey was obtained by eavesdropping to OBN in 2015 and was our earliest test of acquisition in an active injector. The monitor survey was a stand-alone VSP in 2017 with twice sparser shot lines for quick acquisition (100 m crossline; 6 days) and a smaller source (1660 in^3 vs. 5100 in^3 in the 2015 OBN), which could be handled by a lower cost vessel. The fact that baseline and monitor were acquired with vastly different sources is a complication for 4D processing. Receiver positions in baseline and monitor were at different locations along the well (both acquired at approximately 8 m spacing, 40 m gauge length, and ODH4 interrogator), and baseline depths were uncertain due to immature depth calibration procedures in 2015. The deviation of the well produced the typical uneven illumination pattern (Figure 6.5c). 4D targets (two deep reservoirs undergoing water injection) fell in the suboptimally illuminated area, about 5,000 ft below the deviated part of the DAS well (Figure 6.5d). Injection in one of those deep reservoirs (mapped in Figure 6.5e) had been active for less than 6 months prior to the monitor.

In short, every possible aspect of this survey was challenging; no aspect was favorable. Yet, the obtained 4D results were very good. Repeatability was excellent in the well-illuminated areas, with a normalized root mean square (NRMS) level of about ≈6% (Figure 6.6a). Repeatability in the less illuminated area was lower, with an NRMS of ≈10% at the target level, but could have been improved by supplementing the image with data from additional wells (Figure 6.6b). We did not have a baseline in W3 and W4 from 2015, and that is why we used only well W2 for 4D imaging. Still, even with that single well, that repeatability was enough to make useful observations on injection signals in the target reservoirs (Figure 6.7). For example, we observed that the first 5–6 months of injection in one of the reservoirs produced a water signal that was stronger toward the toe of the new horizontal injector (Figure 6.7a), which was not expected from reservoir model predictions (Figure 6.7b). That prompted an internal discussion on the possible explanations and on the potential follow-up. In the other reservoir, the water sweep was seen progressing directly updip from a previously known waterfront location (compare panels (c) and (d) in Figure 6.7), appearing to follow a preferential path but advancing more slowly than in the reservoir model (Figure 6.7e). Such information could help update the reservoir model.

At the time these observations were first made, there was no other time-lapse information available to corroborate them. On the one hand, that made the findings more informative; on the other hand, it made them less trusted. However, in early 2018, they were confirmed by a repeat of the stand-alone DAS VSP that told essentially the same

	NRMS	
	1 well	3 wells
12,000′	6%	6%
14,000′	9%	7%
16,000′	10%	7.5%

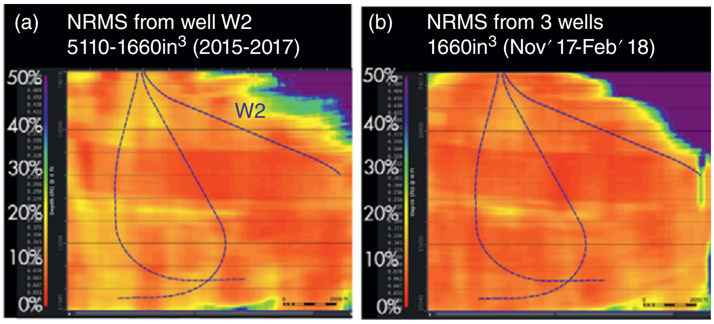

Figure 6.6 Repeatability of DAS VSP images from flowing wells: (a) From Well W2 alone; (b) from three wells combined. The table on the left shows average repeatability at different depths, the toe of W2 being at about 12,000 ft.

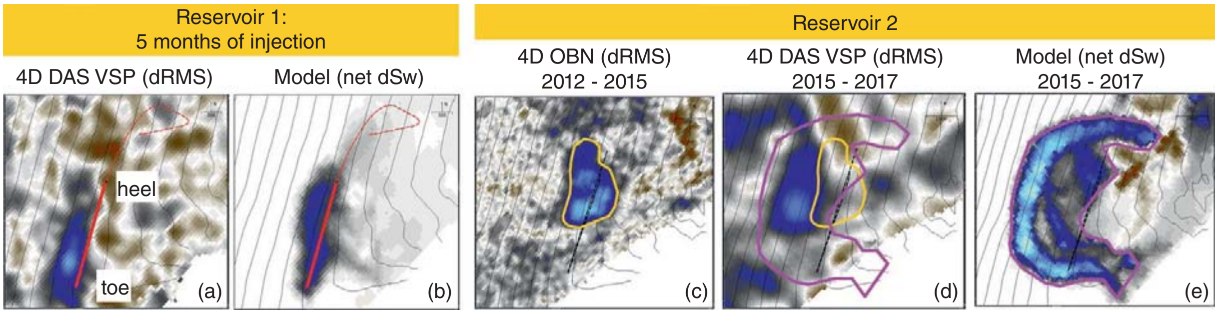

Figure 6.7 4D signals obtained from DAS VSP in Well W2 (2015–2017) compared to other time-lapse data.

story. Later in 2018, another vintage of OBN was acquired, with DAS eavesdropping to it, allowing us to benchmark 4D DAS VSP in this most challenging well against 4D OBN 2015-2018 and prove the ability of DAS to provide valid information within its area of illumination at a fraction of the cost of a traditional seismic survey. This paves the way for future DAS utilization in this field.

Telling this remarkable story in more detail and in the broader context of reservoir surveillance will be the subject of a future case-study paper. Here, our purpose was simply to illustrate that while DAS challenges are real, they can be overcome.

6.6. CONCLUSIONS

It is important to understand the practical implications of the most noted weaknesses of DAS – depth uncertainty, lack of broadside sensitivity, and noise. If properly handled, none of them is a showstopper for harnessing the power of DAS VSP.

Minimizing depth uncertainty requires efforts both by DAS vendors and end users. Vendors must provide reasonable depth estimates by combining several types of information and communicate those clearly and timely to the client. End users may be able to refine those initial depth estimates based on additional in-house information, in 3D and 4D. Relative depth refinements for 4D are easier and are most important for deviated wells.

DAS directionality, together with well trajectory, governs the area of VSP illumination. Knowing what can and cannot be illuminated is critical for both survey planning and final image interpretation. That is why directionality must be taken into account during acquisition modeling by considering only rays in a limited cone, the orientation of which tracks the well path.

Optical noises are present in DAS data, but other noises related to well conditions tend to dominate. Most DAS noises can be suppressed in processing via filtering, stacking, and receiver selection. The main threat to image quality is artifacts from certain immature VSP processing steps, not unique to DAS, rather than noise in the raw data.

Finally, field tests in deep water have proven that 3D/4D DAS VSP imaging is remarkably robust against multiple adverse conditions compounded in a single acquisition. That robustness, together with affordability and nonintrusiveness, makes DAS VSP an enabler of frequent monitoring in deep water.

ACKNOWLEDGMENTS

The authors thank their past and present colleagues from the Areal Surveillance Technology team and collaborators from other Shell technology teams who have greatly contributed to their collective understanding of DAS VSP. The authors also thank all Shell assets who participated in numerous field trials, and particularly the deep water assets who provided invaluable feedback. None of this would have been possible without the tireless efforts of colleagues from Shell's Geophysical Operations and helpers from across Shell. The authors are grateful to OptaSense for the fruitful collaboration over the years.

REFERENCES

Al Ismail, M. (2017). *On the relationship between compressional wave velocity of saturated porous rocks and density: Theory and application* (MSc thesis). Massachusetts Institute of Technology. Department of Earth, Atmospheric, and Planetary Sciences. URI: http://hdl.handle.net/1721.1/108912

Bacci, V., O'Brien, S., Frank, J., & Anderson, M. (2017). Using a walk-away DAS time-lapse VSP for CO2 plume monitoring at the quest CCS project. *Recorder*, *42*(3), 18–21.

Binder, G., Titov, A., Tamayo, D., Simmons, J., Tura, A., Byerley, G., & Monk, D. (2019). *Time-lapse seismic monitoring of individual hydraulic frac stages using a downhole distributed acoustic sensing array. Proceedings of the 7th Unconventional Resources Technology Conference* 2019, Denver, CO. https://doi.org/10.15530/urtec-2019-409

Chalenski, D., Tatanova, M., Du, Y., Mateeva, A., Lopez, J., & Potters, H. (2016). *Climbing the staircase of ultra-low-cost 4D monitoring of deepwater fields using DAS-VSP*. SEG Technical Program Expanded Abstracts 2016 (pp. 5441–5445).

Cox, B. Wills, P., Kiyashchenko, D., Mestayer, J., Lopez, J., Bourne, S., et al. (2012), Distributed acoustic sensing for geophysical measurement, monitoring and verification. *Recorder*, *37*(2).

Daley, T., Freifeld, B., Ajo-Franklin, J., Dou, S., Pevzner, R., Shulakova, et al. (2013). Field testing of fiber-optic distributed acoustic sensing (DAS) for subsurface seismic monitoring. *The Leading Edge*, *32*, 699–706, https://doi.org/10.1190/tle32060699.1

Den Boer, H., Mateeva, A., Pearce, J., Mestayer, J., Birch, W., Lopez, J., et al. (2013). Detecting broadside acoustic signals with a fiber optical distributed acoustic sensing (DAS) assembly. WO Patent PC-T/US2012/069,464.

Dy, T. (2018). *DAS VSP processing and imaging—a marine case study in a highly deviated well*. Paper presented at SEG Summer Research Workshop: Recent Advances and Applications in Borehole Geophysics, Galveston, TX.

Ellmauthaler, A., Willis, M., Barfoot, D., Wu, X., Erdemir, C., Barrios-Lopez, O., et al. (2016). *Depth calibration for DAS VSP: Lessons learned from two field trials*. SEG Technical Program Expanded Abstracts 2016 (pp. 632–636).

Gordon, A., Lawton, D., Hall, K., Freifeld, B., Daley, T., & Cook P. (2018). Depth registration of VSP DAS fiber. SEG Technical Program Expanded Abstracts 2018 (pp. 5427–5431).

Hornman, J., Mateeva, A., Potters, H., & Lopez, J. (2015). *New concepts for lowering the cost of frequent seismic Reservoir monitoring onshore*. SEG Technical Program Expanded Abstracts 2015 (pp. 5518–5522). doi: http://dx.doi.org/10.1190/segam2015-5826463.1

Hornman, J. (2017). Field trial of seismic recording using distributed acoustic sensing with broadside sensitive fibre-optic cables. *Geophysical Prospecting*, *65*, 35–46. doi:10.1111/1365-2478.12358

Innanen, K. (2017). *Determination of seismic-tensor strain from Helical Wound Cable-Distributed Acoustic Sensing cable with arbitrary and nested-helix winds*. SEG Technical Program Expanded Abstracts 2017 (pp. 926–930). https://doi.org/10.1190/segam2017-17664060.1

Kiyashchenko, D., Duan, Y., Mateeva, A., Johnson, D., Pugh, J., Geisslinger, A., & Lopez. J. (2019). *Maturing 4D DAS VSP for on-demand seismic monitoring in deepwater*. SEG Technical Program Expanded Abstracts 2019 (pp. 5285–5289). https://doi.org/10.1190/segam2019-3216625.1

Kuvshinov, B. (2016). Interaction of helically wound fibre-optic cables with plane seismic waves. *Geophysical Prospecting*, *64*, 671–688. doi:10.1111/1365-2478.12303

Lawton, D., Hall, K., & Gordon, A. (2018). *Advances in DAS seismic monitoring for CO2 storage*. SEG Technical Program Expanded Abstracts 2018 (pp. 5500–5500).

Li, Y., Wu, H., Wong, W., Hewett, B., Liu, Z., Mateeva, A. & Lopez J. (2015). Velocity analysis and update with 3D DAS-VSP to improve borehole/surface seismic images. SEG Technical Program Expanded Abstracts 2015 (pp. 5285–5288). doi: http://dx.doi.org/10.1190/segam2015-5864923.1

Lumens, P., Franzen, A., Hornman, K., Karam, S., Hemink, G., Kuvshinov, B., et al. (2013). *Cable development for distributed geophysical sensing with a field trial in surface seismic*. Fifth European Workshop on Optical Fibre Sensors, International Society for Optics and Photonics (pp. 879435–879435).

Lumens, P. G. E. (2014). *Fibre-optic sensing for application in oil and gas wells*. Technische Universiteit Eindhoven.

Mateeva, A., Mestayer, J., Cox, B., Kiyashchenko, D., Wills, P., Lopez, J., et al. (2012). *Advances in Distributed Acoustic Sensing (DAS) for VSP*. SEG Technical Program Expanded Abstracts 2012.

Madsen, K., Tøndel, R., & Kvam, Ø. (2016). Data-driven depth calibration for distributed acoustic sensing. *The Leading Edge*, *35*(7), 610–614.

Mateeva, A., Lopez, J., Mestayer, J., Wills, P., Cox, B., Kiyashchenko, D., et al. (2013). Distributed acoustic sensing for reservoir monitoring with VSP. *The Leading Edge, 32*(10), 1278–1283.

Mateeva, A., Mestayer, J., Yang, Z., Lopez, J., Wills, P., Roy, J., & Bown, T. (2013). Dual-well 3D VSP in deepwater made possible by DAS. SEG Technical Program Expanded Abstracts 2013 (pp. 5062–5066).

Mateeva, A., Lopez, J., Potters, H., Mestayer, J., Cox, B., Kiyashchenko, D., et al. (2014). Distributed acoustic sensing for reservoir monitoring with vertical seismic profiling. *Geophysical Prospecting*, *62*, 679–692. doi:10.1111/1365-2478.12116

Mateeva, A., & Zwartjes, P. (2017). *Depth calibration of DAS VSP channels: A new data-driven method*. Paper presented at 79th EAGE Conference & Exhibition, Expanded Abstracts 2017.

Mateeva, A., Hornman, K., Grandi, S., Potters, H., Lopez, J., & Follett, J. (2016). *Monitoring IOR/EOR onshore with frequent time-lapse seismic—status and survey adaptations for the Middle East*. *Society of Petroleum Engineers.* doi:10.2118/179824-MS

Mateeva, A., Lopez, J., Chalenski, D., Tatanova, M., Zwartjes, P., Yang, Z., et al. (2017). 4D DAS VSP as a tool for frequent seismic monitoring in deep water. *The Leading Edge*, *36*(12), 995–1000. https://doi.org/10.1190/tle36120995.1

Ning, I. L. C., & Sava, P. (2016). *Multicomponent distributed acoustic sensing*. SEG Technical Program Expanded Abstracts 2016 (pp. 5597–5602). https://doi.org/10.1190/segam2016-13952981.1

Pevzner, R., Gurevich, B., Tertyshnikov, K., Pirogova, A., & Glubokovskikh, S. (2018). *Repeat logging using distributed acoustic sensors and earthquakes*. EAGE Conference on Reservoir Geoscience, Dec 3–5, 2018, Kuala Lumpur, Expanded Abstracts.

Webster, P., Cox, B., & Molenaar, M. (2013). *Developments in diagnostic tools for hydraulic fracture geometry analysis*. Unconventional Resources Technology Conference (URTeC): *1619968* (pp. 218–224). doi:10.15530/URTEC-1619968-MS

Webster, P., Molenaar, M., & Perkins, C. (2016). DAS microseismic. *Recorder*, *41*(6).

Webster, P., Wall, J., Perkins, C., & Molenaar, M. (2013). *Micro-seismic detection using distributed acoustic sensing*. SEG Technical Program Expanded Abstracts 2013 (pp. 2459–2463). https://doi.org/10.1190/segam2013-0182.1

Wu, H., Wong, W., Yang, Z., Wills, P., Lopez, J., Li, Y., et al. (2015). Dual-well 3D vertical seismic profile enabled by distributed acoustic sensing in deep-water Gulf of Mexico. *Interpretation, 3*(3), SW11–SW25. doi: 10.1190/INT-2014-0248.1

Zhou, R., Willis, M., & Palacios, W. (2019). *Detecting hydraulic fracture induced velocity change using rapid time-lapse DAS VSP*. SEG Technical Program Expanded Abstracts 2019 (pp. 4859-4863). doi: 10.1190/segam2019-3214042.1

Zwartjes P., & Mateeva A. (2015). *High resolution Walkaway VSP at Kapuni recorded on multi-fiber DAS and geophones*. Paper presented at 77th EAGE Conference & Exhibition 2015, Madrid, Expanded Abstracts.

Zwartjes, P., Mateeva, A., Chalenski, D., Duan, Y., Kiyashchenko, D., & Lopez, J. (2018). *Frequent, multi-well, stand-alone 3D DAS VSP for low-cost reservoir monitoring in Deepwater*. SEG Technical Program Expanded Abstracts 2018.

7

Denoising Analysis and Processing Methods of Distributed Acoustic Sensing (DAS) Vertical Seismic Profiling (VSP) Data

Yuan-Zhong Chen[1,2], Guang-Min Hu[1], Jun-Jun Wu[2], Gang Yu[1,2], Yan-Peng Li[2], Jian-Hua Huang[2], Shi-Ze Wang[2], and Fei Li[2]

ABSTRACT

Vertical Seismic Profiling (VSP) using Distributed Acoustic Sensing (DAS) technique has become a significant development direction for the borehole seismic survey because of its advantages of full-well coverage, high density, high efficiency, low cost, high temperature and high pressure resistance. This section of the book has mainly discussed DAS-VSP data denoising methods, analyzing the noise difference of data sets collected by different coupling methods of optical fiber cable and different optical cable structures in the well. It has also discussed the methods of subtracting the inverse coupling noise and eliminating the ringing noise, suppressing the random noise in the F-X domain, and improving the signal-to-noise (SRN) ratio by traces group combination. This paper proposed some denoising methods, which will greatly reduce the cable resonance interference and random interference noise. By applying these techniques, we were able to reduce DAS-VSP interference and significantly improve the SNR of the data while maintaining effective seismic wave integrity.

7.1. INTRODUCTION

At present, most existing oil and gas fields have oil wells into the middle and later stages of resource exploration and development. As these oil wells become more ubiquitous, new exploration and production technologies are urgently needed to provide high-precision accuracy reservoir descriptions around the well in order to guide further oil and gas field development. As borehole seismic technique continues to mature and downhole large geophone array instrumentation becomes more sophisticated, vertical seismic profiling (VSP) data have evolved beyond their original purpose of time-to-depth relationship for seismic-well ties to become a geophysical technique with applications in high-resolution seismic imaging around the borehole (Blias & Hughes 2015; Lee et al., 2016), amplitude vs. offset (AVO) analysis (Wu et al., 2015), fracture prediction, and anisotropy analysis of reservoir strata.

Distributed acoustic sensing (DAS) uses optical fibers as both a seismic/vibration sensor and a transmission medium to record external disturbances (such as seismic waves, temperature and pressure fluctuations, etc.) in the form of acoustic waves. These acoustic signals are transmitted through and cause tiny changes in the tensile strain in optical fibers, leading to phase changes in modulated backscattered signals that can be captured and recorded as temperature or strain changes at different

[1]*School of Information and Communication Engineering, University of Electronic Science and Technology of China, Chengdu, China*

[2]*BGP Inc., China National Petroleum Corporation, Zhuozhou, China*

Distributed Acoustic Sensing in Geophysics: Methods and Applications, Geophysical Monograph 268, First Edition.
Edited by Yingping Li, Martin Karrenbach, and Jonathan B. Ajo-Franklin.

DOI:10.1002/9781119521808.ch07

positions along optical fibers by demodulating equipment. DAS-VSP surveys are becoming more prevalent in borehole seismic studies because the armored optical cables are more easily and quickly deployed, high efficient at collecting data, and resistant to high pressures and temperatures (Correa et al., 2017; Didraga, 2015; Bakku et al., 2014; Jiang et al., 2016; Mateeva et al., 2012, 2014).

As a result, significant effort has put (gone) into developing DAS-VSP data denoising techniques, which include synthetic modeling cable slapping to reduce ringing noise (Yu et al., 2016), suppressing the DAS cable resonance noise using a wavelet and discrete cosine transform dictionary based on sparse optimization (Chen et al., 2018), VSP denoising via sparse representation (Flórez et al., 2017), and suppressing the random noise of DAS-VSP data (Kimura et al., 2018).

7.2. FIBER DEPLOYMENT TYPES AND NOISE SOURCES

There are three ways to deploy a DAS-VSP system (Figure 7.1). The first way is to permanently fix optical fibers outside the casing. To this end, optical fibers are coupled with strata, which translates into high signal-to-noise ratio (SNR) values (Jiang et al., 2016). These high-quality data are well suited for the exploration of potential sites for new wells, dynamically monitoring existing wells, and gathering time-lapse VSP data. The second way is to fix optical fibers on the inner edges of the oil tubing. Since this deployment method relies on the internal integrity of pipes, optical fibers are more easily disturbed; as a result, this method is best used for semipermanent seismic monitoring. The third way is to pull optical fibers through the casing without attaching them to pipe walls; these instruments are easy to deploy, but because optical fibers are not coupled to well walls, cable resonance can significantly affect VSP data (Constantinou et al., 2016).

Figure 7.2 shows VSP data collected using the second deployment method, where optical fibers are attached to the interior of casing pipes. When the contact between optical fiber cables and casing pipe walls is not maintained, the projecting point at the interface of fiber-optic cables and casing pipes will cause fiber-optic cables to vibrate, like a tight string, independent of the arrival of seismic waves. These waves will vibrate at resonance along fiber-optic cables, thus generating energetic coupled waves that can disguise genuine seismic signals.

Figure 7.3 shows examples of VSP data gathered in fresh water-filled oil wells by way of flexible (Figure 7.3a) and armored (Figure 7.3b) cables that are not fixed to pipe walls. There are three kinds of strong interference in the data collected with bare optical fibers: (1) cable resonance, (2) casing wave, and (3) abnormal background interference. While distinct seismic arrivals are clearly visible, reflection wave groups are noticeable and continuous, as shown in Figure 7.3a. Unlike armored optical fibers, bare fiber-optic cables experience strong coupling interference, and the result is an obvious tube wave. Since armored fiber-optic cables are heavy and well constructed, they have a good casing pipe coupling and a high SNR.

7.3. CABLE RESONANCE REMOVAL

Cable resonance is caused by poor coupling between the cable and borehole walls, and is exacerbated when the well trajectory changes. Since the apparent velocity, frequency, and energy of cable resonance are stable, cable resonance can be quantified with the fitting inversion method. In the fitting inversion method, we first determine the time and depth range of the interference. Then, using the stable propagation law, we define the amplitude, frequency and phase of the cable interference, and subtract it from the seismic signal using Equation 7.1:

$$\min \sum_{i=n_1}^{n_2} | D_i - W * R_i | \tag{7.1}$$

where D_i is the ith channel data, W is the wavelet, R_i is the reflection coefficient of the ith channel, and n_1 and n_2 are the channel sequence numbers.

By analyzing the energy difference between channels, we define the sequence numbers n_1 and n_2 as the beginning and ending channels of the interference wave. After scanning the propagation speed of the coupling interference, we determine the reflection coefficient R_i by measuring the energy of each channel. As the initial inversion wavelet W arrives, we subtract the fitting noise $W * R_i$ from the first channel data D_1 to calculate the data after denoising. When the downstream wave arrives, the uncoupled fiber oscillates in the pipe, resulting in coupling interference (Figure 7.4).

In suppressing the cable resonance, we see that DAS-VSP data (Figure 7.5b) have a much higher SNR than the initial DAS-VSP data (Figure 7.5a). This denoising method can remove signal interference while preserving both the amplitude and the reflection information of the relevant seismic data.

7.4. RANDOM NOISE SUPPRESSION

As shown in Figure 7.6a, random noise can detract from VSP signal strength and make feature interpretation more difficult. To that end, we can suppress random noise in the F-X domain. According to the regularity of the linear time difference of multichannel signals, the predictable signal (governed by a linear time difference law) is strengthened by predictive filtering, while the unpredictable signal is suppressed. To apply predictive filtering and

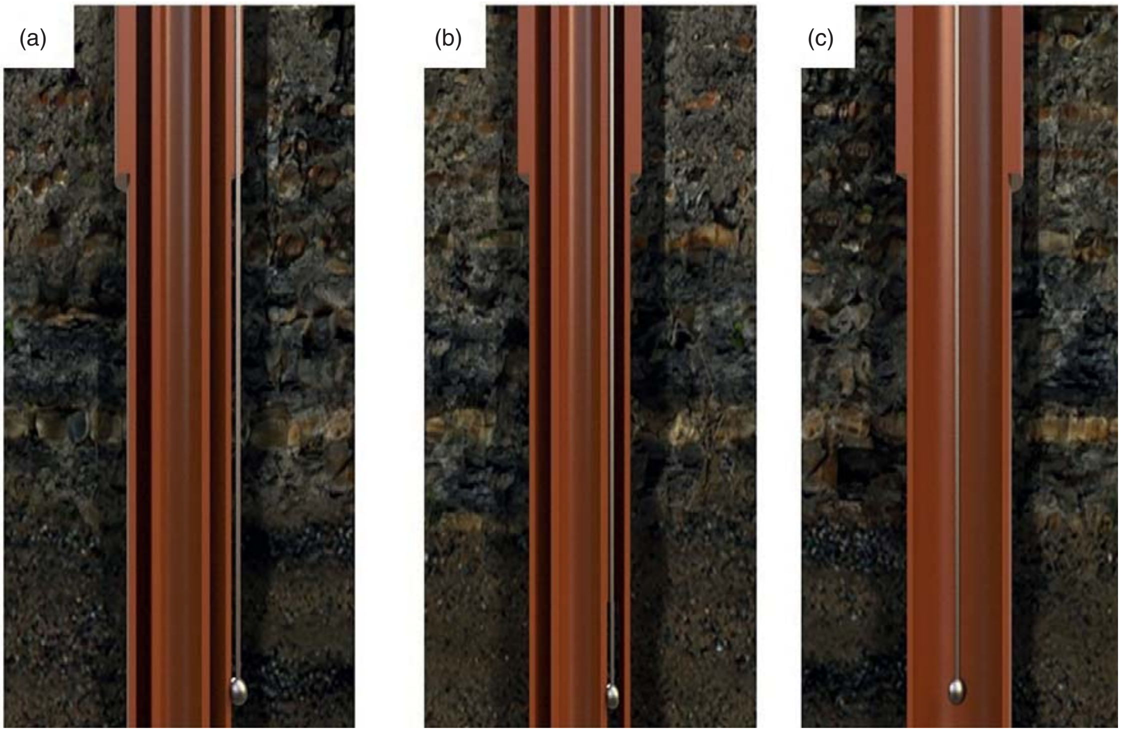

Figure 7.1 Three types of DAS-VSP optical fiber deployment in a borehole. (a) Placement during cementing and outside the casing, (b) placement outside and fixing the oil tube together, and (c) placement inside the casing.

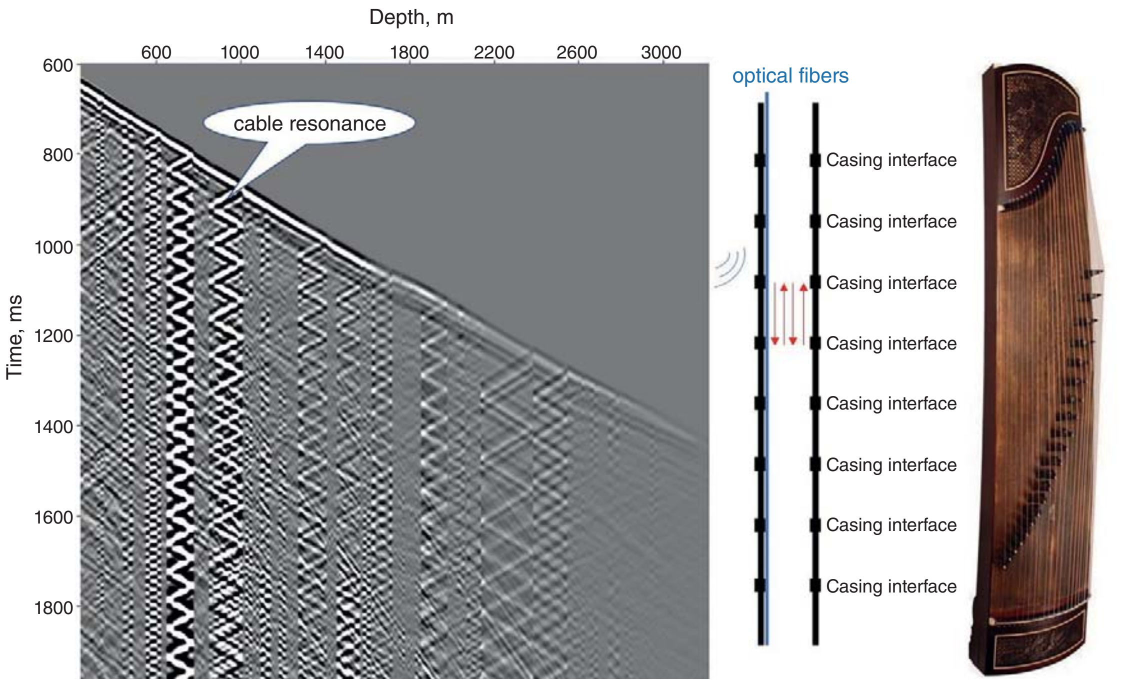

Figure 7.2 DAS-VSP data received by optical fibers freely suspended in the casing.

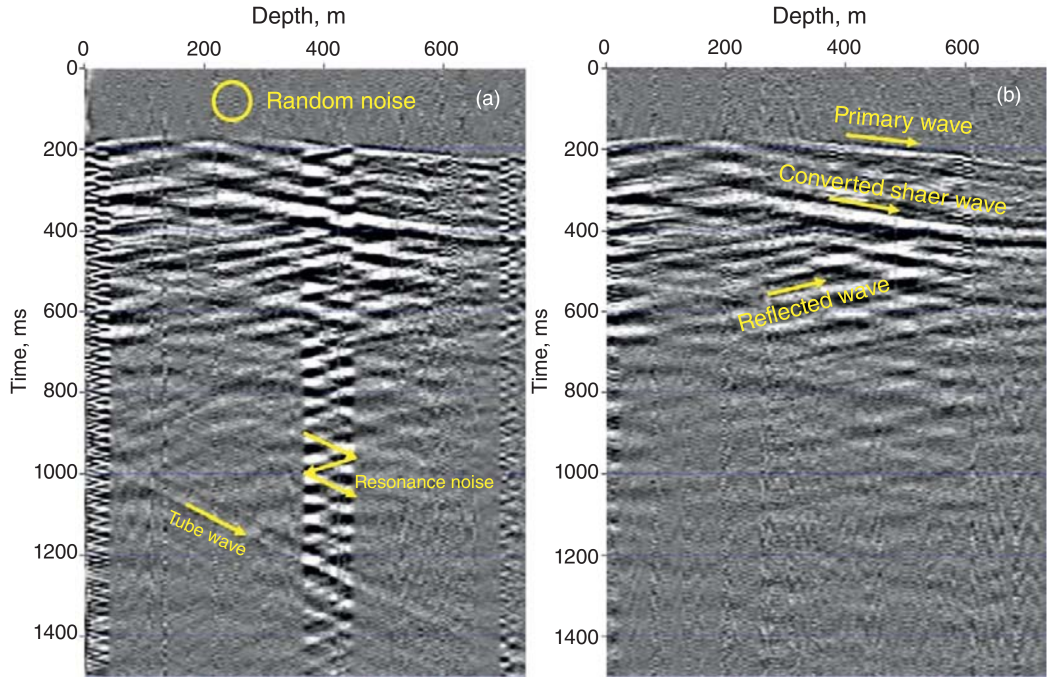

Figure 7.3 Comparison of VSP single-shot record received from (a) flexible optical fiber cables and (b) armored optical fibers.

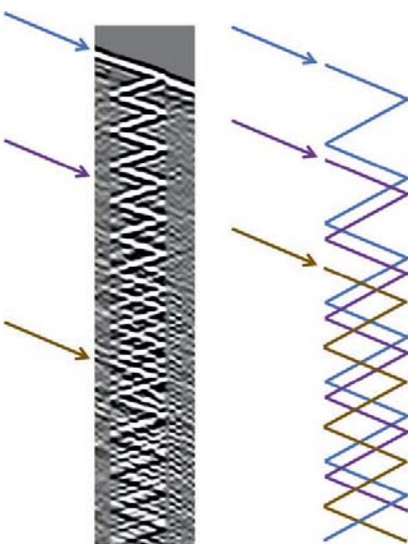

Figure 7.4 Diagram of cable resonance interference.

remove random noise, we need to solve for a set of polynomials $P_f(x)$:

$$\overline{P}_f(x) = \sum_{i=0}^{n} a_i x^i \tag{7.2}$$

that will fit the seismic data $S_f(x)$:

$$\{S_f(x_k), x_k\}, k = 0, 1, \ldots, m \tag{7.3}$$

To identify these polynomials, we solve the following regular equation:

$$\sum_{k=0}^{m} \sum_{i=0}^{n} a_i x_k^{i=j} = \sum_{k=0}^{m} S_f(x_k) x_k^i (j = 0, 1, \ldots, n) \tag{7.4}$$

using the matrix formulation:

$$\overline{\mathbf{X}}\mathbf{a} = \mathbf{b} \tag{7.5}$$

$$\mathrm{X} = \begin{bmatrix} x_0^0 & x_0^1 & \cdots & x_0^n \\ x_1^0 & x_1^1 & \cdots & x_1^n \\ \vdots & \vdots & \ddots & \vdots \\ x_m^0 & x_m^1 & \cdots & x_m^n \end{bmatrix} \tag{7.6}$$

The coefficient matrix of Equation 7.5 is a positive definite symmetric matrix, and therefore we calculate the coefficients of the fitting polynomial by solving the equation. In order to ensure the stability of the solution process, we add a white noise factor to the positive diagonal elements of the coefficient matrix. To solve Equation 7.5, we first transform the T-X signal into the F-X domain, then determine the fitting polynomial coefficients by solving the equation. Using the polynomial expressions, we can recover the complex frequency spectrum of the effective signals. Lastly, we employ an inverse

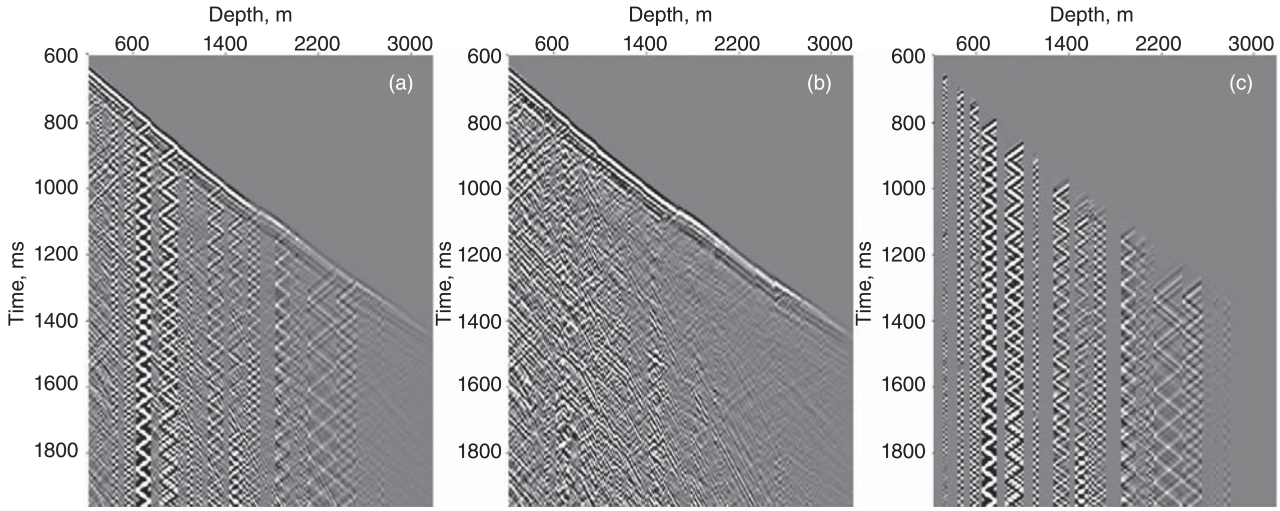

Figure 7.5 The denoising effect of cable resonance. (a) Record before denoising, (b) record after denoising, and (c) removed cable resonance.

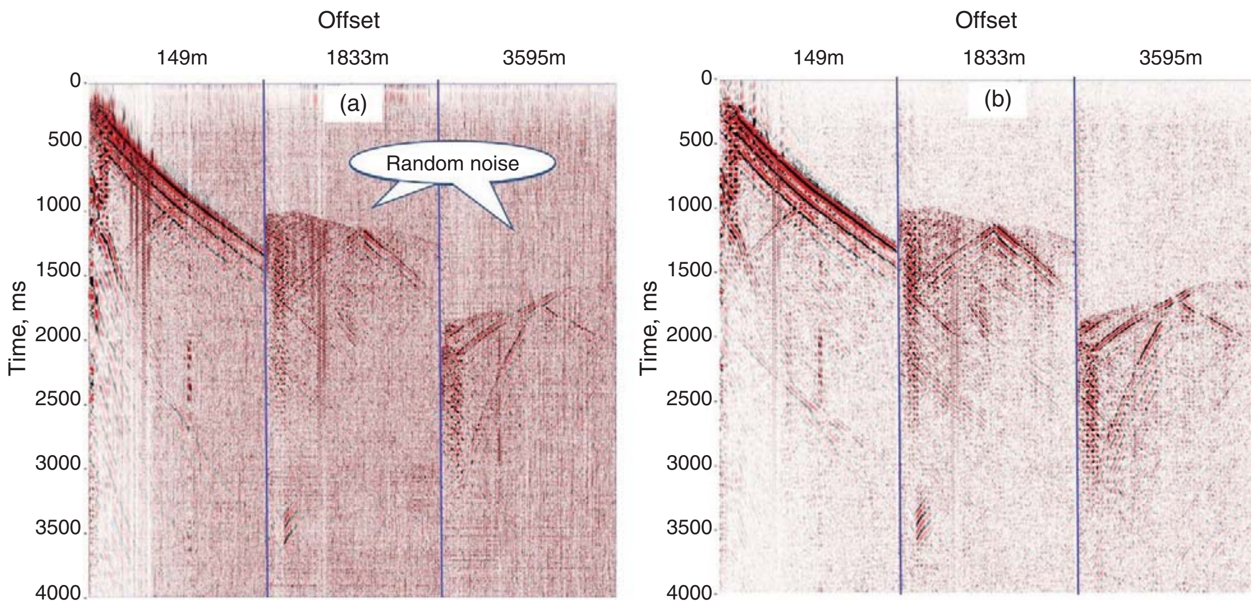

Figure 7.6 DAS-VSP recording before (a) and after (b) F-X denoising.

Fourier transform, which translates the effective signal, now with random noise removed, back into the T-X domain.

Figure 7.6 shows DAS-VSP data with different source spacing before (Figure 7.6a) and after (Figure 7.6b) denoising in the F-X domain. After denoising, we have attenuated the random interference and improved the effective SNR.

7.5. SNR ENHANCEMENT

While removing noise is vital to the process of improving data quality, additional techniques are required to further improve the SNR of DAS-VSP data. To improve the SNR of DAS-VSP data, we capitalize on the DAS path distance and high instrument density in the prestack processing stage. Group forming via multitrace combination

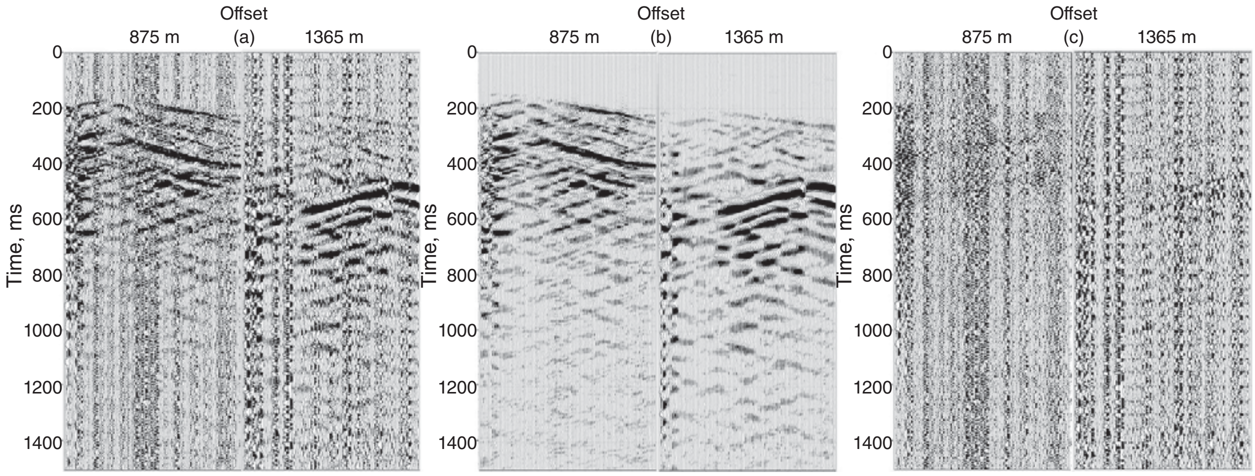

Figure 7.7 Before and after improved SNR processing common shot point gathers. (a) Raw DAS data, interval: 8 m; (b) DAS data after group forming, interval: 8 m; and (c) difference between raw data and denoising data.

is a targeted processing method that increases the effective SNR by combining upgoing and downgoing wave components.

First, we select raw DAS data and capture the first arrival time of the direct wave, and then we separate upgoing and downgoing waves using a median filter. Now the downgoing wave is aligned based on the first arrival time, and then we apply the normal moveout (NMO) correction to the upgoing wave. The next step involves applying median dilution to the downward-stretching and upstream-stretching profiles, which downsamples the data by sampling 21 median points on the first 10 channels and the last 10 channels of the current channel (for a total of 21 channels). Once downsampled, we then align the downward-stretching profile and apply an anti-NMO correction to the upstream wave, and merge the two profiles to generate a rendering of the DAS data, now with a higher SNR value.

At a depth of 0.8 m, the original DAS data (Figure 7.7a) are plagued by noise and have a low SNR value. After applying the group-forming multitrace combination method (Figure 7.7b), the effective wave group is clearer, the continuity and recognition of upper and lower waves are enhanced, and the SNR is significantly improved. Figure 7.7c shows the difference between raw data and denoising data.

7.6. CONCLUSION

DAS-VSP is becoming an increasingly popular technique for near-well imaging in gas and oil fields. It is an efficient way to gather seismic data because of its low cost, full wellbore coverage, and resistance to high temperatures and pressures. In spite of all efforts made to attenuate interference noise in the field, DAS-VSP data are still plagued by noise. We have proposed a number of denoising methods that will greatly mitigate cable resonance interference and random interference noise. After applying these techniques, we were able to mitigate the DAS-VSP interference and significantly improve the SNR, while still maintaining the integrity of effective seismic waves.

REFERENCES

Bakku, S., Wills, P., Fehler, M., Mestayer, J., Mateeva, A., & Lopez, J. (2014). *Vertical seismic profiling using distributed acoustic sensing in a hydrofrac treatment well*. Paper presented at 84th Annual International Meeting, SEG, Expanded Abstracts (pp. 5024–5028). https://doi.org/10.1190/segam2014-1559.1

Blias, E., & Hughes, B. (2015). *3D VSP imaging: Some general problems*. 85th Annual International Meeting, SEG, Expanded Abstracts (pp. 5630–5634). https://doi.org/10.1190/segam2015-5807268.1

Chen, J., Chen, W., Wang, X., Zhou, Y., & Zhang, G. (2018). *DAS coupling noise suppression using wavelet and DCT dictionary based on sparse optimization*. Paper presented at 88th Annual International Meeting, SEG, Expanded Abstracts (pp. 4938–4942). https://doi.org/10.1190/segam2018-2996038.1

Constantinou, A., Farahani, A., Cuny, T., & Hartog, A. (2016). *Improving DAS acquisition by real-time monitoring of wireline cable coupling*. Paper presented at 86th Annual International Meeting, SEG, Expanded Abstracts (pp. 5603–5607). https://doi.org/10.1190/segam2016-13950092.1

Correa, J., Egorov, A., Tertyshnikov, K., Bona, A., Pevzner, R., Dean, T., et al. (2017). Analysis of signal to noise and directivity characteristics of DAS VSP at near and far offsets—A

CO2CRC Otway Project data example. *The Leading Edge*, *36* (12), 994a1–994a7. https://doi.org/10.1190/tle36120994a1.1

Didraga, C. (2015). *DAS VSP recorded simultaneously in cemented and tubing installed fiber optic cables*. Paper presented at 77th EAGE Conference and Exhibition. https://doi.org/10.3997/2214-4609.201412738.

Flórez, R.S. Paredes, J.L., & Mejía, F.A.V. (2017). *A Sparse representation technique for interpolation and denoising: Application on VSP data*. Paper presented at 15th International Congress of the Brazilian Geophysical Society & EXPOGEF. https://doi.org/10.1190/sbgf2017-269

Jiang, T., Zhan, G., Hance, T., Sugianto, S., & Kjos, E. (2016). *Valhall dual-well 3D DAS VSP field trial and imaging for active wells*. Paper presented at 86th Annual International Meeting, SEG, Expanded Abstracts(pp. 5582–5586). https://doi.org/10.1190/segam2016-13871754.1

Kimura, T., Suzuki, K., Ali, S., Breninger, J., & Hajjaj, S. (2018). *Hybrid 3D VSP using fiber-optic technology and a conventional borehole seismic array tool*. Paper presented at 80th EAGE Conference and Exhibition. https://doi.org/10.3997/2214-4609.201801499

Lee, C. C., Gou, W., Rollins, F., Li, Q., Jia, T., & Chakraborty, S. (2016). *3D VSP processing and imaging: A case study at Mad Dog, Gulf of Mexico*. Paper presented at 86th Annual International Meeting, SEG, Expanded Abstracts (pp. 5562–5566). https://doi.org/10.1190/segam2016-13960363.1

Mateeva, A., Lopez, J., Potters, H., Mestayer, J., Cox, B., Kiyashchenko, D., et al. (2014). Distributed acoustic sensing for reservoir monitoring with vertical seismic profiling. *Geophysical Prospecting, 62*(4), 679–692. https://doi.org/10.1111/1365-2478.12116

Mateeva, A., Mestayer, J., Cox, B., Kiyashchenko, D., Wills, P., & Lopez, S. (2012). *Advances in Distributed Acoustic Sensing (DAS) for VSP*. Paper presented at 82nd Annual International Meeting, SEG, Expanded Abstracts (pp. 1–5). https://doi.org/10.1190/segam2012-0739.1

Wu, B., Lawton, D. C., & Hall, K. W. (2015). *Processing and interpretation of multicomponent walkaway vertical seismic profile data—a case study of a heavy oil reservoir*. Paper presented at 85th Annual International Meeting, SEG, Expanded Abstracts (pp. 752–756). https://doi.org/10.1190/segam2015-5873920.1

Yu, G., Cai, Z., Chen, Y., Wang, X., Zhang, Q., & Li, Y. (2016). Walkaway VSP using multimode optical fibers in a hybrid wireline. *The Leading Edge, 35*(7), 615–619. https://doi.org/10.1190/tle35070615.1

8

High-Resolution Shallow Structure at Brady Hot Springs Using Ambient Noise Tomography (ANT) on a Trenched Distributed Acoustic Sensing (DAS) Array

Xiangfang Zeng[1,2], Clifford H. Thurber[2], Herbert F. Wang[2], Dante Fratta[3], and Kurt L. Feigl[2]

ABSTRACT

An ~8700 m fiber-optic cable is installed in surface trenches at the Brady Hot Springs geothermal site in Nevada, USA. A distributed acoustic sensing (DAS) system is applied to use this fiber-optic cable to record seismic ambient noise. Noise cross-correlation functions (NCFs) of channel pairs on one linear DAS segment and on two in-line DAS segments are obtained, from which the Rayleigh wave signal emerges. The dispersive group and phase velocities in a high-frequency band of 2–18 Hz are measured with two different methods (multichannel analysis of surface waves (MASW) and frequency-time analysis (FTAN)) and then used to invert shear wave velocities at shallow depths. The obtained velocity model successfully reveals low-velocity zones (LVZs) in warm ground areas. Our results demonstrate that using a DAS array with ambient noise tomography (ANT) to image near-surface seismic structure is feasible.

8.1. INTRODUCTION

Seismic tomography is one of the most important approaches for imaging Earth's interior. It has been widely used in seismic studies and resource exploration, especially in the oil and gas industry. The potential of seismic tomography in geothermal reservoir imaging and monitoring has also been demonstrated in numerous studies. Since the seismic velocity parameters (V_p, V_s, V_p/V_s, and anisotropy) are sensitive to lithology, including porosity, fracture network, and other reservoir characteristics (e.g., Vécsey et al., 1998; Zhang & Lin, 2014), seismic tomography can be effectively applied in geothermal reservoir imaging. One of the key factors of seismic tomography is that resolution is strongly dependent on seismic ray coverage. Recently, dense arrays have been used to provide high-resolution images of volcanic and geothermal systems (e.g., Lehujeur et al., 2018; Wang et al., 2017). Previous studies reveal that low-velocity anomalies correlate well with surface geology at shallow depths, whereas porosity plays an important role at greater depths (Lehujeur et al., 2018).

To further understand mechanisms and evaluate poroelastic properties of a geothermal reservoir, a three-part seismic acquisition system was deployed at the Brady Hot Springs geothermal field in Nevada for 15 days in March 2016 (Feigl & PoroTomo Team, 2018). In general,

[1]State Key Laboratory of Geodesy and Earth's Dynamics, Innovation Academy for Precision Measurement Science and Technology, Chinese Academy of Sciences, Wuhan, China
[2]Department of Geoscience, University of Wisconsin–Madison, Madison, Wisconsin, USA
[3]Department of Civil and Environmental Engineering, University of Wisconsin–Madison, Madison, Wisconsin, USA

Distributed Acoustic Sensing in Geophysics: Methods and Applications, Geophysical Monograph 268, First Edition.
Edited by Yingping Li, Martin Karrenbach, and Jonathan B. Ajo-Franklin.

DOI:10.1002/9781119521808.ch08

both active source (controlled explosions, vibroseis trucks, etc.) and passive source (naturally occurring noise or cultural noise) can be used for tomography. Active-source data consisting of body-wave and surface-wave signals excited by a vibroseis truck have been analyzed and used in previous tomography studies (Matzel et al., 2017; Parker et al., 2018; Song et al., 2018). One passive-source method is based on the analysis of continuous ambient noise that is generated by natural and anthropogenic activities, such as ocean waves, wind, and traffic. Although the origin of ambient noise tomography (ANT) came into existence as early as the 1950s, its great progress was achieved in the 2000s with more available high-quality continuous records (Campillo & Roux, 2015). The ANT technique makes it possible to construct high-resolution models of shallow shear wave structures without costly active-source operation (Dou et al., 2017; Zeng, Lancelle, et al., 2017). The feasibility of using DAS for ANT has been tested successfully with a small data set acquired in September 2013 at a test site in Garner Valley, California (Zeng, Lancelle, et al., 2017).

In this study, we use continuous records from a surface DAS array to compute high-quality NCFs of channel pairs on individual linear segments and on pairs of two in-line, but separated, segments. The Rayleigh wave signal is analyzed with MASW and FTAN methods to obtain frequency-dependent group and phase velocity measurements. Then, the shallow shear wave structure is inverted from the group and phase velocities. The inverted model is compared with models obtained from other methods and surface geology.

8.2. DATA AND METHODS

The power plant at the Brady Hot Springs geothermal field has been operating since 1992. Cold fluid is injected at about 300 m depth in two wells in the northeast part of the site (Figure 8.1), and the production wells are situated in the southwest part. An elliptical area of subsidence was observed with satellite interferometric synthetic aperture radar, and inverse modeling suggests it is the result of volumetric contraction at shallow depths (Ali et al., 2016). The seismic acquisition systems deployed at the Brady Hot Springs geothermal field included a surface geophone array consisting of 238 short-period three-component sensors, an ~8600 m DAS array installed in surface trenches, and an ~350 m DAS array installed in an observation well. Two seismic tomography techniques with different sources were planned. The active source was a 440 kN force vibroseis truck that occupied 191 locations within and surrounding the DAS array during the four stages of the experiment. Planned passive source included traffic and more general ambient noise.

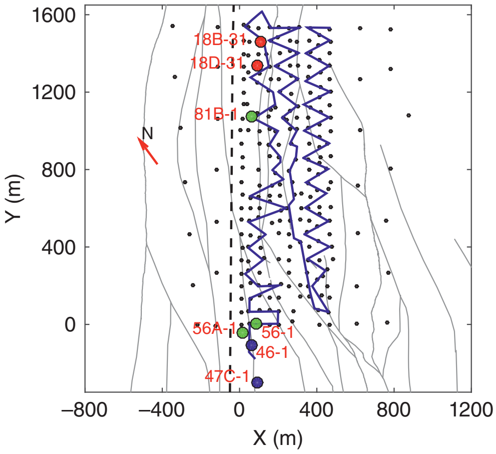

Figure 8.1 Seismic acquisition systems in the Brady Hot Springs geothermal site in Nevada. The trenched DAS cable is shown by the blue line. Black solid circles denote geophones. Wells are denoted by various colored solid circles: Injection wells (red), observation wells (green), and production wells (blue). Gray lines represent faults in Faulds et al. (2017). The green open circles denote the channel pair on two in-line segments, whereas the red ones denote the channel pair along one segment. The highway and service road are shown by a black dashed line and a pink line, respectively.

The DAS array was installed very near the surface of a 1500 × 500 × 400 m target volume (natural laboratory) on the main area of subsidence, in trenches that are about 30–50 cm deep and backfilled with loose soil. Since DAS is sensitive to the strain along the axis of the fiber-optic cable, geometry was designed in a zigzag shape to capture signals from vibroseis sources from different directions as much as possible (Figure 8.1). However, the channels around the corner suffered interference from two segments, we deleted 10 channels around each corner. Gauge length was set at 10 m with a channel spacing of 1 m (Parker et al., 2014). To reduce storage and computational cost, the raw data were resampled from 1000 to 100 Hz.

According to a power spectral density map from the geophone array, there are three dominant ambient noise sources at the Brady Hot Springs geothermal site, which include traffic on the highway, traffic on a service road crossing the target area from southwest to northeast, and pumping noise from the injection wells (Zeng, Thurber, et al., 2017). Due to the varying coupling between the DAS cable and the soil, the noise level across the DAS array is complicated (Figure 8.2). For example, one segment ($x \sim 300$ m, $y \sim 900$ m) crossing a ditch was exposed to the air, and the dangling of the cable generated an extremely strong noise signal. The interrogator was installed in a mobile laboratory that was a modified

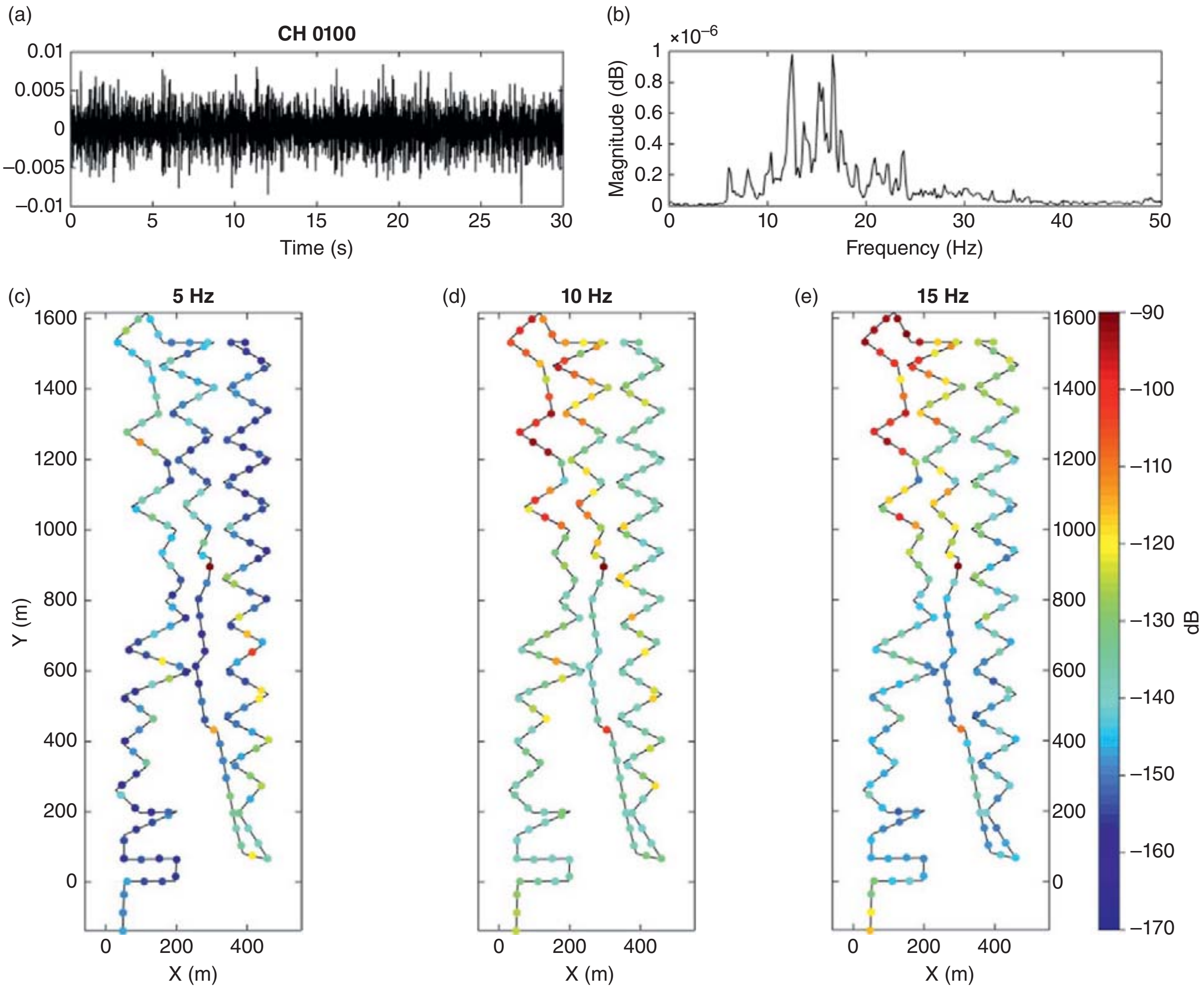

Figure 8.2 (a) Thirty seconds of raw data recorded by Channel 0100 in the southwest part of the study area. (b) The spectrum of the waveform shown in (a). (c)–(e) Power spectral density of every 15th channel at 5, 10, and 15 Hz.

shipping container. The shaking of the mobile laboratory due to door closing, chairs moving, and other activities also caused strong coherent signals across the array. The strongest noise is in the range of 5–35 Hz, and several spectral peaks are also observed in the spectrum.

Several standard processing steps are applied to the raw data (Zeng, Lancelle, et al., 2017; Figure 8.3). As mentioned earlier in this chapter, the shaking of the interrogator causes a coherent noise signal across the whole array, the array mean and segment mean are subtracted at first. Strong transient signals are reduced with temporal and frequency domain normalization (Bensen et al., 2007). Then, the processed waveforms of two receivers in a short time window (30 s) are used to compute individual NCFs. To remove the effect of uneven source distribution and enhance signal-to-noise ratio, individual cross-correlation functions over a long time period are stacked to obtain final NCFs.

Signal-to-noise ratio of the NCFs increases steadily with increasing length of the stacking time period and then converges at some point that is the optimal stacking time period (Seats et al., 2012). One straightforward way to determine the optimal stacking time period is using a cross-correlation analysis. The NCF of a long time period is used as the reference trace. Since traffic is one of the most important noise sources, the individual NCFs show diurnal variations (Zeng, Lancelle, et al., 2017). We use the NCFs of 10 hours, including daytime and nighttime, as reference traces. The cross-correlation coefficients between NCFs of time periods ranging from 1 to 10 hours and the reference trace are computed. The point at which the cross-correlation coefficient curve reaches a particular

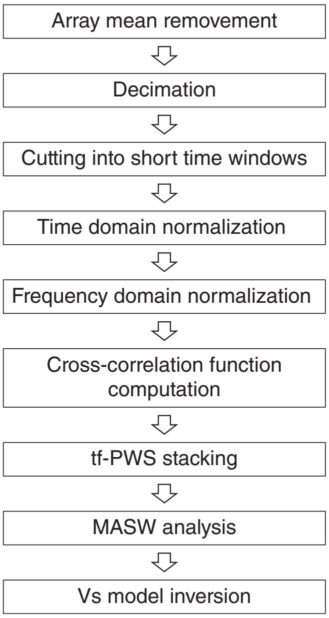

Figure 8.3 The data preparation and modeling process used in this study.

threshold is chosen. Two examples of different channel pairs are shown in Figure 8.4. The first example is Channel Pair CH0462-CH0580 (Figure 8.1) that is on the same segment, which is perpendicular to the highway. The cross-correlation coefficient reaches over 0.8 when the number of stacked traces exceeds 450 (~3.75 hours; Figure 8.4a). The second example is Channel Pair CH0110-CH0640 on two in-line segments (Figure 8.1), in this case, and it is parallel to the highway. The convergence rate is similar to the first example (Figure 8.4b). Therefore, we chose 4 hours (half during nighttime and half during daytime) as the stacking time period for all channel pairs used in this study.

Although the body-wave signal in NCFs has been reported (e.g., Zhan et al., 2010), the surface-wave signal is generally much clearer and its dispersion curve or waveform can be used as the observed data in tomography (e.g., Lee et al., 2015; Shapiro et al., 2005). After extracting the surface-wave signal, the surface-wave phase and/or group velocity dispersion curves need to be determined. The MASW method, based on slant stacks in the frequency domain, is utilized to determine phase velocity between channels along the same segment of the fiber-optic cable (denoted by red open circles in Figure 8.1). Group velocity is measured for channels on two in-line segments (denoted by green open circles in Figure 8.1) with multiple filtering technique (MFT), which has been widely used since the 1960s (Dziewonski et al., 1969). A series of narrow band-pass filters that are defined as Gaussian functions in the frequency domain are applied to the waveform, and then travel times of the maximum energy for each frequency are picked for group velocity computation. Group velocities are computed by channel separation divided by the respective travel times. The dispersion curves obtained from these steps are used to determine layered shear wave velocity structures using two linearized inversion methods for different dispersion

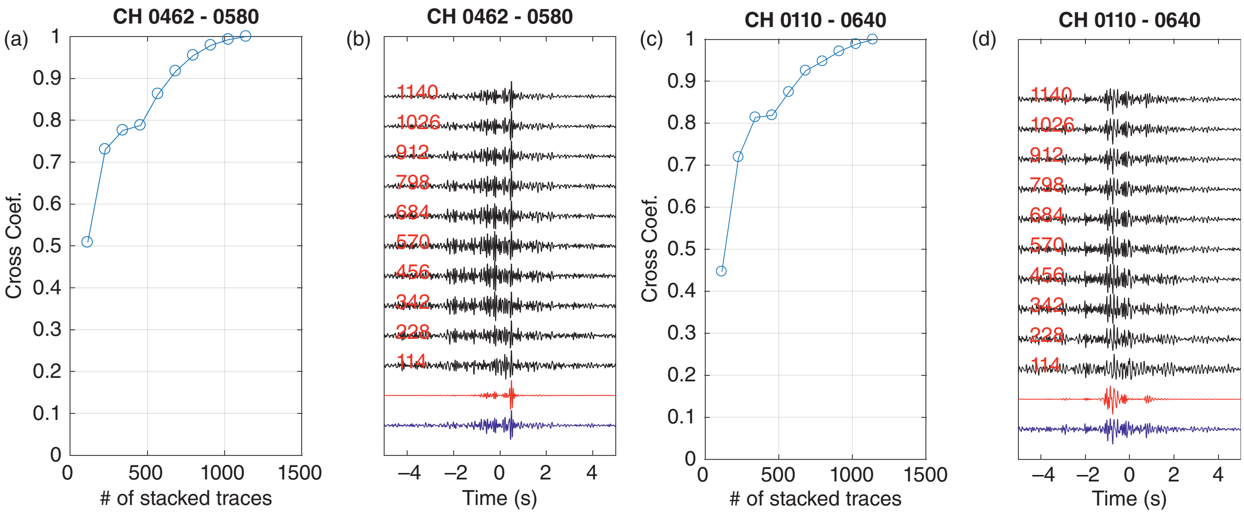

Figure 8.4 (a) Correlation coefficient to the reference trace vs. the number of stacked traces for Channel Pair CH0462-CH0580 (denoted by red open circles in Figure 8.1). (b) The reference NCF (blue), time frequency-phase weight stacking NCF (red), and different time period NCFs (black). (c) and (d) Correlation coefficient to the reference trace vs. the number of stacked traces for Channel Pair CH0110-CH0640 (denoted by purple open circles in Figure 8.1).

curves. The final three-dimensional (3D) model is interpolated from multiple layered models.

8.3. NCF RESULTS

The Rayleigh wave signal can be observed on both vertical-vertical and radial-radial component NCFs of traditional three-component seismic sensors, where radial direction is along the line connecting the two receivers in a laterally homogenous structure. Since each DAS channel is equivalent to one horizontal component geophone, there are two possible channel pairs that could be used: two channels on the same linear segment or channels on two in-line segments with cable orientations that are the same as the path between the two channels. The first case includes 61 segments, whereas the second case includes 51 segment pairs in total.

One example of a channel pair on one linear segment is shown in Figure 8.5. The NCF shows strong asymmetry that reflects more energy coming from the highway side. The Rayleigh wave signal clearly emerges, and the strongest energy propagates with a velocity of ~300 m/s. For the channel pairs on two in-line segments, the greater offset makes it difficult to extract a clear signal due to strong scattering. Therefore, the array interferometry technique, which has been successfully used to extract weak signals from NCFs (Lin et al., 2013; Nakata et al., 2015), is adopted to improve signal quality. This method requires computing NCFs of all possible receiver pairs across arrays (segments in our case) and then stacking NCFs of receiver pairs in particular distance bins. To reduce computational cost, only 10% of all channel pairs between two in-line segments are computed and the NCFs in 10 m distance bins are stacked into one trace. Figure 8.6 shows

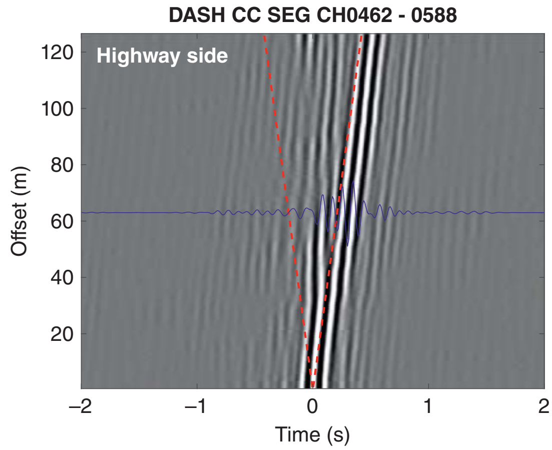

Figure 8.5 Record section of NCFs between channel pairs along one segment (denoted by red open circles in Figure 8.1). The dashed red lines denote a velocity of 300 m/s and one sample trace is shown in blue.

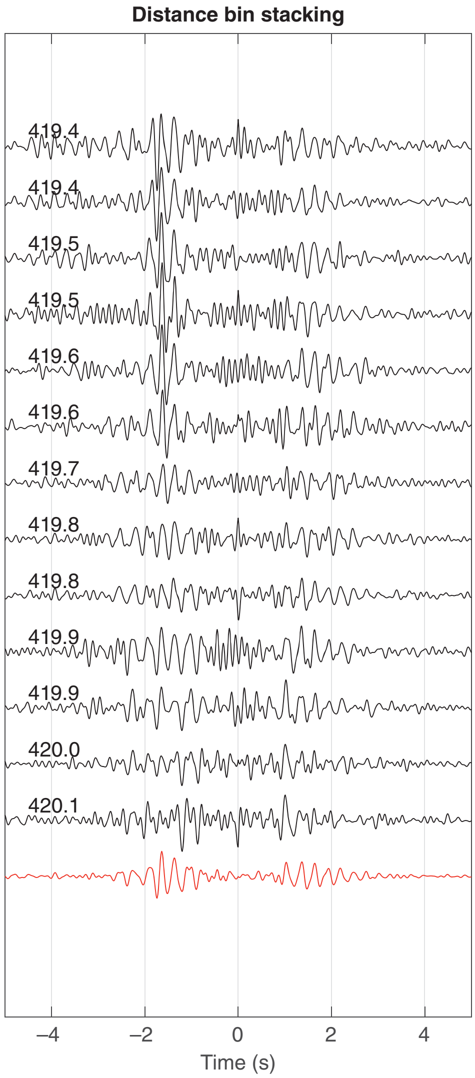

Figure 8.6 Individual NCFs (black) in a distance bin and the stacked trace (red). The number on each trace indicates the offset in meters.

NCFs of 13 channel pairs with the offset ranging from 419.4 to 420.1 m, and the stacked traces. Rayleigh wave signals on both negative and positive lags are enhanced, while random noise is substantially suppressed. The cross-segment NCFs in the southeast part of the study area are shown in Figure 8.7. The Rayleigh wave signal can be traced up to 600 m, making it possible to measure dispersion information in a lower frequency band.

8.4. DISPERSION MEASUREMENT RESULTS

The MASW method is used to measure Rayleigh wave phase velocities from NCFs of channel pairs along single linear segments. Since the MASW method measures the

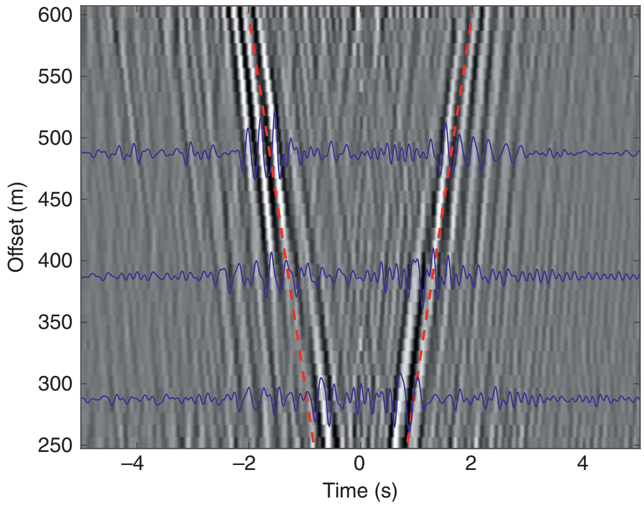

Figure 8.7 Record section of NCFs between channel pairs along two in-line segments (denoted by green open circles in Figure 8.1). The dashed red lines denote a velocity of 300 m/s and sample traces are shown in blue.

phase difference between receivers, phase velocity is controlled by the seismic structure beneath the segment. The denser spacing theoretically reduces aliasing in the wavenumber domain, meaning it is possible to see relatively high-frequency components. On the other hand, the length of the segment also limits both the resolution in the wavenumber domain and the maximum wavelength that controls the maximum depth of investigation. An empirical criterion is the maximum wavelength is about twice the segment length, whereas the maximum depth of investigation is very close to the segment length (Park & Carnevale, 2010). One MASW picking example is shown in Figure 8.8. The MASW picked dispersion curves for the profile shown in Figure 8.5 were used to compare with the result obtained with active source signals (Song et al., 2018). Dispersive trends agree well and the difference between the two results is less than 25 m/s. The histogram shown in Figure 8.8b suggests that the number of picks reaches a peak around 10 Hz, corresponding to a wavelength of about 30 m.

The distance bin stacked NCFs mainly reflect average seismic structure of the whole path rather than that beneath a given segment. The phase velocity measured with the MASW method will be affected by the structures beneath both segments, which has been averaged by distance bin stacking. Therefore, the multiple-filter technique is used to measure group velocities. Similar to the MASW method, the greater offset makes it possible to

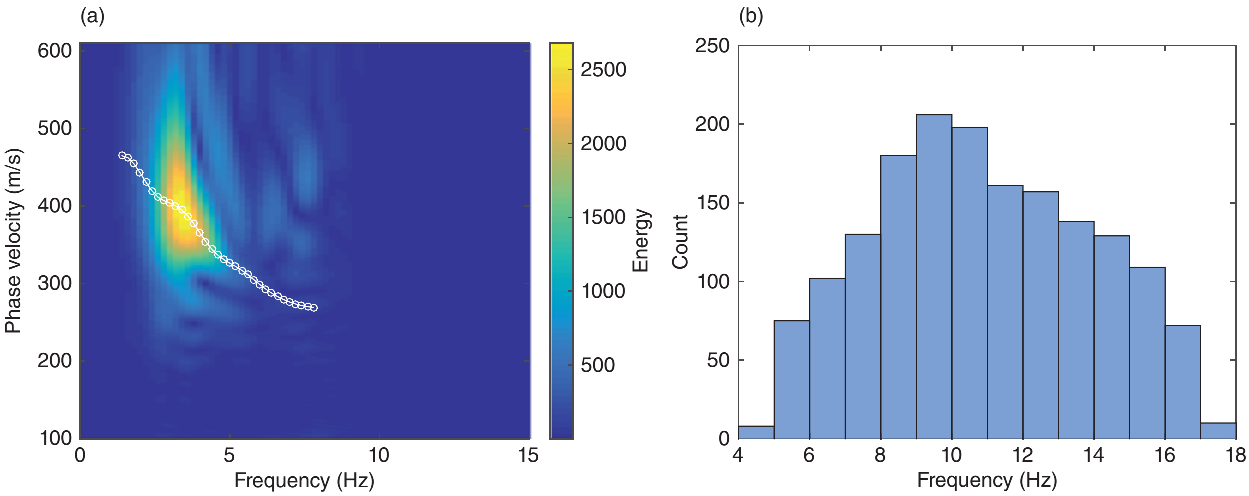

Figure 8.8 (a) One MASW measurement example. The color represents stacking energy, and the picked velocities are marked with white circles at the energy maximum. (b) A histogram of MASW measurements.

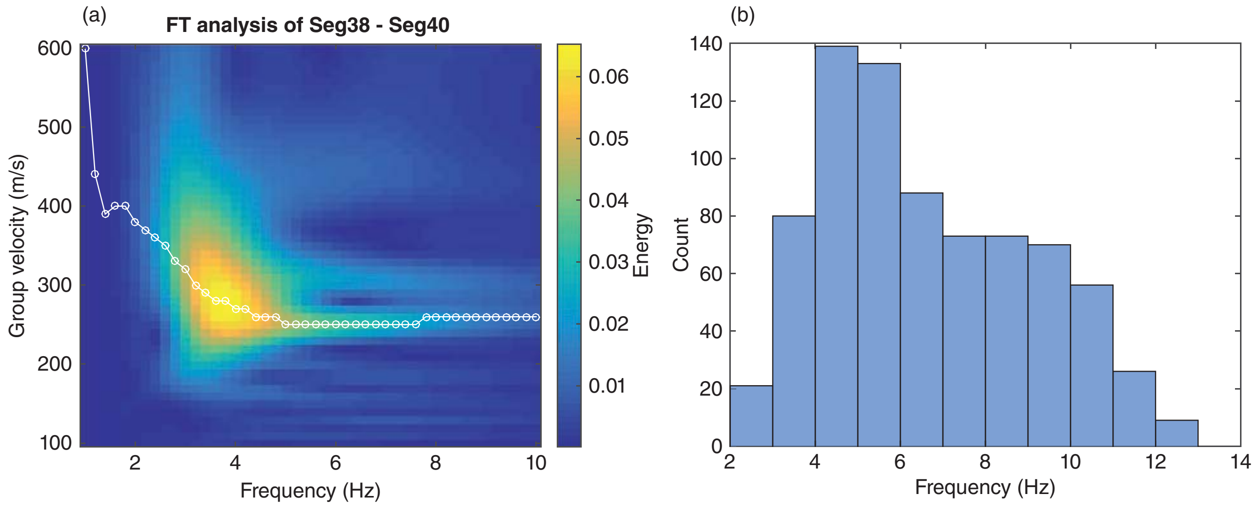

Figure 8.9 (a) One MFT measurement example. The color represents stacking energy, and the picked velocities are marked with white circles. (b) A histogram of MFT measurements.

measure dispersion in a lower frequency band (Bensen et al., 2007). As is shown in Figure 8.9, peak frequency with MFT measurements is around 5 Hz, which is much lower than the frequency for the maximum MASW measurements.

Finally, 1,409 phase velocities and 768 group velocities are measured and used in the next inversion step. Dispersion data between 2 and 18 Hz are sensitive to shear wave velocity at a shallow depth. The rule of thumb in surface-wave inversion is that the dispersion of the fundamental mode Rayleigh wave is sensitive to a depth of about 0.5–0.6 times the wavelength. As an example, we used a typical model to compute example sensitivity kernels for our data set (Figure 8.10). Group

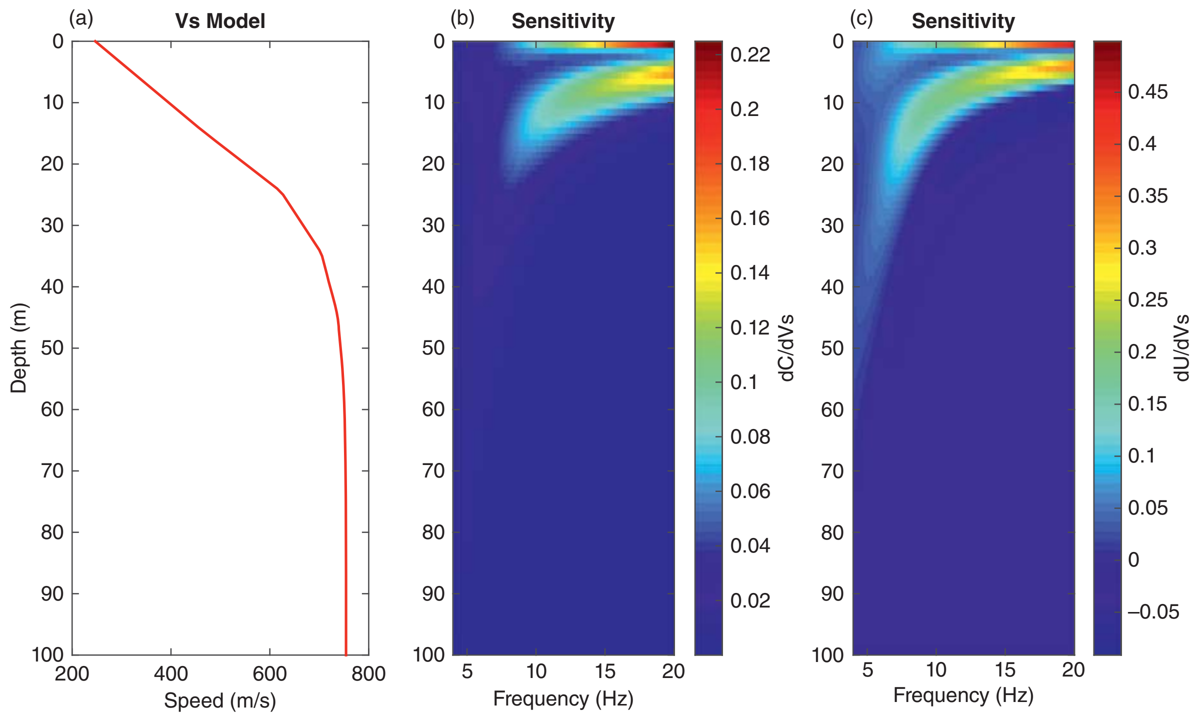

Figure 8.10 (a) The layered model used in sensitivity kernel computation. (b) Sensitivity kernels of Rayleigh wave phase velocity. (c) Sensitivity kernels of Rayleigh wave group velocity.

velocity is more sensitive than phase velocity and the maximum depth of meaningful sensitivity is about 30–40 m in this model.

8.5. SHEAR WAVE VELOCITY MODEL

The last step of ANT is the inversion of dispersion curves to construct layered models at sample points. The sample point is defined as the center point of the segment for the same segment data set and the middle point of the two segments for the two in-line segment data set. Figure 8.11a shows the sample points provided by two data sets. The NCFs of channel pairs of the two in-line segments sample the warm ground zone that supplement the NCFs of channel pairs along one segment. Two inversion methods were implemented to solve shear wave velocity profiles at sample points. The surface wave analysis, modelling and inversion (SWAMI) code (Constable et al., 1987; Lai, 1998), based on Occam's inversion, is used to invert phase velocities, whereas group velocities are inverted with a linearized inversion code from the Computer Programs in Seismology software suite (Herrmann, 2013). The pseudo-3D shear wave velocity model is interpolated from all layered models (Figures 8.11b–d).

At very shallow depth (Z = 5, 10 m), a LVZ is observed in the warm ground zone (Figures 8.11b and 11c). The area around injection wells 18–31 and 18D–31 also shows a relatively low velocity. At greater depth, a velocity contrast emerges across the fault zone in the southern part. Other tomography techniques were also used to image the 3D seismic structure at the Brady Hot Springs geothermal site. The shot interferometry (SI) technique with geophone array data provided 3D V_p and V_s models (Matzel et al., 2017). Parker et al. (2018) used P-wave arrival times from a vibroseis truck on DAS and geophone arrays to invert a 3D V_p model. Figure 8.12 shows a comparison among these three models at 20 m depth. Generally, the SI V_s model shows a higher velocity that might be due to different initial models and/or inversion strategy. The LVZ near the injection wells is imaged in the two V_s models, but it is not clear in the V_p model. The other LVZ in the southwest part (x ~ 400, y ~ 100–400) is evident in our V_s and V_p models.

Distributed temperature sensing (DTS) measurements reveal the spatial surface temperature variation that is strongly affected by the fumaroles and fracture density. Therefore, surface temperature can be regarded as an index of porosity in the natural laboratory. Since seismic velocity decreases with increasing porosity, an anticorrelation between surface temperature and seismic velocity is expected. Our result reflects this relationship well (Figures 8.11a and 8.11b).

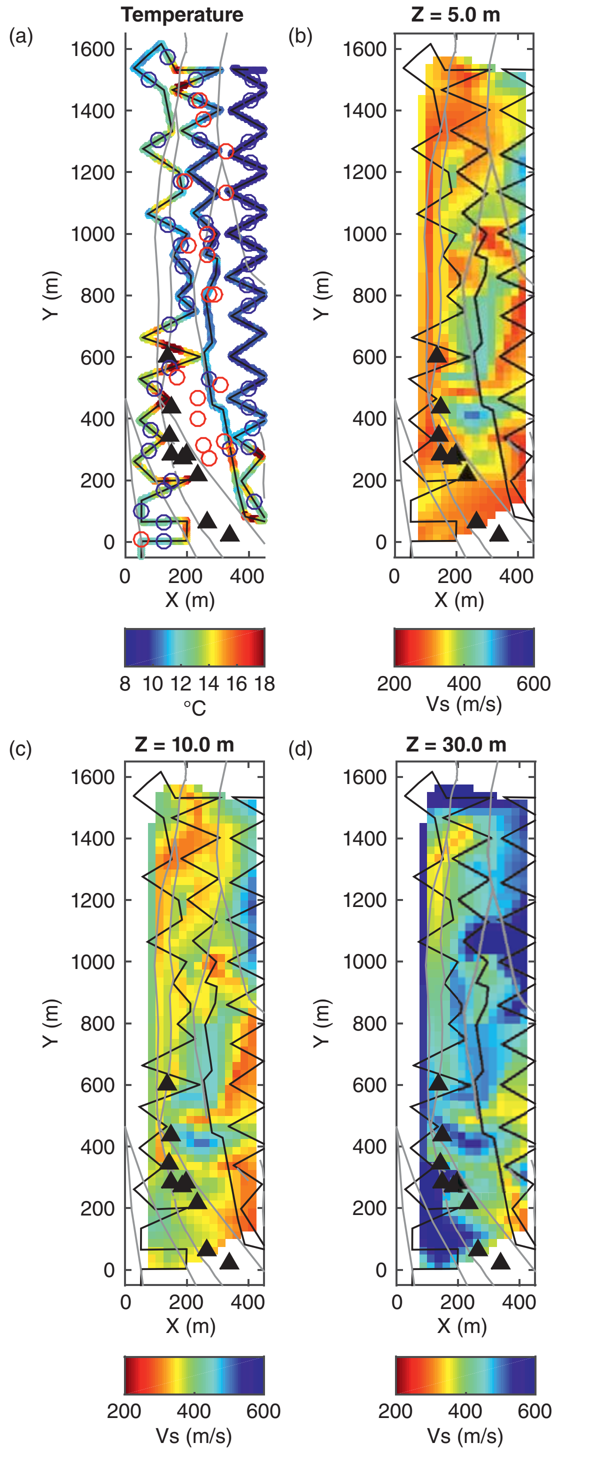

Figure 8.11 (a) Daily average surface temperature of 14 March 2016. (b) Shear wave velocity at 5 m depth. (c) Shear wave velocity at 10 m depth. (d) Shear wave velocity at 30 m depth. The fumaroles are shown by black triangles, and gray lines denote faults. Open circles on panel (a) denote sample points (red: cross-segment; blue: same segment).

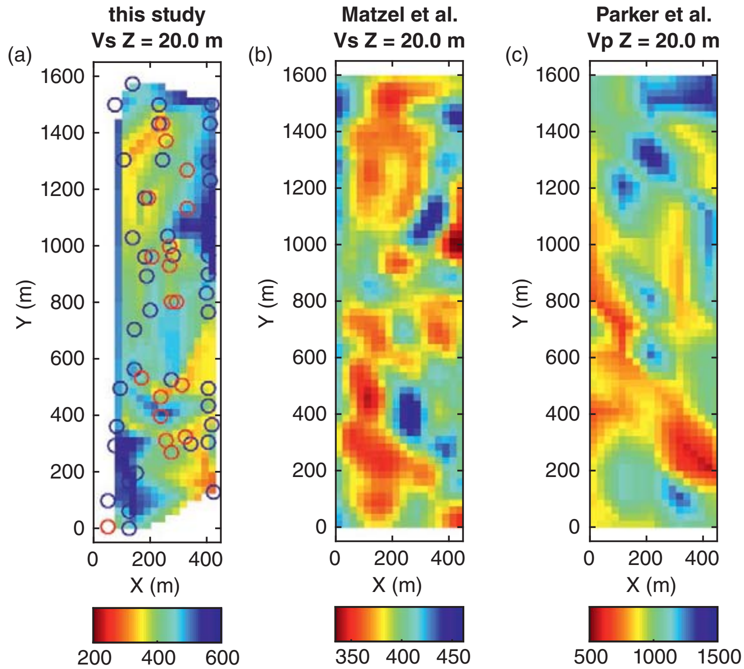

Figure 8.12 Velocity models at 20 m depth. (a) V_s model in this study, (b) V_s model from Matzel et al. (2017), and (c) V_p model from Parker et al. (2018). The open circles on panel (a) denote the sample points of this study. Source: Based on (b) Matzel et al. (2017); (c) Parker et al. (2018).

Due to the array geometry, lower frequency surface waves that are sensitive to deeper structure were not extracted in this study. With longer straight segments, this method could be used to image structure to about 100 m depth (e.g., Zeng et al., 2019). In this study, only a small portion of all possible channel pairs are used, which limits spatial sampling and model resolution. The reason is Rayleigh and Love waves are mixed on the NCFs of channel pairs for two segments that are not in a line. A new method has been proposed to handle this challenge (Song et al., 2020), which will expand usable data set and help to improve resolution.

8.6. CONCLUSIONS

In this study, the NCFs of channel pairs in individual linear DAS segments and pairs of in-line segments are computed following standard ambient noise processing procedures. Distance bin stacking is used to enhance signal-to-noise ratio of NCFs for channel pairs belonging to two in-line segments at the greater offset. Combining the two data sets improves coverage and makes it possible to build a 3D V_s model. Both group and phase velocities of Rayleigh waves in a high-frequency band (2–18 Hz) are used to invert shear wave velocity structure at shallow depth. The velocity model correlates with some surface features and matches some features seen in models obtained with the use of other methods.

ACKNOWLEDGMENTS

This study was funded in part by the Office of Energy Efficiency and Renewable Energy (EERE), U.S. Department of Energy, under Award Number DE-EE0006760. X. Zeng acknowledges support from the Natural Science Foundation of China (41974067) and the LU JIAXI International Team Program supported by the K.C. Wong Education Foundation and the Chinese Academy of Sciences (GJTD-2018-12).

REFERENCES

Ali, S. T., Akerley, J., Baluyut, E. C., Cardiff, M., Davatzes, N. C., Feigl, K. L., et al. (2016). Time-series analysis of surface deformation at Brady Hot Springs geothermal field (Nevada) using interferometric synthetic aperture radar. *Geothermics*, *61*, 114–120.

Bensen, G. D., Ritzwoller, M. H., Barmin, M. P., Levshin, A. L., Lin, F., Moschetti, M. P., et al. (2007). Processing seismic ambient noise data to obtain reliable broad-band surface wave dispersion measurements. *Geophysical Journal International*, *169*(3), 1239–1260.

Campillo, M., & Roux, P. (2015). 1.12—crust and lithospheric structure—seismic imaging and monitoring with ambient noise correlations. *Treatise on Geophysics*, 391–417.

Constable, S. C., Parker, R. L., & Constable, G. G. (1987). Occam's inversion: a practical algorithm for generating smooth models from electromagnetic sounding data. *Geophysics*, *52*, 289–300.

Dou, S., Lindsey, N., Wagner, A. M., Daley, T. M., Freifeld, B., Robertson, M., et al. (2017). Distributed acoustic sensing for seismic monitoring of the near surface: A traffic-noise interferometry case study. *Scientific Reports*, *7*(1), 11620.

Dziewonski, A. M., Bloch, S., & Landisman, M. (1969). A technique for the analysis of transient seismic signals. *Bulletin of the Seismological Society of America*, *59*, 427–444.

Faulds, J. E., Ramelli, A. R., Gardised, L. J., Coolbaugh, M. F., & Green, H. L. (2017). Preliminary geologic map of the Bradys geothermal area, Churchill County, Nevada. Nevada Bureau of Mines and Geology, Open-File Report, 12-5.

Feigl, K. L., & PoroTomo Team. (2018). *Overview and preliminary results from the PoroTomo project at Brady Hot Springs, Nevada: Poroelastic tomography by adjoint inverse modeling of data from seismology, geodesy, and hydrology*. Proceedings: 43rd Workshop on Geothermal Reservoir Engineering, Stanford University, Stanford, California, 12–14 February 2018.

Herrmann, R. B. (2013). Computer programs in seismology: An evolving tool for instruction and research. *Seismological Research Letters*, *84*, 1081–1088.

Lai, C. G. (1998). Simultaneous inversion of Rayleigh phase velocity and attenuation for near-surface site characterization (PhD dissertation), Georgia Institute of Technology.

Lee, E.-J., Chen, P., Jordan, T. H., Maechling, P. B., Denolle, M. A. M., & Beroza, G. C. (2015). Full 3D tomography for crustal structure in southern California based on the scattering-integral and the adjoint-wavefield methods. *Journal of Geophysical Research Solid Earth*, *119*(8), 6421–6451.

Lehujeur, M., Vergne, J., Schmittbuhl, J., Zigone, D., & Chenadec, A. L. (2018). Reservoir imaging using ambient noise correlation from a dense seismic network. *Journal of Geophysical Research Solid Earth*, *123*, 6671–6686, doi:10.1029/2018JB015440.

Lin, F.-C., Tsai, V. C., Schmandt, B., Duputel, Z., & Zhan, Z. (2013). Extracting seismic core phases with array interferometry. *Geophysical Research Letters*, *40*(6), 1049–1053.

Matzel, E., Zeng, X., Thurber, C., Luo, Y., & Morency, C. (2017). *Seismic interferometry using the dense array at the Brady geothermal field*. Proceedings: 42nd Workshop on Geothermal Reservoir Engineering. Stanford University, Stanford, California, 13–15 February 2017.

Nakata, N., Chang, J. P., Lawrence, J. F., & Boué, P. (2015). Body wave extraction and tomography at Long Beach, California, with ambient noise interferometry. *Journal of Geophysical Research Solid Earth*, *120*(2), 1159–1173.

Park, C., & Carnevale, M. (2010). *Optimum MASW survey-revisit after a decade of use*. GeoFlorida 2010: Advances in Analysis, Modeling and Design. ASCE Conference Proceedings, 20–24 February 2010, West Palm Beach, FL.

Parker, T., Shatalin, S. V., & Farhadiroushan, M. (2014). Distributed acoustic sensing—a new tool for seismic applications, *First Break*, *32*(2), 61–69.

Parker, L., Thurber, C., Zeng, X., Li, P., Lord, N., Fratta, D., et al. (2018). Active-source seismic tomography at the Brady geothermal field, Nevada, with dense nodal and fiber-optic seismic arrays. *Seismological Research Letters*, *89*(5), 1629–1640.

Seats, K. J., Lawrence, J. F., & Prieto, G. A. (2012). Improved ambient noise correlation functions using Welch's method. *Geophysical Journal International*, *188*(2), 513–523.

Shapiro, N., Campillo, M., Stehly, L., & Ritzwoller, M. (2005). High-resolution surface-wave tomography from ambient seismic noise. *Science*, *307*(5715), 1615–1618.

Song, Z., Zeng, X., Thurber, C., Wang, H., & Fratta, D. (2018). Imaging shallow structure with active-source surface wave signal recorded by distributed acoustic sensing arrays. *Earthquake Science*, *31*, 207–213.

Song, Z., Zeng, X., & Thurber. C. (2021). Surface-wave dispersion spectrum inversion method applied to Love and Rayleigh waves recorded by DAS, *Geophysics*, *86*(1), EN1–EN12.

Vécsey, G., Holliger, K., Pratt, R. G., Dyer, B. C., & Green, A. G. (1998). Anisotropic seismic tomography of a potential hot dry rock reservoir before and during induced pressurization. *Geophysical Research Letters*, *25*(11), 1991–1994.

Wang, Y., Lin, F.-C., Schmandt, B., & Farrell, J. (2017). Ambient noise tomography across Mount St. Helens using a dense seismic array. *Journal of Geophysical Research Solid Earth*, *122*, 4492–4508. doi:10.1002/2016JB013769

Wang, H. F., Zeng, X., Miller, D. E., Fratta, D., Feigl, K. L., Thurber, C. H., & Mellors, R. (2018). Ground motion response to a Ml 4.3 earthquake using co-located distributed acoustic sensing and seismometer arrays. *Geophysical Journal International*, *213*(3), 2020–2036.

Zeng, X., Lancelle, C., Thurber, C., Fratta, D., Wang, H., Lord, N., et al. (2017). Properties of noise cross-correlation functions obtained from a distributed acoustic sensing array at Garner Valley, California. *Bulletin of the Seismological Society of America*, *107*(2), 603–610.

Zeng, X., Thurber, C., Fratta, D., Wang, H., Fratta, D., Matzel, E., & PoroTomo Team (2017). *High-resolution shallow structure revealed with ambient noise tomography on a dense array*. Proceedings: 42nd Workshop on Geothermal Reservoir Engineering. Stanford University, Stanford, California, 13–15 February 2017.

Zeng, X., Wang, B., Li, X., Xu, W., Xu, S., & Song, Z. (2019). *Shallow Vs structure imaged with the ambient noise recorded by a telecommunication fiber-optic cable in urban area*. Paper presented at 2019 Seismological Society of America Annual Meeting, Seattle, WA, USA, 23–26 April 2019.

Zhan, Z., Ni, S., Helmberger, D. V., & Clayton, R. W. (2010). Retrieval of Moho-reflected shear wave arrivals from ambient seismic noise. *Geophysical Journal International*, *182*(1), 408–420.

Zhang, Q., & Lin, G. (2014). Three-dimensional Vp and Vp/Vs models in the Coso geothermal area, California: Seismic characterization of the magmatic system. *Journal of Geophysical Research: Solid Earth*, *119*(6), 4907–4922.

Part III

Distributed Acoustic Sensing (DAS) Applications in Monitoring of Deformations, Earthquakes, and Microseisms by Fracturing

9

Introduction to Interferometry of Fiber-Optic Strain Measurements

Eileen R. Martin[1], Nathaniel J. Lindsey[2], Jonathan B. Ajo-Franklin[3,4], and Biondo L. Biondi[5,6]

ABSTRACT

Distributed acoustic sensing (DAS) measures the average axial strain (strain rate) along a subset of a fiber-optic cable, as opposed to the particle displacement (velocity) at a particular small point sensor. In shifting from measuring a vector field to a tensor field, DAS changes the directional sensitivity of measurements of every type of seismic wave when compared to single-component geophones, particularly Love and *S* waves. We show this through theoretical analysis of planar Rayleigh, Love, *P*, and *S* waves over both infinitesimally small and realistic gauge lengths. We extend the analysis of individual sensor detection of surface plane waves to inter-receiver cross-correlations of these recordings. Finally, we simulate random sources distributed around traditional seismometers and DAS channels in several configurations. The extraction of Rayleigh wave signals from ambient noise interferometry is more straightforward than Love wave signals. However, with some receiver geometries and source distributions, both Rayleigh and Love wave arrival times may be extracted over a range of offsets.

9.1. INTRODUCTION

The cost of long-term seismic studies using dense arrays has historically been too expensive to maintain for many applications. By performing interferometry on ambient noise recorded by seismometers or geophones, researchers can extract coherent signals mimicking surface wave Green's functions (Lin et al., 2008; Wapenaar et al., 2010). This avoids the cost and permitting of a source crew, but long-term maintenance of a dense geophone array is still too costly for some investigations. Underground fiber-optic DAS arrays are an attractive alternative to geophone arrays due to ease of installation (potentially even using existing telecommunications infrastructure), durability, and the requirement for a single power source for thousands of sensors at meter-scale spacing. DAS measures average axial strain rate along a subset of fiber, while geophones measure particle velocity in the vertical direction and sometimes both horizontal directions. This transition from a vector (particle velocity) to a tensor quantity (strain rate) leads to significant changes in the sensors' angular sensitivities, particularly for waves with particle motion orthogonal to the direction of propagation.

Over the past few years, researchers have extracted coherent signals from ambient noise recorded by colinear channels at multiple surface DAS arrays installed in

[1]Department of Mathematics, Virginia Polytechnic Institute and State University, Blacksburg, Virginia, USA

[2]FiberSense, Sydney, Australia

[3]Energy Geosciences Division, Lawrence Berkeley National Laboratory, Berkeley, California, USA

[4]Department of Earth, Environmental and Planetary Sciences, Rice University, Houston, Texas, USA

[5]Department of Geophysics, Stanford University, Stanford, California, USA

[6]Institute for Computational and Mathematical Engineering, Stanford, California, USA

Distributed Acoustic Sensing in Geophysics: Methods and Applications, Geophysical Monograph 268, First Edition.
Edited by Yingping Li, Martin Karrenbach, and Jonathan B. Ajo-Franklin.

DOI:10.1002/9781119521808.ch09

different ways (Dou et al., 2017; Lancelle, 2016; Martin et al., 2015, 2016; Zeng et al., 2017). These channels are in radial-radial alignment, so the noise correlation functions are interpreted as estimates of Rayleigh wave Green's functions. These results show promise for recovering near-surface structure directly beneath fiber-optic cables, but do not provide information about the subsurface between cables.

More recently, we observed coherent signals in noise correlation functions between fiber-optic lines at a trenched array (Ajo-Franklin et al., 2017; Lindsey, Dou, et al., 2017) and an array using fiber optics in existing telecommunications conduits (Martin & Biondi, 2017; Martin et al., 2018). We were previously unable to interpret these signals for use in subsurface imaging between fiber-optic lines. In this chapter, we develop a simple analytic model of ambient noise interferometry for fiber channels at arbitrary orientations and distances in the hope of expanding the coverage of ambient noise interferometry for near-surface imaging to include regions between fiber-optic lines.

In addition to ambient noise interferometry studies, DAS has become increasingly popular for microseismicity monitoring during energy production (Kahn et al., 2017; Webster et al., 2013) and is being investigated for earthquake monitoring at larger scales (Lindsey, Martin, et al., 2017). Detection of small seismic events often relies on cross-correlations of recordings, so understanding the effect of directional sensitivity on both directly recorded signals and cross-correlations of signals could have implications for quantifying potential biases in statistics describing the distribution of these events estimated with a given array geometry.

In this chapter, we review the differences between theoretical geophone and DAS measurements of plane waves: Both body waves and surface waves. A very different type of strain measurement device was studied nearly a century ago in Benioff (1935), so Figures 7 and 8 of that paper also appear in our analysis. We analyze geophone and DAS cross-correlations for individual plane wave events and point sources. Using theoretical point source responses and cross-correlations, we perform a simple thought experiment inspired by the thought experiment provided in Wapenaar et al. (2010) demonstrating how ambient noise interferometry works for random point sources recorded by both horizontal geophones and DAS in radial-radial and transverse-transverse configurations. Building on this thought experiment, we simulate noise correlation functions of signals recorded by two parallel fiber lines and two orthogonal fiber lines. While DAS sensing of uniformly distributed Love waves is prone to biased arrival time estimates, biases caused by uneven source distributions for geophones and DAS are different and DAS is sometimes more robust.

9.1.1. DAS Measurement Process

Let a wave be described by particle velocity $\dot{\mathbf{u}}(x,y,z,t) = \left(\dot{u}_x(x,y,z,t), \dot{u}_y(x,y,z,t), \dot{u}_z(x,y,z,t)\right)$, and then the axial strain rate in the x-direction at a point is $\frac{\partial \dot{u}_x}{\partial x}\Big|_{(x,y,z,t)}$. Let us say more generally we want to observe this wavefield using a horizontal fiber measuring an axial strain rate in the $(\cos(\theta), \sin(\theta), 0)$ direction. By applying tensor rotation matrices, the axial strain rate observed in the $(\cos(\theta), \sin(\theta), 0)$ direction at that point is:

$$\dot{\epsilon}_\theta = \mathcal{C}_\theta^2 \frac{\partial \dot{u}_x}{\partial x} + \mathcal{C}_\theta \mathcal{S}_\theta \left(\frac{\partial \dot{u}_x}{\partial y} + \frac{\partial \dot{u}_y}{\partial x} \right) + \mathcal{S}_\theta^2 \frac{\partial \dot{u}_y}{\partial y} \tag{9.1}$$

where we use $\mathcal{C}_\theta$ and $\mathcal{S}_\theta$ as short notation for $\cos(\theta)$ and $\sin(\theta)$, respectively, and $\dot{\epsilon}_\theta$ and all derivatives of $\dot{\mathbf{u}}$ are evaluated at (x,y,z,t). The measurement that would be detected by a fiber-optic channel at that same θ orientation centered on (x,y,z) is the average axial strain rate over a gauge length of straight fiber:

$$\dot{\epsilon}_{\theta,g}(x,y,z,t) = \int_{-g/2}^{g/2} \dot{\epsilon}_\theta(x + \nu\mathcal{C}_\theta, y + \nu\mathcal{S}_\theta, z, t)\,d\nu \tag{9.2}$$

The gauge length g over which the interrogator unit averages the axial strain is in general different from the channel spacing. The channel spacing is the distance between the starting point of new segments. For example, if the channel spacing were 1 m and the gauge length were 10 m, there would be a channel observing the average axial strain along the fiber between 1 and 11 m from the interrogator, the next channel would record the average axial strain between distances of 2 and 12 m, etc. The ability of the user to vary gauge length and channel spacing varies depending on manufacturer and model of interrogator.

We make the simplifying assumption that geophones measure $\dot{\mathbf{u}}$ at a point with true amplitude response at all frequencies. We make two simplifying assumptions on DAS systems: (1) The axial strain rates along all points of the gauge are weighted equally. It is possible some DAS implementations may use a different weighted averaging over the gauge length, and the signal may vary depending on pulse shape and gauge length (Bona et al., 2017). (2) We assume the average along the gauge length of the axial strain rate of the medium is observed. In reality, there is a scaling coefficient provided by each manufacturer, and the Lamé parameters of the fiber and jacket, as well as the friction between the fiber, jacket, and ground, affect measurements. More details on this effect can be found in Kuvshinov (2016). To first order, we expect this simplified model to explain the most significant changes observed when switching from geophone to DAS measurements, but more accurate modeling of any given data set could account for implementation-specific details (if provided by the interrogator unit manufacturer).

9.2. SENSITIVITY OF DAS TO FAR-FIELD SOURCES

We are interested in understanding from which directions far-field sources are emphasized when recorded by a horizontal sensor array. Far away sources are generally well represented by plane waves, so we study this approximation. Depending on whether the wave detected is a P, S, Rayleigh, or Love wave, different source angles are emphasized. We assume these are monochromatic plane waves traveling in a half-space at phase velocity c, wavenumber k, and frequency $\omega = kc$. For each type of wave, we use the following parameters to describe their particle displacement and velocity, as shown in Table 9.1. We are interested in the sensitivity of a horizontal fiber oriented in the direction $(\mathcal{C}_\theta, \mathcal{S}_\theta, 0)$ to surface waves (Rayleigh and Love) propagating in the direction $\left(\mathcal{C}_\phi, \mathcal{S}_\phi, 0\right)$, as drawn in Figure 9.1. Similarly, we are interested in the sensitivity to body waves (P and S) propagating in the direction $\left(\mathcal{C}_{\phi_1}\mathcal{C}_{\phi_2}, \mathcal{S}_{\phi_1}\mathcal{C}_{\phi_2}, \mathcal{S}_{\phi_2}\right)$.

- **Rayleigh waves:** We assume a homogeneous half-space. Let α and β be the velocities of the irrotational and solenoidal parts of the solution to the elastic wave equation (so $\mathbf{u}_\alpha + \mathbf{u}_\beta = \mathbf{u}$, $\nabla \times \mathbf{u}_\alpha = 0$, and $\nabla \cdot \mathbf{u}_\beta = 0$). Then define $\gamma_\alpha = \sqrt{1 - \frac{c^2}{\alpha^2}}$ and $\gamma_\beta = \sqrt{1 - \frac{c^2}{\beta^2}}$. A and B are amplitude factors, whose ratio defines the ellipticity of the Rayleigh wave.
- **Love waves:** We assume a homogeneous half-space with group velocity β_2 underneath a top layer of thickness H with group velocity β_1. In this chapter, we consider only surface seismic, so we just use the displacement in the top H meters of the subsurface. Let A and B be amplitude terms of the depth factor in the top layer (independent of the A and B used to describe Rayleigh waves), and $\eta_1 = \sqrt{\frac{c^2}{\beta_1^2} - 1}$.
- ***P* waves:** We assume a homogeneous half-space. Let A be an amplitude factor (independent of amplitudes of other wave types). All other notation is common to all plane waves.
- ***S* waves:** We assume a homogeneous half-space. We split the S-wave motion into two parts: SH, which is just the horizontal particle motion, and SV, which occurs in the plane spanned by the z-axis and the direction of propagation. Let A be an amplitude factor (independent of amplitudes of other wave types). All other notation is common to all plane waves.

As summarized in Table 9.2, we calculate the geophone particle velocity response to each type of wave in the

Table 9.1 Plane Wave Particle Displacements and Velocities.

Wave Type	Quantity	Value	Quantity	Value
Rayleigh	Propagation direction	$(\mathcal{C}_\phi, \mathcal{S}_\phi, 0)$		
	u_x	$\mathcal{C}_\phi\left(Ae^{-\gamma_\alpha kz} + iB\gamma_\beta e^{-\gamma_\beta kz}\right)o_{RL}$	$\dot{u}_x$	$ikc\mathcal{C}_\phi\left(Ae^{-\gamma_\alpha kz} + iB\gamma_\beta e^{-\gamma_\beta kz}\right)o_{RL}$
	u_y	$\mathcal{S}_\phi\left(Ae^{-\gamma_\alpha kz} + iB\gamma_\beta e^{-\gamma_\beta kz}\right)o_{RL}$	$\dot{u}_y$	$ikc\mathcal{S}_\phi\left(Ae^{-\gamma_\alpha kz} + iB\gamma_\beta e^{-\gamma_\beta kz}\right)o_{RL}$
	u_z	$\left(-i\gamma_\alpha Ae^{-\gamma_\alpha kz} + Be^{-\gamma_\beta kz}\right)o_{RL}$	$\dot{u}_z$	$ikc\left(-i\gamma_\alpha Ae^{-\gamma_\alpha kz} + Be^{-\gamma_\beta kz}\right)o_{RL}$
Love	Propagation direction	$(\mathcal{C}_\phi, \mathcal{S}_\phi, 0)$		
	u_x	$-\mathcal{S}_\phi\left(Ae^{-i\eta_1 kz} + Be^{i\eta_1 kz}\right)o_{RL}$	$\dot{u}_x$	$-ikc\mathcal{S}_\phi\left(Ae^{-i\eta_1 kz} + Be^{i\eta_1 kz}\right)o_{RL}$
	u_y	$\mathcal{C}_\phi\left(Ae^{-i\eta_1 kz} + Be^{i\eta_1 kz}\right)o_{RL}$	$\dot{u}_y$	$ikc\mathcal{C}_\phi\left(Ae^{-i\eta_1 kz} + Be^{i\eta_1 kz}\right)o_{RL}$
	u_z	0	$\dot{u}_z$	0
P	Propagation direction	$\left(\mathcal{C}_{\phi_1}\mathcal{C}_{\phi_2}, \mathcal{S}_{\phi_1}\mathcal{C}_{\phi_2}, \mathcal{S}_{\phi_2}\right)$		
	u_x	$A\mathcal{C}_{\phi_1}\mathcal{C}_{\phi_2}o_{PS}$	$\dot{u}_x$	$ikcA\mathcal{C}_{\phi_1}\mathcal{C}_{\phi_2}o_{PS}$
	u_y	$A\mathcal{S}_{\phi_1}\mathcal{C}_{\phi_2}o_{PS}$	$\dot{u}_y$	$ikcA\mathcal{S}_{\phi_1}\mathcal{C}_{\phi_2}o_{PS}$
	u_z	$A\mathcal{S}_{\phi_2}o_{PS}$	$\dot{u}_z$	$ikcA\mathcal{S}_{\phi_2}o_{PS}$
SV	Propagation direction	$\left(\mathcal{C}_{\phi_1}\mathcal{C}_{\phi_2}, \mathcal{S}_{\phi_1}\mathcal{C}_{\phi_2}, \mathcal{S}_{\phi_2}\right)$		
	u_x	$-A\mathcal{C}_{\phi_1}\mathcal{S}_{\phi_2}o_{PS}$	$\dot{u}_x$	$-ikcA\mathcal{C}_{\phi_1}\mathcal{S}_{\phi_2}o_{PS}$
	u_y	$-A\mathcal{S}_{\phi_1}\mathcal{S}_{\phi_2}o_{PS}$	$\dot{u}_y$	$-ikcA\mathcal{S}_{\phi_1}\mathcal{S}_{\phi_2}o_{PS}$
	u_z	$A\mathcal{C}_{\phi_2}o_{PS}$	$\dot{u}_z$	$ikcA\mathcal{C}_{\phi_2}o_{PS}$
SH	Propagation direction	$\left(\mathcal{C}_{\phi_1}\mathcal{C}_{\phi_2}, \mathcal{S}_{\phi_1}\mathcal{C}_{\phi_2}, \mathcal{S}_{\phi_2}\right)$		
	u_x	$A\mathcal{S}_{\phi_1}o_{PS}$	$\dot{u}_x$	$ikcA\mathcal{S}_{\phi_1}o_{PS}$
	u_y	$-A\mathcal{C}_{\phi_1}o_{PS}$	$\dot{u}_y$	$-ikcA\mathcal{C}_{\phi_1}o_{PS}$
	u_z	0	$\dot{u}_z$	0

Note. The oscillatory factor o_{RL} in the surface waves is $o_RL = e^{ik\left(ct - x\mathcal{C}_\phi - y\mathcal{S}_\phi\right)}$, and the oscillatory factor o_{PS} in the body waves is $o_{PS} = e^{ik\left(ct - x\mathcal{C}_{\phi_1}\mathcal{C}_{\phi_2} - y\mathcal{S}_{\phi_1}\mathcal{C}_{\phi_2} - z\mathcal{S}_{\phi_2}\right)}$

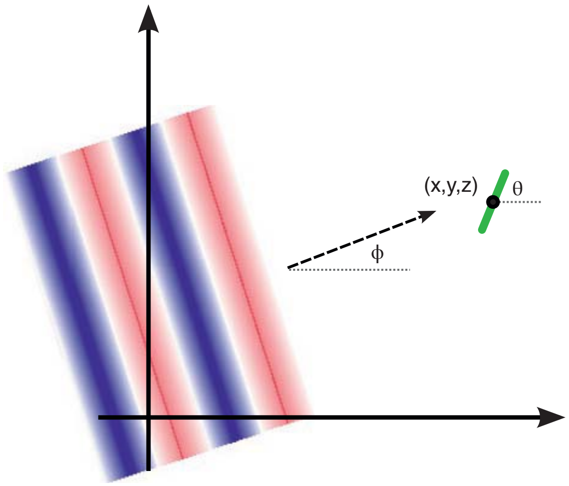

Figure 9.1 We study surface waves (indicated by the red and blue bars) that propagate in the direction $\left(\mathcal{C}_\phi, \mathcal{S}_\phi, 0\right)$ as they are observed by horizontal sensors (indicated by the green line) at (x, y, z) oriented in the $(\mathcal{C}_\theta, \mathcal{S}_\theta, 0)$ direction.

$(\mathcal{C}_\theta, \mathcal{S}_\theta, 0)$ direction, which we denote by $\dot{u}_\theta(x, y, z, t)$. We also calculate the point-wise axial strain rate in the same direction $\dot{\epsilon}_\theta(x, y, z, t)$ and the expected DAS signal denoted by $\dot{\epsilon}_{\theta,g}(x, y, z, t)$. Note that in the long wavelength ($k \rightarrow 0$) limit, a DAS channel with a finite gauge length is predicted to yield the same signal as a point-wise axial strain rate measurement.

Given a predicted measurement, $\dot{u}_\theta, \dot{\epsilon}_\theta, \dot{\epsilon}_{\theta,g}$, to a particular wave, define its "sensitivity" as the measurement disregarding any oscillatory terms. In general, for $\dot{u}_\theta, \dot{\epsilon}_\theta$ and $\dot{\epsilon}_{\theta,g}$ when g is short enough relative to the wavelength, the sensitivity is similar for P waves, SV waves, and Rayleigh waves (a two-lobed sensitivity pattern). Love waves and SH waves are similar to each other, but, $\dot{u}_\theta$ has a $\pi/2$ rotated two-lobed sensitivity pattern, while $\dot{\epsilon}_\theta$ and $\dot{\epsilon}_{\theta,g}$ (for small enough g) have four-lobed sensitivity patterns.

First, we plot the sensitivity to Rayleigh and Love waves coming from different angles in Figure 9.2 for a geophone, a point-wise axial strain rate measurement, and a DAS channel with a gauge length of 10 m (a typical

Table 9.2 Plane Wave Particle Velocity, $\dot{u}_\theta$, Point-Wise Axial Strain Rate, $\dot{\epsilon}_\theta$, and Strain Rate Averaged Over a Gauge Length, $\bar{\epsilon}_\theta$, in the $(\mathcal{C}_\theta, \mathcal{S}_\theta, 0)$ Direction.

Wave Type	Quantity	Value
Rayleigh	Propagation direction	$\left(\mathcal{C}_\phi, \mathcal{S}_\phi, 0\right)$
	$\dot{u}_\theta$	$ick\mathcal{C}_{(\phi-\theta)}\left(Ae^{-\gamma_\alpha kz} + iB\gamma_\beta e^{-\gamma_\beta kz}\right)o_{RL}$
	$\dot{\epsilon}_\theta$	$ck^2\mathcal{C}^2_{(\phi-\theta)}\left(Ae^{-\gamma_\alpha kz} + iB\gamma_\beta e^{-\gamma_\beta kz}\right)o_{RL}$
	$\dot{\epsilon}_{\theta,g}$	$\frac{2ck}{g}\mathcal{C}_{(\phi-\theta)}\sin\left(\frac{kg\mathcal{C}_{(\theta-\phi)}}{2}\right)\left(Ae^{-\gamma_\alpha kz} + iB\gamma_\beta e^{-\gamma_\beta kz}\right)o_{RL}$
Love	Propagation direction	$\left(\mathcal{C}_\phi, \mathcal{S}_\phi, 0\right)$
	$\dot{u}_\theta$	$-ick\mathcal{S}_{(\phi-\theta)}\left(Ae^{-i\eta_1 kz} + Be^{i\eta_1 kz}\right)o_{RL}$
	$\dot{\epsilon}_\theta$	$-\frac{ck^2}{2}\mathcal{S}_{2(\phi-\theta)}\left(Ae^{-i\eta_1 kz} + Be^{i\eta_1 kz}\right)o_{RL}$
	$\dot{\epsilon}_{\theta,g}$	$-\frac{2ck}{g}\mathcal{S}_{(\phi-\theta)}\sin\left(\frac{kg\mathcal{C}_{(\phi-\theta)}}{2}\right)\left(Ae^{-i\eta_1 kz} + Be^{i\eta_1 kz}\right)o_{RL}$
P	Propagation direction	$\left(\mathcal{C}_{\phi_1}\mathcal{C}_{\phi_2}, \mathcal{S}_{\phi_1}\mathcal{C}_{\phi_2}, \mathcal{S}_{\phi_2}\right)$
	$\dot{u}_\theta$	$ick\mathcal{C}_{(\phi_1-\theta)}\mathcal{C}_{\phi_2}Ao_{PS}$
	$\dot{\epsilon}_\theta$	$ck^2\mathcal{C}^2_{(\phi_1-\theta)}\mathcal{C}^2_{\phi_2}Ao_{PS}$
	$\dot{\epsilon}_{\theta,g}$	$\frac{2ck}{g}\mathcal{C}_{(\phi_1-\theta)}\mathcal{C}_{\phi_2}\sin\left(\frac{gk\mathcal{C}_{(\phi_1-\theta)}\mathcal{C}_{\phi_2}}{2}\right)Ao_{PS}$
SV	Propagation direction	$\left(\mathcal{C}_{\phi_1}\mathcal{C}_{\phi_2}, \mathcal{S}_{\phi_1}\mathcal{C}_{\phi_2}, \mathcal{S}_{\phi_2}\right)$
	$\dot{u}_\theta$	$-ick\mathcal{C}_{(\phi_1-\theta)}\mathcal{S}_{\phi_2}Ao_{PS}$
	$\dot{\epsilon}_\theta$	$-\frac{ck^2}{2}\mathcal{C}^2_{(\phi_1-\theta)}\mathcal{S}_{2\phi_2}Ao_{PS}$
	$\dot{\epsilon}_{\theta,g}$	$-\frac{ck}{g}\frac{\mathcal{C}_{(\phi_1-\theta)}\mathcal{S}_{2\phi_2}}{\mathcal{C}_{\phi_2}}\sin\left(\frac{kg\mathcal{C}_{(\phi_1-\theta)}\mathcal{C}_{\phi_2}}{2}\right)Ao_{PS}$
SH	Propagation direction	$\left(\mathcal{C}_{\phi_1}\mathcal{C}_{\phi_2}, \mathcal{S}_{\phi_1}\mathcal{C}_{\phi_2}, \mathcal{S}_{\phi_2}\right)$
	$\dot{u}_\theta$	$ick\mathcal{S}_{(\phi_1-\theta)}Ao_{PS}$
	$\dot{\epsilon}_\theta$	$\frac{ck^2}{2}\mathcal{S}_{2(\phi_1-\theta)}\mathcal{C}_{\phi_2}Ao_{PS}$
	$\dot{\epsilon}_{\theta,g}$	$\frac{2ck}{g}\mathcal{S}_{(\phi_1-\theta)}\sin\left(\frac{kg\mathcal{C}_{(\phi_1-\theta)}\mathcal{C}_{\phi_2}}{2}\right)Ao_{PS}$

Note. The oscillatory factor o_{RL} in the surface waves is $o_{RL} = e^{ik\left(ct - x\mathcal{C}_\phi - y\mathcal{S}_\phi\right)}$, and the oscillatory factor o_{PS} in the body waves is $o_{PS} = e^{ik\left(ct - x\mathcal{C}_{\phi_1}\mathcal{C}_{\phi_2} - y\mathcal{S}_{\phi_1}\mathcal{C}_{\phi_2} - z\mathcal{S}_{\phi_2}\right)}$

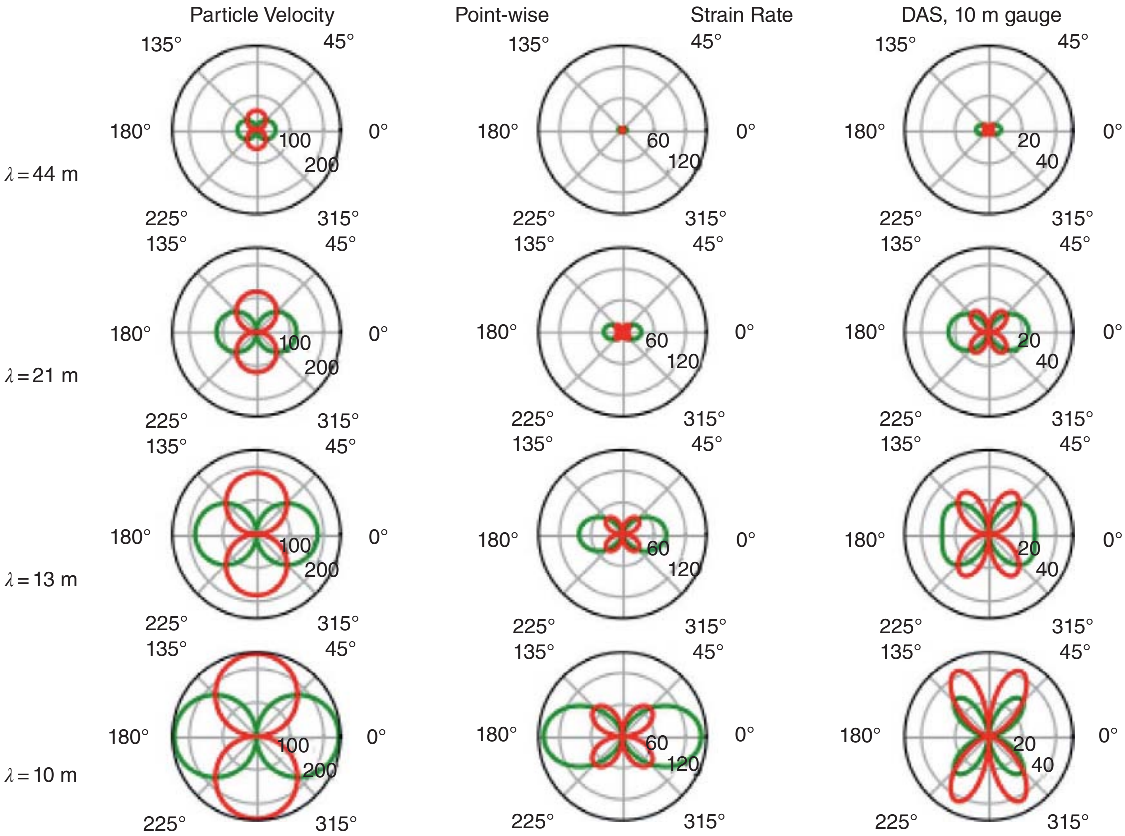

Figure 9.2 Each polar plot shows the amplitude response of a measurement to planar surface waves of varying azimuth and wavelength. The radius of each line represents the sensitivity of a point-wise particle velocity (left), a point-wise strain rate (middle) and a DAS measurement with 10 meter gauge length (right) responding to a range of wavelengths in a 400 m/s velocity material for both Rayleigh (green) and Love (red) plane waves coming from each angle. The plots represent sensitivities for 9 Hz (top), 19 Hz (second row), 29 Hz (third row), and 39 Hz (bottom).

setting for seismic acquisition). At each angle, the radius is equal to the absolute value of expected measured data for a wave coming in at that angle relative to the sensor with $A = 1$, $B = 1$ (this is the case for Figures 9.2–9.7). While the geophone is most sensitive to Rayleigh waves with $\phi - \theta = 0, \pi$, it is equally sensitive to Love waves with $\phi - \theta = \pm \pi/2$ in the sense that these sensitivity patterns are just rotated versions of each other. Like the geophone, the point-wise axial strain rate measurement is also most sensitive to Rayleigh waves such that $\phi - \theta = 0, \pi$, but the sensitivity is more concentrated around these peak angles (i.e., is scaled by an extra $k\mathcal{C}_{(\phi-\theta)}$ compared to the geophone). Unlike the geophone, the point-wise axial strain rate has a four-lobed sensitivity to Love waves with peak sensitivity to Love waves coming in at $\phi - \theta = \pm \pi/4, \pm 3\pi/4$. Further, at the angles of peak Love wave sensitivity, the point-wise axial strain rate measurement only detects half the amplitude that would be detected by the same theoretical sensor to Rayleigh waves at $\phi - \theta = 0, \pi$. Thus, the switch to strain means Love wave sensitivity is weaker and distributed over more angles.

There is a further consideration in real DAS data: The gauge length. For wavelengths a few times longer than g, the sensitivity patterns of $\dot{\epsilon}_\theta$ well-approximate the sensitivity of $\dot{\epsilon}_{\theta,g}$. As seen in Figure 9.2, for wavelengths just slightly longer than g, the sensitivity patterns become more flattened out near peak sensitivity angles, and then for wavelengths shorter than g, additional sensitivity lobes form, consistent with the description for P waves in Dean et al. (2017). This trend can be seen in more detail in Figure 9.3, which shows that for larger gauge lengths, these strange behaviors (deviating from the two-lobe and four-lobe trends) can occur at even longer wavelengths.

The response to body waves is slightly more complicated depending on how vertically the wave is propagating, indicated by ϕ_2. We plot the sensitivity for $\phi_2 = 3\pi/8$, $\pi/4$,and $\pi/8$ in Figures 9.4, 9.5, and 9.6, respectively. In general, the P-wave and SV-wave sensitivity patterns are more like Rayleigh wave sensitivity (two lobed), while the SH-wave sensitivity is more like Love wave sensitivity (four lobed). When ϕ_2 is closer to $\pi/2$, it means the wave is

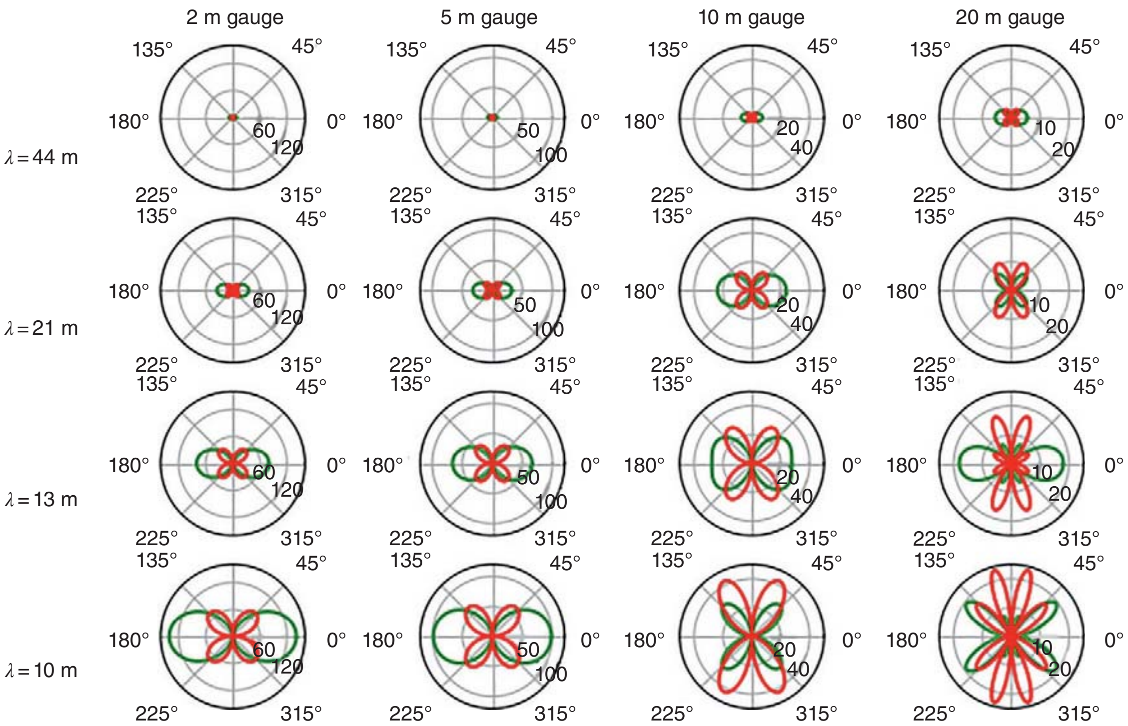

Figure 9.3 The radius of each line represents the sensitivity of DAS with a 2 m (left), 5 m (second column), 10 m (third column), and 20 m (right) gauge length to a range of wavelengths in a 400 m/s velocity material for both Rayleigh (green) and Love (red) plane waves coming from each angle. The plots represent sensitivities for 9 Hz (top), 19 Hz (second row), 29 Hz (third row), and 39 Hz (bottom).

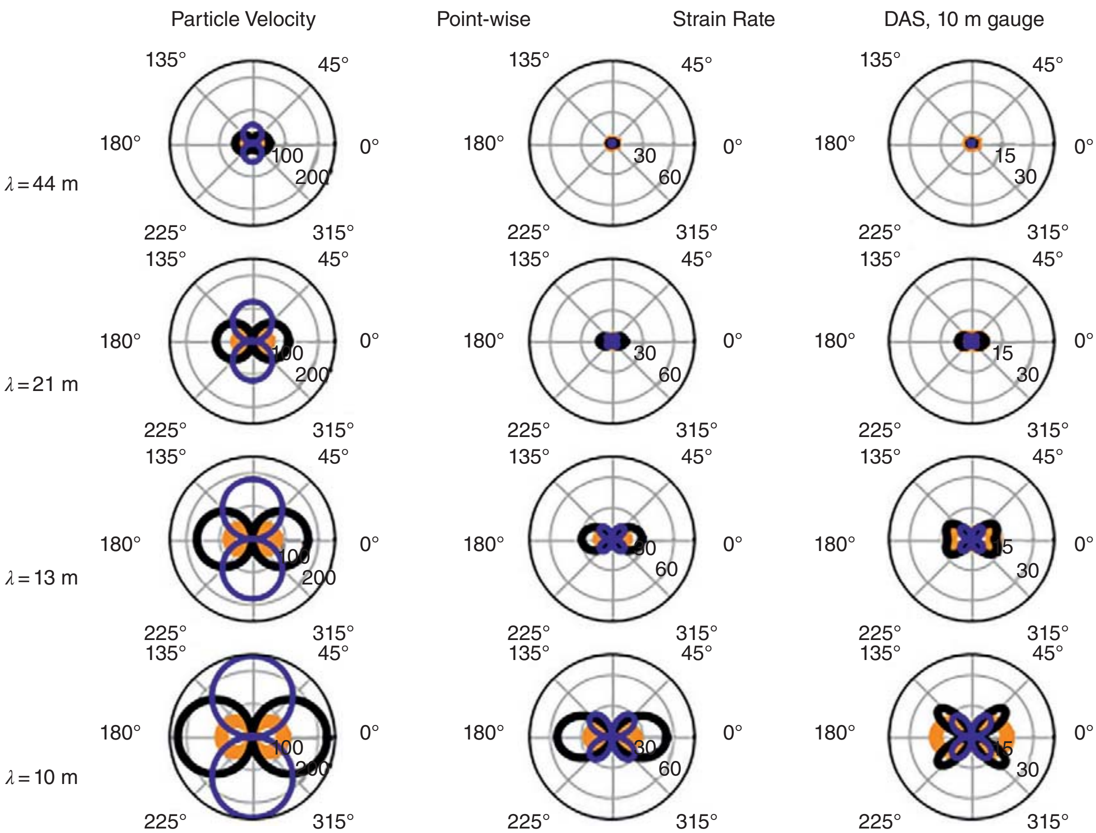

Figure 9.4 The radius of each line represents the sensitivity of geophones (left), point-wise strain measurements (middle), and DAS with a 10 m gauge length (right) to a different wavelength in a 400 m/s velocity material for *P* (orange), *SH* (blue), and *SV* (black) plane waves coming from each horizontal angle $\phi_1 - \theta$ and vertical angle $\phi_2 = 3\pi/8$. The plots represent sensitivities for 9 Hz (top), 19 Hz (second row), 29 Hz (third row), and 39 Hz (bottom).

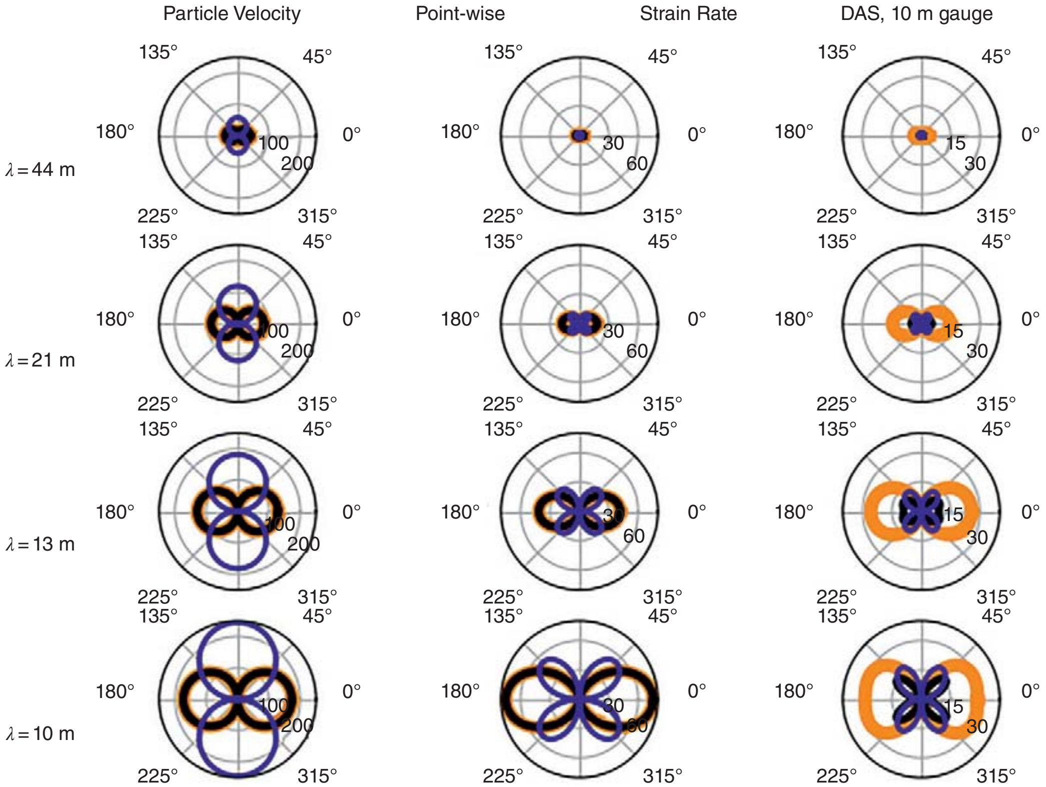

Figure 9.5 The radius of each line represents the sensitivity of geophones (left), point-wise strain measurements (middle), and DAS with a 10 m gauge length (right) to a different wavelength in a 400 m/s velocity material for *P* (orange), *SH* (blue), and *SV* (black) plane waves coming from each horizontal angle $\phi_1 - \theta$ and vertical angle $\phi_2 = \pi/4$. The plots represent sensitivities for 9 Hz (top), 19 Hz (second row), 29 Hz (third row), and 39 Hz (bottom).

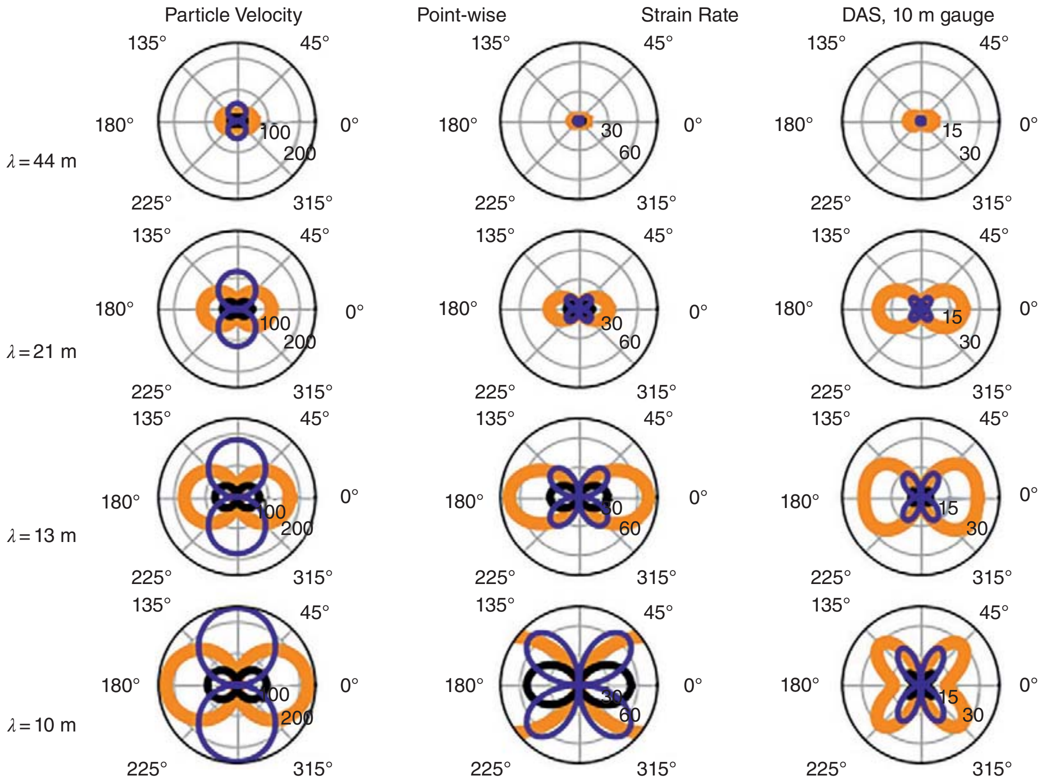

Figure 9.6 The radius of each line represents the sensitivity of geophones (left), point-wise strain measurements (middle), and DAS with a 10 m gauge length (right) to a different wavelength in a 400 m/s velocity material for *P* (orange), *SH* (blue), and *SV* (black) plane waves coming from each horizontal angle $\phi_1 - \theta$ and vertical angle $\phi_2 = \pi/8$. The plots represent sensitivities for 9 Hz (top), 19 Hz (second row), 29 Hz (third row), and 39 Hz (bottom).

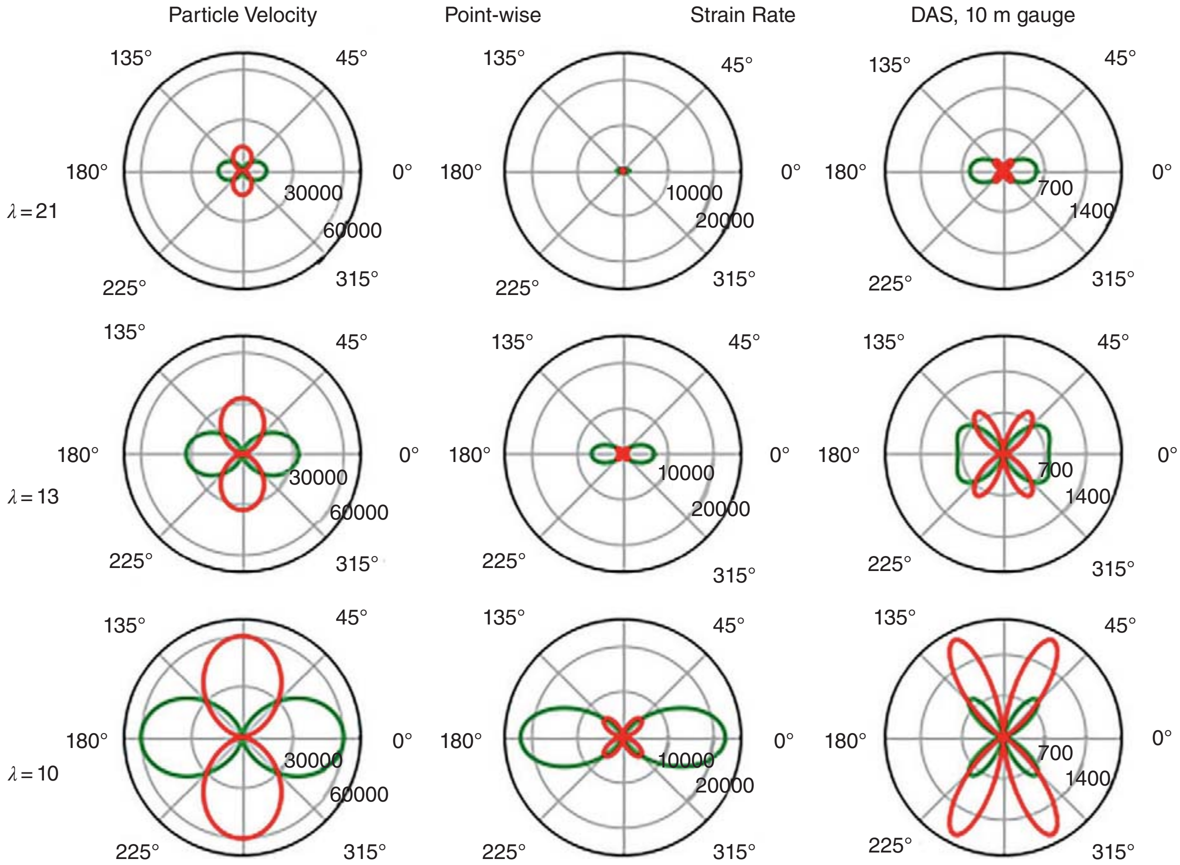

Figure 9.7 The radius of each line represents the sensitivity of radial-radial ($\theta_1 = \theta_2 = 0$) cross-correlation geophones (left), point-wise strain measurements (middle), and DAS with a 10 m gauge length (right) to a range of wavelengths in a 400 m/s velocity material for both Rayleigh (green) and Love (red) plane waves coming from each angle. The plots represent sensitivities for 19 Hz (top), 29 Hz (second row), and 39 Hz (bottom). The plot to represent sensitivity for 9 Hz was not pictured because the responses are too small to see.

nearly vertically propagating, so most particle displacement is closer to vertical and there is less P-wave sensitivity for all three horizontal measurements compared to P waves traveling at smaller ϕ_2 values. While SV geophone response is maximized for nearly vertically propagating waves ($\phi_2 = \pi/2$) and minimized for nearly horizontally propagating waves ($\phi_2 = 0$), the point-wise strain rate and DAS responses are minimized for both horizontally and vertically propagating waves and maximized when there is as much vertical as there is horizontal propagation ($\phi_2 = \pi/4$). On the other hand, the geophone response to SH waves is independent of how much energy is propagating vertically, but the point-wise strain rate and DAS measurements are maximized when an SH wave is propagating horizontally ($\phi_2 = 0$).

9.3. SENSITIVITY OF DAS CROSS-CORRELATIONS TO PLANE WAVE SOURCES

When attempting to use weak signals, as in ambient noise interferometry or some microseismicity detection methods, we often cross-correlate two time series signals, $s(x_1, y_1, z_1, t)$ and $s(x_2, y_2, z_2, t)$, recorded concurrently at different sensors to bring their joint signal, $C(\tau) = \frac{1}{2T}\int_{-T}^{T} s(x_1, y_1, z_1, t)s^*(x_2, y_2, z_2, t+\tau)dt$, above the noise level. In particular, this is used to more accurately detect and locate microseismic events using an array, and this is also used to extract surface wave Green's function approximations from ambient noise recorded by surface arrays. While the extensive sensor coverage of DAS is an advantage in microseismicity detection, could the use of certain channel geometries relative to events lead to different biases in the estimated statistical distribution of events? When performing ambient noise interferometry in the presence of an ideal noise field, does the extracted signal actually approximate the same arrival times as the true Green's functions?

The answers to these questions can be found by studying the differences between cross-correlations of pairs of geophones, point-wise axial strain rate measurements, and DAS channels responding to plane waves. When using three-component geophones, we can rotate any pair of sensors into radial and transverse horizontal components that clearly yield Rayleigh and Love wave

Table 9.3 Cross-Correlations of Measurements at (x_1, y_1, z_1) in the $(\mathcal{C}_{\theta_1}, \mathcal{S}_{\theta_1}, 0)$ Direction with Measurements at (x_2, y_2, z_2) in the $(\mathcal{C}_{\theta_2}, \mathcal{S}_{\theta_2}, 0)$ Direction.

Wave Type	Quantity	Value
Rayleigh	Propagation direction	$(\mathcal{C}_\phi, \mathcal{S}_\phi, 0)$
	$\dot{u}_{\theta_1}(x_1, y_1, z_1) \star \dot{u}_{\theta_2}(x_2, y_2, z_2)$	$c^2k^2\mathcal{C}_{(\phi-\theta_1)}\mathcal{C}_{(\phi-\theta_2)}\left(A^2e^{-2\gamma_\alpha kz} + B^2\gamma_\beta^2e^{-2\gamma_\beta kz}\right)o_{RL}^\tau$
	$\dot{\epsilon}_{\theta_1}(x_1, y_1, z_1) \star \dot{\epsilon}_{\theta_2}(x_2, y_2, z_2)$	$c^2k^4\mathcal{C}^2_{(\phi-\theta_1)}\mathcal{C}^2_{(\phi-\theta_2)}\left(A^2e^{-2\gamma_\alpha kz} + B^2\gamma_\beta^2e^{-2\gamma_\beta kz}\right)o_{RL}^\tau$
	$\dot{\epsilon}_{\theta_1,g}(x_1, y_1, z_1) \star \dot{\epsilon}_{\theta_2,g}(x_2, y_2, z_2)$	$\frac{4c^2k^2}{g^2}\mathcal{C}_{(\phi-\theta_1)}\mathcal{C}_{(\phi-\theta_2)}\sin\left(\frac{kg}{2}\mathcal{C}_{(\phi-\theta_1)}\right)\sin\left(\frac{kg}{2}\mathcal{C}_{(\phi-\theta_2)}\right)\left(A^2e^{-2\gamma_\alpha kz} + B^2\gamma_\beta^2e^{-2\gamma_\beta kz}\right)o_{RL}^\tau$
Love	Propagation direction	$(\mathcal{C}_\phi, \mathcal{S}_\phi, 0)$
	$\dot{u}_{\theta_1}(x_1, y_1, z_1) \star \dot{u}_{\theta_2}(x_2, y_2, z_2)$	$c^2k^2\mathcal{S}_{(\phi-\theta_1)}\mathcal{S}_{(\phi-\theta_2)}\left(A^2 + AB\left(e^{2i\eta_1kz} + e^{-2i\eta_1kz}\right) + B^2\right)o_{RL}^\tau$
	$\dot{\epsilon}_{\theta_1}(x_1, y_1, z_1) \star \dot{\epsilon}_{\theta_2}(x_2, y_2, z_2)$	$\frac{c^2k^4}{4}\mathcal{S}_{2(\phi-\theta_1)}\mathcal{S}_{2(\phi-\theta_2)}\left(A^2 + 2AB\cos(2\eta_1kz) + B^2\right)o_{RL}^\tau$
	$\dot{\epsilon}_{\theta_1,g}(x_1, y_1, z_1) \star \dot{\epsilon}_{\theta_2,g}(x_2, y_2, z_2)$	$\frac{4c^2k^2}{g^2}\mathcal{S}_{(\phi-\theta_1)}\mathcal{S}_{(\phi-\theta_2)}\sin\left(\frac{kg}{2}\mathcal{C}_{(\phi-\theta_1)}\right)\sin\left(\frac{kg}{2}\mathcal{C}_{(\phi-\theta_2)}\right)\left(A^2 + 2AB\cos(2\eta_1kz) + B^2\right)o_{RL}^\tau$
P	Propagation direction	$(\mathcal{C}_{\phi_1}\mathcal{C}_{\phi_2}, \mathcal{S}_{\phi_1}\mathcal{C}_{\phi_2}, \mathcal{S}_{\phi_2})$
	$\dot{u}_{\theta_1}(x_1, y_1, z_1) \star \dot{u}_{\theta_2}(x_2, y_2, z_2)$	$c^2k^2\mathcal{C}_{(\phi_1-\theta_1)}\mathcal{C}_{(\phi_1-\theta_2)}\mathcal{C}^2_{\phi_2}A^2o_{PS}^\tau$
	$\dot{\epsilon}_{\theta_1}(x_1, y_1, z_1) \star \dot{\epsilon}_{\theta_2}(x_2, y_2, z_2)$	$c^2k^4\mathcal{C}^2_{(\phi_1-\theta_1)}\mathcal{C}^2_{(\phi_1-\theta_2)}\mathcal{C}^4_{\phi_2}A^2o_{PS}^\tau$
	$\dot{\varepsilon}_{\theta_1,g}(x_1, y_1, z_1) \star \dot{\varepsilon}_{\theta_2,g}(x_2, y_2, z_2)$	$\frac{4c^2k^2}{g^2}\mathcal{C}_{(\phi_1-\theta_1)}\mathcal{C}_{(\phi_1-\theta_2)}\mathcal{C}^2_{\phi_2}\sin\left(\frac{kg}{2}\mathcal{C}_{(\phi_1-\theta_1)}\mathcal{C}_{\phi_2}\right)\sin\left(\frac{kg}{2}\mathcal{C}_{(\phi_1-\theta_2)}\mathcal{C}_{\phi_2}\right)A^2o_{PS}^\tau$
SV	Propagation direction	$(\mathcal{C}_{\phi_1}\mathcal{C}_{\phi_2}, \mathcal{S}_{\phi_1}\mathcal{C}_{\phi_2}, \mathcal{S}_{\phi_2})$
	$\dot{u}_{\theta_1}(x_1, y_1, z_1) \star \dot{u}_{\theta_2}(x_2, y_2, z_2)$	$c^2k^2\mathcal{C}_{(\phi_1-\theta_1)}C_{(\phi_1-\theta_2)}\mathcal{S}^2_{\phi_2}A^2o_{PS}^\tau$
	$\dot{\epsilon}_{\theta_1}(x_1, y_1, z_1) \star \dot{\epsilon}_{\theta_2}(x_2, y_2, z_2)$	$\frac{c^2k^4}{4}\mathcal{C}^2_{(\phi_1-\theta_1)}\mathcal{C}^2_{(\phi_1-\theta_2)}\mathcal{S}^2_{2\phi_2}A^2o_{PS}^\tau$
	$\dot{\epsilon}_{\theta_1,g}(x_1, y_1, z_1) \star \dot{\epsilon}_{\theta_2,g}(x_2, y_2, z_2)$	$\frac{c^2k^2}{g^2}\cdot\frac{\mathcal{C}_{(\phi_1-\theta_1)}\mathcal{C}_{(\phi_1-\theta_2)}\mathcal{S}^2_{2\phi_2}}{\mathcal{C}^2_{\phi_2}}\sin\left(\frac{kg}{2}\mathcal{C}_{(\phi_1-\theta_1)}\mathcal{C}_{\phi_2}\right)\sin\left(\frac{kg}{2}\mathcal{C}_{(\phi_1-\theta_2)}\mathcal{C}_{\phi_2}\right)A^2o_{PS}^\tau$
SH	Propagation direction	$(\mathcal{C}_{\phi_1}\mathcal{C}_{\phi_2}, \mathcal{S}_{\phi_1}\mathcal{C}_{\phi_2}, \mathcal{S}_{\phi_2})$
	$\dot{u}_{\theta_1}(x_1, y_1, z_1) \star \dot{u}_{\theta_2}(x_2, y_2, z_2)$	$c^2k^2S_{(\phi_1-\theta_1)}S_{(\phi_1-\theta_2)}A^2o_{PS}^\tau$
	$\dot{\epsilon}_{\theta_1}(x_1, y_1, z_1) \star \dot{\epsilon}_{\theta_2}(x_2, y_2, z_2)$	$\frac{c^2k^4}{4}\mathcal{S}_{2(\phi_1-\theta_1)}\mathcal{S}_{2(\phi_1-\theta_2)}\mathcal{C}^2_{\phi_2}A^2o_{PS}^\tau$
	$\dot{\epsilon}_{\theta_1,g}(x_1, y_1, z_1) \star \dot{\epsilon}_{\theta_2,g}(x_2, y_2, z_2)$	$\frac{4c^2k^2}{g^2}\mathcal{S}_{(\phi_1-\theta_1)}\mathcal{S}_{(\phi_1-\theta_2)}\sin\left(\frac{kg}{2}\mathcal{C}_{(\phi_1-\theta_1)}\mathcal{C}_{\phi_2}\right)\sin\left(\frac{kg}{2}\mathcal{C}_{(\phi_1-\theta_2)}\mathcal{C}_{\phi_2}\right)A^2o_{PS}^\tau$

Note. To keep the notation short, we introduce notation for common oscillatory terms: $o_{RL}^\tau = e^{-ik\left(c\tau + (x_1-x_2)\mathcal{C}_\phi + (y_1-y_2)\mathcal{S}_\phi\right)}$ and $o_{PS}^\tau = e^{-ik\left(c\tau + (x_1-x_2)\mathcal{C}_{\phi_1}\mathcal{C}_{\phi_2} + (y_1-y_2)\mathcal{S}_{\phi_1}\mathcal{C}_{\phi_2}\right)}$

components (Lin et al., 2008), but as we only observe one component of the strain tensor with fiber, we cannot do the same with a horizontal fiber array. Thus, we calculate cross-correlations between a sensor at (x_1, y_1, z_1) oriented in the $(\mathcal{C}_{\theta_1}, \mathcal{S}_{\theta_1}, 0)$ direction and a second sensor at (x_2, y_2, z_2) oriented in the $(\mathcal{C}_{\theta_2}, \mathcal{S}_{\theta_2}, 0)$ direction. These cross-correlations are summarized in Table 9.3.

Say we have two sensors at two surface locations $\mathbf{x}_1$ and $\mathbf{x}_2$ such that $\frac{\mathbf{x}_1 - \mathbf{x}_2}{\| \mathbf{x}_1 - \mathbf{x}_2 \|} = (1, 0, 0)$. A plane surface wave coming in from angle $\phi = 0$ or π would hit $\mathbf{x}_1$ and $\mathbf{x}_2$ at what appears to be the true velocity, but a plane wave coming in from angle $\phi = \pm\pi/2$ would arrive at $\mathbf{x}_1$ and $\mathbf{x}_2$ at the same time at an infinitely fast velocity, and any angle in between will have some fast biased apparent velocity, so ideally, we want whichever wave type we are trying to detect to be emphasized close to $\phi = 0, \pi$.

Ignoring the oscillatory terms and exponentially decaying depth-dependent surface wave terms, we have plotted cross-correlation sensitivities for sensors at $\mathbf{x}_1$ and $\mathbf{x}_2$ in a radial-radial orientation ($\theta_1 = \theta_2 = 0$) if they were geophones, point-wise strain rates, and DAS responding to surface waves. The transverse-transverse ($\theta_1 = \theta_2 = \pi/2$) cross-correlation sensitivities are the same as the radial-radial sensitivities, just rotated by $\pi/2$. These are the cross-correlations we use to extract Rayleigh waves and Love waves, respectively, from geophones, and, as expected, the radial-radial cross-correlation in

Figure 9.7 is very sensitive to Rayleigh waves at $\phi = 0, \pi$, and the transverse-transverse cross-correlation is very sensitive to Love waves at $\phi = \pi/2, 3\pi/2$. However, when we look at the point-wise strain rate sensitivities, the radial-radial correlations are very sensitive to Rayleigh waves at $\phi = 0, \pi$, but the transverse-transverse correlations are not very sensitive to any waves at $\phi = 0, \pi$ and in fact are very sensitive to Rayleigh waves that would yield a very fast (even infinite) velocity.

How do we detect any Love waves from cross-correlations? The transverse-transverse cross-correlations are sensitive to Love waves coming from $\phi = \pm\pi/4, \pm 3\pi/4$, just not as sensitive as they are to Rayleigh waves near $\phi = \pm\pi/2$, which would appear to have an extremely fast velocity. If we have reason to believe that Love waves dominate the wavefield, then transverse-transverse cross-correlations will result in an apparent velocity that is $c/\cos(\Phi)$, where c is the true Love wave velocity at that frequency and Φ is the peak Love wave cross-correlation sensitivity angle within the frequency band of interest ($\Phi = \pi/4$ for longer wavelengths relative to the gauge length).

9.4. THOUGHT EXPERIMENT DEMONSTRATING AMBIENT NOISE INTERFEROMETRY TRENDS

A simple thought experiment to understand why hydrophone (pressure) and vertical geophone ambient noise cross-correlations averaged over many sources yield a signal with its peak around the Green's function arrival time of one of the receivers responding to a virtual source at the other can be found in Wapenaar et al. (2010). Here, we recreate that thought experiment at the same scale, but study the cross-correlations of the particle velocity and point-wise axial strain response to random sources that travel either like Rayleigh waves or Love waves (although at a faster velocity than surface waves and without dispersion). Further, we test a range of geometries encountered in the experiments examined in this thesis: A virtual source that is a fiber-optic channel cross-correlated with a set of receivers on a parallel cable, and a fiber-optic virtual source cross-correlated with a set of receivers on an orthogonal cable.

Here, we assume a simple model of surface wave point sources: A Ricker wavelet set off at a point that has either particle motion in the direction of propagation (Rayleigh wave) or horizontal and orthogonal to the direction of propagation (Love wave). This is described in detail along with the derivations of the expected response of the x- and y-components of the particle velocity and axial strain rate to these point sources in Martin (2018). These responses are summarized in Table 9.4.

9.4.1. Simple Case: Radial-Radial Cross-Correlations

Prior work has shown in practice that it is possible to retrieve reasonable geology from surface wave inversion using cross-correlations of data recorded on collinear DAS channels (Dou et al., 2017). This section aims to better understand why this works. Following the thought

Table 9.4 Horizontal Particle Velocity and Point-Wise Axial Strain Rate Responses at $\boldsymbol{x}$ to a Simplified Model of Rayleigh and Love Wave Point Sources at $\boldsymbol{x}_s$ That Emit a Ricker Wavelet at Frequency f.

Wave Type	Quantity	Value
Ray-leigh	$\dot{u}_0(\mathbf{x}, t)$	$o_f \frac{x - x_s}{R^2}\left(-6\pi^2 f^2 \tau + 4\pi^4 f^4 \tau^3\right)$
	$\dot{u}_{\pi/2}(\mathbf{x}, t)$	$o_f \frac{y - y_s}{R^2}\left(-6\pi^2 f^2 \tau + 4\pi^4 f^4 \tau^3\right)$
	$\dot{\epsilon}_0(\mathbf{x}), t$	$o_f \frac{(x - x_s)^2}{R^3}\left(\frac{6\pi^2 f^2}{c} + \frac{12\pi^2 f^2}{R}\tau - \frac{24\pi^4 f^4}{c}\tau^2 - \frac{8\pi^4 f^4}{R}\tau^3 + \frac{8\pi^6 f^6}{c}\tau^4\right)$
	$\dot{\epsilon}_{\pi/2}(\mathbf{x}, t)$	$o_f \frac{\left(y - y_s\right)^2}{R^3}\left(\frac{6\pi^2 f^2}{c} + \frac{12\pi^2 f^2}{R}\tau - \frac{24\pi^4 f^4}{c}\tau^2 - \frac{8\pi^4 f^4}{R}\tau^3 + \frac{8\pi^6 f^6}{c}\tau^4\right)$
Love	$\dot{u}_0(\mathbf{x}, t)$	$o_f \frac{y - y_s}{R^2}\left(-6\pi^2 f^2 \tau + 4\pi^4 f^4 \tau^3\right)$
	$\dot{u}_{\pi/2}(\mathbf{x}, t)$	$o_f \frac{x_s - x}{R^2}\left(-6\pi^2 f^2 \tau + 4\pi^4 f^4 \tau^3\right)$
	$\dot{\epsilon}_0(\mathbf{x}), t$	$o_f \frac{\left(y - y_s\right)\left(x - x_s\right)}{R^3}\left(\frac{6\pi^2 f^2}{c} + \frac{12\pi^2 f^2}{R}\tau - \frac{24\pi^4 f^4}{c}\tau^2 - \frac{8\pi^4 f^4}{R}\tau^3 + \frac{4\pi^6 f^6 2}{c}\tau^4\right)$
	$\dot{\epsilon}_{\pi/2}(\mathbf{x}, t)$	$o_f \frac{(x_s - x)\left(y - y_s\right)}{R^3}\left(\frac{6\pi^2 f^2}{c} + \frac{12\pi^2 f^2}{R}\tau - \frac{24\pi^4 f^4}{c}\tau^2 - \frac{8\pi^4 f^4}{R}\tau^3 + \frac{8\pi^6 f^6}{c}\tau^4\right)$

Note. To keep the notation short, let $R = \|\mathbf{x} - \mathbf{x}_s\|$, $\tau = t - \frac{R}{C}$, and $o_f = e^{-\pi^2 f^2 \left(t - \frac{R}{c}\right)^2}$

experiment of Wapenaar et al. (2010), imagine two receivers at $\mathbf{x}_1 = (-600,0,0)$ and $\mathbf{x}_2 = (600,0,0)$ surrounded by 5,000 point sources randomly distributed on an annulus with inner and outer radii of 2000 and 3000 m (uniformly distributed azimuth in $[0, 2\pi]$ and uniformly distributed radius in $[2000, 3000]$). While the original experiment studied a scalar response (pressure), in this section, we are interested in the radial-radial cross-correlations of geophones or DAS channels oriented following the geometries shown in Figure 9.8, so $\theta_1 = \theta_2 = \pi/2$.

The recordings of these sources (every eighth source for visualization) on both sensors acting as geophones (particle velocity) and as DAS channels (point-wise strain rate) are shown in Figure 9.9. Both the geophones and the fiber optics emphasize sources with ϕ_{Src} close to 0 and π (i.e., sources that are not observed with any apparent velocity bias), and in fact, the relative emphasis of these sources by the fiber channels is stronger than the relative emphasis observed by the geophone. This is also seen in the cross-correlations for each source. As in Wapenaar et al. (2010), even though the initial recordings had random time lags due to their radius being chosen over a range between 2000 and 3000 m, their relative arrival times at $\mathbf{x}_1$ and $\mathbf{x}_2$ are consistent, so the cross-correlations show a clear trend. When we average the source-wise cross-correlations, we get a clear signal with a peak at ± 0.6 s for both the geophone and DAS experiments. Because $\mathbf{x}_1$ and $\mathbf{x}_2$ are 1200 m apart in a 2000 m/s medium, that is the arrival time we would expect for a source emitted from one receiver's location and recorded at the other receiver.

While the average of single-source cross-correlations can start to give some intuition about why ambient noise interferometry works, in reality, each window of noise contains the responses to many sources. If a finite number, N, of point sources go off during a particular time window, then the cross-correlation of two traces (denoted by u) recording these sources would include both single-source cross-correlations and cross-terms between different sources. This is apparent when the cross-correlations are written as a product of Green's functions, G, and source functions, f:

$$
\begin{aligned}
C(\tau) &= \int_{-T}^{T} u(\mathbf{x}_1, t) u^*(\mathbf{x}_2, t+\tau) dt \\
&= \sum_{i=1}^{N} \int_{-T}^{T} G(\mathbf{x}_1, t; \mathbf{x}_i^s) f(\mathbf{x}_i^s, t) G^*(\mathbf{x}_2, t+\tau; \mathbf{x}_i^s) f^*(\mathbf{x}_i^s, t+\tau) dt \\
&+ \sum_{j=1}^{N} \sum_{i \neq j} \int_{-T}^{T} G(\mathbf{x}_1, t; \mathbf{x}_i^s) f(\mathbf{x}_i^s, t) G^*\left(\mathbf{x}_2, t+\tau; \mathbf{x}_j^s\right) f^*\left(\mathbf{x}_j^s, t+\tau\right) dt
\end{aligned}
$$

Only the first term (single-source cross-correlations) is explained by Figure 9.9. Thus, Wapenaar et al. (2010) performed a test to ensure these cross-source-terms did not add up to make coherent changes in the extracted velocity: Many random sources are recorded at both $\mathbf{x}_1$ and $\mathbf{x}_2$ (and we repeat this for both a particle velocity and a point-wise strain rate). Then a single cross-correlation is done

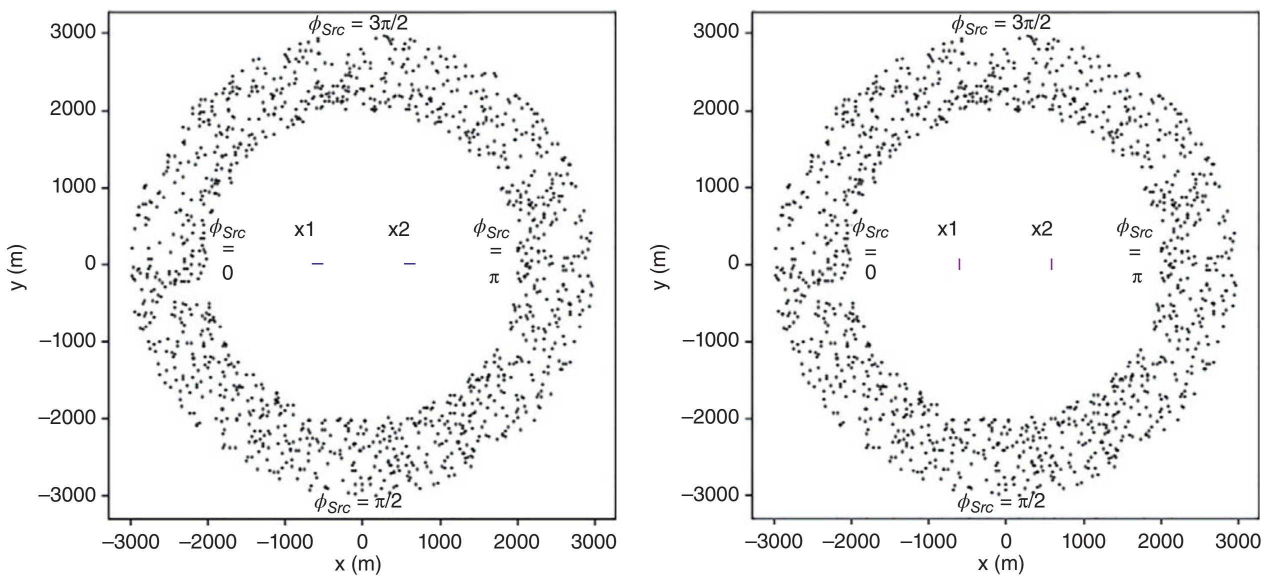

Figure 9.8 We study the cross-correlation response of two sensors at $\mathbf{x}_1 = (-600,0,0)$ and $\mathbf{x}_2 = (600,0,0)$ oriented in a radial-radial $\theta_1 = \theta_2 = 0$ configuration (left) and transverse-transverse $\theta_1 = \theta_2 = \pi/2$ configuration (right) to sources randomly distributed in an azimuth at azimuth ϕ_{Src} and radius between 2000 and 3000 m. Only one fourth of the sources are shown for clarity. Source: Adapted from Wapenaar et al. (2010).

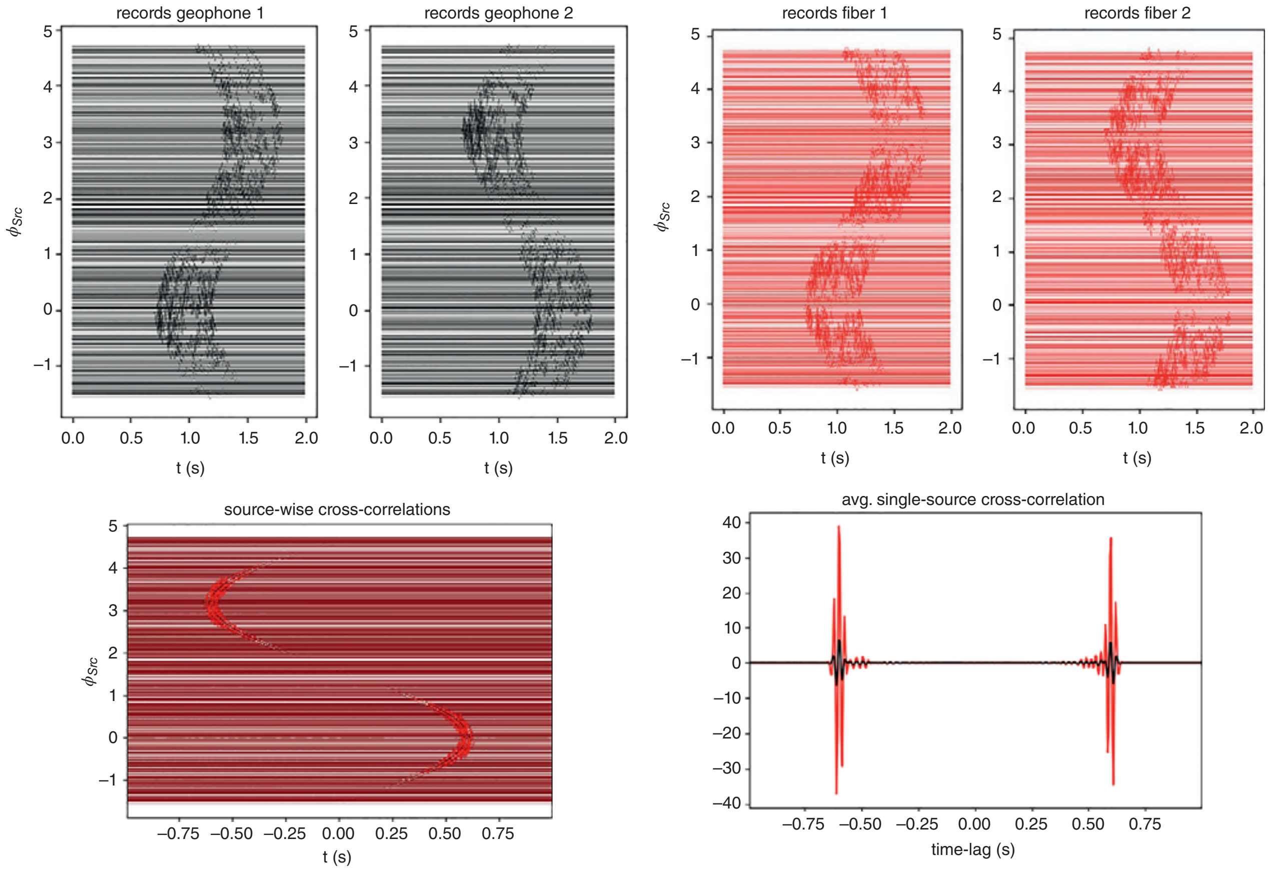

Figure 9.9 Random synthetic point sources emitting Rayleigh waves were recorded via particle velocity and strain rate at $\mathbf{x}_1$ and $\mathbf{x}_2$ in the (1,0,0) direction. Only every eighth source is shown. (Top left) The geophones and (top right) fiber channels both respond strongly to Rayleigh waves coming from the $\phi_{Src} = 0, \pi$ directions. (Bottom left) For each source, the geophone cross-correlation is plotted in black and the fiber cross-correlation is plotted in red, and the cross-correlations are very similar for both sensor types. (Bottom right) The average of these source-wise cross-correlations is plotted for the geophones in black and for the fiber in red.

between the long window of data at $\mathbf{x}_1$ with the data at $\mathbf{x}_2$. The resulting single-window cross-correlations for both fiber and geophones responding to 1,000 random Rayleigh wave point sources throughout a 40000 s window are shown in Figure 9.10. Also shown are the cross-correlations of the same experiment repeated with 1,000 random Rayleigh wave point sources and 1,000 random Love wave point sources of the same amplitude. The signal extracted when both Rayleigh and Love waves are present is a bit noisier than when just Rayleigh waves are present, but the peak at ±0.6 s is easy to pick for both the fiber and geophone responses.

9.4.2. Transverse-Transverse Cross-Correlations

The radial-radial cross-correlations yield a clear peak at the correct ±0.6 s time lags for both geophones and DAS. The analysis of radial-radial cross-correlations is relatively intuitive because both sensors involved in the cross-correlation respond strongly to Rayleigh wave sources at $\phi = 0, \pi$ (the azimuths corresponding to true velocity sources). The same simple scenario does not apply to transverse-transverse cross-correlations in the setup pictured in Figure 9.8. To better understand transverse-transverse cross-correlations, we repeated the exercise from Wapenaar et al. (2010), but with just Love wave sources; the results can be seen in Figure 9.11. While the geophones emphasize Love wave sources at $\phi_{Src} = 0, \pi$, the fiber channels emphasize Love wave sources at $\phi_{Src} = -\pi/4, \pi/4, 3\pi/4, 5\pi/4$. This relative difference is even more pronounced in the cross-correlations of the records for each of these sources. As has already been confirmed in practice (Lin et al., 2008), the average geophone cross-correlation has a strong peak at ±0.6 s, which is the correct arrival time. The average fiber cross-correlation is much more spread out, which may be in part because wavelets do not cancel as cleanly away from peak sensitivity angles, but also due to the amplitude difference

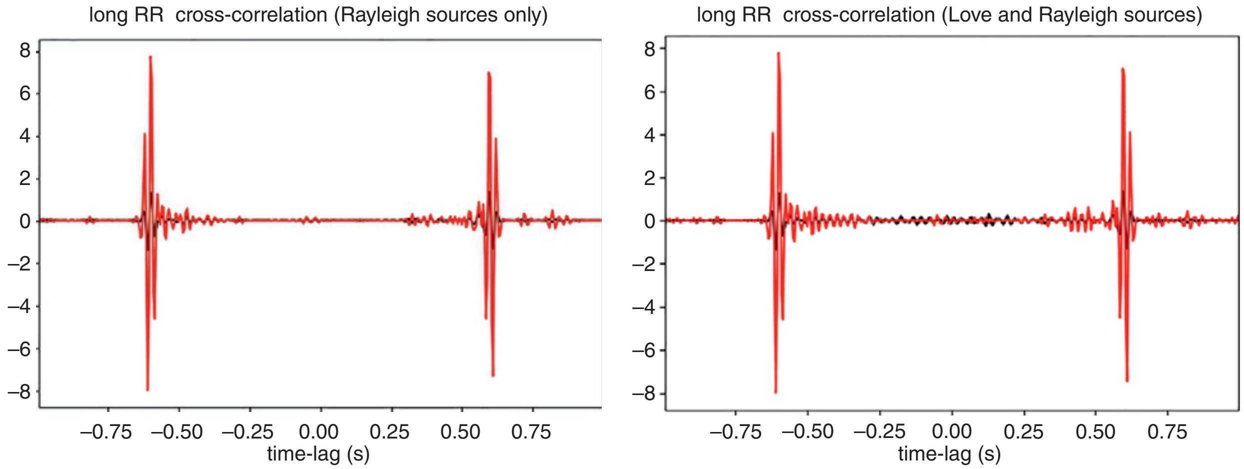

Figure 9.10 A single long radial-radial cross-correlation of synthetic geophone (black) data recorded in the presence of many Rayleigh wave point sources (left) yields a coherent signal with the correct arrival time of ±0.6 s, and the same holds true for the process repeated with synthetic fiber (red) data. (Right) Even when Love wave sources are present at equal amplitudes to the Rayleigh wave sources, the correct arrival time can still be picked clearly.

predicted in Table 9.3. As predicted, the peak of the average fiber cross-correlation is between ±0.4 and ±0.5 s (since 0.42 s = 0.6 s/$\sqrt{2}$).

We also repeated the exercise from Wapenaar et al. (2010) recording 1,000 random Love wave point sources spanning a 40000 s long trace for each location in both particle velocity and strain rate measurements, then doing a single cross-correlation for each type of measurement, pictured in Figure 9.12. Again, because there is only a single window with cross-terms due to many sources rather than averaging over multiple windows that each have a single source, the resulting cross-correlations are noisier than the cross-correlations shown in Figure 9.11. The geophone cross-correlation again yields correct peaks at ±0.6 s, but again, the fiber signal is spread out with a peak somewhere less than ±0.5 s.

We repeated this exercise in the presence of 1,000 Love wave sources and 1,000 Rayleigh wave sources of equal amplitude, also shown in Figure 9.12. There might be some hope of recovering a Love wave signal (that can be corrected) from this receiver geometry when only in the presence of Love wave sources. *However*, it appears that the sensitivity to very apparently fast Rayleigh wave sources near $\phi_{Src} = \pi/2, 3\pi/2$ dominates the signal too much to recover a Love wave signal.

9.5. SIMULATED AMBIENT NOISE INTERFEROMETRY ALONG CABLES

The exercises in Section 9.4 explore the signals extracted by ambient noise interferometry of $\dot{\epsilon}_\theta$ in two common setups: Radial-radial and transverse-transverse; however, even in simple fiber arrays made up of parallel or orthogonal lines, we wish to understand the signals extracted from a wider range of ray paths. In real data, we have observed clear signals extracted from orthogonal and parallel channel pairs that are neither radial-radial nor transverse-transverse (Lindsey, Dou, et al., 2017; Martin & Biondi, 2017; Martin et al., 2018). Here, we perform synthetic experiments to characterize these signals.

9.5.1. Signals Extracted Between two Parallel Fiber Cables

Although the transverse-transverse fiber geometry in Section 9.2 does not yield a clear signal, it seems reasonable that cross-correlations of parallel channels such that $\mathbf{x}_1 - \mathbf{x}_2$ is in a direction close to $\left(\mathcal{C}_{\pi/4}, \mathcal{S}_{\pi/4}, 0\right)$ would have a Love wave signal since this is the direction that is most sensitive to Love waves. However, these sensors also have significant sensitivity to Rayleigh waves, so it seems plausible that the cross-correlations might include both Rayleigh wave and Love wave signals.

We again use a 30 Hz Ricker wavelet (same expressions as in the previous section) with 10,000 random Love wave and 10,000 random Rayleigh wave sources uniformly distributed over an annulus with an inner radius of 2000 m and an outer radius of 3000 m. These are recorded during a 400000 s record. The Rayleigh wave velocity is again 2000 m/s, but the Love wave is 20% faster, i.e., 2400 m/s. As pictured in Figure 9.13, the virtual source is a pointwise axial strain measurement oriented in the (0,1,0) direction and sits at (425,425,0), and there are seven other point-wise axial strain receivers on a parallel line, each

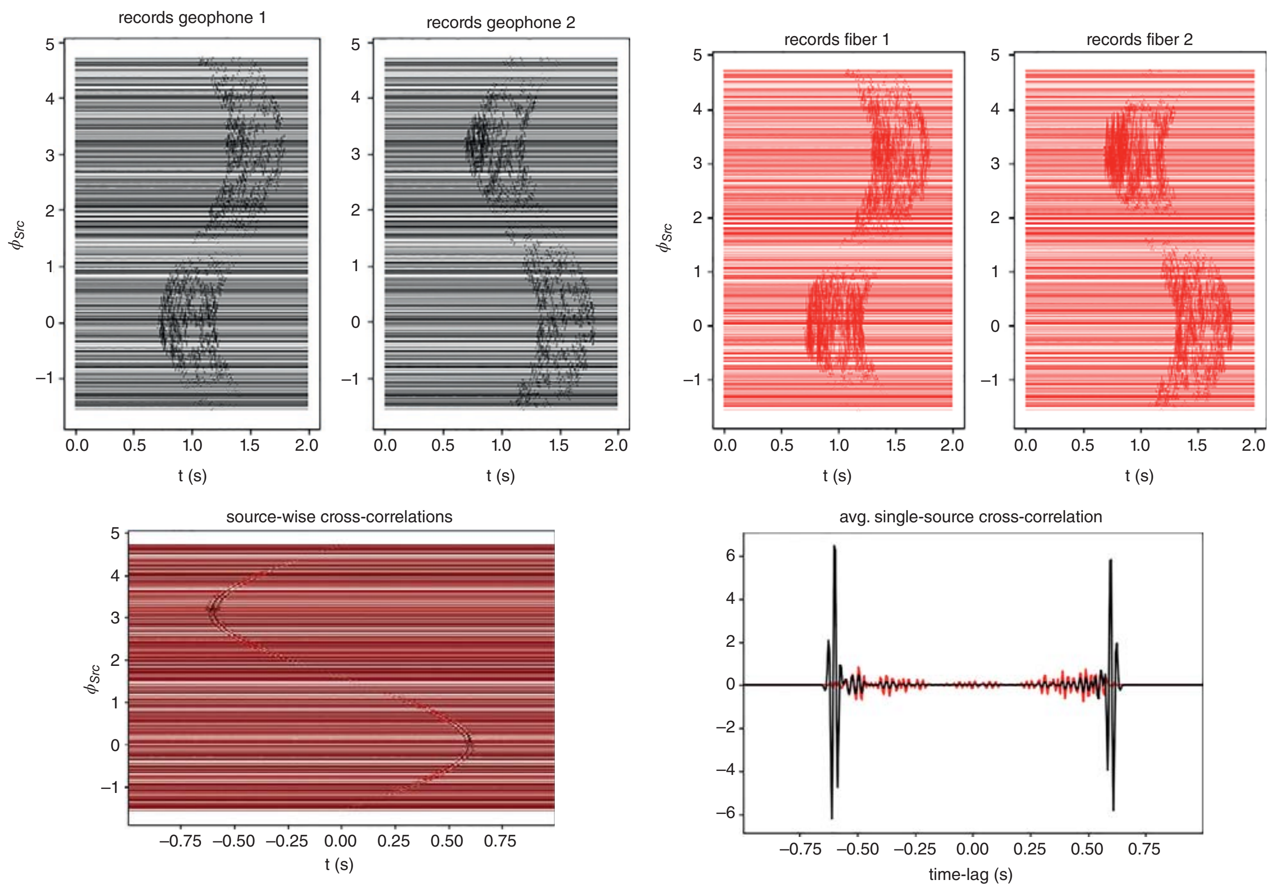

Figure 9.11 Random synthetic point sources emitting Love waves were recorded via particle velocity and strain rate at $\mathbf{x}_1$ and $\mathbf{x}_2$ in the (0,1,0) direction. (Top left) The geophones respond strongly to Love waves coming from the $\phi_{Src} = 0, \pi$ directions. (Top right) The fiber channels respond strongly to Love waves coming from the $\phi_{Src} = -\pi/4, \pi/4, 3\pi/4, 5\pi/4$ directions. (Bottom left) For each source, the geophone cross-correlation is plotted in black and the fiber cross-correlation is plotted in red. (Bottom right) The average of these source-wise cross-correlations is plotted for the geophones in black and for the fiber in red. The peak geophone signal is of around ±0.6 s, and the peak fiber signal is more spread in time with a peak in the ±0.4 to ±0.5 s range.

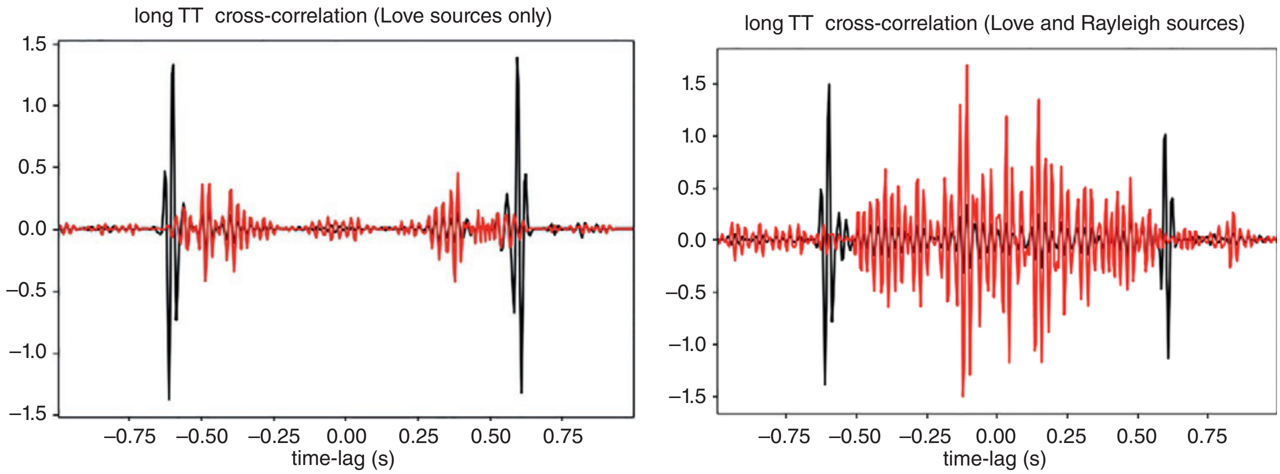

Figure 9.12 (Left) A single long transverse-transverse cross-correlation of strain rate data (red) recorded in the presence of many Love wave point sources yields a coherent signal at an apparently fast velocity by a factor of $\sqrt{2}$. (Right) No discernible arrival can be picked when both Love and Rayleigh wave point sources of equal amplitude and number are recorded as strain rate data (red), but the particle velocity cross-correlation (black) still shows the correct arrival time in the presence of both types of sources.

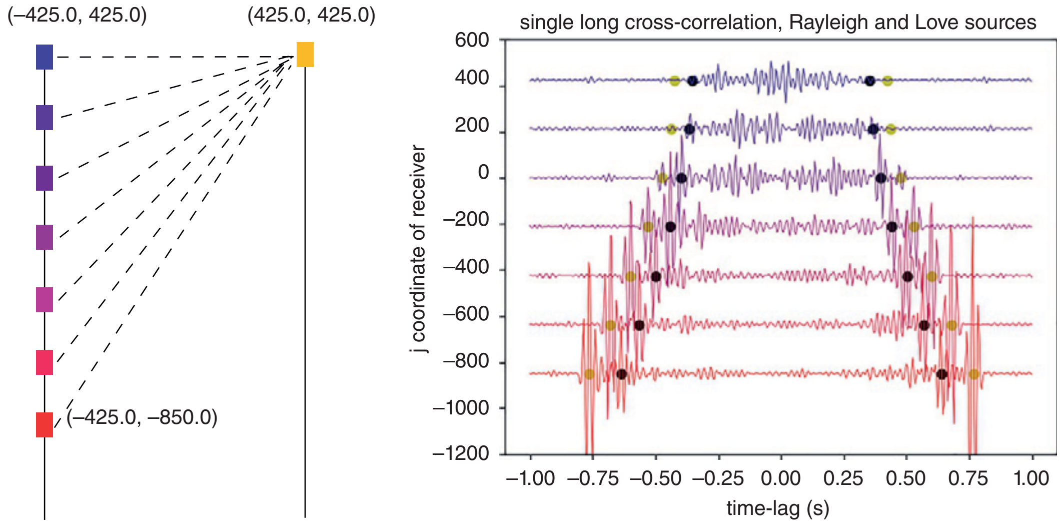

Figure 9.13 (Left) A virtual source is marked in yellow along one fiber line, and along a parallel cable are other receivers marked in blue, purple, and red. (Right) Some of the receiver-color-coded cross-correlations show clear peaks at the correct positive and negative arrival time lags, where Rayleigh waves are marked with yellow dots and Love waves are marked with blue dots.

oriented in the (0,1,0) direction and evenly spaced between (−425, −850,0) and (−425,425,0) (so this last receiver is in the transverse-transverse setup with the virtual source).

The cross-correlations of these long records for each receiver against the virtual source are shown in Figure 9.13. For the receivers within a 15° offset of the transverse-transverse orientation, there is a lot of energy from the very apparently fast velocity Rayleigh wave sources from $\phi_{Src} = \pm\pi/2$, so there is no clear arrival at the true Love and Rayleigh wave arrival times. Moving down to the third receiver, about a 25° offset, there is still quite a bit of this fast energy, but there is also a strong peak at the true Love wave velocity and a smaller peak (although not nearly as clear) at the true Rayleigh wave velocity. All of the receivers farther down have both clear Rayleigh and Love arrivals and less of the early arrival energy. The Rayleigh wave arrivals get increasingly strong moving down the line because the orientation between the receivers and the virtual source gets closer to the two channels being collinear (like a radial-radial setup).

9.5.2. Virtual Source Perpendicular to Receiver Cable

At corners of arrays, it would be ideal to be able to use the ray paths between those two orthogonal lines. To understand this situation, we test a virtual source on one line at (425,425,0) oriented in the (1,0,0) direction, and seven equally spaced receivers oriented in the (0,1,0) direction between (−425, −800,0) and (−425,425,0), as pictured in Figure 9.14. The same velocities and configuration of Rayleigh and Love wave point sources were used as in the previous section.

The cross-correlation results are shown in Figure 9.14. No clear signal is visible in the cross-correlation with the top receiver that is directly across from the virtual source, but for all other offsets, both the Rayleigh and Love wave signals are clearly visible. While the relative amplitudes between the Rayleigh and Love wave signal peaks varied significantly with offset in the parallel lines' setup, the relative amplitudes of the Rayleigh and Love wave peaks stay consistent over offsets in this orthogonal lines' setup. Overall, the orthogonal lines' setup has more pairs of channels from which we can reliably simultaneously extract both Rayleigh and Love wave signals than the parallel lines' setup.

9.6. CONCLUSIONS

Compared to particle velocity measurements, strain rate measurements more strongly respond to longitudinal waves from sources in line with the sensor orientation. When responding to transverse waves, strain rate measurements emphasize sources at four angles offset by 45° from the two source angles that particle velocity measurements respond to most strongly. Many significant features of how DAS data differ from geophone data at medium to low frequencies are primarily explained by the change to strain rate from particle velocity. However, when responding to shorter wavelength vibrations

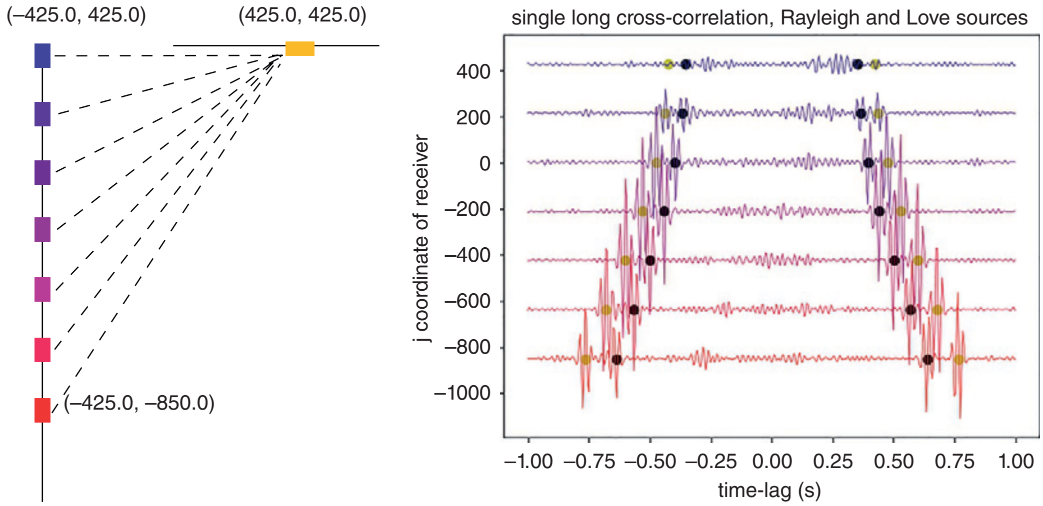

Figure 9.14 (Left) A virtual source is marked in yellow along one fiber line, and along an orthogonal cable are other receivers marked in blue, purple, and red. (Right) Some of the receiver-color-coded cross-correlations show clear peaks at the correct positive and negative arrival time lags, where Rayleigh waves are marked with yellow dots and Love waves are marked with blue dots.

(wavelength approaching the gauge length), DAS data develop a more complicated sensitivity pattern with multiple additional angles of peak sensitivity.

The amplitude of cross-correlations between any pair of sensors has more extreme sensitivity patterns than either sensor on its own. Radial-radial cross-correlations of two DAS channels overemphasize seismic sources in line with the radial direction between the two channels compared to two geophones in the same orientation. This suggests radial-radial cross-correlations between DAS channels are more robust to nonideal noise distributions than radial-radial geophone cross-correlations for ambient noise interferometry. Transverse-transverse cross-correlations between DAS channels mix Rayleigh and Love wave responses, with the Love wave responses often showing apparently fast velocities. For any receiver geometry, the expected cross-correlations between sensor pairs must be simulated to determine which pairs will yield reliable Rayleigh and Love wave Green's function arrival time estimates. We present this analysis for two common fiber orientations: Parallel and perpendicular cables, showing that the nearest sensor pairs do not always have the strongest or most reliable signals when performing ambient noise interferometry with DAS data.

ACKNOWLEDGMENTS

The authors are grateful for useful discussions about aspects of this chapter with J. Chang (Stanford University), R. Clapp (Stanford University), N. Nakata (University of Oklahoma (OU)), S. Dou (Lawrence Berkeley National Laboratory (LBNL)), S. Yuan (Stanford University), and J. Claerbout (Stanford University). This work was financially supported in part by affiliates of the Stanford Exploration Project (E. Martin and B. Biondi), the U.S. Department of Energy (DE-FG02-97ER25308; E. Martin), a Schlumberger Innovation Fellowship (E. Martin), the National Science Foundation Graduate Research Fellowship Program (N. Lindsey), the U.S. Department of Defense under SERDP Grant RC-2437 "Developing Smart Infrastructure for a Changing Arctic Environment Using Distributed Fiber-Optic Sensing Methods," and affiliates of the Stanford Exploration Project.

REFERENCES

Ajo-Franklin, J., Dou, S., Daley, T., Freifeld, B., Robertson, M., Ulrich, C., et al. (2017). *Time-lapse surface wave monitoring of permafrost thaw using distributed acoustic sensing and a permanent automated seismic source*. Expanded Abstracts of the 87th Annual International Meeting of Society of Exploration Geophysicists (pp. 5223–5227).

Benioff, H. (1935). A linear strain seismograph. *Bulletin of the Seismological Society of America*, *25*(4), 283–309.

Bona, A., Dean, T., Correa, J., Pevzner, R., Tertyshnikov, K., & Zaanen, L. V. (2017). *Amplitude and phase response of das receivers*. 79th EAGE Conference and Exhibition in Paris, France, We *A5* 13. doi: 10.3997/2214-4609.201701200

Dean, T., Cuny, T., & Hartog, A. (2017). The effect of gauge length on axially incident p-waves measured using fibre optic distributed vibration sensing. *Geophysical Prospecting*, *65*(1), 184–193.

Dou, S., Lindsey, N., Wagner, A., Daley, T., Freideld, B., Robertson, M., et al. (2017). Distributed acoustic sensing for seismic monitoring of the near surface: A traffic-noise interferometry case study. *Scientific Reports, 7, article number* 11620.

High-resolution shallow structure revealed with ambient noise tomography on a dense array. (2017). Stanford University, Proceedings of the 42nd Workshop on Geothermal Reservoir Engineering.

Kahn, M. K. D., Cole, S., Ridge, A., Boone, K., Rich, J., Silver, K., & Langton, D. (2017). Hydraulic-fracturing-induced strain and microseismic using in situ distributed fiber-optic sensing. *The Leading Edge*, *36*(10), 837–844.

Kuvshinov, B. (2016). Interaction of helically wound fibre-optic cables with plane seismic waves. *Geophysical Prospecting*, *64* (3), 671–688.

Lancelle, C. (2016). Distributed acoustic sensing for imaging near-surface geology and monitoring traffic at garner valley, California, Dissertation at University of Wisconsin-Madison.

Lin, F., Moschetti, M., & Ritzwoller, M. (2008). Surface wave tomography of the western united states from ambient seismic noise: Rayleigh and love wave phase velocity maps. *Geophysical Journal International*, *173*, 281–298.

Lindsey, N., Dou, S., Martin, E., Wagner, A., Ajo-Franklin, J., & Team, L.-C. F. P. E. (2017). 4-D permafrost thaw observations from ambient road traffic noise and a very dense distributed fiber optic sensing array. *American Geophysical Union*¸ Fall Meeting (S31A-0804).

Lindsey, N., Martin, E., Dreger, D., Freifeld, B., Cole, S., James, S., et al. (2017). Fiber-optic network observations of earthquake wavefields. *Geophysical Research Letters*, *44* (23), 11,792–11,799.

Martin, E. (2018). Passive imaging and characterization of the subsurface with distributed acoustic sensing. Dissertation and Stanford University.

Martin, E., Ajo-Franklin, J., Lindsey, N., Daley, T., Freifeld, B., Robertson, M., et al. (2015). *Interferometry of ambient noise from a trenched distributed acoustic sensing array*. Society of Exploration Geophysicists Expanded Abstracts of the 85th Annual International Meeting (pp. 2445–2450).

Martin, E., & Biondi, B. (2017). *Ambient noise interferometry across two-dimensional das arrays*. Society of Exploration Geophysicists Expanded Abstracts of the 87th Annual International Meeting (pp. 2642–2646).

Martin, E., Huot, F., Ma, Y., Cieplicki, R., Cole, S., Karrenbach, M., & Biondi, B. (2018). A seismic shift in scalable acquisition demands new processing: Fiber-optic seismic signal retrieval in urban areas with unsupervised learning for coherent noise removal. *IEEE Signal Processing Magazine*, *35*(2), 31–40.

Martin, E., Lindsey, N., Dou, S., Ajo-Franklin, J., Wagner, A., Bjella, K., et al. (2016). *Interferometry of a roadside das array in Fairbanks, AK*. Society of Exploration Geophysicists Expanded Abstracts of the 86th Annual International Meeting (pp. 2725–2729).

Wapenaar, K., Draganov, D., Snieder, R., Campman, X., & Verdel, A. (2010). Tutorial on seismic interferometry: Part 1—basic principles and applications. *Geophysics*, *75*(5), 75A195–75A209.

Webster, P., Wall, J., Perkins, C., & Molenaar, M. (2013). *Micro-seismic detection using distributed acoustic sensing*. Society of Exploration Geophysicists Expanded Abstracts of the 83rd Annual International Meeting (pp. 2459–2463).

Zeng, X., Lancelle, C., Thurber, C., Fratta, D., Wang, H., Lord, N., et al. (2017). Properties of noise cross-correlation functions obtained from a distributed acoustic sensing array at garner valley, California. *Bulletin of the Seismological Society of America*, *107*(2), 603–610.

10

Using Telecommunication Fiber Infrastructure for Earthquake Monitoring and Near-Surface Characterization

Biondo L. Biondi[1,2], Siyuan Yuan[1], Eileen R. Martin[3], Fantine Huot[1], and Robert G. Clapp[1]

ABSTRACT

The Stanford Fiber Seismic Observatory (SFSO) has been recording data using a distributed acoustic sensing (DAS) laser interrogator attached to a fiber-optic cable that was deployed in telecommunication conduits buried under the Stanford University campus. Analysis of a sequence of local earthquakes demonstrates that using SFSO data, we could detect a weak event that was not previously cataloged. The comparison of signal amplitudes of data recorded by the SFSO array with data recorded by two nearby broadband seismometers demonstrates that DAS arrays could be useful in determining event magnitudes. Time-lapse seismic noise interferometry results show that repeatable virtual source gathers and frequency-velocity spectra can be computed from SFSO data. Time-lapse interferometry using arrivals from quarry blasts shows changes in time delays that can be related to changes in ground conditions caused by excavation of a building foundation. Comparing data recorded by two laser interrogators of different sensitivity, we show that data quality improves with the sensitivity of the interrogator. This result demonstrates that data quality could improve in the future as interrogator technology advances. We also show that new machine-learning algorithms could tackle the challenges of processing, analyzing, and interpreting huge data streams that would be recorded if we scaled up the SFSO experiment.

10.1. INTRODUCTION

Seismologists strive to acquire data using denser and denser arrays of seismic sensors. However, the cost and logistic challenges of deploying and maintaining dense arrays, as well as collecting data from a large number of sensors, are enormous. Recording data using fiber-optic cables buried underground by using distributed acoustic sensing (DAS) technology may provide a significant reduction in cost and complexity, and greatly improve the spatial and temporal resolution and reliability of information subsurface processes that we can extract from seismic data. If we could leverage existing telecommunication fiber infrastructure by using existing unused cables deployed to provide telecommunication services (aka dark fiber), and/or by deploying new cables in existing conduits, the potential impact on seismology would be even greater (Ajo-Franklin, Lindsey, et al., 2017; Jousset et al., 2018; Martin, Biondi, et al., 2017). Many large metropolitan areas that are located in earthquake-prone regions also feature extensive networks of fiber-optic cables to provide the telecommunication services essential to modern life. If we can exploit such networks, we could possibly build

[1]*Department of Geophysics, Stanford University, Stanford, California, USA*

[2]*Institute for Computational and Mathematical Engineering, Stanford, California, USA*

[3]*Department of Mathematics, Virginia Polytechnic Institute and State University, Blacksburg, Virginia, USA*

Distributed Acoustic Sensing in Geophysics: Methods and Applications, Geophysical Monograph 268, First Edition.
Edited by Yingping Li, Martin Karrenbach, and Jonathan B. Ajo-Franklin.

DOI:10.1002/9781119521808.ch10

dense networks that span tens of kilometers under these metropolitan areas and encompass millions of seismic sensors, and could still be able to do it at reasonable cost and collect data in real time, or at least in "useful" time, for the specific application.

To validate the hypothesis that large seismic networks can be built using existing telecomunication infrastructure, we have been conducting a permanent seismic recording experiment since September 2016. We continuously recorded data utilizing fiber-optic cables lying in polyvinyl chloride (PVC) conduits buried in the ground under the Stanford University campus. These conduits existed prior to our experiment and are shared with other fiber cables used to support Internet traffic across the campus. Coupling between the fiber cable and surrounding rocks relies exclusively on gravity and friction. Therefore, ground coupling, and consequently data quality, is expected to be lower than that in other experiments utilizing directly buried horizontal fiber cables, and be similar to data quality that we would have observed if we were using one of the preexisting cables.

As we reported in several publications (Biondi et al., 2017; Martin & Biondi, 2017; Martin, Biondi, et al., 2017; Martin, Castillo, et al., 2017), the data recorded by the Stanford Fiber Seismic Observatory (SFSO) contain coherent and repeatable waveforms originated by natural and anthropogenic seismic sources. These data could be used to study earthquakes, as well as extracting near-surface parameters by interferometry. Our results are consistent with the results from one preceding field experiment (Jousset et al., 2018) and two subsequent ones (Ajo-Franklin et al., 2019; Yu et al., 2019), which recorded useful signal using preexisting telecommunication fiber cables. In this chapter, we further analyze recorded data and discuss the advantage and disadvantage of a DAS-based network for two important applications: (1) Continuous monitoring and analysis of regional and local earthquakes (Lindsey et al., 2017) and (2) high-resolution and continuous subsurface characterization using interferometry (Ajo-Franklin, Dou, et al., 2017; Martin, 2018). We think that these two applications have the potential of providing Earth scientists with information at a resolution and scale that would be impossible using conventional data-recording methods.

For these two applications, as well as for all other possible applications of large-scale DAS arrays based on existing telecomunication infrastructure, there are several important issues to be further addressed. In this chapter, we discuss three critical issues. First, is the suboptimal coupling between the fiber cable and the ground going to hamper the development of the technology and its deployment to large-scale arrays? To start addressing this question, we simultaneously recorded data using two different laser interrogators, each interrogating a different fiber strand packaged in the same cable. The interrogators have different sensitivity, and by comparing the data we draw some preliminary conclusions. Second, large DAS arrays will produce a huge amount of data at extremely high rates. For example, the latest generation of interrogators may geneate about 4 TBytes of data per day when recording at 100 Hz. Our current workflows for analyzing and interpreting seismic data are inadequate to effectively manage this large data stream, in particular when data are recorded in urban, or suburban, areas. One example of new challenges is the identification of noise generated by diverse anthropogenic activities, which are typically nonstationary but coherent in time and space and with variable characteristics. Automatic identification would enable automatic attenuation of such unwanted events. Third, if we leverage telecomunication infrastructure, we may not have direct physical access to the sensors, and thus there is the problem of estimating the location of the virtual receivers in the physical space. We started developing algorithms based on modern data science to tackle this problems and present results at the end of this chapter.

10.2. THE SFSO

The SFSO has been continuously recording seismic data as sensed by a fiber-optic cable placed in telecommunication conduits under the Stanford University campus. The data have been recorded by an OptaSense ODH 3.1 laser interrogator and subsampled to temporal Nyquist frequency of 25 Hz for permanent storage. Virtual sensors were set to be 8 m apart, and the gauge length was set to be 7 m. The gauge windows were not overlapping but contiguous. The total length of the fiber cable is about 2.45 km; at the opposite end of the cable from the laser interrogator, two fiber strands that share the same jacket are connected and the "returning" fiber strand is terminated at the same location as the laser interrogator. Therefore, the total linear length of the arrays is about 4.9 km, but the effective length is half of that, with two sets of sensors sharing the same spatial location, though slightly shifted with respect to each other. The total number of channels is 610. Our fiber cable shares the conduits with other telecommunication cables; the number of these other cables varies depending on the array segment. Figure 10.1 shows the geometry of the array and the position of the channels located at the corners of the array for the forward half of the array, i.e., before the loop back. Channel #5 is just outside of the building where the interrogator is installed. The channel location was mapped by performing tap tests along the roue and matching them with the recorded data. Accurate time synchronization is assured by a GPS antenna placed close to the roof of

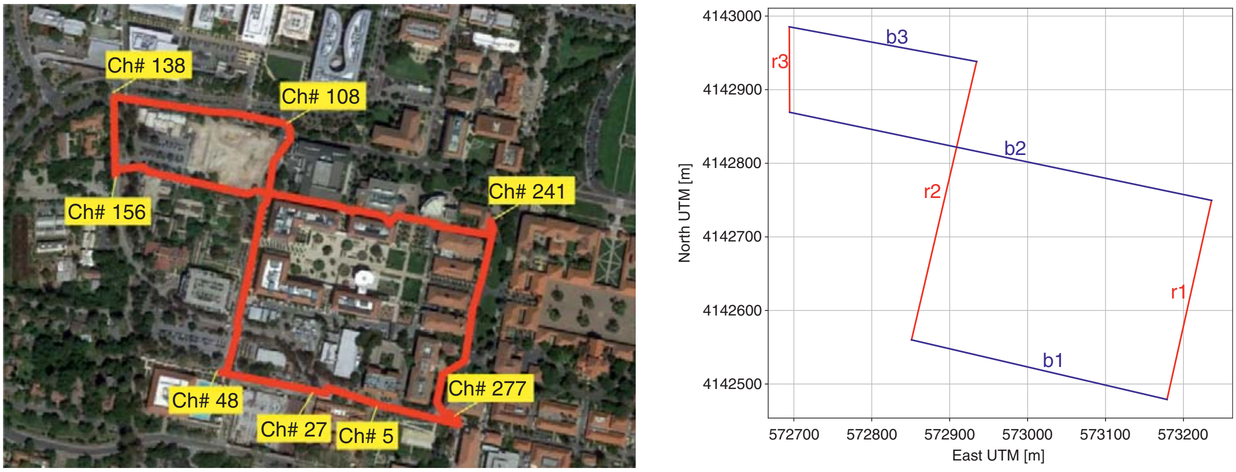

Figure 10.1 (Left) Trace of the array overlaid to an aerial photo of the campus; notice the construction site located at southwest of Channel #108. (Right) Sketch of array geometry with array segments labeled according to their geographical orientation: Red segments (r1, r2, and r3) are oriented approximately north-south, whereas blue segments (b1, b2, and b3) are oriented approximately east-west.

the building hosting the equipment. To better understand the DAS data, we have also used data recorded by two broadband seismometers installed on the Stanford campus and managed by the Berkeley Digital Seismic Network: The Jasper Ridge seismic station (JRSC) and the Stanford Telescope station (JSFB). Their locations with respect to the DAS arrays are shown in Figure 10.2.

10.3. CONTINUOUS MONITORING AND ANALYSIS OF LOCAL AND REGIONAL EARTHQUAKES

The spatial extent and the sensitivity enabled by large DAS arrays may completely change the way that we monitor and analyze local and regional earthquakes. This is particularly true in tectonic active zones (e.g., the San Francisco Bay Area) where numerous events occur and where their sampling with dense arrays would enable the recording and analysis of coherent unaliased arrivals at much higher frequencies. Images and maps of subsurface geology and fault systems would then become available at a higher resolution than would be practical by using arrays of conventional seismometers because the cost of continuous recording using dense arrays would be much higher if conventional seismometers were employed.

In previous publications, we have analyzed the repeatability of the signal recorded form both natural and man-made (e.g., quarry blasts) events (Biondi et al., 2017; Martin, Biondi, et al., 2017). In this chapter, we show the capability of fairly small DAS arrays to detect small earthquakes that have not been cataloged in the USGS online database. We also analyze the recorded amplitudes to investigate whether DAS arrays can provide useful information for estimating event magnitudes; this information is important for both characterizing low-amplitude events and early warning of large destructive events.

We focus our attention on a sequence of five earthquakes that occurred under Felt Lake in the hills behind the Stanford campus during the May–July 2017 period. Three of these events are in the USGS catalog, but two of them are too weak (with a magnitude of lower than 1) to be in the catalog and we identified them by applying template matching to the DAS recording, as described further in this chapter. One of these weak events (*FeltLake #4*) occurred in May, and thus it may be a precursor of the main event, whereas the other one was the last of the series and may be considered a weak aftershock. The parameters of these five events are listed in Table 10.1; magnitude, depth of the hypocenter, and distance of the hypocenter from the SFSO array are listed for the three events in the USGS catalog. The location of the epicenters of these three events is also marked in Figure 10.2. Figure 10.2 also shows the location of the SFSO array and that of two broadband stations located on the Stanford campus that we used for our analysis: JRSC and JSFB; their approximate distances from the hypocenters of the events are also marked on the map. Notice that the Stanford Telescope station is located at less than half the distance from Felt Lake as the SFSO array is, whereas the JRSC is located little less than a mile further from Felt Lake than the SFSO array is.

Figure 10.3 shows the data recorded for all the Felt Lake events shown in the same order as in Table 10.1;

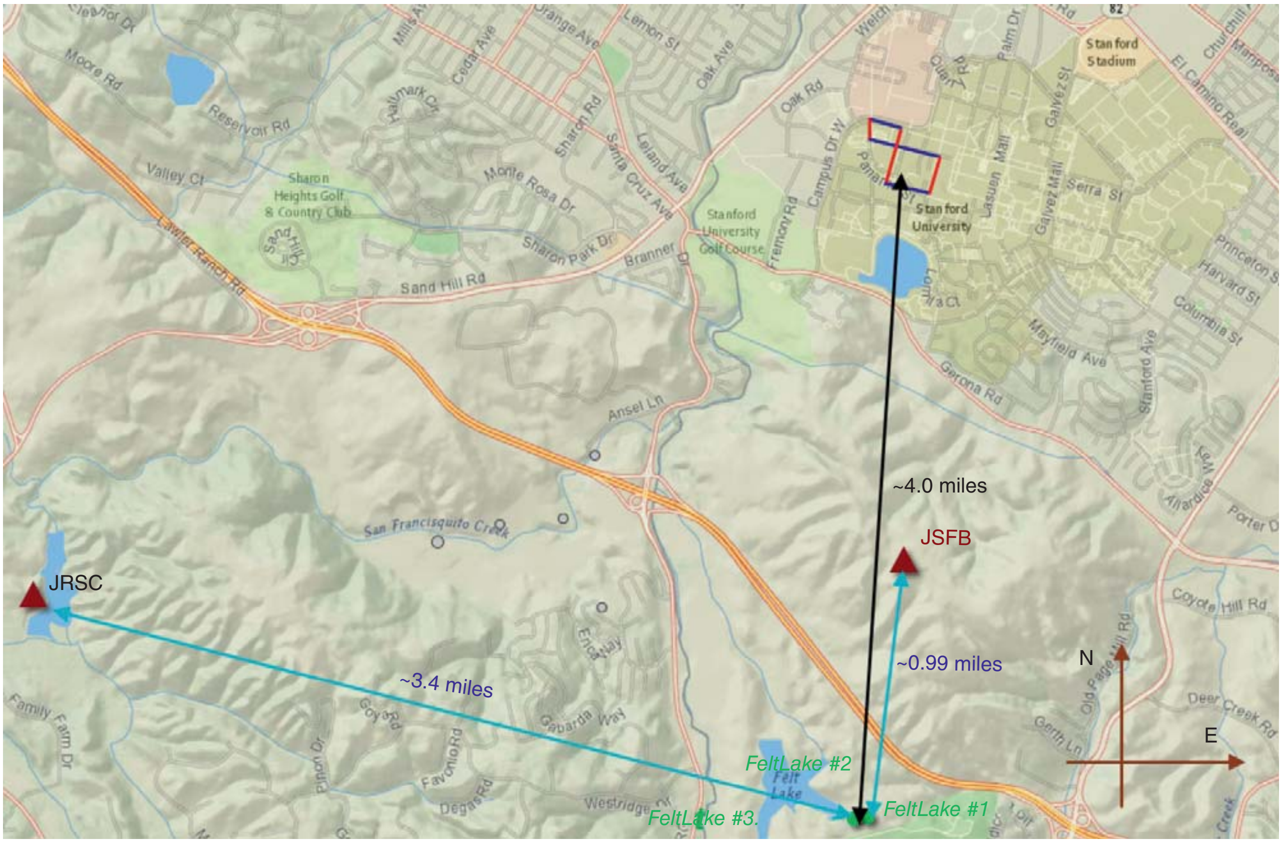

Figure 10.2 Map of the southwest region of the Stanford campus. It shows the location of the SFSO array and that of two broadband stations that we used for our analysis: JRSC and JSFB. It also shows the locations of the epicenters of *FeltLake #1*, *FeltLake #2*, and *FeltLake #3* events, together to their approximate distances from SFSO, JRSC, and JSFB.

Table 10.1 Local Earthquake Recorded by the SFSO DAS Array.

Event Name	Date	Time	M_d	Depth of hypocenter [km]	Distance of SFSO hypocenter [km]
FeltLake #1	12 July 2017	18:46:41	1.34	3.24	5.45
FeltLake #2	12 July 2017	18:47:50	0.95	3.05	5.34
FeltLake #3	13 July 2017	04:02:49	0.81	3.64	5.72
FeltLake #4	10May 2017	06:35:38	-	-	-
FeltLake #5	13 July 2017	05:56:06	-	-	-

Note. The first three events are in the online USGS catalog, whereas the other two events were too weak (with an magnitude of lower than 1) to be catalogd, and thus there is no available information on their magnitude, depth, and distance from the SFSO DAS array.

starting from display (a) through display (e). In each composite display, the DAS data are shown in the upper panels; the vertical components of JRSC and JSFB are shown in the two wiggle plots below the DAS data, with JRSC data shown above JSFB data. The DAS data were band-passed from 0.5 to 20 Hz; the JRSC data were band-passed from 1.5 to 20 Hz; and the JSFB data were band-passed from 0.5 to 50 Hz. Each of the displays is scaled independently to maximize the use of the display dynamic range. In the plots, the time origin corresponds to the event time that was extracted from the USGS catalog for panels (a), (b), and (c), and estimated from the data for the last two events. The DAS array channels are displayed in six different subpanels corresponding to different segments of the array. The data corresponding to segments of the array approximately oriented along the north-south direction (see the right panel in Figure 10.1) are labeled as r1, r2, and r3; red continuous lines separate them. The data corresponding to segments of the array approximately oriented along the east-west

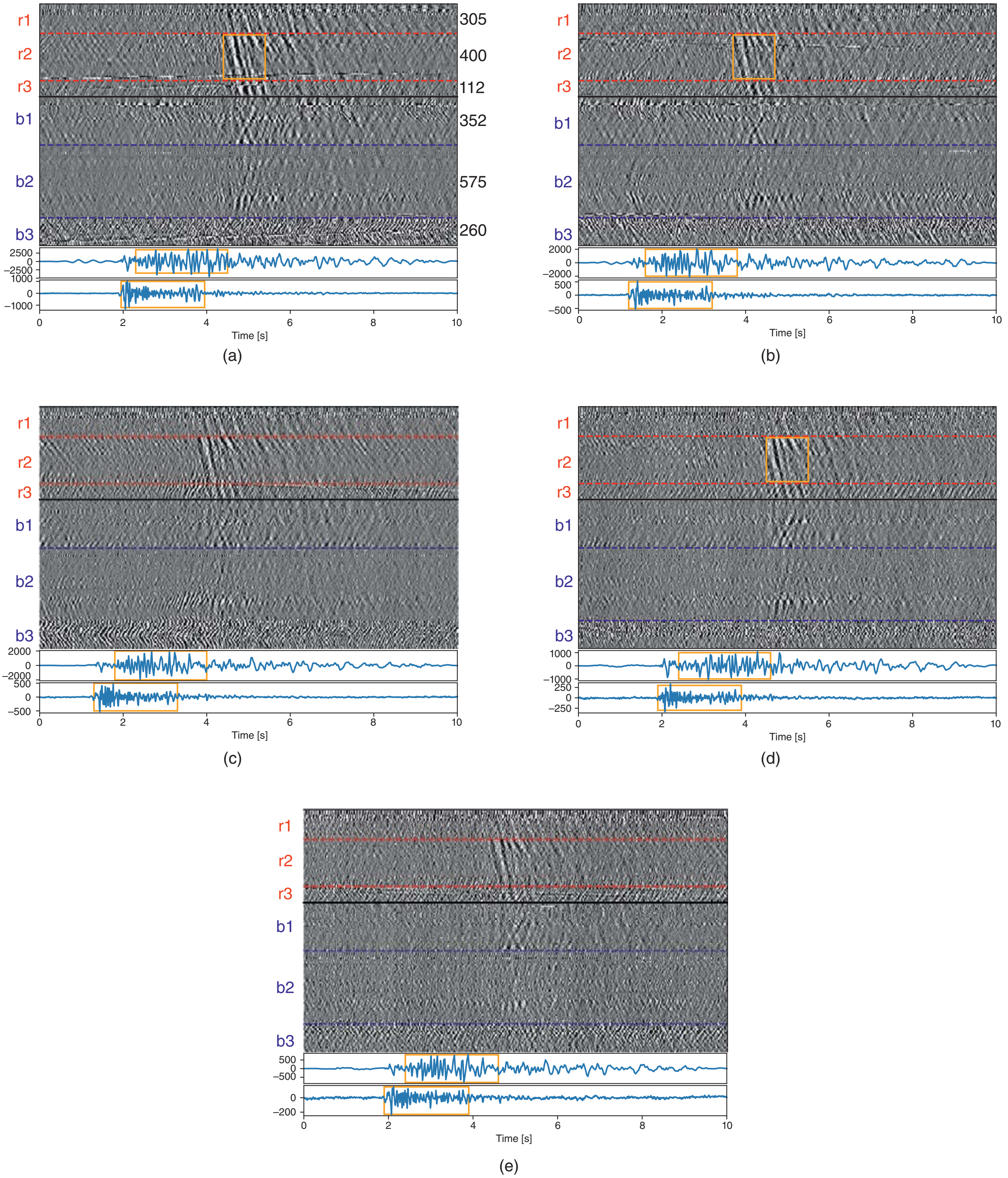

Figure 10.3 Data recorded for all the Felt Lake events shown in the same order as in Table 10.1. The DAS data are shown in the upper panels of each composite display; the vertical components of JRSC and JSFB are shown in the two wiggle plots below the DAS data, with JRSC data shown above JSFB data. Each of the displays is scaled independently to maximize the use of the display dynamic range. The origin of the time axis corresponds to the estimated time of each event. The DAS array channels are displayed in six different subpanels corresponding to segments of the array as they are labeled in the sketch shown in Figure 10.1. On the right of the top-left panel, we have marked the linear lengths (in meters) of the six segments of the array.

direction are labeled as b1, b2, and b3; blue continuous lines separate them. The linear lengths (in meters) of the six segments of the array are indicated on the right of the top-left panel in Figure 10.3.

Not surprisingly, the DAS data corresponding to *FeltLake #1* show more coherent arrivals than for all other events, since this event was substantially stronger than the others. In Figure 10.3a, we can identify the arrival of *P* energy around 2 s; *P* arrivals would be difficult to identify in other panels. In contrast, the *Alum Rock* event presented in Section 10.5 and the examples of DAS data recorded from a series of events originating from another local fault we previously presented in Martin, Castillo, et al. (2017) and Yuan, Biondi, and Clapp (2018) show a strong stepwise onset of recorded energy corresponding to the arrival time of *P* waves. We still need to reach a full understanding of the nature of *P*-arrival recordings by SFSO from local earthquakes, which is consistent with known event source mechanism and known directionality in sensitivity of DAS arrays (Martin, 2018).

10.3.1. Weak Event Detection by Template Matching

Template matching is a well-known method for detecting weak earthquakes that are similar to stronger ones (Shelley et al., 2007). It was initially developed for data recorded from ensembles of isolated seismometers, but the concept is easily generalized to array data. Li and Zhan (2018) applied template matching to data recorded from a DAS array trenched over a geothermal field. We applied template matching to our DAS data recorded from fiber cables free-floating in telecom conduits and identified the two events that were not in the USGS catalog: *FeltLake #4* and *FeltLake #5*. We then applied it to the data recorded by the two broadband seismometers on the Stanford campus (JRSC and JSFB) and compared the results obtained using these two different types of recording technology. Yuan et al. (2018) show results for all the Felt Lake events, as well as for the events originating on another local fault under the community of Ladera. Here we just show the results of template matching for the first weak Felt Lake event (*FeltLake #4*).

Figure 10.4 shows the results of applying template matching to the data recorded by SFSO, JRSC, and JSFB during a 24 hour time window in May 2017 that includes the time of the *FeltLake #4* weak event. The templates being matched are 10 s time windows recorded by the corresponding sensor (or sensor array) around the strongest Felt Lake event (*FeltLake #1*).

For the broadband seismometers (Figures 10.4b and 10.4c), we show the normalized cross correlations of the data recorded in 10 s overlapping windows spaced by 0.02 s. The normalized cross correlations span the range between −1 and 1; when the template is cross-correlated with itself, which did not occur in this time window, the value is 1. For the DAS data (Figure 10.4a), we show the median from the normalized cross correlations of the template for each channel with data recorded at the same channel, with the same window length and overlap as for the seismometers. By taking the median, we take advantage of the redundancy of the data provided by an array measurement, but at the same time we make the results more robust with respect to the strong nonstationary noises recorded by the array (see DAS data shown in Figure 10.3).

Comparing the three panels in Figure 10.4, we notice that the *FeltLake #4* weak event can be detected using data from each of the instruments (shown in red in the figure). However, JRSC template matching shows one false positive, and JSFB matching shows two false positives (shown in black in the figure). We determined that the peaks displayed in black were indeed found false positives by a visual inspection of the recorded traces. The absolute values of the peaks of the normalized cross correlation corresponding to the two broadband seismometers are higher than the peaks for the DAS array, but the correlations for the broadband seismometers have much higher background values. These differences are related to the differences between instruments; DAS traces are more noisy than the corresponding seismometers traces, and thus the correlation at the time of the event is lower. However, the large number of DAS traces more than compensates for noise and makes the detection based on DAS data more robust than the one based on seismometer data. We computed a signal-to-noise ratio (SNR) measure for the peaks corresponding to the *FeltLake #4* event. To compute SNR, we took the ratio between the peak values at the event with the 99.95 percentile (indicated by the orange lines in Figure 10.4) of the absolute values of the normalized cross correlations computed over the whole 24 hour period. The SNR was 5.56 for SFSO, 4.14 for JRSC, and 4.00 for JSFB.

Figure 10.5 shows the results of applying template matching to the data recorded by SFSO, JRSC, and JSFB during a 24 hour time window in July 2017 that includes the time of the *FeltLake #1* and *FeltLake #2* events. As expected, the cross correlation is equal to 1 for *FeltLake #1* and high, but less than 1, for *FeltLake #2*. Again, we can observe a false positive (displayed in black) for the detection using JSFB.

10.3.2. Estimates of Event Amplitudes

In the previous subsection, we showed that DAS data could be used to detect weak local earthquakes that are not in the USGS catalog. In addition to detecting events, these data would be useful to be able to estimate the magnitudes of these events so that they

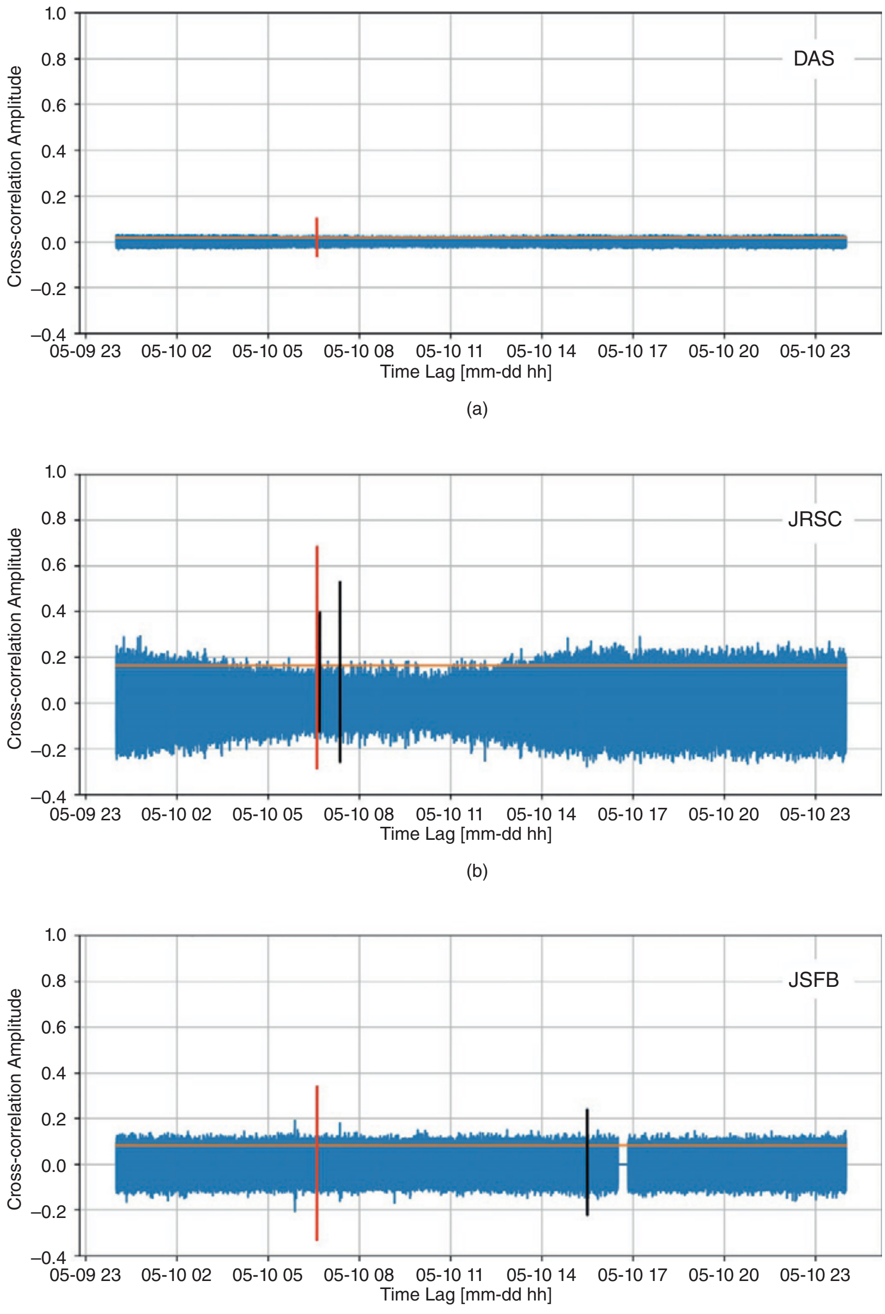

Figure 10.4 Results of template matching for data recorded by SFSO ((a), JRSC (b), and JSFB (c) during a 24-hour time window in May 2017 that includes the time of the Felt Lake weak event (*FeltLake #4*). True detected events are shown in red, whereas false positives are shown in black. This event can be detected using data from each of the instruments; however, JRSC template matching shows one false positive and JSFB matching shows two false positives. The SNR was 5.56 for SFSO, 4.14 for JRSC, and 4.00 for JSFB.

can be better characterized. The estimation of event magnitude would also be extremely important if DAS arrays were to be integrated in early warning systems for large earthquakes. The joint analysis of data recorded by DAS arrays with data recorded by conventional broadband seismometers has the potential of providing crucial information on the accuracy of the amplitude response of DAS arrays. Furthermore,

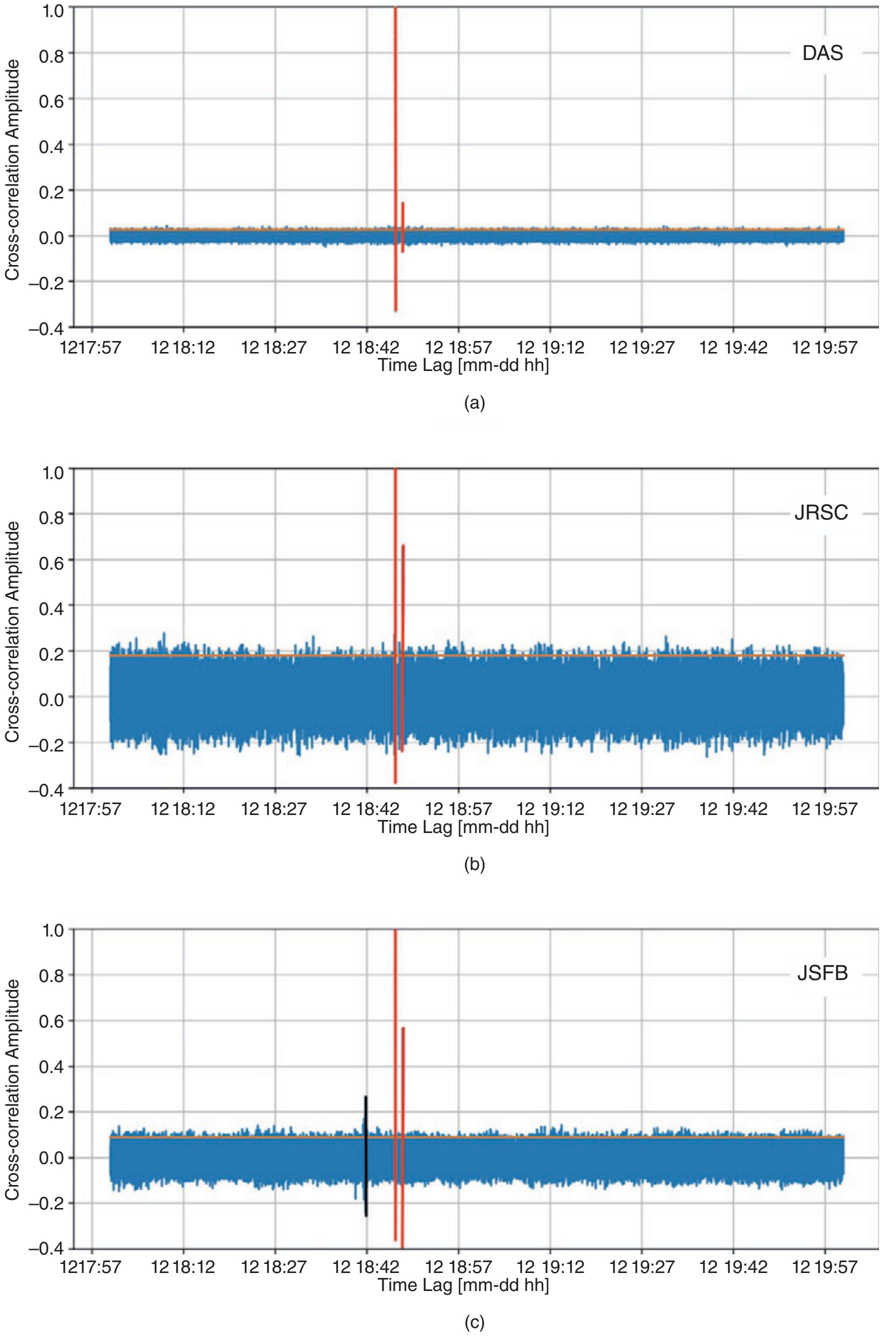

Figure 10.5 Results of template matching for data recorded by SFSO (a), JRSC (b), and JSFB (c) during a 24 hour time window in July 2017 that includes the time of the Felt Lake (*FeltLake #1*) that we use as a template and the immediate aftershock *FeltLake #2* event. True detected events are shown in red, whereas false positives are shown in black.

sequences of earthquakes with similar source mechanism but different magnitudes, such as the Felt Lake sequence, provide the opportunity to perform robust relative analysis across a range of magnitudes. Therefore, we analyzed the amplitudes observed on the data recorded by each recording system for all the Felt Lake events.

Table 10.2 summarizes the results of this analysis in terms of relative amplitudes; it lists the reciprocal of the ratios between the amplitudes measured for each event and the amplitudes measured for the strongest event (*FeltLake #1*). To compute the amplitudes for DAS recording, we selected a window containing the highest coherency arrivals that correspond to the data within

Table 10.2 Estimates of Relative Amplitudes of the Data Generated by Five Local Earthquakes Under Felt Lake as Recorded by SFSO DAS array and by the JRSC and JSFB Broadband Seismometers.

Event Name	SFSO	JRSC	JSFB
FeltLake #1	1.00	1.00	1.00
FeltLake #2	1.66	1.92	1.67
FeltLake #3	2.02	2.03	2.14
FeltLake #4	2.87	3.97	3.85
FeltLake #5	3.98	4.72	6.09

Note. The values shown in the table are the ratios between the amplitudes measured by each recording instrument for the strongest event (*FeltLake #1*) and the other events, respectively.

the orange rectangles shown in Figure 10.3. The length of the windows was chose to maximize the amount of coherent energy used for calculation. We then removed the data samples with absolute amplitudes lower than the 80th percentile and computed the sample-by-sample ratios for all the remaining data samples and then averaged all these sample-by-sample ratios. We used the same algorithm for the broadband instruments starting also from the data included in the orange rectangles in Figure 10.3, with the exception that we first detrended the data by subtracting their median value to remove the effects of the very low frequency noise.

The amplitude ratios monotonously increase from *FeltLake #2* to *FeltLake #5* consistently for all the instruments. For the two strongest events (*FeltLake #2* and *FeltLake #3*), the ratios for SFSO are in broad agreement with ones measured by the two broadband seismometers. For the two weakest earthquakes (*FeltLake #4* and *FeltLake #5*), the ratio is lower for SFSO than that for JRSC and JSFB. One possible explanation is that nonlinear phenomena occured in the coupling between the fiber cable and the ground with stronger events, such as slippage of the fiber cables with respect to the ground. The slippage reduced the sensitivity of the DAS array for those events and consequently reduced the ratios between the strongest events and the weakest events. Another possible explanation is that the source mechanism was slightly different and caused different variation in amplitudes on the data recorded by DAS than on the data recorded by seismometers (based on which the magnitude was estimated) because of different directivity between the instruments.

10.4. CONTINUOUS MONITORING OF NEAR-SURFACE CONDITIONS BY INTEFEROMETRY

Another possible game-changing application for DAS recording based on telecomunication infrastructure is enabling the production of high-resolution maps of near-surface parameters using seismic inteferometry. Furthermore, since the fiber cables are permanently installed, these maps can be continuously updated in a time-lapse sense. Depending on the local seismicity of the recording area, inteferometry can be applied either by exploiting ambient seismic noise to produce virtual source gathers or by using repeatable discrete events to perform intra-array tomography using time delays estimated by cross correlation. Luckily, the SFSO is situated in an area where both methods are possible. Low-frequency ambient noise is generated by natural sources (ocean waves in the nearby Pacific Ocean) and anthropogenic sources (vehicles' traffic). In addition to the natural seismicity continuously shaking the San Francisco Bay Area, an active quarry located about 13.3 km south of the Stanford campus generates repeatable events on a weekly basis. In the following two subsections, we present and discuss time-lapse interferometric results using both ambient noise and quarry blasts.

10.4.1. Time-Lapse Inteferometry Using Raleigh Waves Synthesized by Ambient Noise

Martin in her PhD thesis (Martin, 2018) describes conceptual foundations for applying ambient-noise inteferometry to data recorded by a DAS array. She discusses how the results of interferometry can be affected by the directivity of DAS systems that record only the longitudinal component of the strain sensor (at least when using conventional telecomunication cables). The data recorded by horizontal DAS arrays, such as the SFSO array, are therefore well suited to be used for interferometric synthesis of Rayleigh waves propagating along straight segments of the array (Dou et al., 2017), but are more challenging when we want to perform noise interferometry across parallel or orthogonal segments and/or synthesize Love waves (Martin, 2018; Martin & Biondi, 2017, 2018).

Interferometry results shown in Martin (2018) demonstrate that the SFSO array records data with sufficiently high sensitivity to be used for time-lapse noise interferometry of Rayleigh waves. The left column in Figure 10.6 shows the results of applying cross-coherency to data recorded along one of the north-south segments (segment labeled r2 in Figure 10.1) of the array to generate virtual source gathers with the source located in the middle of the segment. Each of the virtual source gathers was computed by applying cross-coherency to 1 month of recording. Starting from the top, the panels show the results produced from processing data sets that were recorded 6 months apart in September 2016, March 2017, September 2017, and March 2018, respectively. All the gathers contain coherent surface wave arrivals that could be used for estimating time-varying profiles of the

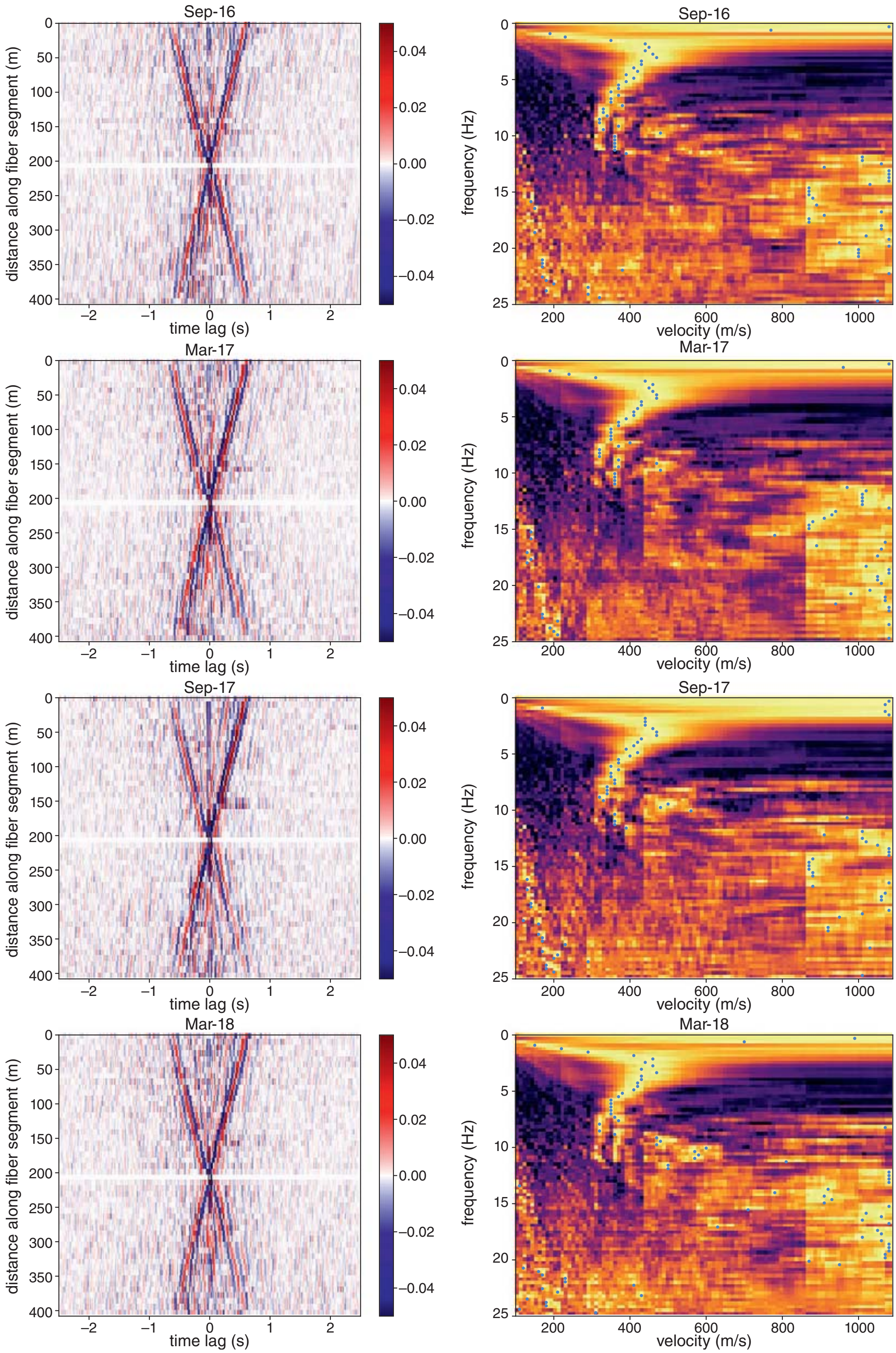

Figure 10.6 (Left) Virtual source gathers computed by cross-coherency applied to 1 month of data recorded along one of the north-south segments of the array. (Right) Dispersion images corresponding to the virtual source gathers on the left. Yellow denotes more energy traveling at a particular frequency and velocity. Dark areas have less energy. Dots mark frequency-wise peak velocities.

near-surface parameters by conventional surface wave dispersion analysis.

The right column in Figure 10.6 shows the horizontal phase velocity vs. frequency spectra corresponding to the gathers shown on the left. Coherent energy peaks can be picked from all these panels from about 1.5 Hz to about 8 Hz. The lower end of the spectrum is likely illuminated by noise coming from the ocean, whereas the higher end is likely to be generated by vehicle traffic. We observe consistent trends of velocity decreasing with frequencies starting at about 500 m/s at low frequencies and ending at about 350 m/s at higher frequencies, indicating velocity increase with depth. As discussed by Martin (2018), these results are consistent with geotechnical surveys conducted on the Stanford campus with active sources.

10.4.2. Time-Lapse Interferometry Using Surface Waves Generated by Quarry Blasts

In areas of substantial natural seismic activity, such as the San Francisco Bay Area, we can also use surface waves generated by discrete detectable events to perform interferometric measurements of travel times between receivers of a DAS array. The potential advantage of using discrete events is that their frequency band might be broader than using either natural or anthropogenic ambient noise; 15 Hz is probably the highest frequency at which traffic noise can be used (Chang et al., 2016). Furthermore, the theory of ambient-noise interferometry relies on the assumption that the ambient noise propagates in all directions. When this assumption is violated in practice, the accuracy of the kinematic measurements extracted from the arrivals synthesized in virtual source gathers by cross-correlation or cross-coherency might be negatively affected. In contrast, when we use discrete events we know their arrival directions, and we can take them into account to avoid biases in parameter estimates.

Fang et al. (2018) recently showed an example of time-lapse interferometric measurements of time delays across the SFSO DAS array using the arrivals from dynamite blasts generated at a quarry located about 13.3 km south of the Stanford campus. The authors used quarry blasts because they were repeatable with a predictable time interval and thus easy to extract from the continuously recorded data. However, similar methods could be used using repeatable natural earthquakes, such as the sequence occurring under Felt Lake, as shown in Figure 10.3.

Figures 10.7 and 10.8 show the time-lapse results of applying a normalized cross correlation to the data recorded at Channel #27 (channel numbers are marked on the map shown in the left panel of Figure 10.1) with the data recorded by many receivers located along two

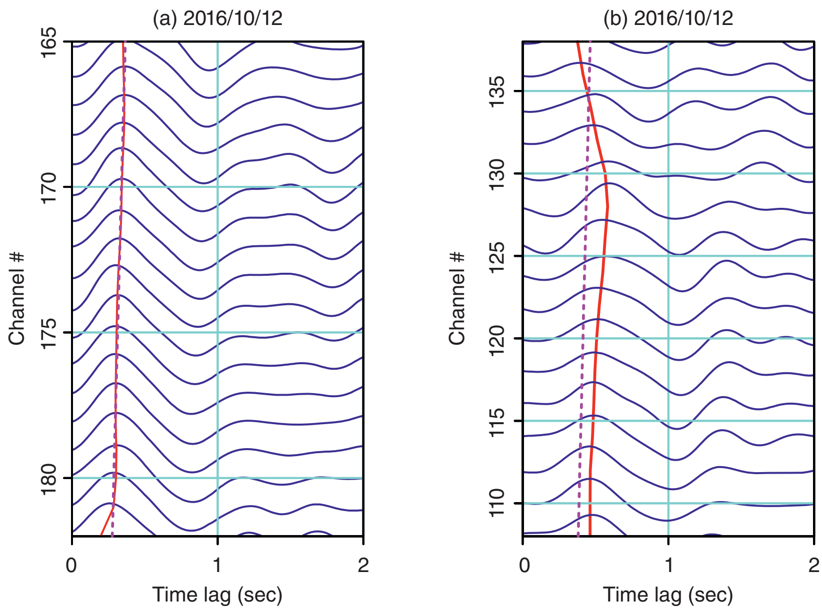

Figure 10.7 Cross correlations between data recorded by Channel #27 and (left) data recorded by Channel #165–Channel #183 and (right) Channel #108–Channel #136 (subsampled by a factor of 2) on 12 October 2016. The solid red lines mark the time delays picked from the cross correlations, whereas the dashed pink lines correspond to modeled time delays computed assuming a constant reference velocity of 816 m/s. This figure was taken from Fang et al. (2018) with the permission of the authors.

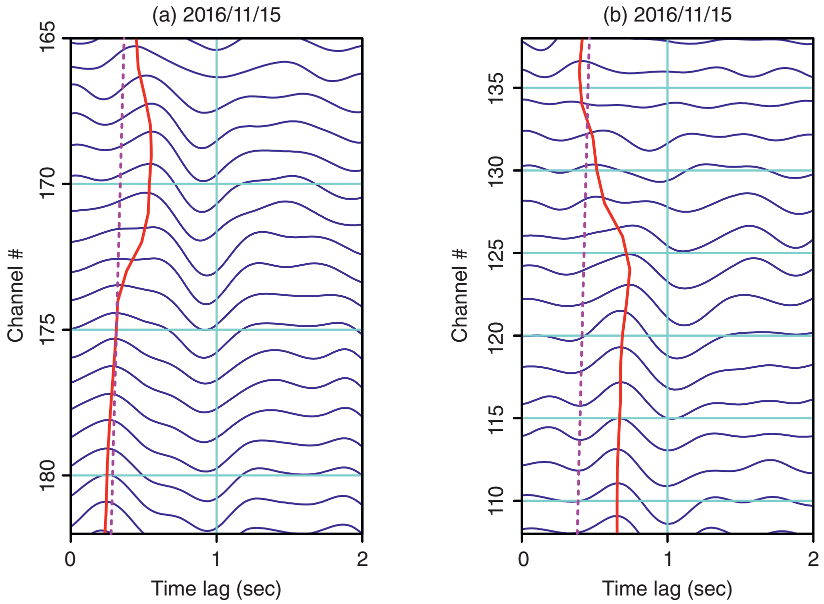

Figure 10.8 Cross correlations between data recorded by Channel #27 and (left) data recorded by Channel #165–Channel #183 and (right) Channel #108–Channel #136 (subsampled by a factor of 2) on 15 November 2016. The solid red lines mark the time delays picked from the cross correlations, whereas the dashed pink lines correspond to modeled time delays computed assuming a constant reference velocity of 816 m/s. Notice the increased time delays at Channel #108–Channel #125. This figure was taken from Fang et al. (2018) with the permission of the authors.

different segments of the array: Left panels correspond to the segment between Channel #165 and Channel #183 and right panels correspond to the segment between Channel #108 and Channel #136. Figure 10.7 shows the results obtained from data recorded on 12 October 2016, whereas Figure 10.8 shows the results obtained from data recorded about a month later, i.e., on 15 November 2016. The solid red lines in Figures 10.7 and 10.8 show the time delays picked from the cross correlations, whereas the dashed pink lines correspond to modeled time delays computed assuming a constant reference velocity of 816 m/s. The recorded surface waves from the quarry blasts were low frequency and the data were band-passed between 0.25 and 2.5 Hz before processing; therefore, the time resolution of the time-lapse results is limited.

During the intervening month between the two quarry blasts, construction proceeded in the excavation of a deep hole to build the foundations for a new building. The construction area is clearly visible at the southwest of the location marked as Channel #108 in Figure 10.1. The time delays between the virtual source and the receiver substantially increase for the receivers behind the construction area (right panels in Figures 10.7 and 10.8). In contrast, the time delays are substantially less affected for the receivers that are in front of the construction area (left panels in Figures 10.7 and 10.8).

10.5. IS THE COUPLING BETWEEN CABLES AND THE GROUND THE LIMITING FACTOR?

When exploiting existing telecomunication infrastructure to build a large DAS array, we can expect that most of the sensing cables are lying in PVC conduits buried in the ground, in a similar configuration to the one of our experiment at Stanford (Ajo-Franklin et al., 2019). Forward looking at the future, and at the possibility of building much larger arrays than SFSO, a crucial question is whether the suboptimal coupling between the cable and the ground will turn out to be the paramount factor limiting the sensitivity, and thus the usefulness, of DAS arrays. We can expect the "effective sensitivity" of arrays to improve, thanks to the increasing number of virtual sensors and laser interrogators' technological advancements, but if we want to exploit existing telecommunication infrastructure, we cannot expect the basic cable/conduit configuration to change in the medium-term future.

To start answering this important question, we recorded data using two different interrogators for a week in October 2017. The interrogators recorded data using two different fiber strands, but these two strands were packaged in the same cable. We can therefore assume that the couplings of the two strands were similar, and assume that differences in data quality are related to the differences in sensitivity of the interrogators, not in couplings. Consequently, if we observe improvements in SNR in the data recorded by the more advanced interrogator, we can infer that the coupling was not the only limiting factor in the SNR of the data recorded by the older interrogator. By induction, we can speculate that we will also be able to measure improvements in data quality when even more sensitive interrogators can be deployed.

The additional interrogator was a model ODH 4.0 by OptaSense Ltd., which is one generation more advanced than the ODH 3.1 we have been using for the continuous recording for more than 2 years. Gauge length and receiver spacing were set to be the same for both interrogators. On 10 October 2017, shortly before 1700 hours, we recorded a magnitude 4.1 earthquake classified as *Alum Rock* by the USGS. The epicenter was located to the southwest of SFSO at a distance of 46 km and the hypocenter was estimated to be at a depth of 9.7 km.

The left panel of Figure 10.9 shows the normalized spectra of the data recorded by the ODH 3.1 interrogator (blue line) and the ODH 4.0 interrogator (red line) for the *Alum Rock* event. Over the whole bandwidth, the spectra are quite different, making the analysis more challenging. As expected from the specifications of the instruments (Karrenbach, personal communication), the ODH 4.0 interrogator has a stronger response at low frequencies. In contrast, above 10 Hz, the frequency spectra are very similar, including small local peaks in the spectra, such as the ones around 18.5 Hz (right panel in Figure 10.9).

Figures 10.10 and 10.11 show the data for interrogators ODH 3.1 and ODH 4.0, respectively. The narrower panels on the left show the *P* arrivals, whereas the wider panels on the right show the *S* and surface wave arrivals. In both figures, the time origin is the event time according to the USGS catalog for the *Alum Rock* event. Because of the time of the day (middle of afternoon rush hour), we can observe several strong arrivals with very low apparent velocity that corresponds to cars passing close to the array. In an attempt to compensate for the different spectral shape of the two data sets (Figure 10.9), we band-passed the data with a Butterworth filter before plotting them and before estimating SNRs. The *P* arrivals (left panels in the figures) were band-passed between 5 and 14 Hz; the *S* arrivals (right panels in the figures) were band-passed between 1 and 6 Hz. Visual comparison of the two figures shows that the waveforms are more coherent in the ODH 4.0 data than in the ODH 3.1 data. In particular, the first break of the *P* arrivals can be more easily interpreted in Figure 10.11 than in Figure 10.10.

Estimation of a meaningful SNR is challenging because of the nonstationary traffic noise visible in the data, but our estimates are consistent with the visual analysis of Figures 10.10 and 10.11. To estimate the SNR, we first muted the same "bad channels" from both recordings; these channels most likely correspond to poorly coupled virtual receivers (e.g., spooled in the manholes). We then selected 80 traces from the *P* arrivals (Channel #160–Channel #240) that were not affected by nonstationary traffic noise in both the "signal" window (shown in the figures) and the "noise" window (taken before the first break between 7.4 and 8.1 s, i.e., as long as the signal window). The signal and noise strengths were estimated as the average of the absolute value of the data in these windows. The resulting SNR was 5.259 for ODH 3.1 data and 6.723 for ODH 4.0 data, which is about 28% higher for the more sensitive interrogator. We applied the same procedure for estimating SNR for the *S* arrivals, except that we used only 20 traces (Channel #160–Channel #180) but longer windows (4.5 s, as long as the data plots in the figures). The resulting SNR was 98.32 for ODH 3.1 data and 115.4 for ODH 4.0 data, which is about 17% higher for the more sensitive interrogator. In both cases, SNR has improved with the more sensitive interrogator, suggesting that the ground coupling was not the only controlling

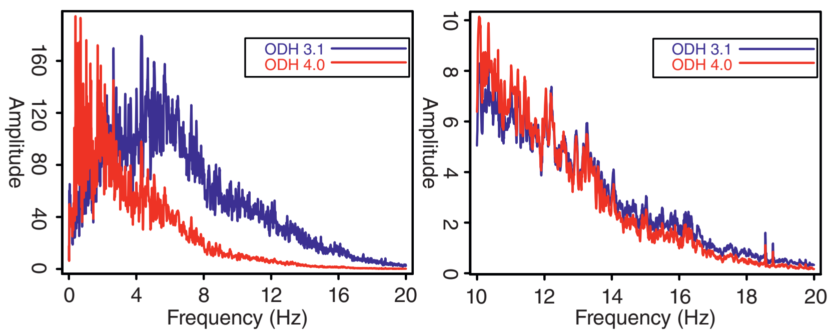

Figure 10.9 (Left) Frequency spectra of the data recorded by the ODH 3.1 interrogator (blue line) and the ODH 4.0 interrogator (red line) for the *Alum Rock* event normalized over the whole frequency range of the data. (Right) Frequency spectra of the data recorded by the ODH 3.1 interrogator (blue line) and the ODH 4.0 interrogator (red line) normalized above 10 Hz. The newer generation interrogator (ODH 4.0) shows stronger energy at the low end of the spectrum than the older one (ODH 3.1). In contrast, the frequency response above 10 Hz is similar.

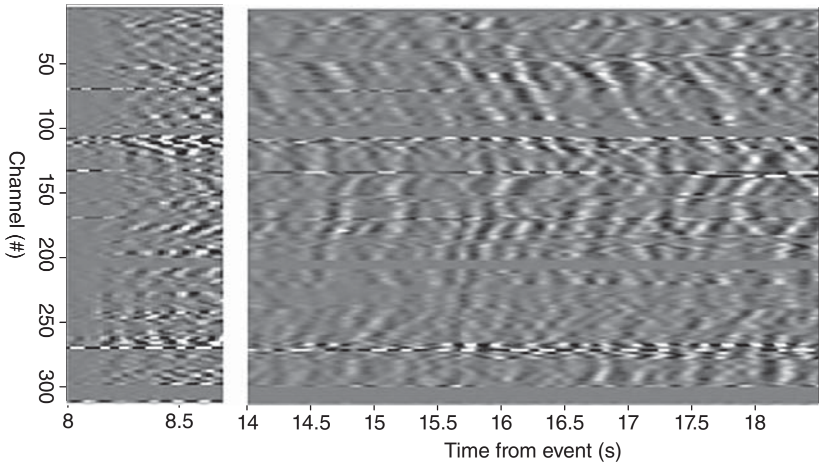

Figure 10.10 The *Alum Rock* event recorded by the ODH 3.1 interrogator. (Left) *P*-wave arrivals and (right) *S* and surface wave arrivals. The time origin is the event time according to the USGS catalog.

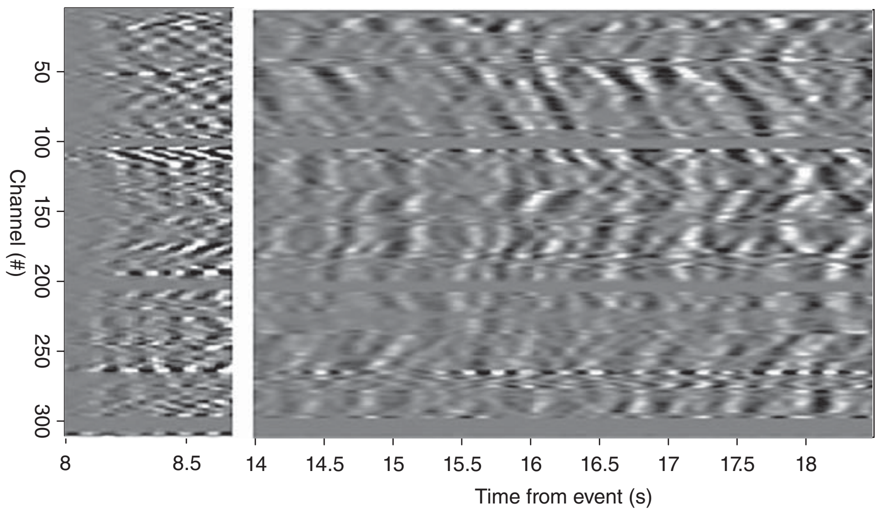

Figure 10.11 The *Alum Rock* event recorded by the ODH 4.0 interrogator. (Left) *P*-wave arrivals and (right) *S* and surface wave arrivals. The time origin is the event time according to the USGS catalog. The most visible difference between the data in this figure and in Figure 10.10 is the more coherent first break of the *P*-wave arrivals.

factor of the sensor sensitivity. Confirming the visual analysis, the *P* arrivals benefited more from the more sensitive interrogator, although the SNR of the *S* arrivals is much higher, because of a much stronger signal.

10.6. PROCESSING CHALLENGES FOR LARGE DAS ARRAYS IN URBAN ENVIRONMENTS

As manual inspection of large, complex data volumes is infeasible, seismic analysis and interpretation requires new processing tools for event detection, signal classification, data editing, and data visualization. Because DAS arrays may rely on preexisting fiber cable networks, even the simple determination of the actual virtual receivers' location may be challenging at large scales.

10.6.1. Analysis in Real Time of a Huge Stream of Data with Nonstationary and UnpredicTable Noise Sources

To identify a variety of common wavefield patterns, we performed unsupervised learning on a subset of the DAS data following the methodology developed by Huot et al. (2017) and Martin et al. (2018). We used clustering algorithms on 7 days of data to capture the daily variations in the noise field. We selected features from different wavelet attributes that capture the temporal and spatial variations of the signal. We computed these attributes by applying continuous wavelet transforms (CWTs) with a Morlet wavelet both along the temporal and spatial axes. CWT is frequently used in pattern recognition to decompose complex patterns into elementary forms by comparing the input signal to shifted and compressed or stretched versions of an analyzing wavelet. The Morlet wavelet is frequently used in signal processing because it is complex, symmetric, and smooth.

We then performed clustering on the computed features to group the repeating patterns. For computational efficiency, we selected the minibatch optimization implementation for *k*-means clustering. We experimented with different numbers of clusters and empirically settled on four main clusters, shown in Figure 10.12, as more clusters merely yielded subdivisions of these main clusters that were not always more interpretable. Once the main types of patterns are identified and have been grouped into clusters, the trained algorithm can be applied to new data to classify them within the identified clusters.

This approach allows us to automate data exploration with the aim of speeding up the overall ambient noise workflow and reducing human bias. The obtained clusters correspond to different types of seismic noise, automatically separating noise generated by cars from incoherent background noise without requiring any information related to the geometry of the array.

Figure 10.12 shows the results of our wave-mode classification; by examining cluster counts over time and over the channels, it appeared that the largest cluster (light gray) corresponded to ambient background noise. The small red cluster showed diurnal trends and appeared mostly on main roads open to cars, so it was interpreted as nearby vehicle noise. The yellow cluster behaved similarly to red, but was more spread in space. We interpreted it as noise associated with vehicle traffic but not necessarily showing the particular space-time pattern of nearby individual cars.

10.6.2. Automatic Identification and Muting of Bad Channels

The aforementioned methodology for transient noise sources can be extended to the automatic identification, quantification, and selective muting of bad channels. This approach allows us to mute channels with high noise levels, in order to remove biases from interferometric results (Section 10.4) or facilitate the automatic detection of weak events (Section 10.3).

10.6.3. Semiautomatic Determination of Virtual Receivers' Location in DAS Arrays

Mapping the recorded data to their spatial coordinates is a costly and time-consuming task, requiring tap tests and active surveys. This manual process is not scalable, and would be a potential bottleneck in broader deployment of urban DAS arrays built by exploiting telecommunication infrastructure. We developed a methodology combining a CNN classifier and a MDP to retrieve the location of the actual receivers directly from the recorded data.

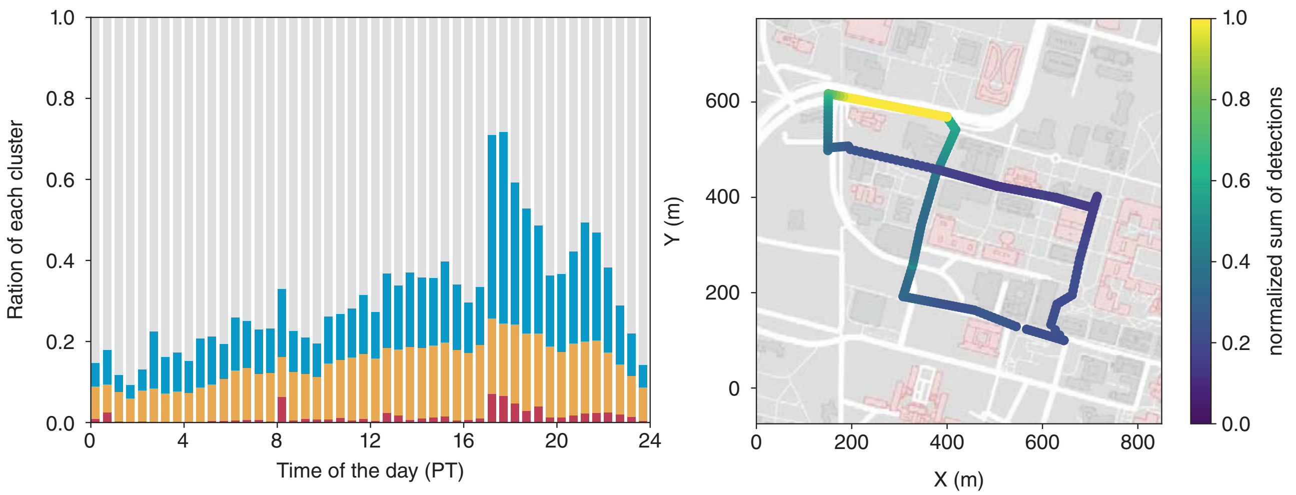

Figure 10.12 (Left) The different types of identified wave-mode clusters averaged over the full array for each hour of the day. (Right) The proportion of time windows that are identified as cars plotted for each channel, with the yellow segments containing higher counts of the red cluster (from left). The segment with the most cars is a major but low-speed route around the campus, and mostly north-south lines in the western half of the array have a moderate amount of slow traffic.

Using the geometry information inferred by tap tests as labels, we trained a CNN to determine whether each portion of data corresponds to a straight portion of the fiber, a turn, or a manhole. We used the first half of sensors as training data and the second half as unseen test data. We trained the neural network over a day of continuous data, divided into overlapping windows of five channels over 20 s. The labels were discretized, with turning angles ranging from 0 to 180° divided into 10° bins and an additional label for manholes. We then mapped each portion of the data to a normalized probability of being a straight line, a turn, or a manhole. However, when tested on unseen data, this classifier often predicted incorrect turning angles. Indeed, when the fiber turns, there is no way of telling directly from the data alone whether it is turning left or right.

With uncertain labels, geometry mapping is a challenging task, and the number of possible geometry mappings increases. To overcome this problem, we built an MDP to reconstruct the array geometry. MDP provides a mathematical framework for modeling decision-making in situations where outcomes are partly random and partly under control of a decision maker.

The MDP starts at the first receiver channel and determines the relative positions of all the contiguous channels until reaching the last channel. The successive states in the MDP represent the channels along the fiber. The transition probabilities from one channel to the next are governed by the probability distribution output by the aforementioned CNN classifier. When turning, we set an equal probability for turning left or right. We added a small exploration probability (0.1) to all turn directions and normalized all the probabilities. We constrained the mapping by defining a guiding path: A list of coordinates defining an initial guess as to where the fiber lies, with a certain error margin. We defined the MDP reward function as the mean square error distance between the computed path and the initial guiding path.

We solved the MDP using the value iteration algorithm. An example of one of the realizations is presented in Figure 10.13. While there still remains uncertainty in the mapping process, this methodology generates approximate mappings at low cost, since human input is limited to defining the guiding path. The proposed solution can compute the mapping of the channels within seconds, while it originally took several weeks of manual labor, iterating between performing tap tests and manually inspecting the data (Martin, Castillo, et al., 2017), to assign locations to the SFSO DAS array channels. Moreover, to this day, the manually assigned geometry may not accurately reflect some of the small features deviating from straight line paths. For future applications, we plan on adding additional functionalities to the MDP, such as the possibility of constraining the mapping process further by defining which receiver channel corresponds to manholes and sharp turns, in order to adapt the proposed algorithm to DAS arrays for which this information is available.

Figure 10.13 Array geometry automatically estimated by combining a convolutional neural network (CNN) classifier with a Markov decision process (MDP). The MDP generates approximate mappings at low cost (red), since human input is limited to defining the guiding path (green).

10.7. CONCLUSIONS

Large-scale arrays of fiber-optic seismic sensors that leverage existing telecommunication infrastructure have the potential of radically improving our ability to study, understand, and monitor seismic activity and fault systems under metropolitan areas prone to seismic hazards. However, before embarking on large-scale experiments, we must evaluate whether the challenges encountered when exploiting preexisting telecommunication infrastructure would prevent us from fully exploiting the potential of the technology.

Our analysis of the data that have been recorded for more than 2 years by the SFSO indicates that DAS seismic arrays could provide information that sparse arrays of conventional seismometers are unlikely to be able to provide at affordable costs. In previous publications, we analyzed several local and regional seismic events (natural and anthropogenic); in this chapter, we present a more detailed analysis of an earthquake sequence generated by a fault located in the Stanford foothills. We show how two weak events that were not cataloged in the USGS online database were detected using template matching applied to SFSO data. We also show that the signal amplitudes of SFSO data follow a trend similar to the one followed by the amplitudes of signals recorded by two nearby broadband seismometers. This result demonstrates that DAS arrays, such as SFSO, could be useful in determining magnitudes of local events.

The possibility of producing high-resolution time-lapse maps of near-surface properties is another application that makes the deployment of DAS arrays built using telecommunication infrastructure attractive. We showed that the SFSO data have a sufficiently high signal-to-noise characteristic to be used for computing repeatable virtual source gathers by noise interferometry and for performing velocity-dispersion analysis of Rayleigh waves generated by ocean waves or local freeways traffic. We also showed an example of time-lapse interferometry using arrivals from repeatable discrete events (quarry blasts) that manifest time-delay changes that can be related to nearby excavations of a large hole in the ground.

Our analysis of the data recorded by two laser interrogators of different sensitivity but interrogating two fiber strands sharing the same cable demonstrates that the suboptimal coupling between the fiber cable and the ground is not the only controlling factor determining data quality. The interrogator with higher sensitivity recorded measurably higher quality data than the lower sensitivity interrogator.

Important practical challenges related to effective use of DAS data recorded by large "virtual" arrays of telecomunication fiber cables are related to a huge stream of data that are potentially generated by such arrays. We show that machine-learning algorithms can be effectively applied to identify nonstationary noise sources, such as vehicles transiting on nearby roads. Typically these algorithms can perform real-time event identification, although they may require more computational time to be properly trained. We also show how a combination of CNN and MDP algorithms can be applied to the semiautomatic determination of DAS channels' physical locations, without requiring direct physical access to the fiber cables.

ACKNOWLEDGMENTS

The authors would like to thank Martin Karrenbach and Steve Cole with OptaSense Ltd. for all the help and support throughout the SFSO project. The authors would like to thank all the affiliate members of the Stanford Exploration Project (SEP) for financial support. Among SEP affiliates, the authors would like to particularly thank OptaSense Ltd. for making DAS recording equipment available. Eileen Martin was supported by DOE CSGF under Grant DE-FG02-97ER25308, Schlumberger Innovation Fellowship, and the SEP affiliate companies. The authors would also like to thank Gregory Kersey, Paul Narcisse, and Gary Gutfeld with the Fiber Team within Stanford IT Services for their help and patience. The Stanford Center for Computational Earth and Environmental Science (CEES) provided us with computing resources. The authors would also like to thank all authors of Fang et al. (2018) for granting their permission to include the results shown in Figures 10.7 and 10.8 in this chapter. Careful reviews by Zhongwen Zhan and an anonymous reviewer helped us to improve the final version of the manuscript.

REFERENCES

Ajo-Franklin, J., Dou, S., Daley, T., Freifeld, B., Robertson, M., Ulrich, C., et al. (2017). *Time-lapse surface wave monitoring of permafrost thaw using distributed acoustic sensing and a permanent automated seismic source*. Expanded Abstracts of the 87th Annual International Meeting of Society of Exploration Geophysicists (pp. 5223–5227).

Ajo-Franklin, J., Dou, S., Lindsey, N., Monga, I., Tracy, C., Robertson, M., et al. (2019). Dark fiber and distributed acoustic sensing: Applications to monitoring seismicity and near-surface properties. *Scientific Reports*, *9*, 1328. doi: 10.1038/s41598-018-36675-8

Ajo-Franklin, J., Lindsey, N., Dou, S., Freifeld, B., Tracy, C., Monga, I. et al. (2017). *Distributed acoustic sensing using dark fiber for near-surface characterization and broadband seismic event detection*. Abstracts of American Geophysical Union, Fall Meeting.

Biondi, B., Martin, E., Cole, S., Karrenbach, M., & Lindsey, N. (2017). *Earthquakes analysis using data recorded by the Stanford DAS array*. Expanded Abstracts of the 87th Annual International Meeting. of Society of Exploration Geophysicists (pp. 2752–2756). doi: 10.1190/ segam2017-17745041.1

Chang, J., de Ridder, S., & Biondi, B. (2016). High-frequency Rayleigh-wave tomography using traffic noise from Long Beach, California. *Geophysics*, B43–B53. doi: 10.1190/geo2015-0415.1

Dou, S., Lindsey, N., Wagner, A., Daley, T., Freideld, B., Robertson, M., et al. (2017). Distributed acoustic sensing for seismic monitoring of the near surface: A traffic-noise interferometry case study. *Scientific Reports*, *7*, 11620. doi: 10.1038/s41598-017-11986-4

Fang, G., Li, Y., Yue, D., Martin, E., & Yu, D. (2018). *Near-surface monitoring enabled by distributed acoustic sensing: An example of the Stanford Array data*. Expanded Abstracts of the 88th Annual International Meeting. of Society of Exploration Geophysicists (pp. 2677–2681). doi: 10.1190/segam2018-2998119.1

Huot, F., Ma, Y., Cieplicki, R., Martin, E., & Biondi, B. (2017). *Near-surface monitoring enabled by distributed acoustic sensing: An example of the Stanford Array data*. Expanded Abstracts of the 87th Annual International Meeting of Society of Exploration Geophysicists (pp. 5027–5032). doi: 10.1190/segam2017-17774369.1

Jousset, P., Reinsch, T., Ryberg, T., Blanck, H., Clarke, A., Aghayev, R., et al. (2018). Dynamic strain determination using fibre-optic cables allows imaging of seismological and structural features. *Nature Communications*, *9*, 2509. doi: 10.1038/s41467-018-04860-y

Li, Z., & Zhan, Z. (2018). Pushing the limit of earthquake detection with distributed acoustic sensing and template matching: A case study at the Brady geothermal field. *Geophysical Journal International*, 3, 1583–1593.

Lindsey, N., Martin, E., Dreger, D., Freifeld, B., Cole, S., James, S., et al. (2017). Fiber-optic network observations of earthquake wavefields. *Geophysical Research Letters*, *44* (23). doi: 10.1002/2017GL075722

Martin, E. (2018). *Passive imaging and characterization of the subsurface with distributed acoustic sensing* (Doctoral dissertation, Stanford University). Retrieved from http://sepwww.stanford.edu/doku.php?id=sep:research: theses:sep173

Martin, E., & Biondi, B. (2017). *Ambient noise interferometry across two- dimensional DAS arrays*. Expanded Abstracts of the 87th Annual International Meeting of Society of Exploration Geophysicists(pp. 2642–2646). doi: 0.1190/segam2017-17677759.1

Martin, E., & Biondi, B. (2018). *Eighteen months of continuous near-surface monitoring with DAS data collected under Stanford University*. Expanded Abstracts of the 88th Annual International Meeting of Society of Exploration Geophysicists (pp. 4958–4962). doi: 10.1190/segam2018-2997853.1

Martin, E., Biondi, B., Karrenbach, M., & Cole, S. (2017). *Continuous subsurface monitoring by passive seismic with distributed acoustic sensors: the "Stanford Array" experiment*. Expanded Abstracts of the First Workshop on "Practical Reservoir Monitoring" of the European Association of Geoscientists & Engineers. doi: 10.3997/2214-4609.201700017

Martin, E., Castillo, C., Cole, S., Sawsdee, P., Yuan, S., & Biondi, R. C. B. (2017). Seismic monitoring leveraging existing telecom infrastructure at the SDASA: Active, passive, and ambient-noise analysis. *The Leading Edge*, *36*(12), 1025–1031. doi: 0.1190/tle36121025.1

Martin, E., Huot, F., Ma, Y., Cieplicki, R., Cole, S., Karrenbach, M., & Biondi, B. (2018). A seismic shift in scalable acquisition demands new processing: Fiber-optic seismic signal retrieval in urban areas with unsupervised learning for coherent noise removal. *IEEE Signal Processing Magazine*, *35*(2), 31–40.

Shelley, D., Beroza, G., & Ide, S. (2007). Non-volcanic tremor and low frequency earthquake swarms. *Nature*, *446*, 305–307. doi: 10.1038/nature05666

Yu, C., Zhan, Z., Lindsey, N., Ajo-Franklin, J., & Robertson, M. (2019). The potential of DAS in teleseismic studies: Insights from the Goldstone experiment. *Geophysical Research Letters*, *46*, 320,1328. doi: 10.1029/2018GL081195

Yuan, S., Biondi, B., & Clapp, R. (2018). Earthquake detection through cross-correlation of the Stanford Fiber Seismic Observatory (SFSO) data. *Stanford Exploration Project Report*, *174*, 55–72.

11

Production Distributed Temperature Sensing versus Stimulation Distributed Acoustic Sensing for the Marcellus Shale

Payam Kavousi Ghahfarokhi, Timothy Robert Carr, Cody Wilson, and Keithan Martin

ABSTRACT

The MIP-3H well is a horizontal well in the dry gas area of the Marcellus Shale near Morgantown, West Virginia. During hydraulic fracturing, distributed acoustic sensing (DAS) and distributed temperature sensing (DTS) were recorded via a fiber-optic cable permanently attached to the outer part of the well casing. We process more than 2 years of DTS data, recorded during the production from May 2016 to August 2018, and continue to monitor DTS. Plotting DTS attributes with time shows that production varies and that gas production varies significantly among stages. We then compare these DTS attributes with the calculated energy attribute and energy variance attribute of DAS data that were recorded during the stimulation process. The resulted stimulation DAS energy uniformity (standard deviation) or DAS energy attribute may not be a simple indication of long-term stage production efficiency. A stage might show a uniform stimulation on DAS data; however, based on DTS data, it may turn into a relatively warming stage, suggestive of reduced production, during the life of the reservoir. In contrast, there are stages that showed poor performance with regard to stimulation DAS, but turned into cooling stages by time.

11.1. INTRODUCTION

11.1.1. Marcellus Shale Energy and Environment Laboratory

The multidisciplinary and multi-institutional team involved in the Marcellus Shale Energy and Environment Laboratory (MSEEL) works on geoscience, engineering, and environmental research in collaboration with Northeast Natural Energy, LLC, several industrial partners, and the National Energy Technology Laboratory of the US Department of Energy. The MIP-3H well is in the dry gas area of the core play area of the Marcellus Shale in Monongalia County, West Virginia. The Marcellus Shale spans 95,000 mi^2 (246,000 km^2) across six states in the northeastern United States, which makes it the most extensive shale gas play in North America (Carr et al., 2011; Wang & Carr, 2013). Currently, gas production in the Appalachian basin is dominated by the wells of the Marcellus Shale, which is the largest gas-producing region in the United States accounting for almost 30% of total US gas production (EIA, 2018a, b). The lateral of the MIP-3H well successfully landed and stayed in the target zone just above the Cherry Valley Limestone of the Marcellus Shale (Figure 11.1).

The lateral of the MIP-3H well was hydraulically stimulated in 28 stages by injection at an average of 8500 psi (58.6 MPa) to establish high permeable fracture pathways in the Marcellus Shale. The stimulation started from the

Department of Geology and Geography, West Virginia University, Morgantown, West Virginia, USA

Distributed Acoustic Sensing in Geophysics: Methods and Applications, Geophysical Monograph 268, First Edition.
Edited by Yingping Li, Martin Karrenbach, and Jonathan B. Ajo-Franklin.

DOI:10.1002/9781119521808.ch11

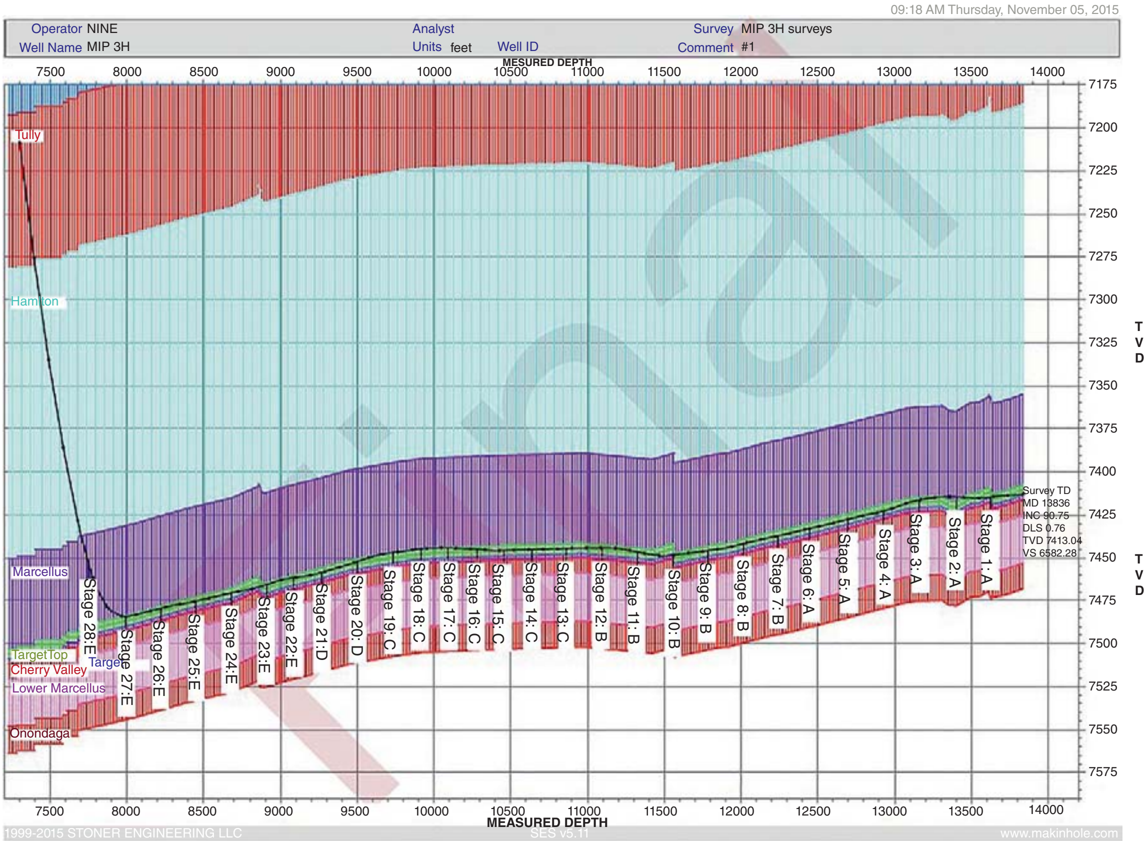

Figure 11.1 The MIP-3H well trajectory. The lateral landed and stayed in the target zone just above the Cherry Valley Limestone of the Marcellus Shale for almost 6,000 feet measured depth (1829 m). Due to the geometry of the formation, the toe of the well is approximately 60 ft true vertical depth (18 m) higher structurally than the heel of the well.

toe of the well and proceeded to the heel, stage by stage. Each stage is of around 200 feet (61 m) long and with four to five perforation clusters consisting of four to five shots per foot. Stages are 20–50 feet (6–15 m) apart with an average of 24 feet (7 m) between plug depths to the nearest cluster in the previous stage. The MIP-3H well is a dry gas well, and after initial production and outside of the cleanup associated with the production logging, it produces less than 10 barrels of water per day.

Shale reservoir heterogeneity presents a challenge for an efficient hydraulic fracture stimulation. Chorn et al. (2014) studied production performance for 100 wells drilled in the Barnett Shale by an operator; although the drilling and stimulation design were kept constant, a significant production variability was observed. The MIP-3H well was completed with a mix of geometrical completion and engineered completion, and with different fracturing fluids for each section of the well to test new completion techniques. Geometrical completion has been a common method for development of unconventional plays. In this method, heterogeneity along the lateral is not accounted for. Cipolla et al. (2011) implemented a statistical analysis on 100 production logs from geometrically completed horizontal wells; and only 60% of the perforation clusters were found contributing to production. Enhanced engineered completion design for several stages was undertaken in the MIP-3H well. Various geomechanical data acquired by well logging were used to optimize the stage length, cluster spacing, and treatment parameters. Stages were strategically placed in segments with similar gamma ray, minimum horizontal stress, and natural fracture intensity.

Figure 11.2 shows that the completion was carried out in five sections from the toe to the heel: Sections A, B, C, D, and E. Sections A and B were completed using a geometrical approach in which variations in geomechanical parameters, such as fracture closure stress and fracture intensity, are not accounted for. Two types of proppants were used for hydraulic fracturing of the MIP-3H well: 100 mesh sand and 40/70 white sand. Section A has around 35% 100 mesh proppants and 65% 40/70 white sand, while Section B has 75% 100 mesh proppants and

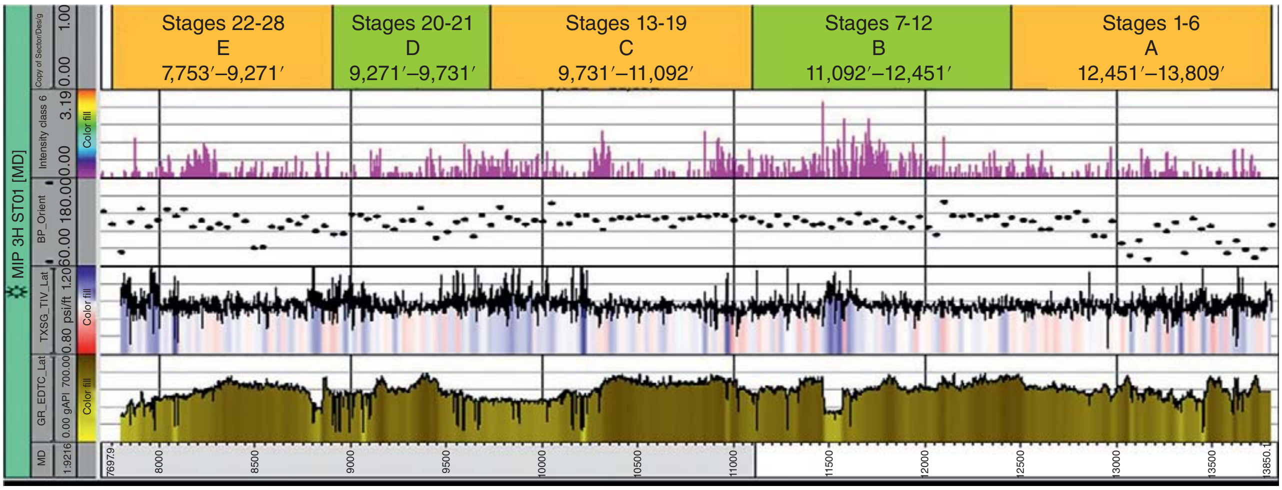

Figure 11.2 Logs acquired along the lateral of the MIP-3H well. Curves from bottom to top are gamma ray, closure stress, perforation phase, fracture intensity, and Sections A–E with varying completion strategies.

25% 40/70 white sand. The completion extends to Section C, in which completions were engineered. Stages and cluster spacing in Section C were designed by appraising geomechanical parameters from the well logs to set each stage with similar fracture closure stress, fracture intensity, and gamma ray. The proportion of proppants vary between stages in Section C: Stages 13, 14, 15, 17, and 19 have 35% 100 mesh while Stage 16 has 67% 100 mesh and Stage 18 has around 43% 100 mesh. In addition, a limited entry approach was undertaken by decreasing the number of shots per cluster to enhance stimulation efficiency (Ingram et al., 2014). In Section D, a new guar-free viscoelastic fracturing fluid was used in Stages 20 and 21. Section E, involving Stages 22–28, was completed using various engineered approaches with variations in pumping schedule.

Wilson et al. (2016) analyzed natural fractures in the lateral of the MIP-3H well and the MIP-3H pilot well (the vertical well) and extracted the trends of the natural fractures. A single-fracture set oriented in N79°E was observed in the lateral of the MIP-3H well. The image logs from the vertical MIP-3H pilot well showed two sets of fractures: An open-fracture set oriented in N57°E and a healed fracture set in N87°E (Figure 11.3). Preexisting

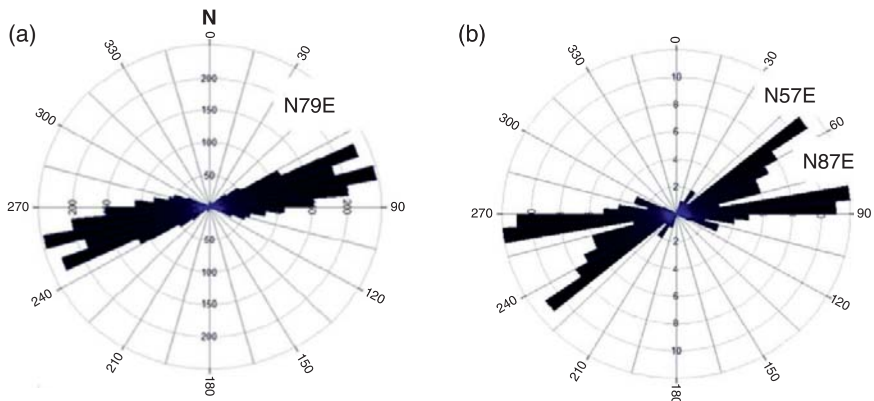

Figure 11.3 Rose diagrams of natural fractures (a) observed along the length of the lateral of the MIP-3H well (N = 1,640) and (b) in the vertical pilot well (N = 91). Fractures observed in the vertical well consist of 21 open fractures in the N57 E cluster and 70 healed fractures mainly concentrated in the N87 E cluster with a smaller fraction falling in the N57 E cluster. Source: Courtesy of Wilson et al. (2018).

natural fractures can affect the stimulation process even when they are healed fractures. Gale et al. (2008) analyzed the natural fractures of Barnett Shale core from Pecos County, Texas. The tensile testing on the cores showed failure along fractures even though fractures were sealed. They proposed that the Barnett Shale in the Fort Worth Basin has sealed natural fractures that affect hydraulic fracture propagation as a result of reactivation of natural fractures and hence hydraulic fracture propagation at natural fracture tips. The computerized tomography (CT) scan of the vertical core from the MIP-3H pilot hole shows several natural fractures in the Marcellus Shale that are mineral filled (Figure 11.4). More than 1,500 resistive (healed) fractures were documented from the wireline image logs in the lateral of the MIP-3H well.

We focus on geometrically completed Stage 10 as it has 160 natural fractures and 2 faults. Wilson et al. (2018) showed that most of the fractures undergo shear failure when pore pressure increases. Kavousi et al. (2017) showed that there is an inverse relationship between fracture intensity and DAS energy for the engineered stages in Section C. Stages with more natural fractures showed less vibration, while stages with a smaller number of fractures caused more vibration of the fiber-optic cable in the MIP-3H well. However, this relationship does not exist in other sections of the well. Kavousi et al. (2017) suggested that engineered stages show a more uniform stimulation in clusters than geometrical stages. A more uniform vibration (strain) in all clusters across a stage is assumed to be a sign of successful fracturing, while an individual quiet cluster within a successful stage is interpreted as a poorly stimulated or even a failed cluster, which could affect production or Estimated Ultimate Recovery (EUR). They suggested that the engineered stages could be more productive than geometric stages. Here, we process more than 2 years of DTS data to compare them with stimulation DAS data to better understand long-term behavior of stimulated stages and completion strategies.

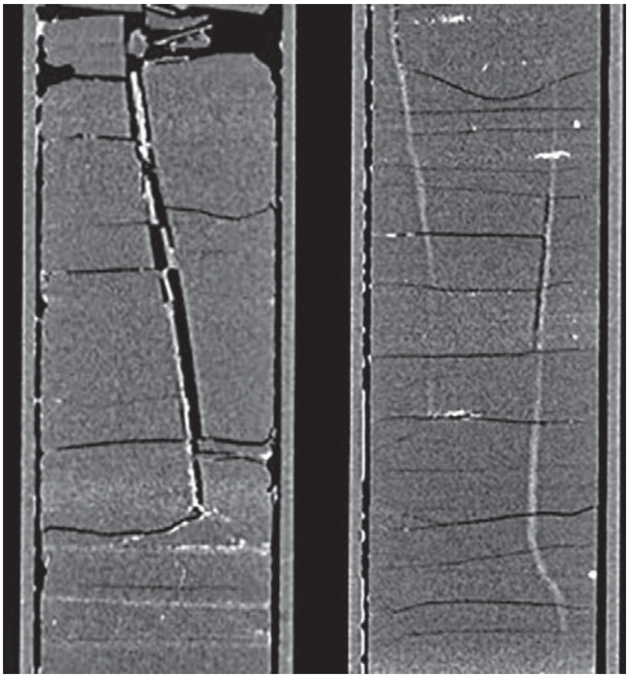

Figure 11.4 Vertical CT scan of the MIP-3H pilot core (7508–7509 feet). Vertical fractures filled with calcite. Horizontal white areas are heavy minerals.

11.1.2. Fiber-Optic Technology and its Applications

Traditionally, surface pressure and subsurface pressure gauges, well head rates, and radioactive tracers are the only monitoring tools for completion engineers during hydraulic fracturing (Molenaar et al., 2012). Shallow depth of investigation limits the application of the traditional techniques in complex reservoirs (Molenaar et al., 2012). The need for more robust diagnostic tools opened the way to the use of fiber-optic technology. Fiber-optic sensing technology has been applied to the oil and gas reservoirs from 1990s to monitor steam injection, injection profiling, acid injection profiling, and hydraulic fracture diagnostics (Glasbergen et al., 2010; Holley and Kalia, 2015; Karaman et al., 1996; Rahman et al., 2011; Sierra et al., 2008). An early application of fiber-optic technology was DTS, which was only able to record the temperature. DTS is still widely used for unconventional oil and gas reservoirs to monitor the temperature in the subsurface during stimulation, production, or injection. DAS technology was later introduced to the industry to perform additional robust diagnostics of the subsurface (Molenaar et al., 2012).

A fiber-optic cable is composed of a light-carrying core, and a cladding, which provides the lower refractive index for total internal light reflection throughout the cable (Nath et al., 2005, 2006). A fiber-optic system emits laser pulses at 10 ns or less down the length of the optical fiber. Incident light pulses collide with the molecular and lattice structure of the fiber medium, and photons are scattered from the fiber medium. Most photons that collide with the atoms in the fiber medium are elastically scattered and have the same frequency and wavelength as the incident light. This energy preserved scattering, which is the strongest signal, and this scattering is called Rayleigh scattering. Brillouin scattering is an inelastic scattering that occurs when acoustic waves vibrate the fiber lattice at the molecular level and cause a fluctuation in density and hence affect the local refractive index of the optical fiber. Thus, the energy of backscattered light will be different than that of the incident light. This energy variation expressed as frequency and wavelength shift depends on both the local temperature and fiber-optic cable strain. Furthermore, a part of incident photons is scattered through the inelastic Raman effect, in which the scattered photon might be excited to a higher energy or lose energy to the fiber medium (Brown, 2006). Figure 11.5 shows that the Raman scattering energy shift is much higher than the Brillouin scattering. The scattered photon could gain energy from displacing the fiber molecules to a lower vibrational energy state (anti-Stokes scattering) or lose energy to the fiber medium molecules and raise them to a higher vibrational energy state (Stokes scattering). The energy of a photon is inversely proportional to its wavelength: Higher-energy anti-Stokes scattered photons have shorter wavelength than lower energy Stokes scattering. The intensity of the anti-Stokes Raman scattering is strongly dependent on the temperature, while the longer wavelength Stokes Raman signal is less temperature dependent. The ratio of these intensities is directly proportional to the temperature of the optical fiber at the point where backscattering takes place. In a DTS system, backscattered lights are filtered to remove the Rayleigh and Brillouin backscatters to evaluate the intensity ratio of Stoke and anti-Stoke Raman waves, while in a DAS system, the focus is on the Brillouin backscatters. The velocity of light in the optical fiber can be stated as:

$$v = \frac{c}{n} \tag{11.1}$$

where c is the speed of the light and n is the fiber refractive index, which is usually between 1.5 and 1.7 (Smolen & van der Spek, 2003). Thus, a 10 ns long laser will correspond to approximately a 2 m segment of the fiber, with a refractive index of 1.5. This will turn the optical fiber into a multipoint sensor for temperature and strain in the subsurface. This superiority over single-point temperature and strain measurement gauges has made fiber-optic technology an excellent downhole measurement tool.

11.2. METHODOLOGY

A permanent fiber-optic cable was attached along the outer part of the casing to record fiber strains (DAS) during stimulation of each stage and monitor the temperature around the fiber-optic cable (DTS). After the stimulation, the fiber-optic cable has been used only as a DTS system to monitor temperature at intervals of several times per day around the fiber. Gas production in horizontal wells is associated with a pressure drop and volume increase, which is therefore accompanied by a change in temperature. The Joule-Thompson effect describes the temperature change for a real gas or liquid when it is forced through a porous plug (throttling) in an adiabatic process (Roy, 2002). This temperature variation is governed by the Joule-Thompson coefficient (μ_{JT}) as:

$$\mu_{JT} = \left(\frac{\partial T}{\partial P}\right)_h \tag{11.2}$$

where T is temperature, P is pressure, and h is specific enthalpy (Çengel & Boles, 2008). The equation shows the rate of change of temperature vs. pressure, at constant enthalpy. During a sudden pressure drop, the sign of the μ_{JT} describes the temperature variation as:

$\mu_{JT} < 0$, temperature increase
$\mu_{JT} = 0$, temperature remains constant
$\mu_{JT} > 0$, temperature decreases

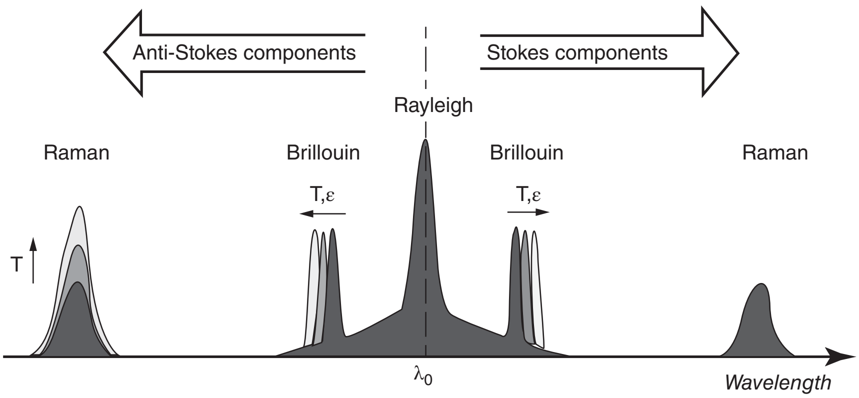

Figure 11.5 The incident laser is backscattered in different wavelength Raman and Brillouin waves; however, majority of the incident laser is backscattered with the same wavelength as the incident laser through Rayleigh scattering. Brillouin waves are sensitive to both temperature and strain. An increase in temperature (T) results in movement of the Brillouin waves and an increase in the anti-Stokes components of Raman waves. Source: Mishra et al. (2017).

Pinto et al. (2013) carried out a linear mixing approach to predict μ_{JT} for a natural gas, with methane as the major component, at various pressures and temperatures. Their study revealed a positive μ_{JT} for pressure ranges from 72.5 to 3625.9 psi at temperatures of −9.4°F, 35.6°F, 80.6°F, and 170.6°F. Brown (2006) suggested that the temperature usually decreases when gas enters the wellbore and increases when oil or water enters the wellbore. Wang et al. (2008) carried out analytical and numerical modeling and showed that the Joule-Thompson cooling (JTC) effect usually happens in gas wells except in very high bottom hole pressures of around 8000 psi where a warming effect might occur. A negative JTC effect (cooling) is expected to occur in tight gas reservoirs, such as the Marcellus Shale, which have significant pressure drawdowns close to the horizontal wellbores. The cooling effect for gas can vary between 2 and >20°F/1000 psi pressure drawdown; in contrast, water produces a warming effect of around 3°F/1000 psi (Johnson et al., 2006).

We processed over 2 years of DTS data, around 1.2 million data points, in a waterfall plot to show dynamic nature of subsurface temperature. The MIP-3H well along with the three other wells on the pad is capable of providing all the gas for the City of Morgantown, and with no other market outlet, production varies with change in consumption due to temperature. Consequently, gas production is less in warmer months than during winter. Figure 11.6a shows that DTS temperature has been changing as the gas production varies during time. The MIP-3H well achieved its maximum production in the last quarter of 2017 and began a natural decline, which was again interrupted due to warmer weather in the summer of 2018. Water production from the MIP-3H well has been less than 10 barrels per day, except during late winter of 2017 when, in order to clean out the well prior to production logging, it was washed with water and nitrogen foam.

Although temperature along the lateral varied significantly from day to day and seasonally with periods of relatively higher and cooler temperatures, there is a general cooling trend that is progressing from the toe of the lateral to the heel (decreasing measured depth).

We detrended the DTS, as shown in Figure 11.6, by subtracting average daily DTS along the entire lateral from the measured DTS. This removes the seasonal and daily trends induced in DTS data because of the changes in gas and water production. The resulted detrended DTS attribute is plotted by stage and shows that stages vary in relative temperature and change through time (Figure 11.7). In general, there is an increased contrast through time between the toe and the heel. In addition, geometric Stage 9 and, particularly, Stage 10 are warmer than the other stages indicating that gas production is lower and/or water production is higher than adjoining stages. The engineered stages of Section C (13–19) show cooler temperatures while that of Section D (Stages 20 and 21) with the new viscoelastic fracturing fluid are warmer. Much of this contrast is muted with continued production and appears to be related to decreased overall water production from the reservoir and its effect on the DTS. Again, we relate the DTS temperature attribute contrast to production efficiency and demonstrate that the production is very dynamic.

Of the 28 stages, Stage 10 appears, after significant production is established in the winter of 2016–2017, warmer than its adjacent stages and remains warmer (Figure 11.7). Using image logs, 2 faults and 160 natural fractures in Stage 10 were independently interpreted by a service company. Ghahfarokhi et al. (2018) studied this stage DAS data and microseismic data. They documented low-frequency (10–80 Hz) long-period events from microseismic and DAS data. They suggested that Stage 10 underwent long-period long-duration deformation during hydraulic fracturing. This deformation resulted in a cross-stage flow communication expressed as a warming in the previous stage (Stage 9) and lowered stimulation efficiency.

The production DTS provides the opportunity to compare the long-term behavior of the reservoir with its stimulation efficiency measured by available DAS data. To conduct this analysis, we processed DAS data of 28 stages by calculating energy attribute for each stage. The lateral of the MIP-3H well is covered by 493 traces in the DAS data with a spacing of 16.74 feet and a gauge length of 64 feet. There is one SEG-Y file for every 30 s of stimulation process. Each SEG-Y file has 493 traces with a sampling frequency of 2000 Hz. Each trace is a signal with 30 s length and 60,000 samples. The energy of a discrete signal can be calculated as:

$$E = \sum_{n=-\infty}^{\infty} |x(n)|^2 \tag{11.3}$$

A 30 s window energy attribute for DAS SEG-Y files can be calculated as (Kavousi et al., 2017):

$$E_{ik} = \sum_{j=1}^{m} x_k(j)^2 \; i = 1\ldots\text{number of DAS traces,} \quad k = 1\ldots\text{number of SEG-Y files} \tag{11.4}$$

where $x_k(j)$ is sample j from m samples in trace i from k^{th} SEG-Y file. Figure 11.8 shows waterfall plots of the calculated energy attribute for selected stages from the geometric Section B (Stages 5 and 10) and Stage 18 from engineered Section C, Stage 21 from Section D, and Stage 25 from Section E.

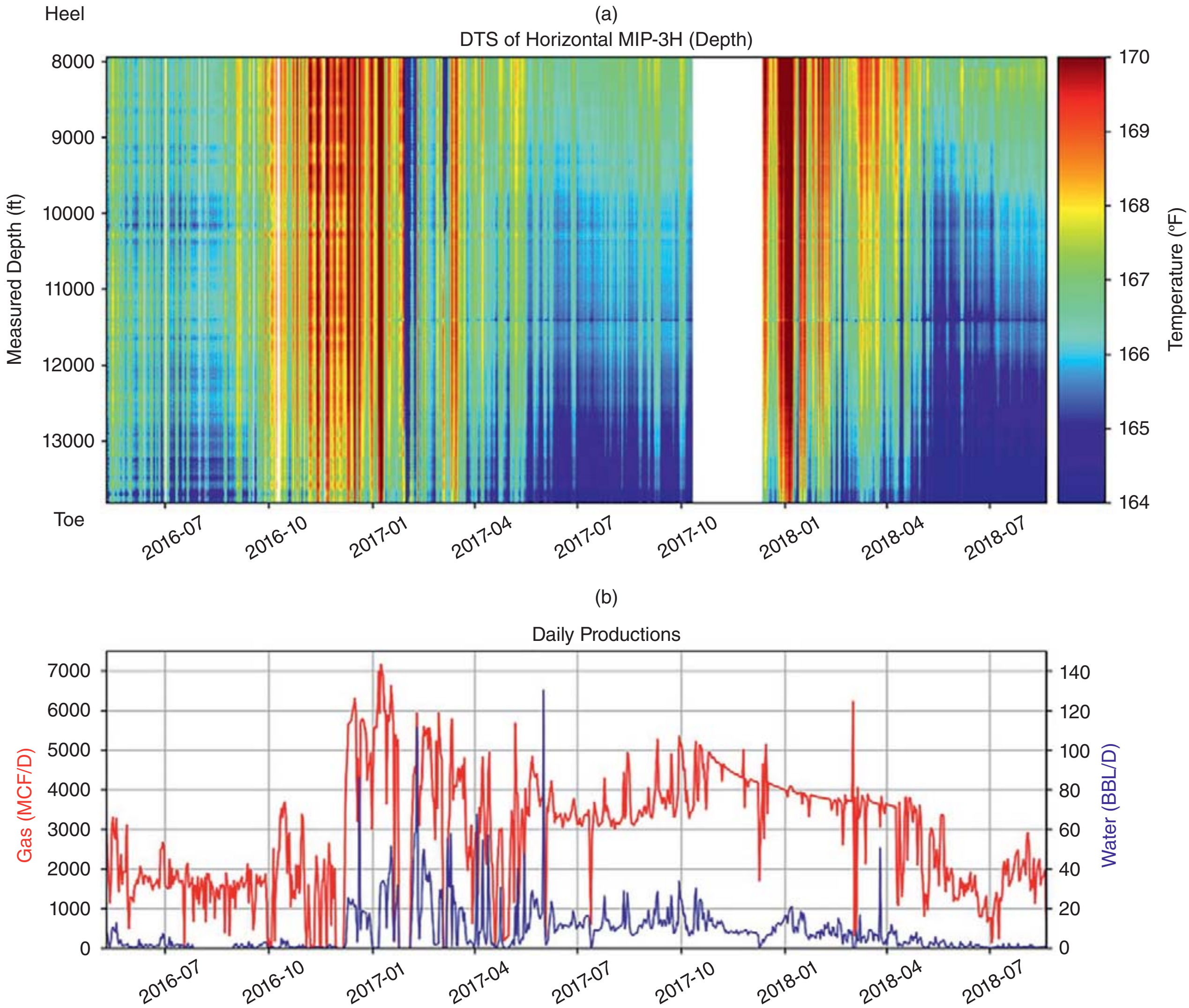

Figure 11.6 (a) Upper plot shows the measured DTS from May 2016 to May 2018 from the heel (lower measured depth) to the toe (greater measured depth) of the lateral of the MIP-3H well displayed as a waterfall plot. (b) Gas and water production shows seasonal variation between warmer and colder time periods, and the lower water production except during the late winter of 2017 when the well was being cleaned out with water and nitrogen foam for production logging. The large white section corresponds to missing data because of equipment issues.

Vertical distribution of microseismic events was visualized for Stages 7–28. Figure 11.9 shows that Section C of the well (Engineered Completion) has more events in the target zone than their sections. This finding is consistent with more uniform DAS energy in Engineered Completion stages in Section C.

11.3. RESULTS AND DISCUSSIONS

The DAS energy attribute was calculated and normalized by the service company for all perforation clusters in the MIP-3H well. Figure 11.10a shows a normalized DAS energy score for all clusters in the MIP-3H well. Geometric stages in Sections A and B have individual clusters with much higher energy than other sections, while clusters in the engineered Section C show more uniform energy distribution. Clusters in Sections D and E were engineered, but subjected to varying completion processes, such as use of a specialized fracturing fluid and pumping schedules. Energy standard deviation of each stage is calculated to show how uniform a stage DAS energy is on its clusters (Figure 11.10b). Stages with higher standard

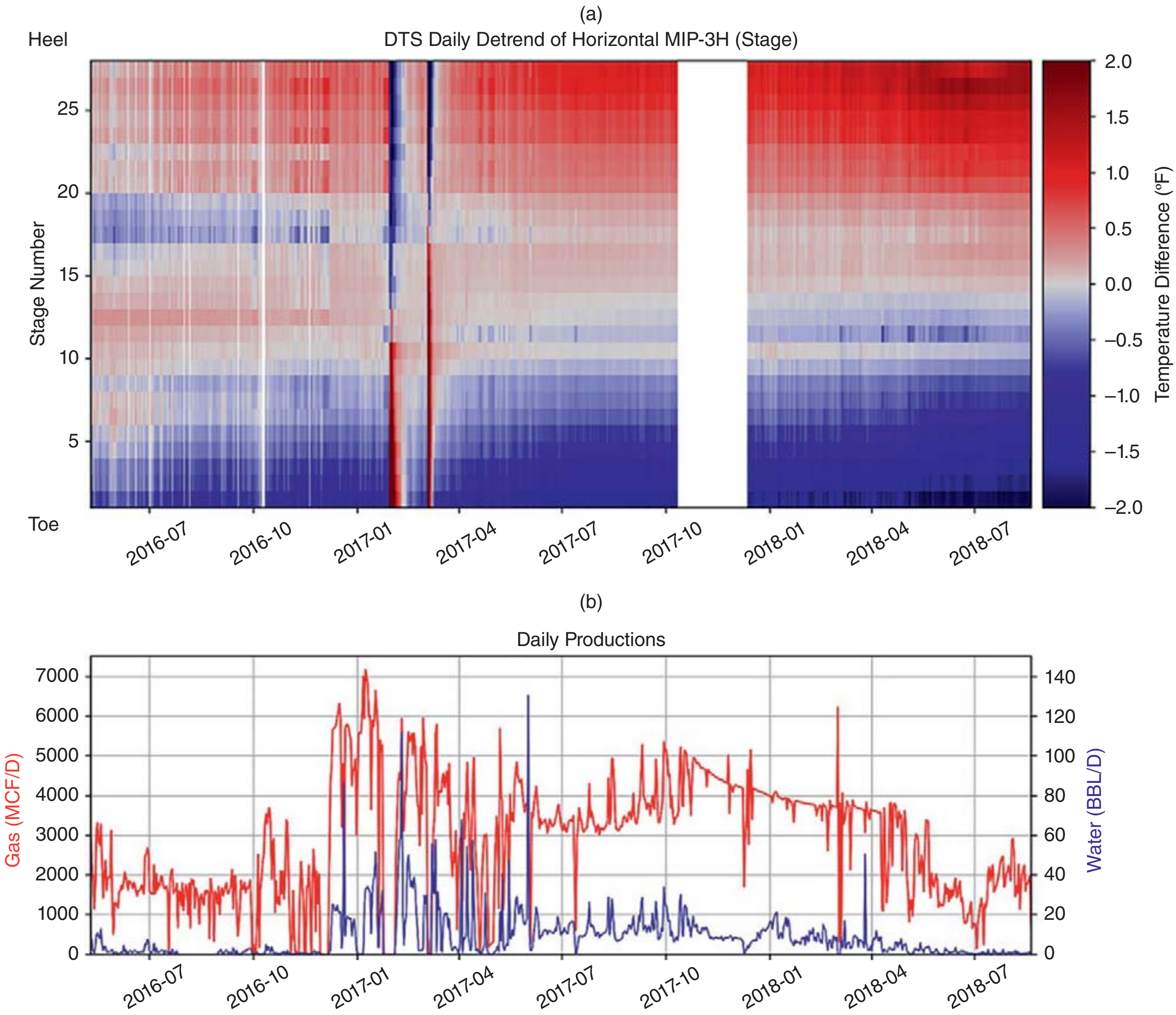

Figure 11.7 The detrended DTS attribute is averaged to the stage scale. The two vertical anomalies between January and April 2017 show the time that the MIP-3H well was washed with water and then with nitrogen foam prior to production logging.

deviations have less uniform energy distributions over their clusters. The analysis of DAS data suggests that engineered stages had active clusters during the stimulation (e.g., Figures 11.8c–d). In contrast, geometric stages (Sections A and B) stimulation efficiencies were interpreted to be lower than engineered stages because of increased heterogeneity of DAS energy over their clusters (e.g., Figures 11.8a and 11.8b). The DTS data indicate that in this toe-up well, the stages at the toe are cooler than that at the heel, and this trend is increasing with time of production. However, geometric Stages 10–12 are warmer than the adjacent engineered Stages 13–19. We suggest that this trend is the result of the toe-up geometry of the well and the effect of increased water production recognized on production logs from Stage 10 to Stage 12 and pooling at the heel. The single production log did not show any recognizable gas production trend.

The detrended DTS temperature attribute and DTS detrended attribute show that the subsurface temperature does not remain constant during the production life of the reservoir and is very dynamic. Some stages turn from warming to cooling and vice versa. This behavior can also be seen in Figure 11.7 where geometric stages at the toe switch from relative warming to cooling through time and engineered stages at the heel switch from cooling to warming. Although geometric stages have nonuniform DAS energy attribute, they have individual clusters with

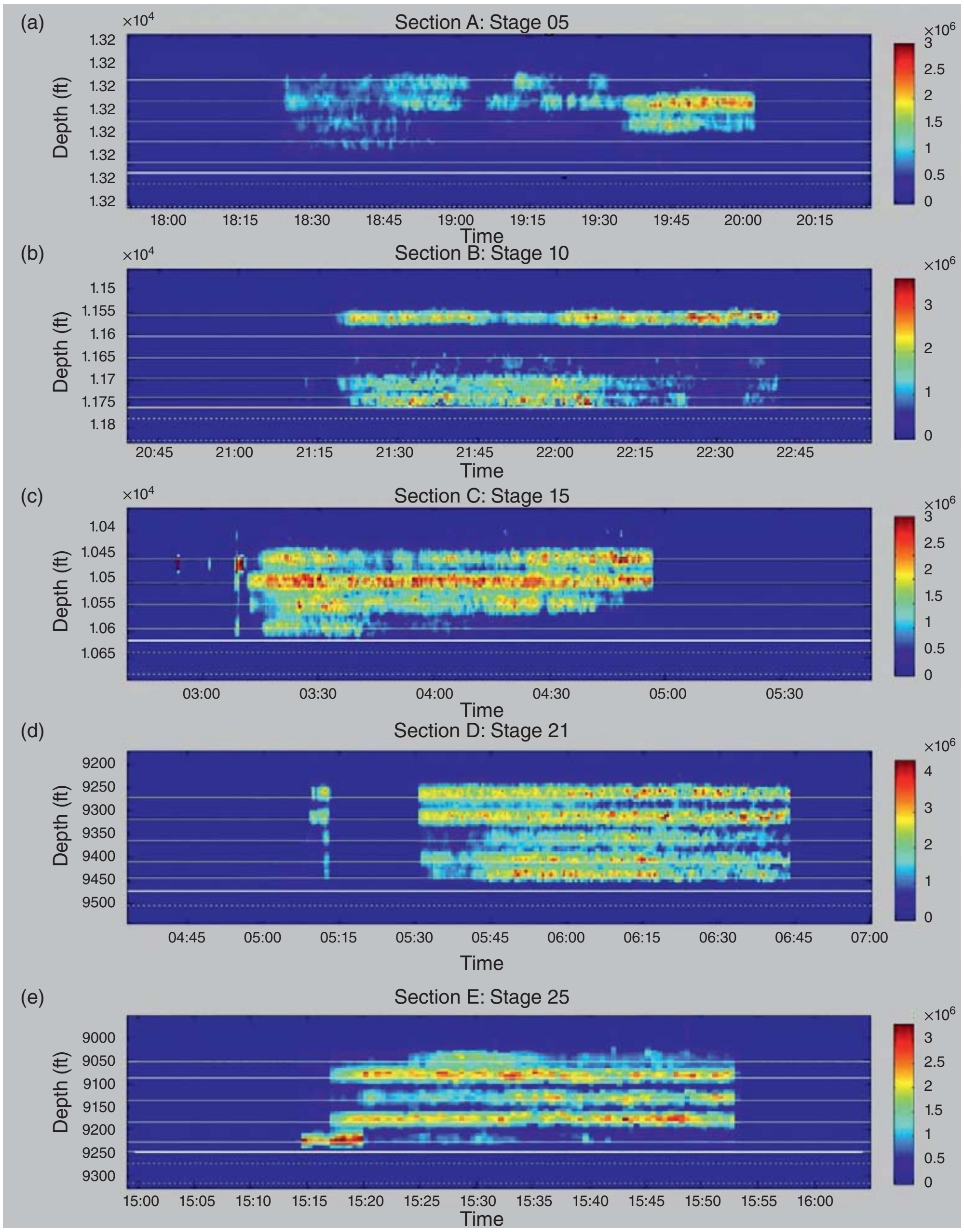

Figure 11.8 Energy attribute for Stage 5 (a) and Stage 10 (b) stimulation from the geometric completions. Energy attribute for Stages 15, 21, and 25 stimulation from the engineered stimulation using different completion approaches. It appears that engineered stages show higher energy more evenly distributed across the clusters.

higher energy than Sections C, D, and E (Figure 11.10). The geometric stages are not initially cool, but start to cool with time. One possible explanation could be changes in the fluid flow regime in the MIP-3H well, which we will investigate with additional production and modeling as production constraints are reduced. However, Heckman et al. (2013) analyzed gas production of several ultralow permeability shale reservoirs in the United States, and showed that dry gas wells usually start to have linear flow between 3 and 6 months after stimulation. In the linear flow, fractures could show reduced interference with each other, and the flow regime would change to stimulated reservoir volume (SRV) flow. SRV flow usually starts within 9–36 months after the stimulation. Then, the reservoir might end up in a pseudo-elliptical flow regime (flow from matrix to collection of fractures). The MIP-3H well

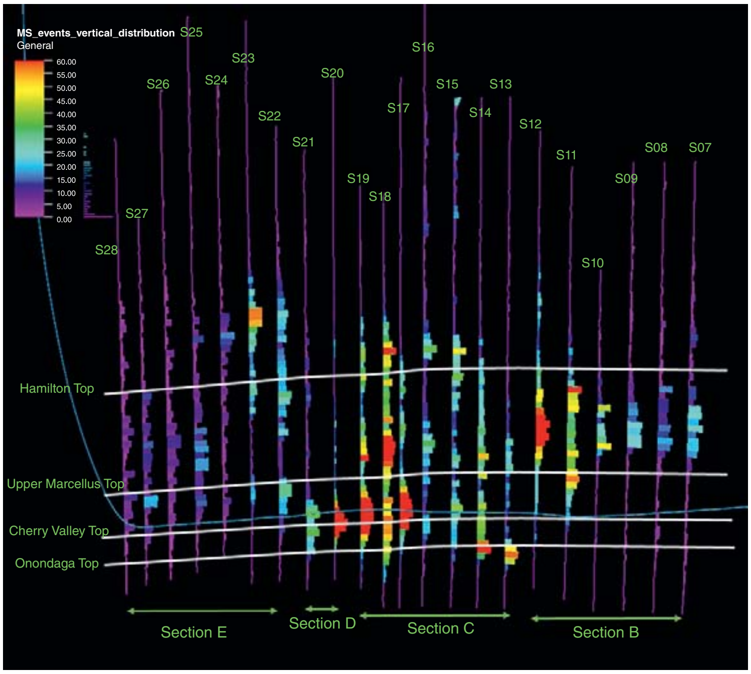

Figure 11.9 Microseismic events' distribution is illustrated for Stages 7–28 in vertical depth above the center of corresponding stage. Microseismic events for Stages 1–6 were not recorded. Warmer color means more microseismic events. Section C has the most concentration of microseismic events in the target zone.

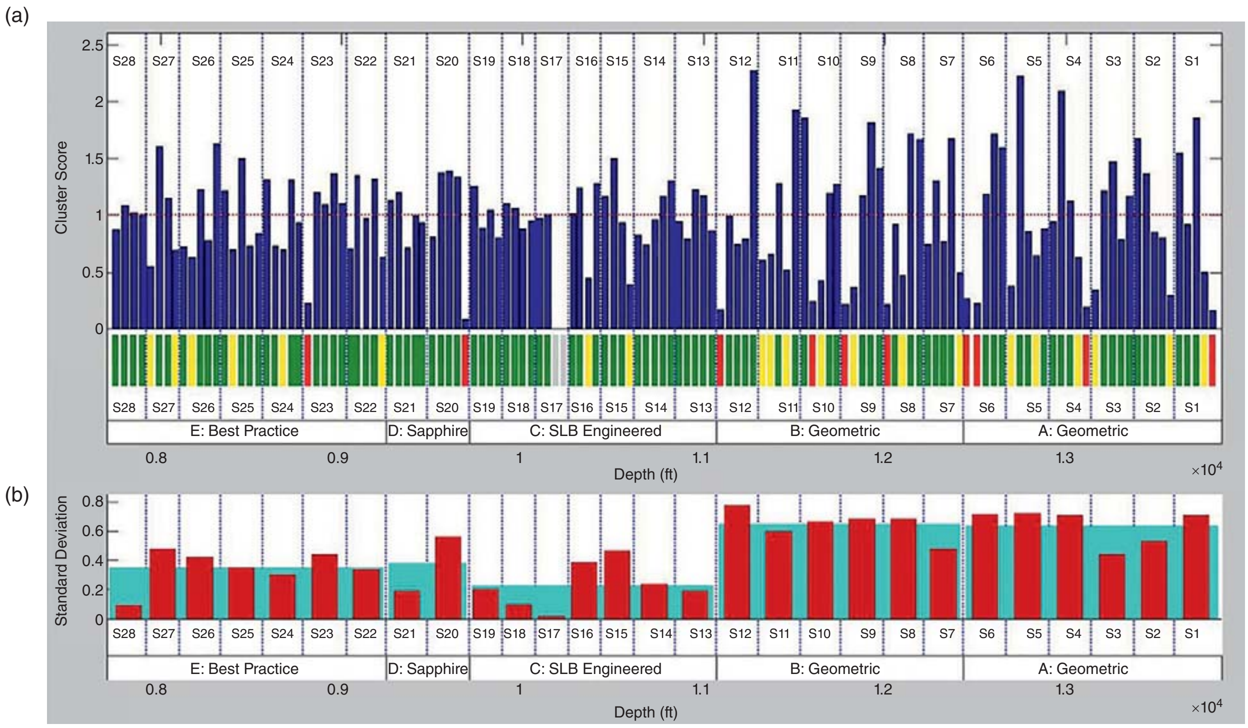

Figure 11.10 (a) A cluster score is calculated for each cluster for every stage of the MIP-3H well based on normalized energy attribute. (b) Energy standard deviation of clusters in each stage showing the uniformity of DAS energy. Geometric Stages 1–12 have higher-energy deviation between clusters than engineered stages and interpreted lower stimulation efficiency (Courtesy Schlumberger). Cluster stimulation efficiency is the percentage of clusters that receive effective stimulation in a given stage. A higher-efficiency value indicates a greater number of highly conductive fractures with more uniform half-lengths and fewer gaps in the fracture network along the lateral that could affect flow rates and possibly enhance EUR. Source: Ingram et al. (2014). Reproduced with permission of Society of Petroleum Engineers

has been supplying the gas demands of Morgantown, West Virginia, since early 2016. During the warm seasons, the well can be in a constrained mode of production for several hours per day, making the analysis of the flow regime hard to determine.

11.4. CONCLUSIONS

The recorded DAS data of the stimulation process of the MIP-3H well were processed and energy attributes were calculated for 28 stages. The processed DTS data of more than 2 years of production show that the subsurface temperature along the producing lateral is changing through time. The gas production could cause a JTC effect (cooling) while water production could cause a warming effect detectable by DTS system. DAS data are used as hydraulic fracture monitoring to assess the stimulation efficiency. Geometric stages showed less uniform DAS energy distribution over their clusters than other sections of the well. This was interpreted as poorer stimulation. However, after 2 years of production and decreased water production, it is difficult to use DTS data to assess production efficiency. Subsequent analysis of the production DTS revealed that geometric stages at the toe and at less depth (toe-up) are cooler than other engineered stages at a lower elevation near the heel. In contrast, engineered stages showed more uniform DAS energy over their clusters, but relative temperature is increasing with time. The general cooling and changes in relative temperature between stages may be the result of decreased produced water, declining gas production rates, and warming of gas and water vapor along the lateral due to the elevation change along the lateral. The overall change in the DTS data may be a result of the change to SRV, where fractures and differences in stimulation efficiency between clusters do not interfere with each other.

ACKNOWLEDGMENTS

This research was funded by the National Energy Technology Laboratory of the U.S. Department of Energy (DOE) as part of their Marcellus Shale Energy and Environment Laboratory (MSEEL) (DOE Award No.: DE-FE0024297). The authors appreciate Northeast Natural Energy, LLC for providing data and technical support, and Schlumberger for providing access to the fiber-optic data.

REFERENCES

Brown, G. A. (2006). *Monitoring multilayered reservoir pressures and GOR changes over time using permanently installed distributed temperature measurements*. Paper presented at SPE Annual Technical Conference and Exhibition. https://doi.org/10.2118/101886-ms

Carr, T. R., Wang, G., Boyce, M. L., & Yanni, A. (2011). Understanding controls on deposition of organic content in the Middle Devonian organic-rich shale intervals of West Virginia and western Pennsylvania. In *Geological Society of America Abstracts with Programs: Northeast (46th Annual) and North-Central (45th Annual) Joint Meeting* (Vol. *43*, No. 1, p. 50). Pittsburgh.

Çengel, Y. A., & Boles, M. A. (2008). *Thermodynamics: An engineering approach*. Boston, Massachusetts: McGraw-Hill.

Chorn, L., Stegent, N., & Yarus, J. (2014). *Optimizing lateral lengths in horizontal wells for a heterogeneous shale play*. Paper presented at SPE/EAGE European Unconventional Resources Conference and Exhibition. https://doi.org/10.2118/167692-ms

Cipolla, C. L., Weng, X., Onda, H., Nadaraja, T., Ganguly, U., & Malpani, R. (2011). *New algorithms and integrated workflow for tight gas and shale completions*. Paper presented at SPE Annual Technical Conference and Exhibition. https://doi.org/10.2118/146872-ms

EIA (2018a). Drilling Productivity Report. US Energy Information Administration, Released July *16*, 2018. https://www.eia.gov/petroleum/drilling/archive/2018/07/

EIA (2018b). Natural Gas Gross Withdrawals and Production. US Energy Information Administration. https://www.eia.gov/dnav/ng/ng_prod_sum_a_EPG0_FGW_mmcfpd_m.htm

Gale, J. F., Reed, R. M., Becker, S. P., & Ali, W. (2008). Natural fractures in the Barnett Shale in the Delaware Basin, Pecos Co. West Texas: Comparison with the Barnett Shale in the Fort Worth Basin. *AAPG Convention*.

Ghahfarokhi, P. K., Carr, T. R., Song, L., Shukla, P., & Pankaj, P. (2018). *Seismic attributes application for the distributed acoustic sensing data for the Marcellus Shale: New insights to cross-stage flow communication*. SPE Hydraulic Fracturing Technology Conference and Exhibition. https://doi.org/10.2118/189888-ms

Glasbergen, G., Yeager, V. J., Reyes, R. P., & Everett, D. M. (2010). Fluid-diversion monitoring: the key to treatment optimization. *SPE Production & Operations*, *25*(03), 262–274. https://doi.org/10.2118/122353-pa

Heckman, T., Olsen, G., Scott, K., Seiller, B., Simpson, M., & Blasingame, T. (2013). *Best practices for reserves estimation in unconventional reservoirs: Present and future considerations*. In Keynote presentation presented at the 2013 SPE Unconventional Resources Conference, The Woodlands, TX (USA).

Holley, E. H., & Kalia, N. (2015). *Fiber-optic monitoring: Stimulation results from unconventional reservoirs*. Unconventional Resources Technology Conference. https://doi.org/10.2118/178520-ms

Ingram, S. R., Lahman, M., & Persac, S. (2014). Methods improve stimulation efficiency of perforation clusters in completions. *Journal Petroleum Technology*, *66*(4). https://pubs.spe.org/en/jpt/jpt-article-detail/?art=1853

Johnson, D., Sierra, J., Kaura, J., & Gualtieri, D. (2006). *Successful flow profiling of gas wells using distributed temperature sensing data*. Proceedings of SPE Annual Technical Conference and Exhibition. https://doi.org/10.2523/103097-ms

Karaman, O. S., Kutlik, R. L., &. Kluth, E. L. (1996). *A field trial to test fiber optic sensors for downhole temperature and pressure measurements, West Coalinga Field, California*. SPE Western Regional Meeting. https://doi.org/10.2118/35685-ms

Kavousi, P., Carr, T. R., Wilson, T. H., Amini, S., Wilson, C., Thomas, M., et al. (2017). *Correlating distributed acoustic sensing (DAS) to natural fracture intensity for the Marcellus Shale*. SEG Technical Program Expanded Abstracts 2017. https://doi.org/10.1190/segam2017-17675576.1

Mishra, A., Al Gabani, S. H., & Jumaa Al Hosany, A. (2017). *Pipeline leakage detection using fiber optics distributed temperature sensing DTS*. In Abu Dhabi International Petroleum Exhibition & Conference. Society of Petroleum Engineers. https://doi.org/10.2118/188407-MS

Molenaar, M. M., Hill, D., Webster, P., Fidan, E., & Birch, B. (2012). First downhole application of distributed acoustic sensing for hydraulic-fracturing monitoring and diagnostics. *SPE Drilling & Completion*, *27*(01), 32–38. https://doi.org/10.2118/140561-PA

Nath, D., Sugianto, R., & Finley, D. (2005). *Fiber-optic distributed temperature sensing technology used for reservoir monitoring in an Indonesia Steam Flood*. Paper presented at SPE International Thermal Operations and Heavy Oil Symposium. https://doi.org/10.2118/97912-ms

Nath, D. K., Finley, D. B., & Kaura, J. D. (2006). *Real-time fiber-optic distributed temperature sensing (DTS)—new applications in the oilfield*. Paper presented at SPE Annual Technical Conference and Exhibition. https://doi.org/10.2118/103069-ms

Pinto, M. C., Karale, C., & Das, P. (2013). A simple and reliable approach for the estimation of the Joule-Thomson coefficient of reservoir gas at bottomhole conditions. *SPE Journal*, *18* (05), 960–968. https://doi.org/10.2118/158116-pa

Rahman, M., Zannitto, P. J., Reed, D. A., & Allan, M. E. (2011). *Application of fiber-optic distributed temperature sensing technology for monitoring injection profile in Belridge Field, diatomite reservoir*. Paper presented at SPE Digital Energy Conference and Exhibition. https://doi.org/10.2118/144116-ms

Roy, B. N. (2002). *Fundamentals of classical and statistical thermodynamics*. West Sussex, England: John Wiley.

Sierra, J. R., Kaura, J. D., Gualtieri, D., Glasbergen, G., Sarker, D., & Johnson, D. (2008). *DTS monitoring of hydraulic fracturing: Experiences and lessons learned*. Paper presented at SPE Annual Technical Conference and Exhibition. https://doi.org/10.2118/116182-ms

Smolen, J. J., & van der Spek, A. (2003). *Distributed Temperature Sensing—A DTS primer for Oil and Gas Production*. http://w3.energistics.org/schema/witsml_v1.3.1_data/doc/Shell_DTS_Primer.pdf

Wang, X., Lee, J., Thigpen, B., Vachon, G. P., Poland, S. H., & Norton, D. (2008). *Modeling flow profile using Distributed Temperature Sensor (DTS) system*. Paper presented at Intelligent Energy Conference and Exhibition. https://doi.org/10.2118/111790-ms

Wang, G., & Carr, T. R. (2013). Organic-rich Marcellus Shale lithofacies modeling and distribution pattern analysis in the Appalachian Basin. *AAPG Bulletin*, *97*(12), 2173–2205. https://doi.org/10.1306/05141312135

Wilson, T. H., Carr, T. R., Carney, B. J., Hewitt, J., Costello, I., Jordon, E., et al. (2016). *Microseismic and model stimulation of natural fracture networks in the Marcellus Shale, West Virginia*. SEG Technical Program Expanded Abstracts 2016. https://doi.org/10.1190/segam2016-13866107.1

Wilson, T. H., Carr, T. R., Carney, B. J., Yates, M., MacPhail, K., Morales, A., et al. (2018). Marcellus Shale model stimulation tests and microseismic response yield insights into mechanical properties and the reservoir discrete fracture network. *Interpretation*, *6*(2). https://doi.org/10.1190/int-2016-0199.1

12

Coalescence Microseismic Mapping for Distributed Acoustic Sensing (DAS) and Geophone Hybrid Array: A Model-Based Feasibility Study

Takashi Mizuno, Joel Le Calvez, and Daniel Raymer

ABSTRACT

Application of distributed acoustic sensing (DAS) has been studied in several areas in seismology. One of the areas is microseismic reservoir monitoring. Given the present limitations of DAS, which include relatively low signal-to-noise ratio (SNR) and absence of three-component (3C) polarization measurements, a DAS-3C geophone hybrid array is an option, particularly in the case of a single monitoring array. Considering the large volume of data, a source-scanning-type algorithm is a reasonable choice, especially for real-time monitoring. This algorithm must handle both DAS measurement, which is a finite differentiation of particle displacement along the borehole axis, and particle velocity/acceleration for 3C geophones. We develop an end-to-end workflow starting from generating synthetic data for the DAS-geophone hybrid array to testing the algorithm to prove the concept. We demonstrate the coalescence microseismic mapping (CMM) algorithm is capable to locate events since it migrates short-time average to long-time average (STA/LTA) of DAS, as well as geophone data, and also incorporate polarization of geophone data to focus the image to locate events even in the case of a single horizontal monitoring array. Considering the long hybrid array, we expect that only a small number of high SNR events will be detected throughout a large aperture encompassing the hybrid array; therefore, the aperture is to be optimized dynamically to eliminate noisy channels for most events. Hence, the CMM algorithm is revised to incorporate automatic receiver selection. Testing results show that automatic receiver rejection improves detectability of the array. This model-driven research approach should be applicable to other geophysical processing studies for a DAS acquisition system.

12.1. INTRODUCTION

Monitoring of reservoir seismicity has been used for hydraulic fracturing monitoring for tight and unconventional reservoirs (e.g., Warpinski, Branagan, Peterson, & Wolhart, 1998; Warpinski Branagan, Peterson, and Wolhart, & Uhl, 1998). Because the magnitude of hydraulically induced events is usually less than 0, such events are referred to as microseismic events. Because a fracture network usually has a spatial scale in the hundreds of meters, the monitoring system is usually configured as a downhole sensor array installed in single or multiple wells close to the hydraulic fracturing operation. This configuration maximizes sensitivity for seismic events, as well as

Schlumberger, Houston, Texas, USA

Distributed Acoustic Sensing in Geophysics: Methods and Applications, Geophysical Monograph 268, First Edition.
Edited by Yingping Li, Martin Karrenbach, and Jonathan B. Ajo-Franklin.

DOI:10.1002/9781119521808.ch12

accuracy for the event locations and other source parameters. A single monitoring array is the preferable option because the project cost is scaled by the number of monitoring wells, and there is often a limited availability of wells.

Historically, a sensor is configured with a three-component (3C) geophone system to provide polarization of seismic data, and a mechanical or magnetic clamp is equipped with the housing of the geophone to secure the coupling to the formation and avoid borehole modes. The travel time of direct arrivals and polarizations are used for event location, and its time domain amplitude and frequency domain amplitude are used to infer source parameters. This is applicable to single-well monitoring since both travel time and polarization are provided by geophone.

Distributed acoustic sensing (DAS) has been introduced as a new technology for a borehole seismic array system and applied in microseismic monitoring (e.g., Karrenbach et al., 2017; Molteni et al., 2017; Webster et al., 2013). Table 12.1 provides a high-level summary of geophone and DAS systems. The DAS system has a wide aperture extending from the surface to the bottom of the monitoring well, which is an advantage over geophone arrays for event location and source parameter estimation. However, currently, polarization cannot be obtained because the measurement is still limited to a single component. This limits application of the DAS-only system to single-well monitoring. Due to lack of polarization information, we are not able to infer the direction of event, which is necessary for event location in single-well monitoring. Also, it limits detection capability since identification of *P*- and *S*-waves cannot make use of polarization information. We anticipate the combination of DAS and geophone system provides better capability than the geophone or DAS-only monitoring system for a single-well monitoring case.

In addition to the availability of polarization, there are a couple of differences in measurements by geophone and DAS. DAS measures a spatial derivative of the wavefield whereas the geophone measurement is a point measurement. Therefore, the geophone response can be described as a frequency response whereas that of DAS is a wavenumber response (i.e., frequency response could be changed by phase velocity). In terms of noise, in addition to the difference in the source of noise, it was observed in field experiments that the signal-to-noise ratio (SNR) of DAS is low when compared to that of geophones (e.g., Molteni et al., 2017). To prove the concept of the DAS-geophone monitoring system, one may consider the end-to-end workflow, including model generation, of processing for the hybrid monitoring system. However, the study of modeling of microseismic data in DAS is still quite limited (e.g., Baird et al., 2019), particularly for the DAS-geophone hybrid system. We developed a modeling-based evaluation workflow for the DAS-geophone hybrid microseismic monitoring system, in which a synthetic microseismic seismogram of DAS and geophone hybrid array is generated and the location algorithm is applied to prove the concept. In the present study, we studied a single monitoring well configuration as it is a preferable option in the industry.

The inversion methods of event location are characterized in three types: Travel-time-based methods, characteristic-function-based (migration-based) methods, and full-waveform-based methods. A time-pick-based method, such as the so-called Geiger method (Geiger, 1912), is often employed in earthquake seismology. However, time-pick-based processing is not practical for a DAS-geophone array, particularly in real time, because obtaining time picks for thousands of receiver points is time consuming. A full-waveform method (e.g., Jarillo Michel & Tsvankin, 2014a, 2014b) is another end member that does not require time picks. However, this problem requires solving the moment tensor because waveform is a function of event location and moment tensor, which is known to be challenging for a single-well configuration (Vavrycuk, 2007). A characteristic-function-based method (migration-based method) does not require time pick and phase information because the characteristic function cancels phase information. This method consists of two parts: The first step is to calculate characteristic function, which represents arrival of seismic phases, and the second step is to migrate the function in time and space and find the peak of the migrated function as the event location and origin time. In terms of characteristic function, several functions have

Table 12.1 Comparison of Specifications of Geophone and DAS Arrays.

	Geophone array	DAS
Aperture	600 m (40-level tool)	From wellhead to total depth
Number of Components	3C	1C
Measurement	Particle velocity/acceleration at the receiver	Phase difference between two measurement points separated with gauge length (L_G)
Frequency/Wavenumber Response	Flat response over the given frequency band	Gauge length related wavenumber (frequency and apparent phase velocity) response
Source of Noise	Environment noise Electric noise (low frequency)	Environment noise Optical noise

been proposed, e.g., energy trace (e.g., Kao & Shan, 2004), envelope trace (e.g., Gharti et al., 2010), short-time average to long-time average (STA/LTA; e.g., Drew et al., 2005), and high-order statistics, like kurtosis (e.g., Lagnet et al., 2014); and performance has been compared (Cesca & Grigoli, 2015). In the present study, we study the applicability of coalescence microseismic mapping (CMM) (Drew et al., 2005), which uses STA/LTA, as a case study of the applicability of a migration-based method to a DAS-geophone hybrid array.

12.2. DAS SYNTHETIC DATA FOR MICROSEISMIC EVENTS

12.2.1. Expected Signature of DAS Microseismic Data

DAS responds to displacement wavefield along the borehole. The one-dimensional (1-D) wave equation in terms of displacement is defined as:

$$u(x,t) = A \exp i(kx - \omega t) \tag{12.1}$$

where u is displacement, A is amplitude, x is coordinate along the borehole, t is time, k is wavenumber (angular wavenumber c/ω), and ω is angular frequency.

We employ a simple model of DAS measurement (Bona et al., 2017):

$$d(x,t) = \frac{1}{L_G}\int_{-\infty}^{\infty}\left(u\left(x - \frac{L_G}{2} + l, t\right) - u\left(x + \frac{L_G}{2} + l, t\right)\right) w(l)\,dl \tag{12.2}$$

where d is the DAS measurement of difference of displacement of neighboring points with gauge length L_G and laser pulse length l. Function w defines forms of the laser pulse. To further simplify, the pulse width of the laser is considered a delta function. Then, Equation 12.2 becomes:

$$d(x,t) = \frac{1}{L_G}\int_{-\infty}^{\infty}\left(u\left(x - \frac{L_G}{2} + l, t\right) - u\left(x + \frac{L_G}{2} + l, t\right)\right) \delta(l)\,dl \tag{12.3}$$

Therefore,

$$d(x,t) = \frac{1}{L_G}\left[u\left(x - \frac{L_G}{2}, t\right) - u\left(x + \frac{L_G}{2}, t\right)\right] \tag{12.4}$$

Equation 12.4 can be expressed using the 1-D wave equation (Equation 12.1) by:

$$d(x,t) = \frac{1}{L_G}\left[A \exp i\left(k\left(x - \frac{L_G}{2}\right) - \omega t\right) - A \exp i\left(k\left(x + \frac{L_G}{2}\right) - \omega t\right)\right] \tag{12.5}$$

Therefore,

$$d(x,t) = -\frac{2i}{L_G}\left(\sin k\left(\frac{L_G}{2}\right)\right) A \exp i(kx - \omega t) \tag{12.6}$$

Using particle velocity, DAS data can be written as:

$$d(x,t) = \frac{2}{\omega L_G}\left(\sin k\left(\frac{L_G}{2}\right)\right) v(x,t) \tag{12.7}$$

Equation 12.7 indicates DAS is in the same phase as particle velocity, but amplitude is a function of gauge length and wave number. This is often called "gauge length effect". The amplitude becomes 0 (notch) at every case where the following condition is fulfilled:

$$k\left(\frac{L_G}{2}\right) = n\pi \tag{12.8}$$

In the case of microseismic data, the omega-squared displacement spectrum model is often observed (e.g., Fehler & Phillips, 1991):

$$\Omega(\omega) = \frac{\Omega_0}{\left(1 + \left(\frac{f}{f_c}\right)^2\right)} \tag{12.9}$$

Therefore, the spectrum of DAS microseismic data is expected to be:

$$d(\omega) = \frac{2}{L_G}\left(\sin k\left(\frac{L_G}{2}\right)\right)\frac{\Omega_0}{\left(1 + \left(\frac{f}{f_c}\right)^2\right)} \tag{12.10}$$

Figure 12.1 shows the displacement spectrum and DAS synthetic spectrum. To demonstrate the shear wave case, we consider two cases: One in which the phase velocity is set to 2000 m/s and the other with a phase velocity of 4000 m/s, both with corner frequency set to 150 Hz. To simplify, signal moment Ω_0 was set to 1 m/Hz. As shown, the omega-squared falloff at high frequency is observed in DAS as in the displacement spectrum. In addition, a spectrum is slightly changed by apparent phase velocity c. More significantly, the low-frequency signature shows a difference from the displacement spectrum with the amplitude dropping off toward lower frequencies. Figure 12.2 shows the comparison of DAS spectrum with particle velocity. It demonstrates that the low-frequency spectrum of DAS is comparable with that seen for particle velocity.

It is often observed that DAS is comparable to geophone (particle velocity) in the time domain for both vertical seismic profiles (VSPs) (e.g., Daley et al., 2016;

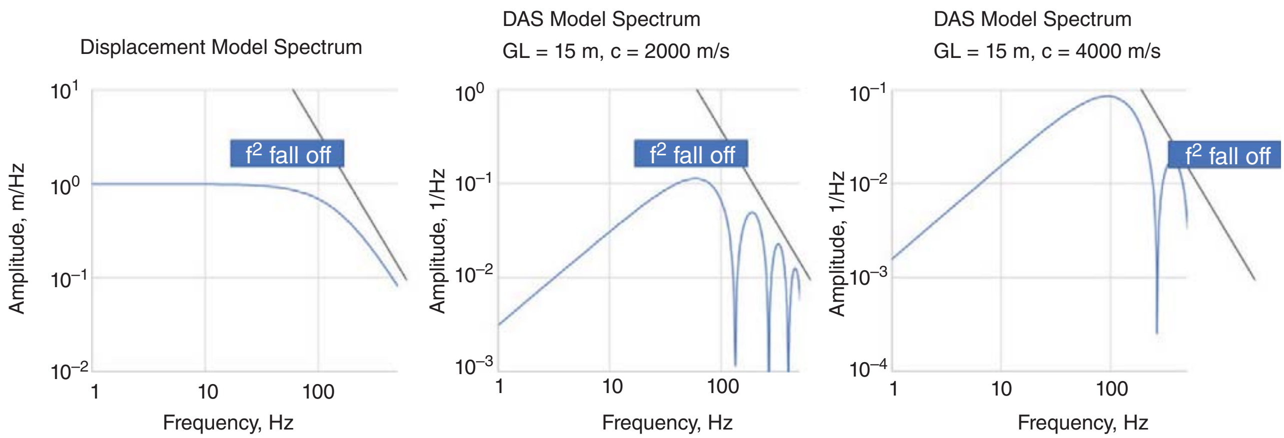

Figure 12.1 Comparison of spectrum of microseismic synthetic data for an event with $\Omega_0 = 1$ m/Hz and a corner frequency of 150 Hz. (Left) Model displacement. (Center) DAS model with $L_G = 15$ m for $c = 2000$ m/s. (Right) DAS model with $L_G = 15$ m for $c = 4000$ m/s.

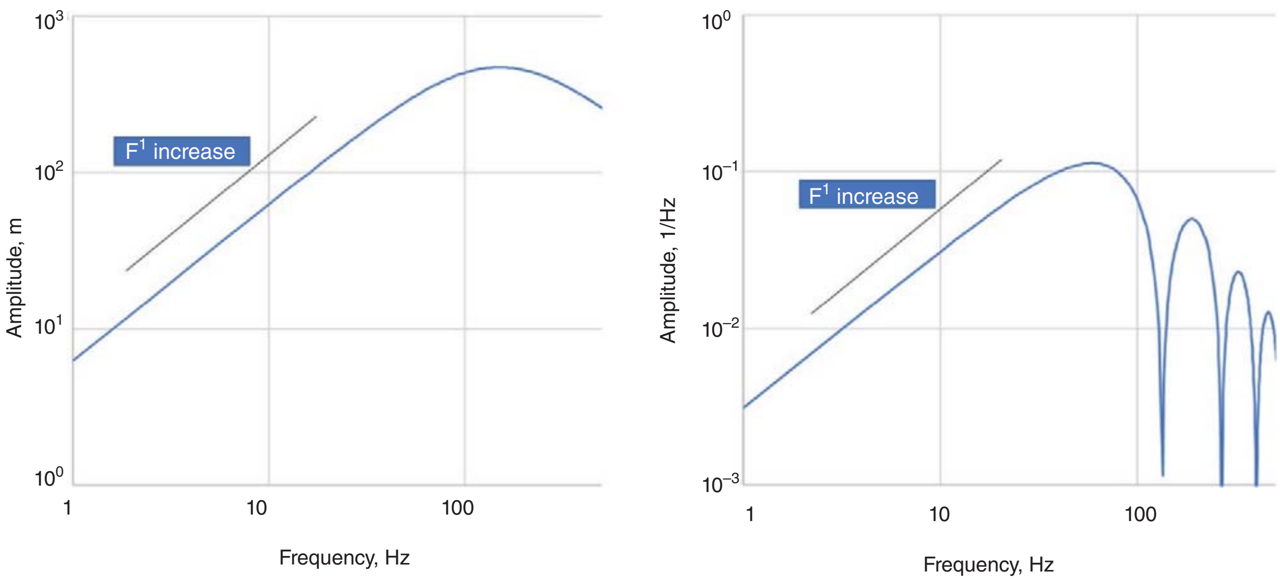

Figure 12.2 Comparison of spectrum of microseismic synthetic data. (Left) Particle velocity. (Right) DAS model with $L_G = 15$ m for $c = 2000$ m/s.

Willis, et al., 2016) and microseismic data (Molteni et al., 2017). This is explained by (1) the DAS data being in the same phase with particle velocity (Equation 12.7) and (2) the similarity of the DAS spectrum with particle velocity for low frequency (Figure 12.2). However, this is still an approximation of DAS data because we expect the footprint of gauge length in the response function of the DAS measurement as seen in Figure 12.2. In our study, we use Equation 12.4 to simulate the DAS measurement for further study.

12.2.2. Simulation of DAS and Geophone Data for a Single Monitoring Array

Figure 12.3 shows the geometry of the monitoring configuration in this study. We assume single-well monitoring because it is the most practical approach in the industry. The monitoring well was configured with vertical and horizontal sections because we often use a production well for monitoring. Twelve geophones were installed at the toe section of the horizontal well. The geophone spacing

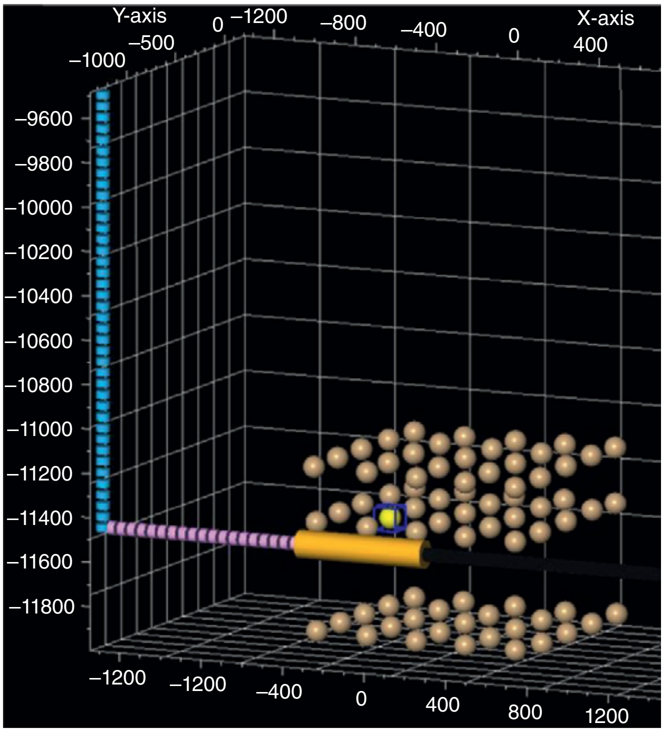

Figure 12.3 Event location and receiver array used in this study. Length unit is feet. Brown dots, blue dots, and purple dots are locations for event, vertical section of DAS, and horizontal section of DAS, respectively. Geophones are installed in the yellow section in the horizontal well with 50 ft spacing.

was 50 ft. DAS was deployed from the horizontal well through the vertical portion of the well.

We applied the workflow described in Figure 12.4 to generate the geophone synthetic and DAS synthetic. First, we generated particle velocity with a ray theory synthetic (Leaney, 2014) at every 50 ft along the well. Right lateral strike-slip faulting is assumed, and the strike of the fault was set to north-south assuming fracture growth normal to the direction of the horizontal well. Although the algorithm is capable of simulating wavefield in vertical transverse isotropic (VTI) layered structure, we assumed a homogenous isotropic model of V_p = 11308 ft/s and V_s = 6486 ft/s. The corner frequency is assumed as 150 Hz considering a moment magnitude of -2 and empirical seismic moment-corner frequency relation in microseismic events at reservoirs (Mizuno, Le Calvez, et al., 2019). To simulate realistic source spectrum in frequency domain, Brune's pulse (Brune, 1970) is assumed as the source pulse. After the particle velocity is obtained, the displacement is calculated by time domain integration. Finally, we apply Equation 12.4 to simulate DAS at the midpoint between neighboring receivers. Since the receiver spacing is 50 ft, the operation is equivalent to generating synthetic for the DAS system using 50 ft (15.2 m) gauge length.

To study the performance of the event location algorithm in a noisy environment, low-noise and high-noise data sets were generated by adding white noise to the synthetic data. Because geophones represent a better SNR compared to DAS (e.g., Molteni et al., 2017), the geophone SNR was set six times higher compared to the DAS SNR. We assumed the constant noise level for each DAS and geophone system. In low-noise data, the average SNR = 120 for geophone, and the average SNR = 20 for DAS. In high-noise data, the average SNR = 30 for geophone, and the average SNR = 5 for DAS.

Figure 12.5 shows an example of the DAS synthetic data generated. The shape of time domain pulse is not displacement (one-sided pulse) anymore and is similar to particle velocity of Brune's pulse as expected from Equation 12.7.

The signature of the DAS synthetic is further reviewed to validate the workflow. The DAS synthetic is sensitive to the displacement along the borehole: The horizontal section of the well is to be correlated to the easting component of displacement, and the vertical section is to be correlated to the vertical component of displacement. The following is a summary of DAS synthetic signatures:

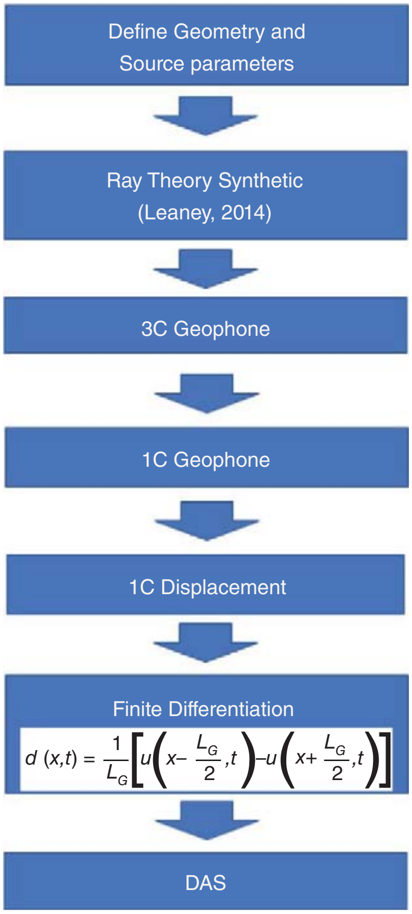

Figure 12.4 Workflow to generate the DAS synthetic waveforms in this study.

- Vertical section
  - The amplitude of the *P*-wave of DAS is weak, particularly at the bottom of the vertical section of the well. This is because projection of *P*-wave particle motion to the well is small and the wavenumber is approaching 0.
  - Duration of the wave train of the *S*-wave changes with depth. This can be interpreted as the gauge length effect in the dominant frequency (Figure 12.1).
- Horizontal section
  - *P*-wave amplitude is higher at the heel due to (1) the radiation pattern and (2) the projection of *P*-wave particle motion to make an angle of about 60° to the well.
  - The *S*-wave is diminished at the intersection of the *SH* nodal plane (*A* in Equation 12.7 approaching 0).
  - *SH* amplitude is diminished at DAS in the toe section. This is because apparent velocity approaches infinite (k ➔ 0 in Equation 12.7).

Because we could explain the signatures of DAS synthetic data from the analytical DAS model, we concluded that the synthetic data were generated as expected.

12.3. THE LOCATION ALGORITHM FOR DAS-GEOPHONE HYBRID ARRAY

Figure 12.6 represents the high-level processing flow of a migration-based event location approach and its implementation in CMM for a DAS-geophone hybrid array. In CMM, the STA/LTA of the envelope of the waveform is used (Drew et al., 2005; Drew et al., 2013). To calculate the STA/LTA, the envelope function E is defined as follows:

$$E_r(t) = \sum_i H(d_i(t))^2 \tag{12.11}$$

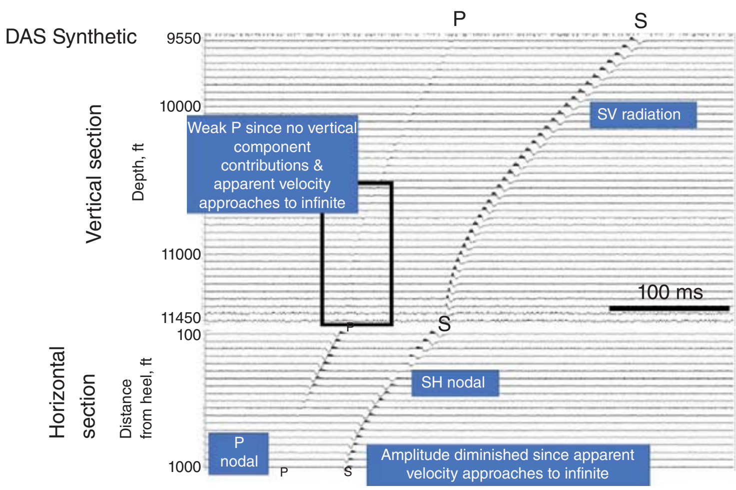

Figure 12.5 An example of a synthetic waveform of DAS. The event is located at yellow dots in Figure 12.3. The top section corresponds to the vertical section of DAS, and the bottom section corresponds to the horizontal section of DAS. Amplitudes are normalized trace by trace.

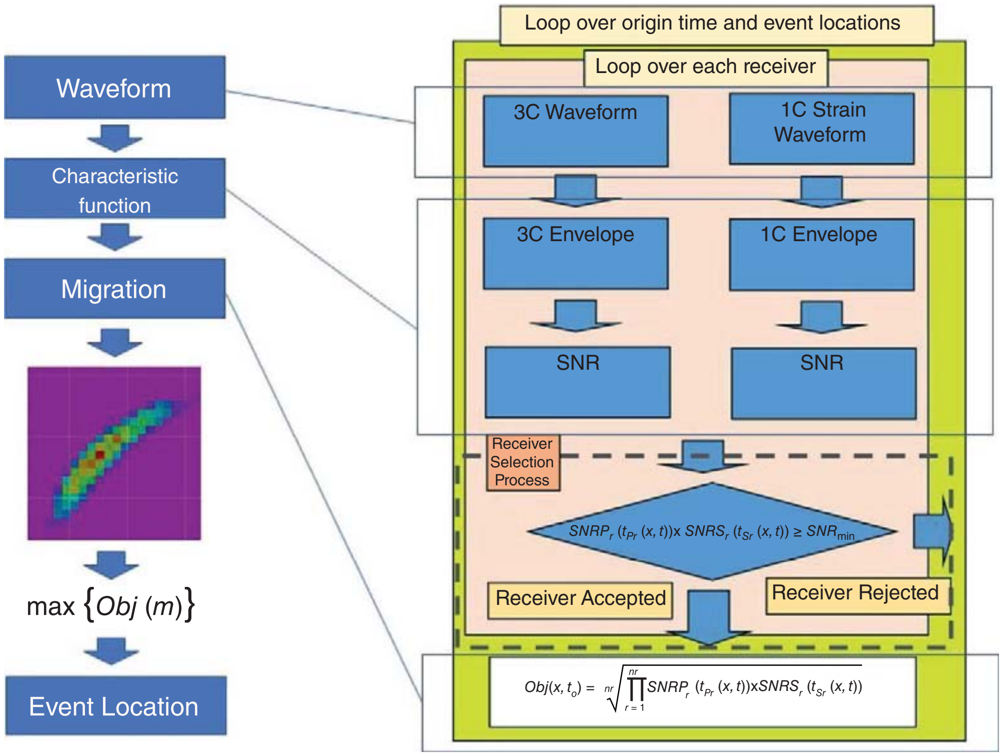

Figure 12.6 (Left) High-level design of migration-based event location algorithm. (Right) Specific design for CMM for DAS and geophone hybrid configuration. Receiver selection process is needed to handle noisy DAS data.

where d is data, H is the operator to calculate the envelope, r is receiver index, t is the time index, and i is the component index. Because this equation is applicable to a one-component (1C) geophone and a 3C geophone, it could be applicable to a mixed 1C and 3C system, such as a DAS-geophone system. The SNR (STA/LTA function) is calculated as follows:

$$\mathrm{SNR}_{rj}(t) = \sqrt{\frac{n\sum_{s} E(t+s)}{s\sum_{n} E(t-n)}} \tag{12.12}$$

where s and n are the number of samples in the signal and the noise window, respectively, and j is the phase index (P-wave or S-wave). If data are separated in terms of P- and S-waves using *a priori* information of polarization, the SNR function will have different signatures for the P- and S-waves. In the case of DAS, we expect the P- and S-wave SNR values will be the same because polarization cannot be used. Drew et al. (2013) demonstrate that Equation 12.12 represents the onset of phase reasonably when the time window for noise and signal is set. Then, the SNR function is migrated to time and space, and a map of the objective function in time and space is generated. The peak of the objective function is searched for to infer origin time and event location. Details of this implementation can be found in Drew et al. (2005), Drew et al. (2013), and Hirabayashi (2016).

CMM can be naturally extended to the DAS-geophone problem because (1) CMM is applicable to 1C and 3C, and (2) the algorithm is applicable to the mixture of different responses of receivers because the dimension of data, as well as phase information, is dropped in the STA/LTA calculation. However, because STA/LTA does not carry phase information that original data contain, noise is rather preserved in objective function compared to the case that the original data are migrated. Gendrin et al. (2016) studied the application of coalescence mapping to microseismic monitoring at the surface array where the SNR of data is significantly lower than the downhole and concluded that nonlinear stacking (Ozbek et al., 2013) for the subarray is a useful data-conditioning step prior to CMM. In the present study, we attempt to remove noisy data instead, in a manner comparable to the approach a seismologist would attempt in manual processing. The following logic is implemented in CMM before the objective function (Figure 12.6, right) is calculated in detail:

• *P*-wave SNR (STA/LTA) and *S*-wave SNR (STA/LTA) are calculated at each given event location and origin time candidate.
• If the average (arithmetic mean or geometric mean) of SNR for *P*- and *S*-waves is below threshold, the receiver is excluded to calculate the objective function to this event location.
• To avoid false detection, a condition of a minimum number of receivers is employed. Given an event location and origin time candidate, if the number of receivers is below the threshold, the objective function for this event location and origin time is excluded.

12.4. TESTS

Two scenarios of the DAS and geophone hybrid array were considered in the present study. Test Case 1 covers the scenario that only the horizontal section is available, and Test Case 2 is for when the whole array (vertical and horizontal sections) is available. Test Case 1 demonstrates the limitation of DAS-only array, provides an example that CMM handles hybrid array data as expected, and shows an example that the hybrid array reduces uncertainty of location compared to the geophone-only array. The low-noise data set is used. In Test Case 2, we will see the importance of selection of receiver in CMM for detectability improvement in the case of a wide aperture array. Table 12.2 summarizes the processing parameters used in this study. It is to be noted that receiver SNR and the minimum number of receivers are used for Test Case 2.

12.4.1. Test Case 1: Monitoring Only at the Horizontal Section of the Array

Figures 12.7a and 12.7b show the comparison of event location with geophone and DAS. With geophone, CMM is able to locate all events as expected. However, CMM could not locate the events when only the horizontal section of DAS is available. As shown in Figure 12.7b, CMM is able to locate events normal to the x axis for both geophone and DAS while not in the y and z coordinates for the DAS case. Figure 12.7c shows an example of a cross-sectional view of the objective function by the CMM algorithm in the case that only the horizontal section of DAS is available. CMM constrained the event location in the x axis; however, it was not the case in the y and z axes. This is expected since only travel time information is available in DAS, and travel time data are only enough to constrain event location in terms of distance from the well in a horizontal monitoring well configuration. Figure 12.7d shows the comparison of objective function by only geophone and DAS and geophone hybrid array. By adding travel time information of DAS, a sharper image is obtained in the x-y plane, which indicates a reduction in uncertainty of event location.

12.4.2. Test Case 2: Monitoring by large aperture array

Because all events are located for the low-noise conditions, we discuss the performance of the method in the high-noise condition. Figure 12.8 shows the event locations estimated by the algorithm. From the comparison of Figure 12.8 with Figure 12.3, it can be seen that the horizontal and vertical extension and the layering structure of microseismic cloud are obtained as expected, although some events are not located. Figure 12.8 also shows the histogram of the number of events detected at each receiver. This is automatically defined during the event location. Overall, the bottom of the vertical section of the borehole is poor when compared to other portions of DAS, and the horizontal section of DAS and rest of the vertical section of the DAS are utilized 100%. This is expected from the configuration of the receivers, as well as the mechanism, as shown in Figure 12.5. More importantly, geophone utilization is 100%, as expected. Figure 12.9 shows the comparison of model phase arrival with actual phase arrival. The blue and red bars indicate expected phase arrivals for *P*- and *S*-waves calculated from event location estimates. The modeled phase arrivals explain the data well. Figure 12.9 also shows receiver utilization information. In terms of receivers in the bottom of the vertical section (Figure 12.9b), receivers are automatically deselected because the noise level is relatively high compared to the signal for those receivers. These observations indicate that microseismic events can be located using the DAS-geophone array using CMM, and automatic receiver selection works as expected.

Table 12.2 CMM Algorithm Parameters Used in This Study.

Parameter	Values
STA/LTA Window	Signal: 5 ms Noise: 30 ms
Event Location Threshold	SNR = 2.0
Receiver Threshold	SNR = 1.3
Minimum Number of Receivers' Threshold	30
Objective Function	*P*-wave SNR and *S*-wave SNR arithmetic mean

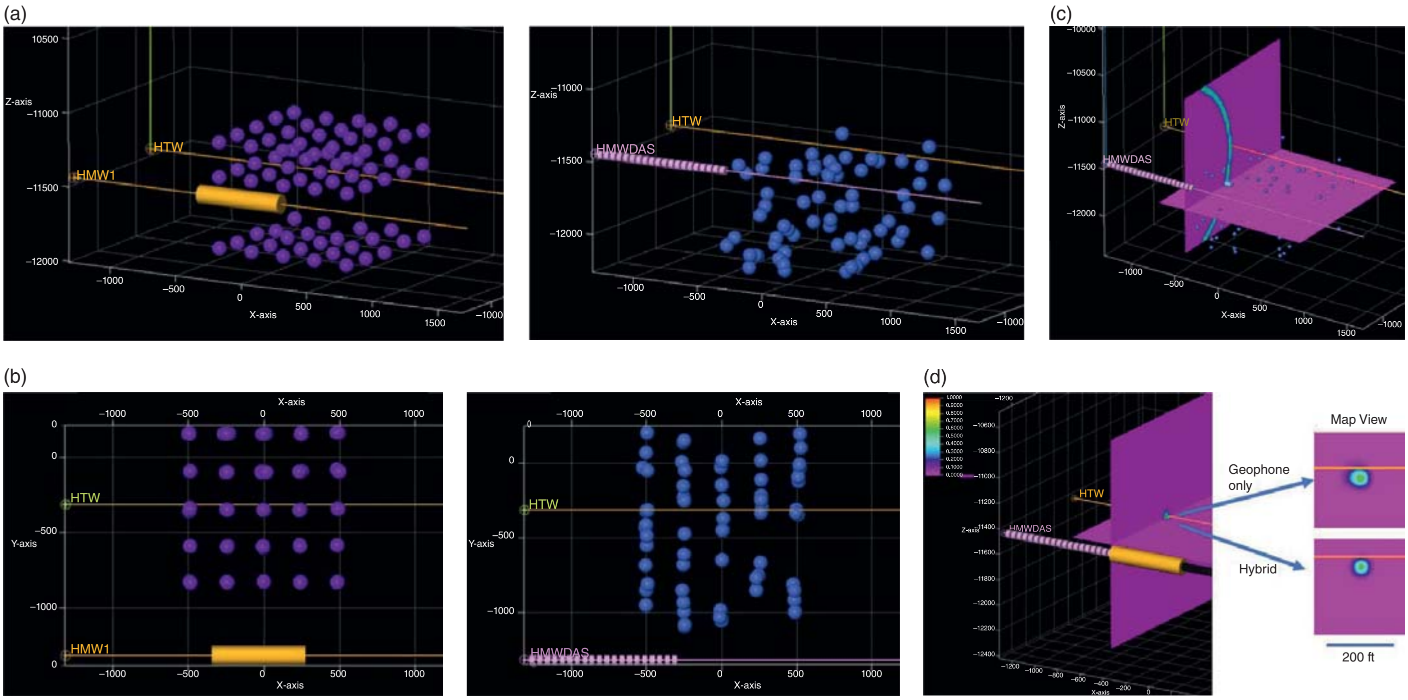

Figure 12.7 Event locations estimated by CMM for data set only at the horizontal section of the well. Length unit is feet. Comparison between (left) geophone and (right) DAS in 3-D view from (a) southeast and top view (b). (c) The example of the objective function when only horizontal section of DAS is used in 3-D view. (d) The example of the objective function in the case where only geophone is used (left) with map view close-up comparison of geophone (top right) and DAS-geophone hybrid (bottom right) cases showing objective function peak.

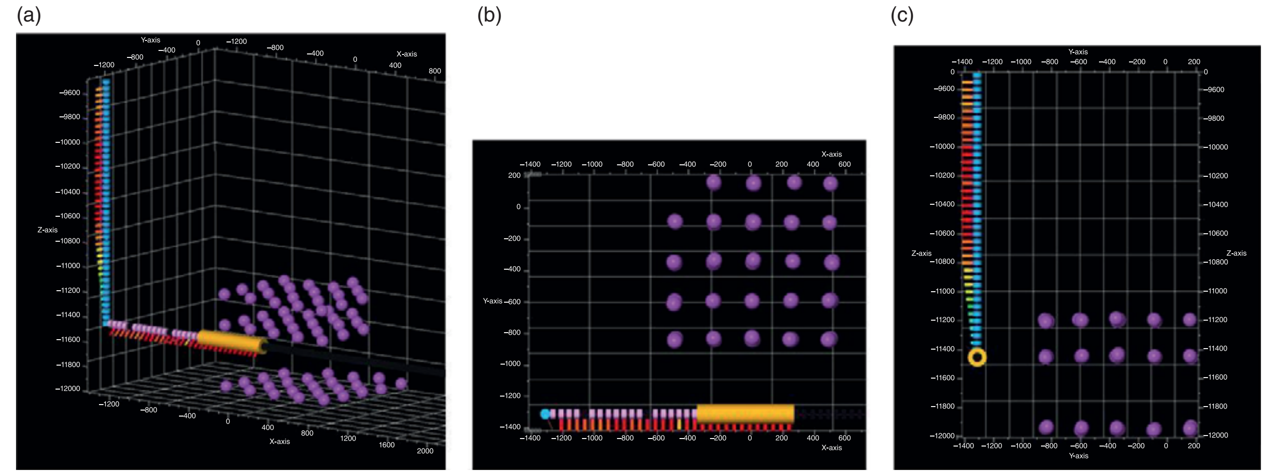

Figure 12.8 Event locations (purple) estimated by CMM with automatic receiver rejection. Length unit is feet. (a) 3-D view from southeast, (b) top view, and (c) cross-sectional view from east. The number of events detected at each receiver is shown as the length of the bar next to a receiver on the well.

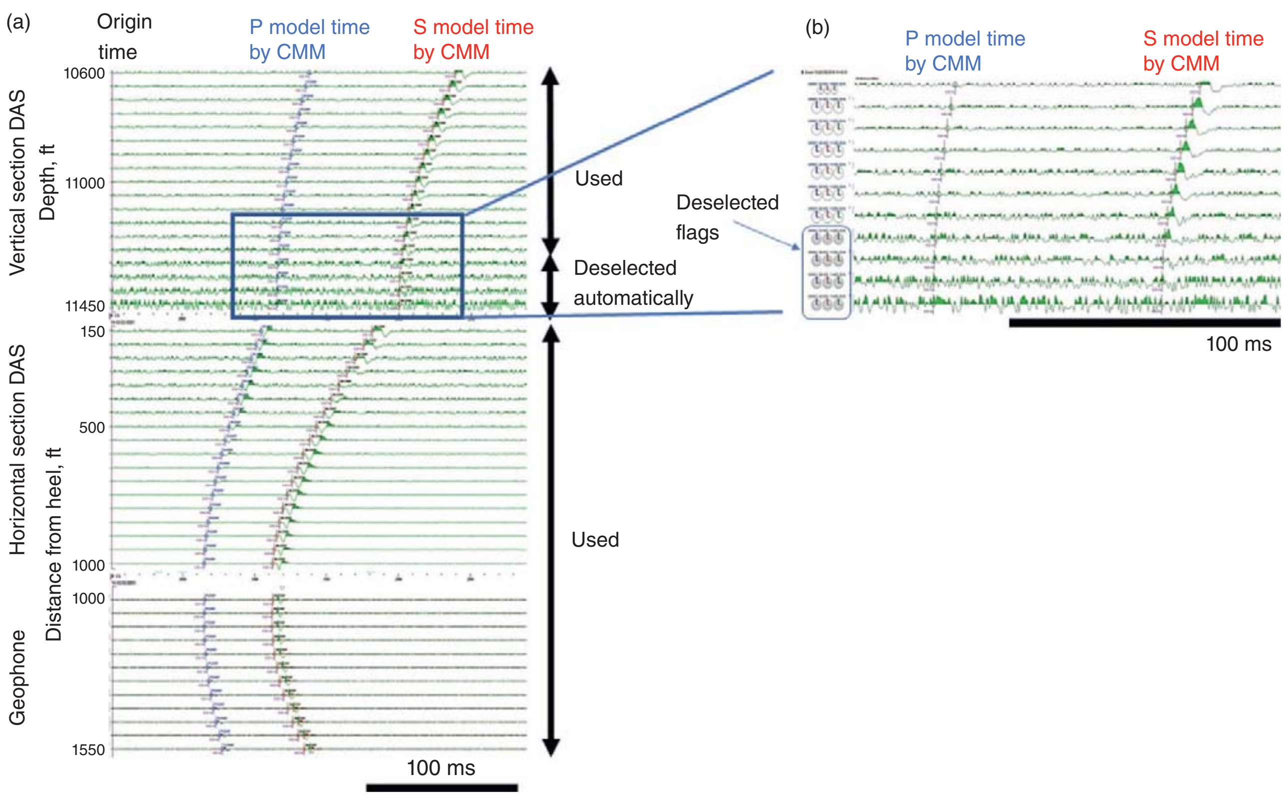

Figure 12.9 An example of a flag for receiver selection and model time picks calculated from event location. Blue is for *P* waves, and red is for *S* waves. (a) For all receivers and (b) for bottom of the vertical section. The clock symbols with a gray background indicate the algorithm deselected those receivers, and the receivers were not used for event location.

To evaluate the importance of the automatic receiver rejection process, the algorithm was run without receiver rejection. Figure 12.10 shows the comparison of the event locations with and without automatic receiver rejection. Without receiver rejection, only 20% of the events are located, and the structure of the microseismic cloud (Figure 12.10a, left) is different from that expected (Figure 12.3), particularly for the extension of the cloud away from the monitoring well. Figure 12.10b shows the comparison of the value of the objective function. Although it varies event by event, automatic event detection brings a higher objective function, increased by between 0.2 and 0.9 in this example, and more events are detected. This is of practical importance because we can add a DAS acquisition system to an existing array based on geophones without changing processing parameters. We conclude that DAS-geophone microseismic monitoring is applicable with minimal changes to a migration-based algorithm.

12.5. DISCUSSION AND CONCLUSION

Borehole geophysics, including microseismic monitoring, has been entering a new era with the availability of DAS measurements because DAS will produce a massive amount of data. This imposes challenges in processing technology in two aspects. One is the volume of data and the other is validation/redefinition of processing physics built in the last several decades. The second point is brought up from the fact that the DAS measurement is not the conventional particle velocity measurement, but the spatial gradient of the wavefield along the fiber. To validate processing physics, we propose a synthetic-based workflow, including generation of a synthetic using a DAS model and testing the algorithm being developed. In this chapter, we introduced our application to the microseismic event location inversion problem for a single monitoring array, which is often favorable configuration for borehole observation. We confirmed that a single-well DAS-only system is not feasible for microseismic

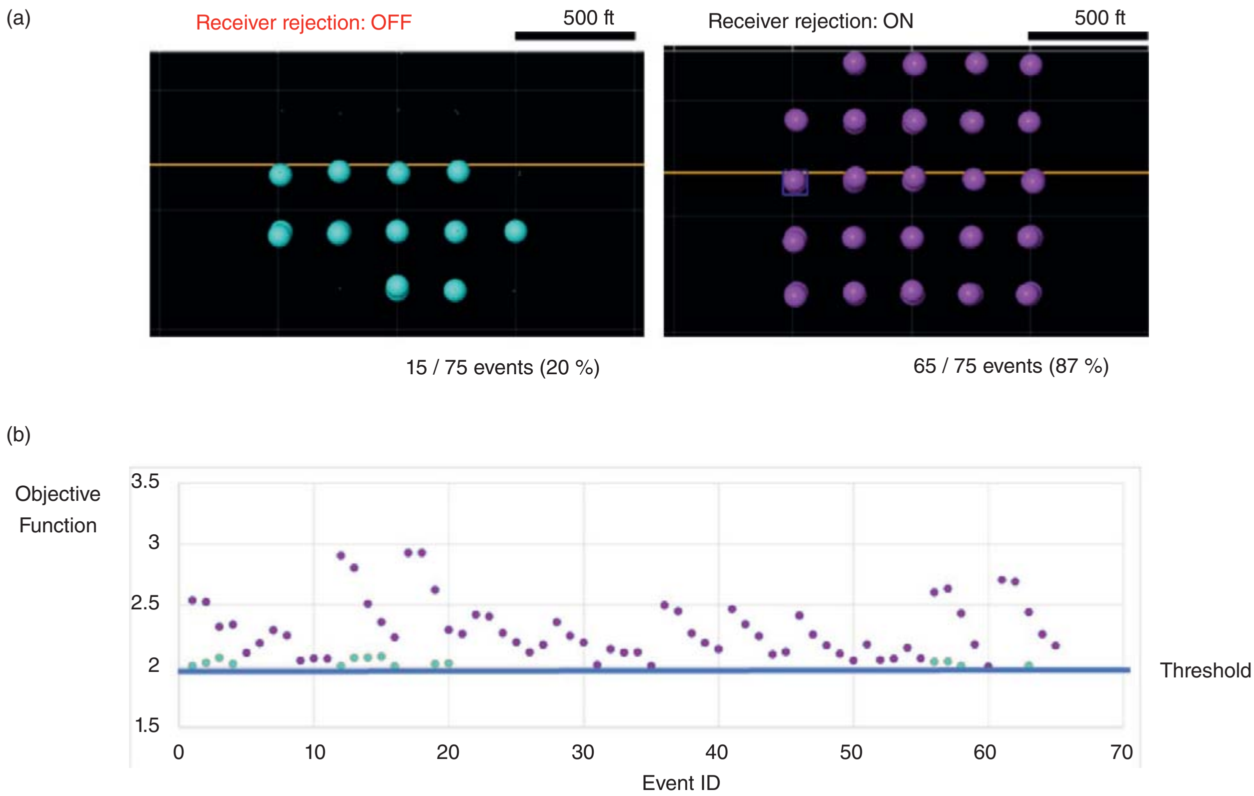

Figure 12.10 Comparison of event location with and without automatic receiver rejection in CMM. (a) Map view of event location: (left) No receiver rejection is used and (right) automatic receiver rejection is used. (b) Comparison of objective function value for (blue) no receiver rejection and for (purple) automatic receiver rejection. The blue horizontal bar represents the threshold, which, in this case, is set to 2, as shown in Table 12.2.

location, and a DAS-geophone hybrid array is making single-well monitoring feasible by a migration-based method, like CMM, with an improvement in uncertainty. To handle a wide range of data quality condition, which is anticipated for a long array in a single monitoring well, we demonstrated that the introduction of automatic selection of receivers into the migration-based algorithm improved the detectability. As a next step, testing with real data is required to confirm the conclusion obtained in this study.

Although it is not under the scope of this study, we can apply this workflow to the survey design or simulation of microseismic monitoring using DAS. In this study, we tried to incorporate a realistic source model: Strike-slip fault mechanism that is usually dominated in the reservoir (e.g., Rutledge et al., 2004), and assumed a corner frequency of 150 Hz, which is typical for reservoir seismicity (Mizuno, Le Calvez, et al., 2019). Although we assumed a homogeneous isotropic model in the present study, the forward modeling engine used in the study (Leaney, 2014) is applicable to a 1-D VTI layered model, which is used for the microseismic location after the calibration (Mizuno et al., 2010). If we consider the full wavefield simulation, including reflections as well as head waves, we may need to consider a numerical wavefield solver rather than a ray-based method used in this study. In terms of the amplitude of DAS data, the present study incorporates the gauge length effect, which has primary importance for interpretation of DAS VSP and microseismic data (e.g., Mizuno, Leaney, et al., 2019). However, it is not enough to simulate noise of DAS data we have seen. Williams et al. (2019) developed the method to simulate raw optical backscatter from geophysical simulations, and it is capable of simulating DAS data precisely, including noise. The upgrade of the DAS measurement model in the workflow brings us more accurate forward modeling, including noise, and it will be applicable from concept validation to real survey simulation.

REFERENCES

Baird, A., Stork, Al., Horne, S., Naldrett, G., Kendall, M., Wookey, J., et al. (2019). *Modelling of fibre-optic DAS response to microseismic arrivals in anisotropic media*. Paper presented at 81st EAGE Conference and Exhibition, We-R09-08.

Bona, A., Dean, T., Correa, J., Pevzner, R., Tertyshnikov, K. V., & Zaanen, L. V. (2017). *Amplitude and phase response of DAS receivers*. Paper presented at 79th EAGE Conference and Exhibition, We-A5-13. https://doi.org/10.3997/2214-4609.201701200

Brune, J. (1970). Tectonic stress and the spectra of seismic shear waves from earthquakes. *Journal of Geophysical Research*, *75*, 4997–5009.

Cesca, S., & Grigoli, F. (2015). Full waveform seismological advances for microseismic monitoring. *Advances in Geophysics*, *56*, 169–225. https://doi.org/10.1016/bs.agph.2014.12.002

Daley, T. M., Miller, D. M., Dodds, K., Cook, P., & Freifeld, B. M. (2016). Field testing of modular borehole monitoring with simultaneous distributed acoustic sensing and geophone vertical seismic profiles at Citronelle, Alabama. *Geophysical Prospecting*, *64*, 1318–1334. https://doi.org/10.1111/1365-2478.12324

Drew, J., Leslie, D., Armstrong, P., & Michaud, G. (2005). *Automated microseismic event detection and location by continuous spatial mapping*. Paper SPE-5513-MS presented at the SPE Annual Technical Conference and Exhibition, Dallas, Texas. https://doi.org/10.2118/95513-MS.

Drew, J., White, R., Tilmann, F., & Tarasewicz, J. (2013). Coalescence microseismic mapping. *Geophysical Journal International*, *195*, 1773–1785. https://doi.org/10.1093/gji/ggt331

Fehler, M., & Phillips, W.S. (1991). Simultaneous inversion for Q and source parameters of microearthquakes accompanying hydraulic fracturing in granitic rock. *Bulletin of the Seismological Society of America*, *81*, 553–575.

Geiger, L. (1912). Probability method for the determination of earthquake epicenters from the arrival time only. *Bulletin of St. Louis University*, *8*, 60–71.

Gharti, H. N., Oye, V., Roth, M., & Kuehn, D. (2010). Automated microearthquake location using envelope stacking and robust global optimization. *Geophysics*, *75*, MA 27–MA 46. https://doi.org/10.1190/1.3432784

Gendrin, A, Ozbek, A., Probert, T., Bradford, I., & Le Calvez, J. (2016). *Toward an optimized data conditioning for surface-acquired microseismic data*. Paper presented at 78th EAGE Conference and Exhibition, We-STZ2-12. https://doi.org/10.3997/2214-4609.201601261

Hirabayashi, N. (2016). Real-time event location using model-based estimation of arrival times and back azimuths of seismic phases. *Geophysics*, *81*, KS25–KS40. https://doi.org/10.1190/geo2014-0357.1

Jarillo Michel, O., & Tsvankin, I. (2014a). Gradient calculation for waveform inversion of microseismic data in VTI media. *Journal of Seismic Exploration*, *23*, 201–217.

Jarillo Michel, O., & Tsuvankin, I. (2014b). Waveform inversion for parameters of microseismic sources in VTI media. Paper presented at SEG Technical Program Expanded Abstracts 2014 (pp. 1045–1048). https://doi.org/10.1190/segam2018-2990944.1

Kao, H., & Shan, S. J. (2004). The source-scanning algorithm: Mapping the distribution of seismic sources in time and space. *Geophysical Journal International*, *157*, 589–594. https://doi.org/10.1111/j.1365-246x.2004.02276.x

Karrenbach, M., Ridge, A., Cole, S., Boone, K., Kahn, D., Rich, J., et al. (2017). *DAS microseismic monitoring and integration with strain measurement in hydraulic fracture profiling. Presented at the Unconventional Resource Technology Conference*, Austin, Texas. https://doi.org/10.15530/URTEC-2017-2670716.

Lagnet, N., Maggi, A., Michelini, A., & Brenguier, F. (2014). Continuous kurtosis-based migration for seismic event detection and location, with application to Piton de la Fournaise

Volcano, La Reunion. *Bulletin of the Seismological Society of America*, *14*, 229–246. https://doi.org/10.1785/0120130107

Leaney, S. (2014). Microseismic source inversion in anisotropic media (Doctoral dissertation). Retrieved from the University of British Columbia Open Collections. (https://open.library.ubc.ca/cIRcle/collections/ubctheses/24/items/1.0165970). Vancouver, BC: University of British Columbia.

Mizuno, T., Leaney, S., & Michaud, G. (2010). *Anisotropic velocity model calibration for imaging the microseismic cloud*. Paper presented at 72nd EAGE Conference & Exhibition incorporating SPE EUROPEC, F 14.

Mizuno, T., Leaney, S., Le Calvez, J., Naseer, F., & Lal Khaitan, M. (2019). The significance of gauge length in particle velocity estimation from DAS data: VSP and microseismic cases. SEG Technical Program Expanded Abstracts 2019 (pp. 4869–4873).

Mizuno, T., Le Calvez, J., & Rutledge, J. (2019). Variation of seismic scalar moment-corner frequency relationship during development of a hydraulic fracture system. *Leading Edge*, *38*, 123–129.

Molteni, D., Williams, M. J., & Wilson, C. (2017). Detecting microseismicity using distributed vibration. *First Break*, *35*, 51–55.

Ozbek, A., Probert, T., Raymer, D., & Drew, J. (2013). *Nonlinear processing methods for detection and location of microseismic events*. 75th EAGE Conference and Exhibition incorporating SPE EUROPEC 2013. https://doi.org/10.3997/2214-4609.20130397.

Rutledge, J. T., Philips, W. S., & Mayerfofer, M. J. (2004). Faulting induced by forced fluid injection and fluid flow forced by faulting: An interpretation of hydraulic-fracture microseismicity, Carthage Cotton Valley gas field, Texas. *Bulletin of the Seismological Society of America, 94*, 1817–1830.

Vavrycuk, V. (2007). On the retrieval of moment tensors from borehole data. *Geophysical Prospecting*, *55*, 381–391. https://doi.org/10.1111/j.1365-2478.2007.00624.x

Warpinski, N. R., Branagan, P. T., Peterson, R. E., & Wolhart, S. L. (1998). *An interpretation of M-Site hydraulic fracture diagnostic results*. Paper SPE-39950-MS presented at the SPE Rocky Mountain Regional/Low Permeability Reservoirs Symposium, Denver, Colorado. https://doi.org/10.2118/39950-MS

Warpinski, N. R., Branagan, P. T., Peterson, R. E., Wolhart, S. L., & Uhl, J. E. (1998). *Mapping hydraulic fracture growth and geometry using microseismic events detected by a wireline retrievable accelerometer array*. Paper SPE-40014-MS presented at the SPE Gas Technology Symposium, Calgary, Alberta. https://doi.org/10.2118/40014-MS

Webster, P., Wall, J., Perkins, C., & Molenaar, M. (2013). Micro-seismic detection using distributed acoustic sensing. SEG Technical Program Expanded Abstracts 2013 (pp. 2459–2463). https://doi.org/10.1190/segam2013-0182.1

Williams, M. Le Calvez, J., Wilson, C., & Rodriguez-Herrera, A. (2019). *Integrated geomechanical interpretation of hydraulic stimulation operations using distributed vibration sensing*. Unconventional Resources Technology Conference, 184.

Willis, M. E., Ellmauthaler, A., Wu, X., Barfoot, D., Erdemir, C., Barrios-Lopez, O. A., et al. (2016). *Calibration of distributed acoustic sensing (DAS) VSP data*. Paper presented at 78th EAGE Conference and Exhibition, Th-ST22-02. https://doi.org/10.3997/2214-4609.201601599

Part IV

Distributed Acoustic Sensing (DAS) Applications in Environmental and Shallow Geophysics

13

Continuous Downhole Seismic Monitoring Using Surface Orbital Vibrators and Distributed Acoustic Sensing at the CO2CRC Otway Project: Field Trial for Optimum Configuration

Julia Correa[1,2,3], Roman Pevzner[1,2], Barry M. Freifeld[4], Michelle Robertson[3], Thomas M. Daley[3], Todd Wood[3], Konstantin Tertyshnikov[1,2], Sinem Yavuz[1,2], and Stanislav Glubokovskikh[1,2]

ABSTRACT

Active time-lapse seismic monitoring has successfully detected and tracked injected carbon dioxide (CO_2) in a number of carbon capture and storage (CCS) projects. Usually, this involves successive acquisition of three-dimensional (3-D) reflection seismic surveys, which requires deployment of large seismic receiver arrays and, for land sites, mobile vibroseis sources. An alternative approach to continuous monitoring is to use permanently installed fiber-optic cables as distributed acoustic sensors (DASs) and permanent seismic sources known as surface orbital vibrators (SOVs). This technology was tested as part of the CO2CRC Otway Project Stage 3 design phase by acquiring vertical seismic profile (VSP) surveys using two SOV sources located 380 m and 630 m from a borehole instrumented with two DAS cables cemented behind the casing. The cemented DAS cables include a standard fiber and an enhanced fiber engineered to increase its sensitivity. To improve the frequency range, each SOV was equipped with one large (higher force) motor and one small (lower force) motor, sweeping to frequencies of up to 80 Hz and 160 Hz, respectively. The VSP records from both SOV source locations show well-resolved *P*-wave reflections, *S*-waves, and *PS* conversions recorded by the enhanced fiber. For the standard fiber, the signal-to-noise ratio (SNR) is lower by 15–20 dB, but still shows *P*-wave reflections from the large motor. After processing, both the engineered fiber and the standard fiber provide similar images, though the standard fiber image is noisier at deep intervals. The large motor shows a higher SNR in comparison with the small motor, but the latter increases the spatial resolution of the image due to higher frequency content. The results demonstrate that the DAS/SOV combination is able to image the subsurface at least up to 1500 m deep.

13.1. INTRODUCTION

Onshore seismic monitoring applications typically require the deployment of seismic receiver arrays and mobile sources to image the subsurface. Conventional time-lapse (TL) surveys rely on the accurate positioning of source points and receivers to monitor changes in the reservoir (Lumley, 2001). Common land access issues and the imprecise positioning of seismic equipment contribute to a significant and irreversible TL signal loss. Furthermore, such surveys require significant labor as a large amount of seismic equipment needs to be deployed and then retrieved for each survey. As a result, the high cost of conventional TL surveys coupled with the considerable environmental impact of the large acquisition footprint results in sparse temporal data.

[1]*Centre for Exploration Geophysics, Curtin University, Perth, Australia*

[2]*CO2CRC Limited, Melbourne, Australia*

[3]*Energy Geosciences Division, Lawrence Berkeley National Laboratory, Berkeley, California, USA*

[4]*Class VI Solutions Inc., Oakland, California, USA*

Distributed Acoustic Sensing in Geophysics: Methods and Applications, Geophysical Monograph 268, First Edition.
Edited by Yingping Li, Martin Karrenbach, and Jonathan B. Ajo-Franklin.

DOI:10.1002/9781119521808.ch13

Carbon capture and storage (CCS) is the process of capturing carbon dioxide (CO_2) emissions from sources of the gas, such as power plants or refinery operations, and injecting and storing it inside dedicated geological reservoirs. Seismic monitoring of the injected CO_2 is a crucial step in the life of a CCS project as it provides assurance that the injected gas is safely stored in the subsurface. In the context of CCS, cost-effective reservoir monitoring techniques are especially desirable given that monitoring may need to be conducted across multidecadal time scales. Given the large footprint of a potential CO_2 injection plume, a methodology that minimizes impacts on surface-rights owners is essential.

To reduce the cost and land impact, permanently installed distributed acoustic sensors/distributed acoustic sensing (DAS) (Parker et al., 2014) can be utilized in conjunction with permanently installed surface orbital vibrators (SOVs) to create an on-demand permanent seismic monitoring array. SOVs consist of common alternating current induction motors driving eccentric weights to generate acoustic signals at the ground surface. SOVs produce vibrations as an effect of the rotation of the eccentric weights, which produce compressional waves and vertically and horizontally polarized shear waves (Daley & Cox, 2001). The sources generate vibroseis-type sweeps while rotating in both clockwise (CW) direction and counterclockwise (CCW) direction. The two directions are combined to synthesize linearly polarized waves. One can adjust the eccentric weights' setting to vary the maximum force of the source. The instantaneous force of the source varies as the frequency squares off the SOVs' rotational velocity. With their low capital and operating cost and high output force, SOVs can be a good alternative to common seismic sources. Yet, they have only been explored for niche applications and have not seen widespread adoption as seismic sources for permanent reservoir monitoring.

DAS technology enables the acquisition of on-demand vertical seismic profile (VSP) by using a permanently installed fiber-optic cable in a well, which is highly complementary to SOVs. DAS can acquire seismic data along the entire length of the fiber simultaneously, at small spatial intervals (Parker et al., 2014). Due to the potentially long lifetime of fiber cables and their inherent affordability compared to conventional seismic sensors, the permanent installation of a fiber-optic cable for acoustic sensing is becoming significantly more attractive and viable. The use of DAS for monitoring has been tested in the seismic industry, showing that DAS is an ideal cost-efficient nonintrusive seismic receiver when applied to three-dimensional (3-D) VSP applications (Mateeva et al., 2014; Mestayer et al., 2011).

DAS is rapidly becoming the sensor of choice for long-term seismic monitoring applications in CO_2 sequestration projects. Small-scale CCS projects tend to implement cutting-edge technologies, such as DAS, to demonstrate their applicability and to serve as an example for industrial-scale projects. Projects, such as the Ketzin pilot project, Citronelle CCS, and Aquistore Carbon Capture (Daley et al., 2013; Götz et al., 2018; Harris et al., 2017), showed in a variety of field tests that DAS can be used for long-term monitoring.

Stage 3 of the CO2CRC Otway Project is focused on the development of a suite of low-invasive downhole-based techniques, which could be used to conduct risk-based continuous or on-demand monitoring of industrial-scale CCS projects (Jenkins et al., 2017). TL seismic has two distinct goals within the Stage 3 project scope: (1) To develop novel approaches for downhole data acquisition and analysis, which would reduce the cost and level of invasiveness of conventional TL seismic monitoring, and (2) to reduce the considerable time lag between the acquisition of the data and availability of the interpretable results. These goals led to acquisition designed with continuous downhole seismic monitoring using an array of wells instrumented with multimode, standard single-mode and engineered fibers, and SOV sources on the surface. The aim is to automate data acquisition and processing and conduct close to daily updates of plume propagation along the transects between the wells and surface source locations.

Freifeld et al. (2016) presented an initial look at DAS/SOV data collected with a DAS/SOV array at the CO2CRC Otway Project site. Dou et al. (2016) analyzed the data acquired with buried surface fibers. Their results are discussed in the next section. In 2017, the CRC-3 well was drilled at the CO2CRC Otway Project site and instrumented with a combination of single-mode, multimode, and engineered fibers cemented behind the well casing. A series of offset VSP surveys were conducted using the cemented DAS and three-component geophones as receivers and a conventional vibroseis source. The cemented DAS VSP showed impressive results, presenting signal-to-noise ratio (SNR) values similar to those acquired by the geophone VSP (Correa et al., 2017).

In this chapter, we present the analysis of a follow-up study at the CO2CRC Otway Project using a series of offset VSPs acquired with the cemented DAS in the CRC-3 well and the permanently installed SOV sources. The surveys were acquired as field trials to test the performance of DAS/SOV, as well as establishing an optimum configuration of SOV power and frequency band to be applied in the Stage 3 monitoring program. Two field trials were conducted. In the first field trial, we compared the performance of DAS/SOV acquired using a conventional single-mode fiber and an enhanced sensitivity fiber. In the second field trial, DAS/SOV data were acquired using different source power and frequency settings. The results from this study help to shape Stage 3 of the CO2CRC Otway Project, which aims to develop more cost-effective seismic monitoring approaches.

13.2. PERMANENT MONITORING AT THE CO2CRC OTWAY PROJECT

The CO2CRC Otway Research Facility is Australia's first demonstration of deep geological storage of CO_2 (Figure 13.1). In 2015, a seismic monitoring array was installed permanently on-site. The array consists of a combination of buried geophones, approximately 40 km of fiber-optic cables for DAS acquisition, and two permanently installed SOVs. The fiber cables are deployed in 0.8 m deep trenches and along the tubing of the injector well (CRC-2). The SOV sources are installed atop a 2 m deep concrete foundation, deployed next to the Naylor-1 and CRC-2 wells. On each SOV pad, two sources are mounted: A small motor source with a maximum rotational speed of 200 Hz and a large motor source with a maximum speed of 80 Hz. The two SOV sources are installed at offsets of approximately 630 m (SOV1) and 380 m (SOV2) from the CRC-3 well.

During Stage 2C of the project, 15 kt of CO_2/methane gas mixture was injected at a depth of approximately1500 m. To image the development of the gas plume, a series of 3-D surface seismic surveys and VSP surveys were acquired using a 26,000 lbs vibroseis source (Pevzner et al., 2017). Five monitor surveys were acquired over a 2-year period after the gas injection, using 3-D surface seismic and VSP acquisition (Pevzner et al., 2020). The previous stages of the project were focused on the use of conventional technologies for monitoring, while simultaneously testing new technologies, such as DAS and SOVs. The surface DAS/SOV combination was evaluated using the buried fiber-optic cable. The results from early field trials show that DAS/SOV could potentially be used as an economical approach for acquiring TL surveys (Dou et al., 2016). The tubing-deployed DAS showed low SNR, possibly due to poor coupling of the fiber with the formation (Freifeld et al., 2016). However, after further processing of the 3-D VSP survey, the on-tubing fiber presented enough sensitivity to record reflections from the main interfaces (Correa et al., 2019).

Stage 3 of the Otway Project plans to inject 15 kt of CO_2 commencing in the second half of 2020. A unique feature of Stage 3 is that it is focused on a multiwell monitoring strategy to develop continuous on-demand reservoir monitoring using remotely operated sources and receivers. This approach aims to reduce the acquisition footprint, minimizing environmental and social impacts associated

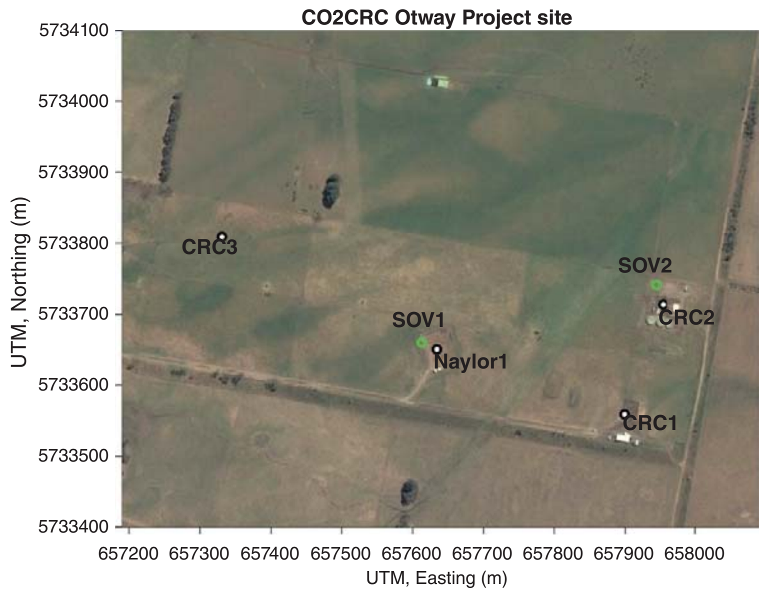

Figure 13.1 The CO2CRC Otway Project site location and satellite image. The locations of the CRC-1, CRC-2, CRC-3, and Naylor-1 wells are displayed. The locations for SOV1 and SOV2 sources are also marked in green.

with data acquisition. The CRC-3 well, which was drilled in 2017 and is the future injector for Stage 3, is instrumented with a pair of fiber-optic cables. The fiber-optic cables were cemented behind the casing of the well, aiming to increase the coupling to the formation and thus improving SNR of the VSP records. One cable contains a set of single-mode and multimode fibers that were deployed to a depth of 1430 m. The other cable contains single-mode, multimode, and "enhanced" sensitivity fibers engineered to increase the light backscatter (commercial name is "constellation fiber"), which were deployed over the total depth of the well. Recent VSP acquisitions with DAS in CRC-3 demonstrated the ability of DAS to effectively image the plume, using both the standard single-mode fiber and the engineered fiber (Correa et al., 2017).

The monitoring plan for Stage 3 uses seven wells, both vertical and directionally drilled (wells CRC-2 to CRC-7 are instrumented with fiber optics, and CRC-1 is instrumented with three-component geophones), combined with nine SOV sources (Figure 13.2). The proposed monitoring plan consists of daily automatic acquisition of DAS/SOV VSP data. The acquired data will be processed through a standard VSP processing flow that will run automatically. The final product of the processing flow will be a series of two-dimensional (2-D) images for each well-SOV pair that intersects the injected CO_2 plume, providing daily images of the subsurface movement of gas. The proposed seismic processing will use full-waveform inversion to provide a quantitative interpretation of the rock properties within the injection interval (Egorov et al., 2018). With this, the CO2CRC Otway Project hopes to provide the industry with a template for cost-effective, permanent, on-demand reservoir monitoring.

13.3. FIELD EXPERIMENTS WITH DAS AND SOV SOURCES AT THE CO2CRC OTWAY PROJECT

Preparation for the Stage 3 monitoring program included a set of field experiments to test the performance of SOV sources in conjunction with cemented DAS in CRC-3. The primary objective was to determine the capability of DAS/SOV to image the target horizon (1500 m) by testing the performance of a series of offset VSP surveys acquired with a standard single-mode fiber and an engineered fiber designed to increase DAS sensitivity. Additionally, the field trials aimed to test different SOV source types and sweep designs to determine the optimum parameters for imaging at the CO2CRC Otway Project.

The first DAS/SOV field trial was acquired in May 2017 to compare DAS VSP from a standard fiber with an enhanced fiber, using the SOV sources. DAS VSP was acquired at 0.5 m spatial sampling along the fiber cable. During the first field trial, DAS VSP was acquired using the longer of the two installed fiber cables (maximum depth of 1660 m) in the CRC-3 well. The standard fiber-optic cable was connected to an interrogator unit

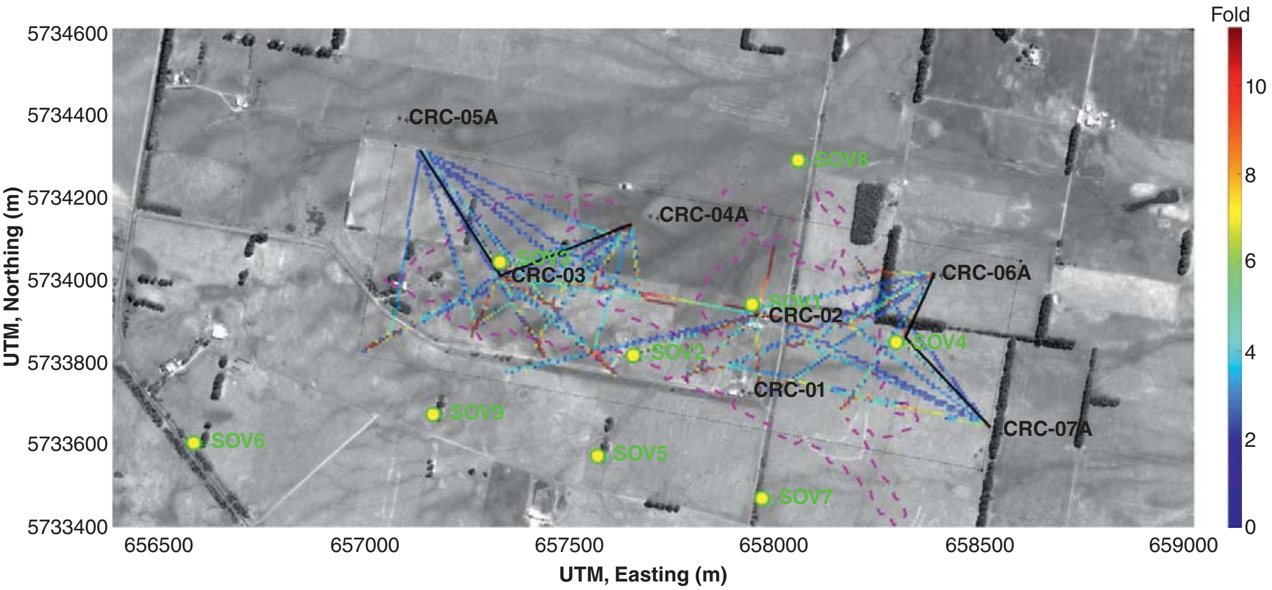

Figure 13.2 Seismic fold (color bar) given by a combination of seven wells (CRC-1–CRC-7) and nine SOV sources (SOV1–SOV9). Outlined with a purple dashed line is the predicted plume after injection in CRC-3, combined with the previously injected plume in CRC-2.

(iDASv2) and the engineered fiber (constellation fiber) was connected to an upgraded version of this interrogator unit (iDASv3). Both interrogators and constellation fiber are a proprietary of Silixa Ltd. A 10 m gauge length was used in both interrogators. SOV1 and SOV2 sources (with large motors) were used in the acquisition for this trial. The sources used sweeps of 155 s (30 s upsweep, 5 s hold, and 120 s downsweep) from 0 to 80 Hz (Table 13.1). The large motors can generate a force of 20,000 lbf at 60 Hz. Assuming the force is proportional to frequency squared, at 80 Hz the source generates a force of approximately 10 t with weights set to 55% force. The weight setting of 55% was chosen to limit the SOV motor to its rated load capacity.

The second field trial was conducted in November 2018 to test source sweep designs to obtain optimal parameters for the monitoring program. DAS VSP was acquired using the shorter cemented cable, with standard single-mode fiber, and interrogator unit iDASv2 at 0.5 m spatial intervals. Small and large motors were used for both SOV1 and SOV2. The small motors can generate a force of 5,000 lbf at 60 Hz. SOV1 used sweeps from 0 to 80 Hz for the large motor, and from 0 to 120 Hz for the small motor. SOV2 was also set to produce sweeps from 0 to 80 Hz with large motor, while the small motor had sweeps from 0 to 120 Hz and from 0 to 160 Hz (Table 13.2). Given the specifications for the small motors, at 120 Hz the source force is 5 t, using 100% of the weight setting but modifying the weights to half their initial mass. For the test from 0 to 160 Hz, the weight setting was 50%, using the modified weights, which gave a force of 4.5 t at 160 Hz. Multiple sweeps were recorded for each test. Table 13.1 and Table 13.2 summarize the main parameters for each test.

13.4. OFFSET VSP PROCESSING

The processing flow applied to the offset VSP acquired with DAS/SOV consists of three stages (Table 13.3). The first stage is performed using MatLab and aims to deconvolve the recorded data with a source wavelet; the second stage performs wavefield separation to obtain the upgoing *P*-waves; and the third stage performs VSP-CDP transform of the upgoing *P*-waves.

When using conventional vibroseis sources that generate a phase- and amplitude-controlled sweep, the data are correlated with the source signal (theoretical or measured) to obtain a zero-phase wavelet (e.g., Yilmaz, 2001). Due to the unbalanced frequency spectrum of the orbital vibes, where the force increases as frequency squares, if the source sweep is autocorrelated, the resulting frequency spectrum has amplitudes increasing with fourth power of the frequencies. This yields a wavelet with pronounced side lobes. To reduce this effect, the sweep is deconvolved (division in frequency domain), which normalizes the amplitudes and reduces wavelet side lobes (Daley & Cox, 2001). During the deconvolution process, the amplitude spectrum of the recorded data is divided by the amplitude spectrum of the sweep, and the phase spectrum of the recorded data is subtracted by the phase spectrum of the sweep. To stabilize due to division by zero, a water level (or white noise) factor of 0.1 is multiplied by the maximum amplitude of the sweep and added to the denominator.

After deconvolution, the resulting data sets are processed using commercial seismic processing software (RadExPro). For each sweep, the eccentric mass of the source starts at a different position, which results in sweeps that vary by a static phase shift, which can leave

Table 13.1 Acquisition Parameters for the May 2017 Field Trial.

SOV1	SOV2
Large motors, 0–80 Hz, 55% weight setting, 100% weights, 10 t force at peak frequency, 28 sweeps	Large motors, 0–80 Hz, 55% weight setting, 100% weights, 10 t force at peak frequency, 28 sweeps

Table 13.2 Acquisition Parameters for the November 2017 Field Trial.

SOV1	SOV2
Large motors, 0–80 Hz, 55% weight setting, 100% weights, 10 t force at peak frequency, 20 sweeps	Large motors, 0–80 Hz, 55% weight setting, 100% weights, 10 t force at peak frequency, 20 sweeps
Small motors, 0–120 Hz, 100% weight setting, 50% weights, 5 t force at peak frequency, 32 sweeps	Small motors, 0–120 Hz, 100% weight setting, 50% weights, 5 t force at peak frequency, 32 sweeps
	Small motors, 0–160 Hz, 50% weight setting, 50% weights, 4.5 t force at peak frequency, 10 sweeps

Table 13.3 Offset VSP Processing Flow.

Processing step	Comments
Data input	Measured data were in strain rate
Deterministic source signature deconvolution	Deconvolution with source sweep. Water level factor of 0.1 was added
Source statics	Correct source delays
Stack of multiple sweeps	Stack sweeps and average (mean)
Geometry assignment	Assignment of coordinates
Band-pass filtering	8–14–50–82 Hz for sweeps up to 80 Hz 8–14–100–122 Hz for sweeps up to 120 Hz 8–14–120–160 Hz for sweeps up to 160 Hz
Wavefield separation (FK filter)	Separation of upgoing and downgoing wavefields by using a polygon in the FK domain
***S*- and *PS*-wave attenuation (FK filter)**	Flattening of first breaks and separation of *P* from *S* and *PS* by using a polygon in the FK domain
Amplitude correction	Multiplied by travel time squared
VSP to CDP transform	Raytracing procedure to remap amplitudes using a one-dimensional velocity model
Summation of CW and CCW directions	Summation of both directions of rotation to result in the vertical component of the source

a residual time shift after decon. Therefore, each sweep had statics applied by picking the first break for each sweep and correcting the difference in time between them. After statics correction, the sweeps were stacked to reduce random noise and increase SNR. For the May test, SOV1 and SOV2 had 14 repeated sweeps stacked for each CW and CCW rotation. For the November test, DAS data sets with large motors were stacked with 10 repeated sweeps, data sets with small motors up to 120 Hz were stacked with 16 repeated sweeps, and for small motors up to 160 Hz, 5 repeated sweeps were stacked.

After stacking the sweeps, the geometry for each data set was assigned where each trace was matched with the depth and the geographical positions of the source and receiver. Assigning depth to a DAS VSP channel can require some calculation due to extra fiber length (e.g., Daley et al., 2016). A band-pass filter was applied to the data, passing the dominant frequency band of the respective sweep. In the next step, wavefield separation was applied to the data set using an FK filter to remove the downgoing wavefield by applying a polygon in the FK domain. The upgoing wavefield contains a combination of *P*-, *S*-, and *PS*-waves. To proceed with the *P*-wave processing, the first breaks were flattened, and an extra pass of FK filtering was applied in order to filter out *S*- and *PS*-upgoing waves by also using a polygon in the FK domain. The amplitudes were compensated for spherical divergence by multiplying by the travel time squared. The upgoing filtered *P*-waves were stacked using 5 m spatial intervals.

The data were remapped to surface equivalent through VSP to CDP transform, using a one-dimensional velocity model. During VSP to CDP transform (often referred to as "mapping"), the reflected wave energy is relocated through raytracing to the position on the image which would correspond to the location of the reflection point. However, unlike in migration, no summation over the travel time curves of diffracted waves happens at this stage. The velocity model utilized in this step was obtained and tuned numerous times in previous analyses done on data sets acquired at the CO2CRC Otway Project with geophones. After the transform, the CW and CCW directions were summed to result in the total vertical component of the source (Daley & Cox, 2001).

13.5. MAY 2017 FIELD TRIAL: CONVENTIONAL SINGLE-MODE FIBER VS. CONSTELLATION FIBER

The use of DAS combined with SOV sources has enormous potential in permanent reservoir monitoring applications, as it offers reduced environmental and social impact, while imaging the changes in the reservoir. However, it is important to address issues limiting the capability of SOV/DAS, such as the narrow bandwidth of SOVs and the lower sensitivity of DAS (Dean et al., 2016; Willis et al., 2016). In order to study how these issues affect SOV/DAS, we analyze the data quality of the VSP acquired by DAS using both SOV sources deployed on-site (Figure 13.1).

Figure 13.3 shows the SOV/DAS data acquired using the standard fiber and the constellation fiber. Each display shows a stack of 14 repeated shots in the CW direction, after the geometry assignment processing step. A band-pass filter was applied to select frequencies from 5 to 140 Hz (the filter tapers over 5–10 Hz and 80–140 Hz). Figures 13.3a and 13.3b show the VSP data acquired

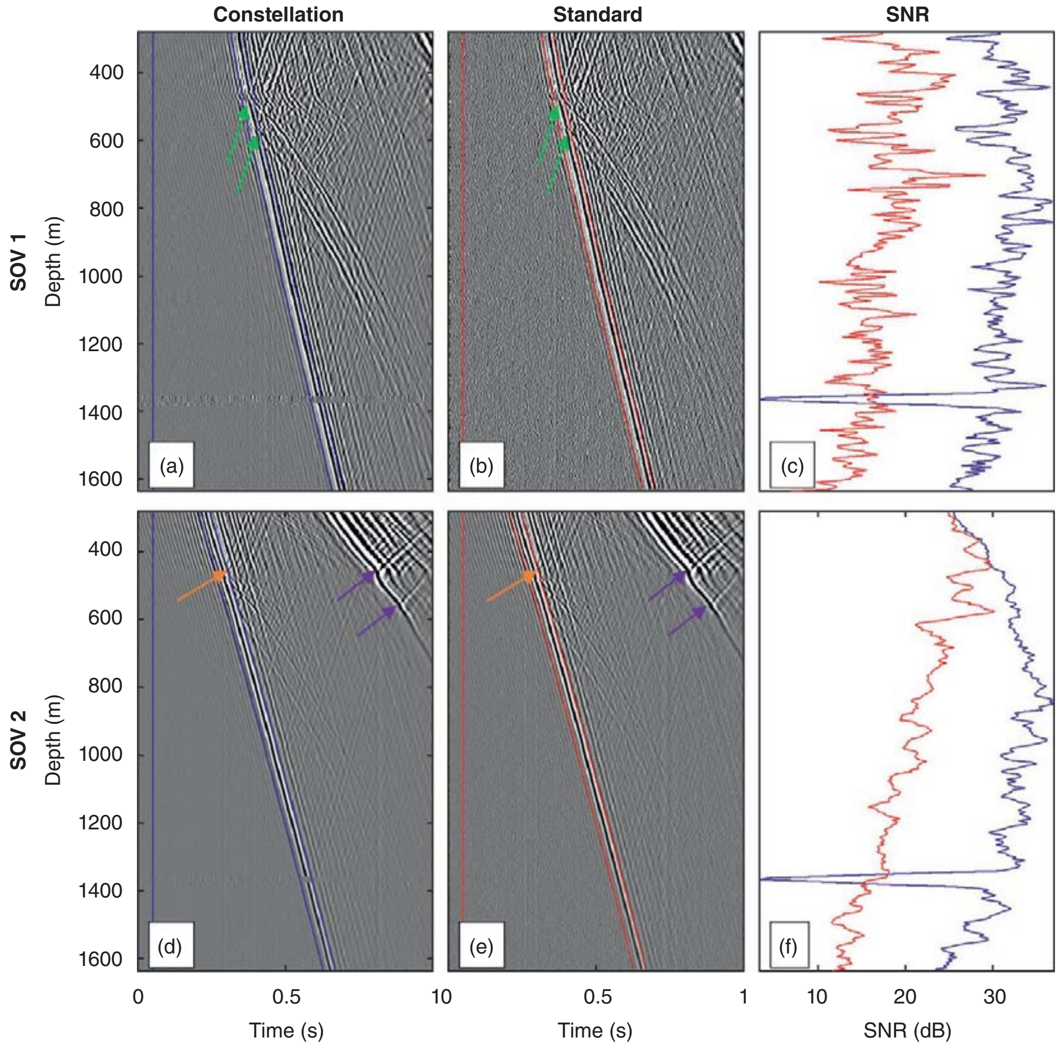

Figure 13.3 DAS-SOV VSP records acquired for SOV1 [(a) and (b)] and SOV 2 [(d) and (e)], for a stack of 14 sweeps in the CW direction. The normalized SNR for SOV1 and SOV2 is shown in (c) and (f), respectively. Sweeps were acquired with frequencies from 0 to 80 Hz, using a motor of 10 t force at maximum frequency. Data were acquired during the May 2017 test. Each display is normalized individually by its maximum amplitude. Acquisition parameters can be found in Table 13.1.

for SOV1 (a 630 m distance from the well). By comparing qualitatively the data acquired with the engineered fiber (Figure 13.3a) and the standard single-mode fiber (Figure 13.3b), the engineered fiber shows improved data quality. The enhanced fiber is engineered to increase light backscatter, which increases the sensitivity of the fiber. Therefore, the apparent reduction of noise in the engineered fiber can be explained by normalizing the stronger amplitudes of the reflections in relation to the background noise itself. The data from the enhanced fiber contain a set of "blind" traces corresponding to a depth of approximately 1390 m as a result of a section of the fiber not receiving the enhancing treatment during the manufacturing process. Also, it is possible to note "common-mode" noise at approximately 400 ms in Figure 13.3a and at 300 ms in Figure 13.3b, which affects all depths. The common-mode noise is seen frequently in DAS data and it occurs when the interrogator unit is disturbed (vibrated). The data acquired with the standard fiber are noisier; however, these were still able to detect the *P*-wave reflections present on the enhanced fiber. The green arrows show an example of upgoing *P* reflections that appear on both engineered and standard fibers. Figures 13.3d and 13.3e show the data acquired with SOV2, at 320 m distance from the well. Both fibers are able to detect seismic reflections. The orange arrow shows a *PS*-wave reflection sensed by both fibers, while the purple arrow shows *S*-wave reflections.

SNR was calculated by dividing the root-mean-square (RMS) amplitude of a 50 ms window centered around the first breaks and a 50 ms window of noise at the start of the record. Figure 13.3c shows the SNR for SOV1 and the engineered fiber is approximately 15–20 dB higher than the standard fiber. Figure 13.3f shows SNR calculated for SOV2 and the engineered fiber shows approximately 15 dB higher SNR than the standard fiber.

The amplitude spectrum for both engineered fiber and standard fiber is shown in Figure 13.4. The amplitude spectrum uses the unfiltered data (no band pass). By comparing the frequency content in each fiber type, it is possible to note that they show the same trend within the signal band (up to 80 Hz). However, the engineered fiber shows significantly lower noise floor, approximately 15 dB lower than the standard fiber, which is seen on the frequencies above the sweep range (above 80 Hz). Below approximately 10 Hz, the force that the SOV source is able to generate is relatively weak. The difference of the amplitude spectrum between the constellation fiber and the standard fiber suggests that the improvement in SNR of the constellation fiber can be attributed to lowering its noise floor.

Figure 13.5 shows the results of applying VSP to CDP transform for each data set acquired during the May test. After the transform, both CW and CCW directions were summed, which results in the vertical component of the source. The 2-D lines produced for SOV1 and SOV2 are displayed side by side; the well location is displayed in blue where both lines meet. Note that the reflections on the 2-D lines of SOV1 and SOV2 match well, for both engineered fiber (Figure 13.5a) and standard fiber (Figure 13.5b). Both fibers provide similar results, although the standard fiber shows a higher level of random noise, which is more apparent at the end of the record where the signal level decreases (orange square).

After VSP to CDP transform, the 2-D images produced from each data set were converted from depth to time to facilitate a comparison with a conventional seismic data set. Figure 13.6 shows a comparison of the 2-D image generated from SOV1 using constellation fiber after VSP to CDP transform, and a crossline of a previously acquired data set using conventional surface geophone data acquired during Stage 2C monitor 5 survey (Pevzner et al., 2020). The surface geophone survey was the main monitoring tool for Stage 2C of the CO2CRC Otway Project, as previously mentioned in Section 13.2. It should be noted that the conventional geophone seismic surveys were acquired using a vibroseis source with approximately 4,000 source points and sweeps of up to 150 Hz. Figure 13.6 shows the surface seismic crossline that intersects with the SOV/DAS 2-D image at the well location. Despite the differences in acquisition of the conventional and SOV/DAS surveys, the 2-D image generated from SOV1 and DAS shows a good match with the crossline from the surface geophone data. Comparison can be made for reflections at the approximate times of 500 ms, 600 ms, 1100, and 1200 ms, with the last corresponding to the injection interval. The SOV/DAS data contain good-quality signal and low levels of noise and correspond well with the image produced from the conventional acquisition, though it is important to note that the image produced from a single SOV source position and one well has a significantly narrower illumination

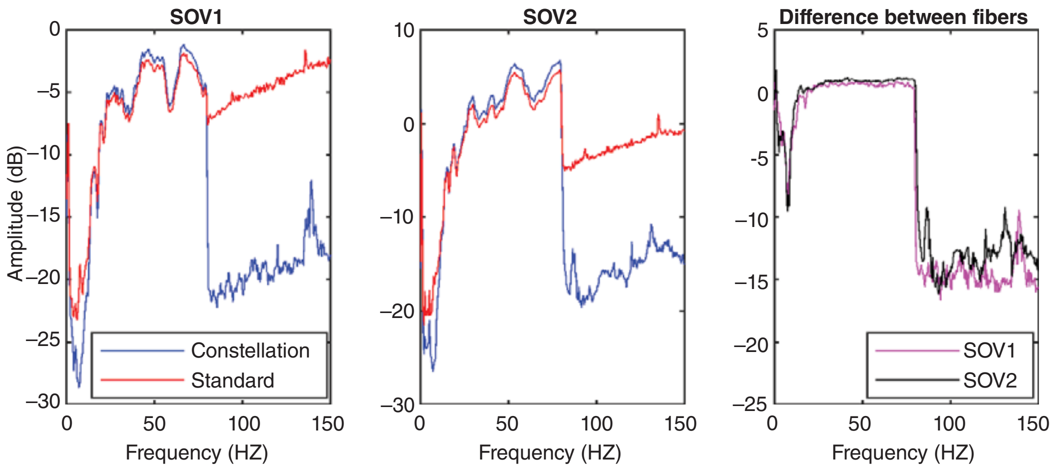

Figure 13.4 Amplitude spectrum for the constellation fiber (blue curve) and the standard fiber (red curve) acquired with SOV1 and SOV2. The difference between constellation fiber and standard fiber amplitudes is displayed for SOV1 (purple curve) and SOV2 (black curve). The amplitude spectrum was calculated over unfiltered data. Amplitude spectrum was normalized using 90 dB as reference.

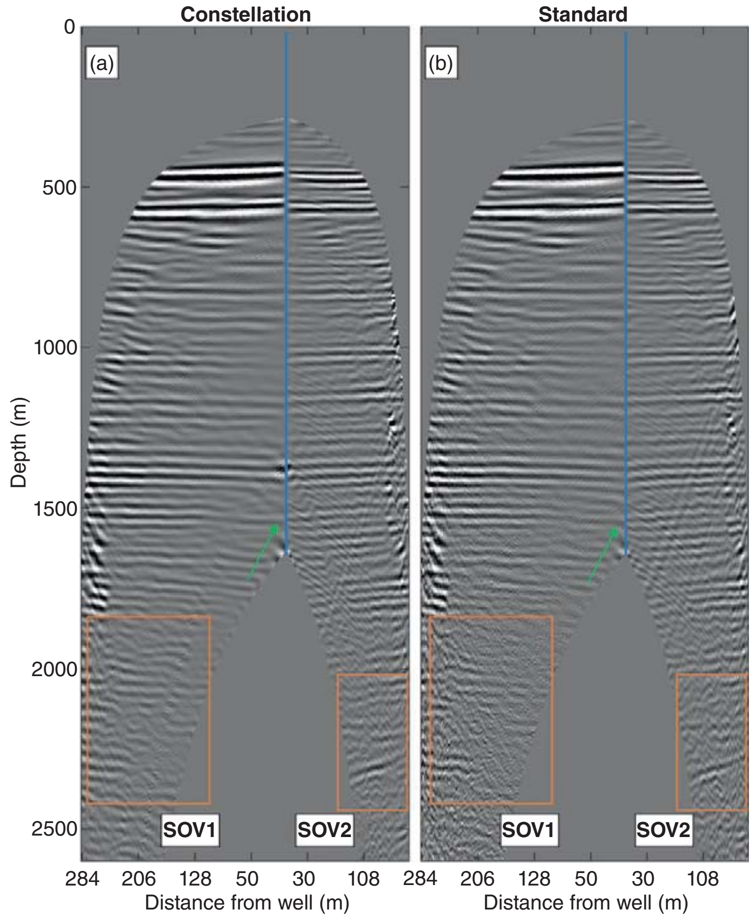

Figure 13.5 VSP to CDP transform for the constellation fiber (a) and the standard fiber (b). The 2-D lines corresponding to SOV1 and SOV2 are displayed side by side. Well location is displayed in blue. Sweeps were acquired with frequencies from 0 to 80 Hz, using a motor of 10 t force at maximum frequency. Each direction of rotation (CW and CCW) was summed following deconvolution to obtain the vertical force. Data were acquired during the May 2017 test. The green arrow points at the injection interval. Acquisition parameters can be found in Table 13.1.

pattern when compared to conventional acquisitions, giving a short 2-D line. This imposes limitations on the application of DAS/SOV to 3-D reservoir monitoring with a limited number of sources and wells on a site.

13.6. NOVEMBER 2017 FIELD TRIAL: PERFORMANCE OF SMALL AND LARGE MOTORS

Tests of a range of sweep designs conducted using both large and small motors at SOV1 and SOV2 locations were recorded with the standard fiber-optic cable in the CRC-3 well. Since the SOV force output is proportional to frequency squared, the force while sweeping through low frequencies is small compared to the force during high frequencies. To generate sufficient energy at low frequencies, large SOV motors, which can produce approximately 10 t force at peak frequency (80 Hz), are best. To acquire higher frequency data, small motors, which reliably operate at frequencies up to 160 Hz, are best though reaching a force of only 4.5 t at peak frequency.

Figure 13.7 shows the data recorded for CW direction using the standard single-mode fiber with large motors (up to 80 Hz) and small motors (up to 120 Hz), after geometry assignment. For display purposes, a band-pass filter of 5–10–80–140 Hz was applied to the large motor data, and a band-pass filter of 5–10–120–140 Hz was applied to the small motor data. For both sweep design tests, DAS was able to record upgoing *P*- and *S*-waves. As expected, large motors provide stronger signal with better defined reflections than small motors, since they

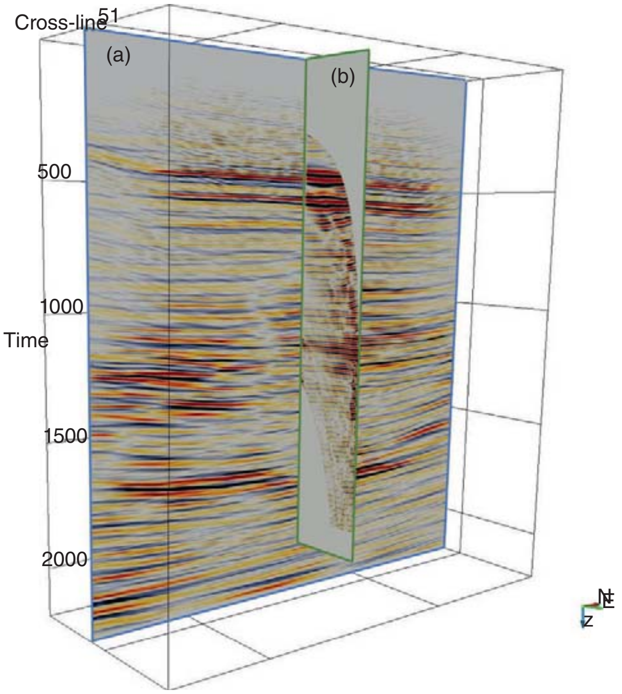

Figure 13.6 Crossline from a conventional vibroseis-geophone surface seismic survey acquired during Otway monitor 5 (a) intersected by the DAS/SOV1 2-D line after VSP to CDP transform acquired with the engineered fiber (b). The two lines intersect at the well location.

are able to provide higher force. Even with the small motor, DAS was still able to record *P*-wave reflections at the far offset (Figure 13.7b). At the near offset with SOV2, DAS was able to sense *PS*-upgoing reflections using both motors (denoted by an orange arrow). However, the small motor was not sufficiently strong to generate clear reflections from deep interfaces. The green rectangle emphasizes the main differences between the large and small motors, where the large motor has strong *P* reflections and the small motor shows weak reflections and noisy data.

The SNR was calculated by dividing the RMS amplitude of the record in a 50 ms window centered at the first breaks with the RMS amplitude of a 50 ms window of noise at the start of the record (Figures 13.7c and 13.7f). The large motors provide higher SNR, reaching approximately 20 to 30 dB at both locations, while the SNR of small motors is approximately 5 to 10 dB. The apparent difference in the background noise can be explained by normalizing the peak signal amplitude, which reduces visible noise for the higher amplitude source.

To analyze the effect of the different sweeps, each data set was processed using the same seismic processing flow (Table 13.3) as the previous test. The VSP to CDP transform for CW and CCW directions was stacked to obtain the vertical component for one 2-D line. Figure 13.8 shows a 2-D line for three sweeps. The test using sweeps from 0 to 80 Hz (Figure 13.8a) produces good *P*-wave reflections, and both lines corresponding to SOV1 and SOV2 match well. When using the small motors with sweeps from 0 to 120 Hz (Figure 13.8b), DAS reveals reflections only up to approximately the target depth of 1500 m, as the low power of the source results in low SNR of the data set (Figure 13.8b). The test with sweeps from 0 to 160 Hz (Figure 13.8c) was acquired only for SOV2, and, even at a near offset, the source power is not sufficient to image reflections beyond 800 m depth. Although the large motors provide higher SNR data sets, the higher frequency of the small motors can improve resolution and sharpness of the reflections. The improved resolution from the higher frequency sweeps can be seen, for example, by comparing the reflection at 500 m, as shown in Figure 13.8.

13.7. SUMMARY AND CONCLUSIONS

Restricted land accessibility, poor repeatability, and long survey durations are common issues that limit onshore reservoir monitoring applications. For CCS projects, reservoir monitoring is used to ensure safe and leakage-free storage of CO_2. In CCS projects, where the surveillance of the reservoir is likely to go on for decades after the injection, it is crucial to develop monitoring techniques that are cost-effective and easily operated, and minimize the environmental and land impact. The seismic monitoring program of Stage 3 of the CO2CRC Otway Project aims to demonstrate a safe and efficient method for monitoring that can be applied to commercial-scale CCS projects and has long-term potential. Preparation for Stage 3 of the CO2CRC Otway Project involved a series of tests to explore optimal DAS/SOV configurations. Two separate VSP surveys were acquired with cemented fiber-optic cables using SOV sources at two offset locations: Approximately 380 m (SOV2) and approximately 630 m (SOV1) from the injector well (CRC-3). The first field trial had the objective to test the performance of DAS using a standard fiber-optic cable and an "enhanced" sensitivity cable engineered to increase light backscatter. The second field trial tested the optimal performance of the SOV source by acquiring a range of sweeps using large and small motors at different frequency ranges – up to 80 Hz for large motors and 160 Hz for small motors.

In the first test, DAS acquired with the engineered fiber shows approximately 15 dB higher SNR in comparison with the standard single-mode fiber. Despite the lower

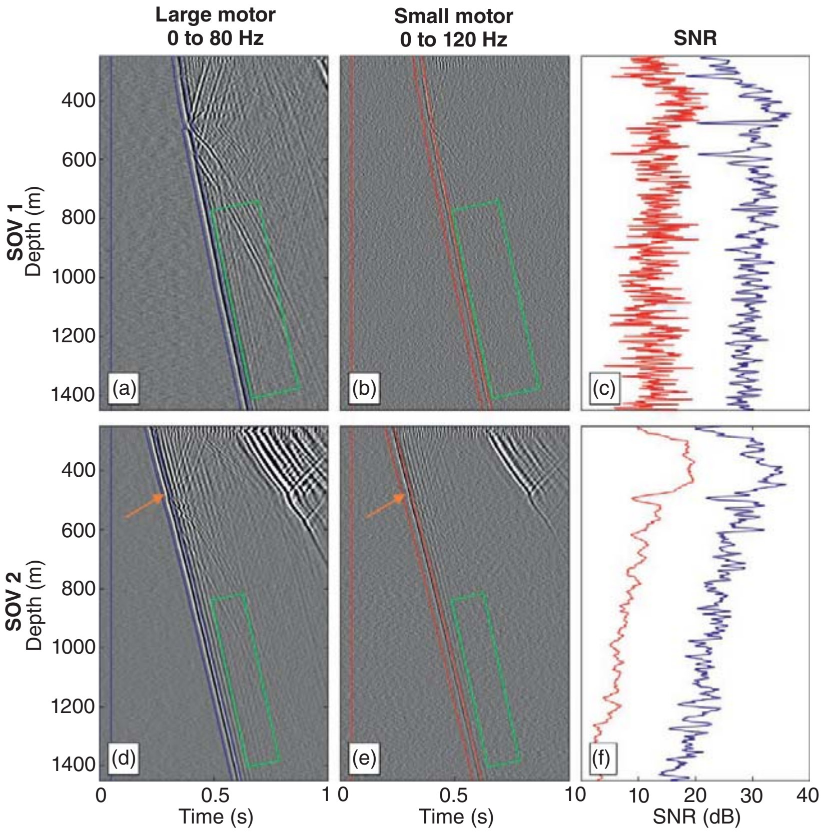

Figure 13.7 VSP acquired with DAS using large and small motors at SOV1 [(a) and (b)] and at SOV2 [(d) and (e)] during the November 2017 test. CW direction is displayed. Large motor plot was stacked using 10 sweeps, and small motor plot was stacked using 16 sweeps. SNR was calculated for DAS with SOV1 (c) and DAS with SOV2 (f). Acquisition parameters can be found in Table 13.2. The plots are normalized by their maximum amplitude.

SNR, the standard fiber was able to record the clear *P*-wave reflections with large motors. After VSP to CDP transform, both the engineered fiber and the standard fiber provide similar images, though the standard fiber is noisier at deep intervals. The second test shows that large motors provide higher signal-to-noise levels, as expected given the higher source power. The small motors can be utilized in conjunction with the large motors to improve the resolution, due to their ability to sweep up to high frequencies. Sweeps up to 80 Hz and up to 120 Hz both generated measurable reflections from the target depth at 1500 m.

The results of these tests show that a VSP acquired with DAS using a cemented cable and SOVs yields high-quality data, which are sufficient to image and monitor the injection interval. At both SOV locations, DAS was able to acquire *P*-wave reflections, as well as converted *PS*-waves and *S*-waves. Thus, these results demonstrate a proof of concept of using borehole DAS/SOV for seismic imaging as an efficient alternative methodology for permanent reservoir monitoring. The use of DAS in conjunction with SOV sources and an automated processing flow has the potential to autonomously acquire good-quality VSP surveys.

Pairing SOVs with engineered fibers has the potential of decreasing some of the disadvantages associated with SOVs, such as the narrow frequency band of the sweep signal. Since its force is proportional to frequency squared, the low-frequency content is especially affected. However, the detection of weak signals, like those at low frequencies, can be improved by using engineered fibers. Engineered fibers should also have an advantage when acquiring data from small motors. The increased sensitivity of the engineered fiber should improve the recording of seismic data with the higher frequencies achieved by the small motors, while the standard fiber was not sensitive enough to detect their weak signal. Another advantage is that engineered fibers should permit acquisition of

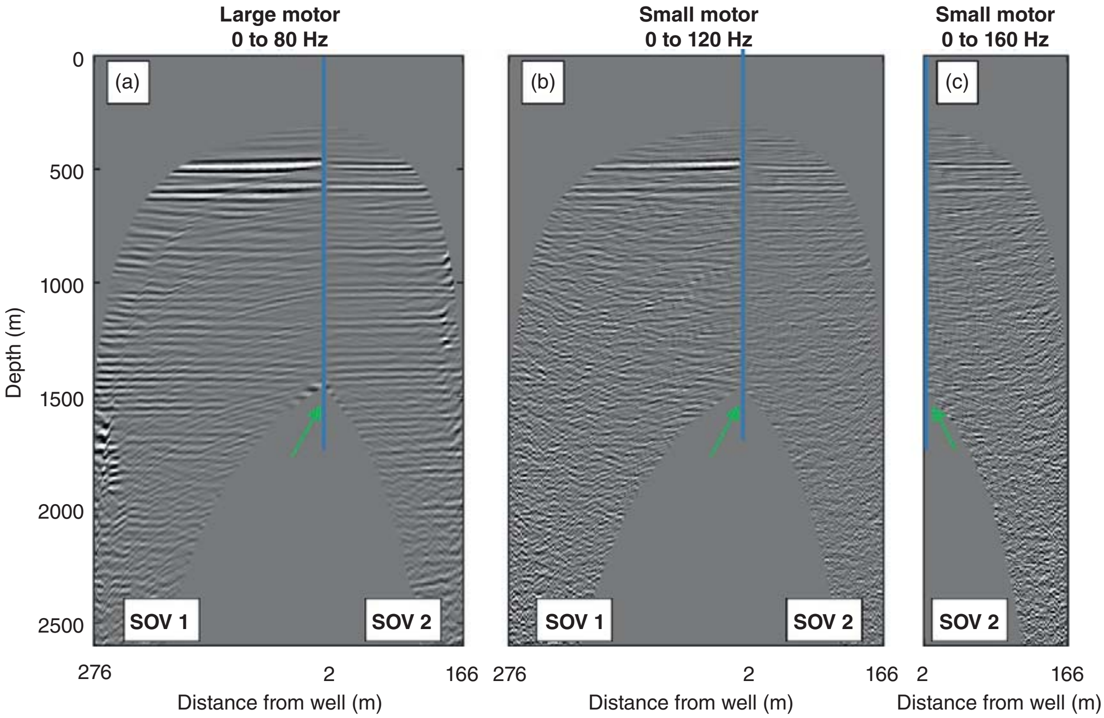

Figure 13.8 Results of VSP to CDP transform for test with sweeps from 0 to 80 Hz using large motors (a), from 0 to 120 Hz using small motors (b), and from 0 to 160 Hz using small motors at SOV2 (c). The data were acquired with the shorter standard single-mode cable. The 2-D lines corresponding to SOV1 and SOV2 are displayed side by side. Well path is displayed in blue. The injection interval is shown by the green arrow. Acquisition parameters can be found in Table 13.2.

SOVs at longer offsets, increasing the illumination range and providing a better estimation of the migration of the CO_2 plume.

Based on these results, VSP acquisition for Stage 3 of the CO2CRC Otway Project will use both large and small motors, and, in most wells, engineered fibers. The tests performed with DAS and SOVs shown here demonstrate considerable benefits of utilizing the large motors with sweeps from 0 to 80 Hz, as well as small motors with sweeps from 0 to 120 Hz. The Stage 3 monitoring plan will involve nine SOVs (as displayed in Figure 13.2), incorporating both large and small motors, and seven wells, six of which have fiber installed permanently. This arrangement will be used to generate a series of daily 2-D images intersecting the injected CO_2 plume, providing real-time monitoring of the reservoir, while improving our understanding of the behavior of the injected CO_2 and increasing the safety of operations.

ACKNOWLEDGMENTS

The CO2CRC Otway Project received CO2CRC funding through its industry members and research partners, the Australian Government under the CCS Flagships Programme, the Victorian State Government, and the Global CCS Institute. The authors wish to acknowledge financial assistance provided through Australian National Low Emissions Coal Research and Development (ANLEC R&D) supported by Australian Coal Association Low Emissions Technology Limited and the Australian Government through the Clean Energy Initiative. Funding for Lawrence Berkeley National Laboratory was provided through the Carbon Storage Program, U.S. Department of Energy, Assistant Secretary for Fossil Energy, Office of Clean Coal and Carbon Management through the National Energy Technology Laboratory, under Contract No. DE-AC02- 05CH11231.

REFERENCES

Correa, J., Egorov, A., Tertyshnikov, K., Bona, A., Pevzner, R., Dean, T., et al. (2017). Analysis of signal to noise and directivity characteristics of DAS VSP at near and far offsets—A CO2CRC Otway Project data example. *The Leading Edge*, *36*(12), 994a1–994a7. https://doi.org/10.1190/tle36120994a1.1

Correa, J., Pevzner, R., Bona, A., Tertyshnikov, K., Freifeld, B., Robertson, M., & Daley, T. (2019). 3D VSP acquired with DAS on tubing installation: A case study from the CO2CRC

Otway Project. *Interpretation*, *7*(1), SA11–SA19. https://doi.org/10.1190/INT-2018-0086.1

Daley, T. M., & Cox, D. (2001). Orbital vibrator seismic source for simultaneous P- and S-wave crosswell acquisition. *Geophysics*, *66*, 1471–1480. doi:10.1190/1.1487092

Daley, T. M., Freifeld, B. M., Ajo-Franklin, J., Dou, S., Pevzner, R., Shulakova, V., et al. (2013). Field testing of fiber-optic distributed acoustic sensing (DAS) for subsurface seismic monitoring. *The Leading Edge*, *32*(6), 699–706, http://dx.doi.org/10.1190/tle32060699.1

Daley, T.M., Miller, D. E., Dodds, K., Cook, P., &Freifeld, B. M. (2016). Field testing of modular borehole monitoring with simultaneous distributed acoustic sensing and geophone vertical seismic profile at Citronelle, Alabama. *Geophysical Prospecting*, *64*(5), 1318–1334, doi: 10.1111/1365-2478.12324

Dean, T., Brice, T., Hartog, A., KraghE., Molteni, D., & O'Connell, K. (2016). *Distributed vibration sensing for seismic acquisition. The Leading Edge*, *35*(7), 600–604. doi:10.1190/tle35070600.1

Dou, S., Ajo-Franklin, J., Daley, T., Robertson, M., Wood, T., Freifeld, B., et al. (2016). *Surface orbital vibrator (SOV) and fiber-optic DAS: Field demonstration of economical, continuous-land seismic time-lapse monitoring from the Australian CO2CRC Otway site*. SEG Technical Program Expanded Abstracts (5552–5556). doi: 10.1190/segam2016-13974161.1

Egorov, A., Correa, J., Bóna, A., Pevzner, R., Tertyshnikov, K., Glubokovskikh, S., et al. (2018). Elastic full-waveform inversion of vertical seismic profile data acquired with distributed acoustic sensors. *Geophysics*, *83*, R273–R281. https://doi.org/10.1190/geo2017-0718.1

Freifeld, B. M., Pevzner, R., Dou, S., Correa, J., Daley, T. M., Robertson, M., et al. (2016). *The CO2CRC Otway Project deployment of a distributed acoustic sensing network coupled with permanent rotary sources*. 78th EAGE Conference and Exhibition, Extended Abstract. doi. 10.3997/2214-4609.201600577.

Götz, J., Lüth, S., Henninges, J., & Reinsch, T. (2018). Vertical seismic profiling using a daisy-chained deployment of fibre-optic cables in four wells simultaneously—Case study at the Ketzin carbon dioxide storage site. *Geophysical Prospecting, 66*(6), 1201–1214.

Harris, K., Don, W., & Samson, C. (2017). Imaging the Aquistore reservoir after 36 kilotonnes of CO2 injection using distributed acoustic sensing. *Geophysics*, *82*(6), M81–M96. doi: 10.1190/geo2017-0174.1

Jenkins, C., Marshall, S., Dance, T., Ennis-King, J., Glubokovskikh, S., Gurevich, B., et al. (2017). Validating subsurface monitoring as an alternative option to surface M&V – The CO2CRC's Otway Stage 3 injection. *Energy Procedia*, *114*, 3374–3384. doi: 10.1016/j.egypro.2017.03.1469

Lumley, D. E. (2001). Time-lapse seismic reservoir monitoring. *Geophysics*, *66*(1), 50–53. doi: 10.1190/1.1444921

Mateeva, A., Lopez, J., Potters, H., Mestayer, J., Cox, B., Kiyashchenko, D., et al. (2014). Distributed acoustic sensing for reservoir monitoring with vertical seismic profiling: *Geophysical Prospecting*, *62*, 679–692.

Mestayer, J., Cox, B., Wills, P., Kiyashchenko, D., Lopez, J., Costello, M., et al. (2011). *Field trials of distributed acoustic sensing for geophysical monitoring. Paper presented at 81st SEG Annual International Meeting*.

Parker, T., Shatalin, S., & Farhadiroushan, M. (2014). Distributed Acoustic Sensing—a new tool for seismic applications. *First Break*, *32*(2), 61–69. doi: 10.3997/1365-2397.2013034

Pevzner, R., Urosevic, M., Popik, D., Shulakova, V., Tertyshnikov, K., Caspari E., et al. (2017). 4D surface seismic tracks small supercritical CO2 injection into the subsurface: CO2CRC Otway Project. *International Journal of Greenhouse Gas Control*, *63*, 150–157. doi: 10.1016/j.ijggc.2017.05.008

Pevzner, R., Urosevic, M., Tertyshnikov, K., AlNasser, H., Caspari, E., Correa, J., et al. (2020). Active surface and borehole seismic monitoring of a small supercritical CO2 injection into the subsurface: Experience from the CO2CRC Otway Project. In J. Kasahara, M. S. Zhdanov, & H. Mikada (Eds.), *Active Geophysical Monitoring (Second Edition)* (pp. 497–522). *Elsevier*. https://doi.org/10.1016/B978-0-08-102684-7.00024-8

Willis, M. E., Barfoot, D., Ellmauthaler, A., Wu, X., Barrios, O., Erdemir, C., et al. (2016). Quantitative quality of distributed acoustic sensing vertical seismic profile data. *The Leading Edge*, *35*(7), 605–609.doi: 10.1190/tle35070605.1

Yilmaz, O. (2001). *Fundamentals of signal processing. Seismic data analysis*. In Investigations in Geophysics. Seismic data analysis: Processing, inversion, and interpretation of seismic data (pp. 25–158). Society of Exploration Geophysics. doi:10.1190/1.9781560801580.ch1

14

Introduction to Distributed Acoustic Sensing (DAS) Applications for Characterization of Near-Surface Processes

Whitney Trainor-Guitton[1,2] and Thomas Coleman[3]

ABSTRACT

Improvements in DAS measurement and processing technologies have increased the acceptance of DAS technology as powerful monitoring and characterization tool for situations beyond vertical seismic profiles for oil and gas applications. This chapter reviews this evolution of DAS for near-surface, including examples of applications where DAS has been applied to better understand shallow processes and properties. In particular, horizontal fiber, originally was thought to be insensitive to wave energy that informed about the subsurface, can be utilized to characterize shallow aquifers.

14.1. INTRODUCTION

The last 5 years have brought many exciting technological and application area advances for distributed acoustic sensing (DAS), including demonstrations of its four-dimensional (4-D) repeatability (Mateeva et al., 2014), applicability to earthquake seismology (Lindsey et al., 2017), use in the imaging of subsurface structures (Jreij et al., 2018), microseismic monitoring capability (Grandi et al., 2013), potential fracture characterization (Bakku et al., 2014), and fluid flow monitoring ability (Martinez et al., 2014). Due to early adoption of DAS by the oil and gas industry, many applications of DAS, including the prior examples, are deeper in the subsurface. However, DAS has additionally been applied to the shallow subsurface (generally defined as the top 500 m of the subsurface) due to its inherent capability that allows high spatial coverage over long distances. A detailed and accurate understanding of the shallow subsurface is important for understanding geological and hydrological processes and resources. The applications in this chapter are either isolated in the near surface or require an understanding of the near surface. For example, carbon dioxide (CO_2) sequestration in deep reservoirs requires careful monitoring of drinking water aquifers for signs of leakage (Carroll et al., 2014). Many geothermal reservoirs require spatially dense characterization of the near surface to identify and understand surface-originated recharge (Feigl et al., 2018). This chapter focuses on recent advances that utilize DAS measurements to understand static and dynamic properties for solving environmental and shallow subsurface problems.

Characterization of the near surface has been important for groundwater resources and seismic risk assessment, but it will become ever more critical with changing climate and increasing urban population densities. The California drought demonstrated the risk to agriculture and communities heavily reliant on groundwater resources (Xiao et al., 2017). The melting of permafrost will bring about costly damages to infrastructure. Earthquakes pose a continued hazard to infrastructure and life. Acceptance of and advances in DAS technology, including improvements in

[1]*Department of Geophysics, Colorado School of Mines, Golden, Colorado, USA*
[2]*W Team Geosolutions, Twin Falls, Idaho, USA*
[3]*Silixa LLC, Missoula, Montana, USA*

Distributed Acoustic Sensing in Geophysics: Methods and Applications, Geophysical Monograph 268, First Edition.
Edited by Yingping Li, Martin Karrenbach, and Jonathan B. Ajo-Franklin.

DOI:10.1002/9781119521808.ch14

interrogators, new data processing techniques, and above all the understanding of the tools' sensitivity to different acoustic events and acquisition geometries, have made it possible to consider DAS as an important and uniquely powerful monitoring and characterization tool.

14.2. CONSIDERATIONS FOR DEPLOYMENTS

The physical scales of interest for resource and risk monitoring are vast. The inherent ability to collect spatially and temporally continuous seismic data at meter-scale sampling resolution, along tens of kilometers of a passive fiber-optic cable, is a significant advantage of DAS when compared with traditional sensors. In other words, distributed sensing with fiber optics provides a tool to the geophysical community that can allow measurements not only at much finer resolutions, but also at an array scale much greater than is practically achievable with point sensors. We briefly review some previous work that has advanced the understanding and application of DAS within the shallow subsurface – the focus of this chapter.

14.2.1. A Continuous Sensor Array, Signal-to-noise Ratio, and Bandwidth

The measurement array capability provided by amplitude and phase coherent DAS opens a range of array-processing possibilities, such as beamforming. Environmental geophysical investigations often demand characterization at fine spatial resolution in the shallow subsurface, while simultaneously desiring measurement capability that can be extended from local to regional scales. DAS inherently provides direct measurements at these scales while also allowing for directional sensing capability using array analysis techniques. Achieving fine spatial measurements over long lengths of fiber, while maintaining high signal-to-noise ratio (SNR), can be a challenge for DAS systems and has been an area of continued development. Thus, increasing SNR has been desired for the wider application of DAS to measuring the subsurface, including shallow subsurface applications. Recent advances in DAS have made significant strides with maintaining a long-range continuous coherent sensor array, while simultaneously refining the spatial resolution and improving SNR (Correa et al., 2017). Perhaps one of the greatest advantages of DAS is its wide acoustic bandwidth capability, with measurements down to earth tide frequencies of 23 μHz demonstrated in the lab (Becker & Coleman, 2019) and the upper limit in the tens of kilohertz dictated by fiber length and associated sampling frequencies.

14.2.2. Signal-to-fiber Coupling

Coupling of the fiber to the formation is a primary control of SNR and on whether DAS measurements represent deformations and signals of interest in the subsurface, and is therefore key for maximizing data quality. Papp et al. (2017) provide laboratory measurements that explore signals from highly coupled experiments (adhering the sensors to the medium with putty) vs. loosely coupled experiments (using staples to mimic the case of a fiber lying on the medium surface). The latter case is particularly applicable to horizontal buried/trenched cable deployments, which are discussed in the majority of the case studies presented in this chapter. As expected, the strength of the signal decreases with decreased coupling. However, as seen in Lindsey et al. (2017), earthquakes were detected from a horizontal DAS fiber lying in underground communications conduits, without controlled contact with the subsurface. Munn et al. (2017) describe a DAS cable installation method that ensures improved coupling of the DAS fiber to the formation in shallow wells and discuss coupling methods used for deeper installations. Even without this system, "slickline" deployments relying on frictional coupling alone (e.g., a loosely vertically installed fiber) recorded signals that when migrated were consistent with fault locations up to 1 km away (Trainor-Guitton et al., 2018), and "wireline" deployments have been used in industry for both microseismic and low-frequency strain measurements (Richter et al., 2019).

DAS is based on measurements of fiber dynamic strain in the axial direction. Thus, sensitivity is greatest to particle motion parallel to the optical fiber and lowest to particle motion perpendicular to the optical fiber. Survey geometry should consider the angular response of DAS to maximize SNR. A helically wound fiber-optic cable has been developed to lessen the angular response by improving omnidirectionality if making the sensitivity of the fiber-optic cable more omnidirectional (Ning & Sava, 2018). Fiber coupling mechanisms and angle response are both critical components of any deployment. Advancement in cable design is ongoing and is likely an area to see further improvement over the next several years.

14.2.3. Economics for Near-surface Characterization

Perhaps one of the challenges in near-surface applications is that unlike the energy industry, there often exists less monetary incentive for research and development efforts. The cost of DAS interrogators can still be considered relatively high for extended duration deployments for small-scale investigations. However, when compared with large-scale deployment of point sensors and scientific value considered, benefits are realized for cost-sensitive applications. In the environmental field, distributed temperature sensing (DTS) was adopted rapidly for hydrology and groundwater applications, and other problems that use temperature as an environmental tracer. Selker et al. (2006) and Bense et al. (2016) provided a review of DTS methods for hydrological and downhole hydrogeological applications, respectively. DTS systems are generally lower in cost than DAS, and reliable, commercially available systems were available in the decade prior to DAS commercialization. Thus, DTS has seen wider adoption for environmental monitoring than DAS to date, which is reflected in the longer publication record of DTS studies for the near surface compared to DAS; however, deployments of DAS are rapidly increasing as the full measurement capability and benefits are yet to be realized.

A general economic advantage of DAS installations in the near surface is the low cost of cable and cable installation. For deep downhole installations in the oil/gas industry, cable itself is commonly tens of dollars per meter and the installation costs are substantial due to the hazards and associated complexity involved with installations in harsh environments. Telecommunication grade fiber, which is commonly available, is suitable for shallow borehole and surface deployments, and can cost only a few dollars per meter with substantially reduced installation costs. Having a permanent receiver array is an economic advantage for time-lapse DAS surveys, eliminating the requirement for costly interventions with a DAS interrogator needed on-site only when measurements are required (Mateeva et al., 2014). Significant economic efficiencies can be achieved by connecting to existing optical fiber originally installed for telecommunications as most telecommunication cables have a significant excess fiber count included, which can be utilized for DAS.

14.3. SPECIFIC TOPICS IN THIS CHAPTER

14.3.1. Ambient Noise Tomography

Since the proposed methodology in Bensen et al. (2007), ambient noise tomography has become a viable technology for using passive acoustic sources along with temporally continuous observations. This method has allowed for acoustic measurements that do not rely on expensive active sources, such as dynamite or vibroseis trucks, which are often necessary or utilized for near-surface applications. The advancing methodology is now viable for constructing multidimensional models of the subsurface that allow for interpretations of fluid-saturation content (Ajo-Franklin et al., 2015; Matzel et al., 2017).

Dou et al. (2017) utilized traffic energy to probe the upper 20 m of the subsurface. The repeatability of their recovered shear-wave velocity models (with 2% data-fitting error) would allow inferences into water-content changes. DAS could be utilized to transform infrastructure noise in the 2–30 Hz band (e.g., surface waves generated by cars, trucks, and trains) into accurate and stable one-dimensional (1-D) estimates of shear-wave velocity of the upper 30 m using DAS.

14.3.2. 4-D Time-lapse Imaging

DAS has economic advantages for time-lapse surveys due to the relatively low cost of permanently installing fiber-optic cable when compared to multiple well interventions or deployments with surface receivers. Combining the technical capabilities of DAS with the economic advantages for long-term monitoring has led to a high level of adoption for monitoring carbon sequestration for imaging CO_2 injection and migration within the reservoir.

Carbon sequestration [or carbon capture and storage (CCS)] is one potential mitigation method that has been studied to abate climate change by injecting supercritical CO_2 into intermediate depth formations. CCS applications are generally deeper than other near-surface geophysical deployments; however, CO_2 sequestration can be categorized as an environmental geophysical problem and thus has been included in this chapter. The concept of CCS is that instead of venting CO_2 from power plants and other industrial sources into the atmosphere, it can be injected into reservoirs for long-term storage, thus diminishing the climate-changing effects of greenhouse gas through reduced atmospheric emissions. The EPA has ruled what kind of monitoring must be performed to reduce the risk of CO_2 leakage from these deep reservoirs into shallow, drinking water aquifers (Rose & Bayer, 2010). The ability for cost-effective permanent deployment of a spatially dense and continuous array of receivers has enabled DAS to be considered as one of the primary tools for monitoring CO_2 injection and propagation (Dou et al., 2016).

14.3.3. Multichannel Analyses of Surface Waves

Multichannel analyses of surface waves (MASW) is a relatively new technique that utilizes dispersive properties of the surface wavefield along with recording at numerous channels to image shear-wave velocity structures in the shallow near surface. The MASW method involves three sequential steps in wavefield transformation: (1) Multichannel surface wave data acquisition, (2) dispersion curve construction, and (3) 1-D layered model parameter inversion. Both active and passive source methods can be applied. The inherent multichannel nature of DAS allows for dense channel spacing over long distances, which makes DAS measurements attractive for near-surface characterization. Dou et al. (2017) successfully obtained shear-wave velocity profiles using ambient traffic noise recorded on a dedicated DAS array and demonstrated repeatability of the method. Yamauchi et al. (2018) tested both active and passive MASW techniques using DAS. MASW and DAS are enabling technologies for transforming dark fiber into cost-effective arrays to monitor seismic structures over vast distances. These studies have mainly focused on linear fiber segments without fully exploiting the advantage of a two-dimensional (2-D) DAS array geometry. Luo et al. (2020) demonstrate that orthogonal, horizontal fibers can distinguish Rayleigh and Love wave dispersion information from ambient recordings, by stacking the orthogonal DAS noise correlation functions.

14.3.4. Utilization of Dark Fiber

Since DAS can be applied to telecommunication grade optical fiber, the possibility exists to transform existing fiber infrastructure into vast sensor networks, which would fundamentally transform our monitoring and characterization capabilities. Dark fiber is a currently installed unutilized fiber, which in many cases can be readily adopted for DAS measurements through simple connection of a DAS interrogator. Dark fiber provides the advantages of not requiring substantial installation costs or permitting us to install fit-for-purpose sensors, and can thus collect data similarly in urban, suburban, and rural environments.

Dark fiber makes near-surface characterization at basin scale seem plausible, and importantly, the characterization can be with much higher resolution than kilometers, which is what is provided by satellite, point source, or airborne techniques (Xiao et al., 2017). Optical fiber cables are commonly installed along existing highway, rail, and pipeline right of ways, enabling the potential to monitor these assets, the environment around them, and transform existing cables into smart infrastructure for the autonomous transportation and Internet of Things era.

Jousset et al. (2018) present interpretations of the ambient recordings from 15 km long fiber-optic cable layout on the Reykjanes Peninsula, southwest Iceland. They use cross-correlation techniques along with static deformation theory to make interpretations of the near-surface fault structure and soil properties. Ajo-Franklin et al. (2019) have provided a study using 27 km of dark fiber and MASW techniques to construct shear-wave velocity models of the subsurface to enable mapping of shallow structures and groundwater depth.

14.3.5. Opportunities and Challenges

The application of DAS to the near surface is still in its infancy, with a multitude of potential applications easily imaginable offering an opportunity for scientists, engineers, and operators. Infrastructure monitoring is an area that will likely see a growth in applications in the coming years. Climate change poses an increasing danger to infrastructure in extreme latitudes, as melting permafrost will heave. An early study in this area by Ajo-Franklin et al. (2017) describes a semipermanent surface orbital vibrator (SOV) source and DAS to measure variations in surface wave propagation while monitoring the active heating and thus melting of permafrost. Seepage and erosion are major causes of failure in embankment dams and levees. DTS has been used for monitoring these structures for two decades (Johansson & Sjödahl, 2004; Khan et al., 2010); however, the application of DAS for dam and levee monitoring is also in the early stages.

DAS provides opportunities to collect seismic data at vast scales suitable for high-resolution structural imaging using large N array analysis concepts. Given the massive amount of DAS data that could potentially be available (specifically the spatial density), it is paramount to completely harvest the directional data and construct fully three-dimensional (3-D) subsurface models. Full wavefield migrations can more accurately represent the wave energy in the 3-D subsurface and reproduce the DAS observations (Trainor-Guitton et al., 2019).

Deployed at scale, regional or global DAS arrays could record many petabytes of data per day as the data sets are both temporally and spatially extensive. Thus, as pointed out by Miah and Potter (2017), handling large data sets can be the bottleneck in taking full advantage of the fiber-optic sensing technology. This poses an opportunity for new artificial intelligence, machine learning, and data analytics techniques to efficiently reduce the data to the features or signals that can accurately identify anomalies or important changes. Computationally efficient analysis techniques will be necessary, and the development of machine learning may enable characterization and monitoring of both naturally occurring and anthropogenically induced processes and events autonomously. Though, continual advances in data storage, transmission, and processing capability, including the possibility of quantum computing, will also play key roles in reducing the volumetric data burden.

14.4. CONCLUSIONS

DAS has proven to be a valuable tool for characterizing the near surface. This chapter includes examples of applications where DAS has been applied to better understand shallow processes and properties, and attempts to prime the reader for a variety of opportunities and considerations particular to DAS measurements. The introduction and subsequent entries focused herein primarily on geophysical methods are not exhaustive; geotechnical (Michlmayr et al., 2017; Schenato, 2017) and hydrological (Becker, Ciervo, et al., 2017; Becker, Coleman, et al., 2017) advances of DAS techniques for near-surface applications have also been significant. The combination of methodology refinements and vast opportunity provides an exciting outlook for the future of DAS.

REFERENCES

Ajo-Franklin, J., Lindsey, N., Daley, T. M., Freifeld, B., Robertson, M., Ulrich, C., et al. (2015). *A field test of distributed acoustic sensing for ambient noise recording*. SEG Technical Program Expanded Abstracts 2015 (pp. 2620–2624). doi: 10.1190/segam2015-5926936.1

Ajo-Franklin, J., Dou, S., Daley, T., Freifeld, B., Robertson, M., Ulrich, C., et al. (2017). *Time-lapse surface wave monitoring of permafrost thaw using distributed acoustic sensing and a permanent automated seismic source*. SEG Technical Program Expanded Abstracts 2017 (pp. 5223–5227). doi: 10.1190/segam2017-17774027.1

Ajo-Franklin, J., Dou, S., Lindsey, N., Monga, I., Tracy, C., Robertson, M., et al. (2019). Using dark fiber and distributed acoustic sensing for near-surface characterization and broadband seismic event detection. *Scientific Reports*, v. 9. doi: 10.1038/s41598-018-36675-8.

Bakku, S. K., Wills, P., Fehler, M., Mestayer, J., Mateeva, A., & Lopez, J. (2014). Vertical seismic profiling using distributed acoustic sensing in a hydrofrac treatment well. Paper presented at SEG Denver 2014 Annual Meeting (pp. 5024–5028). doi: 10.1190/segam2014-1559.1

Becker, M. W., Ciervo, C., Cole, M., Coleman, T., & Mondanos, M. (2017). Fracture hydromechanical response measured by fiber optic distributed acoustic sensing at milliHertz frequencies. *Geophysical Research Letters*, *44*, 7295–7302. doi: 10.1002/2017GL073931

Becker, M. W., & Coleman, T. I. (2019). Distributed acoustic sensing of strain at earth tide frequencies. *Sensors (Switzerland)*, *19*. doi: 10.3390/s19091975

Becker, M., Coleman, T., Ciervo, C., Cole, M., & Mondanos, M. (2017). Fluid pressure sensing with fiber-optic distributed acoustic sensing. *The Leading Edge*, *36*, 1018–1023, doi: 10.1190/tle36121018.1

Bense, V. F., Read, T., Bour, O., Le Borgne, T., Coleman, T., Krause, S., et al. (2016). Distributed Temperature Sensing as a downhole tool in hydrogeology. *Water Resources Research*, *52*, 9259–9273. doi: 10.1002/2016WR018869.

Bensen, G. D., Ritzwoller, M. H., Barmin, M. P., Levshin, A. L., Lin, F., Moschetti, M. P., et al. (2007). Processing seismic ambient noise data to obtain reliable broad-band surface wave dispersion measurements. *Geophysical Journal International*, *169*, 1239–1260. doi: 10.1111/j.1365-246X.2007.03374.x.

Carroll, S. A., Keating, E., Mansoor, K., Dai, Z., Sun, Y., Trainor-Guitton, W., et al. (2014). Key factors for determining groundwater impacts due to leakage from geologic carbon sequestration reservoirs. *International Journal of Greenhouse Gas Control*, *29*, 153–168. doi: 10.1016/j.ijggc.2014.07.007.

Correa, J., Egorov, A., Tertyshnikov, K., Bona, A., Pevzner, R., Dean, T., et al. (2017). Analysis of signal to noise and directivity characteristics of DAS VSP at near and far offsets—a CO2CRC Otway Project data example. *The Leading Edge*, *36*, 994a1–994a7. doi: 10.1190/tle36120994a1.1.

Dou, S., Ajo-Franklin, J., Daley, T., Robertson, M., Wood, T., Freifeld, B., et al. (2016). *Surface orbital vibrator (SOV) and fiber-optic DAS: Field demonstration of economical, continuous-land seismic time-lapse monitoring from the Australian CO_2 CRC Otway site*. SEG Technical Program Expanded Abstracts 2016 (pp. 5552–5556). doi: 10.1190/segam2016-13974161.1.

Dou, S., Lindsey, N., Wagner, A. M., Daley, T. M., Freifeld, B., Robertson, M., et al. (2017). Distributed acoustic sensing for seismic monitoring of the near surface: A traffic-noise interferometry case study. *Nature: Scientific Reports*, *7*, 11620. doi: 10.1038/s41598-017-11986-4.

Feigl, K. L., Lancelle, C., Lim, D. D., Parker, L., Reinisch, E. C., Ali, S. T., et al. (2018). *Overview and preliminary results from the PoroTomo Project at Brady Hot Springs, Nevada: Poroelastic Tomography by Adjoint Inverse Modeling of Data from Seismology, Geodesy, and Hydrology*. In 42nd Workshop on Geothermal Reservoir Engineering (pp. 1–15). Stanford University.

Grandi, S., Webster, P., Hornman, K., Lumens, P., Franzen, A., & Berlang, W. (2013). *Micro-seismic applications using DAS*. In Fourth Passive Seismic Workshop Optimizing Development of Unconventional Reservoirs, EAGE.

Johansson, S., & Sjödahl, P. (2004). *Downstream seepage detection using temperature measurements and visual inspection—Monitoring experiences from Røsvatn field test dam and large embankment dams in Sweden*. In Proceedings of the International Seminar on Stability and Breaching of Embankment Dams (pp. 1–20). Oslo, Norway.

Jousset, P., Reinsch, T., Ryberg, T., Blanck, H., Clarke, A., Aghayev, R., et al. (2018). Dynamic strain determination using fibre-optic cables allows imaging of seismological and structural features. *Nature Communications*, *9*. doi: 10.1038/s41467-018-04860-y

Jreij, S., Trainor-Guitton, W., & Simmons, J. (2018). *Improving point-sensor image resolution with distributed acoustic sensing at Brady's enhanced geothermal system*. In Stanford Geothermal Workshop, Stanford, California.

Khan, A. A., Vrabie, V., Mars, J. I., Girard, A., & D'Urso, G. (2010). Automatic monitoring system for singularity detection in dikes by DTS data measurement. *IEEE Transactions on Instrumentation and Measurement*, *59*, 2167–2175. doi: 10.1109/TIM.2009.2032880.

Lindsey, N. J., Martin, E. R., Dreger, D. S., Freifeld, B., Cole, S., James, S. R., et al. (2017). Fiber-optic network observations of earthquake wavefields. *Geophysical Research Letters*, *44*, 11,792–11,799. doi: 10.1002/2017GL075722

Luo, B., Trainor-Guitton, W., Bozdağ, E., LaFlame, L., Cole, S., & Karrenbach, M. (2020). Horizontally orthogonal distributed acoustic sensing array for earthquake- and ambient-noise-based multichannel surface wave analysis. *Geophysical Journal International*, *222*, 2147–2161.

Martinez, R., Hill, A., & Zhu, D. (2014). Diagnosis of fracture flow conditions with acoustic sensing. SPE Hydraulic Fracturing Technology Conference (pp. 4–6).

Mateeva, A., Lopez, J., Potters, H., Mestayer, J., Cox, B., Kiyashchenko, D., et al. (2014). Distributed acoustic sensing for reservoir monitoring with vertical seismic profiling. *Geophysical Prospecting*, *62*, 679–692. doi: 10.1111/1365-2478.12116.

Matzel, E., Zeng, X., Thurber, C., Luo, Y., & Morency, C. (2017). *Seismic interferometry using the dense array at the Brady geothermal field*. In 42nd Stanford Geothermal Workshop on Geothermal Reservoir Engineering (pp. 3–6).

Miah, K., & Potter, D. K. (2017). A review of hybrid fiber-optic distributed simultaneous vibration and temperature sensing technology and its geophysical applications. *Sensors (Switzerland)*, *17*, 1–26. doi: 10.3390/s17112511.

Michlmayr, G., Chalari, A., Clarke, A., & Or, D. (2017). Fiber-optic high-resolution acoustic emission (AE) monitoring of slope failure. *Landslides*, *14*, 1139–1146. doi: 10.1007/s10346-016-0776-5

Munn, J. D., Coleman, T. I., Parker, B. L., Mondanos, M. J., & Chalari, A. (2017). Novel cable coupling technique for improved shallow distributed acoustic sensor VSPs. *Journal of Applied Geophysics*, *138*, 72–79. doi: 10.1016/j.jappgeo.2017.01.007.

Ning, I. L. C., & Sava, P. (2018). Multicomponent distributed acoustic sensing: Concept and theory. *Geophysics*, *83*, P1–P8, doi: 10.1190/GEO2017-0327.1.

Papp, B., Donno, D., Martin, J. E., & Hartog, A. H. (2017). A study of the geophysical response of distributed fibre optic acoustic sensors through laboratory-scale experiments. *Geophysical Prospecting*, *65*, 1186–1204. doi: 10.1111/1365-2478.12471

Richter, P., Parker, T., Woerpel, C., Wu, W., Rufino, R., & Farhadiroushan, M. (2019). *High-resolution distributed acoustic sensor using engineered fiber for hydraulic fracture monitoring and optimization in unconventional completions*. SEG Technical Program Expanded Abstracts (pp. 4874–4878). doi: 10.1190/segam2019-3215860.1.

Rose, M., & Bayer, M. (2010). Environmental Protection Agency. *Federal Register*, *75*, 77230–77303.

Schenato, L. (2017). A review of distributed fibre optic sensors for geo-hydrological applications. *Applied Sciences*, *7*, 896, doi: 10.3390/app7090896

Selker, J. S., Thévenaz, L., Huwald, H., Mallet, A., Luxemburg, W., Van De Giesen, N., et al. (2006). Distributed fiber-optic temperature sensing for hydrologic systems. *Water Resources Research*, *42*, 1–8. doi: 10.1029/2006WR005326.

Trainor-Guitton, W., Guitton, A., Jreij, S., Powers, H., & Sullivan, C. B. (2018). *3D Imaging from vertical DAS fiber at Brady's Natural Laboratory*. In Proceedings, 43rd Workshop on Geothermal Reservoir Engineering,.

Trainor-Guitton, W., Guitton, A., Jreij, S., Powers, H., & Sullivan, B. (2019). 3D Imaging of Geothermal Faults from a Vertical DAS. *Energies*, *12*. doi: 10.3390/en12071401.

Xiao, M., Koppa, A., Mekonnen, Z., Pagán, B. R., Zhan, S., Cao, Q., et al. (2017). How much groundwater did California's Central Valley lose during the 2012–2016 drought? *Geophysical Research Letters*, *44*, 4872–4879. doi: 10.1002/2017GL073333.

Yamauchi, Y., Kasahara, J., Hasada, Y., & Kawashima, H. (2018). *Surface wave analysis using DAS (Distributed Acoustic Sensor) in active and passive method*. In Society of Exploration Geophysicist of Japan, Tokyo, Japan.

15

Surface Wave Imaging Using Distributed Acoustic Sensing Deployed on Dark Fiber: Moving Beyond High-Frequency Noise

Verónica Rodríguez Tribaldos[1], Jonathan B. Ajo-Franklin[1,2], Shan Dou[3], Nathaniel J. Lindsey[4], Craig Ulrich[1], Michelle Robertson[1], Barry M. Freifeld[5], Thomas Daley[1], Inder Monga[6], and Chris Tracy[6]

ABSTRACT

Several recent studies have demonstrated that "distributed acoustic sensing" (DAS) can utilize existing subsurface telecommunication fiber (i.e., dark fiber) for high-quality seismic measurements. Researchers to date have shown that this sensing combination, coupled with ambient noise interferometry techniques, can effectively image the shallow subsurface (<30 m) using vehicle and infrastructure noise (f = 8–30 Hz). We present a long-offset surface wave inversion study targeting deeper (≈500 m) structure using DAS and dark fiber. This study utilizes a previously acquired data set collected on a 23 km fiber section between West Sacramento and Woodland, California, part of the Energy Sciences Network (ESnet) of the U.S. Department of Energy. By targeting noise generated by a colinear rail line, broadband and rich in low frequencies (down to f = 1 Hz), and long array offsets, we generate high-quality interferometric gathers suitable for inversion. Subsequent surface wave inversions using a multimode Monte Carlo sampling algorithm are consistent with geology and available confirmatory data sets derived from colocated sonic logs. The relatively sparse confirmatory data demonstrate, by comparison, the utility of the high spatial sampling provided by DAS. These results open the door to larger regional DAS studies targeting deeper targets, but with resolutions higher than those afforded by the use of persistent low-frequency (f < 1 Hz) ocean microseism-related noise.

15.1. INTRODUCTION

The characterization of the top several hundred meters of the Earth's subsurface is crucial for understanding a variety of phenomena, including near-surface property variations for geohazard evaluation or distribution and accessibility to water and other resources. However, our current understanding of the subsurface at these depths is limited by our ability to image its structure and temporal variations at high resolution using classical geophysical approaches. In seismological studies, specifically, the high cost of active surveys and long-term deployments and the sparse coverage of permanent arrays make it challenging to acquire high-resolution data at regional scale. These limitations result in missed information that can lead to restricted understanding of geological structures and unidentified hazards (e.g., fault zones and collapse structures), as well as limited capacity for process monitoring.

[1]*Energy Geosciences Division, Lawrence Berkeley National Laboratory, Berkeley, California, USA*

[2]*Department of Earth, Environmental and Planetary Sciences, Rice University, Houston, Texas, USA*

[3]*Visier Inc., Vancouver, British Columbia, Canada*

[4]*FiberSense, Sydney, Australia*

[5]*Class VI Solutions Inc., Oakland, California, USA*

[6]*Energy Sciences Network, Lawrence Berkeley National Laboratory, Berkeley, California, USA*

Distributed Acoustic Sensing in Geophysics: Methods and Applications, Geophysical Monograph 268, First Edition.
Edited by Yingping Li, Martin Karrenbach, and Jonathan B. Ajo-Franklin.

DOI:10.1002/9781119521808.ch15

Recently, the combination of novel sensing techniques with the use of already existing sensing networks has offered an attractive alternative to classical seismological studies. Here, we explore the applicability of "distributed acoustic sensing" (DAS) using so-called "dark fiber" networks. These networks consist of subsurface fiber-optic cables that were originally deployed for telecommunication purposes – but are currently not in use for data transmission. Because of the high cost of commercial fiber installation, it is common practice to install significantly more fiber than needed for current demand. This custom in combination with technological advances in available bandwidth per cable yields an excess of fiber that is not in use. These dark fiber networks are widespread, are found both onshore and offshore, and are often available for lease and purchase to be repurposed as sensing arrays. Recent studies have demonstrated the potential of combining DAS and dark fiber networks for near-surface imaging and earthquake seismology (Ajo-Franklin et al., 2019; Dou et al., 2017; Jousset et al., 2018).

DAS is an innovative and rapidly developing technology that uses the principles of coherent optical time-domain reflectometry to make spatially distributed measurements of extensional strain or strain rate along an optical fiber (Hartog et al., 2017; Parker et al., 2014). A laser pulse sent down the fiber-optic cable is backscattered by impurities in the fiber (Rayleigh scattering) and measured by an interferometric system. When strain is applied at a location along the cable, the phase of the backscattered light changes. The system correlates these changes at specific locations along the cable with strain in the fiber at those positions. Differences in phase and amplitude of the backscattered light profile are measured over short subsets of the cable, which is referred to as the gauge length. DAS technology enables acquisition of high-resolution seismological data at frequencies from kilohertz to millihertz for long distances (tens of kilometers) and at very dense spatial samplings (down to 1 m) in contexts in which the use of conventional sensors is intricate and/or costly (Becker et al., 2017; Daley et al., 2016). DAS is incrementally being adopted in the field of applied geophysics, and a variety of studies have demonstrated its suitability for a range of applications, such as vertical seismic profiling (Daley et al., 2013; Mateeva et al., 2013; Wu et al., 2015; Wu et al., 2017), time-lapse monitoring of near-surface properties (Ajo-Franklin et al., 2019; Dou et al., 2017), earthquake detection (Ajo-Franklin et al., 2019; Li & Zhan, 2018; Lindsey et al., 2017), and hydrological monitoring (Becker et al., 2017).

In this study, we investigate the potential of combining DAS and dark fiber networks for ambient noise imaging at intermediate depths. In the past decade, many studies have shown that ubiquitous vibrations generated by natural and anthropogenic sources (e.g., wind, rivers, ocean waves, traffic) can be analyzed to recover subsurface information. By cross-correlating ambient seismic noise recordings at two receivers, subsurface velocity structure between the two receivers can be retrieved using interferometric approaches (Bensen et al, 2007; Campillo & Roux, 2015; Snieder & Larose, 2013). Because most of the noise has its origin on the surface, the observed ambient seismic noise has a strong component of surface waves that can be exploited for a variety of imaging purposes (Campillo & Roux, 2015). A large number of ambient seismic noise studies utilize broadband sensors located tens of kilometers apart for subsurface imaging at the crustal or lithospheric scale (Li et al., 2010; Molinari et al., 2015; Shapiro et al., 2005; Yang et al., 2008). These works generally exploit natural ambient seismic noise in the microseism band (5 s and above) to reach depths of tens of kilometers or greater with resolution of several tens of kilometers. In near-surface and geotechnical applications, classical methods, such as multichannel analysis of surface waves (MASW), exploit noise at high frequencies (typically 10 Hz or greater) to image the V_s structure of the top 30 m of the subsurface (Kaufmann et al., 2005; Park et al., 1999; E. H. Parker & Hawman, 2012; Xia, 2014). These studies commonly use short arrays of densely spaced short-period sensors (e.g., geophones). These arrays provide velocity information with vertical resolution in the order of a few meters, but their lateral extent and spatial coverage is limited. These constraints restrict the applicability of these sensors for investigating local structures. The opposite is true for studies of the top hundreds of meters of the Earth's subsurface. Whereas spatial coverage and deep penetration can be achieved with extensive, broadband arrays, dense spacing is not feasible with conventional sensors due to their high cost, which results in poor lateral resolution.

In this context, DAS is an excellent alternative to bridge the gap between low-frequency, regional studies and high-resolution, local investigations. DAS allows deployments of seismic arrays capable of recording broadband data at high spatial resolution for distances of several kilometers. Telecommunication fiber-optic networks, in turn, are commonly routed along road and railway right of ways – areas which are rich in ambient noise. In a previous study, we demonstrated that ambient noise interferometry could be applied to DAS ambient noise recordings generated by a train traveling parallel to a section of a dark fiber network (Ajo-Franklin et al., 2019). In this work, ambient noise analyses at frequencies in the traffic band were used to image the top 50 m of the subsurface and to monitor groundwater level variations. To date, only a few other studies have successfully used train-generated noise for imaging purposes (Brenguier et al., 2019; Nakata et al., 2011; Quiros et al., 2016). In their study, Quiros et al. (2016) show that the ambient field generated by trains can be utilized to produce virtual records of surface and body waves that can be analyzed for subsurface imaging down to ≈200 m. A recent study by Inbal et al. (2018) demonstrates that noise generated by freight trains can be recorded in borehole arrays at distances of up to 50 km from the railway, and it is used to estimate average attenuation values for depths between 200 and 500 m.

In this study, we use a DAS data set acquired as part of the Fiber-Optic Sacramento Seismic Array (FOSSA) experiment introduced in Ajo-Franklin et al. (2019) to explore the potential of exploiting train-generated noise recorded by a dark fiber network for imaging the subsurface down to 500 m and compare the results to exploration sonic well logs available along the profile. We find that the inverted V_s profiles are consistent with available data and are well constrained for the upper 300 m with higher uncertainty in lower units due to the limited coherent energy generated by the train below 0.5 Hz.

15.2. DARK FIBER NETWORKS: THE ESNET DARK FIBER TESTBED

The data set analyzed in this study was acquired using the fiber-optic cable installation maintained as part of the Dark Fiber Testbed of the Energy Sciences Network (ESnet). ESnet is a nationwide U.S. Department of Energy Office (DOE) user facility. It provides high-performance, unclassified infrastructure that connects DOE research sites (including supercomputer facilities and major scientific instruments), as well as research and commercial networks. The Dark Fiber Testbed itself consists of a 20,920 km (13,000 miles) network of short- and long-haul telecommunication fiber used for network communication research. This network utilizes single-mode telecommunication fiber-optic cables of varying age and installation modes. However, none was installed with sensing in mind; hence, making it a representative example of currently available commercial networks and expected DAS data quality.

15.3. STUDY SITE AND DATA ACQUISITION

The study site under investigation is located on the Sacramento River floodplain, northwest of the city of Sacramento, California (Figure 15.1). It is located within the southern portion of the Sacramento Valley, which constitutes the northern arm of California's Central Valley. The shallow stratigraphy of the site mainly consists of Quaternary floodplain deposits comprised of an intercalation of clays, silts, fine sands, and gravels that can reach thicknesses of up to 46 m in the area. Regionally, these young sediments are underlain by alluvial deposits of Pliocene age, which are composed of loose to moderately compacted clays, silts, sand, and gravels, and by the partially lithified deposits of the Tehama formation, which includes silts, clays, and fine sands that enclose sand and silt, gravel and silt, and cemented conglomerate lenses (Olmsted & Davis, 1961). Deeper horizons include fill sediments in the Markley Gorge (600–800 mbgs; see Pepper-Kittredge & Wilson, 1984), which overly the late Cretaceous Mokelumne River Formation (≈800–1000 mbgs), which produces gas at commercial quantities. The study site is in close proximity to the Conway Ranch gas field (Campion Jr., 1980), as well as the Todhunter Lake field (Hunter et al., 1984); as a result, numerous wells have been drilled along the transect, all with available logs.

Within this region, data were acquired along a 23.29 km long transect of the ESnet's Dark Fiber Testbed that runs between West Sacramento and the town of Woodland in Yolo County (Figure 15.1). This section of the network extends from urban areas in West Sacramento into farmland close to the Sacramento River, crossing Interstate 5 before bending westward toward Woodland. For most of its length, the network runs along a rail line and a local road.

This study builds on the work presented in Ajo-Franklin et al. (2019), which uses the same data set for imaging near-surface structure, monitoring groundwater table variations, and detecting teleseismic earthquakes. Data were acquired using a single DAS interrogator between 28 July 2017 and 4 March 2018. The DAS interrogation unit (Silixa iDAS, Elstree, UK) was installed on a vibration-isolated table inside a telecommunication point-of-presence facility in West Sacramento. The authors refer to Ajo-Franklin et al. (2019) for more details on hardware and installation conditions. Ambient noise was recorded at a sampling rate of 500 Hz (2 ms), with spatial sampling of 2 m and a gauge length of 10 m. Data were continuously recorded and stored in the form of 1 minute files in 8 TB external hard drives that were manually exchanged weekly during the duration of the experiment.

Mapping of linear distances along the fiber cable and actual location coordinates was established by carrying out impact tests at surface locations and identifying their response along the cable. These points were surveyed with a high-accuracy differential GPS and associated with the corresponding distance along the fiber. Linear interpolation was performed between the known points. As a result, the uncertainty associated with the final subsurface geometry of the cable is in the order of 5 m (Ajo-Franklin et al., 2019).

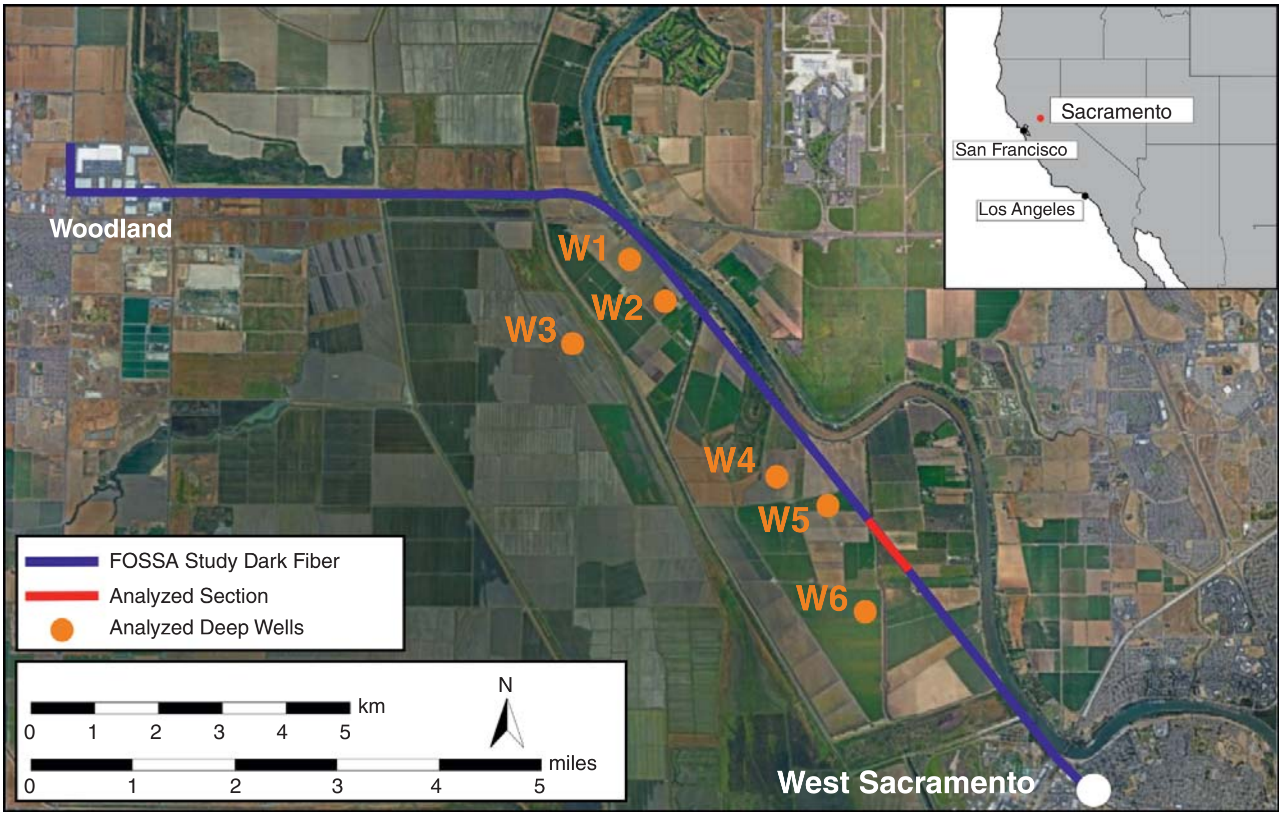

Figure 15.1 An aerial photograph showing location of the study site and transect of the ESnet Dark Fiber Testbed used in this study. Labelled orange circles are deep boreholes with sonic log information used for ground truth of ambient noise analysis results. W1 = Hanks 3-4; W2 = Unit 1-1; W3 = Conway 4-2; W4 = Rivercat 11-2; W5 = Mattos 1; and W6 = Agriventure Ensher (AE) 19-1.

15.4. DATA CHARACTERISTICS AND ANALYSIS OF NOISE SOURCES

Following the establishment of the correct geometry, the characteristics of the ambient noise signals recorded by the DAS array were analyzed. Due to its location straddling an urban area and farmland and its proximity to major infrastructure, this network is an excellent natural laboratory to test the applicability of DAS using dark fiber networks for recording seismic noise from different sources.

Figure 15.2a shows a 10 s recording of ambient seismic noise across the entire fiber-optic cable, starting in West Sacramento and finishing near Woodland. The most evident feature is the deterioration in data quality along the array at significant distances from the recording unit. Clear infrastructure-related seismic signals are observed for the first 16 km of the profile, where the data are relatively clean and have sufficient signal-to-noise ratio to observe discrete signals. Beyond that location, the signal slowly degrades and is dominated by optical noise at the distal end of the profile. The cause of this signal degradation is the weakening of the light pulse as it travels along the cable and is scattered at the fiber impurities. At large distances, not enough photons can be returned to the interrogation unit and only noise is recorded. Several localized noisy sections are also observed toward the beginning of the profile. Within the first 0.5 km of the profile, data are affected by noise inside the point of presence where the recording unit sits. At a distance of about 3.5–4 km, data quality is affected by poor coupling of the fiber-optic cable, which is attached to a bridge in this section. After this evaluation, noisy sections were disregarded for further analysis.

Besides data quality variability, differences in the character of the recorded ambient noise signals are also observable. Most of the energy recorded corresponds to traffic noise along local roads and along regional highways located to the north of the study site, as well as diffuse urban noise originating in West Sacramento. The signal with the highest amplitude corresponds to noise generated by a train traveling along the railway that runs

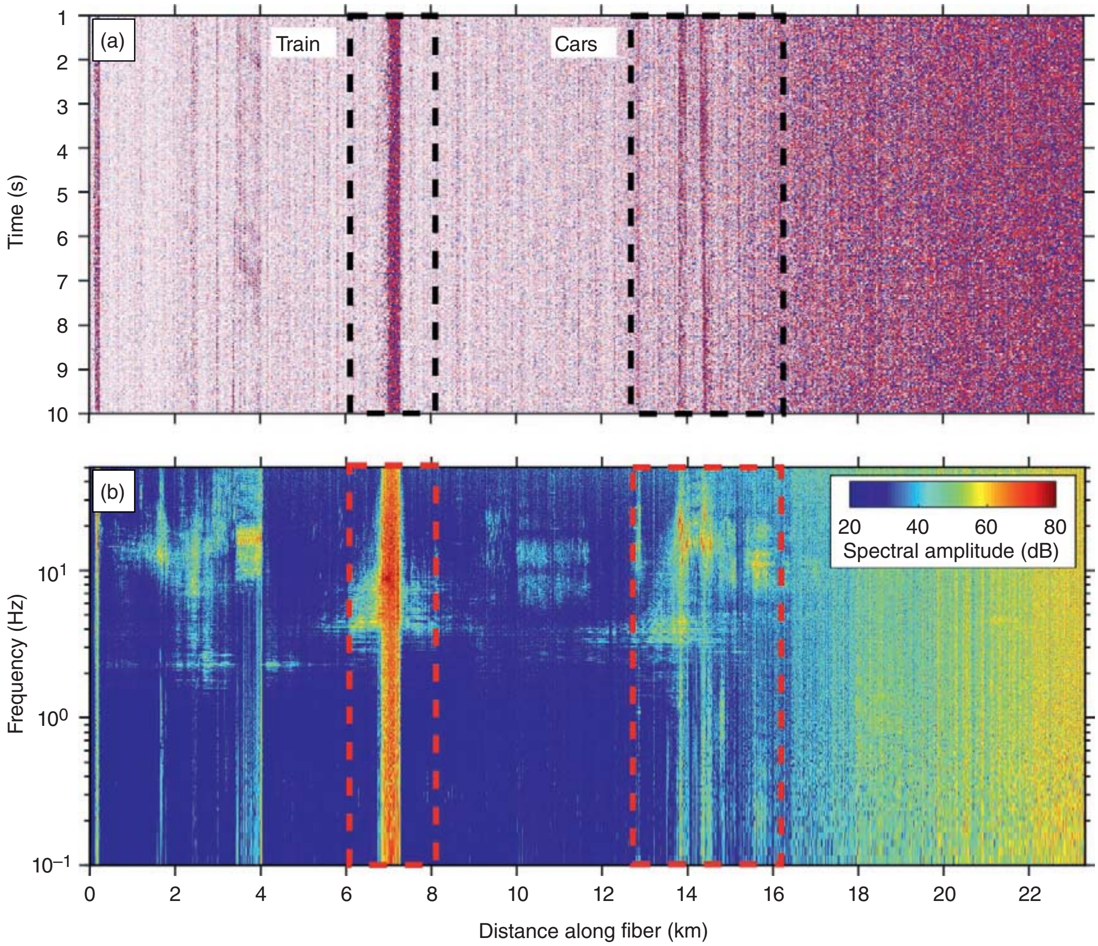

Figure 15.2 Data characteristics along the dark fiber array. (a) A 10 s recording of raw ambient seismic noise data. Traffic noise generated by a freight train running in line with the array and by cars traveling along a road nearby presents the most conspicuous signals. (b) Frequency content variation across the array. Red, dashed-line rectangles correspond to sections containing noise generated by the train and cars indicated in panel (a).

parallel to the fiber-optic line. The railway runs parallel to the entire FOSSA study dark fiber. The distance between the train tracks and the fiber-optic cable varies along the line, with a minimum separation of 3 m and a maximum separation of 30 m. For the section analyzed here, the distance between the railway and the cable is ≈10 m, which is also the average distance for most of the line. The train traveling along this railway and generating the surface wave energy under analysis here corresponds to a freight train that travels at a velocity of 3–5 m/s.

In Figure 15.2b, the frequency content of the corresponding 1 minute of data is analyzed as a function of distance along the cable. Shown are spectral amplitudes normalized with respect to the maximum amplitude value in decibels (dB) for all noise sources. As is to be expected, the traffic-generated noise dominates the spectrum and is concentrated within a frequency band between 3 and 30 Hz. Noise associated with railroad activity, however, is characterized by a broadband signal that varies as the train is approaching and departing a particular location along the cable. Differences in the frequency spectrum of the distinct noise signals are more evident, as shown in Figure 15.3, where normalized spectral amplitudes of the three main types of noise signals identified in the data are shown. The background noise spectrum shown in blue in Figure 15.3a corresponds to the frequency content of a 1 minute file recorded during nighttime, when traffic noise is minimal. These data have the smallest amplitude at all frequencies, and their spectrum is characterized by an increasing trend toward high frequencies. A small peak is observed at a frequency of approximately 4 Hz, which most likely corresponds to urban noise from nearby Sacramento. As expected, car-generated noise has higher amplitudes than background noise, and most of its energy

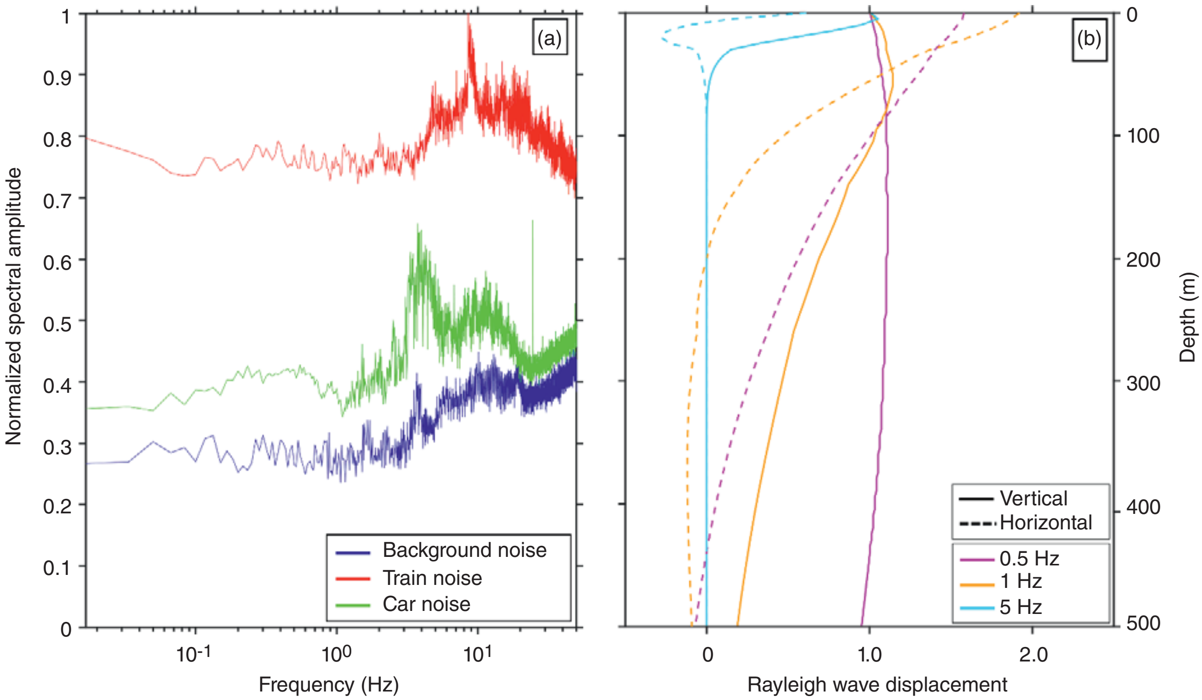

Figure 15.3 (a) Comparison of spectral amplitude of the distinct noise signals sensed in our study site for a 1 minute seismic noise recording. Blue = background noise recorded at night, where traffic noise was minimal; green = noise generated by moving cars; and red = noise generated by an approaching train. (b) Sensitivity kernels represented by the displacement of the vertical and horizontal components of a synthetic Rayleigh wave as a function of depth for distinct frequencies contained in the train-generated noise used for ambient noise analysis, calculated for a simple six-layer V_s model. For the horizontal component of displacement, positive values indicate prograde motions, whereas negative values indicate retrograde motions.

is concentrated at frequencies between 3 and 20 Hz, with the highest peak being at 4 Hz (spectrum denoted by the green curve in Figure 15.3a). In comparison with these two types of noise sources, energy generated by the train is characterized by much higher amplitudes at all frequencies. Even though most of the energy is concentrated in the traffic band, the spectral content at lower frequencies (i.e., below 3 Hz) is significantly higher. This characteristic frequency spectrum makes train-generated noise the most energetic and most broadband signal present in our study area, and hence the most appropriate ambient seismic noise for the purposes of intermediate-to-large-scale imaging of the subsurface.

A more quantitative analysis of the depth penetration of train-generated noise in our site can be obtained by calculating sensitivity curves at the different frequencies contained in our ambient noise recordings. Figure 15.3b illustrates the vertical and horizontal components of displacement for the fundamental mode of a synthetic Rayleigh wave as a function of depth and frequency for a six-layer subsurface model with increasing velocity derived from this study. These curves show that sensitivity rapidly decreases with depth for both components of displacement, especially for high frequencies (>3 Hz). This decay is more acute for the horizontal component of displacement (denoted by dashed lines in Figure 15.3b). For this velocity structure, maximum sensitivity is obtained for depths between 50 and 100 m. Significant sensitivity is achieved at depths down to ≈300 m for waves with a frequency of 1 Hz, but frequencies as low as 0.5 Hz are needed in order for Rayleigh wave energy to be sufficiently excited at the deepest sections of the profile. Hence, train noise is best suited for deeper imaging.

15.5. PROCESSING STRATEGY

Based on the previous analysis, an approach similar to that used in Ajo-Franklin et al. (2019) is used in this study. Infrastructure noise generated by a freight train running along the dark fiber cable is exploited to retrieve the shear-wave velocity structure of the topmost few hundred meters beneath the cable. The complete processing workflow is illustrated in Figure 15.4, which starts with the acquired 1 minute noise records and ends with one-dimensional (1-D) shear-wave velocity profiles. This processing framework is very similar to that of Ajo-Franklin

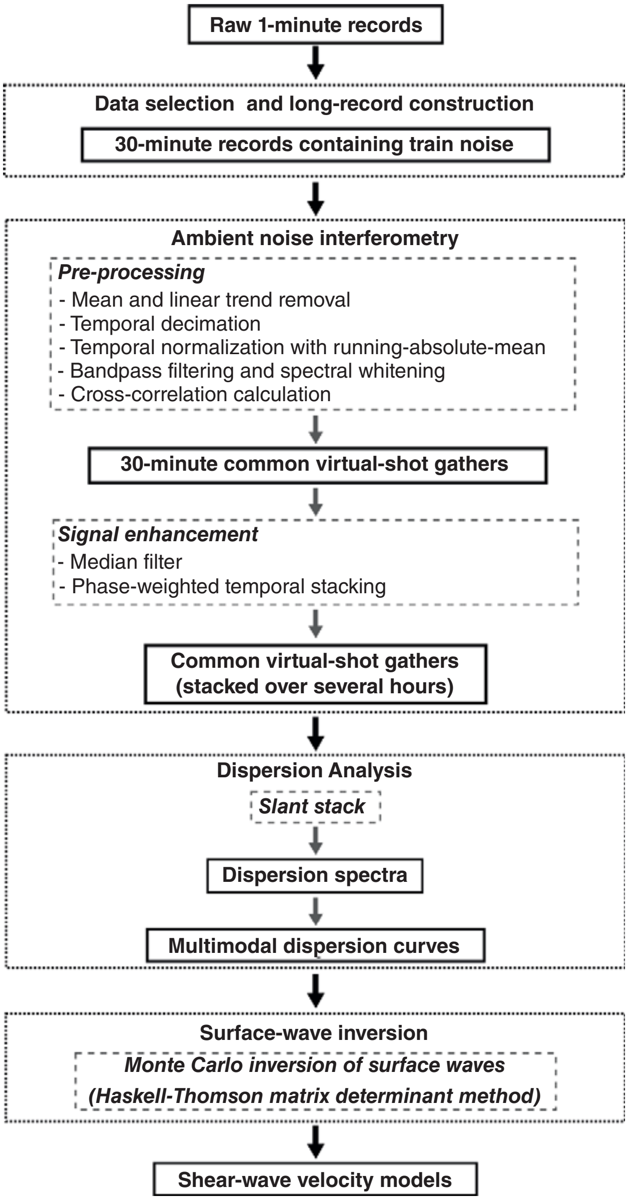

Figure 15.4 Ambient noise processing flow for V_s recovery at intermediate depths.

et al. (2019), slightly modified to achieve deeper imaging, and is based on well-established ambient noise analysis procedures (e.g., Bensen et al., 2007). A key difference with the processing sequence used in Ajo-Franklin et al. (2019) is that 30 minute long records instead of 1 minute long records are processed.

15.5.1. Data Selection

The analysis is performed on 1 km long segments of the array. These sections allow retrieving surface wave energy at long offsets, which is necessary for large-scale imaging using long wavelengths, but are still assumed to be adequate for 1-D analysis of subsurface structure. In order to obtain sampling of deep structure and surface wave energy retrieval at long distances, it is important that enough low-frequency energy is captured. With this objective, the acquired noise data are organized into 30 minute long records to ensure that low-frequency (i.e., long wavelength) phases are included (e.g., Seats et al., 2012).

As shown in Figure 15.3a, train energy is the most energetic and broadband source available in our study site. Accordingly, the data selected for analysis consist exclusively of records containing energy created by an approaching or departing train. For each 1 km long section, 1 minute records containing train energy are identified by scanning trace windowed root-mean-square (RMS) amplitude on the raw data and are tagged as “train pass” (Ajo-Franklin et al., 2019). Next, 1 minute files acquired between 31 and 1 minutes before “train passes” in our selected cable section are concatenated into the 30 minute long records to which ambient noise interferometry is subsequently applied. The logic behind selecting noise records between 31 and 1 minutes before the train arrives at the section of cable under investigation lies on the intensity of the train signal and the dynamic range of the interrogator unit. When the train is directly above our selected cable section, the intensity of the train-generated signal surpasses the dynamic range of the instrument, resulting in a very noisy signal with no interpretable waves (e.g., Figure 15.2). To avoid this effect, we select noise recorded before the arrival of the train, which contains usable surface wave energy.

15.5.2. Ambient Noise Interferometry and Dispersion Analysis

After construction of these longer records, preprocessing of the raw data is needed in order to prepare them for cross correlation (Bensen et al., 2007; Dou et al., 2017). Static offsets and linear trends are removed from the raw, 30 minute long noise records, followed by temporal decimation down to a sampling rate of 8 ms (f = 125 Hz). Temporal normalization is applied using a running absolute-mean procedure with a running window of 0.5 s, in order to reduce the effect of undesired signals, such as earthquakes. Next, the data are band-passed between 0.002 and 15 Hz and these frequencies are balanced using spectral whitening. Following these preparation steps, for each of the 30 minute long records, the southernmost receiver of the 1 km long section is treated as the virtual source and cross-correlated with all other receivers in that section to construct common virtual-source gathers. As observed in Figures 15.5a and 15.5c, the resultant gathers are contaminated by horizontal (infinite velocity) noise that affects all channels and is especially strong at zero lag time. This noise is most likely the effect of

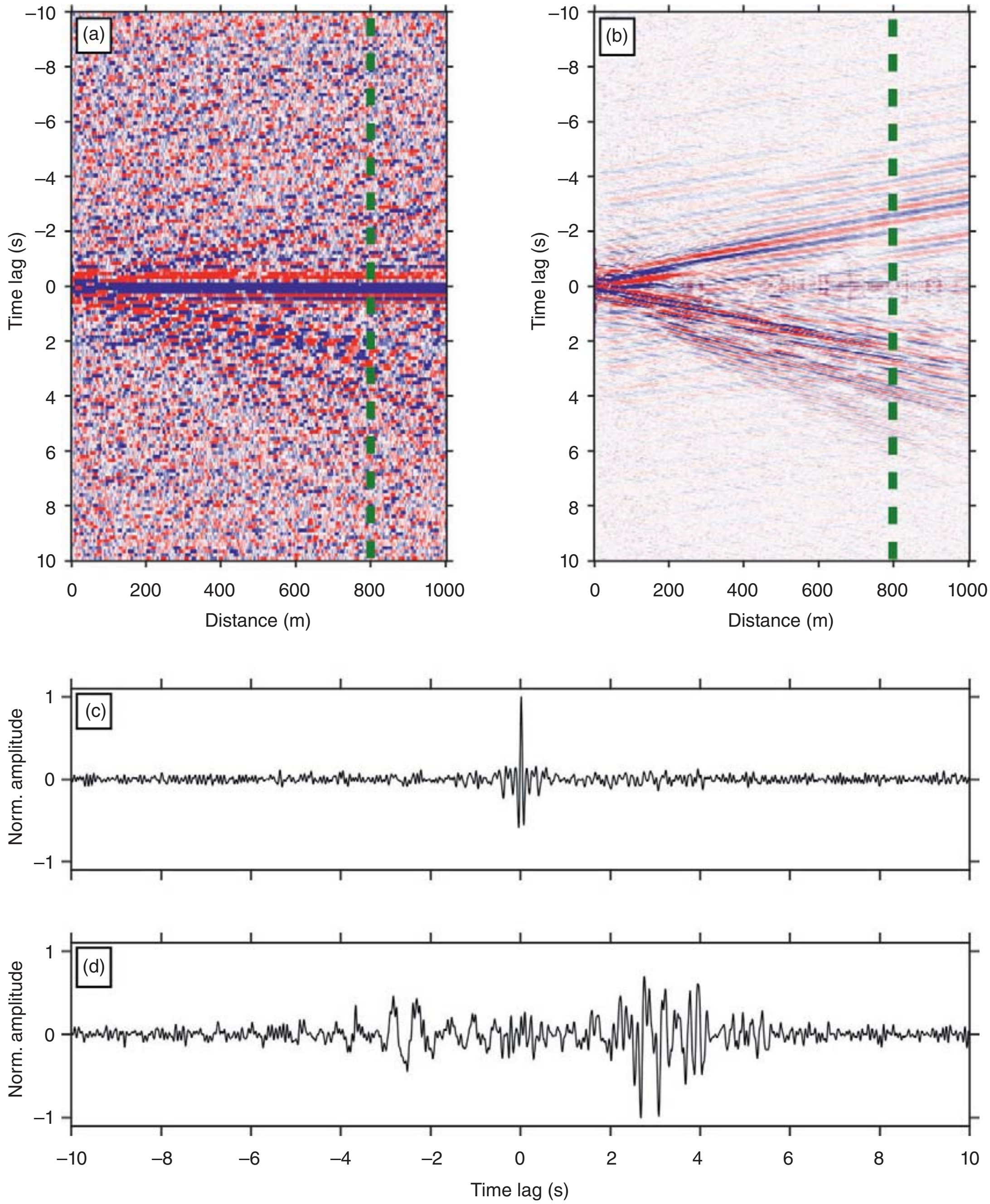

Figure 15.5 Comparison between a 30 minute single virtual shot gather and phase-weighted stack of 42 virtual shot gathers. (a) Time-distance display of single cross-correlation. The green dashed line indicates trace shown in panel (c). (b) Same as panel (a), but for phase-weighted stack. (c) Normalized amplitude-time lag close-up view of a single trace at offset indicated in panel (a). Note signal is dominated by horizontal noise at 0 s time lag. (d) Same as panel (c), but for a trace in virtual stack shown in panel (b). Note the high amplitude group arrival between −2 and −3 s and between 2 and 4 s.

cross-correlating coherent optical noise generated by the DAS unit. This noise is suppressed by calculating the median amplitude of all traces in the gather and later subtracting it from each trace. Further signal enhancement and signal-to-noise ratio improvement is achieved by temporally stacking multiple 30 minute long records, which suppresses incoherent signals. The phase-weighted stacking method of Schimmel & Paulssen (1997) is used, which allows data quality improvement with fewer records than what would be needed if a mean stack were performed. In this approach, the coherency of the unstacked traces is calculated based on their instantaneous phase. This measure of coherency is then used to weight every sample of the linear stack. In this way, this nonlinear stacking technique enhances coherent signals through the reduction of incoherent noise and enables the detection of weak signals even for small amounts of data. Here, 45 records are stacked, corresponding to 22.5 hours of train noise (Figures 15.5b and 15.5d).

Ambient noise interferometry is followed by dispersion analysis. Slant stacking is applied to the common virtual-shot gathers to transform the data from the time-distance domain to the frequency-velocity (dispersion) domain. Once the dispersion spectrum is calculated, multimodal dispersion curves are manually extracted and used as input for a multimodal surface wave inversion.

15.5.3. Multimodal Inversion Using the Haskell-Thomson Determinant Method

As discussed in Dou et al. (2017) and Ajo-Franklin et al. (2019), mode numbering can be difficult to assign in DAS data sets. Consequently, we adopt the inversion approach developed by Maraschini et al. (2010), which does not require explicit mode numbering. As opposed to minimizing the misfit between observed and calculated dispersion curves, this inversion algorithm minimizes the determinant of the model-predicted Haskell-Thomson propagator matrix. This matrix describes the propagating media, and its determinant depends on model parameters such as V_s, V_p (or V_p/V_s ratio), density and thickness of each model layer, as well as the frequency-velocity point at which the determinant is calculated. The algorithm evaluates the determinant misfit function at the frequency-velocity pairs of our observed dispersion curves and finds the model that minimizes the function at these data appoints using the L1 norm. Details on the calculation of the determinant misfit function and the inversion algorithm can be found in Maraschini et al. (2010) and Maraschini & Foti (2010).

A Monte Carlo (MC) sampling approach is adopted to allow for a sparse parameterization of the model space (Maraschini & Foti, 2010). Initially, three approaches are tested to construct the velocity model: (1) Choosing a specific number of layers, with broad bounds in both velocity and layer thickness to allow for efficient model exploration; (2) defining large number of thin layers with a gradual increase in velocity, to allow for gradual changes in velocity instead of sharp velocity contrasts; and (3) selecting a specific number of layers with the same constant velocity bounds, to allow for an even broader exploration of the parameter space. Of these approaches, (2) and (3) made the inversion very unstable and were discarded. The main reason for this instability is most likely the nature of the determinant method inversion technique itself. As a result, the model is constructed as a series of distinct layers over a half space.

Thorough parameter testing suggests that a six-layer model (five layers plus the half space) is most adequate to describe the subsurface below the selected cable section. This choice is made based on a combination of two factors: Achieving small RMS misfits for the determinant function and obtaining the best match between our observed dispersion curve and the synthetic dispersion curve calculated from the best fit inversion model for each run. In this procedure, models with less than five layers and more than six layers yielded very high RMS misfits and the derived synthetic dispersion curves did not match the observations. Misfits for models with five and six layers were very similar, but the model with six layers provided a slightly better fit to the observed dispersion curves. In this inversion approach, both V_s and layer thickness are inverted for.

For each MC run, a pool size of 1 x 10^6 models is defined and specified search bounds for both parameters are broad, allowing model exploration. Search bounds for each model parameter are specified in Table 15.1. After inversion, all models are ranked by their L1 norm misfit and the top 0.1% best fit models are selected for analysis and interpretation. The Haskell-Thomson determinant method provides the advantage of multimodal, nonlabelled data to be used as inversion input. However, it is important to note that this approach comes with the pitfall that several local minima are present in the misfit function. In some cases, this feature will make the resultant velocity inversion highly dependent on the choice of model bounds, since there is the risk of the inversion to converge into a local minimum.

Table 15.1 Upper and Lower Bounds of MC Sampling for Inversion Parameters.

Model layer	V_s lower bound [m/s]	V_s upper bound [m/s]	Thickness lower bound [m]	Thickness upper bound [m]
1	250	700	10	60
2	300	900	30	100
3	400	1,000	30	100
4	600	1,200	50	100
5	900	1,600	50	100
6 (half space)	1,000	2,000	-	-

15.6. RESULTS

15.6.1. Site Comparison Data

To assist in evaluating the inversion results, we made use of a large number of archival sonic logs acquired in gas wells drilled near the fiber profile. Well logs were obtained from the California Department of Oil, Gas, and Geothermal Resources (DOGGR) online database, picked, and digitized to Log ASCII Standard (LAS) format. Sonic logs dated from the 1960s to early 2000s and their quality were highly variable. In all cases, only *P*-wave sonic logs were available, necessitating development of a V_p/V_s model for direct comparison with our V_s inversion profiles. Additionally, no wells were logged to surface; therefore, our available constraints extend only from ≈180 m depth to the extent of our inversion profile. Well locations and corresponding API (American Petroleum Institute) identification numbers are detailed in Table 15.2. The relatively sparse distribution of well data (despite the area's history of natural gas exploration) highlights the potential of dark fiber DAS to provide subsurface information with high spatial sampling.

Figure 15.6a shows the catalog of log data used in developing our comparison model. The colored dots represent V_p measurements for the six wells considered. As

Table 15.2 Location and American Petroleum Institute (API) Identification Numbers of Well Logs From the DOGGR Database Used in This Study to Evaluate Inversion Results.

Well name	Longitude	Latitude	API number
Hanks 3-4	−121.62443	38.669974	11320756
Unit 1-1	−121.61713	38.662796	11320931
Conway 4-2	−121.637443	38.655187	11321126
Rivercat 11-2	−121.600432	38.636183	11321189
Mattos 1	−121.588339	38.633324	11320751
Agriventure Ensher (AE) 19-1	−121.581496	38.617168	11321099

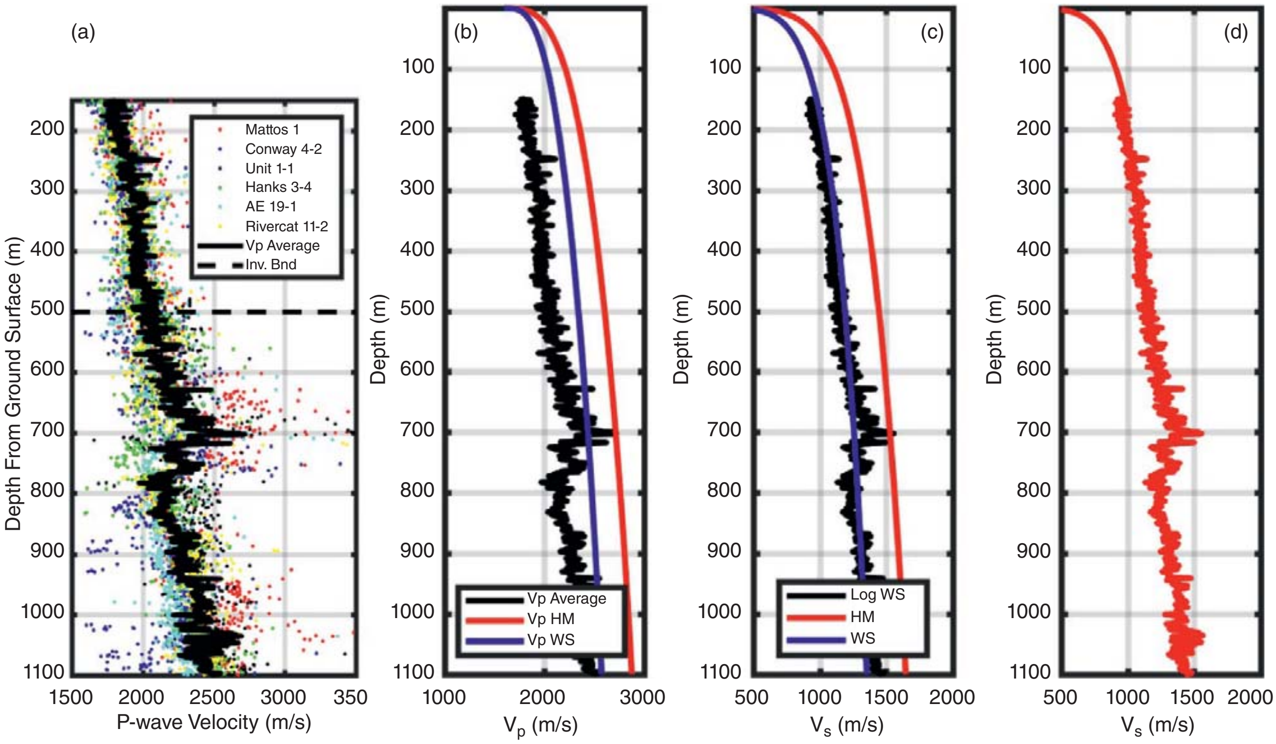

Figure 15.6 Data sets and development of a reference $V_s(z)$ model; panel (a) shows available sonic logs (colored dots) near the DAS profile, as well as a V_p depth average (black line). Panel (b) shows a comparison of the mean V_p log with two analytical contact theory models Hertz-Mindlin, HM, and Walton Smooth, WS, models. Panel (c) shows the mean sonic log (black) converted into V_s using a depth-dependent V_p/V_s model derived from the WS model. Panel (d) shows the final reference $V_s(z)$ model consisting of the converted logs below 150 m and the WS model above.

can be seen, while structural variations exist between the wells, as would be expected given the different log vintages and departures from 1-D geological structure, the first 600 m lacks any units with distinct *P*-wave properties. This zone appears to have a consistent depth gradient, likely driven by increasing overburden stress given the relatively young age of the sediments and known absence of cementation at these depths. Based on this observation, we decided to average the logs to develop a larger scale 1-D model; in Figure 15.6a, this is denoted by the bold black line.

To convert this mean log V_p profile to a V_s model, we explored a variety of empirical as well as analytical models to generate an appropriate V_p/V_s ratio. Our first attempts made use of classical empirical models, such as the regression set proposed by Brocher (2008) for Northern California. The depth regressions in Brocher yielded higher *P*-wave velocities than observed in our log database suggesting they are not well suited for this site.

Based on the observed depth trend, we evaluated the use of several contact-theory-based models to develop an appropriate V_p/V_s ratio model. Following the summary available in Mavko et al. (1998), we tested the Hertz-Mindlin (HM) and Walton Smooth (WS) models (Mindlin, 1949; Walton, 1987) for both predicting the observed *P*-wave trend and for V_p/V_s ratio estimation. We used these two contact theory models assuming a lithostatic stress trend of 0.022 MPa/m (equivalent to 1 psi/ft) and a standard hydrostatic pore pressure trend. We assumed a constant porosity of 0.34, an empirical porosity/coordination number conversion, and that the grain properties are that of pure quartz. After dry frame properties were calculated, we estimated water-saturated properties using Gassmann fluid substitution (Mavko et al., 1998). A volumetric average was used to calculate density. Figure 15.6b compares the resulting HM and WS predictions to the average *P*-wave velocity trend. The WS model with these parameters appears to capture the trend effectively, although slightly overestimates velocity, likely due to the many simplifying assumptions.

A V_p/V_s ratio based on the WS model was then used to convert the *P*-wave sonic logs to V_s estimates. Figure 15.6c shows the converted sonic logs (black) with the analytical HM and WS predictions; the close correspondence between the analytical WS model and converted log estimates suggests that this approach is reasonable. This correspondence also justified utilization of the WS model for prediction of the shallower shear velocity structure. Figure 15.6d shows the integrated V_s model used for our inversion comparisons consisting of the log conversion below ≈150 m and the WS estimation at shallower depths.

15.6.2. Inverted V_s Structure and Comparison with Ground Truth Data

Here, we present the results of applying the described processing approach to a 1 km long section located toward the southern end of the profile (denoted by a red line in Figure 15.1). Figure 15.7 shows the results of the dispersion analysis and the associated best fit V_s model obtained from the inversion. The inverted profile reveals an increasing velocity gradient within the top 250 m, with no significant velocity variations (Figure 15.7c). The interfaces that characterize the model are most likely due to the nature of the inversion process, which does not allow modeling of velocity gradients but discrete layers only. Shear-wave velocities increase from about 250 m/s at shallow depths to ≈1000 m/s at a depth of 260 m. Velocities remain the same down to 500 m, which is the maximum depth of our model. Synthetic dispersion curves are calculated using the inverted model and can be seen to agree well with our dispersion observations (Figures 15.7a and 15.7b). Model uncertainty can be evaluated by examining the results of the top 0.1% best fit V_s profiles. To do that, we have divided the model parameter space into bins of 5 m depth by 25 m/s V_s and have calculated how many models fall within these bins. The spread of these results is taken as the uncertainty bounds of our best-fit model. As illustrated in Figure 15.7c, uncertainty increases with depth. As expected, lowest uncertainty is achieved for depths down to ≈100 m, with slightly higher uncertainties for depths between 100 and ≈250 m. Higher model variability is observed at deeper depths, where uncertainty in V_s is mostly within 500 m/s. These results are expected, since the low-frequency content shown in our frequency-velocity spectra shows low amplitudes below ≈1 Hz (Figures 15.7a and 15.7b). Stacking of longer ambient noise recordings in combination with spatial stacking of a few contiguous channels would potentially help recover more energy at the low-frequency end of the spectra.

In order to evaluate the applicability of DAS ambient noise analysis for imaging at intermediate scales, we compare our V_s model with the integrated V_s model converted from well log data as described in the previous section. Our results show that the inverted velocity structure agrees with the converted well log V_s profile (Figure 15.7c). Our model can capture the increasing velocity gradient described by the log data and matches the very little velocity variation at depth. At depths between 150 and 250 m, our best fit model predicts shear-wave velocities that are slightly lower than those defined by the converted well logs, but the latter fall within the inversion uncertainty bounds. Well log data for depths shallower than 150 m are not available, which again highlights the utility of dark fiber DAS data sets to

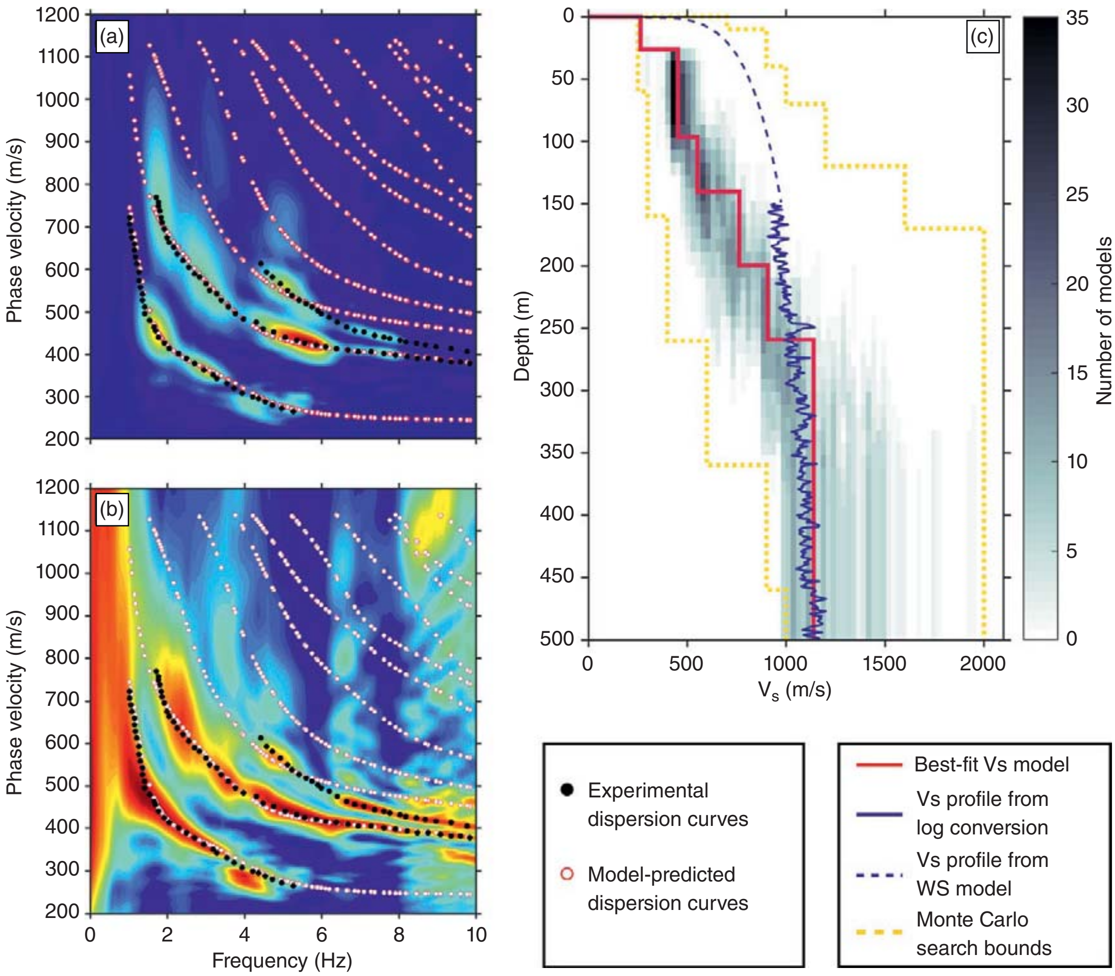

Figure 15.7 Results of multimodal inversion of the analyzed 1 km long virtual shot gather. (a) Amplitude normalized dispersion spectra in the frequency-velocity domain. Experimental (black) and model-predicted (white/red) dispersion curves. (b) As for panel (a), but dispersion spectrum is frequency normalized. (c) Comparison of inverted velocity model with average V_s converted sonic well log. The number of models within bins of 5 m in depth by 25 m/s in V_s is shown for the top 0.1% best-fit models as a measure of uncertainty. Model bounds are also illustrated.

retrieve subsurface velocity information at high resolution. As described in the previous section, the dashed line illustrated here at those shallower depths corresponds to the V_s trend estimated by the WS model. The model predicts velocities that are higher than our inverted velocity structure. Subsurface properties at these depths, however, are highly variable. It is expected that, due to many simplifying assumptions, the WS model is not able to adequately capture the complexity of properties at these depths, resulting in a discrepancy between the two estimated profiles. More detailed information on lithology, porosity, water saturation, etc., at these depths and the application of a more sophisticated model for the shallower section of the profile would help alleviate this issue.

15.7. DISCUSSION

Our study illustrates that DAS data sets acquired using existing telecommunication networks are suitable for applying ambient noise analysis to image the top several hundreds of meters of the subsurface. To date, only a few works have focused on investigating the subsurface between several tens of meters to several hundreds of meters using ambient noise approaches. Some recent examples include applications such as reservoir-scale imaging and monitoring (de Ridder & Biondi, 2013; Mordret et al., 2014), landslide imaging (Renalier et al., 2010), and basin-scale groundwater monitoring (Clements & Denolle, 2018). This lack of intermediate-scale studies is mainly due to the paucity of noise sources between the microseism band and higher frequency infrastructure noise sources, as well as the absence of appropriate recording geometries. As previously discussed, waves with frequencies between 0.5 Hz and 1–2 Hz are needed to sample depths between 100 m and ≈1 km (Figure 15.3b). In our investigation, we have shown that railway activity generates enough energy at these frequencies; DAS arrays located along or nearby railway tracks are suitable for recovering this noise. Along with this lower frequency component, DAS also allows for recording waves at the traffic frequency band, which enables high-resolution imaging of the shallow (top tens of meters) subsurface. Low-frequency components are better recovered when cross-correlating noise at receivers separated by long offsets. In contrast, high-frequency surface waves scatter off near-surface features and attenuate rapidly; dense receiver spacing is required in order to fully capture them. In our study, we have proven that DAS recorded on dark fiber meets both requirements, enabling the acquisition of high-quality, broadband ambient noise data sets at unprecedented spatial resolution for distances of several kilometers without the necessity of sensor installation or a power source.

Interesting applications of retrieving shear-wave velocity structure at depths of hundreds of meters include their use in seismic reflection processing routines. First, accurate velocity models at these depth scales and spatial density would be useful for precise *S*-wave static corrections. When the shallow velocity model at a site is not known, corrections are applied using constant velocities. In complex environments, this simplification can result in significant distortion of reflector geometries (Yilmaz, 2001). Second, such velocity models could potentially be used in later migration steps, which are indispensable for the correct relocation of imaged structures. Lastly, the combination of shallow and intermediate depth V_s models should find application in understanding earthquake ground motion, particularly in basins where the combination of basement depth as well as near-surface soil properties is required for prediction of amplification and structure performance. Ultimately, the potential of combining dark fiber DAS data sets with ambient noise analysis for intermediate depth imaging, demonstrated in this study, paves the way for efficient high-resolution imaging at a regional scale. Recent studies in the field of ambient seismic noise interferometry have demonstrated that not only surface waves but also body waves can be recovered from noise recordings and used for seismic reflection imaging and *P*-wave tomography (Draganov et al., 2007; Nakata et al., 2015; Nakata et al., 2016; Ryberg, 2011). In an interferometric experiment carried out in the Sirte basin in Libya using a classical geophone array and 11 hours of ambient seismic noise at high frequencies (6–24 Hz), the authors are able to retrieve a reflection image of the subsurface that compares to data sets acquired using active source data down to 1 s two-way travel time (Draganov et al., 2009, 2013). Within the Sacramento basin, most academic geophysical works have focused on characterizing the basement and crustal structure of the Great Valley forearc basin (e.g., Constenius et al., 2000; Godfrey et al., 1997), whereas a few others have investigated the stratigraphic architecture of the Jurassic–Cretaceous Great Valley Group (Williams & Graham, 2013). The acquisition of high spatial resolution DAS-based ambient noise data would provide means to characterize the stratigraphic framework and structure of the youngest (Paleogene-Quaternary) sedimentary sequences of the basin infill. With the current dark fiber infrastructure, much of the length of the Sacramento basin could be probed using only four independent interrogator units (Ajo-Franklin et al., 2019). Investigations of this caliber are rarely feasible with conventional sensors due to instrument, deployment, and maintenance costs. This approach can be applied to other geological structures and environments where conventional deployments are challenging or costly, such as basin-scale mapping of geothermal systems, reservoir characterization, or hazard evaluation in urban areas.

15.8. CONCLUSIONS

This study shows that ambient seismic noise interferometry can be applied to DAS data sets acquired in existing telecommunication networks to retrieve shear-wave structure down to depths of 500 m. DAS-based ambient seismic noise data were acquired along a 23.29 km long dark fiber network that crosses part of the Sacramento Basin between northwest Sacramento and the city of Woodland for a period of approximately 7 months. Noise originating from rail traffic in line with the fiber array proved to be the most energetic and broadband noise source and is exploited to perform interferometric analysis and inversion of surface wave data to retrieve 1-D shear-wave velocity models beneath the array. Results of a 1 km long section located in the southern end of the array reveal that we can resolve subsurface velocity structure down to a depth of 500 m, with increasing uncertainty below a depth of ≈300 m. Our resultant *S*-wave velocity model agrees well with an average V_s profile converted from seven sonic well logs acquired in gas wells in the vicinity of the DAS array. The potential of combining DAS-based seismic data sets acquired in unused telecommunication networks with analysis of ambient seismic noise opens up possibilities for efficient, high-resolution, basin-scale imaging.

ACKNOWLEDGMENTS

This work was supported by the Laboratory Directed Research and Development (LDRD) Program of Lawrence Berkeley National Laboratory under U.S. DOE Contract No. DE-AC02-05CH11231. This research used resources of the ESnet Dark Fiber Testbed , which is supported by the Office of Science of the U.S. DOE under Contract DE-AC02-05CH11231. Nate Lindsey was supported by the National Science Foundation Graduate Research Fellowship under Grant No. DGE 1106400. The authors would like to thank Silixa for long-term support of their DAS acquisition efforts. The authors would like to thank Dr. Sebastiano Foti (Politecnico di Torino) for providing the original version of the multimodal surface wave inversion code utilized in authors' ambient noise analysis, as well as pioneering the inversion approach with his collaborators and students. Finally, the authors would like to thank CenturyLink for providing installation protocol details on the network section utilized in this study.

REFERENCES

Ajo-Franklin, J. B., Dou, S., Lindsey, N. J., Monga, I., Tracy, C., Robertson, M., et al. (2019). Distributed acoustic sensing using dark fiber for near-surface characterization and broadband seismic event detection. *Scientific Reports*, *9*(1328).

Becker, M. W., Ciervo, C., Cole, M., Coleman, T., & Mondanos, M. (2017). Fracture hydromechanical response measured by fiber optic distributed acoustic sensing at milliHertz frequencies. *Geophysical Research Letters*, *44*(14), 7295–7302. https://doi.org/10.1002/2017GL073931

Bensen, G. D., Ritzwoller, M. H., Barmin, M. P., Levshin, A. L., Lin, F., Moschetti, M. P., et al. (2007). Processing seismic ambient noise data to obtain reliable broad-band surface wave dispersion measurements. *Geophysical Journal International*, *169*, 1239–1260. https://doi.org/10.1111/j.1365-246X.2007.03374.x

Brenguier, F., Boué, P., Ben-Zion, Y., Vernon, F., Johnson, C. W., Mordret, A., et al. (2019) Train traffic as a powerful noise source for monitoring active faults with seismic interferometry. *Geophysical Research Letters*, *46*, 9529–9536. https://doi.org/10.1029/2019GL083438

Brocher, T. M. (2008). Compressional and shear-wave velocity versus depth relations for common rock types in northern California. *Bulletin of the Seismological Society of America*, *98*(2), 950–968. https://doi.org/10.1785/0120060403

Campillo, M., & Roux, P. (2015). Crust and Lithospheric Structure—Seismic imaging and monitoring with ambient noise correlations. In *Treatise on Geophysics: Second Edition* (Vol. *1*, pp. 391–417). Elsevier B.V. https://doi.org/10.1016/B978-0-444-53802-4.00024-5

Campion, Jr., J. T. (1980). Conway Ranch gas field. California Division of Oil and Gas Publication TR 24.

Clements, T., & Denolle, M. A. (2018). Tracking groundwater levels using the ambient seismic field. *Geophysical Research Letters*, *45*, 1–7. https://doi.org/10.1029/2018GL077706

Constenius, K. N., Johnson, R. A., Dickinson, W. R., & Williams, T. A. (2000). Tectonic evolution of the Jurassic–Cretaceous Great Valley forearc, California: Implications for the Franciscan thrust-wedge hypothesis. *Bulletin of the Geological Society of America*, *112*(11), 1703–1723. https://doi.org/10.1130/0016-7606(2000)112<1703:TEOTJC>2.0.CO;2

Daley, T. M., Freifeld, B. M., Ajo-Franklin, J., Dou, S., Pevzner, R., Shulakova, V., et al. (2013). Field testing of fiber-optic distributed acoustic sensing (DAS) for subsurface seismic monitoring. *The Leading Edge* (June). https://doi.org/S0016-6480(10)00349-7 [pii]10.1016/j.ygcen.2010.10.003

Daley, T. M., Miller, D. E., Dodds, K., Cook, P., & Freifeld, B. M. (2016). Field testing of modular borehole monitoring with simultaneous distributed acoustic sensing and geophone vertical seismic profiles at Citronelle, Alabama. *Geophysical Prospecting*, *64*(5), 1318–1334. https://doi.org/10.1111/1365-2478.12324

Dou, S., Lindsey, N., Wagner, A. M., Daley, T. M., Freifeld, B., Robertson, M., et al. (2017). Distributed acoustic sensing for seismic monitoring of the near surface: A traffic-noise interferometry case study. *Scientific Reports*, *7*(1), 1–12. https://doi.org/10.1038/s41598-017-11986-4

Draganov, D., Campman, X., Thorbecke, J., Verdel, A., & Wapenaar, K. (2009). Reflection images from ambient seismic noise. *Geophysics*, *74*(5), A63–A67. https://doi.org/10.1190/1.3193529

Draganov, D., Campman, X., Thorbecke, J., Verdel, A., & Wapenaar, K. (2013). Seismic exploration-scale velocities and structure from ambient seismic noise (> 1 Hz). *Journal of Geophysical Research: Solid Earth*, *118*, 4345–4360. https://doi.org/10.1002/jgrb.50339

Draganov, D. S., Wapenaar, K., Mulder, W., Singer, J., & Verdel, A. (2007). Retrieval of reflections from seismic background-noise measurements. *Geophysical Research Letters*, *34*(4), 2–5. https://doi.org/10.1029/2006GL028735

Godfrey, N. J., Beaudoin, B. C., & Klemperer, S. L. (1997). Ophiolitic basement to the Great Valley forearc basin, California, from seismic and gravity data: Implications for crustal growth at the North American continental margin. *Geological Society of America Bulletin*, (*12*), 1536–1562. https://doi.org/10.1130/0016-7606(1997)109<1536

Hartog, A. H., Rao, Y.-J., Ran, Z.-L., Gong, Y., Güemes, A., & Sierra Perez, J. (2017). In A. H. Hartog (Ed.), *An introduction to distributed optical fibre sensors*. Boca Raton, FL: Taylor and Francis Group.

Hunter, W. A., Kenworthy, L. G., & Bowersox, J. R. (1984). Geology of the Todhunters lake gas field. In A. A. Almgren & P. D. Hacker (Eds.), *Paleogene submarine canyons of the Sacramento Valley* (Vol. *1*, pp. 151–163). California: AAPG Pacific Section.

Inbal, A., Cristea-Platon, T., Ampuero, J., Hillers, G., Agnew, D., & Hough, S. E. (2018). Sources of long-range anthropogenic noise in Southern California and Implications for Tectonic Tremor Detection. *Bulletin of the Seismological*

Society of America, *108*(6), 3511–3527. https://doi.org/10.1785/0120180130

Jousset, P., Reinsch, T., Ryberg, T., Blanck, H., Clarke, A., Aghayev, R., et al. (2018). Dynamic strain determination using fibre-optic cables allows imaging of seismological and structural features. *Nature Communications*, *9*(2509). https://doi.org/10.1038/s41467-018-04860-y

Kaufmann, R. D., Xia, J., Benson, R. C., Yuhr, L. B., Casto, D. W., & Park, C. B. (2005). Evaluation of MASW data acquired with a hydrophone streamer in a shallow marine environment. *Journal of Environmental & Engineering Geophysics*, *10*(2), 87–98. https://doi.org/10.2113/jeeg10.2.87

Li, H., Bernardi, F., & Michelini, A. (2010). Surface wave dispersion measurements from ambient seismic noise analysis in Italy. *Geophysical Journal International*, *180*(3), 1242–1252. https://doi.org/10.1111/j.1365-246X.2009.04476.x

Li, Z., & Zhan, Z. (2018). Pushing the limit of earthquake detection with distributed acoustic sensing and template matching: a case study at the Brady geothermal field. *Geophysical Journal International*, *215*, 1583–1593.

Lindsey, N. J., Martin, E. R., Dreger, D. S., Freifeld, B., Cole, S., James, S. R., et al. (2017). Fiber-optic network observations of earthquake wavefields. *Geophysical Research Letters*, *44*(23), 11,792–11,799. https://doi.org/10.1002/2017GL075722

Maraschini, M., & Foti, S. (2010). A Monte Carlo multimodal inversion of surface waves. *Geophysical Journal International*, *182*(3), 1557–1566. https://doi.org/10.1111/j.1365-246X.2010.04703.x

Maraschini, M., Ernst, F., Foti, S., & Socco, L. V. (2010). A new misfit function for multimodal inversion of surface waves. *Geophysics*, *75*(4), G31–G43. https://doi.org/10.1190/1.3436539

Mateeva, A., Lopez, J., Mestayer, J., Wills, P., Cox, B., Kiyashchenko, D., et al. (2013). Distributed acoustic sensing for reservoir monitoring with VSP. *The Leading Edge*, (October), 3–7. Retrieved from http://library.seg.org/doi/10.1190/INT-2014-0248.1

Mavko, G., Mukerji, T., & Dvorkin, J. (1998). *The rock physics handbook*. Cambridge University Press.

Mindlin, R. D. (1949). Compliance of elastic bodies in contact. *Journal of Applied Mechanics*, *16*, 259268.

Molinari, I., Verbeke, J., Boschi, L., Kissling, E., & Morelli, A. (2015). Italian and Alpine three-dimensional crustal structure imaged by ambient-noise surface-wave dispersion. *Geochemistry Geophysics Geosystems*, *18*(1–2), 1541–1576. https://doi.org/10.1002/2014GC005684.Key

Mordret, A., Landés, M., Shapiro, N. M., Singh, S. C., & Roux, P. (2014). Ambient noise surface wave tomography to determine the shallow shear velocity structure at Valhall: Depth inversion with a Neighbourhood Algorithm. *Geophysical Journal International*, *198*(3), 1514–1525. https://doi.org/10.1093/gji/ggu217

Nakata, N., Snieder, R., Tsuji, T., Larner, K., & Matsuoka, T. (2011). Shear wave imaging from traffic noise using seismic interferometry by cross-coherence. *Geophysics*, *76*(6), SA97–SA106. https://doi.org/10.1190/geo2010-0188.1

Nakata, N., Chang, J. P., Lawrence, J. F., & Boué, P. (2015). Body wave extraction and tomography at Long Beach, California, with ambient-noise interferometry. *Journal of Geophysical Research: Solid Earth*, *120*(2), 1159–1173. https://doi.org/10.1002/2015JB011870

Nakata, N., Boué, P., Brenguier, F., Roux, P., Ferrazzini, V., & Campillo, M. (2016). Body and surface wave reconstruction from seismic noise correlations between arrays at Piton de la Fournaise volcano. *Geophysical Research Letters*, *43*(3), 1047–1054. https://doi.org/10.1002/2015GL066997

Olmsted, F. H., & Davis, G. H. (1961). Geologic features and ground-water storage capacity of the Sacramento Valley, California. U.S. Geological Survey Water-Supply Paper 1497, 241.

Park, C. B., Miller, R. D., & Xia, J. (1999). Multichannel analysis of surface waves. *Geophysics*, *64*(3), 800–808. https://doi.org/10.1190/1.1444590

Parker, E. H., & Hawman, R. B. (2012). Multi-channel Analysis of Surface Waves (MASW) in Karst Terrain, Southwest Georgia: Implications for detecting anomalous features and fracture zones. *Journal of Environmental & Engineering Geophysics*, *17*, 129–150. https://doi.org/10.2113/JEEG17.3.129

Parker, T., Shatalin, S., & Farhadiroushan, M. (2014). Distributed Acoustic Sensing—a new tool for seismic applications. *First Break*, *32*(February), 61–69.

Pepper-Kittredge, O., & Wilson, M. L. (1984). The Markley Submarine Valley and its stratigraphic relationships, Sacramento Valley, California. In A. A. Almgren & Paul D Hacker (Eds.), *Paleogene submarine canyons of the Sacramento Valley* (Vol. *1*, pp. 81–99). California: AAPG Pacific Section.

Quiros, D. A., Brown, L. D., & Kim, D. (2016). Seismic interferometry of railroad induced ground motions: Body and surface wave imaging. *Geophysical Journal International*, *205*(1), 301–313. https://doi.org/10.1093/gji/ggw033

Renalier, F., Jongmans, D., Campillo, M., & Bard, P. Y. (2010). Shear wave velocity imaging of the Avignonet landslide (France) using ambient noise cross correlation. *Journal of Geophysical Research: Earth Surface*, *115*(3), 1–14. https://doi.org/10.1029/2009JF001538

de Ridder, S. A. L., & Biondi, B. L. (2013). Daily reservoir-scale subsurface monitoring using ambient seismic noise. *Geophysical Research Letters*, *40*(12), 2969–2974. https://doi.org/10.1002/grl.50594

Ryberg, T. (2011). Body wave observations from cross-correlations of ambient seismic noise: A case study from the Karoo, RSA. *Geophysical Research Letters*, *38*(13), 1–5. https://doi.org/10.1029/2011GL047665

Schimmel, M., & Paulssen, H. (1997). Noise reduction and detection of weak, coherent signals through phase weighted stacks. *Geophysical Journal International*, *130*, 497–505. https://doi.org/10.1111/j.1365-246X.1997.tb05664.x

Seats, K. J., Lawrence, J. F., & Prieto, G. A. (2012). Improved ambient noise correlation functions using Welch's method. *Geophysical Journal International*, *188*(2), 513–523. https://doi.org/10.1111/j.1365-246X.2011.05263.x

Shapiro, N. M., Campillo, M., Stehly, L., & Ritzwoller, M. H. (2005). High-resolution surface-wave tomography from ambient seismic noise. *Science*, *307*(5715), 1615–1618. https://doi.org/10.1126/science.1108339

Snieder, R., & Larose, E. (2013). Extracting Earth's elastic wave response from noise measurements. *Annual Review of Earth* *and Planetary Sciences*, *41*(1), 183–206. https://doi.org/10.1146/annurev-earth-050212-123936

Walton, K. (1987). The effective elastic moduli of a random pack of spheres. *Journal of the Mechanics and Physics of Solids*, *35*, 213–226.

Williams, T. A., & Graham, S. A. (2013). Controls on forearc basin architecture from seismic and sequence stratigraphy of the Upper Cretaceous Great Valley Group, central Sacramento Basin, California. *International Geology Review*, *55*(16), 2030–2059. https://doi.org/10.1080/00206814.2013.817520

Wu, H., Wong, W.-F., Yang, Z., Wills, P. B., Lopez, J. L., Li, Y., et al. (2015). Dual-well 3D vertical seismic profile enabled by distributed acoustic sensing in deepwater Gulf of Mexico. *Interpretation*, *3*(3), SW11–SW25. https://doi.org/10.1190/INT-2014-0248.1

Wu, X., Willis, M. E., Palacios, W., Ellmauthaler, A., Barrios, O., Shaw, S., & Quinn, D. (2017). Compressional- and shear-wave studies of distributed acoustic sensing acquired vertical seismic profile data. *The Leading Edge*, *36*(12), 987–993. https://doi.org/10.1190/tle36120987.1

Xia, J. (2014). Estimation of near-surface shear-wave velocities and quality factors using multichannel analysis of surface-wave methods. *Journal of Applied Geophysics*, *103*, 140–151. https://doi.org/10.1016/j.jappgeo.2014.01.016

Yang, Y., Ritzwoller, M. H., Lin, F. C., Moschetti, M. P., & Shapiro, N. M. (2008). Structure of the crust and uppermost mantle beneath the western United States revealed by ambient noise and earthquake tomography. *Journal of Geophysical Research: Solid Earth*, *113*(12), 1–9. https://doi.org/10.1029/2008JB005833

Yilmaz, O. (2001). *Seismic data analysis: Processing, inversion and interpretation of seismic data*. Tulsa: Society of Exploration Geophysics Press.

16

Using Distributed Acoustic Sensing (DAS) for Multichannel Analysis of Surface Waves (MASW)

Chelsea E. Lancelle[1], Jonathan A. Baldwin[2], Neal Lord[3], Dante Fratta[4], Athena Chalari[5], and Herbert F. Wang[3]

ABSTRACT

A field experiment in Garner Valley, California, evaluated the use of a distributed acoustic sensing (DAS) array for obtaining surface-wave dispersion curves and a shear-wave velocity profile by a modified multichannel analysis of surface waves (MASW) method incorporating moving window cross-correlation in a 762 m long, rectangular layout. Traditional geophysical instruments were also deployed along parts of the array. The interpretation of DAS response against traditional seismic sensors must consider the nature, directivity, and length of measurements and bandwidth of the different measurements. After all these phenomena were considered, it was found that the dispersion curve results for DAS and accelerometers agreed within 10 m/s for frequencies greater than 7 Hz. Previous vibroseis surveys in the vicinity of the site were also used for comparison of dispersion curve results, though the velocities for each frequency calculated by DAS ranged from 10 to 50 m/s, which were different than those found previously at the site. Overall, the distributed nature of DAS array is well positioned for its use in the collection of the MASW data as it allows following propagation of the seismic waves from complex seismic sources and near-surface structures. Data collected with DAS were successfully used to calculate a dispersion curve using MASW and inverted for the evaluation of near-surface shear-wave velocity distributions.

16.1. INTRODUCTION

Distributed acoustic sensing (DAS) is a recent fiber-optic sensing technology being used largely for vertical seismic profiling in oil and gas reservoirs (Johannessen et al., 2012; Madsen et al., 2013; Mateeva et al., 2014). A relatively small number of DAS surface layouts have also been described. These include a 90 m triangular array on lake ice (Castongia et al., 2017) and a 150 m receiver line at a carbon sequestration site (Daley et al., 2013). Short parallel DAS lines have been used to collect impact source data for the interpretation of spectral analysis of surface waves (SASW – parallel and perpendicular lines to the direction of the surface waves; Costley et al., 2018) and multichannel analysis of surface waves (MASW – parallel lines to the direction of the surface waves; Galan-Comas, 2015) using impact sources. Larger deployments include a 17 km array at the Nevada Test Site (Mellors et al., 2014), a 36 km array at the Australian CO2CRC Otway Project site (Freifeld et al., 2016; Yavuz

[1]Department of Civil and Environmental Engineering, University of Wisconsin–Platteville, Platteville, Wisconsin, USA
[2]U.S. Army Corps of Engineers, Washington, District of Columbia, USA
[3]Department of Geoscience, University of Wisconsin–Madison, Madison, Wisconsin, USA
[4]Department of Civil and Environmental Engineering, University of Wisconsin–Madison, Madison, Wisconsin, USA
[5]Silixa Ltd., Elstree, UK

Distributed Acoustic Sensing in Geophysics: Methods and Applications, Geophysical Monograph 268, First Edition.
Edited by Yingping Li, Martin Karrenbach, and Jonathan B. Ajo-Franklin.

DOI:10.1002/9781119521808.ch16

et al., 2016), and a 9 km array at the Brady Hot Springs, Nevada geothermal site (Feigl et al., 2016). Recently, Dou et al. (2017) presented a 100 m × 110 m perpendicular array to show the combined interpretation of traffic noise for an interferometry study for MASW.

In this chapter, we report on the results of MASW using a swept-frequency source and an intermediate-sized 160 m × 80 m DAS array at Garner Valley, California. The study was motivated by a desire to assess the use of the dense spatial sensing of DAS for shallow geophysical applications. The field site and large shaker were part of the George E. Brown Jr. Network for Earthquake Engineering Simulation (NEES) funded by the National Science Foundation (NSF). The near-surface geology at the testing site had been characterized previously by boreholes (Youd, Steidl, & Nigbor, 2004) and by SASW (Stokoe et al., 2004).

The organization of this chapter is as follows: Section 16.2 describes basic principles of DAS technology; Section 16.3 provides information on the near-surface geology at the Garner Valley testing site; Section 16.4 throws light on the layout of active source and sensors; and Sections 16.5–16.7 cover the procedure for obtaining surface-wave dispersion. These sections are followed by a discussion and conclusions (Sections 16.8 and 16.9) that assess the use of DAS-collected data for shallow subsurface geology characterization in comparison with conventional sensors.

16.2. DAS MEASUREMENT PRINCIPLES

DAS is a measurement methodology for ground motion that is similar to distributed temperature sensing (e.g., Tyler et al., 2009) or distributed strain sensing (e.g., Froggatt & Moore, 1998) in which a fiber-optic cable is the sensor and the spacing of measurements is on the order of 1 m. However, rather than temperature or static strain, DAS senses vibrations along the fiber-optic length by sending a short pulse of laser light and monitoring returning signals from Rayleigh backscattering that occurs along the silica in the fiber (Johannessen et al., 2012). Phase changes of consecutive pulses from the same region of fiber are linearly proportional to changes in the length of a segment of fiber. The length of fiber over which the change in length is measured is called the gauge length, which sets the spatial resolution (10 m in our case) (Dean et al., 2017; Martin et al., 2018). Because DAS systems measure the change in length over the gauge length between consecutive laser pulses, the output of the DAS system is strain rate averaged over the gauge length (Daley et al., 2015; Parker et al., 2014). The center of the gauge length is called a channel. The DAS technique is capable of sampling strain rate every meter over distances of up to tens of kilometers of cable length with sampling rates as fast as 100 kHz (Johannessen et al., 2012; Madsen et al., 2013; Miller et al., 2012; Parker et al., 2014). This sampling rate far exceeds what is needed for seismic applications. Typically, DAS data are downsampled to 1 kHz or 200 Hz. A standard, single-mode fiber-optic cable can be used, although cables specifically made to work with DAS may improve performance (Madsen et al., 2013; Parker et al., 2014).

Several studies have utilized DAS in borehole and near-surface horizontal arrays. Daley et al. (2013) deployed fiber-optic cables in boreholes and surface trenches to monitor seismic waves created by a drop-weight source. The cable was placed in the surface trench in order to compare the DAS data with colocated geophone responses along the fiber-optic cable. The captured data showed high-quality surface waves. Correa et al. (2017) used two different fiber-optic cables deployed in a borehole along with a conventional three-component geophone to test the relative signal-to-noise ratios and directivity characteristics of each receiver type. They found the signal-to-noise ratio for DAS using a standard fiber to be around 10 dB below that of the geophone, while DAS using an enhanced fiber had a signal-to-noise ratio that was not significantly different from the geophone. Hornman (2016) used a helically wound cable to test the validity of using DAS for seismic recording on land. The helically wound cable was designed to have broadside sensitivity, something a horizontal fiber lacks. The helically wound cable was placed in a shallow borehole and compared with a colocated streamer. The data from the cable showed that the helically wound cable could successfully be used for seismic monitoring on land. Castongia et al. (2017) utilized a fiber-optic cable laid out in a triangular array and frozen into the ice of Lake Mendota (Madison, WI, USA). Two types of fiber-optic cables (i.e., tightly buffered and loose-tube cables) were used and the fiber-optic cable was looped multiple times around the array to compare fiber types and the effect of signal attenuation along colocated points in the fiber. The study also assessed directional sensitivity of the cable and compared DAS data with geophone responses.

Several DAS studies have also involved the deployment of fiber-optic cables in boreholes (Bakku, 2015; Daley et al., 2013, 2015; Johannessen et al., 2012; Madsen et al., 2013). In these studies, fiber-optic cables were coupled to the borehole by being cemented behind casing or clamped to tubing. The DAS response was assessed with colocated geophones. Most recently, a kilometer-scale DAS array was deployed for monitoring the carbon dioxide sequestration at Otway in Australia (Freifeld et al., 2016; Yavuz et al., 2016). Continuous monitoring of the reservoir is achieved using 90 kN sources that are permanently mounted on foundations. All these studies demonstrated that quality of the signal and noise level are comparable to those of geophones, but with the advantage of a more densely spaced sensor array.

In summary, two advantages of DAS are that (1) fiber-optic cable is installed once for use in repeat surveys and (2) a single interrogator can sense hundreds to tens of thousands of meters with a spatial resolution of as fine as 1 m. Limitations of DAS are that it is sensitive only to the strain in the direction of the fiber and the measurement technique limits the bandwidth to wavelengths larger than the DAS gauge length.

16.3. STUDY AREA AND EQUIPMENT LAYOUT

A DAS trial was conducted at the former University of California Santa Barbara's George E. Brown Jr. NEES facility (http://nees.ucsb.edu/facilities/GVDA) at the Garner Valley Downhole Array (GVDA) field site in Southern California in September 2013. The GVDA is 20 km southwest of Palm Springs, CA, USA (Figure 16.1, inset). It is in a seismically active region 7 km east of the San Jacinto Fault and 35 km west of the San Andreas Fault. The near-surface geology of the site is well known, and the local sediments have been fully characterized with geotechnical engineering logs (Youd, Bartholomew, & Proctor, 2004) and surface-wave analysis (Stokoe et al., 2004). From a fairly flat surface to about 16 m depth, the subsurface is composed mostly of silty and sandy soils (Figure 16.2). Below that is weathered granite to a depth of about 90 m, and that is underlain by granitic bedrock. The water table varies seasonally and ranged between 1 and 3 m deep in 2010 (Steidl et al., 2012). The shallowest water table occurs in the winter and spring, decreasing gradually through the summer to its deepest levels in September through December.

At the site, 762 m of fiber-optic cable was laid in a trench at a depth of about 0.30 m in a rectangular design with two interior diagonal segments (Figure 16.1). The approximately rectangular perimeter measures about 160 m × 80 m. The trench was backfilled and left for 3 months during which time sandy soil settled back into the trench, effectively coupling the cable to the ground. An Optical Cable Corporation fiber-optic cable with two single-mode and two multimode tightly buffered fibers in the same jacket was used in the study. The two single-mode fibers were spliced together at the end of the line to allow for two colocated measurements at each meter of fiber.

Sensors at the field site included two GVDA surface Kinematics EPI ES-T accelerometers (nees@UCSB,

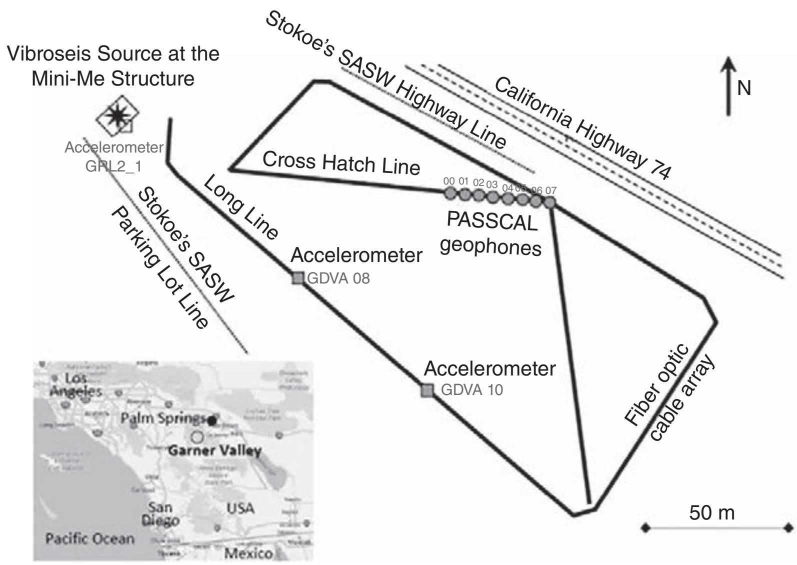

Figure 16.1 Map of the Garner Valley field site. The thick line is the layout of the fiber. The two fibers in the same jacket are spliced together at the cable end to create two measurement points at each channel location. California Highway 74 runs parallel to the long axis of the array and it is the main source of noise. Locations of Stokoe et al. (2004)'s SASW lines and those of PASSCAL geophones and GVDA accelerometers are also shown. The inset shows the location of the field site in Southern California. Source: Modified from Stokoe et al. (2004).

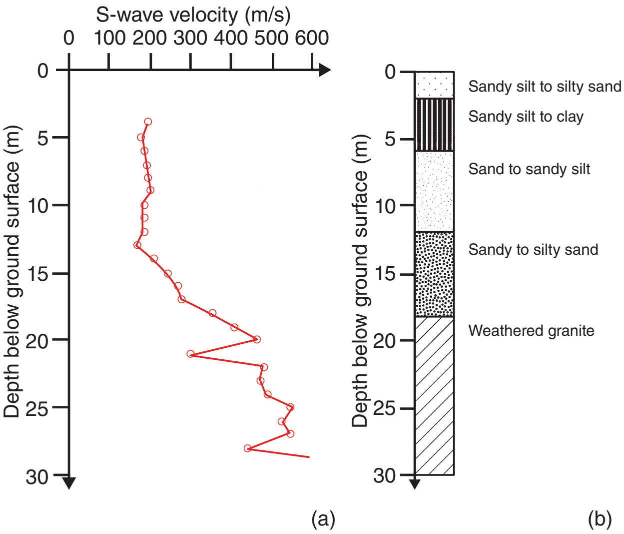

Figure 16.2 Subsurface geology at Garner Valley. (a) Shear-wave velocity profile from sonic logs and (b) near-surface lithologic profile. Source: Star et al. (2015). With permission of SAGE Publications.

2008) that were used in this study. Further details are also available at http://nees.ucsb.edu/facilities/GVDA. A 48-channel seismometer array was also deployed. It consisted of two Geometrics GEODE 24-channel seismographs provided by the Incorporated Research Institutions for Seismology Program for Portable Array Seismic Studies of the Continental Lithosphere (PASSCAL) together with 18 triaxial 4.5 Hz L-28-3D geophones (details are available at https://www.passcal.nmt.edu/content/instrumentation/sensors). Eight of the geophones were positioned 5 m apart on the first diagonal segment (denoted by a crosshatch in Figure 16.1.) Seven University of California, Los Angeles (UCLA) (http://nees.ucla.edu/sensors.html) triaxial accelerometers were used to monitor the source vibration on the Mini-Me structure (Figure 16.3a), a one-story tall structure, which was built as part of the NEES facility to assess the response of simple structures to local seismic excitations (http://nees.ucsb.edu/facilities/GVDA).

16.4. LARGE SHAKER SEISMIC SOURCE

The active source for the MASW results reported in this chapter was a stationary 45 kN eccentric mass shaker located on top of the Mini-Me structure (Figure 16.3a). MASW has been used previously with a mass shaker similar to UCLA's for monitoring carbon sequestration (Ikeda et al., 2015). The Mini-Me and its larger counterpart, "Dr. Evil", were developed to determine interactions between the structure and the subsurface under different loadings (Givens, 2013; Star et al., 2015). The Mini-Me is a steel moment frame consisting of a reinforced concrete slab supported by four columns anchored to a reinforced concrete foundation. The structure's dimensions are 4.28 m × 2.13 m at its base and its height is 2.13 m. The short axis is oriented at an azimuth of 326° (y axis). The UCLA 4600A shaker consists of two counter-rotating eccentric masses that force the structure to rock. The total eccentricity yields a maximum moment of 111 Nm. The shaker was swept from direct current (DC) to 10 Hz and back to DC over a 60 s excitation period. This sweep was followed by a 3 s listening time, making the length of each file 63 s long. The shaker produces strong vertical ground motion by rocking the Mini-Me structure about its x axis. The induced vibrations were measured on the Mini-Me and in the ground using NEES@UCLA EpiSensor accelerometers (http://nees.ucsb.edu/facilities/GVDA). Figure 16.3b shows all three components of acceleration on the southeast corner of the Mini-Me foundation, as well as those of a "free-field" sensor in the ground a few meters southwest of the Mini-Me structure. The responses of the accelerometer on the Mini-Me are very similar in magnitude and character to those presented by Givens (2013) in his Figures 5-17a and 5-17c. Resonance of the Mini-Me structure was reached at around 5 Hz, creating a small deviation from the otherwise linear excitation sweep. External triggering was used to synchronize the source and the PASSCAL geophones and the DAS system. Ten repeats of the source at 100% power were run to vibrate the structure and excite the field.

16.5. DAS AND GEOPHONE SENSORS

The characteristics of the DAS and geophone recordings of the Mini-Me source are described in this section. The two single-mode fibers within the cable were spliced together at the end of the array, doubling the number of channels to 1,524 at a spatial sampling of 1 m and a gauge length of 10 m. However, no discernible difference could be seen in waveforms from channels sensed at the same location. The geophone array was deployed with a spacing of 5 m along two 35 m segments of the diagonals of the array, as shown on the cable map in Figure 16.1.

Colocated DAS Channel 774 and geophone G01-East traces are shown for the large shaker source in Figures 16.4 and 16.5. Channel 774 and geophone G01 are located along the east-trending diagonal about 35 m from the intersection of the diagonals with the cable segment parallel to Highway 74. The raw DAS data were provided as a phase rate in radians per second. These values were converted into strain rate based on a conversion factor of 11.6 nanostrain per radian. The DAS strain rate and geophone ground velocity responses were band-pass filtered between 5 and 95 Hz and then downsampled from 1,000 to 200 samples per second. Then, the filtered

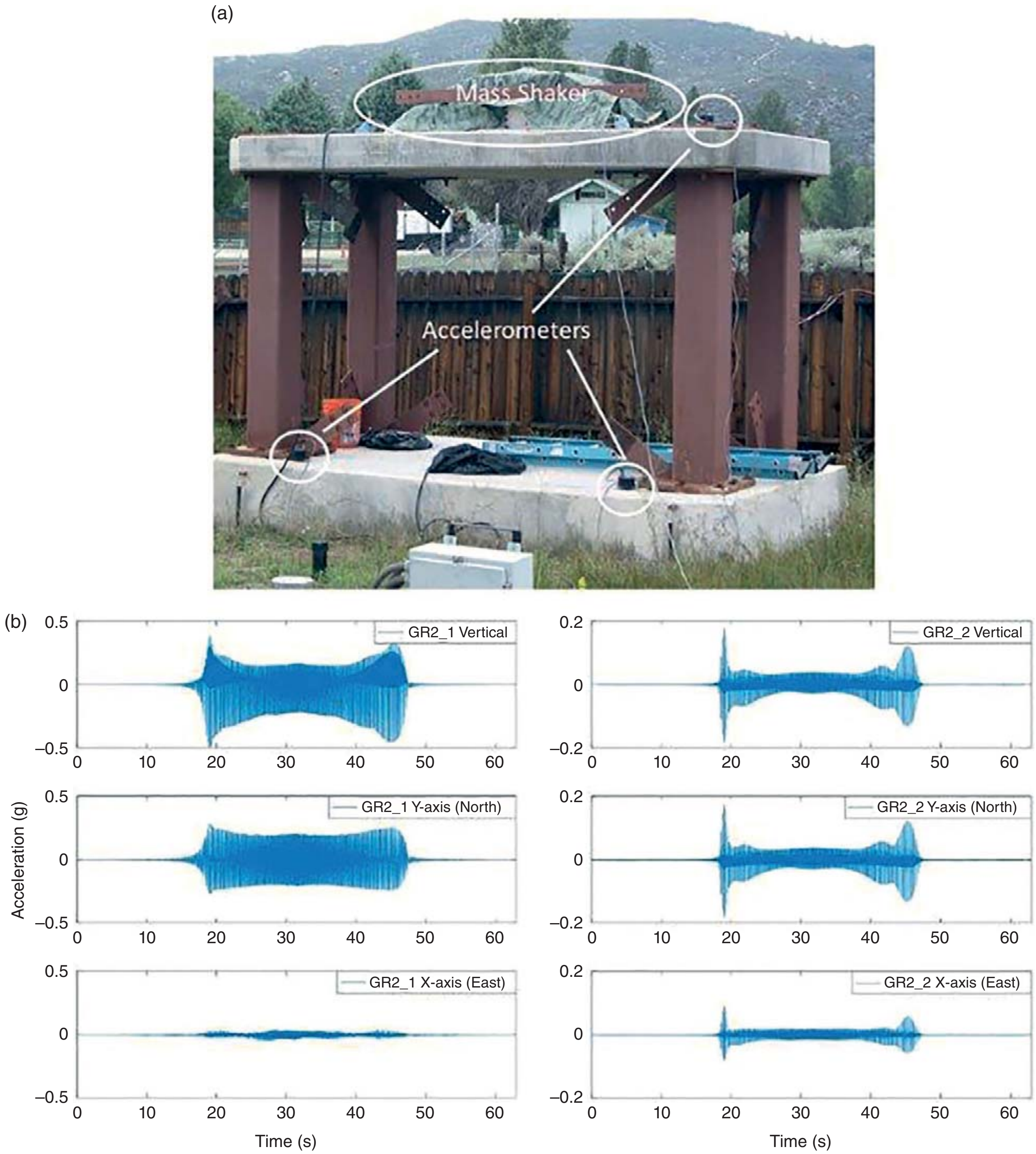

Figure 16.3 (a) Mini-Me structure. Locations of eccentric mass shaker and foundation accelerometer GR2_1 are shown. (b) Three components of accelerometers on the southeast corner of the Mini-Me foundation (left) and in the ground (free field) (right).

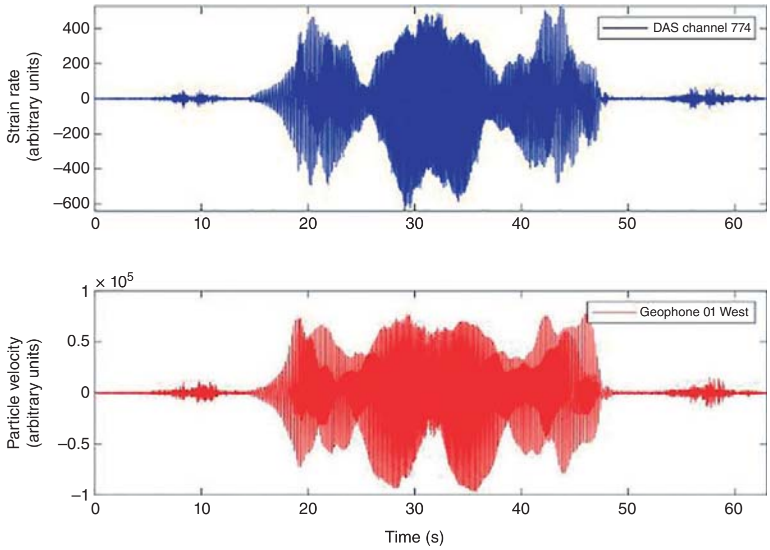

Figure 16.4 Plots of 63 s of data for a colocated DAS channel 774 (top) and east component of colocated seismometer (bottom). Noise in both the DAS and seismometer plots at around 10 and 57 s is from passing vehicles on Highway 74.

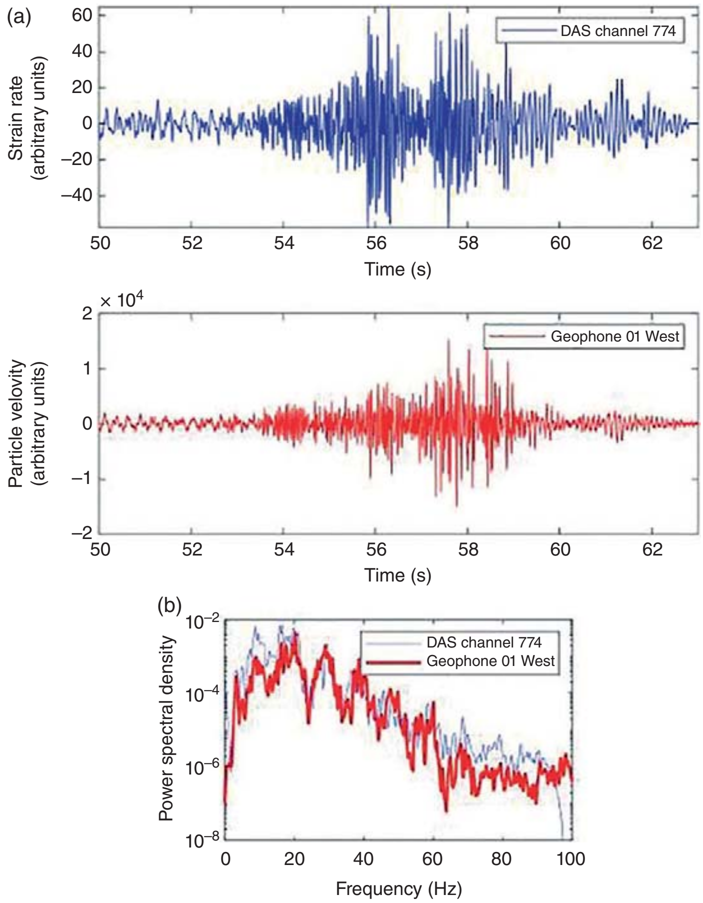

Figure 16.5 (a) Expanded plots of 13 s of data showing passing traffic for a colocated DAS channel 774 (top) and east component of colocated seismometer (bottom). (b) Power spectra for DAS strain and geophone horizontal particle velocity east (each trace normalized by its zero-frequency value).

DAS strain rate was integrated with respect to time to yield strain vs. time. The energy buildup from the large shaker is very gradual at low frequencies and increases rapidly at around 13 s, or a frequency of 4 Hz. Figure 16.4 shows the complete 63 s of record in which the first 30 s are the source upsweep from rest to 10 Hz followed by a downsweep back to rest over the next 30 s with an additional 3 s of listening time. Traffic noise can be seen at about 5 s and again between 53 and 63 s in the DAS and geophone responses (Figure 16.4). The traffic noise response of DAS Channel 774 and geophone G01 between 53 and 63 s and their frequency response are shown in more detail in Figure 16.5. The DAS strain and geophone ground velocity show highly similar ground motion because the ratio of strain ε to particle velocity $\dot{u}$ is the reciprocal of the phase velocity c (i.e., $\varepsilon/\dot{u} = 1/c$) (Daley et al., 2015).

Because the angle between the radial direction of wave propagation from the Mini-Me structure and the diagonal DAS cable line at geophone G01 is about 7°, the true phase velocity differs by only 1% from the apparent phase velocity. The calculated phase velocities are factors of 2–3 slower than any of the surface-wave velocities obtained by MASW described in the following section. The results, however, are based on amplitudes of DAS and geophone signals, which might be sensitive to the details of their coupling to the ground.

Other comparisons can be made between the colocated DAS Channel 774 and geophone G01-East. The background noise level of DAS is greater than that of the geophones. The root mean square (RMS) average of DAS noise between 50 and 53 s is 0.57 cm/s whereas that of the geophone is 0.34 cm/s. Spectra of DAS strain (scaled by apparent velocity) are compared with geophone ground velocity in Figure 16.5 for traffic noise between 50 and 63 s. Power spectra for DAS strain and east horizontal geophone are very similar. The lower sensitivity could be related to the greater directional sensitivity of DAS in the cable direction, which is at a high angle relative to the highway or due to bandwidth limitation of the DAS response. Wavelengths larger than the gauge lengths are needed for DAS to correctly capture the strain rate.

16.6. MULTICHANNEL ANALYSIS OF SURFACE WAVES (MASW)

Much of the energy from seismic sources at the surface goes into Rayleigh waves. Rayleigh waves in geological settings are dispersive because they propagate in a medium with a vertical stiffness distribution (Park et al., 1999). If the formation stiffness increases with depth, then lower frequency waves propagate at higher phase velocities because they penetrate deeper into the formation. The dispersive response of Rayleigh waves in a vertically heterogeneous media can be inverted for the *S*-wave velocity distribution vs. depth. The results of the dispersion analyses are then used to determine the stiffness and dynamic behavior of near-surface formations and to study geological structures.

Both active and passive sources of surface waves are used in geological and geotechnical engineering applications to assess the dynamic properties of the near surface (Foti et al., 2015; Picozzi et al., 2009). The active techniques, which use seismic sources, such as a hammer impact or vibroseis, are SASW (Rix et al., 1991) and MASW (Miller et al., 1999; Park et al., 1999). Passive techniques include refraction microtremor (Louie, 2001) and ambient noise tomography (Lin et al., 2007). In the case of SASW, two sensors capture the phase velocity of a propagating surface wave as a function of frequency by performing a spectral analysis of the captured signals (Rix et al., 1991). In the case of MASW, multiple channels capture the arrival of surface waves.

The two active-source techniques have advantages and disadvantages. The main advantage of SASW is that only two sensors are needed. However, in order to obtain a dispersion curve, many frequencies need to be sampled, and that may require reconfiguring the sensors in the field by changing the separations of both sensors and seismic sources, which can make the process time consuming and labor intensive. Moreover, the SASW method assumes that only fundamental mode surface waves exist in the field (Rix et al., 1991) and therefore other propagation modes may be missed with the use of only two sensors. MASW overcomes some of the disadvantages in SASW. The use of multiple sensors allows for multiple propagation modes to be identified. It also allows for less time in the field between source locations because reconfiguring the sensors is not required (Park et al., 1999). Larger numbers of sensors used in MASW allow for more straightforward identification of propagation modes. Although trenching in fiber-optic cable is labor intensive and the need to contract a DAS interrogator is one of the current barriers, the low cost of cable and the acquisition of data from long lines of DAS channels make it inherently suitable for MASW. A disadvantage of the DAS array response for interpretation of Rayleigh waves is that DAS only senses vibrations in the direction of the cable and it is then prone to potential interference from Love waves.

For a linear array of sensors and a swept-frequency source, MASW requires that the receiver traces be filtered for a range of specific frequencies (Park et al., 1999, 2007). In this study, the phase velocity of individual frequencies was then obtained using a modified version of MASW incorporating moving window cross-correlation (MWCC) (Sun et al., 2009). Two processing steps were performed on the receiver traces. First, a source synchronous filter (SSF) (Lord et al., 2016) was applied to all the receiver traces. The SSF was developed for a swept-frequency source to remove out-of-band noise and unwanted source harmonics. The SSF is a narrow-band filter synchronized with the source frequency, which for the Mini-Me shaker was taken to be an idealized sweep from DC to 10 Hz and back to DC linearly over 60 s. The narrow-band filter had a bandwidth of 2 Hz to account for the time-varying source function and the maximum travel-time delay (less than 1 s) for surface waves propagating across the array. The largest sources of noise removed by the SSF are source harmonics and passing vehicles. The SSF was applied to all receiver signals before further analysis. For the PASSCAL geophones, a pole-zero compensation was applied to remove the 4.5 Hz geophone response, and automatic gain control was applied to reduce amplitude variations in all data.

Following the SSF processing, MWCC was applied to the processed time-domain traces. For MWCC, a small, tapered time window of the source waveform (with its restricted range of frequency) is cross-correlated with a set of receiver signals over a range of distances. The source waveform used in the MWCC technique is the y axis (north-south) component of one of the UCLA accelerometers on top of the Mini-Me structure that has been converted from acceleration to displacement. The source window is filtered to remove high-frequency noise and harmonics using SSF prior to the cross-correlation. One peak of the cross-correlation function is chosen for tracking over a range of receiver distances. The slope of the line is the phase velocity for the frequency of the source within the corresponding small-time window.

16.7. SURFACE-WAVE DISPERSION ANALYSIS RESULTS

The procedure described in the previous section was applied to the long line and crosshatch sections of the cable shown in Figure 16.1. Only the upsweep of the source from 2 to 10 Hz was used to create the dispersion curves, as this allowed the different phases to spread out rather than overtake each other as lower frequencies have higher phase velocities. Below 2 Hz, the energy of the source was too low to obtain a coherent phase, so those frequencies did not contribute to the dispersion curve.

The source time windows used for cross-correlation were 6 s wide, corresponding to a frequency width of 2 Hz. This width was chosen to fully capture the desired frequencies while excluding any frequencies away from the central frequency of interest. The source time windows were spaced every 1.5 s, meaning the frequency shifted by 0.5 Hz between each window. The source time windows were tapered using a Tukey cosine window. The power spectral density of each windowed signal was taken to determine the dominant frequency. These tapered windowed signals were then cross-correlated with the vertical component of the seismometers' and accelerometers' responses, and with the DAS array horizontal response.

The long line is oriented in a radial direction from the large shear shaker. Figure 16.6 compares 30 m of raw DAS data with SSF-filtered data. The time window from 6 to 12 s corresponds to source frequencies from 2 to 4 Hz, which is within the 2 Hz band pass at the receiver because the seismic travel-time is less than 1 s. Note that almost all noise from passing vehicles was removed even when the signal energy was quite low.

Figure 16.7 shows every fifth channel of 30 m of fiber-optic cable along the long line of the DAS array. Frequencies of 2, 4, 6, and 8 Hz are shown and the moveout of each phase is marked by best fit line. The standard deviation of the slope is approximately 20 m/s based on the best fit slope of multiple time of arrival picks made for each frequency. Each of these best fit slopes is plotted in Figure 16.8 to produce the experimental dispersion curve for the DAS array's long line (median and range are presented). The same basic analysis was made using data from GVDA three-component Kinematrics EpiSensor accelerometers GDVA 08 and GDVA 10 colocated along the long line. Vertical components were used. As only two accelerometers were used, the dispersion curve was obtained using SASW interpretation. The SASW method assumes that only fundamental mode surface waves exist in the field (Rix et al., 1991) and therefore other propagation modes may be missed. Lord et al. (2016) show how DAS interpretation of the same data set allows capturing higher modes. The accelerometer dispersion results are plotted in Figure 16.8.

The second section of cable for which a dispersion curve is obtained is aligned with the PASSCAL sensors on the east-trending diagonal, referred to as the crosshatch (Figure 16.1). The same procedure was followed as for the GVDA accelerometers. The radial direction of the crosshatch differs by only 7° from the cable direction at the location of the geophones so that the apparent velocities, which are plotted on the dispersion curves shown in Figure 16.9, differ by only a percent from the true phase velocities and were not corrected. The agreement between PASSCAL geophones and DAS array is not as strong as for the long line, and the velocities are different by up to 200 m/s for low frequencies, though the results do agree within 10 m/s or less for frequencies above 7 Hz. DAS results for the crosshatch segment of cable tend to have lower velocities at lower frequencies in comparison with the geophones. The differences at low frequencies may

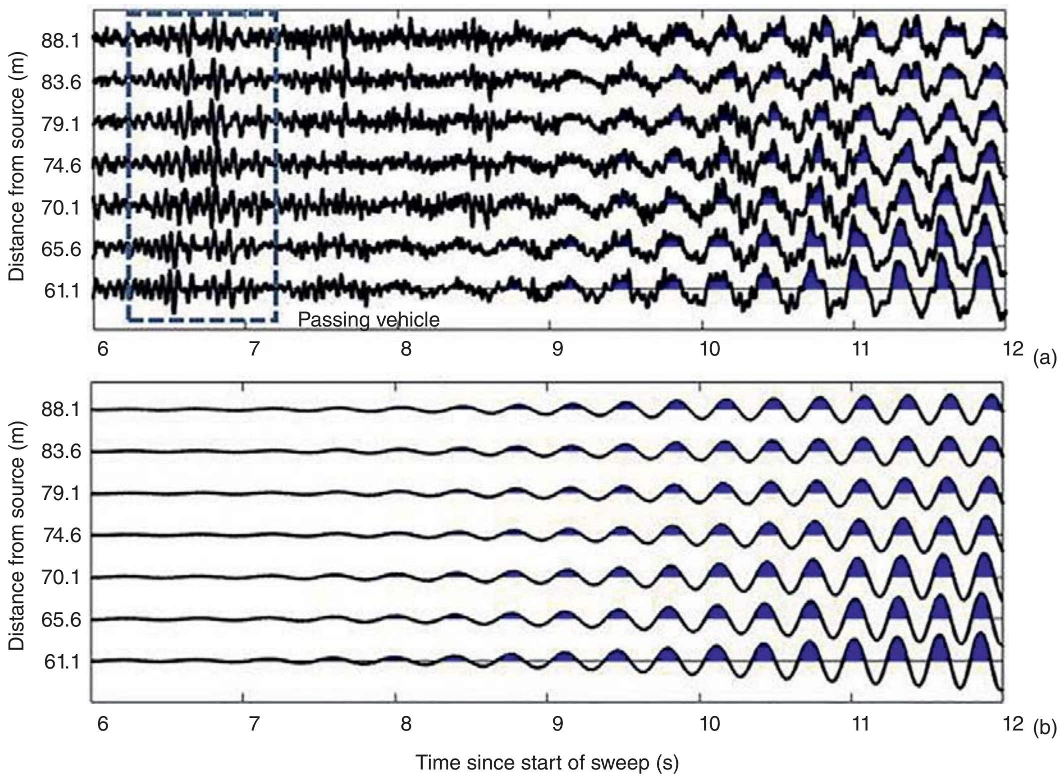

Figure 16.6 (a) Plot of 30 m of unfiltered DAS data. Channels are spaced 5 m apart and distances to the 45 kN source are given. The source was sweeping from 2 to 4 Hz during this time window. A passing vehicle arrival can be seen around 6.5 s. (b) Source synchronous filtered DAS data plotted over the same 30 m and the same time interval. Note that source harmonics and traffic noise are removed.

be due to the possibilities listed previously for the long line. Issues for all of these dispersion curves could arise from misidentification of the arrival time due to interference between waves along the cable.

Figures 16.8 and 16.9 present the dispersion curves as median and range of phase velocity obtained for repeated source excitations. DAS data show similar repeatability as the data collected with accelerometers and geophones, and these data are similar to the ones reported by Lai et al. (2005) for surface-wave analysis performed in Italy. The coefficient of variation in phase velocity determination (and therefore the uncertainty in the inversion analysis) in all cases increases at lower frequencies.

The final step in MASW analysis is to invert the dispersion curves obtained by different sensors for a shear-wave velocity profile. In our study, we used the surface-wave analysis, modeling, and inversion (SWAMI) tool (Lai & Rix, 1998; Rix et al., 2001). The required inputs to SWAMI are the number of layers and their thicknesses, densities, and Poisson's ratios, as well as the frequencies and corresponding velocities from the dispersion curves. The inversion methodology finds the solution with the smoothest profile of shear-wave velocities subject to the constraint of a specified misfit between the experimental and theoretical dispersion curves.

Inversion of DAS dispersion curve results is compared in Figure 16.10 with those from a previous study at the site by Stokoe et al. (2004) for which a large vibroseis truck was used as the source. Results were obtained using the SASW method for two lines: One is the parking lot line and the other is the highway line (Figure 16.1). Only qualitative comparisons were made with the highway line because the parking lot line is across a poorly graded gravel layer, which is inconsistent with the rest of the site and yielded increased variability in Stokoe et al.'s results.

A simple three-layer model was chosen with tops at the surface, 5.5 m, 17 m, and 25 m, below which is the "half space". No layering present in the Stokoe et al.'s profile was incorporated in the top 5.5 m as our highest frequency of 10 Hz and a velocity of approximately 200 m/s means that the half wavelength is 10 m, which is unable to resolve even 5 m. At the low-frequency end, the first usable

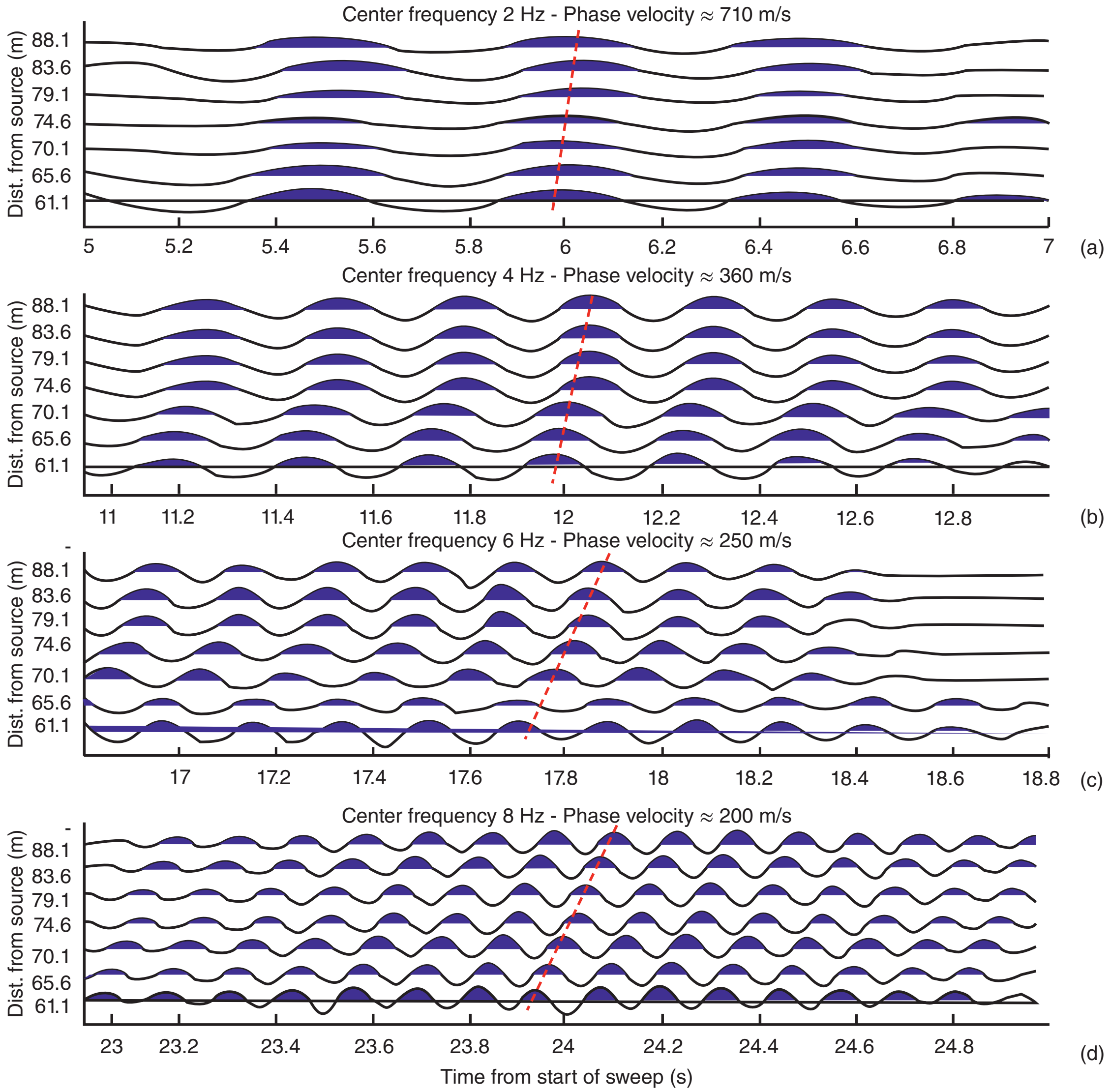

Figure 16.7 Plots (a) through (d) show source synchronous filtered MWCC DAS data at frequencies of 2, 4, 6, and 8 Hz (approximate phase velocities shown in figures). Thirty meters of cable are shown with every fifth channel plotted. Distance from the 45 kN shaker source is shown. The frequencies are based on what the source was outputting at that time assuming a linear sweep (e.g., at 6 s the source frequency was 2 Hz). The dashed line follows the moveout of a phase (the slope of the line gets steeper as the frequency decreases).

frequency was of approximately 4 Hz, which leads to a half wavelength of 75 m for a phase velocity of 600 m/s. The bottom of the model was therefore displayed to a depth of 50 m based on the depth achievable by Stokoe et al.

Several of the frequency-velocity values in the University of California, Santa Barbara (UCSB) accelerometer appeared anomalous around the 5 Hz resonance of the Mini-Me structure and were not included in the inversion. Also, data below 2.6 Hz had to be removed in order to obtain a converging solution. The poor phase velocity results at low frequency are probably related to the small amount of energy from the large shaker before 10 s into the sweep (Figure 16.3b).

The resulting shear-wave velocity profiles for the long line are shown in Figure 16.10 for DAS and two UCSB accelerometers along the long line. Also plotted is the profile obtained by inverting Stokoe et al.'s (2004) theoretical dispersion curve (Figure 16.10a) obtained from a forward model of their inversion of the highway line. This dispersion curve is considerably smoothed from the raw SASW data. Their highway line parallels the DAS long line and is

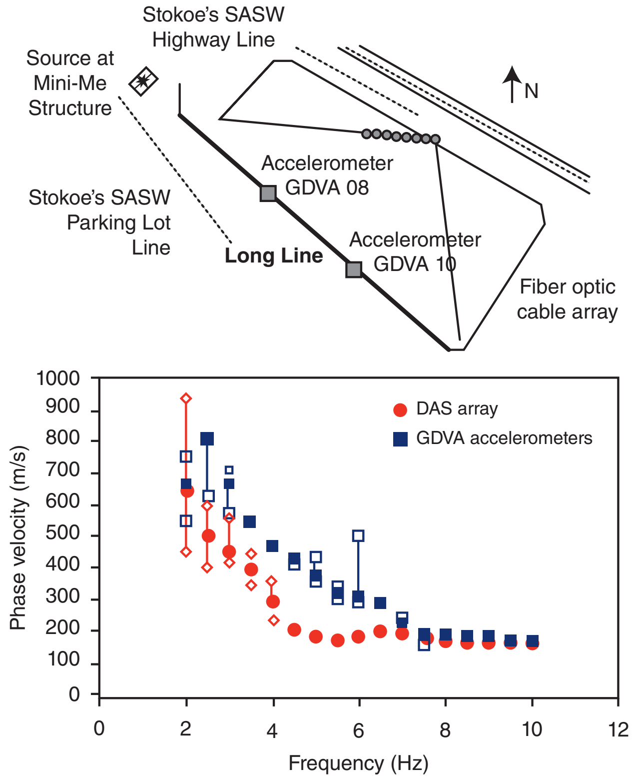

Figure 16.8 Dispersion curve results for the DAS and GVDA accelerometers numbered 8 and 10 along the long line. Filled symbols indicate the median while the open symbols indicate the range of the calculated phase velocities.

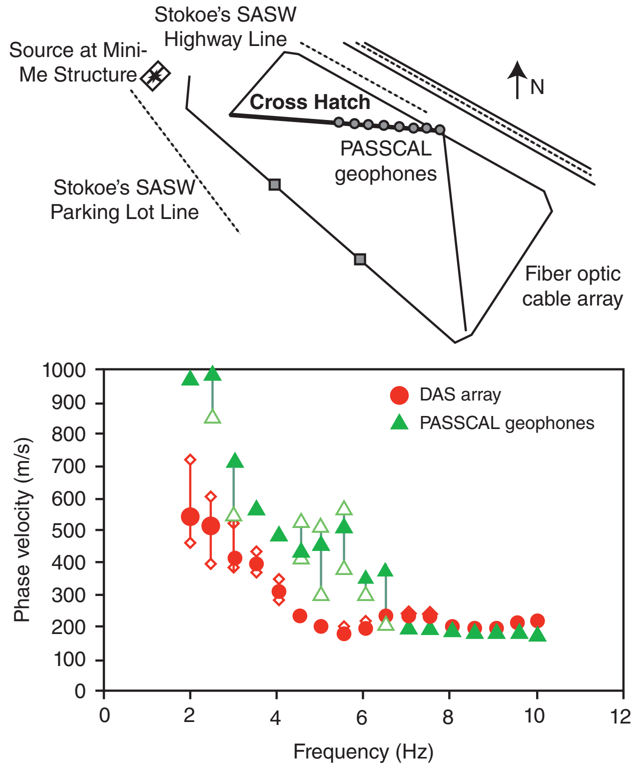

Figure 16.9 Dispersion curve results from the DAS crosshatch line, as well as the PASSCAL geophones along the crosshatch. Filled symbols indicate the median while the open symbols indicate the range of the calculated phase velocities.

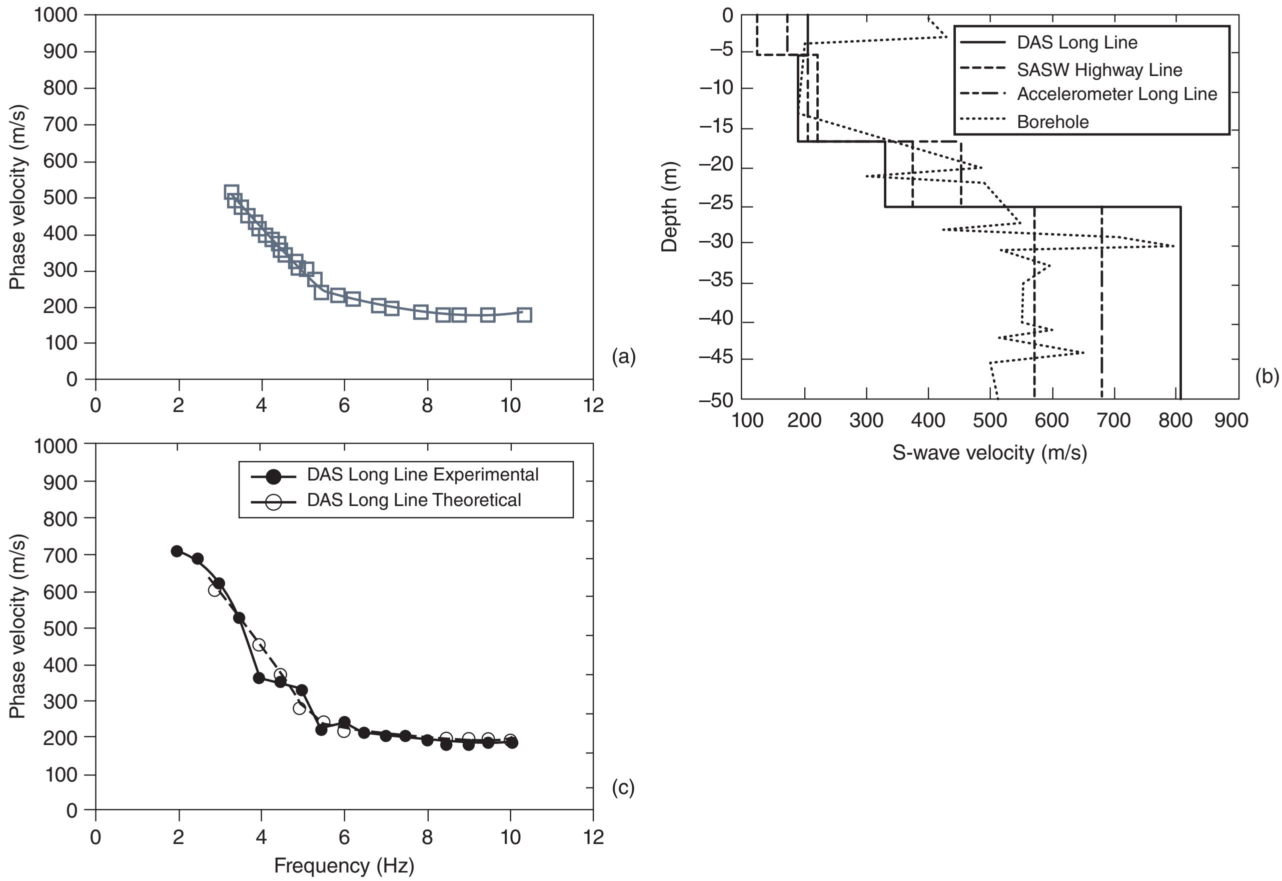

Figure 16.10 (a) Modeled dispersion curve obtained by Stokoe et al. (2004) along the highway line. (b) Shear-wave velocity profile inverted from dispersion curves from the DAS long line, GVDA accelerometers on the long line, Stokoe et al.'s highway line, and borehole geophysical logs from Steller (1996). (c) Comparison of measured and modeled velocity dispersion. Source: (a) Modified from Stokoe et al. (2004). (b) Modified from Steller (1996).

Table 16.1 Parameters Used in SWAMI Inversion.

Top of layer depth [m]	Layer thickness [m]	*P*-wave velocity [m/s]	*S*-wave velocity [m/s]	Poisson's ratio	Density [kg/m^3]
0	5.5	1,524	200	0.40	1,762
5.5	11.5	1,524	300	0.49	1,762
17.0	8.0	1,524	450	0.43	2,002
25.0	Half space	1,524	600	0.41	2,002

likely more similar to their parking lot line. The input layering and layer parameters (Table 16.1) used for all of the SWAMI inversions – DAS long line, two GVDA accelerometers along the long line, and the highway line – were the same except for their dispersion values. These values were based on the layering reported for the inversion results of the SASW highway line from Stokoe et al. (2004).

The shear-wave velocity profile calculated from the DAS long line dispersion curve is compared with that obtained from Stokoe et al.'s highway line in Figure 16.10b. Only velocities for frequencies below 10 Hz were used from the Stokoe et al. theoretical dispersion curve. Results from borehole geophysical logs at the site by Steller (1996) are also plotted in Figure 16.10b for comparison with both inversion results. Figure 16.10c shows the experimental and theoretical dispersion curves for the DAS long line.

For the three-layer plus half-space model, the three velocity profiles range between 125 and 210 m/s in the first layer and between 180 and 270 m/s in the layer between 5.5 and 17 m depth. The velocity profiles then increase to between 350 and 500 m/s in the third layer before reaching values between 560 and 810 m/s in the half-space layer beginning at a depth of 25 m. The shear-velocity profiles all generally increase below 5.5 m depth, but the results for the different data sets vary between 10% and 33%.

16.8. DISCUSSION

The field trial at Garner Valley provided an opportunity to study characteristics of DAS traces of ground motion and to employ them for MASW at a well-characterized site. The deployment of 18 geophones along portions of the DAS layout and the presence of surface accelerometers that were part of the GVDA facility enabled some comparisons between the different sensor types.

DAS records ground motion as strain rate in the direction of the cable. Integrating strain rate with respect to time allows DAS traces to be interpreted as "virtual geophones" based on the plane-wave relationship that is $\varepsilon/\dot{u} = 1/c$, where ε is strain, $\dot{u}$ is particle velocity, and c is phase velocity (Daley et al., 2015). Here it is understood that the strain and particle velocity are in the direction of the cable. The proportionality is shown to hold well based on the similarity of the DAS strain and geophone traces in Figures 16.4 and 16.5. The proportionality constant, however, leads to a particle velocity that is slower than measured, implying that the measured amplitude of the strain is relatively higher than that of the geophones. At face value, the result implies relatively better coupling of DAS, which may be related to the cable being in contact with the alluvium over its 10 m gauge length rather than at a single point in the case of the geophone. More calibrated tests would be needed to test this hypothesis because the results will depend heavily on details of how the sensor is coupled to ground motion.

The strain-rate value obtained at each DAS channel is an average over a 10 m segment of cable. Then the 10 m segment shifts 1 m to represent the next channel. Possible aliasing could arise if the seismic wavelengths were less than 20 m. In our study, wavelengths are generally greater than 20 m, but near 10 Hz, the upper range of our frequencies, the wavelength falls to about 18 m. Also, the gauge length of 10 m means that nearby channels share part of the cable segment over which the strain rate is obtained. Thus, the channels spaced 5 m apart, plotted in Figure 16.7, share 5 m of sampling distance between them. While this could possibly be a concern, clear moveout is seen for the 5 m separation, and clear time differences in the arrivals of phases are seen when every channel spaced 1 m apart is plotted.

Figures 16.8 and 16.9 compare results from lines of the DAS array with the corresponding GVDA accelerometers and PASSCAL geophones, respectively. In all cases, the dispersion relationship between phase velocity and frequency is in general agreement (both for mean and range) and velocity tends to decrease with increasing frequency. When looking at results from the long line in Figure 16.8, the curves match within about 10 m/s for frequencies greater than 7 Hz, but deviation between the DAS and accelerometer curves occurs for frequencies less than 7 Hz. This deviation may be linked to several factors. One possibility is related to the resonance of the structure at about 5 Hz (Star et al., 2015). The structure may be introducing more complex waveforms into the ground at the resonant frequency, which might lead to more surface-wave propagation modes and make it more difficult to interpret the dispersion. The larger number of DAS channels means that the signal was still clearly identifiable from the noise. Having only two accelerometers made this identification more difficult and thus the results may have been more affected by the resonance of the structure. A second possibility for the difference relates to the occurrence of a phase offset between DAS channels. The offset appears to be due to interference between different propagation modes that is most prominent for frequencies between 4 and 6 Hz. Lord et al. (2016) documented the presence of different propagation modes and higher harmonics captured with DAS for the data set presented in this study. When interference occurs, only channels unaffected by the phase offset were used to obtain phase velocity. However, the mode interference may still be causing a perturbation in the velocities near affected frequencies. The denser spatial sampling of DAS allowed a better understanding of the different propagation modes. The 10 m, running spatial average of DAS data means that the traces are low-pass filtered and when combined with using 30 channels can explain its better suppression of noise and being less affected by the structural resonance in comparison with that of the accelerometers. A third possibility for the difference in the dispersion curves relates to differences in sensor orientation. Surface-wave analysis generally uses measurements from vertically oriented seismometer components to avoid interference from Love waves, so that is what was used in this study for the accelerometers and geophones. However, DAS is sensitive to axial strain along the length of the fiber (Mateeva et al., 2014). The fiber-optic cable along the long line will be most sensitive to motion in the radial direction away from the Mini-Me source. Finally, a fourth hypothesis is related to the repeatability of the

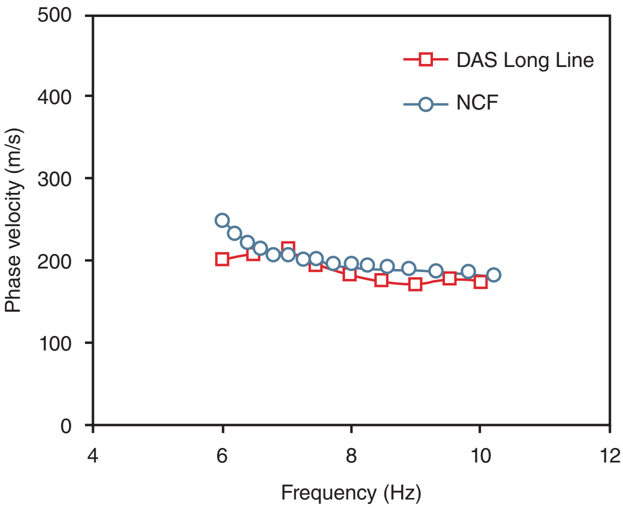

Figure 16.11 Dispersion curves obtained from the DAS long line active source traces and the NCF passive source result. Source: Modified from Zeng et al. (2016).

phase velocity determination. Data presented in this chapter and elsewhere (Lai et al., 2005) show uncertainty increases with decreasing frequencies.

The same DAS array used for active source MASW can be used for an ambient noise source. At the Garner Valley testing site, California Highway 74 runs parallel to the main axis of the DAS array (Figure 16.1). Zeng et al. (2016) used 8 hours of continuous overnight recording from the same DAS array presented in this study to calculate a dispersion curve based on noise cross-correlation functions (NCFs). The prevailing source of noise during the overnight recording was traffic passing on Highway 74. The dominant frequencies from traffic were between 5 and 25 Hz. The NCFs for 1 minute intervals were stacked using phase-weighted stacking to improve the signal. Then MASW was used to calculate a dispersion curve from the NCFs, and the results are plotted along with results from the long line in this study in Figure 16.11. Only the results from frequencies between 6 and 10 Hz were plotted since the frequencies used in the Zeng et al.'s work were from 5 to 25 Hz. The results from the passive overnight recording match within 10 m/s for frequencies greater than 7 Hz with those from the active tests used in this study; thus, DAS was successfully used in both a passive and an active manner to obtain the same results.

16.9. SUMMARY AND CONCLUSIONS

A field test was conducted in September 2013 in Garner Valley, California, where a DAS array and seismometers and accelerometers were deployed. A 45 kN, swept-frequency shear shaker excited the field between 2 and 10 Hz. DAS records the same active source and traffic events as geophones. Traces and power spectra are similar. A single DAS strain-rate trace can be integrated to strain, which is proportional to ground velocity, and thus, the integrated trace is a single-component "virtual geophone" in the direction of the cable.

While the nature of how DAS measures is different than traditional seismic sensors (i.e., directivity, measurement length, and bandwidth), multiple sensors inherent to a DAS array make it very well suited to MASW analysis to obtain surface-wave dispersion curves. The results from DAS agree with those from the traditional seismic sensors for frequencies greater than 7 Hz, as well as results from previous studies at the same site. The DAS results also match within 10 m/s for frequencies between 7 and 10 Hz with results using NCFs from traffic noise using the same array. Differences in results could be attributed to differences in the number of sensors, in the response associated with a hitch in the source output at the resonant frequency of the structure on which the source was located, in sensing orientation of the receivers, or to multimode wave interference.

ACKNOWLEDGMENTS

This project was supported in part by the NSF Grant CMMI-0900663 (Program Director: R. Fragaszy) and by the U.S. Department of Energy (DOE) Geothermal Technologies Office (GTO) Grant DE-EE0006760 (Program Managers: E. Metcalfe and L. Boyd). Ethan Castongia, Rumen Karaulanov, Robert Nigbor, and James Steidl participated in the experiment planning and data collection; their contribution is greatly appreciated.

REFERENCES

Bakku, S. K. (2015). Fracture characterization from seismic measurements in a borehole (Doctoral dissertation). Cambridge, MA: Massachusetts Institute of Technology.

Castongia, E., Wang, H. F., Lord, N., Fratta, D., Mondanos, M., & Chalari, A. (2017). An experimental investigation of distributed acoustic sensing (DAS) on lake ice. *Journal of Environmental and Engineering Geophysics, 22*(2), 167–176.

Correa, J., Egorov, A., Tertyshnikov, K., Bona, A., Pevzner R., Dean, T., et al. (2017). Analysis of signal to noise and directivity characteristics of DAS VSP at near and far offsets—a CO2CRC Otway Project data example. *The Leading Edge, 36*(12), 994a1–994a7.

Costley, R. D., Galan-Comas, G., Kirkendall, C. K., Simms, J. E., Hathaway, K. K., Parker, M. W., et al. (2018). Spectral analysis of surface waves with simultaneous fiber optic distributed acoustic sensing and vertical geophones. *Journal of Environmental and Engineering Geophysics, 23*(2), 183–195. https://doi.org/10.2113/JEEG23.2.183

Daley, T. M., Freifeld, B. M., Ajo-Franklin, J., Dou, S., Pevzner, R., Shulakova, V., et al. (2013). Field testing of fiber-optic distributed acoustic sensing (DAS) for subsurface seismic monitoring. *The Leading Edge, 32*(6), 699–706. https://doi.org/10.1190/tle32060699.1

Daley, T. M., Miller, D. E., Dodds, K., Cook, P., & Freifeld, B. M. (2015). Field testing of modular borehole monitoring with simultaneous distributed acoustic sensing and geophone vertical seismic profiles at Citronelle, Alabama. *Geophysical Prospecting, 64*(5), 1318–1334. https://doi.org/10.1111/1365-2478.12324

Dean, T., Cuny, T., & Hartog, A. H. (2017). The effect of gauge length on axially incident P-waves measured using fibre optic distributed vibration sensing. *Geophysical Prospecting*, *65*(1), 184–193.

Dou, S., Lindsey, N., Wagner, A. M., Daley, T. M., Freifeld, B., Robertson, M., et al. (2017). Distributed acoustic sensing for seismic monitoring of the near surface: A traffic-noise interferometry case study. *Scientific Reports, 7*, 11620. https://doi.org/10.1038/s41598-017-11986-4.

Feigl, K. L., Cardiff, M. A., Zeng, X., Lancelle, C., Reinisch E. C., Lim D., et al. (2016). *H13O-02: Overview and Preliminary Results from the PoroTomo project at Brady Hot Springs, Nevada: Poroelastic tomography by adjoint inverse modeling of data from seismology, geodesy, and hydrology. Paper presented at the AGU Fall Meeting, December 12–16*, 2016, San Francisco, CA.

Foti, S., Lai, C., Rix, G. L., & Strobia, C. (2015). *Surface wave methods for near surface wave characterization*. Boca Raton, FL: CRC Press.

Freifeld, B. M., Pevzner, R., Don, S., Correa, J., Daley, T. M., Robertson, M., et al. (2016). *The CO2CRC Otway Project deployment of a distributed acoustic sensing network coupled with permanent rotary sources*. Paper presented at the 78th EAGE Conference & Exhibition 2016, Vienna, Austria, 30 May–2 June 2016.

Froggatt, M., & Moore, J. (1998). High-spatial-resolution distributed strain measurement in optical fiber with Rayleigh scatter. *Applied Optics, 37*, 1735–1740.

Galan-Comas, G. (2015). Multichannel analysis of surface waves using distributed fiber optic sensors (Master's thesis). Starkville, MS: Mississippi State University.

Givens, M. J. (2013). Dynamic soil-structure interaction of instrumented buildings and test structures (Doctoral dissertation). Los Angeles, CA: University of California–Los Angeles.

Hornman, J. C. (2016). Field trial of seismic recording using distributed acoustic sensing with broadside sensitive fibre-optic cables. *Geophysical Prospecting, 65*(1), 35–46. https://doi.org/10.1111/1365-2478.12358

Ikeda, T., Tsuji, T., Watanabe, T., & Yamaoka, K. (2015). Development of a surface-wave monitoring system for leaked CO_2 using a continuous and controlled seismic source. *International Journal of Greenhouse Gas Control, 45*, 94–105.

Johannessen, K., Drakeley, B., & Farhadiroushan, M. (2012). *Distributed Acoustic Sensing—a new way of listening to your well/reservoir*. Paper presented at the SPE Intelligent Energy International held in Utrecht, The Netherlands, 27–29 March 2012.

Lai, C. G., Foti, S., & Rix, G. J. (2005). Propagation of data uncertainty in surface wave inversion. *Journal of Environmental and Engineering Geophysics*, *10*(2), 219–228.

Lai, C. G., & Rix, G. J. (1998). *Simultaneous inversions of Rayleigh phase velocity and attenuation for near-surface site characterization* (Rep. GITCEE/GEO-98-2). Atlanta, GA: School of Civil and Environmental Engineering, *Georgia Institute of Technology.*

Lin, F. C., Ritzwoller, M., Townend, J., Bannister, S., & Savage, M. (2007). Ambient noise Rayleigh wave tomography of New Zealand. *Geophysical Journal International, 170*, 649–666.

Lord, N., Wang, H. F., & Fratta, D. (2016). A source-synchronous filter for uncorrelated receiver traces from a swept-frequency seismic source. *Geophysics*, *81*(5), P47–P55. https://doi.org/10.1190/geo2015-0324.1

Louie, J. N. (2001). Faster, better: Shear-wave velocity to 100 meters depth from refraction microtremor arrays. *Bulletin of the Seismological Society of America, 91*(2), 347–364.

Madsen, K. N., Dümmong, S., Kritski, A., Pedersen, Å. S., Finfer, D., Gillies, A., & Travis, P. (2013). *Simultaneous multiwell VSP in the North Sea using distributed acoustic sensing*. Paper presented at the 75th EAGE Conference & Exhibition incorporating SPE EUROPEC 2013, London, UK, 10–13 June 2013.

Martin, E. R., Lindsey, N., Ajo-Franklin, J., & Biondi, B. (2018, June 14). *Introduction to interferometry of fiber optic strain measurements*. https://doi.org/10.31223/osf.io/s2tjd (preprint).

Mateeva, A., Lopez, J., Potters, H., Mestayer, J., Cox, B., Kiyashchenko, D., et al. (2014). Distributed acoustic sensing for reservoir monitoring with vertical seismic profiling. *Geophysical Prospecting, 62*, 679–692, https://doi.org/0.1111/1365-2478.12116

Mellors, R. J., Pitarka, A., Kuhn, M., Stinson, B., Ford, S. R., Snelson, C., & Drachenberg, D. (2014). Fiber optic acoustic sensing (FOAS) far-field observations of SPE 3. *Seismological Research Letters*, 85(2), 450 (abstract).

Miller, D., Parker, T., Kashikar, S., Todorov, M., & Bostick, T. (2012). *Vertical seismic profiling using a fibre-optic cable as a distributed acoustic sensor*. Paper presented at the 74th EAGE Conference & Exhibition incorporating SPE EUROPEC 2012, Copenhagen, Denmark, 4–7 June 2012.

Miller, R. D., Xia, J., Park, C. B., & Ivanov, J. M. (1999). Multichannel analysis of surface waves to map bedrock. *The Leading Edge*, *18*(12), 1392–1396.

nees@UCSB (2008). *GVDA Instrumentation guide*. URL: https://nees.org/data/get/facility/UCSB/Equipment/77/GVDAGuide.pdf [Accessed on November 27, 2016].

Park, C. B., Miller, R. B., & Xia, J. (1999). Multichannel analysis of surface waves. *Geophysics*, *64*(3), 800–808.

Park, C. B., Miller, R. B., Xia, J., & Ivanov, J. (2007). Multichannel analysis of surface waves (MASW)—active and passive methods. *The Leading Edge*, *26*(1), 60–64.

Parker, T., Shatalin, S. V., & Farhadiroushan, M. (2014). Distributed acoustic sensing—a new tool for seismic applications. *First Break, 32*, 61–69.

Picozzi, M., Parolai, S., Bindi, D., & Strollo, A. (2009). Characterization of shallow geology by high-frequency seismic noise tomography. *Geophysical Journal International, 176*, 164–174. https://doi.org/10.1111/j.1365-246X.2008.03966.x

Rix, G., Stokoe, K. H., & Roesset, J. M. (1991). *Experimental study of factors affecting the spectral-analysis-of-surface-waves method* (Rep. 1123-5). Austin, TX: Center for Transportation Research, The University of Texas at Austin. Retrieved from: http://library.ctr.utexas.edu/digitized/texasarchive/phase2/1123-5.pdf

Rix, G., Lai, C. G., Orozco, M. C., Hebeler, G. L., & Roma, V. (2001). *Recent advances in surface wave methods for geotechnical site characterization*. Paper presented at the XV International Conference on Soil Mechanics and Geotechnical Engineering, Istanbul, 27–31 August 2001.

Star, L. M., Givens, M. J., Nigbor, R. L., & Stewart, J. P. (2015). Field-testing of structure on shallow foundation to evaluate soil-structure interaction effects. *Earthquake Spectra*, *31*(4), 2511–2534.

Steidl, J., Gee, R., Seale, S., & Hegarty, P. (2012). *Recent enhancements to the NEES@UCSB permanently instrumented field sites*. Paper presented at the 15th World Conference of Earthquake Engineering. Lisbon, Portugal.

Steller, R. (1996). *New borehole geophysical results at GVDA. Data Report*. Retrieved from: http://nees.ucsb.edu/sites/eot-dev.nees.ucsb.edu/files/facilities/docs/GVDA-Geotech-Stellar1996.pdf

Stokoe, K. H., Kurtulus, A., & Menq, F.-Y. (2004). Data report: SASW measurements at the NEES Garner Valley test site, California, 13 January 2004. Retrieved from: http://nees.ucsb.edu/sites/eot-dev.nees.ucsb.edu/files/facilities/docs/GarnerValley-SASWreport.pdf

Sun, L. F., Milkereit, B., & Schmitt, D. R. (2009). Measuring velocity dispersion and attenuation in the exploration seismic frequency band. *Geophysics, 74*(2), 113–122.

Tyler, S. W., Selker, J. S., Hausner, M. B., Hatch, C. E., Torgersen, T., & Schladow, S. (2009). Environmental temperature sensing using Raman Spectra DTS fiber-optic methods. *Water Resources Research, 4*(187), 673–679.

Yavuz, S., Freifeld, B. M., Pevzner, R., Tertyshnikov, K., Dzunic, A., Ziramov, S., et al. (2016). *Kinmetrics EPI ES-T buried DAS and geophone arrays: Preliminary results from CO2CRC Otway project*. Paper presented at the 78th EAGE Conference & Exhibition 2016, Vienna, Austria, 30 May–2 June 2016.

Youd, T. L., Bartholomew, H. A. J., & Proctor, J. S. (2004). *Geotechnical logs and data from permanently instrumented field sites: Garner Valley Downhole Array (GVDA) and Wildlife Liquefaction Array (WLA)*, Data Report. Retrieved from: http://nees.ucsb.edu/sites/eot-dev.nees.ucsb.edu/files/facilities/docs/geotech-data-report.pdf

Youd, T. L, Steidl, J., & Nigbor, N. (2004). Ground motion, pore water pressure and SFSI monitoring at NEES permanently instrumented field sites. Retrieved from: https://www.researchgate.net/publication/251804811_Ground_Motion_Pore_Water_Pressure_and_SFSI_Monitoring_at_NEES_Permanently_Instrumented_ Field_Sites

Zeng, X., Lancelle, C., Thurber, C., Fratta, D., Wang, H. F., Lord, N., et al. (2016). Properties of noise cross-correlation functions obtained from a distributed acoustic sensing array at Garner Valley, California. *Bulletin of the Seismological Society of America*. https://doi.org/10.1785/0120160168

17

A Literature Review: Distributed Acoustic Sensing (DAS) Geophysical Applications Over the Past 20 Years

Yingping Li[1], Martin Karrenbach[2], and Jonathan B. Ajo-Franklin[3,4]

ABSTRACT

We briefly review the history of distributed acoustic sensing (DAS) as applied to geophysical problems over the past 20 years, including a bibliography of about 900+ DAS-related papers and abstracts. First, we introduce some general reviews and introductory papers on DAS to provide readers with an overview of DAS technologies and their various applications. Second, we discuss geophysical applications of fiber Bragg grating (FBG) based DAS systems. We describe 10 major geophysical applications of DAS technologies based on Rayleigh backscattering systems in Part 3 of this chapter. We then share some of the open problems and promising areas of research in the hope of promoting future development of DAS as a geophysical tool.

17.1. INTRODUCTION

DAS is one of the families of distributed fiber-optic sensing techniques, which utilizes fiber-optical cables to measure acoustic signals. DAS systems are optoelectronic devices that measure small vibrations, typically through quantification of strain or strain rate, along a length of fiber-optic cable with a laser light source and a receiver [together referred to as an interrogator unit (IU)]. These measurements typically have a fine spatial resolution and a wide bandwidth, which are two attributes that make DAS an appealing tool for geophysics. Rayleigh backscattering (Hartog & Gold, 1984; Healey, 1985) based DAS systems (Juskaitis et al., 1994; Shatalin et al., 1998) use the entire fiber-optic cables to provide distributed strain or strain-rate sensing. In a fiber Bragg grating (FBG) technique (Hill et al., 1978), "sensors" are crafted onto a small segment of the fiber core to sense vibrations in a "discrete" manner. When multiple FBG sensors are made along a very long optical fiber, the discrete FOS enables distributed FOS measurements. Therefore, "discrete acoustic sensing" by FBG can be viewed as qDAS.

Geophysical applications of FBG-based qDAS were reported at the beginning of this century (Bostick, 2000; Kersey, 2000). Rayleigh backscattering based DAS systems were first applied by the oil and gas industry to borehole measurements (e.g., Allanic, 2012; Barberan et al., 2012; Cox et al., 2012; Johannessen et al., 2012; Koelman, 2011; Li Q. et al., 2013; Madsen et al., 2012; Mateeva et al., 2012; Mestayer et al., 2011; Miller et al., 2012; Molenaar, Hill, & Koelman, 2011; Molenaar, Hill, et al., 2011; Parker et al., 2012; Webster,

[1]*BlueSkyDas (formerly Shell), Houston, Texas, USA*

[2]*OptaSense Inc. (A LUNA Company), Brea, California, USA*

[3]*Department of Earth, Environmental and Planetary Sciences, Rice University, Houston, Texas, USA*

[4]*Energy Geosciences Division, Lawrence Berkeley National Laboratory, Berkeley, California, USA*

Distributed Acoustic Sensing in Geophysics: Methods and Applications, Geophysical Monograph 268, First Edition.
Edited by Yingping Li, Martin Karrenbach, and Jonathan B. Ajo-Franklin.

DOI:10.1002/9781119521808.ch17

Cox, et al., 2013) and were then rapidly adopted by the broader geophysical community (e.g., Ajo-Franklin et al., 2015; Becker et al., 2016a; Biondi et al., 2017; Daley et al., 2013; Dou et al., 2016; Jousset et al., 2016; Lindsey, Martin, et al., 2017; Lord et al., 2016; Martin et al., 2015; Reinsch et al., 2015; Wang H. et al., 2014). Advantages of qDAS technologies with the FBG method mainly include three-component (3C) "sensors" and less depth uncertainties of qDAS-VSP measurements. However, crafting many discrete "sensors" with a small sensor spacing (a few meters) over a long fiber cable (up to a few tens to hundreds of kilometers) is a great technical challenge. It is very expensive to build, install, and maintain such FBG-qDAS systems. In contrast, DAS technologies based on Rayleigh backscattering use the entire fiber up to tens to hundreds of kilometers as "sensors" to record acoustic signals. Major disadvantages of DAS technologies involve "single" component, amplitude directivity, and depth uncertainties of channels ("sensors") for DAS-VSP surveys, etc. However, utilizing existing or abandoned communication fiber cables with little cost is one of the major factors for the rapid development of DAS geophysical applications.

As DAS technologies advance, a large volume of successful geophysical DAS applications have been reported and published throughout various geophysical and seismological journals, abstracts, and proceedings of technical conferences, including the AGU (American Geophysical Union), SEG (Society of Exploration Geophysicists), EAGE (European Association of Geophysicists and Engineers), and SSA (Seismological Society of America). Figure 17.1 compares the number of papers published related to DAS and qDAS (FBG) applications in geophysics over the past 20 years. These geophysical DAS publications have dramatically increased in the last 10 years due to the apparent advantages of the technology. Since 2011, the number of geophysical DAS publications quickly increased, slowed down in 2015, then rapidly picked up since 2016 and reached a high plateau in 2018. Geophysical applications of DAS are currently pursued in both industry and academia. AGU, EAGE, and SEG have hosted many DAS-related workshops since 2014. For example, Figure 17.2 summarizes statistical results of the SEG DAS workshops from 2014 to 2020. These results show the dramatically increasing interest in DAS technologies among geophysicists, seismologists, and engineers, as well as with increasing contributions to the SEG DAS workshops from academia and DAS service sectors since 2017.

At the 2017 AGU Fall Meeting, scientists and engineers from both industry and academia gathered in New Orleans to share their research outcomes on DAS technologies and applications in geophysics and seismology. They believed that effective communication between experts in both industry and academia could significantly advance DAS technologies. In the oil and gas industry, DAS systems are widely installed in boreholes to monitor microseismicity during hydraulic fracturing stages (Farhadiroushan et al., 2017; Kahn et al., 2017; and Kavousi Ghahfarokhi, Carr, & Mellors, 2017). Modeling and processing methods to detect and locate microseismic events with DAS data were quickly developed (Mellors et al., 2017; Mizuno et al., 2017; and Williams A. et al., 2017). Parallel to industrial DAS monitoring of microseismicity and hydraulic fracturing, DAS observation systems are used for earthquake seismology at local and regional scales (Ajo-Franklin, Lindsey, et al., 2017; Karrenbach, Cole, et al., 2017; and Martin, Biondi, Karrenbach, et al., 2017). A 2.4 km campus DAS array (Martin, Biondi, Karrenbach, et al., 2017), a 20 km "dark fiber" array (Ajo-Franklin, Lindsey, et al., 2017), and a 320 km pipeline DAS array (Karrenbach, Cole, et al., 2017) all recorded the 2017 M8.1 and M7.2 Mexico great earthquakes. These DAS arrays were also extensively used to study both local earthquakes and teleseismic events. DAS systems were also used to observe vertical strain at the San Andreas Fault Observatory at Depth (Ellsworth et al., 2017) and to monitor deformation of a seafloor fault in Europe (Gutscher et al., 2017). These

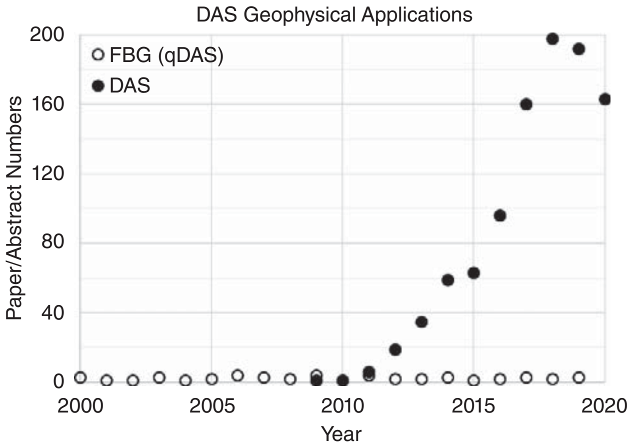

Figure 17.1 Trend of collected journal and conference papers/abstracts related to DAS and FBG-based qDAS over the last 20 years. Geophysical DAS publications have been quickly increasing since 2011, with a slowdown in 2015 when a major oil/gas industry downturn occurred. Since 2016, the number of publications has more rapidly picked up and reached a high plateau in 2018. Statistics include data for only nine months of 2020.

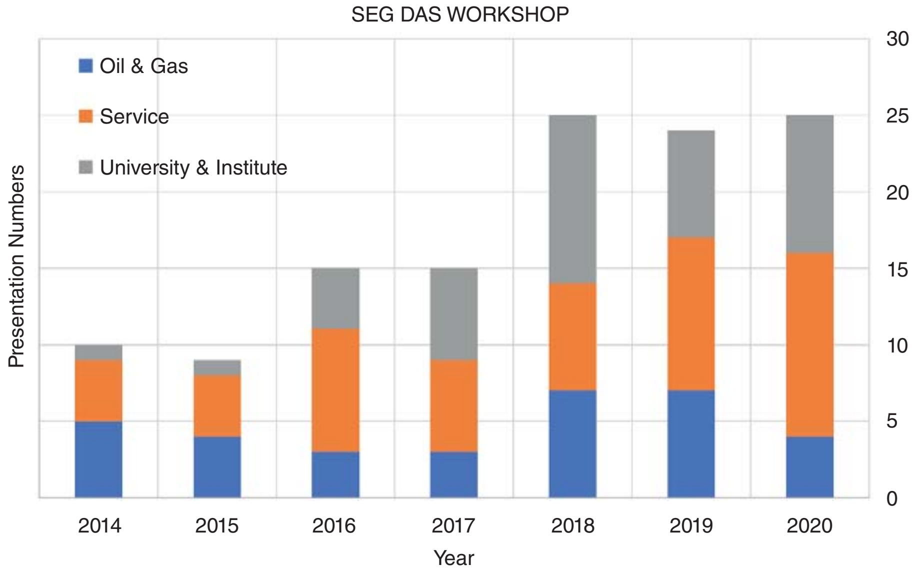

Figure 17.2 Histogram of papers presented at the SEG DAS workshops since 2014. Contributions from academia and service sectors have been dramatically increasing since 2017.

examples demonstrate that the broadband nature of DAS systems may monitor extremely low frequency strain and its variations.

DAS technologies are now also utilized in mining, geothermal energy industries (Cronin et al., 2017; Feigl et al., 2017; Nesladek et al., 2017; Thurber et al., 2017; Wang et al., 2017; Zeng, Thurber, Wang, Fratta, & PoroTomo Team, 2017), in shallow geophysical monitoring of carbon dioxide (CO_2) injection (Freifeld et al., 2017), in examining the mechanical response of fractured bedrock aquifers (Ciervo et al., 2017), and in the imaging of shallow surface structures with ambient noise interferometry and tomography (Ajo-Franklin, Lindsey, et al., 2017; Ciocca et al., 2017; Martin, Biondi, Yuan, et al., 2017; Paitz & Fichtner, 2017; Zeng, Thurber, Wang, Fratta, & PoroTomo Team, 2017). Since DAS can measure ground motion at thousands of locations at high data rates (exceeding 10 s of TBs/day), “big data” challenges are generated by the resulting data sets. Recent research has explored approaches to effectively optimize and manage storage systems (Dou, Wood, et al., 2017), as well as innovating data compression and retrieval techniques (Muir & Zhan, 2017). With the rapid advance of DAS technologies and applications, many attendees of the DAS sessions in the 2017 AGU Fall Meeting expressed that there is a need for a book on DAS geophysical applications. With support from the AGU Publication Committee and AGU Book, as well as contributions from DAS experts, this AGU DAS monograph was initiated and will be published.

Many of the chapters of the DAS book are derived from presentations at the 2017 AGU Fall Meeting in New Orleans. This DAS monograph covers the DAS principle and applications in industries (oil, gas, geothermal, and mining), in earthquake seismology, and in environmental and near-surface geophysics. However, some aspects of wider DAS geophysical applications are not covered and some new advances on the DAS geophysical applications since 2018 are not included either in this book. To overcome such a shortcoming of this monograph, we have collected 900+ published papers and abstracts related to DAS geophysical applications to provide readers with useful materials for further study of DAS technologies as related to geophysics. This chapter, rather than being considered a review, should be viewed as an extended historical bibliography attempting to capture relevant papers in the field as of the 2019–2020 time frames.

Tables 17.1.1 and 17.1.2 list 19 review articles and 23 introductory papers for readers to obtain an overview of DAS technologies and various applications. The advantage of the DAS technology has enabled rapid adoption across a range of applications, including geophysics, geotechnical engineering (railroad, tunnel, and bridge monitoring), hazard mitigation and prevention, and safety and security fields. Readers may refer to review papers and introductory papers in Table 17.1.1 for DAS applications in geophysics (Cannon & Aminzadeh, 2013; Hartog, 2017; Miah & Potter, 2017), geohydrology (Schenato, 2017), environmental monitoring (Joe et al., 2018; Shanafield et al., 2018), and civil engineering (Barrias et al., 2016).

In Section 17.2, we briefly review the history of geophysical applications of FBG-based qDAS systems in the last 20 years with 49 papers listed in Table 17.2.

In Section 17.3, we introduce various DAS geophysical applications using the Rayleigh backscattering based DAS systems (with a few exceptions) in Tables 17.3–17.12.

Table 17.3: DAS Principle, Instrument, Installation, Tests, and Advance
Table 17.4: DAS-VSP (Borehole Seismic) Applications
Table 17.5: DAS in Downhole Surveillance and Flow Monitoring
Table 17.6: DAS in Monitoring Hydraulic Fracturing and Microseismicity
Table 17.7: DAS in Carbon Capture and Storage (CCS) and CO_2 Injection Monitoring
Table 17.8: DAS in Surface Seismic Exploration
Table 17.9: DAS in Geothermal System, Mining, and Mineral Exploration
Table 17.10: DAS in Monitoring Safety and Security

Table 17.1 Review and Introduction for DAS Applications.

17.1.1 *Review* – 19
Johannessen et al. (2012[2]), Distributed Acoustic Sensing: Listening to Your Well/Reservoir;
Cannon & Aminzadeh (2013), Distributed Acoustic Sensing: State of the Art;
Palmieri & Schenato (2013), FOS-Rayleigh Scattering;
Zhang, J. et al. (2013[2]), Pipeline Leak Detection;
Warpinski (2014[2]), Fracture Induced Microseismicity;
Baldwin (2015), Upstream Oil and Gas Industry;
Barrias et al. (2016), Civil Engineering;
Jaroszewicz et al. (2016), Fibre-Optic Rotational Seismometers;
Masoudi & Newson (2016), Distributed Optical Fibre Dynamic Strain Sensing;
Allwood et al. (2017[2]), Fiber Bragg Grating Sensors;
Hartog (2017), DAS Introduction Book;
Miah & Potter (2017), DAS/DTS Sensors & Geophysical Applications;
Schenato (2017), Geo-Hydrological Applications;
Tejedor et al. (2017[3]), Machine Learning for Pipeline Surveillance;
Hveding & Bukhamsin (2018), Upstream Oil and Gas Applications;
Joe et al. (2018), Environmental Monitoring;
Shanafield et al. (2018), Environmental Monitoring for Water Resources;
Sheydayev et al. (2018), Downhole Surveillance History;
Soroush et al. (2019); Wellbore Monitoring
17.1.2 *Introduction* – 23
Denney (2012[2]);
Elesztos & Dookhee (2013); Eriksrud & Kringlebotn (2013); Forster & Dria (2013);
Jacobs (2014); Kamal (2014); Rassenfoss (2014);
Carpenter (2015); Gardner et al. (2015); Li M. et al. (2015);
Carpenter (2016a, 2016b); Webster (2016);
Carpenter (2017a, 2017b, 2017c); Willis, Ajo-Franklin, et al. (2017);
Carpenter (2018[2]);
Carpenter (2019); Egan (2019); Rassenfoss (2019); Zhan et al. (2019)
Alcantara Santos (2020)

Note. Papers with superscripts discuss more than one topic or appear in several different tables.

Table 17.2 FBG-Based qDAS Applications in Geophysics.

FBG optical sensing – 49
Hill et al. (1978);
Udd et al. (1998);
Bostick (2000); Kersey (2000); Udd et al. (2000);
Kragas et al. (2001);
Kragas et al. (2002);
Bostick et al. (2003); Hornby et al. (2003); Knudsen et al. (2003);
MacDougall & Sanders (2004);
Hornby et al. (2005); Keul et al. (2005);
Blanco et al. (2006); Hornby et al. (2006); Knudsen et al. (2006); Thompson et al. (2006);
Hornby, Barkved, Askim, et al. (2007); Hornby, Barkved, Williams, et al. (2007); Thompson et al. (2007);
Hornby & Burch (2008); Langhammer et al. (2008);
Eriksrud et al. (2009); Langhammer et al. (2009a, 2009b); Morton et al. (2009);
Eriksrud (2010);
Gaston & Bostick (2011); Lescanne et al. (2011); Nakstad et al. (2011); Wu H. et al. (2011);
Gaston & Bostick (2012); Hornby et al. (2012);
Eriksrud & Kringlebton (2013); Prinet et al. (2013);
Bostick & Travis (2014); Paulsson et al. (2014); Rassenfoss (2014);
Paulsson et al. (2015);
Paulsson et al. (2016); Singer et al. (2016);
Allwood et al. (2017[2]); Paulsson (2017); Staveley et al. (2017[2]);
Alfataierge et al. (2018[2]); Krietsch et al. (2018[2]);
Alfataierge et al. (2019a[2], 2019b[2]); Paulsson et al. (2019)

Note. Papers with superscripts discuss more than one topic or appear in several different tables.

Table 17.11: DAS for Seismology, Fault, and Deformation
Table 17.12: DAS Data Exchange, Management, Processing, and Deep Learning

In Section 17.4, we will discuss the most recent DAS developments since 2018 and focus on their significances for future DAS advances and some DAS missions from impossible to become possible. We conclude this review chapter in Section 17.5, followed by acknowledgments and an extensive reference list.

In Tables 17.1–17.12, we include 900+ papers and abstracts on DAS geophysical applications. We aim to build "a library catalog" for as much DAS literature as possible to satisfy the individual needs for so many different readers in such a diverse field within general geophysics. Some readers may feel that the references are too much to read and digest. The tables for different DAS geophysical applications are designed to partially solve such a problem to effectively and efficiently read the literature. Readers who are interested in a general knowledge of DAS geophysical applications may select a few review or introductory papers (e.g., Allwood et al., 2017; Cannon & Aminzadeh, 2013; Hartog, 2017; and Johannessen et al., 2012) in Table 17.1 to obtain an overview of DAS technologies and associated applications. For readers who are interested in a particular field, such as DAS-VSP, we would like to recommend them to check Table 17.4 and to read the earliest three to four papers for original ideas and the initial application. Then, they may read three to four most recent papers listed in the table to follow the most recent developments and to trace back literature in the table for more details. We anticipate that readers can use this simple approach to quickly familiarize themselves with DAS references in a particular field.

17.2. FBG-BASED QDAS GEOPHYSICAL APPLICATIONS

The first geophysical (borehole seismic) application of a discrete FOS system (qDAS) in the oil and gas industry was reported by Bostick (2000) and Kersey (2000). Bostick (2000) successfully conducted a field test with an FBG-based FOS system (Hill et al., 1978), which was installed in a 433 ft test well in Texas, the United States of America (USA), to record seismic signals generated by weight-drop sources and drilling bit noise and to compare the recorded seismic signals with those recorded by a 3C geophone. Multiaxis FBG technique (Udd et al., 1998, 2000) enables this FOS system with

Table 17.3 DAS Principle, Instrument, Installation, Tests, and Advance.

Principle, instrument systems, installation, advance, and tests – 134
Hartog & Gold (1984);
Healey (1985);
Juskaitis et al. (1994);
Shatalin et al. (1998);
Tanimola & Hill (2009[2]);
Mullens et al. (2010[2]);
Koelman (2011[2]); Mestayer et al. (2011[4]); Molenaar, Hill, & Koelman (2011[2]);
Barberan et al. (2012[4]); Madsen et al. (2012[3]); Mateeva et al. (2012[4]); Miller et al. (2012[3]); Parker T. et al. (2012[2]);
Barfoot (2013[2]); Bateman et al. (2013[2]); Cheng L. et al. (2013); Daley et al. (2013[5]); Hartog et al. (2013); Hill (2013); Li Q. et al. (2013[3]); Mateeva, Mestayer, Cox, et al.(2013[3]); Parker T. et al. (2013[3]);
Daley, White, et al. (2014[3]); Drakeley et al. (2014[2]); Mateeva, Lopez, Potters, et al. (2014[4]); Papp et al. (2014); Parker T. (2014); Parker, Gillies, et al. (2014); Parker, Shatalin, et al. (2014[3]); Poletto, Corubolo, et al. (2014);
Blount et al. (2015); Dean, Constantinou, et al. (2015[2]); Dean, Papp, et al. (2015); Didraga (2015); Hill (2015); Li Y. Wu, et al. (2015[2]); Longton (2015[2]); Loranger et al. (2015);
Constantinou (2016); Constantinou, Schmitt, et al. (2016); Constantinou, Farahani, et al. (2016); Dean, Brice, et al. (2016[2]); Dean, Hartog, et al. (2016); Ellmauthaler, Willis, Wu, et al. (2016); Farhadiroushan (2016[2]); Gabai & Eyal (2016a, 2016b); Hartog et al. (2016); Lim Chen Ning & Sava (2016[2]); Madsen et al. (2016[2]); Miller et al. (2016[4]); Molteni, Hopperstad, et al. (2016); Morshed & El-Sayed (2016); Nishiguchi (2016); Schilke et al. (2016); Servette & Lamour (2016); Willis, Ellmauthaler, et al. (2016[3]); Wu X. et al. (2016[2]);
Bernard et al. (2017); Bona et al. (2017[2]); Constantinou et al. (2017); Correa, Dean, et al. (2017[3]); Correa, Van Zaanen, et al. (2017[2]); De Jong et al. (2017[2]); Ellmauthaler et al. (2017); Eyal et al. (2017); Farhadiroushan et al. (2017[2]); Gabai & Eyal (2017); Hartog (2017); Henninges et al. (2017); Higginson et al. (2017); Hornby (2017); Lim Chen Ning & Sava (2017[2]); Liu et al. (2017); Miah & Potter (2017); Munn et al. (2017); Nöther (2017); Papp et al. (2017); Podgornova et al. (2017); Reinsch et al. (2017); Schilke et al. (2017); Wu X. et al. (2017[2]); Zaanen et al. (2017[2]);
Chalari (2018); Coleman (2018); Farhadiroushan (2018a); Ferla et al. (2018[4]); Hartog, Liokumovich, et al. (2018); Hartog, Belal, et al. (2018); Karrenbach (2018a); Lim Chen Ning & Sava (2018a[2], 2018b[2]); Mellors (2018); Mellors, Sherman, Messerly, et al. (2018); Mellors, Yu, Mart, et al. (2018); Miah (2018); Miah & Ha (2018); Nakatsukasa et al. (2018a, 2018b, 2018c); Naruse et al. (2018); Pevzner, Bona, et al. (2018); Thomas et al. (2018[2]); Wang C. (2018); Willis, Ellmauthaler, et al. (2018); Willis et al. (2018a, 2018b);
Bostick et al. (2019); Correa (2019); Dean & Nguyen (2019); Dean et al. (2019); Ellmauthaler (2019); Farhadiroushan (2019); Farhadiroushan et al. (2019b[2]); Hill (2019); Karrenbach, Cole, Minto, et al. (2019); Pevzner et al. (2019[3]); Sherman (2019); Vera et al. (2019a, 2019b); Wang Y. et al. (2019); Williams M., Cuny, et al (2019); Willis et al. (2019[3]);
Aldawood et al. (2020[3]); Clement et al. (2020); Ellmauthaler, LeBlanc, et al. (2020); Ellmauthaler, Maida, et al. (2020); He et al. (2020); Karrenbach & Laing (2020); Naldrett, Parker, et al. (2020); Naldrett, Soulas, et al. (2020); Pevzner et al. (2020[3]); Stork et al. (2020[3]); Tertyshnikov & Pevzner (2020); Zeng et al. (2020)

Note. Papers with superscripts discussed more than one topic and appear in several tables.

3C accelerometers to obtain reliable measurements of the vector seismic wavefield. Endurable features of fiber under high pressure and high temperature in a downhole harsh environment allow the FOS system to measure seismic waves, pressure, temperature, and flow simultaneously with the same fiber cable in a cost-effective manner (Bostick, 2000; Kersey, 2000; Kragas et al., 2001, 2002; MacDougall & Sanders, 2004).

3C FOS systems were quickly installed in onshore wells in the USA to test installation methods (Hornby et al., 2003, 2005) of the passive seismic mandrel and the active seismic clamp for recording offset vertical seismic profiling (OVSP) and walkaway VSP (WVSP). In France, FOS systems were installed to run time-lapse WVSP surveys with six sets of FOS 3C accelerometers for time-lapse subsurface seismic images (Blanco et al., 2006; Bostick et al., 2003; Keul et al., 2005; Knudsen et al., 2003) and to test the FOS system performance tube-conveyed into a well with flow-induced noise (Knudsen et al., 2006).

After successful tests in onshore wells, FOS systems were immediately installed in offshore wells to test their performance in a deepwater environment. Five sets of the FOS 3C accelerometers were first installed in an offshore production well at Valhall in the North Sea in 2006 for active time-lapse VSP surveys and passive microseismic monitoring (Hornby et al., 2006). A high-resolution three-dimensional (3-D) VSP image of

Table 17.4 DAS-VSP (Borehole Seismic) Applications.

17.4.1 *DAS-VSP Trails, Comparison, Calibration, and Validation* – 62

Mestayer et al. (2011[4]);
Barberan et al. (2012[4]); Koelman et al. (2012a[2]); Madsen et al. (2012[3]); Mateeva et al. (2012[4]); Mestayer et al. (2012[2]); Miller et al. (2012[3]);
Daley et al. (2013[5]); Kiyashchenko et al. (2013[3]); Li Q. et al. (2013[3]); Madsen, Dümmong, Parker, et al. (2013)[2]; Madsen, Dümmong, Kritski, et al. (2013)[2]; Madsen, Thompson, et al. (2013[2]); Mateeva, Lopez, Mestayer, et al. (2013[2]); Parker T. et al. (2013[3]);
Daley, Miller, et al., 2014[2]; Daley, White, et al., 2014[3]; Cocker et al. (2014[2]); Hornby et al. (2014); Mateeva, Lopez, Hornman, et al. (2014[2]); Mateeva, Lopez, Potters, et al. (2014[4]); Parker Shatalin, et al. (2014[3]); Poletto, Clarke, et al. (2014[2]);
Dean, Hartog, et al. (2015); Longton et al. (2015[2]); Verliac et al. (2015[2]);
Borland et al. (2016[3]); Daley, Freifeld, et al. (2016[4]); Daley, Miller, et al. (2016[2]); Dean, Cuny, Constantinou, et al., (2016); Dean, Hartog, et al. (2016); Ellmauthaler, Willis, Barfoot, et al. (2016); Kimura et al. (2016[3]); Madsen et al. (2016[2]); Miller et al. (2016[4]); Willis, Ellmauthaler, et al. (2016[3]); Willis, Erdemir, et al. (2016[2]);
Correa, Dean, et al. (2017[3]); Correa, Egorov, et al. (2017[2]); Correa, Van Zaanen, et al. (2017[2]); Mateeva & Zwartjes (2017); Nesladek et al. (2017[3]); Olofsson & Martinez (2017[2]); Zaanen et al. (2017[2]);
Alfataierge et al. (2018[2]); Dean et al. (2018); Duan et al. (2018); Ferla et al. (2018[4]); Gordon et al. (2018); Hall et al. (2018[3]); Percher & Valishin (2018[3]); Pevner, Tertshnikv & Bona (2018); Pevner, Tertshnikv, Bona, Correa, et al. (2018); Riedel et al. (2018a[3], 2018b[3]); Spackman & Lawton (2018);
Alfataierge et al. (2019a[2]); Hall et al. (2019[3]); Tertyshnikov & Pevzner (2019);
Aldawood et al. (2020[3]); Martinez A. et al. (2020[2]); Stork et al. (2020[3])

17.4.2 *DAS-VSP Measurement and Imaging* – 116

Mestayer et al. (2011[4]);
Allanic (2012[2]); Barberan et al. (2012[4]); Koelman et al. (2012b[2]); Lopez et al. (2012); Madsen et al. (2012[3]); Mateeva et al. (2012[4]); Mestayer et al. (2012[2]); Miller et al. (2012[3]);
Al Adawi et al. (2013); Kiyashchenko et al. (2013[3]); Li Q. et al. (2013[3]); Madsen, Dümmong, Parker, et al. (2013)[2]; Madsen, Dümmong, Kritski, et al. (2013)[2]; Madsen, Thompson, et al. (2013[2]); Mateeva, Lopez, Mestayer, et al. (2013[2]); Mateeva, Mestayer, Cox, et al.(2013[3]); Mateeva, Mestayer, Yang, et al. (2013);
Al-Hinai et al. (2014); Bakku, Wills, Fehler, Mestayer, et al. (2014); Lesnikov & Allanic (2014); Madsen et al. (2014); Mateeva, Lopez, Detomo, et al. (2014); Mateeva, Lopez, Hornman, et al. (2014[2]); Mateeva, Lopez, Potters, et al. (2014[4]); Wu H. et al. (2014);
Alabri (2015); Bettinelli & Puech (2015); Götz et al. (2015[3]); Li Y., Chang, et al. (2015); Li Y. Wu, et al. (2015[2]); Longton (2015); Lopez, Wills, et al. (2015); Nizkous et al. (2015); Verliac et al. (2015[2]); Wong et al. (2015); Wu H. et al. (2015); Zhan et al. (2015); Zwartjes & Mateeva (2015a, 2015b);
Borland et al. (2016[3]); Dean, Clark, et al. (2016); Gerritsen et al. (2016a, 2016b); Hance et al. (2016); Jiang et al. (2016); Kimura et al. (2016[3]); Koller et al. (2016); Leclercq et al. (2016); Miller et al. (2016[4]); Tatanova et al. (2016[2]); Teff et al. (2016[3]); Willis, Ellmauthaler, et al. (2016[3]); Willis, Erdemir, et al. (2016[2]); Wu X. et al. (2016[2]); Yu G., Chen, et al. (2016[2]); Yu G. et al. (2016a[3], 2016b[2]); Zhan et al. (2016);
Abdul Rahim, Ghazali, et al. (2017); Abdul Rahim, Hardy, et al. (2017); Ball et al. (2017); Clarke et al. (2017); Correa, Dean, et al. (2017[3]); Dean & Correa (2017); Lopez et al. (2017); Muhammed et al. (2017[2]); Pevzner, Urosevic, Popik, Shulakova, et al. (2017[4]); Pevzner, Urosevic, Popik, Tertyshnikov, et al. (2017[4]); Pevzner, Urosevic, Tertyshnikov, et al. (2017[4]); Tatanova et al. (2017[2]); Wu J. et al. (2017); Wu X. et al. (2017[2]);
Abdul Rahim et al. (2018); Aldawood et al. (2018); Chen, Hu, et al. (2018); Chen, Yu, et al. (2018); Dy et al. (2018); Ferla et al. (2018[4]); Ghazali et al. (2018); Gordon & Lawton (2018); Götz et al. (2018[3]); Li Y. et al. (2018); Lim Chen Ning & Sava (2018c); Lopez et al. (2018); Riedel et al. (2018a[3], 2018b[3]); Saxton et al. (2018); Trainor-Guitton, Guitton, et al. (2018[2]); Willis, Wu, et al. (2018); Zhou, Cheng, & Barrios (2018); Zhou, Cheng, Zhao, Barrios, Palacios, & George Knapo (2018); Zhou, Cheng, Zhao, Barrios, Palacios, & Knapo (2018);
Cai et al. (2019); Chavarria et al. (2019[2]); Ferla et al. (2019[2]); Ghazali et al. (2019); Hall et al. (2019[3]); Li Y. et al. (2019); Lim Chen Ning & Sava (2019); Lim Chen Ning et al. (2019); Mad Zahir et al. (2019); Muhammed et al. (2019); Shultz & Simmons (2019); Sidenko et al. (2019[2]); Tertyshnikov, Pevzner, Freifeld, Ricard, Gillies, et al. (2019[2]); Yu G. et al. (2019); Wang X. et al. (2019);
Aldawood et al. (2020[3]); An et al. (2020); Booth et al. (2020); Chavarria et al. (2020); Pierre & Le Calvez (2020); Yu, G., Chen, et al. (2020); Yu, G., Xiong, et al. (2020)

(*Continued*)

Table 17.4 (*Continued*)

17.4.3 *Time-Lapse DAS-VSP* – 55
Mateeva et al. (2012[4]);
Kiyashchenko et al. (2013[3]); Mateeva, Mestayer, Cox, et al.(2013[3]);
Hill (2014);
Lopez, Przybysz-Jarnut, et al. (2015); Mateeva et al. (2015); Zwaan et al. (2015[2]);
Chalenski et al. (2016); Daley, Freifeld, et al. (2016[4]); Effiom (2016); Harris et al. (2016[2]); Mateeva et al. (2016); Tatanova et al. (2016[2]); Teff et al. (2016[3]);
Chalenski, Hatchell, et al. (2017); Chalenski, Wang, et al. (2017); Grandi et al. (2017); Mateeva et al. (2017); Meek et al. (2017[2]); Oropeza Bacci, Halladay, O'Brien, Anderson, et al. (2017[2]); Oropeza Bacci, O'Brien, et al. (2017[2]); Pevzner, Urosevic, Popik, Shulakova, et al. (2017[4]); Pevzner, Urosevic, Popik, Tertyshnikov, et al. (2017[4]); Pevzner, Urosevic, Tertyshnikov, et al. (2017[4]); Wang K. et al. (2017); White et al. (2017[2]); Zwartjes et al. (2017);
Binder (2018[2]); Byerley, Monk, Aaron, et al. (2018[2]); Byerley, Monk, Yates, et al. (2018[2]); Carpenter (2018[2]); Chalenski, Hatchell, et al. (2018); Chalenski, Lopez, et al. (2018); Charara et al. (2018[2]); Chavarria (2018a[2], 2018b[2]); Cheraghi et al. (2018[2]); Egorov et al. (2018); Hall et al. (2018[3]); Halladay, A., Orpeza Bacci, et al. (2018[2]); Harris & White (2018[2]); Mateeva et al. (2018); Meek et al. (2018[2]); Zwartjes et al. (2018);
Chavarria et al. (2019[2]); Grindei et al. (2019[2]); Kiyashchenko et al. (2019); Langton et al. (2019[2]); Mateeva (2019); Pevzner et al. (2019[3]); Tertyshnikov, Pevzner, Freifeld, Ricard, & Avijegon (2019[2]); Wang K. et al. (2019); White et al. (2019[2]); Zhou et al. (2019[2]);
Pevzner et al. (2020[3])
17.4.4 *DAS-Geophone Hybrid Tool and Coiled Tubing Conveyed DAS* – 28
Frignet & Hartog (2014); Hartog, Frignet, Mackie, & Allard (2014); Hartog, Frignet, Mackie, & Clark (2014); Hartog et al. (2014);
Dean, Constantinou, et al. (2015[2]); Götz et al. (2015[3]);
Borland et al. (2016[3]); Kimura et al. (2016[3]); Yu G., Chen, et al. (2016[2]); Yu G. et al. (2016a[3], 2016b[2]);
Kimura & Galybin (2017); Kimura et al. (2017);
Ferla et al. (2018[4]); Götz et al. (2018[3]); Haldorsen & Hilton (2018); Haldorsen et al. (2018a, 2018b); Kimura et al. (2018); Percher & Valishin (2018[3]);
Ellmauthaler et al. (2019); Ferla et al. (2019[2]); Leaney et al. (2019); Martuganova et al. (2019[2]); Valishin (2019a); Willis et al. (2019[3]);
Ellmauthaler, Willis et al. (2020); Martinez A. et al. (2020[2])

Note. Papers with superscripts discussed more than one topic and appear in several tables.

subsurface structures was obtained to complement the surface seismic image (Hornby, Barkved, Askim, et al., 2007; Hornby, Barkved, Williams, et al., 2007). In mid-2006, 12 levels of FOS system with 10 vertical components and two sets of 3C accelerometers with spacings of 75 ft were installed in a production well at the Mars site in the deepwater Gulf of Mexico (GOM). Simultaneously, ocean-bottom node (OBN)-VSP surveys were carried out in 2007 and 2010. Finally, the 3-D (Hornby & Burch, 2008) and four-dimensional (4-D) VSP high-resolution images of subsurface structures were delivered (Hornby et al., 2012; Wu et al., 2011).

The FBG-based FOS systems with 3C seismic sensors were also laid out on the ocean bottom (rather than in downhole wells) in the subsea environments to acquire surface seismic data (Eriksrud et al., 2009; Eriksrud, 2010; Langhammer et al., 2008, 2009a, 2009b; Morton et al., 2009; Nakstad et al., 2011; Singer et al., 2016; and Thompson et al., 2006, 2007). The FOS systems with 3C seismic sensors installed in wells were used to monitor induced microseismicity generated by fracturing (Bostick & Travis, 2014; Gaston & Bostick, 2011, 2012) and were applied to both geothermal fields (Paulsson et al., 2014, 2015, 2016; Rassenfoss, 2014) and for carbon capture and storage (CCS) projects (Gaston & Bostick, 2012; Lescanne et al., 2011; Prinet et al., 2013).

Although building an FBG-based qDAS system in a long fiber represents a great technical challenge with cost concerns, there is a continuous effort to develop such systems with up to a few hundred 3C seismic sensors because of its capacity to record vector seismic wavefields (Paulsson et al., 2017, 2019). FBG-based qDAS

Table 17.5 DAS in Downhole Surveillance and Flow Monitoring.

Subsurface surveillance and flow monitoring – 174
Koelman (2011[2]);
Allanic (2012[2]); Denney (2012[2]); Johannessen et al. (2012[2]); Koelman et al. (2012a[2], 2012b[2]); Parker T. et al. (2012[2]);
Allanic et al. (2013); Bateman et al. (2013[2]); Cannon & Aminzadeh (2013[3]); Van Der Horst, Den Boer, et al. (2013); Van Der Horst, Lopez, et al. (2013); Xiao et al. (2013);
Ansari et al. (2014); Bukhamsin & Horne (2014); Danardatu et al. (2014); Drakeley et al. (2014[2]); Finfer et al. (2014); Holley et al. (2014); In't Panhuis et al. (2014); Martinez, Hill, et al. (2014); Martinez, Chen, et al. (2014); Sookprasong et al. (2014); Sookprasong et al. (2014a, 2014b); Ugueto et al. (2014); Van Der Horst et al. (2014); Wheaton et al. (2014); Xiao et al. (2014); Zett et al. (2014);
Baihly et al. (2015); Boone et al. (2015); Carpenter (2015); Chen K. et al. (2015); Finfer et al. (2015); Fitzel et al. (2015); Gonzalez et al. (2015a, 2015b); Holley & Kalia (2015); Hveding & Porturas (2015); Paleja et al. (2015); Richards et al. (2015[2]); Sanghvi et al. (2015); Spain et al. (2015); Ugueto et al. (2015); Van Der Horst (2015); Van Der Horst et al. (2015); Wheaton et al. (2015); Williams T. et al. (2015); Xiao et al. (2015);
Al Shoaibi et al. (2016); Anifowoshe et al. (2016); Baciu et al. (2016); Boone (2016); Bukhamsin & Horne (2016); Carpenter (2016a, 2016b); Chen K. et al. (2016); Dickenson et al. (2016); Evans et al. (2016); Gohari et al. (2016); Hemink et al. (2016); Irvine-Fortescue et al. (2016); Lee et al. (2016); MacPhail et al. (2016); Ramurthy et al. (2016); Sahdev & Cook (2016); Shirdel et al. (2016); Somanchi et al. (2016); Stokely (2016); Thiruvenkatanathan et al. (2016); Ugueto et al. (2016); Van Der Horst (2016); Wheaton et al. (2016); Wu K. et al. (2016); Wu Q. et al. (2016a, 2016b);
Becker, Coleman et al. (2017); Berry et al. (2017); Carpenter (2017b, c); Fidaner (2017); Ghazali et al. (2017); Huckabee et al. (2017); Karrenbach, Kahn, et al. (2017); Kavousi Ghahfarokhi, Carr, & Mellors (2017); Khalifeh et al. (2017); Muhammed et al. (2017[2]); Pakhotina et al. (2017); Sadigov et al. (2017); Shen Y. et al. (2017); Shirdel et al. (2017); Somanchi et al. (2017); Tatanova et al. (2017[2]); Willis, Zhao, et al. (2017); Wu C. et al. (2017); Wu Q. et al. (2017);
Becker (2018); Gustavo et al. (2018); Hemink & Van Der Horst (2018); Hveding & Bukhamsin (2018); Karrenbach (2018b); Kavousi Ghahfarokhi, Carr, Bhattacharya, et al. (2018); Kavousi Ghahfarokhi, Carr, Song, et al. (2018); Naldrett et al. (2018); Park T. et al. (2018[2]); Parkhonyuk et al. (2018[2]); Rachapudi et al. (2018); Rawahi et al. (2018); Sanni et al. (2018); Sherman et al. (2018); Sheydayev et al. (2018); Shuvalov (2018); Somanchi et al. (2018); Titov (2018); Titov et al. (2018); Ugueto et al. (2018); Yi et al. (2018);
Alrashed et al. (2019); Attia et al. (2019); Baker (2019); Banack et al. (2019); Bazyrov et al. (2019); Berlang (2019); Cerrahoglu et al. (2019); Cramer et al. (2019); Feo et al. (2019); Garofoli et al. (2019); Ghazali et al. (2019); Gorham et al. (2019); Ichikawa et al. (2019); Jin (2019); Jin et al. (2019); Kortukov & Williams (2019); Li L. et al. (2019); Mad Zahir et al. (2019); Mali et al. (2019); Mondal et al. (2019); Raab et al. (2019); Sarmah et al. (2019); Sau et al. (2019); Seabrook (2019); Shirdel et al. (2019); Soroush et al. (2019); Stark et al. (2019); Temizel et al. (2019); Titov (2019); Trombin et al. (2019); Trumble et al. (2019); Ugueto, Huckabee, et al. (2019); Ugueto, Todea, et al. (2019); Yi et al. (2019); Wu Q. et al. (2019);
Borodin & Segal (2020); Cramer et al. (2020); Davies et al. (2020); Feder (2020); Franquet (2020); Holley et al. (2020); Hveding (2020); Kruiver et al. (2020); Liang et al. (2020); Mast et al. (2020); McCarthy et al. (2020); Miklashevskiy et al. (2020); Pakhotina et al. (2020); Pellegrini (2020); Shako et al. (2020); Squires et al. (2020); Stark et al. (2020); Titov et al. (2020); Ugueto et al. (2020); Zhang S. et al. (2020); Wu Y. et al. (2020)

Note. Papers with superscripts discussed more than one topic and appear in several tables.

instruments are still used and compared with DAS equipment based on Rayleigh backscattering (Alfataierge et al., 2018, Alfataierge, Dyaur, Li, et al., 2019; Alfataierge, Dyaur, & Stewart, 2019; Staveley et al., 2017) and Brillouin (Krietsch et al., 2018) backscattering. Readers interested in the FBG-based distributed FOS systems and applications may refer to review papers by Eriksrud and Kringlebotn (2013) for applications in the oil and gas fields, and to that by Allwood et al. (2017) for general wider applications. Table 17.2 lists 49 selected pieces of literature on qDAS geophysical applications based on the FBG technology.

17.3. VARIOUS DAS GEOPHYSICAL APPLICATIONS

17.3.1. DAS Principle, Instrument, Installation, Tests, and Advances

Table 17.3 includes 134 papers and abstracts on the principles and instrumentation of Rayleigh backscattering based DAS systems (Hartog et al., 2013; Hill, 2013; Juskaitis et al., 1994; Mateeva et al., 2012; Parker T. et al., 2013; Shatalin et al., 1998), various early DAS tests in fields (Barberan et al., 2012; Koelman, 2011; Madsen

Table 17.6 DAS in Monitoring Hydraulic Fracturing and Microseismicity.

Hydraulic fracturing and microseismicity – 121
Molenaar, Hill, & Koelman (2011[2]); Molenaar, Hill, et al. (2011);
MacPhail et al. (2012); Molenaar, Fidan, et al. (2012); Molenaar, Hill, et al. (2012);
Cannon & Aminzadeh (2013[3]); Grandi et al. (2013); Lowe et al. (2013); Molenaar & Cox (2013); Webster, Cox, et al. (2013); Webster, Wall, et al. (2013);
Bakku, Wills, & Fehler (2014); Cox et al. (2014); Fonseca (2014); Warpinski (2014[2]); Warpinski et al. (2014); Webster et al. (2014);
Cadwallader et al. (2015); Zwaan et al. (2015[2]);
Becker et al. (2016b); Bhatnagar (2016); Cole & Karrenbach (2016); Farhadiroushan (2016); Molteni, Williams, et al. (2016); Teff et al. (2016[3]); Webster et al. (2016);
Ay et al. (2017); Azad et al. (2017); Becker, Ciervo et al. (2017); Carr et al. (2017); Ciervo et al. (2017); Cole et al. (2017); Farhadiroushan et al. (2017); Haustveit et al. (2017); Hull et al. (2017); James et al. (2017[2]); Jin & Roy (2017); Kahn & Fish (2017); Kahn et al. (2017); Karrenbach, Ridge, et al. (2017); Karrenbach, Kahn, et al. (2017[2]); Kavousi Ghahfarokhi, Carr, Wilson, et al. (2017); Meek et al. (2017[2]); Mellors et al. (2017); Mizuno et al. (2017); Molteni et al. (2017); Raterman et al. (2017); Scott et al. (2017); Sherman et al. (2017); Starr (2017); Starr & Jacobi (2017); Wilks, M., Wuestefeld, Thomas, et al. (2017[2]); Wilks, M., Wuestefeld, Oye, et al. (2017[2]); Williams A. et al. (2017); Zhou R. & Willis (2017); Zhou R. et al. (2017);
Binder (2018[2]); Binder et al. (2018); Binder et al. (2018a, 2018b); Byerley, Monk, Aaron, et al. (2018[2]); Byerley, Monk, Yates et al. (2018[2]); Chavarria (2018a[2]); Cole, Karrenbach, Kahn et al. (2018); Drew & Schaeffer (2018); Eaid & Innanen (2018); Eaid et al. (2018); Eisner & Stanek (2018); Farhadiroushan (2018b, c); Heigl et al. (2018); Karrenbach, Kahn, Cole, & Langton, et al. (2018); Karrenbach, Kahn, Cole, Langton, Boone, et al. (2018); Kavousi Ghahfarokhi, Wilson, Carr, et al. (2018); Meek et al. (2018[2]); Mizuno et al. (2018); Raterman et al. (2018); Sahdev et al. (2018); Shurunov et al. (2018); Staněk et al. (2018); Tamayo et al. (2018); Wilks & Wuestefeld (2018); Zhou R.& Pei (2018);
Baird et al. (2019); Binder & Chakraborty (2019); Binder et al. (2019[2]); Carr et al. (2019); Diller & Richter (2019); Farhadiroushan et al. (2019a, 2019b); Heigl et al. (2019); Horne et al. (2019); Hull et al. (2019); Jayaram et al. (2019); Karrenbach (2019b); Karrenbach & Cole (2019); Karrenbach, Cole, Ridge, et al. (2019); Kavousi Ghahfarokhi et al. (2019); Langton et al. (2019[2]); Lellouch, Biondi, et al. (2019); Lellouch, Horne, et al. (2019); Meek et al. (2019); Mellors, Sherman, et al. (2019[2]); Mizuno et al. (2019); Rassenfoss (2019[2]); Raterman et al. (2019); Richter et al. (2019a, 2019b); Sullivan et al. (2019); Titov et al. (2019); Williams, M. J., Le Calvez, et al. (2019); Wilson & Verkhovtseva (2019); Wuestefeld & Wilks (2019); Zhou R. et al. (2019[2]);
Baird (2020); Baird et al. (2020); Haustveit et al. (2020); Lellouch et al. (2020); Li X. et al. (2020); Verdon et al. (2020); Williams A. et al. (2020)

Note. Papers with superscripts discussed more than one topic and appear in several tables.

et al., 2012; Mestayer et al., 2011; Miller et al., 2012; Molenaar, Hill, & Koelman, 2011; Parker et al., 2012), installation methods (Bateman et al., 2013; Bostick et al., 2019; Coleman, 2018; Didraga, 2015; Ellmauthaler et al., 2019; Ellmauthaler, Willis, et al., 2020; Mateeva, Mestayer, Cox, et al., 2013; Willis et al., 2019), discussion on directivity and modes of DAS (Constantinou et al., 2017; Mateeva et al., 2012; Mateeva, Mestayer, Cox, et al., 2013; Mateeva, Lopez, Potters, et al., 2014; Papp et al., 2014; Willis, Ellmauthaler, et al., 2018; Willis et al., 2018a; Wu X. et al., 2016, 2017), recent development and improvement of DAS observation systems (Dean, Clark, et al., 2016; Ellmauthaler, LeBlanc, et al., 2020; Farhadiroushan et al., 2017, 2019; He et al., 2020; Karrenbach & Laing, 2020), etc.

17.3.2. DAS Applications in VSP (Borehole Seismic)

DAS technology was first applied to borehole seismic measurements in the context of VSP about 10 years ago because of three important attributes: (1) Fiber performs well under harsh high-temperature and high-pressure conditions in boreholes; (2) DAS, distributed temperature sensing (DTS), and distributed pressure sensing (DPS) can make measurements with the same downhole fiber cable to significantly reduce costs; and (3) DAS-VSP saves significant costs related to rig downtime in comparison with conventional geophone-VSP acquisition operations. The term *DAS-VSP* here and hereinafter is used to distinguish from conventional VSP surveys, typically acquired using lockable 3C geophones. Mestayer et al. (2011) reported two DAS-VSP downhole trials in a carbon capture and sequestration (CCS) site in September 2010 and in a tight gas field in October to November 2010, with both zero-offset VSP (ZVSP) and WVSP sources. These two DAS experiments focused on comparing DAS measurements to classical sensors, as well as DAS signal-to-noise ratio (SNR). They also compared the resulting subsurface images from the DAS-VSP data with those from WVSP geophone-VSP data to calibrate and validate the DAS method.

Since then, many such DAS-VSP field trials have been conducted on land and marine facilities, including

Table 17.7 *DAS in CCS and CO_2 Injection Monitoring*.

CCS and CO_2 monitoring – 62
Mestayer et al. (2011[4]);
Barberan et al. (2012[3]); Cox et al. (2012);
Daley et al. (2013[5]);
Cocker et al. (2014[2]); Daley, Miller, et al. (2014[2]); Daley, White, et al., (2014[3]);
Bettinelli & Frignet (2015[2]); Götz et al. (2015[3]); Humphries et al. (2015); Longton et al. (2015[2]);
Daley, Freifeld, et al. (2016[4]); Daley, Miller, et al. (2016[2]); Dou et al. (2016); Freifeld et al. (2016); Harris et al. (2016[2]); Humphries et al. (2016); Miller et al. (2016[4]); Yavuz et al. (2016[2]);
Correa, Egorov, et al. (2017[3]); Correa, Freifeld, et al. (2017[2]); Daley et al. (2017[2]); Freifeld et al. (2017); Olofsson & Martinez (2017[2]); Oropeza Bacci, Halladay, O'Brien, Anderson, et al. (2017[2]); Oropeza Bacci, Halladay, O'Brien, Henderson, et al. (2017); Oropeza Bacci, O'Brien, et al. (2017[2]); Pevzner, Urosevic, Popik, Shulakova, et al. (2017[4]); Pevzner, Urosevic, Popik, Tertyshnikov, et al. (2017[4]); Pevzner, Urosevic, Tertyshnikov, et al. (2017[4]); White et al. (2017[2]); Wilks, M., Wuestefeld, Thomas, et al. (2017[2]); Wilks, M., Wuestefeld, Oye, et al. (2017[2]);
Charara et al. (2018[2]); Chavarria (2018b[2]); Cheraghi et al. (2018[2]); Correa, Freifeld, et al. (2018); Correa, Pevzner, et al. (2018); Götz et al. (2018[3]); Halladay, O'Brien, et al. (2018); Halladay, Orpeza Bacci, et al.(2018[2]); Harris & White (2018[2]); Kelley (2018); Kelley et al. (2018); Lawton, Hall, et al. (2018); Lawton, Saeedfar, et al. (2018); Nakatsukasa et al. (2018a, 2018b, 2018c); Thomas et al. (2018[2]);
Grindei et al. (2019[2]); Pevzner et al. (2019[3]); Rodriguez-Tribaldos (2019a); Sidenko et al. (2019[2]); Tertyshnikov, Pevzner, Freifeld, Ricard, & Avijegon (2019[2]); Tertyshnikov, Pevzner, Freifeld, Ricard, Gillies, et al. (2019[2]); White et al. (2019[2]); Wuestefeld (2019); Zhang et al. (2019);
Ringstad et al. (2020[2]); Kobayashi et al. (2020); Pevzner et al. (2020[3])

Note. Papers with superscripts discussed more than one topic and appear in several tables.

Table 17.8 DAS in Surface Seismic Exploration.

17.8.1 *Surface Seismic Survey, Calibration, and Analysis* – 39
Daley et al. (2013[5]); Hornman & Forgues (2013); Parker T. et al. (2013[3]);
Baldwin et al. (2014[3]); Kendall (2014a, 2014b); Lancelle et al. (2014[3]); Mateeva, Lopez, Potters, et al. (2014[4]); Parker, Shatalin, et al. (2014[3]); Poletto, Clarke, et al. (2014[2]); Wang H. et al. (2014[3]);
Hornman et al. (2015); Przybysz-Jarnut et al. (2015);
Daley, Freifeld, et al. (2016[4]); Dean, Brice, et al. (2016); La Follett et al. (2016); Yavuz et al. (2016[3]);
Bakulin et al. (2017); Pevzner, Urosevic, Popik, Shulakova, et al. (2017[4]); Pevzner, Urosevic, Popik, Tertyshnikov, et al. (2017[4]); Pevzner, Urosevic, Tertyshnikov, et al. (2017[4]);
Bakulin, Golikov, Erickson, et al. (2018); Bakulin et al. (2018a, 2018b, 2018c); Bakulin, Silvestrov, et al. (2018); Bakulin, Silvestrov, & Pevzner (2018); Hall et al. (2018[3]); Shiloh et al. (2018[2]);
Alajmi et al. (2019); Almarzoug et al. (2019); Alshuhail et al. (2019); Bakulin, Silvestrov, & Alshuhail (2019); Bakulin, Silvestrov, & Pevzner (2019); Hall et al. (2019[3]); Smith, Bakulin, & Silvestrov (2019); Smith, Bakulin, & Jervis (2019);
Alajmi et al. (2020); Ringstad et al. (2020[2])
17.8.2 *Helical Wound and Shaped Fibers for Surface Seismic* – 14
Hornman et al. (2013); Lumens et al. (2013);
La Follett et al. (2014);
Poletto et al. (2015);
Kuvshinov (2016); Lim Chen Ning & Sava (2016[2]);
Hornman (2017); Innanen (2017a, 2017b); Lim Chen Ning & Sava (2017[2]);
Innanen & Eaid (2018); Lim Chen Ning & Sava (2018a[2], 2018b[2]);
Innanen et al. (2019)

Note. Papers with superscripts discussed more than one topic and appear in several tables.

Table 17.9 DAS in Geothermal System, Mining, and Mineral Exploration.

17.9.1 *Geothermal* – 46
Baldwin et al. (2014[3]); Lancelle et al. (2014[3]); Wang H. et al. (2014[3]);
Reinsch et al. (2015);
Becker et al. (2016a); Lord et al. (2016); Reinsch et al. (2016);
Cronin et al. (2017); De Jong et al. (2017); Feigl & PoroTomo Team (2017); Feigl et al. (2017); Thurber et al. (2017); Zeng, Thurber, et al. (2017[2]); Zeng, Thurber, Wang, Fratta, & PoroTomo Team (2017[2]); Zeng, Lancelle, et al. (2017[2]);
Becker et al. (2018a); Feigl & PoroTomo Team (2018); Jreij, Trainor-Guitton, Simmons, et al. (2018); Mellors, Sherman, Ryerson, et al. (2018); Miller (2018); Miller et al. (2018); Parker L. et al. (2018); Percher & Valishin (2018[3]); Stiller et al. (2018); Trainor-Guitton, Guitton, et al. (2018[2]); Vandeweijer et al. (2018[2]); Wang, Fratta, Lord, et al. (2018[4]); Wang, Zeng, Fratta, et al. (2018[3]);
Chalari et al. (2019); Kasahara (2019); Kasahara, Hasada, & Yamaguchi (2019); Kasahara, Hasada, Kuzume, Fujise, et al. (2019); Kasahara, Hasada, & Kuzume (2019); Martuganova et al. (2019[2]); Mellors, Sherman, et al. (2019); 2019); Mondanos & Coleman (2019); Stork et al. (2019); Trainor-Guitton, Guitton, et al. (2019[2]);
Carpentier et al. (2020); Haberer et al. (2020); Hopp et al. (2020); Jestin et al. (2020); Kasahara et al. (2020); Li D. et al. (2020a, 2020b); Paap et al. (2020); Schoenball et al. (2020)
17.9.2 *Mining and Mineral Exploration* – 14
Brentle & Großwig (2014);
Cheng et al. (2015);
Nesladek et al. (2017[3]); Wang H. et al. (2017);
Bellefleur et al. (2018); Bona & Pevzner (2018); Koivisto et al. (2018); Riedel et al. (2018a[3], 2018b[3]); Urosevic et al. (2018); Wang, Fratta, Lord, et al. (2018[4]); Wang, Zeng, Fratta, et al. (2018[3]);
Urosevic et al. (2019);
Bellefleur et al. (2020)

Note. Papers with superscripts discussed more than one topic and appear in several tables.

production wells and CCS sites around the world (Barberan et al., 2012; Cocker et al., 2014; Correa, Dean, et al., 2017; Correa, Egorov, et al., 2017; Daley et al., 2013; Daley, Miller, et al., 2014; Daley, White, et al., 2014; Dean, Hartog, et al., 2015; Hornby et al., 2014; Kiyashchenko et al., 2013; Li Q. et al., 2013; Longton et al., 2015; Madsen et al., 2012; Madsen, Thompson, et al., 2013; Mateeva et al., 2012, Mateeva, Lopez, Mestayer, et al., 2013; Mateeva, Lopez, Hornman, et al., 2014; Mateeva, Lopez, Potters, et al., 2014; Miller et al., 2012; Parker T. et al., 2013; Parker, Shatalin, et al., 2014; Pevner, Tertshnikv & Bona, 2018; Pevner, Tertshnikv, Bona, Correa, et al., 2018; Poletto, Clarke, et al., 2014; Verliac et al., 2015). As DAS technologies and instrumentation advance, an increasing number DAS-VSP field tests with different goals are being conducted to gradually mature the application (Aldawood et al., 2020; Borland et al., 2016; Correa, Dean, et al., 2017; Correa, Van Zaanen, et al., 2017; Correa, Freifeld, et al., 2018; Correa, Pevzner, et al. 2018; Daley, Freifeld, et al., 2016; Daley, Miller, et al., 2016; Gordon et al., 2018; Kimura et al., 2016; Martinez A. et al., 2020; Miller et al., 2016; Nesladek et al., 2017; Percher & Valishin, 2018; Riedel et al., 2018a, 2018b; Spackman & Lawton, 2018; Tertyshnikov & Pevzner, 2019; Willis, Ellmauthaler, et al., 2016; Willis, Erdemir, et al., 2016; Zaanen et al., 2017). Depth uncertainties of DAS channels present a great challenge for DAS-VSP surveys and DAS acquisition more broadly. Many investigators have sought approaches for solving this problem (Verliac et al., 2015; Dean, Cuny, Constantinou, et al., 2016; Dean et al., 2018; Duan et al., 2018; Ellmauthaler, Willis, Barfoot, et al., 2016; Mateeva & Zwartjes, 2017; Olofsson & Martinez, 2017). Alternative cable designs, including helical and straight fiber, have also been installed in wells with 3C geophones to compare their performance (Hall et al., 2018, 2019; Stork et al., 2020). DAS systems based on Rayleigh backscattering are also compared with FBG-based qDAS systems (Alfataierge et al., 2018; Alfataierge, Dyaur, Li, et al., 2019). We select 62 papers and abstracts listed in Table 17.4.1 on this topic for further study by interested readers.

After a series of field trials in various wells on land for calibration and validation with conventional geophones, DAS-VSP surveys have been used to measure velocity and other physical parameters of subsurface formations and image subsurface structures with wider frequency ranges and higher spatial resolution in the oil and gas

Table 17.10 DAS Monitoring for Safety and Security.

17.10.1 *Monitoring and Detection of Pipeline Leakage and Intrusion* – 31

Tanimola & Hill (2009[2]);
Frings & Walk (2011); Giunta et al. (2011);
Eisler & Lanan (2012); Glisic & Yao (2012); Williams J. (2012);
Idachaba et al. (2013); Zhang J. et al. (2013[2]);
Audouin et al. (2014); Boone et al. (2014); Cramer et al. (2014a, 2014b); Thodi et al. (2014); Worsley et al. (2014);
Cramer et al. (2015); Siebenaler et al. (2015); Thodi et al. (2015);
Baqué (2016); Garcia-Hernandez & Bennett (2016);
Baqué (2017); Carpenter (2017c); Fagbami et al. (2017); Karrenbach, Cole, et al. (2017[2]); Michelin et al. (2017); Pimentel-Niño (2017); Siebenaler et al. (2017); Tejedor et al. (2017[3]);
Lu et al. (2018);
Alfataierge et al. (2019); Svelto et al. (2019);
Velarde et al. (2020)

17.10.2 *Crucial Structure and Facility* – 14

Duckworth & Ku (2013);
Arslan et al. (2015);
Kammerer & MacLaughlin (2017); Karrenbach, Cole, et al. (2017); Williams J. (2017);
Ray (2018); Zhao H. et al. (2018);
Glaser et al. (2019); Karrenbach (2019a[2]); Parikh et al. (2019); Ray et al. (2019);
Cherukupalli & Anders (2020); Sahin et al. (2020[2]); Stork et al. (2020[3])

Note. Papers with superscripts discussed more than one topic and appear in several tables.

industry. Both *P*- and *S*-wave velocities were measured (e.g., Martinez et al., 2020; Miller et al., 2012; Willis, Ellmauthaler, et al., 2016; Wu X. et al., 2016, 2017), and *Q*-factors (e.g., An et al., 2020; Bettinelli & Puech, 2015; Dean & Correa 2017; Pierre & Le Calvez, 2020; Yu, G., Xiong, et al., 2020) were derived using DAS-VSP data. DAS-VSP surveys acquired with OVSP and WVSP sources in wells on land were used to calibrate velocity models and produce subsurface images (e.g., Al Adawi et al., 2013; Aldawood et al., 2018; Booth et al., 2020; Clarke et al., 2017; Chen, Yu, et al., 2018; Ferla et al., 2018, 2019; Kiyashchenko et al., 2013; Leclercq et al., 2016; Li Q. et al., 2013; Lim Chen Ning & Sava, 2018c, 2019; Lim Chen Ning et al., 2019; Mateeva et al., 2012; Mateeva, Lopez, Mestayer, et al., 2011; Mateeva, Lopez, et al., 2013; Zwartjes & Mateeva, 2015a, 2015b; Teff et al., 2016; Yu G. et al., 2016a; Zhan G. et al., 2016). It has been recognized that 3-D DAS-VSP surveys are useful tools to characterize 3-D features of subsurface geological structures (Alabri, 2015; Al-Hinai et al., 2014; Chen, Hu, et al., 2018; Mateeva, Lopez, Hornman, et al., 2014; Mateeva, Lopez, Potters, et al., 2014; Yu G. et al., 2019). 3-D DAS-VSP surveys were also applied to CO_2 sequestration monitoring (Götz et al., 2015, 2018; Miller et al., 2016), geothermal exploration (Trainor-Guitton, Guitton, et al., 2018), and mineral exploration (Riedel et al., 2018a, 2018b).

Following the success of the first marine walk above VSP field trial with a DAS system in the North Sea in November 2011 (Madsen et al., 2012, Madsen, Thompson, et al., 2013), the first dual-well 3-D DAS-VSP survey in a deepwater environment was conducted simultaneously with an ocean bottom seismometer (OBS) survey in the GOM in 2012 (Mateeva, Lopez, Mestayer, et al., 2013; Mateeva, Mestayer, Yang, et al., 2013). This survey was conducted because of the apparent economic advantage of DAS-VSP over a traditional VSP survey where significant rig downtime is required for operation. It has been demonstrated through processing of the first marine dual-well 3-D DAS-VSP data acquired in deep water that DAS-VSP data can accurately update the velocity model using travel time tomography, and migration images of subsurface structures are significantly improved for both OBS and DAS-VSP surveys (Li, Wu, et al., 2015; Li et al., 2018; Wong et al., 2015; Wu et al., 2014, 2015). Since then, numerous marine 3-D DAS-VSP surveys have been acquired to obtain 3-D subsurface structures around the world (Abdul Rahim, Ghazali, et al., 2017; Abdul Rahim, Hardy et al., 2017; Abdul Rahim et al., 2018; Ball et al., 2017; Dy et al., 2018; Gerritsen et al., 2016b; Ghazali

Table 17.11 DAS for Seismology, Fault, and Deformation.

17.11.1 *Earthquake, Explosion, Urban, and Near-Surface Seismology* – 129
Daley et al. (2013[5]);
Baldwin et al. (2014[2]); Lancelle et al. (2014[2]); Mellors et al. (2014); Wang H. et al. (2014[2]);
Ajo-Franklin et al. (2015); Martin et al. (2015);
Ajo-Franklin et al. (2016); Dou et al. (2016); Lord et al. (2016); Martin et al. (2016);
Ajo-Franklin, Dou, et al. (2017); Ajo-Franklin, Lindsey, et al. (2017); Biondi et al. (2017); Castongia et al. (2017); Ciocca et al. (2017); Dou, Lindsey, et al. (2017); Feigl & PoroTomo Team (2017); Feigl et al. (2017); Fratta et al. (2017); Huot et al. (2017); Jousset et al. (2017); Karrenbach, Cole, et al. (2017[2]); Lindsey, Martin, et al. (2017); Lindsey, Dou, et al. (2017); Martin & Biondi (2017); Martin, Biondi, Karrenbach, et al. (2017); Martin, Biondi, Yuan, et al. (2017); Martin, Castillo, Cole, et al. (2017); Martin, Chang, Huot, et al. (2017); Nesladek et al. (2017[3]); Paitz & Fichtner (2017); Raab et al. (2017); Thurber et al. (2017[2]); Williams J. (2017[2]); Zeng, Thurber, et al. (2017[2]); Zeng, Thurber, Wang, Fratta, & PoroTomo Team (2017[2]); Zeng, Lancelle, et al. (2017[2]);
Abbott (2018); Abbott et al. (2018); Fang et al. (2018); Feigl & PoroTomo Team (2018); Fratta (2018); Huot & Biondi (2018); Jousset et al. (2018); Kasahara, Hasada, Kawashima, et al. (2018); Kasahara et al. (2018a, 2018b); Li Z. (2018); Li Z. & Zhan (2018); Lindsey (2018a, 2018b); Marra et al. (2018); Martin (2018); Martin & Biondi (2018); Martin, Biondi, et al. (2018); Martin, Lindsey, et al. (2018); Martin, Huot, et al. (2018); Paitz et al. (2018); Pevzner, Gurevich, et al. (2018); Rodríguez-Tribaldos (2018); Song et al. (2018); Sullivan (2018); Vandeweijer et al. (2018[2]); Wang, Fratta, Lord, et al. (2018[4]); Wang, Zeng, Fratta, et al. (2018[3]); Wang, Zeng, Miller, et al. (2018); Yu C. (2018); Zhan (2018);
Abbott et al. (2019); Ajo-Franklin et al. (2019); Costley, Galan-Comas, Hathaway, et al. (2018); Costley, Galan-Comas, Kirkendall, et al. (2018); Holland et al. (2019); Karrenbach (2019a); Krawczyk et al. (2019); Lellouch, Spica, et al. (2019); Lellouch et al. (2019a, 2019b, 2019c, 2019d, 2019e); Lellouch, Yuan, et al. (2019); Li Z. et al. (2019); Lindsey, Rademacher, Dreger, et al. (2019); Lindsey, Rademacher, & Ajo-franklin (2019); Lindsey, Dawe, & Ajo-franklin (2019[2]); Martin (2019); Mellors, Gok, et al. (2019); Paitz et al. (2019a, 2019b); Rodríguez-Tribaldos, 2019; Rodríguez-Tribaldos et al. (2019); Shragge et al. (2019); Sladen et al. (2019); Trainor-Guitton, Titov, et al. (2019); Wang H. et al. (2019); Williams E. (2019); Williams, E. F., Zhan, et al. (2019); Williams, E. F., Fernández-Ruiz, Magalhaes, et al. (2019); Williams, E. F., Fernández-Ruiz, Magalhaes, et al. (2019); Yu C. et al. (2019); Zhang Z. et al. (2019a, 2019b); Zeng et al. (2019); Zhan Z. (2019); Zhao Y. et al. (2019); Zhu & Stensrud (2019);
Beroza et al. (2020); Edme et al. (2020); Fang et al. (2020); Fernández-Ruiz et al. (2020); Ford et al. (2020); Gok & Mellors (2020); Lindsey, Rademacher, et al. (2020); Mellors et al. (2020); Paitz et al. (2020a, 2020b); Rodríguez-Tribaldos et al. (2020); Smolinski et al. (2020); Song et al. (2020); Spica et al. (2020); Walter et al. (2020); Wang X. et al. (2020); Yang Y. et al. (2020); Young et al. (2020); Zhu & Stensrud (2020); Zhu, Martin, et al. (2020); Zhu, Junzhu Shen, et al. (2020)
17.11.2 *Fault and Deformation Characterization* – 19
Constantinou, Schmitt, et al. (2016); Jousset et al. (2016);
Ellsworth et al. (2017); Gutscher et al. (2017); Kammerer & MacLaughlin (2017);
Becker et al. (2018b); Trainor-Guitton, Jreij, et al. (2018); Zumberge et al. (2018);
Becker & Coleman (2019a, 2019b); Broderick et al. (2019); Gutscher et al. (2019); Lindsey, Dawe, et al. (2019[2]); Trainor-Guitton, Guitton, et al. (2018[2]); Zhang Y. & Xue (2019);
Ajo-Franklin et al. (2020); Clement et al. (2020); Lay et al. (2020); Lindsey, Ajo-Franklin, et al. (2020)

Note. Papers with superscripts discussed more than one topic and appear in several tables.

et al., 2018; Ghazali et al., 2019; Hance et al., 2016; Jiang et al., 2016; Li et al., 2019; Mad Zahir et al., 2019; Muhammed et al., 2017; Muhammed et al., 2019; Nizkous et al., 2015; Saxton et al., 2018; Wang X. et al., 2019; Zhan et al., 2015, 2016, 2018). Li et al. (2019) used a 3-D DAS-VSP acquired inside a salt pile in the GOM to delineate and obtain migration images of salt boundaries. As many repeat 3-D DAS-VSPs are acquired, time-lapse DAS-VSP surveys will be a proven tool to monitor and manage subsurface reservoirs. We have compiled 116 papers and abstracts in Table 17.4.2 on the topic of DAS-VSP measurements and imaging for interested readers.

Time-lapse 3-D surface seismic and VSP surveys (also referred to as 4-D surveys) are useful tools to monitor variations in subsurface properties caused by a variety of processes, including reservoir stress perturbations, fluid injections (e.g., CO_2 or brine), and hydraulic fracturing operations. Mateeva et al. (2012) reported a time-lapse DAS-ZVSP experiment in 2010 and 2011 in a well on land to demonstrate both repeatability and the significant

Table 17.12 *DAS Data Exchange, Management, Processing, and Deep Learning.*

DAS exchange, storage, manage, processing, and machine learning – 43
Dean, Cuny, et al. (2015); Richards et al. (2015[2]);
Yu G. et al. (2016a[3]);
Bello et al. (2017); Cui et al. (2017); Dean et al. (2017); Dou, Wood, et al. (2017); Martins et al. (2017); Muir & Zhan (2017); Tejedor et al. (2017[3]); Williams M. et al. (2017); Yu Z. et al. (2017);
Bello et al. (2018); Chad Trabant (2018); Chen J. et al. (2018); Cole, Karrenbach, Gunn, et al. 2018; Huot & Biondi (2018); Huot, Biondi, et al. (2018); Huot, Martin, et al. (2018); Jreij, Trainor-Guitton & Simmons (2018); LeBlanc et al. (2018); Martin, Huot, et al. (2018[2]); Park et al. (2018[2]); Parkhonyuk et al. (2018[2]); Shiloh et al. (2018[2]); Yang L. et al. (2018);
Alkhalaf et al. (2019); Cheng D. et al. (2019); Clements et al. (2019); Costley et al. (2019); Dean (2019); Martin (2019[2])~~[2]~~; Nelson & Konopczynski (2019); Sherman (2019); Williams, M. J., Le Calvez, & Cuny (2019); Willis et al. (2019[3]); Wilson R. et al. (2019); Yang X. et al. (2019); Zheng et al. (2019);
Cuny et al. (2020); Neri & Philo (2020); Sahin et al. (2020[2]); Schuberth (2020)

Note. Papers with superscripts discussed more than one topic and appear in several tables.

improvements in the DAS-VSP technology. Several repeat 3-D DAS-VSP surveys acquired on land and in deepwater environments (Chalenski et al., 2016, Chalenski, Hatchell, et al., 2017; Chalenski, Wang, et al., 2017; Chalenski, Hatchell, et al., 2018; Chalenski, Lopez, et al., 2018; Effiom, 2016; Grandi et al., 2017; Hill, 2014; Kiyashchenko et al., 2013; Lopez, Przybysz-Jarnut, et al., 2015; Mateeva, Mestayer, Yang, et al., 2013, Mateeva et al., 2015, 2016; Tatanova et al., 2016; Zwaan et al., 2015) demonstrated that time-lapse 4-D DAS-VSP surveys can produce "4-D" migration images to reveal temporal and spatial variations of subsurface reservoirs in a cost-effective manner in comparison with conventional 4-D surface seismic surveys (Kiyashchenko et al., 2019; Mateeva et al., 2017, 2018, 2019; Wang K. et al., 2017, 2019; Zwartjes et al., 2017). Time-lapse DAS-VSP methods were also applied to monitor CO_2 injection process (e.g., Daley, Freifeld, et al., 2016; Grindei et al., 2019; Harris et al., 2016; Oropeza Bacci, O'Brien, et al., 2017; Pevzner, Urosevic, Popik, Shulakova, et al., 2017; Pevzner, Urosevic, Popik, Tertyshnikov, et al., 2017; Pevzner, Urosevic, Tertyshnikov, et al., 2017; Pevzner et al., 2019; Pevzner et al., 2020) and reveal physical property variations in formations induced by hydraulic fracturing treatments (e.g., Byerley, Monk, Aaron, et al., 2018; Langton et al., 2019; Meek et al., 2017; Teff et al., 2016). Readers may refer to Section 17.3.4 (Table 17.6) and Section 17.3.5 (Table 17.7) for more details on time-lapse DAS-VSP applications for monitoring hydraulic fracturing and CO_2 injection. We have assembled 55 papers and abstracts in Table 17.4.3 for further reading on the topic of time-lapse DAS-VSP applications.

Conventional VSP surveys use up to 100 3-C geophones conveyed by a standard heptacable with seven copper connections into a wellbore. DAS-VSP surveys make use of the entire optical fiber as a dense sensor array to record borehole seismic signals with a much larger aperture and a higher spatial resolution as discussed previously. However, you need an optical fiber or fibers permanently or temporarily installed in the wellbore to conduct a DAS-VSP survey. In order to run DAS-VSP surveys without existing installed fibers in wells, hybrid DAS-geophone-VSP systems have been developed (Dean, Constantinou, et al., 2015; Frignet & Hartog, 2014; Haldorsen & Hilton, 2018; Hartog et al., 2014; Hartog, Frignet, Mackie, & Allard, 2014; Hartog, Frignet, Mackie, & Clark, 2014; Percher & Valishin, 2018; Valishin, 2019a; Willis et al., 2019). In these hybrid DAS-geophone-VSP systems, a modified hybrid heptacable with five copper connections and two optical fibers connects to several 3C geophones at the bottom and to an IU at the surface to obtain both 3C geophone data and DAS-VSP data using the optical fibers as DAS "sensors". One can also move the hybrid cable to shallower depths to obtain more 3C geophone data as a conventional wireline VSP operation, as well as obtaining redundant DAS data. This hybrid DAS-geophone-VSP tool has been used in the oil and gas industry for DAS-VSP surveys on land and in an offshore environment (Borland et al., 2016; Ferla et al., 2018, 2019; Haldorsen et al., 2018a, 2018b; Kimura et al., 2016, 2017, 2018; Martinez A. et al., 2020; Willis et al., 2019). It was also used to acquire DAS-geophone-VSP surveys in a CCS site and a geothermal resource area in Germany (Götz et al., 2015, 2018; Martuganova et al., 2019) without fibers permanently installed in the well. Yu, G., Chen, et al. (2016) reported that a hybrid wireline cable was rigged up in a vertical well without geophones but a weight at the bottom to successfully acquire DAS-WVSP data in northeastern China. After removing strong coherent noise caused by cable slapping and ringing along the borehole casing with a newly developed processing method, satisfactory VSP migration images of subsurface structures were obtained (Yu et al., 2016a, 2016b). In addition to the hybrid DAS-VSP cable, successful examples of coiled tubing conveyed DAS-VSPs have been reported (Ellmauthaler et al., 2019; Ellmauthaler, Willis, et al., 2020). Table 17.4.4 lists 28 papers and abstracts we compiled for readers who have interests in hybrid cable and coiled tubing conveyed DAS-VSP.

17.3.3. DAS in Downhole Surveillance and Flow Monitoring

DAS methods play an important role in downhole surveillance and flow monitoring by listening and analyzing acoustic energy levels associated with downhole activities. DAS downhole technologies enable wellbore integrity monitoring, well equipment monitoring, and smart-well completion monitoring (Ansari et al., 2014; Bukhamsin & Horne 2014, 2016; Denney, 2012; Koelman, 2011; Koelman et al., 2012a, 2012b; Parker T. et al., 2012). Downhole DAS systems can also be utilized as tools for sand detection (Carpenter, 2017c; Drakeley et al., 2014; Mullens et al., 2010; Sadigov et al., 2017; Thiruvenkatanathan et al., 2016). DAS can be applied for inflow and injection profiling, gas lift optimization, and production profiling (Bateman et al., 2013; Finfer et al., 2014; Hemink et al., 2016; Hemink & Van Der Horst, 2018; In't panhuis, et al., 2014; Koelman, 2011; Ugueto et al., 2014; Van Der Horst, Den Boer, et al., 2013; Van Der Horst, Lopez, et al., 2013; Van Der Horst et al., 2014). DAS systems are also used for electrical submersible pump and steam-assisted gravity drainage monitoring (Allanic et al., 2013; and Carpenter, 2016b; MacPhail et al., 2016). DAS can measure flow velocities by tracking the acoustic noise up and down the fiber generated by flow with F-K (frequency and wavenumber) domain analysis and obtain the Doppler shift associated with flow (Finfer et al., 2015; Fidaner, 2017; Johannessen et al., 2012; Xiao et al., 2013, 2014, 2015). DAS for downhole surveillance and flow monitoring is one of the most active areas of research for DAS geophysical applications. We have collected 174 papers and abstracts on this topic in Table 17.5 for interested readers.

17.3.4. DAS in Monitoring Hydraulic Fracturing and Microseismicity

Another major application of DAS is for the monitoring of hydraulic fracture stimulation (HFS) stages and to locate and characterize microseismic events (MSE) induced by hydraulic fracturing (Cadwallader et al., 2015; Cannon & Aminzadeh, 2013; Lowe et al., 2013; MacPhail et al., 2012; Molenaar, Hill, & Koelman, 2011; Molenaar, Hill, et al., 2011; Molenaar & Cox, 2013; Warpinski et al., 2014; Webster, Cox, et al., 2013; Webster, Wall, et al., 2013; Webster et al., 2014) in the unconventional oil and gas industry. DAS is applied for near-wellbore monitoring before, during, and after HFS stages to observe acoustic noise energy associated with the setting of packers, dropping of balls, movement of sliding sleeves, and flow of fluid which is behind packers or goes through perforations (Cannon & Aminzadeh, 2013; Cadwallader et al., 2015; Lowe et al., 2013; MacPhail et al., 2012; Molenaar & Cox, 2013; Molenaar, Fidan, et al., 2012; Molenaar, Hill, et al., 2012; Warpinski et al., 2014). Acoustic signatures of downhole events, such as leaky and unset packers, shattered balls, and misfired perforation guns, can be recorded by DAS installed in the well(s) in a real-time manner. This setup enables operators to make quick critical decisions, which increases both operation safety and efficiency and also saves operational costs (Cannon & Aminzadeh, 2013). Variations of amplitudes and durations of acoustic "noise" of each HFS stage recorded by DAS allow operators to quantitatively evaluate the fracturing effectiveness of each fracturing stage (Aminzadeh, 2013; Cadwallader et al., 2015; Cannon & Lowe et al., 2013; Haustveit et al., 2017; Jin & Roy, 2017; Kavousi Ghahfarokhi, Carr, Wilson, et al., 2017; MacPhail et al., 2012; Molenaar & Cox, 2013; Webster et al., 2014).

DAS installed in wells for near-wellbore monitoring of HFS process can also be used to detect *P* and *S* waves generated by microseismic events induced by the hydraulic fracturing stages (Cadwallader et al., 2015; Cole & Karrenbach, 2016; Farhadiroushan, 2016, 2018c; Hull et al., 2017; Molenaar & Cox, 2013; Molteni et al., 2017; Webster, Cox, et al., 2013; Webster, Wall, et al., 2013; Warpinski et al., 2014). Locating induced microseismic events, along with in-well HSF monitoring, allows delineation of fracture network development extending outside of the wellbores and to better characterize the fractures (Carr et al., 2017; Carr et al., 2019; Cole, Karrenbach, Kahn, et al., 2018; Jayaram et al., 2019; Jin & Roy, 2017; Karrenbach, Ridge, et al., 2017; Karrenbach, Kahn, et al., 2017; Rassenfoss, 2019; Raterman et al., 2017, 2018; Shurunov et al., 2018; Warpinski, 2014; Webster, Wall, et al., 2013; Webster et al., 2014; Webster et al., 2016; Verdon et al., 2020). DAS recordings of polarities of *P* and *S* waves from induced microseismic events can provide strong constraints on the fault-plane solutions of source mechanisms and characterize the fractures and local stress field (Baird et al., 2020; Karrenbach & Cole, 2019; Karrenbach, Cole, Ridge, et al., 2019). Time-lapse DAS-VSP surveys were conducted in fractured regions close to the treatment well(s) to monitor variations of physical properties of the fractured zones during hydraulic fracturing (Binder, 2018; Byerley, Monk, Aaron, et al., 2018; Byerley, Monk, Yates, et al., 2018; Chavarria, 2018a; Langton et al., 2019; Meek et al., 2017, 2018; Teff et al., 2016; Zhou et al., 2019). We collect 121 papers and abstracts on this topic in Table 17.6 for further reading. It is interesting to note that the number of papers on this topic rapidly dropped to 2 in 2015, coinciding with the big downturn of the oil and gas industry. The number dramatically increased to about seven times the average number of the previous six years in 2017 and has maintained a high level since then.

17.3.5. DAS in Carbon CCS and CO_2 Injection Monitoring

DAS technology is widely used in various carbon capture and storage (CCS) projects (Daley et al., 2013; Daley, Miller, et al., 2014; Freifeld et al., 2017) to monitor subsurface CO_2 injection (Barberan et al., 2012; Cocker et al., 2014; Daley et al., 2013; Daley, White, et al., 2014; Longton et al., 2015; Mestayer et al., 2011). Since VSP with 3C geophones installed in wells has been a traditional mean to monitor CO_2 injection, many early comprehensive comparison, calibration, and validation of DAS and geophones were carried out at CCS sites around the world (Barberan et al., 2012; Cocker et al., 2014; Correa, Egorov, et al., 2017; Cox et al., 2012; Daley et al., 2013; Daley, White, et al., 2014; Daley, Miller, et al., 2016; Longton et al., 2015; Miller et al., 2016; Mestayer et al., 2011; Olofsson & Martinez, 2017). Single- and multiple-mode DAS were also compared side by side at several CCS sites (Bettinelli & Frignet, 2015; Daley, White, et al., 2014; Longton et al., 2015; Miller et al., 2016). DAS-VSP migration images of subsurface structures (Correa, Pevzner, et al., 2018; Daley, Miller, et al., 2016; Götz et al., 2015, 2018; Humphries et al., 2015, 2016; Kobayashi et al., 2020; Miller et al., 2016; Sidenko et al., 2019) at the CSS sites were generated and compared with the surface seismic (Götz et al., 2015) and geophone-VSP images (Humphries et al., 2015, 2016). DAS cables have also been trenched above CCS sites to enable surface seismic surveys (Daley, Freifeld, et al., 2016; Dou et al., 2016; Freifeld et al., 2016; Yavuz et al., 2016) and joint DAS-VSP and DAS surface seismic surveys (Lawton, Saeedfar, et al., 2018; Pevzner, Urosevic, Tertyshnikov, et al., 2017; Ringstad et al., 2020) for monitoring CO_2 injection. Time-lapse DAS-VSP surveys are widely used to image subsurface variations caused by CO_2 injections (Charara et al., 2018; Chavarria, 2018b; Cheraghi et al., 2018; Daley, Freifeld, et al., 2016; Harris et al., 2016; Grindei et al., 2019; Halladay, Orpeza Bacci, et al., 2018; Harris & White, 2018; Oropeza Bacci, O'Brien, et al., 2017; Pevzner et al., 2020; Tertyshnikov Pevzner, Freifeld, Ricard, & Avijegon, 2019; White et al., 2017). We collected 62 papers and abstracts in Table 17.7 on CO_2-related DAS applications for further investigation by interested readers.

17.3.6. DAS in Surface Seismic Exploration

DAS surface seismic experiments onshore were conducted, following successful DAS-VSP tests in wellbores, by installing optical fibers buried in shallow trenches or in near-surface horizontal borings for subsurface seismic exploration and surveillance (Dean, Brice, et al., 2016; Hornman & Forgues, 2013; Jarnut et al., 2015; Kendall, 2014a, 2014b; La Follett et al., 2016; Mateeva, Lopez, Potters, et al., 2014; Parker T. et al., 2013, Parker, Statalin, et al., 2014; Poletto, Clarke, et al., 2014; Przybysz-Shiloh et al., 2018). DAS methods have revealed shallow geological structures of oil and gas fields (Alajmi et al., 2019; Bakulin et al., 2017; Bakulin, Golikov, Erickson, et al., 2018; Bakulin, Silvestrov, & Pevzner, 2018; Bakulin, Silvestrov, & Pevzner, 2019; Smith, Bakulin, & Silvestrov, 2019) and have been used to monitor CO_2 injection at CCS sites as mentioned previously (Daley et al., 2013; Daley, Freifeld, et al., 2016; Dou et al., 2016; Yavuz et al., 2016; Pevzner, Urosevic, Popik, Shulakova, et al., 2017). Wang et al. (2014) reported an active-source DAS seismic field trail in 2013 with trenched fiber at the Garner Valley site, California, USA, to analyze sensitivity and directivity of the fiber response (Lancelle et al., 2014) and derive *S*-wave velocity profiles with active sources (Baldwin et al., 2014) and ambient noise (Zeng, Lancelle, et al., 2017) using the multispectral analysis of surface wave (MASW) method.

3C geophones or seismometers have also been colocated with the DAS standard fiber cables and helically wound cable (HWC) fibers to make comparison, calibration, and validation (Daley, Freifeld, et al., 2016; Dou et al., 2016; Hall et al., 2018, 2019; Parker T. et al., 2013; Poletto, Corubolo, et al., 2014; Yavuz et al., 2016). To overcome the directivity of DAS fiber disadvantage, HWC fibers (Hornman et al., 2013, 2017; Innanen, 2017a, 2017b; Kuvshinov, 2016; La Follett et al., 2014; Lim Chen Ning & Sava, 2016, 2017, 2018a, 2018b; Lumens et al., 2013; Poletto et al., 2015) and other shaped fibers (Innanen & Eaid, 2018; Innanen et al., 2019; Ringstad et al., 2020) are modeled, investigated, and developed. We gathered 39 papers and abstracts on DAS surface seismic applications in Table 17.8.1 and included 14 papers and abstracts on HWC and other shaped fiber configuration in Table 17.8.2 for further reading.

17.3.7. DAS for Geothermal System, Mining, and Mineral Exploration

Geothermal energy systems utilize harvest natural or injected high-temperature fluids for energy production.

Enhanced geothermal systems (EGS) are engineered subsurface systems where permeability is created in initially tight hot formations for energy production, which is an alternative to naturally occurring hydrothermal reservoirs. EGS technologies enhance and create geothermal resources by a variety of stimulation methods. Durable features of optical fibers in a high-temperature harsh environment have allowed DAS systems to become a favored tool for geophysicists and geoscientists to explore and characterize geothermal resources in the USA (Feigl & PoroTomo Team, 2017; Wang H. et al., 2014; Hopp et al., 2020, Li, D. et al., 2020; Lord et al., 2016; Mellors, Sherman, et al., 2019; Miller et al., 2018), Germany (Haberer et al., 2020; Martuganova et al., 2019; Reinsch et al., 2015; Stiller et al., 2018; Vandeweijer et al., 2018), Iceland (Reinsch et al., 2015), Japan (Kasahara, Hasada, & Yamaguchi, 2019; Kasahara et al., 2020), Belgium (Carpentier et al., 2020), France (Jestin et al., 2020), the Netherlands (Paap et al., 2020), and other countries. In 2016, the PoroTomo project, studying the geothermal field at Brady Hot Spring, in Nevada, USA, used an 8.7 km zigzag fiber in a trench and a 400 m fiber in a well to conduct a comprehensive DAS experiment, producing *S*-velocity profiles with MASW (Lord et al., 2016; Zeng, Thurber, Wang, Fratta, & PoroTomo Team, 2017); 3-D velocity models by tomography with active sources (Parker L. et al., 2018; Thurber et al., 2017) and ambient noise (Zeng, Thurber, et al., 2017); 3-D DAS-VSP migration images of subsurface structures and faults (Jreij, Trainor-Guitton, Simmons, et al., 2018b; Trainor-Guitton, Guitton, et al., 2018; Trainor-Guitton, Guitton, et al., 2019); and assessing the DAS ability to monitor changes in the water table (Cronin et al., 2017).

Mellors, Sherman, et al. (2019) reported on the feasibility of using DAS methods to monitor fractures and microseismicity at the Frontier Observatory for Research in Geothermal Energy (FORGE) EGS site in Utah, USA. The EGS Collab project at the Sanford Underground Research Facility in South Dakota, USA, focused on continuous DAS monitoring during hydraulic stimulations (Hopp et al., 2020; Li, D. et al., 2020a, 2020b; Schoenball et al., 2020). Although both surface and borehole DAS (Feigl & PoroTomo Team, 2017; Miller et al., 2018; Reinsch et al., 2015, 2016) are extensively used in geothermal applications, DAS-VSP in wells (Becker et al., 2016a; Carpentier et al., 2020; Haberer et al., 2020; Jestin et al., 2020; Kasahara, Hasada, & Yamaguchi, 2019; Kasahara et al., 2020; Mellors, Sherman, Ryerson, et al., 2018) is dominant since the wells are closer to the underground geothermal sources. Kasahara, Hasada, & Yamaguchi (2019) proposed to use both surface and borehole DAS along with full-waveform inversion method to improve subsurface images of geothermal resources. Efforts to improve instruments and installation methods for EGS DAS applications were reported (Chalari et al., 2019; De Jong et al., 2017; Percher & Valishin, 2018; Stork et al., 2019). Readers may refer to Paulsson et al. (2014, 2019) in Table 17.2 about development of FBG-based qDAS for EGS applications. We collect 47 papers and abstracts on DAS EGS applications in Table 17.9.1 for further reading.

DAS technology has also been applied in mineral exploration and monitoring mining activities in Australia, Canada, China, Finland, USA, and other countries around the world (Bellefleur et al., 2018, 2020; Bona & Pevzner, 2018; Brentle & Großwig, 2014; Cheng et al., 2015; Koivisto et al., 2018; Nesladek et al., 2017; Riedel et al., 2018a, 2018b; Urosevic et al., 2018, 2019; Wang H. et al., 2017; Wang, Fratta, Lord, et al., 2018; Wang, Zeng, Fratta, et al., 2018). Both DAS-VSP (Bellefleur et al., 2018; Bona & Pevzner, 2018; Koivisto et al., 2018; Riedel et al., 2018a) and DAS surface seismic (Urosevic et al., 2018, 2019) methods have been attempted, using both standard and HWC fibers (Bellefleur et al., 2018, 2020; Urosevic et al., 2018, 2019) to image subsurface geological structures associated with mineral deposits at depths. Colocated DAS and geophones have been compared, calibrated, and validated (Bellefleur et al., 2018, Bona & Pevzner, 2018; Koivisto et al., 2018; Urosevic et al., 2018). DAS systems have been installed in mining areas to monitor activities related to mining (Cheng et al., 2015; Wang H. et al., 2017) and derive velocity structures by tomography for an active room-and-pillar mine (Wang H. et al., 2017; Wang, Fratta, Lord, et al., 2018; Wang, Zeng, Fratta, et al., 2018). Nesladek et al. (2017) conducted DAS experiments in an underground education mining center on a campus to compare and calibrate DAS and geophones for both research and education purposes. Table 17.9.2 lists 14 papers on DAS applications in mining and mineral exploration.

17.3.8. DAS Monitoring for Safety and Security

Pipeline leaks and damage by third-party intrusion present severe safety, economic, environmental, and reputational risks. DTS systems based on Raman/Brillouin scattering have been used to detect pipeline leakage by significant temperature changes (Frings & Walk, 2011; Tanimola & Hill, 2009). However, DAS systems based on Rayleigh backscattering apparently have an advantage over DTS since DAS systems are not only sensitive to sonic changes and the acoustic signatures generated by leaking fluid, but can also capture acoustic and vibration signals generated by third-party interference (Eisler & Lanan, 2012; Frings & Walk, 2011; Giunta et al., 2011; Idachaba et al., 2013; Tanimola & Hill, 2009; Williams J., 2012; Worsley et al., 2014). It has been demonstrated that DAS can detect and locate pipeline leakage with acoustic characterizations of leak-induced vibrations (Idachaba et al., 2013; Tanimola & Hill, 2009; Williams J., 2012) and monitor and record third-party interferences, such as construction activity, manual and excavator digging, hammer impacts and drilling/grinder on pipe shell, humans' walking, vehicle and helicopter driving through nearby storm thunders, and local earthquakes and teleseismic events (Audouin et al., 2014; Glisic & Yao, 2012; Giunta et al., 2011; Karrenbach, Cole, et al., 2017; Williams J., 2012). DAS systems are successfully installed to monitor the integrity and leakage of pipelines built above and on the ground (Audouin et al., 2014; Tanimola & Hill, 2009), buried underground (Baqué, 2016; Giunta et al., 2011; Williams J., 2012), and in arctic regions (Thodi et al., 2014), as well as in offshore and subsea environments (Cramer et al., 2014a; Eisler & Lanan, 2012; Garcia-Hernandez & Bennett, 2016). All successful examples of DAS applications in pipeline security and safety we cite here imply that it is possible to build virtual walls to monitor not only people walking on the surface but also people digging and walking through underground tunnels. Readers are encouraged to further read 31 papers and abstracts listed in Table 17.10.1 for more application examples on monitoring leakage and integrity of pipelines around the world.

In addition to detecting and monitoring pipeline leaks and damage in the oil and gas industry, DAS technologies are also utilized for monitoring infrastructure safety (Duckworth & Ku, 2013; Karrenbach, 2019a), detecting intrusion (Sahin et al., 2020; Williams J., 2017), monitoring geohazards, such as landslides (Arslan et al., 2015; Williams J., 2017), recording earthquakes (Karrenbach, 2019b), assessing highway healthy status (Zhao H. et al., 2018), safety monitoring for power cables (Cherukupalli & Anders, 2020), nuclear reactors (Parikh et al., 2019; Ray 2018), and other industry facilities (Kammerer & MacLaughlin, 2017; Ray et al., 2019; Stork et al., 2020). A snow-coupled DAS device was tested in an extremely cold condition (-70 °C) similar to that of arctic areas for intrusion detection of polar bears (Glaser et al., 2019). We have 14 papers and abstracts collected in Table 17.10.2 for readers as references on this topic of DAS monitoring for critical structures and facilities.

17.3.9. DAS for Near-Surface and Earthquake Seismology, Fault Characterization, and Deformation

DAS borehole and surface seismic field trials for near-surface seismological applications have been reported at a CCS site with a DAS cable built in a borehole (Daley et al., 2013), at an infrastructure test facility (Lancelle et al., 2014; Wang H. et al., 2014), at a university seismic test facility (Ajo-Franklin et al., 2015), and at CO_2 storage sites (Daley et al., 2013; Dou et al., 2016) with DAS cables buried in shallow trenches to prove the DAS concept and to characterize near-surface structures using both active sources (Baldwin et al., 2014; Daley et al., 2013) and ambient noise (Dou, Lindsey, et al., 2017; Martin et al., 2015; Zeng, Thurber, et al., 2017) with the MASW method. DAS systems were then quickly set up in permafrost (Ajo-Franklin et al., 2016; Martin et al., 2016), lake ice (Castongia et al., 2017), and glaciated terrain (Walter et al., 2020), as well as geothermal facilities (Feigl & PoroTomo Team, 2017; Jousset et al., 2017; Lord et al., 2016; Wang, Fratta, et al, 2018) to confirm the durable features of DAS systems under the extremely cold and hot conditions and to characterize near-surface structures in a permafrost area (Ajo-Franklin et al., 2016; Ajo-Franklin, Dou, et al., 2017; Lindsey, Dou, et al., 2017; Martin et al., 2016) and geothermal resource regions (Jousset et al., 2017; Lord et al., 2016; Thurber et al., 2017; Zeng, Thurber, et al., 2017). Time-lapse surface seismic DAS systems observe velocity slowdown during permafrost thaw (Ajo-Franklin, Dou, et al., 2017; Lindsey, Dou, et al., 2017) and by precipitation (Kasahara, Hasada, & Yamaguchi, 2018; Kasahara, Hasada, Kawashima, et al., 2018). Currently, numerous DAS surveys aim to characterize and image near-surface structures with active and passive sources, as well as ambient and traffic noise have been conducted around the world (Costley, Galan-Comas, Hathaway, et al., 2018; Costley, Galan-Comas, Kirkendall, et al., 2018; Fratta et al., 2017; Jousset et al., 2018; Paitz & Fichtner, 2017; Pevzner, Gurevich, et al., 2018; Raab et al., 2017; Rodríguez-Tribaldos 2018; Shragge et al., 2019; Zhang Z. et al., 2019a).

In view of borehole seismic DAS being successfully used to detect and locate tiny microearthquakes with negative magnitudes induced by fracturing in the unconventional oil and gas industry (e.g., Lowe et al., 2013; MacPhail et al., 2012; Molenaar, Hill, & Koelman, 2011; Molenaar & Cox, 2013; Webster, Cox, et al., 2013), DAS systems have been quickly applied to detect and record earthquakes (e.g., Ajo-Franklin, Lindsey, et al., 2017; Ajo-Franklin et al., 2019; Biondi et al., 2017; Fernández-Ruiz, Magalhaes, et al., 2019; Fernández-Ruiz et al., 2020; Jousset et al., 2017, 2018; Karrenbach, Cole, et al., 2017; Lellouch. Spica, et al., 2019; Lellouch, Yuan, Ellsworth, Biondi, 2019; Lellouch, Yuan, et al., 2019a,d,e; Li Z. & Zhan, 2018; Lindsey, Martin, et al., 2017; Lindsey, 2018b; Marra et al., 2018; Martin, Biondi, Yuan, et al., 2017; Mellors, Gok, et al., 2019; Sladen et al., 2019; Wang, Zeng, Fratta, et al., 2018; Wang, Zeng, Miller, et al., 2018; Williams, E. F., Yu C. et al., 2019) and explosions (e.g., Abbott et al., 2018; Ford et al. 2020; Holland et al., 2019; Mellors et al., 2014, 2020; Young et al., 2020) for seismological studies. DAS arrays were set up in a university campus (Biondi et al., 2017; Huot et al., 2017; Li Z. et al., 2019;

Martin, Biondi, Yuan, et al., 2017; Sullivan, 2018; Zhan Z., 2018; Trainor-Guitton, Titov, et al., 2019; Wang X. et al., 2020; Zhu, Martin, et al., 2020; Zhu, Junzhu Shen, et al., 2020) with fibers in existing telecommunication conduits and at other important sites in cities (Fang et al., 2018, 2020; Rodríguez-Tribaldos et al., 2020; Smolinski et al., 2020; Spica et al., 2020; Vandeweijer et al., 2018; Williams, E. F., Zhan, et al., 2019; Zhao Y. et al., 2019) to monitor teleseismicity, as well as local and regional seismicity, and to characterize shallow subsurface structures for unban seismology studies (Beroza et al., 2020; Díaz et al., 2017; Krawczyk et al., 2019). Apertures of DAS arrays range from campus sizes of a few kilometers (Biondi et al., 2017; Nesladek et al., 2017; Zhan Z., 2018; Trainor-Guitton, Titov, et al., 2019; Zhu, Martin, et al., 2020), to 300 km pipeline DAS arrays (Karrenbach, Cole, et al., 2017; Williams J., 2017), to a few tens of thousands of kilometers "dark fiber" arrays on land and submarine seafloor (Ajo-Franklin, Lindsey, et al., 2017; Ajo-Franklin et al., 2019; Marra et al., 2018; Sladen et al., 2019; Williams, E. F., Fernández-Ruiz, Magalhaes, et al., 2019). All of these DAS arrays with different scales will compose a new generation of global seismic antenna networks (Wang H. et al., 2019; Zhan Z., 2019) to monitor global seismic activities and related geohazards. Various DAS arrays have dual roles in monitoring seismicity and characterizing near-surface structures (Ajo-Franklin, Lindsey, et al., 2017; Ajo-Franklin et al., 2019) with active and passive sources and noise (Martin, Castillo, Cole, et al., 2017). DAS methods have also been applied for soil wetness characterization (Ciocca et al., 2017), traffic monitoring (Fratta et al., 2017; Fratta, 2018), thunder quake detection and location (Zhu & Stensrud, 2020), and aftershock monitoring following the 2019 Ridgecrest M7.1 earthquake (Yang Y. et al., 2020). We collected 129 papers and abstracts on DAS seismology topics in Table 17.11.1 for further reading.

DAS methods have also been applied to monitor strain and its variations at magmatic areas (Jousset et al., 2016), in a borehole at the San Andreas Fault Observatory (Ellsworth et al., 2017), in underground facilities (Kammerer & MacLaughlin, 2017), on the seafloors (Zumberge et al., 2018), for water migration (Becker et al., 2018b; Zhang Y. & Xue, 2019), and Earth solid tides (Becker & Coleman, 2019b). DAS surface and borehole seismic techniques have been used to monitor seafloor faults (Gutscher et al., 2017, 2019) and to image and characterize various faults onshore, on seafloor, and in geothermal areas (Ajo-Franklin et al., 2020; Broderick et al., 2019; Constantinou, Schmitt, et al., 2016; Lay et al., 2020; Lindsey, Dawe, & Ajo-franklin, 2019; Trainor-Guitton, Jreij, et al., 2018; Trainor-Guitton, Guitton, et al., 2019). Table 17.11.2 lists 19 papers and abstracts on this DAS strain and deformation topic for readers as reference.

17.3.10. DAS Data Management, Processing, and Machine Learning

Many successful DAS geophysical deployments accumulate huge volumes of data rapidly and force geophysicists and engineers to inevitably face the tremendous challenge of up to PB (petabyte) scale "big data" storage and analysis (Richards et al., 2015; Bello et al., 2017; Clements et al., 2019; Dou, Wood, et al., 2017; Huot, Martin, et al., 2018; Martins et al., 2017). Dou, Wood, et al. (2017) reported their efforts to manage and continuously process DAS seismic monitoring data that accumulated at rates of terabyte/day. They emphasized data management and processing components and explored improved DAS data file structures and data compression schemes to optimize the use of disk space and network bandwidth. Although cloud systems (Le Calvez, & Cuny, 2019; Richards et al., 2015; Williams, M. J., Yang X. et al., 2019; Yang L. et al., 2018) provide sufficient storage and computational ability, new data compression approaches (Cheng D. et al., 2019; Martin, Huot et al, 2018; Martin, 2019; Muir & Zhan, 2017; Wilson et al., 2019) have been explored to reduce the size of raw and processed DAS and to optimize DAS data storage, management, exchange, and public distribution (Chad Trabant, 2018; Dou, Wood, et al., 2017).

Borehole and surface DAS data can be processed by adopting conventional surface seismic and VSP processing workflows. DAS processing approaches mentioned here will deal directly with issues special for DAS surveys only. The signal obtained from DAS systems is a distributed measurement over a length of fiber, which is referred to as the gauge length (Dean, Cuny, et al., 2015). The gauge length is one important acquisition parameter that will be a tradeoff between spatial resolution and SNR. Some efforts were taken to optimize gauge lengths to satisfy different DAS survey requirements (Costley et al., 2019; Dean et al., 2017; LeBlanc et al., 2018). Cuny et al. (2020) proposed a variable gauge length method to maximize DAS SNR with acceptable ranges of spatial resolution. Researchers (Chen, J. et al., 2018; Williams M. et al., 2017; Willis et al., 2019; Yu G. et al., 2016a; Yu, Z. et al., 2017) developed methods to reduce DAS noise caused by bad coupling. Martin, Huot, et al. (2018) introduced a machine learning (ML) method for unsupervised clustering ambient noise recorded by a DAS array and to improve convergence of coherent signals extracted from noise throughout the DAS array. ML approaches were quickly adopted to process DAS data for different geophysical applications (Alkhalaf et al., 2019; Huot, Biondi, et al., 2018; Huot, Martin, et al., 2018; Jreij, Trainor-Guitton, & Simmons, 2018; Park et al., 2018; Parkhonyuk et al., 2018; Sahin et al., 2020; Shiloh et al., 2018; Sherman et al., 2019; Tejedor et al., 2017; Zheng et al., 2019). We compile 43 papers and abstracts in Table 17.12 as further reading materials for readers who are interested in DAS data exchange, management, processing, and ML.

17.4. SOME THOUGHTS ON RECENT ADVANCES AND FUTURE APPLICATIONS

DAS applications in geophysics are one of the fastest growing frontiers in FOS technologies. It is believed that mutual effective communications between scientists and engineers working on DAS in both academia and industry will advance DAS geophysical applications. The 2017 AGU Fall Meeting joint sessions on DAS techniques, the recently established DAS research coordination network (DAS-RCN) funded by the National Science Foundation, as well as the publication of this AGU DAS monograph are parts of the efforts to promote DAS geophysical applications. To initiate such dialog, we would like to share a range of ideas and questions to promote the next steps within the research community.

Currently, most of the comparison and calibration tests in DAS-VSP applications compare DAS data with the vertical component of geophone data only. One direction worth considering would be a more detailed comparison to rotated 3C geophone data, particularly to understand the nature of shear coupling. Because the fiber response directivities to incident *P* and *S* waves are so different, comparing the rotated 3C geophone data with DAS data will help us better understand *P*- and *S*-wave velocity profiles obtained by DAS-VSP acquisitions (e.g., Martinez et al., 2020; Miller et al., 2012; Willis, Ellmauthaler, et al., 2016; Wu X. et al., 2017). DAS directivity is a disadvantage because it distorts DAS signal amplitudes, but some special geometry of a DAS seismic network can naturally separate *P*- and *S*-wave recordings of earthquakes by orthogonal fiber lines (e.g., Biondi et al., 2017). If a few campus DAS arrays are available in a region, can amplitude ratio of *S* and *P* waves from local earthquakes be used to constrain their focal mechanisms?

Microseismic events recorded by DAS in "L"-shaped wells also show strong directivities for both *P* and *S* waves from microearthquakes induced by hydraulic fracturing (Baird et al., 2019, 2020; Cole & Karrenbach, 2016; Cole, Karrenbach, Kahn, et al., 2018; Farhadiroushan, 2016, 2018; Hull et al., 2017; Kahn et al., 2017; Karrenbach, Ridge, et al., 2017; Karrenbach, Kahn, et al., 2017; Karrenbach, Cole, Ridge, et al., 2019; Longston et al., 2019; Molteni, Williams, et al., 2016; Richter et al., 2019b; Webster, Wall, et al., 2013; Webster, 2016; Williams A., et al., 2017; Verdon et al., 2020). A potential topic ripe for future exploration is the optimization of DAS arrays to better utilize this directivity to (a) recover the true multicomponent wavefield and (b) optimize detection and discrimination of distant seismic events. Karrenbach, Ridge, et al. (2017), Karrenbach, Kahn, et al. (2017), Karrenbach et al. (2019), and Karrenbach & Cole (2019) reported comprehensive and integrated studies for microseismic event locations and source mechanisms to characterize hydraulic fractures. In addition to these efforts, some mature seismological methods, such as relative event locations with correlation, rupture direction, and length based on source time function analysis, and stress drops of the microearthquakes induced by fracturing, may be useful to reveal fracture geometries and stress fields associated with fracturing treatments. Joint tomography inversion for both event locations and velocity structures may help us understand structure variations caused by different fracturing stages.

3-D and 4-D DAS-VSP surveys in deepwater environments have been used to image complex 3-D subsurface structures and monitor reservoir variations to optimally manage production because of the technical and economic advantages of DAS technology. Multiple-well DAS data acquired with channels in water and shallow sediments near the ocean bottom are very noisy because of water currents, casing resonance, and noise associated with production activities. It has been shown that the DAS with MASW method can derive *S*-wave profile for shallow structure using active and passive sources, as well as ambient and traffic noise (e.g., Ajo-Franklin, Lindsey, et al., 2017; Baldwin et al., 2014; Dou, Lindsey, et al., 2017; Lancelle et al., 2014, Martin et al., 2015; Zeng, Thurber, et al., 2017; Zeng, Lancelle, et al., 2017). However, there is no such attempt so far to apply the MASW method to marine DAS data for deriving *S*-wave profiles of shallow structures near the ocean bottom, which is important for mitigating shallow hazards in selecting drill spots.

Processing marine 3-D/4-D DAS-VSP data involves diagnosing and updating the velocity model with travel time tomography and migrating reflected waves to obtain subsurface structures. It has been suggested that updating velocity models with large DAS data sets will significantly improve the quality of migration images of subsurface structures for both DAS-VSP data and OBS surface seismic data (e.g., Li, Wu, et al., 2015; Wong et al., 2015; Wu et al., 2014, 2015; Zhan G. et al., 2015, 2016). Zdraveva et al. (2018) tested the joint inversion of both surface seismic and conventional 3-D VSP data to significantly improve the accuracy of the velocity model and quality of the migration images. We believe that multiple-well DAS-VSP first arrival and reflection data, OBS data, and even future DAS data from fibers installed on the seafloor should also be incorporated in joint inversion to update 3-D velocity models to improve migration images of subsurface structures. The marine DAS-VSP processing method with velocity diagnosis/update procedure can be adopted to process 3-D/4-D land DAS data to monitor CO_2 injection and seismic, geothermal, and mineral exploration.

DAS systems connected with existing cables (dark fibers) enable the monitoring and characterization of active seafloor faults (Ajo-Franklin et al., 2020; Gutscher et al., 2017, 2019; Lindsey, Dawe, & Ajo-franklin, 2019; Lindsey, Ajo-Franklin, et al. 2020) and faults on land (Ellsworth et al., 2017; Lay et al., 2020). It has been demonstrated that DAS systems can also record offshore tidal effects (Zumberge et al., 2018) and Earth solid tides (Becker & Coleman, 2019b). When a DAS system is set up with dark fibers along a fault in an earthquake-prone area, such as the San Andreas (Ellsworth et al., 2017), it can monitor deformation of faults and associated seismic activities to complement current GPS and seismic networks in the area. DAS seismic networks have been developed very quickly, from campus size DAS arrays in cities of a few kilometers with existing campus telecommunication fibers (Biondi et al., 2017; Li Z. et al., 2019; Lindsey, Martin, et al., 2017; Trainor-Guitton, Titov, et al., 2019; Zhan Z., 2018; Zhu, Martin, et al., 2020), to DAS arrays with submarine cables of less than 100 km (Ajo-Franklin et al., 2020; Lindsey, Dawe, & Ajo-franklin, 2019; Marra et al., 2018; Williams, E. F., Fernández-Ruiz, Magalhaes, et al., 2019), to pipeline DAS arrays with a length of a few hundred kilometers for pipeline safety and security (Karrenbach, Cole, et al., 2017), and to a 500 km terrestrial DAS array in Italy (Marra et al., 2018). Leveraging existing research test networks, such as the Department of Energy's Dark Fiber Test Bed (Ajo-Franklin, Lindsey, et al., 2017; Ajo-Franklin et al., 2019), provides even greater reach and fiber availability. The rapidly growing DAS seismic networks are expected to extend globally in the near future to use existing and planned submarine telecommunication infrastructure (Marra et al., 2018; Fernández-Ruiz et al., 2020), terrestrial "dark fibers" (Ajo-Franklin et al., 2019), and over 32,000 km pipeline DAS arrays (Williams J., 2017) around the world. The global DAS seismic networks could potentially be developed as an earthquake early warning system (Karrenbach, Cole, et al., 2017). The sharing of pipeline DAS data with researchers and industry may present a challenge, but governments could provide effective policies to promote data sharing. In principle, there is a strong win-win case for such integration, since monitoring earthquake hazards to protect pipelines is one of the objectives for pipeline safety and security monitoring. Current DAS arrays are built with existing or abandoned fibers in a manner designed to reduce costs. However, built-for-purpose fiber networks may be required in the near future for special purposes, such as discriminating earthquakes from explosions; in these cases, radar antenna theory and processing methods, such as phased array radar, could be easily adopted for seismological DAS array studies.

With the rapid growth of DAS seismic array networks, our data analysis methods will require improvements to catch up on the resulting explosion of high spatial resolution seismic observations. If we have recordings of a large earthquake on a few DAS arrays with dimensions comparable to rupture length of the large earthquake, can we directly characterize the rupture process of the earthquake with an array beam forming analysis and processing? Can *P*- and *S*-wave separations by their directivities enable us to constraint earthquake source properties? Ajo-Franklin, Lindsey, et al. (2017) and Ajo-Franklin et al. (2019) pointed out that dark fiber DAS arrays have two major roles for broadband seismic detections, and near-surface characterization, particularly with the MASW method applied to DAS recordings from passive and active sources and ambient or traffic noise (e.g., Cole, Karrenbach, Gunn, et al., 2018; Martin, Castillo, Cole, et al., 2017), can derive shallow structure *S*-wave profile. Thus, this MASW-DAS method can be used to detect underground water levels and monitor the temporal variations of hydraulic features (e.g., Dou, Lindsey, et al., 2017; Rodriguez Tribaldos, 2019). In an earthquake-prone region, integration of DAS array observations on seismic activity increase, underground water variations, solid tide fluctuations, and accumulated strain and deformation of fault(s) may help us identify potential precursors, if they exist, before large magnitude earthquakes. If so-called "earth sound" and "earth temperature increase" indeed exist prior to an imminent large earthquake, DAS and DTS could be the most suitable instruments to detect them. We expect that integrated observations of DAS seismic arrays will greatly contribute to earthquake hazards' mitigation in the near future.

As DAS observation systems rapidly advance, dealing with massive data sets on the PB scale is inevitable. We must seek to enhance our DAS data management and processing capacity to effectively extract more useful geophysical information from DAS recordings of signals embedded within noise. Time-frequency (T-F) analysis should be one very powerful tool to analyze DAS geophysical data. Matching pursuit algorithms (Mallat & Zhang, Z., 1993) are one approach to T-F analysis methods, which could serve dual roles for both analyzing and compressing DAS data. Beyond signal extraction and compression approaches, new data product models should be developed to allow archiving the aspects of DAS data sets useful for each subcommunity. Successful methods in seismology should be adopted in energy exploration industries, especially in unconventional oil and gas business, and vice versa. Algorithms and methods to deal with special DAS issues, such as analysis and compensation of amplitude distortion by directivities, should be quickly developed by the DAS community. As a community, we have demonstrated success in developing DAS acquisition approaches over the past decade, but better solutions and demonstration of value across a diverse range of applications are still required.

17.5. CONCLUSION

DAS applications in geophysics have rapidly advanced over the last 10 years, as indicated by the increasing number and improved quality of papers published in scientific journals and conferences. We briefly review the historical development of qDAS and DAS technologies and their applications in geophysics with a compiled list of about 900+ papers and abstracts related to various DAS geophysical applications. We discuss some current issues and challenges in DAS technologies and make some expectations for some future development in DAS geophysical applications. We hope that readers, particularly early career scientists and engineers who are just entering in this new and rapidly growing field, will find the reading materials useful. Without encouragement, contribution, and support from colleagues and friends in the DAS communities and in the AGU Book Publication, publication of this monograph would not have been possible.

ACKNOWLEDGMENTS

The authors would like to thank AGU for supporting this monograph. The authors appreciate Ali Sayed and two anonymous reviewers for their detailed review and constructive comments and suggestions, which led to the improvement of this manuscript. The authors sincerely thank the team at Wiley, especially Dr. Rituparna Bose, Layla Harden, Noel McGlinchey, Vaishali Rajasekar, Bobby Kilshaw, and others, for their patience, kind help and assistance.

REFERENCES

Abbott, R. (2018). *Borehole DAS recordings of the DAG-1 chemical explosion*. Paper presented at AGU Workshop: Distributed Acoustic Sensing-Principles and Case Studies. Washington, D.C., USA.

Abbott, R. E., Knox, H. A., Mellors, R., Pitarka, A., & Matzel, E. (2018). *Downhole and surface fiber optic DAS recordings of a 1000 kg TNT-equivalent chemical explosion in alluvium*. Paper presented at SEG Postconvention Workshop W-20: DAS-Validating Measurements, Developing Processing Methods, *and Integrating to Optimize Velocity Models for Improving Subsurface Imaging*. Anaheim, CA, USA.

Abbott, R. E., Mellors, R. J., & Pitarka, A. (2019). *Distributed acoustic sensing observations and modeling of the DAG series of chemical explosions*. Seismological Society of America Annual Meeting, Abstract. Seattle, WA, USA.

Abdul Rahim, M. F., Ghazali, A. R., Hardy, R. J. J., Bourdon, L. M., El Kady, M. N., Muhammed, M. D. D., & Konuk, T. (2017). *Estimation of Anisotropy in the presence of gas cloud using 3D DAS VSP*. Asia Petroleum Geoscience Conference and Exhibition, Expanded Abstracts, 43580. https://doi.org/10.3997/2214-4609.201802854

Abdul Rahim, M. F., Hardy, R. J. J., Bourdon, L. M., Chavarria, J. A., Ghazali, A. R., Muhammed, M. D. D., et al. (2017). *Imaging beneath shallow gas using DAS 3DVSP within active dual string producing wells*. 79th EAGE Conference and Exhibition, Expanded Abstracts, Tu P7 15. https://doi.org/10.3997/2214-4609.201701099

Abdul Rahim, M. F., Ghazali, A. R., & Davis, M. D. (2018). *Joint imaging Of 3D fiber optic DAS VSP And OBN to solve shallow gas cloud problem in Bokor Field Malaysia*. EAGE Conference on Reservoir Geoscience, Expanded Abstracts, 145. https://doi.org/10.3997/2214-4609.201803225

Ajo-Franklin, J., Lindsey, N., Dou, S., Daley, T. M., Freifeld, B., Martin, E. R., et al. (2015). *A field test of distributed acoustic sensing for ambient noise recording*. 85th SEG Annual International Meeting, Expanded Abstracts (pp. 2620–2624). https://doi.org/10.1190/segam2015-5926936.1

Ajo-Franklin, J., Wagner, A., Lindsey, N., Dou, S., Martin, E., Daley, T., et al. (2016). *Using distributed fiber-optic methods to track a changing landscape: combining DAS tomography, DSS, & DTS for timelapse permafrost monitoring*. Paper presented at SEG Postconvention workshop W-10: Fiber-optic Sensing for Exploration and Monitoring: Development, Applications, *and Challenges*. Dallas, TX, USA.

Ajo-Franklin, J. B., Dou, S., Daley, T., Freifeld, B., Robertson, M., Ulrich, C., et al. (2017). *Time-lapse surface wave monitoring of permafrost thaw using distributed acoustic sensing and a permanent automated seismic source*. 87th SEG Annual International Meeting, Expanded Abstracts (pp. 5223–5227). https://doi.org/10.1190/segam2017-17774027.1

Ajo-Franklin, J. B., Lindsey, N., Dou, S., Freifeld, B. M., Daley, T. M., Tracy, C., & Monga, I. (2017). *Dark fiber and distributed acoustic sensing: Applications to monitoring seismicity and near-surface properties. AGU Fall Meeting Abstract S33B-2384*.

Ajo-Franklin, J. B., Dou, S., Lindsey, N. J., Monga, I., Tracy, C., Robertson, M., et al. (2019). Distributed acoustic sensing using dark fiber for near-surface characterization and broadband seismic event detection. *Scientific Reports*, 9(1), 1328, https://doi.org/10.1038/s41598-018-36675-8

Ajo-Franklin, J. B., Cheng, F., Shang, Y., Lindsey, N. J., & Dawe, C. (2020). *Utilizing distributed acoustic sensing and ocean bottom fiber optic cables for fault zone characterization*. Seismological Society of America Annual Meeting, *Abstract*. Albuquerque, NM, USA.

Al Adawi, R., Rocco, G., Al Busaidi. S., Al Maamari, A., Salah Al Ghafri, S., Kiyashchenko, D., et al. (2013). *Seismic* *reservoir monitoring of a thermal EOR redevelopment; Thick heavy oil field in Oman*. SPE Middle East Oil and Gas Show and Conference, SPE-164353-MS. https://doi.org/10.2118/164353-MS

Al Shoaibi, S., Kechichian, J., Mjeni, R., Al Rajhi, S., Bakker, G. G., Hemink, G., & Freeman, F. (2016). *Implementing fiber optics distributed sensing as a key surveillance tool*. Abu Dhabi International Petroleum Exhibition & Conference, SPE-183535-MS. https://doi.org/10.2118/183535-MS

Alabri, S. (2015). *Processing 8 Wells DAS 3D VSP from South of Oman*. 3rd EAGE Workshop on Borehole Geophysics. Expanded Abstracts, BG24. https://doi.org/10.3997/2214-4609.201412203

Alajmi, M. S., Pevzner, R., Alkhalifah, T., Qadrouh, A. N., Almalki, M., & Alonaizi, F. A. (2019). *Trialling distributed acoustic sensing in a sand dune environment*. ASEG Extended Abstracts. https://doi.org/10.1080/22020586.2019.12073099

Alajmi, M., Pevzner, R., Alkhalifah, T., Qadrouh, A. N., *Almalki*, M., & Alzahrani, E. (2020). Characterization of *Sand dunes near surface structures using distributed acoustic sensing*. First EAGE Workshop on Fibre Optic Sensing, Expended Abstract. https://doi.org/10.3997/2214-4609.202030036

Alcantara Santos, O. L. (2020). Technology focus: Well integrity. *Journal of Petroleum Technology*, 72(01). 63. https://doi.org/10.2118/0120-0063-JPT

Aldawood, A., Silvestrov, I., & Dmitriev, M. (2018). *Velocity estimation and imaging using walkaway DAS VSP acquired with carbon rod*. International Petroleum Technology Conference IPTC 2018, IPTC-19525-MS

Aldawood, A., Alfataierge E., & Bakulin, A. (2020). *Introducing a New DAS test facility for evaluating emerging DAS technologies*. First EAGE Workshop on Fibre Optic Sensing, Expended Abstract. https://doi.org/10.3997/2214-4609.202030021

Alfataierge, E., Dyaur, N., Ho, M., & Stewart, R. R. (2018). *Fiber-optic motion sensing for marine VSP, monitoring, and communication: A comparison of DAS, FBG, and hydrophone sensors*. Abstract. Presented at SEG Summer Research Workshop: Recent Advances and Applications in Borehole Geophysics. Galveston, TX, USA.

Alfataierge, E., Dyaur, N., Li, C., & Stewart, R. R. (2019). *Marine seismic source characterization using fiber optic sensors*. Offshore Technology Conference, OTC-29267-MS. https://doi.org/10.4043/29267-MS

Alfataierge, E., Dyaur, N., & Stewart, R. R. (2019). *Measuring flow in pipelines via FBG and DAS fiber optic sensors*. Offshore Technology Conference, OTC-29433-MS. https://doi.org/10.4043/29433-MS

Al-Hinai, S. M., Tromp, J. P., Al Manahali, M. O., Belghache, A., Koning, M., Al Rabaani, A. O., et al. (2014). *Maximising steam project value in South Oman through flexible development phasing and integrated reservoir surveillance*. SPE EOR Conference at Oil and Gas West Asia, SPE-169678-MS. https://doi.org/10.2118/169678-MS

Alkhalaf, M., Hveding, F., & Arsalan, M. (2019). *Machine learning approach to classify water cut measurements using DAS fiber optic data*. Abu Dhabi International Petroleum Exhibition & Conference, SPE-197349-MS. https://doi.org/10.2118/197349-MS

Allanic, C. (2012). *Overview of optical distributed sensing for reservoir monitoring in TOTAL E&P*. Abu Dhabi International Petroleum Conference and Exhibition, SPE-161609-MS. https://doi.org/10.2118/161609-MS

Allanic, C., Frangeul, J., Liebeck, M., Carbonnier, B., Naldrett, G. J., Farhadiroushan, M., & Clarke, A. (2013). *Distributed acoustic sensing for ESP understanding and surveillance*. SPE Middle East Intelligent Energy Conference and Exhibition, SPE-167501-MS. https://doi.org/10.2118/167501-MS

Allwood, G., Wild, G., & Hinckley, S. (2017). Fiber Bragg grating sensors for mainstream industrial processes. *Electronics*, 6 (4), 92. https://doi.org/10.3390/electronics6040092

Almarzoug, M., Alshuhail, A., & Aldawood, A. (2019). *Improving signal-to-noise ratio of distributed acoustic sensing data via super-virtual refraction interferometry*. 81st EAGE Conference and Exhibition, Expanded Abstracts, We_P10_01. https://doi.org/10.3997/2214-4609.201901122

Alrashed, A., Miskimins, J., & Tura, A. (2019). *Optimization of hydraulic fracture spacing through the investigation of stress shadowing and reservoir lateral heterogeneity*. SPE Middle East Oil and Gas Show and Conference, SPE-195071-MS. https://doi.org/10.2118/195071-MS

Alshuhail, A., Silvestrov, I., Aldawood, A., Bakulin, A., & Alawaji, M. (2019). *Near-surface characterization using vertical array seismic data from smart DAS upholes*. 89th SEG Annual International Meeting, Expanded Abstracts (pp. 2893–2897). https://doi.org/10.1190/segam2019-3215594.1

An, S., Li, X., Wu, J., Wang, S., W. Su, W., Kong, F., et al. (2020). Industrial application of DAS technique in uphole survey. First EAGE Workshop on Fibre Optic Sensing, Expended Abstract. https://doi.org/10.3997/2214-4609.202030038

Anifowoshe, O., Yates, M., Xu, L., Dickenson, P., Akin, J., Carney, B. J., et al. (2016). *Improving wellbore stimulation coverage in the Marcellus: Integrating lateral measurements with enhanced engineered completion design and fiber optic evaluation*. SPE Eastern Regional Meeting, *SPE-184051-MS*. https://doi.org/10.2118/184051-MS

Ansari, R. Z., Himanshu Yadav, H., Thiruvenkatanathan, P., Zett, A., Spain, D. R., & Gysen, A. (2014). *Advanced petrophysical surveillance improves the understanding of well behavior in unconventional reservoirs*. SPE Annual Technical Conference and Exhibition, *SPE-170878-MS*. https://doi.org/10.2118/170878-MS

Arslan, A., Akgün, H., Koçkar, M. K., Eker, A. M., & Kelam, M. A. (2015). *Slope movement monitoring with optical fiber technology*. ISRM Regional Symposium—EUROC, *ISRM-EUROCK-2015-069*.

Attia, A., Brady, J., Lawrence, M., & Porter, R. (2019). *Validating refrac effectiveness with carbon rod conveyed distributed fiber optics in the Barnett shale for Devon energy*. SPE Hydraulic Fracturing Technology Conference and Exhibition, *SPE-194338-MS*. https://doi.org/10.2118/194338-MS

Audouin, G., Rupert, S., Popineau, D., & Minto, C. (2014). *An operator feedback on the installation of a pipeline intrusion detection system*. Abu Dhabi International Petroleum

Exhibition and Conference, *SPE-171738-MS*. https://doi.org/10.2118/171738-MS

Ay, E., Nigel Payne, N., Le Calvez, J., & Denaclara, H. (2017). *The value of microseismic monitoring and interpretation of microseismic event hypocenters—myths, misconceptions, realities, and opportunities*. Unconventional Resources Technology Conference, *URTEC-2671285-MS*. https://doi.org/10.15530/urtec-2017-2671285

Azad, A., Somanchi, K., Brewer, J. R., & Yang, D. (2017). *Accelerating completions concept select in unconventional plays using diagnostics and frac modeling*. SPE Hydraulic Fracturing Technology Conference and Exhibition, *SPE-184867-MS*. https://doi.org/10.2118/184867-MS

Baciu, C., Groen, L., Chai, C. F., van der Horst, J., Berlang, W., Franzen, A., et al. (2016). *Distributed acoustic sensing for day-to-day well reservoir and facility management*. SPE Intelligent Energy International Conference and Exhibition, *SPE-181095-MS*. https://doi.org/10.2118/181095-MS

Baihly, J. D., Wilson, C., Menkhaus, A., Ejofodomi, E., England, K., & Dickenson, P. (2015). *Fiber-optic revelations from a multistage openhole lateral fracturing treatment*. Unconventional Resources Technology Conference, *URTEC-2172404-MS*, https://doi.org/10.15530/URTEC-2015-2172404

Baird, A. (2020). *Modelling the response of helically wound DAS cables to microseismic arrivals*. First EAGE Workshop on Fibre Optic Sensing, Expended Abstract. https://doi.org/10.3997/2214-4609.202030019

Baird, A., Stork, A., Horne, S., Naldrett, G., Kendall, M., Wookey, J., et al. (2019). *Modelling of fibre-optic DAS response to microseismic arrivals in anisotropic media*. 81st EAGE Conference and Exhibition, Expanded Abstracts, *We_R09_08*. https://doi.org/10.3997/2214-4609.201901244

Baird, A. F., Stork, A. L., Horne, S. A., Naldrett, G., Kendall, J.-M., Wookey, J., et al. (2020). Characteristics of microseismic data recorded by distributed acoustic sensing systems in anisotropic media. *Geophysics, 85*(4), *KS139–KS147*. https://doi.org/10.1190/geo2019-0776.1

Baker, S. A. (2019). *Cutting through the FOG (fiberoptic geophysics) in Subsea Wells*. Paper presented at SEG Postconvention Workshop W-14: DAS Part2: What is next for DAS? *Operator needs versus Technology Suppliers' vision*. San Antonio, TX, USA.

Bakku, S. K., Wills, P., & Fehler, M. (2014). *Monitoring hydraulic fracturing using distributed acoustic sensing in a treatment well*. 84th SEG Annual International Meeting, *Expanded Abstract* (pp. 5003–5008). https://doi.org/10.1190/segam2014-1280.1

Bakku, S. K., Wills, P., Fehler, M., Mestayer, J., Mateeva, A., & Lopez, J. (2014). *Vertical seismic profiling using distributed acoustic sensing in a hydrofrac treatment well*. 84th SEG Annual International Meeting, *Expanded Abstract* (pp. 5024–5028). https://doi.org/10.1190/segam2014-1559.1

Bakulin, A., Golikov, P., Smith, R., Erickson, K., Silvestrov, I., & Al-Ali, M. (2017). Smart DAS upholes for simultaneous land near-surface characterization and subsurface imaging. *The Leading Edge*, 36, 1001–1008. https://doi.org/10.1190/tle36121001.1

Bakulin, A., Golikov, P., Erickson, K., Silvestrov, I., Kim, Y. S., Smith, R., & Al-Ali, M. (2018). *Seismic imaging of vertical array data acquired using smart DAS uphole acquisition system*. 88th SEG Annual International Meeting, *Expanded Abstracts* (pp. 4050–4054). https://doi.org/10.1190/segam2018-2995404.1

Bakulin, A., Golikov, P., Smith, R., Erickson, K., Silvestrov, I., & Al-Ali, M. (2018a). *Reflection seismic imaging using smart DAS upholes*. 80th EAGE Conference and Exhibition, Expended Abstracts, *Th* P7 12. https://doi.org/10.3997/2214-4609.201801626

Bakulin, A., Golikov, P., Smith, R., Erickson, K., Silvestrov, I., & Al-Ali, M. (2018b). *Advances in near-surface characterization and deep imaging with smart DAS upholes*. SPE Kingdom of Saudi Arabia Annual Technical Symposium and Exhibition, *SPE-192310-MS*. https://doi.org/10.2118/192310-MS

Bakulin, A., Golikov, P., Smith, R., Erickson, K., Silvestrov, I., & Al-Ali, M. (2018c). *Smart DAS uphole acquisition system for near-surface characterization and imaging*. 88th SEG Annual International Meeting, *Expanded Abstracts* (pp. 201–205). https://doi.org/10.1190/segam2018-2995883.1

Bakulin, A., Silvestrov, I., Golikov, P., Erickson, K., Kim, Y. S., Smith, R., & Al-Ali, M. (2018). *Simultaneous near-surface model building and deep reflection imaging using smart DAS uphole acquisition system*. Presented at SEG Postconvention Workshop W-20: DAS-Validating Measurements, Developing Processing Methods, *and Integrating to Optimize Velocity Models for Improving Subsurface Imaging*. Anaheim, CA, USA.

Bakulin, A., Silvestrov, I., & Pevzner, R. (2018). *Surface seismic with DAS: Looking deep and shallow at the same time*. 88th SEG Annual International Meeting, *Expanded Abstracts* (pp. 16–20). https://doi.org/10.1190/segam2018-2995870.1

Bakulin, A., Silvestrov, I., & Alshuhail, A. (2019). *Simultaneous acquisition of surface seismic and vertical DAS arrays reduces structural uncertainty for subtle exploration targets*. Paper presented at SEG Postconvention Workshop W-14: DAS Part2: What is next for DAS? *Operator needs versus Technology Suppliers' vision*. San Antonio, TX, USA.

Bakulin, A., Silvestrov, I., & Pevzner, R. (2019). *Surface seismic with DAS changes land acquisition*. SPE Middle East Oil and Gas Show and Conference, *SPE-194950-MS*. https://doi.org/10.2118/194950-MS

Baldwin, C. S. (2015). *Applications for fiber optic sensing in the upstream oil and gas industry*. Proceedings of SPIE 9480, *Fiber Optic Sensors and Applications* XII, 94800D. https://doi.org/10.1117/12.2176226

Baldwin, J. A., Fratta, D., Wang, H. F., Lord, N. E., Chalari, A., Karaulanov, R., et al. (2014). *Using Distributed Acoustic Sensing (DAS) for Multichannel Analysis of Surface Waves (MASW) to evaluate ground stiffness*. Paper presented at the 2014 AGU Fall Meeting, San Francisco, CA, USA. Abstract, *NS31C-3938*.

Ball, M., Mathieson, A., & Soulas, S. (2017). *The evolution of life of field seismic data on the clair field*. 1st EAGE Workshop on Practical Reservoir Monitoring, Expanded Abstracts, We PRM 09. https://doi.org/10.3997/2214-4609.201700018

Banack, B., Burke, L. H., Booy, D., Chineme, E., Lastiwka, M., Gaviria, F., et al. (2019). *Characterization of flow control* *device performance with distributed fiber-optic sensors*. SPE Annual Technical Conference and Exhibition, *SPE-195869-MS*. https://doi.org/10.2118/195869-MS

Baqué, M. (2016). *Fiber optic leak detection FOLD project*. Abu Dhabi International Petroleum Exhibition & Conference, *SPE-183137-MS*. https://doi.org/10.2118/183137-MS

Baqué, M. (2017). *Early gas leak detection EGLD*. Abu Dhabi International Petroleum Exhibition & Conference, *SPE-188669-MS*. https://doi.org/10.2118/188669-MS

Barberan, C., Allanic, C., Avila, D., Hy-Billiot, J., Hartog, A., Frignet, B., & Lees, G. (2012). *Multi-offset seismic acquisition using optical fiber behind tubing*. 74th EAGE Conference and Exhibition, *Expanded Abstracts*, Y003. https://doi.org/10.3997/2214-4609.20148798

Barfoot, D. (2013). *Efficient vertical seismic profiling using fiber-optic distributed acoustic sensing and real-time processing*. 2nd EAGE Borehole Geophysics Workshop, Extended Abstracts, *BG06*. https://doi.org/10.3997/2214-4609.20142554

Barrias, A., Casas, J. R., & Villalba, S. (2016). A review of distributed optical fiber sensors for civil engineering applications. *Sensors (Basel)*, 16(5). 748. https://doi.org/10.3390/s16050748

Bateman, K., Molenaar, M. M., & Brown, M. D. (2013). *Lessons learned from Shell's history of casing conveyed fiber optic deployment*. SPE Unconventional Resources Conference, *SPE-167211-MS*. https://doi.org/10.2118/167211-MS

Bazyrov, I., Galeev, R., Ipatov, A., Kayeshkov, I., Simakov, S., Fayzullin, I., et al. (2019). *Dynamic control of the efficiency of waterflooding of low-permeability reservoirs by horizontal injection wells with transverse multi-stage hydraulic fractures*. SPE Russian Petroleum Technology Conference, *SPE-196739-MS*. https://doi.org/10.2118/196739-MS

Becker, M., Cole, M., Ciervo, C., Coleman, T., & Mondanos, M. (2016a). *Measuring hydraulic connection in fractured bedrock with periodic hydraulic tests and distributed acoustic sensing*. 41st Workshop on Geothermal Reservoir Engineering, PROCEEDINGS, *SGP-TR-209*. 372–382.

Becker, M., Cole, M., Ciervo, C., Coleman, T., & Mondanos, M. (2016b). *Measuring hydraulic connection in fractured bedrock with periodic hydraulic tests and distributed acoustic sensing*. Presented at SEG Postconvention workshop W-10: Fiber-optic Sensing for Exploration and Monitoring: Development, Applications, *and Challenges*. Dallas, TX, USA.

Becker, M., Coleman, T., Ciervo, C., Cole, M., & Mondanos, M. (2017a). Fluid pressure sensing with fiber-optic distributed acoustic sensing. *The Leading Edge* 36.1018–1023. https://doi.org/10.1190/tle36121018.1

Becker, M., Ciervo, C., Cole, M., Coleman, T., & Mondanos, M. (2017a). Fracture hydromechanical response measured by fiber optic distributed acoustic sensing at milli-Hertz frequencies. *Geophysical Research Letters*, 44, 7295–7302. https://doi.org/10.1002/2017GL073931

Becker, M. (2018). *Hydrologic applications of low-frequency DAS*. Paper presented at AGU Workshop: Distributed Acoustic Sensing-Principles and Case Studies. Washington, D.C., *USA*.

Becker, M., Ciervo, C., & Coleman, T. (2018a). *A slimhole approach to measuring distributed hydromechanical strain in fractured geothermal reservoirs*. 43rd Workshop on Geothermal Reservoir Engineering, Proceedings, *SGP-TR-213*. 1–8.

Becker, M., Ciervo, C., & Coleman, T. (2018b). *Laboratory testing of low-frequency strain measured by distributed acoustic sensing (DAS)*. 88th SEG Annual International Meeting, *Expanded Abstracts* (pp. 4963–4966). https://doi.org/10.1190/segam2018-2997900.1

Becker, M., & Coleman, T. (2019a). *Ultra-low frequency strain measurements with Distributed Acoustic Sensing (DAS)*. SAGEEP—32nd Annual Symposium on the Application of Geophysics to Engineering and Environmental Problems, *Expanded Abstracts*.

Becker, M., & Coleman, T. (2019b). Distributed acoustic sensing of strain at Earth tide frequencies. *Sensors*, 19(9), 1975, 1–9. https://doi.org/10.3390/s19091975

Bellefleur, G., Schetselaar, E., Wade, D., & White, D. (2018). *VSP using distributed acoustic sensing with scatter-enhanced fibre-optic cable at the New Afton porphyry deposit, Canada*. 2nd Conference on Geophysics for Mineral Exploration and Mining, Expanded Abstracts, Tu 2MIN P05. https://doi.org/10.3997/2214-4609.201802717

Bellefleur, G., Schetselaar, E., Wade, D., White, D., Enkin, R., & Schmitt, D. R. (2020). Vertical seismic profiling using distributed acoustic sensing with scatter-enhanced fibre-optic cable at the Cu–Au New Afton porphyry deposit, British Columbia, Canada. *Geophysical Prospecting*, 68(1), 313–333. https://doi.org/10.1111/1365-2478.12828

Bello, O., Yang, D., Lazarus, S., Wang, X. S., & Denney, T. (2017). *Next generation downhole big data platform for dynamic data-driven well and reservoir management*. SPE Reservoir Characterisation and Simulation Conference and Exhibition, *SPE-186033-MS*. https://doi.org/10.2118/186033-MS

Bello, O., Bale, D. S., Yang, L., Yang, D., Kb, A., Lajith, M., & Lazarus, S. (2018). *Integrating downhole temperature sensing datasets and visual analytics for improved gas lift well surveillance*. SPE Annual Technical Conference and Exhibition, *SPE-191626-MS*. https://doi.org/10.2118/191626-MS

Berlang, W. (2019). *The value proposition of DAS/DTS (DxS) across the life cycle of a field*. Paper presented at SEG Postconvention Workshop W-14: DAS Part2: What is next for DAS? *Operator needs versus Technology Suppliers' vision*. San Antonio, TX, USA.

Bernard, P., Plantier, G., Brunet, C., Nercessian, A., Sourice, A., Feuilloy, M., et al. (2017). *The LINES high resolution optical seismometer*. EAGE/DGG Workshop on Fibre Optic Technology in Geophysics, Expended Abstracts, Fr SR P06. https://doi.org/10.3997/2214-4609.201700166

Beroza, G. C., Spica, Z. J., Perton, M., Martin, E. R., & Biondi, B. (2020). *Urban seismic site characterization with fiber-optic seismology*. Seismological Society of America Annual Meeting, *Abstract*. Albuquerque, NM, USA.

Berry, S., Cooper, G., Webster, M., & Gysen, A. (2017). *Optical fibre enabled slickline; Enhancing the quality of decision making through intelligent real time surveillance using distributed acoustic sensing and distributed temperature sensing*. SPE Offshore Europe Conference & Exhibition, *SPE-186144-MS*. https://doi.org/10.2118/186144-MS

Bettinelli, P., & Frignet, B. (2015). *Using optical fiber seismic acquisition for well-to-seismic tie at the Ketzin Pilot site (CO2Storage)*. 85th SEG Annual International Meeting, *Expanded Abstracts* (pp. 772–776). https://doi.org/10.1190/segam2015-5846235.1

Bettinelli, P., & Puech, J.-C. (2015). *New method of Q-factor estimation applied to optical fiber VSP data*. 85th SEG Annual International Meeting, *Expanded Abstracts* (pp. 747–751). https://doi.org/10.1190/segam2015-5800169.1

Bhatnagar, A. (2016). *Overcoming challenges in fracture stimulation through advanced fracture diagnostics*. SPE Asia Pacific Hydraulic Fracturing Conference, *SPE-181802-MS*. https://doi.org/10.2118/181802-MS

Binder, G. (2018). *Time-lapse seismic monitoring of individual hydraulic frac stages using a downhole DAS array*. Presented at AGU Workshop: Distributed Acoustic Sensing-Principles and Case Studies. Washington, D.C., *USA*.

Binder, G., Titov, A., Tamayo, D., Liu, Y., Simmons, J., Tura, A., et al. (2018). *Time lapse seismic monitoring of individual hydraulic frac stages using a downhole DAS array*. Presented at SEG Postconvention Workshop W-20: DAS-Validating Measurements, Developing Processing Methods, and Integrating to Optimize Velocity Models for Improving Subsurface Imaging. Anaheim, CA, USA.

Binder, G., Titov, A., Tamayo, D., Simmons, J., Tura, A., Byerley, G., & Monk, D. (2018a). *Time delays from stress-induced velocity changes around fractures in a time-lapse DAS VSP*. 88th SEG Annual International Meeting, *Expanded Abstracts* (pp. 5328–5332). https://doi.org/10.1190/segam2018-2998082.1

Binder, G., Titov, A., Tamayo, D., Simmons, J., Tura, A., Byerley, G., & Monk, D. (2018b). *Time lapse seismic monitoring of individual hydraulic frac stages using a downhole DAS array: Theoretical findings and full wavefield modeling*. Abstract. *Presented at SEG Summer Research Workshop: Recent Advances and Applications in Borehole Geophysics*. Galveston, TX, USA.

Binder, G., & Chakraborty, D. (2019). *Detecting microseismic events in downhole distributed acoustic sensing data using convolutional neural networks*. 89th SEG Annual International Meeting, *Expanded Abstracts* (pp. 4864–4868). https://doi.org/10.1190/segam2019-3214863.1

Binder, G., Titov, A., Tamayo, D., Simmons, J., Tura, A., Byerley, G., & Monk, D. (2019). *Time-lapse seismic monitoring of individual hydraulic frac stages using a downhole distributed acoustic sensing array*. SPE/AAPG/SEG Unconventional Resources Technology Conference, *URTEC-2019-409-MS*. https://doi.org/10.15530/urtec-2019-409

Biondi, B., Martin, E., Cole, S., Karrenbach, M., & Lindsey, N. (2017). *Earthquakes analysis using data recorded by the Stanford DAS array*. 87th SEG Annual International Meeting, *Expanded Abstracts* (pp. 2752–2756). https://doi.org/10.1190/segam2017-17745041.1

Blanco, J., Knudsen G. S., & Bostick, F. X. (2006). *Time-lapse VSP field test for gas reservoir monitoring using permanent fiber optic seismic system*. 76th SEG Annual International Meeting, *Expanded Abstract* (pp. 3447–3451). https://doi.org/10.1190/1.2370250.

Blount, C. G., Friehauf, K. E., Smith, B. E., Smith, D. P., Jaaskelainen, M., & Baldwin, C. S. (2015). Improving *Fiber-optic system reliability in permanent installations*. SPE Annual Technical Conference and Exhibition, *SPE-174928-MS*. https://doi.org/10.2118/174928-MS

Bona, A, & Pevzner, R. (2018). *Distributed acoustic sensing for mineral exploration: Case study*. *ASEG Extended Abstracts*. https://doi.org/10.1071/ASEG2018abW8_4F

Bona, A., Dean, T., Correa, J., Pevzner, R., Tertyshnikov, K., & Van Zaanen, L. (2017). *Amplitude and phase response of DAS receivers*. 79th EAGE Conference and Exhibition, Expanded Abstracts, We A5 13. https://doi.org/10.3997/2214-4609.201701200

Boone, K., Ridge, A., Crickmore, R., & Onen, D. (2014). Detecting *leaks in abandoned gas wells with fibre-optic distributed acoustic sensing*. International Petroleum Technology Conference, Expanded Abstract, *IPTC-17530-MS*. https://doi.org/10.2523/IPTC-17530-MS.

Boone, K., Crickmore, R., Werdeg, Z., Laing, C., & Molenaar, M. (2015). *Monitoring hydraulic fracturing operations using fiber-optic distributed acoustic sensing*. Unconventional Resources Technology Conference, *URTEC-2158449-MS*. https://doi.org/10.15530/URTEC-2015-2158449

Boone, K. (2016). *Locating perforations, plugs, orientation clamps and fractures; and supporting optimal control of hydraulic fracturing using DAS and DTS*. Paper presented at SEG Postconvention workshop W-10: Fiber-optic Sensing for Exploration and Monitoring: Development, Applications, *and Challenges*. Dallas, TX, USA.

Booth, A. D., Christoffersen, P., Schoonman, C., Clarke, A., Hubbard, B., Law, R., et al. (2020). *Distributed Acoustic Sensing (DAS) of seismic properties in a borehole drilled on a fast-flowing Greenlandic Outlet Glacier*. *Geophysical Research Letters*, Accepted. https://doi.org/10.1029/2020GL088148

Borland, W., Hearn, R., & Sayed, A. (2016). *Improving the acquisition efficiency of acquiring borehole seismic data by recording optical distributed acoustic data on a wireline hybrid electrooptical cable*. 86th SEG Annual International Meeting, *Expanded Abstracts* (pp. 800–804). https://doi.org/10.1190/segam2016-13951115.1

Borodin, I., & Segal, A. (2020). *Real-time hydraulic fracturing monitoring via distributed acoustic sensing (das) acquisition of pumping noise*. First EAGE Workshop on Fibre Optic Sensing, Expended Abstract. https://doi.org/10.3997/2214-4609.202030007

Bostick, F. X. (2000). *Field experimental results of three-component fiber-optic seismic sensors*. 70th SEG Annual International Meeting, *Expanded Abstract* (pp. 21–24). http://dx.doi.org/10.1190/1.1815889

Bostick, F., Knudsen, S., Nakstad, H., Blanco, J., & Mastin, E. (2003). *Permanently installed fiber optic multi-station 3-C in-well seismic trial at Izaute field*. 65th EAGE Conference and Exhibition, *Expanded Abstracts*, https://doi.org/10.3997/2214-4609-pdb.6.F45

Bostick, T., & Travis. P. (2014). *Optical multi-component borehole seismic systems continue to deliver unique permanent downhole data*. 76th EAGE Conference and Exhibition, Expanded Abstracts (pp. 413–414). http://dx.doi.org/10.3997/2214-4609.20140609

Bostick, F. X. T., Purkis, D., Feherty, C., Rose, K., & Hitchcock, D. (2019). *Disposable intervention tool for production logging*. SPE/ICoTA Well Intervention Conference and Exhibition, *SPE-194271-MS*. https://doi.org/10.2118/194271-MS

Brentle, J. O., & Großwig, S. (2014). *The application of fibre optic measurement techniques in the Mining Sector, The Oil & Gas Industry as well as in Geothermal Projects*. ISRM International Symposium—8th Asian Rock Mechanics Symposium, *ISRM-ARMS8-2014-265*.

Broderick, N. G. R., Loveday, J., Van Wijk, K., *Townend*, J., & Sutherland, R. (2019). *Optical measurements of temperature and strain of New Zealand's Alpine Fault*. Seismological Society of America Annual Meeting, Abstract. Seattle, WA, USA.

Bukhamsin, A., & Horne, R. N. (2014). *Using distributed acoustic sensors to optimize production in intelligent wells*. SPE Annual Technical Conference and Exhibition, *SPE-170679-MS*. https://doi.org/10.2118/170679-MS

Bukhamsin, A., & Horne, R. (2016). *Cointerpretation of distributed acoustic and temperature sensing for improved smart well inflow profiling*. SPE Western Regional Meeting, Expanded Abstracts, *SPE-180465-MS*. https://doi.org/10.2118/180465-MS

Byerley, G., Monk, D., Aaron, P., & Yates, M. (2018). Time-lapse seismic monitoring of individual hydraulic frac stages using a downhole DAS array. *The Leading Edge*, 37, 802–810. https://doi.org/10.1190/tle37110802.1

Byerley, G., Monk, D., Yates, M., & Aaron, P. (2018). *Time-lapse seismic monitoring of individual hydraulic-frac stages using a downhole DAS array: Part 1—field experiment and observations*. 88th SEG Annual International Meeting, *Expanded Abstracts* (pp. 5293–5297). https://doi.org/10.1190/segam2018-2998281.1

Cadwallader, S., Wampler, J., Sun, T., Sebastian, H., Graff, M., Gil, I., et al. (2015). *An integrated dataset centered around distributed fiber optic monitoring—key to the successful implementation of a geo-engineered completion optimization program in the Eagle Ford Shale*. Unconventional Resources Technology Conference, *URTEC-2171506-MS*. https://doi.org/10.15530/URTEC-2015-2171506

Cai, Z., Wang, S., Liu, W., Li F., Wang, C., Ma, L., & Li, Q. (2019). *Application of Walkaway-VSP based on joint observation by DAS and geophones in the Tarim Basin, northwest China*. 89th SEG Annual International Meeting, *Expanded Abstracts* (pp. 974–978). https://doi.org/10.1190/segam2019-3214449.1

Cannon, R. T., & Aminzadeh, F. (2013). *Distributed Acoustic Sensing: State of the art*. SPE Digital Energy Conference, *SPE-163688-MS*. https://doi.org/10.2118/163688-MS

Carpenter, C. (2015). Fracture-stimulation placement with fiber-optic distributed-sensing diagnostics. *Journal of Petroleum Technology*, 67(09), 134–135. https://doi.org/10.2118/0915-0134-JPT

Carpenter, C. (2016a). Distributed acoustic sensing for downhole production and injection profiling. *Journal of Petroleum Technology*, 68(03), 78–79. https://doi.org/10.2118/0316-0078-JPT

Carpenter, C. (2016b). SAGD and fiber-optic distributed acoustic and temperature sensing. *Journal of Petroleum Technology*, 68(09), 78–80. https://doi.org/10.2118/0916-0078-JPT

Carpenter, C. (2017a). Fiber-optic leak-detection project. *Journal of Petroleum Technology*, 69(04), 71–72. https://doi.org/10.2118/0417-0071-JPT

Carpenter, C. (2017b). Cointerpretation of distributed acoustic and temperature sensing for inflow profiling. *Journal of Petroleum Technology*, 69(05), 64–66. https://doi.org/10.2118/0517-0064-JPT

Carpenter, C. (2017c). Downhole sand-ingress detection with fiber-optic distributed acoustic sensors. *Journal of Petroleum Technology*, 69(10), 99–101. https://doi.org/10.2118/1017-0099-JPT

Carpenter, C. (2018). Advances in 4D seismic and geophysical monitoring of deepwater fields. *Journal of Petroleum Technology*, 70(03). 90–91. https://doi.org/10.2118/0318-0090-JPT

Carpenter, C. (2019). Permanent fiber-optic system monitors oil-rim movement. *Journal of Petroleum Technology*, 71(03). 73–74. https://doi.org/10.2118/0319-0073-JPT

Carpentier, S., Vandeweijer, V., Petitclerc, E., Paap B., & Verdel, A. (2020). *Using fibre-optic DAS surveying to de-risk a shallow geothermal energy storage site in Brussels*, *Belgium*. First EAGE Workshop on Fibre Optic Sensing, Expended Abstract. https://doi.org/10.3997/2214-4609.202030009

Carr, T. R., Wilson, T., Kavousi, P., Amini, S., Sharma, S., Hewitt, J., et al. (2017). *Insights from the Marcellus Shale Energy and Environment Laboratory (MSEEL)*. SPE/AAPG/SEG Unconventional Resources Technology Conference, *URTEC-2670437-MS*. https://doi.org/10.15530/URTEC-2017-2670437

Carr, T., Ghahfarokhi, P., Carney, B. J., Hewitt, J., & Vargnetti, R. (2019). *Marcellus Shale Energy and Environmental Laboratory (MSEEL) results and plans: Improved subsurface reservoir characterization and engineered completions*. SPE/AAPG/SEG Unconventional Resources Technology Conference, *URTEC-2019-415-MS*. https://doi.org/10.15530/urtec-2019-415

Castongia, E., Wang, H. F., Lord, N., Fratta, D., Mondanos, M., & Chalari, A. (2017). An experimental investigation of Distributed Acoustic Sensing (DAS) on Lake Ice. *Journal of Environmental and Engineering Geophysics*, 22, 167–176. https://doi.org/10.2113/JEEG22.2.167

Cerrahoglu, C., Naldrett, G., Vigrass, A., & Aghayev, R. (2019). *Cluster flow identification during multi-rate testing using a wireline tractor conveyed distributed fiber optic sensing system with engineered fiber on a HPHT horizontal unconventional gas producer in the Liard Basin*. SPE Annual Technical Conference and Exhibition, *SPE-196120-MS*. https://doi.org/10.2118/196120-MS

Chad Trabant, C. (2018). *Data management at IRIS*. Presented at AGU Workshop: Distributed Acoustic Sensing-Principles and Case Studies. Washington, D.C., *USA*.

Chalari, A. (2018). *Silixia: Fiber optic distributed sensors and applications*. Presented at AGU Workshop: Distributed Acoustic Sensing-Principles and Case Studies. Washington, D.C., *USA*.

Chalari, A., Mondanos, M., Coleman, T., *Farhadiroushan*, M., & Stork, A. (2019). *Seismic methods for geothermal reservoir characterization and monitoring using fiber optic distributed acoustic and temperature sensor*. EAGE/BVG/FKPE Joint Workshop on Borehole Geophysics and Geothermal Energy, Expended Abstract. https://doi.org/10.3997/2214-4609.201903162

Chalenski, D., Tatanova, M., Du, Y., Mateeva, A., Lopez, J., & Potters, H. (2016). *Climbing the staircase of ultralow-cost 4D monitoring of deepwater fields using DAS-VSP*. 86th SEG Annual International Meeting, *Expanded Abstracts* (pp. 5441–5445). https://doi.org/10.1190/segam2016-13681284.1

Chalenski, D., Hatchell, P., Lopez, J., Ross, M., Potters, H., & Broker, K. (2017). *Rapid autonomous marine 4D (RAM4D): Unmanned time-lapse seismic acquisition*. 87th Annual International Meeting, SEG, Expanded Abstracts (pp. 5968–5973). https://doi.org/10.1190/segam2017-17739013.1

Chalenski, D., Wang, K., Tatanova, M., Lopez, J. L., Hatchell, P., & Dutta, P. (2017). *Small airgun sources for frequent low-cost 4D reservoir surveillance*. First EAGE Workshop on Practical Reservoir Monitoring, Expanded Abstracts, Tu PRM 05. https://doi.org/10.3997/2214-4609.201700003

Chalenski, D. A., Hatchell, P. J., Lopez, J. L., & Broker, K. (2018). *Rapid Autonomous Marine 4D (RAM4D)—an unmanned, time-lapse offshore seismic acquisition system*. 80th EAGE Conference and Exhibition, Expended Abstracts, *WS14*. https://doi.org/10.3997/2214-4609.201801942

Chalenski, D. A., Lopez, J., Hatchell, P., Grandi, S., Broker, K., Hornman, K., et al. (2018). *Rapid autonomous marine 4D (RAM4D): Developing unmanned 4D seismic surveys*. 88th SEG Annual International Meeting, *Expanded Abstracts* (pp. 5288–5292). https://doi.org/10.1190/segam2018-2996863.1

Charara, M., Barnes, C., Tsuchiya, T., & Yamada, N. (2018). *Time-lapse DAS/Geophone VSP viscoelastic full waveform inversion for CO2 monitoring*. Abstract. *Paper presented at SEG Summer Research Workshop: Recent Advances and Applications in Borehole Geophysics*. Galveston, TX, USA.

Chavarria, J. A. (2018a). *Repeatability in DAS seismic measurements: Assessing Fiber Optic Technology for 4D analysis*. EAGE Workshop on 4D Seismic and Reservoir Monitoring, Expended Abstracts, *4DS17*. https://doi.org/10.3997/2214-4609.201900243

Chavarria, J. A. (2018b). *Reservoir monitoring through DAS measurements*. 80th EAGE Conference and Exhibition, Expended Abstracts, *WS08*. https://doi.org/10.3997/2214-4609.201801916

Chavarria, J. A., Kahn, D., Langton, D., Cole, S., & Li, X. (2019). *Time-lapse WAW VSP imaging of an unconventional reservoir using DAS fiber optics*. SPE/AAPG/SEG Unconventional Resources Technology Conference, *URTEC-2019-922-MS*. https://doi.org/10.15530/urtec-2019-922

Chavarria, J. A., Minto, C., Karrenbach, M., *Laing*, C., & Bown, T. (2020). *Offshore DASVSP applications and long-range distributed fiber optic sensing*. First EAGE Workshop on Fibre Optic Sensing, Expended Abstract. https://doi.org/10.3997/2214-4609.202030018

Chen, J., Chen, W., Wang, X., Zhou, Y., Shi, Z., & Zhang, G. (2018). *DAS coupling noise suppression using wavelet and DCT dictionary based on sparse optimization*. 88th SEG Annual International Meeting, *Expanded Abstracts* (pp. 4938–4942). https://doi.org/10.1190/segam2018-2996038.1

Chen, K., Zhu, D., & Hill, A. D. (2015). *Acoustic signature of flow from a fractured wellbore*. SPE Annual Technical Conference and Exhibition, *SPE-174877-MS*. https://doi.org/10.2118/174877-MS

Chen, K., Lee, E., Duncan, R., Howard, J., & Denney, T. (2016). *In-situ production profiling for recovery optimization via fiber-optic monitoring*. Offshore Technology Conference, OTC-26938-MS. https://doi.org/10.4043/26938-MS

Chen, Y., Hu, G., Cai, H., Wu, J., Li, Y., Yu, G., & Li, F. (2018). *Fiber armor acquisition contrast experiment and noise suppression technique in DAS 3D-VSP*. 88th SEG Annual International Meeting, *Expanded Abstracts* (pp. 5506–5510). https://doi.org/10.1190/segam2018-w20-04.1

Chen, Y. Z., Yu, G., Li, Y. P., Guo, X. L., Huang, J. H., & Wu, J. J. (2018). *Comparative study of DAS and geophone VSP data*. 80th EAGE Conference and Exhibition, Expended Abstracts, *WS08*. https://doi.org/10.3997/2214-4609.201801924

Cheng, D., Zhao, M., Willis, M., Zhou, R., Zhang, M., & Quinn, D. (2019). *Channel decimation and impact on DAS VSP data processing*. 89th SEG Annual International Meeting, *Expanded Abstracts* (pp. 5350–5354). https://doi.org/10.1190/segam2019-w1-01.1

Cheng, G., Shi, B., Zhu, H.-H., Zhang, C.-C., & Wu, J.-H. (2015). A field study on distributed fiber optic deformation monitoring of overlying strata during coal mining. *Journal of Civil Structural Health Monitoring*, 5, 553–562. https://doi.org/10.1007/s13349-015-0135-6

Cheng, L. K., Boering, M., & Braal, R. (2013). *Toward the next fiber optic revolution and decision making in the oil and gas industry*. Offshore Technology Conference, *OTC-23966-MS*. https://doi.org/10.4043/23966-MS

Cheraghi, S., White, D., Harris, K., & Roberts, B. (2018). *Initial results of time-lapse processing of VSP Geophone and DAS fiber-optic cable at Aquistore CO2 injection site, Sask*. 80th EAGE Conference and Exhibition, Expended Abstracts, Th F 15. https://doi.org/10.3997/2214-4609.201801472

Cherukupalli, S., & Anders, G. J. (2020). *Use of distributed sensing for strain measurement and acoustic monitoring in power cables*. In *Distributed Fiber Optic Sensing and Dynamic Rating of Power Cables, IEEE*, 2020, pp. 185–209, https://doi.org/10.1002/9781119487739.ch11

Ciervo, C., Becker, M., Cole, M. C., Coleman, T., & Mondanos, M. (2017). *Localizing fracture hydromechanical response using fiber optic distributed acoustic sensing in a fractured bedrock aquifer*. AGU Fall Meeting Abstract S33F-05.

Ciocca, F., Bodet, L., Simon, N., Karaulanov, R., Clarke, A., Abesser, C., et al. (2017). *Towards the wetness characterization of soil subsurface using fibre optic distributed acoustic sensing. AGU Fall Meeting Abstract H21A-0609*.

Clarke, A., Miller, D., Parker, T., & Greer, J. (2017). *Advanced applications of distributed acoustic sensing*. EAGE/DGG Workshop on Fibre Optic Technology in Geophysics, Expended Abstracts, Fr SR 02. https://doi.org/10.3997/2214-4609.201700151

Clements, T., Denolle, M. A., Yu, E., Ross, Z. E., & Hauksson, E. (2019). *Ambient noise processing with Julia*. Seismological Society of America Annual Meeting, *Abstract*. Seattle, WA, USA.

Clement, P., Gabet, R., & Lanticq, V. (2020). *Distributed temperature and strain sensing using Brillouin backscattering*.

First EAGE Workshop on Fibre Optic Sensing, Expended Abstract. https://doi.org/10.3997/2214-4609.202030041

Cocker, J. D., Herkenhoff, E. F., Craven, M. E., Nemeth, T., Daley, T. M., White, D., & Strudley, A. (2014). *Simultaneous acquisition of DAS and conventional down-hole geophone array at Aqusitore, Canada*. 76th EAGE Conference and Exhibition—Workshops, Extended Abstracts, *WS15-C03*. https://doi.org/10.3997/2214-4609.20140616

Cole, S., & Karrenbach, M. (2016). *Cross-well observations using a fiber optic DAS array*. Paper presented at SEG Postconvention workshop W-10: Fiber-optic Sensing for Exploration and Monitoring: Development, Applications, *and Challenges*. Dallas, TX, USA.

Cole, S., Karrenbach, M., Boone, K., Ridge, A., Kahn, D., Rich, J., et al. (2017). Effective *Diffusivity estimates from distributed fiber-optic strain and microseismic measurements*. 87th SEG Annual International Meeting, *Expanded Abstracts* (pp. 2757–2761). https://doi.org/10.1190/segam2017-17680716.1

Cole, S., Karrenbach, M., Gunn, D., & Dashwood, B. (2018). *MASW analysis of DAS fiber-optic data for active and passive seismic sources*. 80th EAGE Conference and Exhibition, Expended Abstracts, Th P8 10. https://doi.org/10.3997/2214-4609.201801640

Cole, S., Karrenbach, M., Kahn, D., Rich, J., Silver, K., & Langton, D. (2018). *Source parameter estimation from DAS microseismic data*. 88th SEG Annual International Meeting, *Expanded Abstracts* (pp. 4928–4932). https://doi.org/10.1190/segam2018-2995716.1

Cole, S., & Karrenbach, M. (2019). *MASW analysis of active-source and passive DAS fiber-optic data*. 89th SEG Annual International Meeting, *Expanded Abstracts* (pp. 968–973). https://doi.org/10.1190/segam2019-3216720.1

Coleman, T. (2018). *Installation considerations for downhole and surface geophysics*. Paper presented at AGU Workshop: Distributed Acoustic Sensing-Principles and Case Studies. Washington, D.C., *USA*.

Constantinou, A. (2016). *Evolution of hDVS performance and applications*. Paper presented at SEG Postconvention workshop W-10: Fiber-optic Sensing for Exploration and Monitoring: Development, Applications, *and Challenges*. Dallas, TX, USA.

Constantinou, A., Schmitt, D., Kofman, R., Kellett, R., Eccles, J., Lawton, D., et al. (2016). *Comparison of fiber-optic sensor and borehole seismometer VSP surveys in a scientific borehole: DFDP-2b, Alpine Fault, New Zealand*. 86th SEG Annual International Meeting, *Expanded Abstracts* (pp. 5608–5612). https://doi.org/10.1190/segam2016-13946302.1

Constantinou, A., Farahani, A., Cuny, T., & Hartog, A. (2016). *Improving DAS acquisition by real-time monitoring of wireline cable coupling*. 86th SEG Annual International Meeting, *Expanded Abstracts* (pp. 5603–5607). https://doi.org/10.1190/segam2016-13950092.1

Constantinou, A., Hartog, A., Dickenson, P., & Lees, G. (2017). *The merits of DAS acquisition on multimode optical fiber*. 4th EAGE Borehole Geophysics Workshop, Extended Abstracts, *BGP11*. https://doi.org/10.3997/2214-4609.201702478

Correa, J. C., Dean, T., Van Zaanen, L., Tertyshnikov, K. V., Pevzner, R., & Bona, A. (2017). *A comparison of DAS and Geophones for VSP acquisition at a dedicated field laboratory*. 79th EAGE Conference and Exhibition, Extended Abstracts, *Tu* P7 16. https://doi.org/10.3997/2214-4609.201701100

Correa, J., Egorov, A., Tertyshnikov, K., Bona, A., Pevzner, R., Dean, T., et al. (2017). Analysis of signal to noise and directivity characteristics of DAS VSP at near and far offsets—A CO2CRC Otway Project data example. *The Leading Edge*, *36*(12). *994a1–994a7*. https://doi.org/10.1190/tle36120994a1.1

Correa, J. C., Freifeld, B. M., Robertson, M., Pevzner, R., Bona, A., Popik, D., et al. (2017). *Distributed acoustic sensing applied to 4d seismic - preliminary results from the CO2CRC Otway site field trials*. 79th EAGE Conference and Exhibition, Extended Abstracts, *Tu* A1 15. https://doi.org/10.3997/2214-4609.201700811

Correa, J., Van Zaanen, L., Tertyshnikov, K., Dean, T., Pevzner, R., & Bona, A. (2017). *DAS versus geophones: A quantitative comparison of a VSP survey at a dedicated field laboratory*. 4th EAGE Borehole Geophysics Workshop, Extended Abstracts, *BGP10*. https://doi.org/10.3997/2214-4609.201702477

Correa, J., Freifeld, B. M., Pevzner, R., Wood, T., Tertyshnikov, K., & Bona, A. (2018). *Continuous DAS VSP monitoring using surface orbital vibrators: Field trials for optimal configuration at the CO2CRC Otway Project*. 80th EAGE Conference and Exhibition, Expended Abstracts, *WS08*. https://doi.org/10.3997/2214-4609.201801917

Correa, J., Pevzner, R., Popik, S., Tertyshnikov, K., Bona, A., & Freifeld, B. (2018). *Application of 3D VSP acquired with DAS and 3C geophones for site characterization and monitoring program design: preliminary results from Stage 3 of the CO2CRC Otway project*. 88th SEG Annual International Meeting, *Expanded Abstracts* (pp. 4933–4937). https://doi.org/10.1190/segam2018-2996035.1

Correa, J. (2019). *Continuous on-demand reservoir monitoring using DAS and permanent surface vibrators: case studies and preliminary results*. Paper presented at SEG Postconvention Workshop W-1: DAS—Part 1: Recent Advances in Subsurface Characterization using Distributed Acoustic Sensing and the Road Ahead. San Antonio, TX, USA.

Costley, R. D., Galan-Comas, G., Hathaway, K. K., Ketcham, S. A., & Kirkendall, C. K. (2018). Distributed acoustic sensing for near-surface seismic applications. *The Journal of the Acoustical Society of America*, 144, 1702. https://doi.org/10.1121/1.5067562

Costley, R. D., Galan-Comas, G., Kirkendall, C. K., Simms, J. E., Hathaway, K. K., Parker, M. W., et al. (2018). Spectral analysis of surface waves with simultaneous fiber optic distributed acoustic sensing and vertical geophones. *Journal of Environmental and Engineering Geophysics*, 23(2). 183–195. https://doi.org/10.2113/JEEG23.2.183

Costley, R. D., Galan-Comas, G., Feigenbaum, D. Z., & Hathaway, K. K. (2019). *Effect of gauge length on response of distributed acoustic sensors*. SAGEEP—32nd Annual Symposium on the Application of Geophysics to Engineering and Environmental Problems, *Expanded Abstracts*.

Cox, B. Wills, P., Kiyashchenko, D., Mestayer, J., Lopez, J., Bourne, S., et al. (2012). Distributed acoustic sensing for geophysical measurement, monitoring and verification. *Recorder*, *37*(2). 7–13.

Cox, B. E., Lehner, R., Webster, P., Molenaar, M., & Azad, A. (2014). *Keynote presentation: Microseismic data integration: How connecting the dots can help solve the unconventionals puzzle*. 5th EAGE Passive Seismic Workshop. Expanded Abstracts, PS25. https://doi.org/10.3997/2214-4609.20142154.

Cramer, D., Friehauf, K., Roberts, G., & Whittaker, J. (2019). *Integrating DAS, treatment pressure analysis and video-based perforation imaging to evaluate limited entry treatment effectiveness*. SPE Hydraulic Fracturing Technology Conference and Exhibition, *SPE-194334-MS*. https://doi.org/10.2118/194334-MS

Cramer, D., Friehauf, K., Roberts, G., & Whittaker, J. (2020). *Integrating Distributed Acoustic Sensing, treatment-pressure analysis, and video-based perforation imaging to evaluate limited-entry-treatment effectiveness*. SPE Production & Operations, *SPE-194334-PA*. https://doi.org/10.2118/194334-PA

Cramer, R., Shaw, D., Tulalian, R., Angelo, P., & van Stuijvenberg, M. (2014a). *Detecting and correcting pipeline leaks before they become a big problem*. SPE Intelligent Energy Conference & Exhibition, *SPE-167874-MS*. https://doi.org/10.2118/167874-MS

Cramer, R., Shaw, D., Tulalian, R., Angelo, P., & van Stuijvenberg, M. (2014b). *Detecting and correcting pipeline leaks before they become a big problem*. SPE Annual Caspian Technical Conference and Exhibition. *SPE-172253-MS*. https://doi.org/10.2118/172253-MS

Cramer, R., Tulalian, R., Angelo, P., Van Stuijvenberg, M., & Shaw, D. (2015). *Detecting and correcting pipeline leaks before they become a big problem*. SPE Middle East Oil & Gas Show and Conference, *SPE-172779-MS*. https://doi.org/10.2118/172779-MS

Cronin, S. P., Whitney Trainor-Guitton, W., PoroTomo Team, Pare, A., Jreij, S., & Powers, H. (2017). *Integration of DAS (distributed acoustic sensing) vertical seismic profile and geostatistically modeled lithology data to characterize an enhanced geothermal system*. AGU Fall Meeting Abstract H43E-1998.

Cui, T., Vasconcelos, I., Rickett, J. E., & Williams, M. J. (2017). *Marchenko Redatuming of the Hdvs signal*. 79th EAGE Conference and Exhibition, Extended Abstracts, *Th* P6 06. https://doi.org/10.3997/2214-4609.201700744

Cuny, T., Bettinelli, P., Le Calvez, J., Parker, R., Guerra, R., & Williams, M. (2020). *Variable gauge length processing: DAS VSP examples*. First EAGE Workshop on Fibre Optic Sensing, Expended Abstract. https://doi.org/10.3997/2214-4609.202030008

Daley, T. M., Freifeld, B. M., Ajo-Franklin, J., Dou, S., Pevzner, R., Shulakova, V., et al. (2013). Field testing of fiber-optic distributed acoustic sensing (DAS) for subsurface seismic monitoring. *The Leading Edge*, 32, 699–706. https://doi.org/10.1190/tle32060699.1

Daley, T. M., Miller, D., Freifeld, B. M., & Dodds, K. (2014). *Results of field testing of simultaneous DAS and Geophone VSP*. 76th EAGE Conference and Exhibition—Workshops, Extended Abstracts, *WS15-D03*. https://doi.org/10.3997/2214-4609.20140619

Daley, T. M., White, D., Miller, D. E., Robertson, M., Freifeld, B. M., Herkenhoff, F., & Cocker, J. (2014). *Simultaneous acquisition of Distributed Acoustic Sensing VSP with multi-mode and single-mode fiber optic cables and 3-component geophones at the Aquistore CO2 storage site*. 84th SEG Annual International Meeting, *Expanded Abstract* (pp. 5014–5018). https://doi.org/10.1190/segam2014-1357.1

Daley, T. M., Freifeld, B. M., Miller, D. E., White, D., Robertson, M., Worth, K., et al. (2016). *DAS experiments at Aquistore CO2 storage site: 4D-VSP, Geophone comparison and other tests*. Paper presented at SEG Postconvention workshop W-10: Fiber-optic Sensing for Exploration and Monitoring: Development, Applications, *and Challenges*. Dallas, TX, USA.

Daley, T. M., Miller, D. E., Dodds, K., Cook, P., & Freifeld, B. M. (2016). Field testing of modular borehole monitoring with simultaneous distributed acoustic sensing and geophone vertical seismic profiles at Citronelle, Alabama. *Geophysical Prospecting*, 64(5), 1318–1334. https://doi.org/10.1111/1365-2478.12324

Daley, T. M., Marchesini, P., Wilt, M., Cook, P., Freifeld, B. M., & Lawton, D. (2017). *Containment and Monitoring Institute—Baseline geophysics for CO2 monitoring with crosswell seismic and electromagnetics*. EAGE/SEG Research Workshop, Extended Abstracts, *Th CO2* 06. https://doi.org/10.3997/2214-4609.201701934

Danardatu, H., Gregersen, S. H. H., Altern, E., & Pellegrini, I. (2014). *Data acquisition and processing of carbon rod conveyed DTS and DAS in very long horizontal wells: First trial in North Sea Danish sector*. SPE Annual Technical Conference and Exhibition, *SPE-170663-MS*. https://doi.org/10.2118/170663-MS

Davies, K., Thornton, D., Stefani, J., *Makedonov*, A., & Katrenov, Z. (2020). *Fiber optics for sub-surface strain forecasting*. First EAGE Workshop on Fibre Optic Sensing, Expended Abstract. https://doi.org/10.3997/2214-4609.202030033

De Jong, W., Jansen, R., & Cheng, L. (2017). *Designing A DAS system for a geothermal well. EAGE/DGG Workshop on Fibre Optic Technology in Geophysics*, Expended Abstracts, Fr SR 03. https://doi.org/10.3997/2214-4609.201700152

Dean, T., Constantinou, A., Curry, T., Frignet, B., Hartog, A., Kimura, T., et al. (2015). *Vertical seismic profiles: Now just another log?* 85th SEG Annual International Meeting, *Expanded Abstracts* (pp. 5544–5548). https://doi.org/10.1190/segam2015-5804007.1

Dean, T., Cuny, T., & Hartog, A. (2015). *Determination of the optimum gauge length for borehole seismic surveys acquired using distributed vibration sensing*. 77th EAGE Conference and Exhibition. Expanded Abstracts. *Tu* N118 16. https://doi.org/10.3997/2214-4609.201412740

Dean, T., Hartog, A., Papp, B., & Frignet, B. (2015). *Fibre optic based vibration sensing: Nature of the measurement*. 3rd EAGE Workshop on Borehole Geophysics, Expanded Abstracts, *BG04*. https://doi.org/10.3997/2214-4609.201412183

Dean, T., Papp, B., & Hartog, A. (2015). *Wavenumber response of data recorded using distributed fibre-optic systems*. 3rd EAGE Workshop on Borehole Geophysics, Expanded Abstracts, *BGP07*. https://doi.org/10.3997/2214-4609.201412215

Dean, T., Brice, T., Hartog, A., Kragh, E., Molteni, D., & O'Connell, K. (2016). Distributed vibration sensing for seismic acquisition. *The Leading Edge*, 35(7), 600–604. https://doi.org/10.1190/tle35070600.1

Dean, T., Clark, M., Cuny, T., & Puech, J. (2016). *Is there value in highly spatially sampled zero-offset vertical seismic profiles?* 78th EAGE Conference and Exhibition, Expanded Abstracts, Tu P4 01. https://doi.org/10.3997/2214-4609.201600678

Dean, T., Cuny, T., Constantinou, A., Dickenson, P., Smith, C., & Hamouche, E. (2016). *Depth calibration of fibre-optic distributed vibration sensing measurements*. 78th EAGE Conference and Exhibition, Expanded Abstracts, Th STZ2 03. https://doi.org/10.3997/2214-4609.201601600

Dean, T., Cuny, T., & Hartog, A. (2016). The use of fiber-optic sensing to efficiently acquire vertical seismic profiles. *CSEG Recorder*, 41(6), 18–21.

Dean, T., Hartog, A., Cuny, T., & Englich, F. (2016). *The effects of pulse width on fibre-optic distributed vibration sensing data*. 78th EAGE Conference and Exhibition, Expanded Abstracts. *Tu* P4 07. https://doi.org/10.3997/2214-4609.201600684

Dean, T., & Correa, J. (2017). *The determination of the seismic quality factor Q from VSP data acquired using Distributed Acoustic Sensing*. 79th EAGE Conference and Exhibition, Extended Abstracts, *We* A5 16. https://doi.org/10.3997/2214-4609.201701203

Dean, T., & Cuny, T., & Hartog, A. (2017). The effect of gauge length on axially incident P-waves measured using fibre optic distributed vibration sensing. *Geophysical Prospecting*, 65(1), 184–193. https://doi.org/10.1111/1365-2478.12419

Dean, T., Cuny, T., Constantinou, A., Dickenson, P., & Hamouche, E. (2018). Depth calibration of fibre-optic distributed vibration sensing measurements. *First Break*, 36(3), 29–34. https://doi.org/10.3997/1365-2397.2017025

Dean, T. (2019). *Improving DAS VSP data quality by overcoming gauge length effects*. Paper presented at SEG Postconvention Workshop W-1: DAS—Part 1: Recent Advances in Subsurface Characterization using Distributed Acoustic Sensing and the Road Ahead. San Antonio, TX, USA.

Dean, T., & Nguyen, H. (2019). *Turning it up to 11: A 10 kN electromagnetic vibrator for downhole and near-surface applications*. 81st EAGE Conference and Exhibition, Expanded Abstracts, *Th_P05_03*. https://doi.org/10.3997/2214-4609.201901404

Dean, T., Tertyshnikov, K., Pevzner, R., Calbris, G., Jestin, C., & Lanticq, V. (2019). *Experimental measurement of the effects of acquisition parameters on DAS data quality*. 81st EAGE Conference and Exhibition, Expanded Abstracts, *We_R09_09*. https://doi.org/10.3997/2214-4609.201901245

Denney, D. (2012). Distributed Acoustic Sensing for hydraulic-fracturing monitoring and diagnostics. *Journal of Petroleum Technology*, *64*(3): 68–74. SPE-0312-0068-JPT. https://doi.org/10.2118/0312-0068-JPT

Díaz, J., Ruiz, M., Sánchez-Pastor, P. S., & Romero, P. (2017). Urban Seismology: On the origin of earth vibrations within a city. *Scientific Reports*, 7, 15296. https://doi.org/10.1038/s41598-017-15499-y

Dickenson, P., Brants-Menard, S., Telsey, M., Stanbridge, A., Wilson, C., Akin, J., et al. (2016). *Real-time interactive remote display of DTS and DAS data for well treatment optimization*. SPE Intelligent Energy International Conference and Exhibition, *SPE-181065-MS*. https://doi.org/10.2118/181065-MS

Didraga, C. (2015). *DAS VSP recorded simultaneously in cemented and tubing installed fiber optic cables*. 77th EAGE Conference and Exhibition. Expanded Abstracts, Tu N118 14. https://doi.org/10.3997/2214-4609.201412738

Diller, D. E., & Richter, P. (2019). *Transformative changes in Distributed Acoustic Sensing (DAS) hydraulic fracture and VSP monitoring*. 16th International Congress of the Brazilian Geophysical Society, Rio de Janeiro, Brazil. https://doi.org/10.22564/16cisbgf2019.342

Dou, S., Ajo-Franklin, J., Daley, T., Robertson, M., Wood, T., Freifeld, B., et al. (2016). *Surface orbital vibrator (SOV) and fiber-optic DAS: Field demonstration of economical, continuous-land seismic time-lapse monitoring from the Australian CO2CRC Otway site*. 86th SEG Annual International Meeting, *Expanded Abstracts* (pp. 5552–5556). https://doi.org/10.1190/segam2016-13974161.1

Dou, S., Lindsey, N. J., Wagner, A., Daley, T. M., Freifeld, B. M., Robertson, M., et al. (2017). Distributed acoustic sensing for seismic monitoring of the near surface: A traffic-noise interferometry case study. *Scientific Reports*, 7(1), 11620. https://doi.org/10.1038/s41598-017-11986-4

Dou, S., Wood, T., Freifeld, B. M., Robertson, M., McDonald, S., Pevzner, R., et al. (2017). *Processing approaches for DAS-enabled continuous seismic monitoring*. *AGU Fall Meeting Abstract S33B-2388*.

Drakeley, B. K., Morrison, F., Grigsby, T., Martinez, S., & Perez. E. (2014). *Integration into the sandface tool system for gravel and frack-pack installations with a fiber optics wetmate connector system*. Offshore Technology Conference, OTC-25195-MS. https://doi.org/10.4043/25195-MS

Drew, J., & Schaeffer, B. (2018). *Fiber-optic microseismic monitoring*. Abstract. *Paper presented at SEG Summer Research Workshop: Recent Advances and Applications in Borehole Geophysics*. Galveston, TX, USA.

Duan, Y., Mateeva, A., Kiyashchenko, D., & Zwartjes, P. (2018). *Do we know where DAS channels are and what well data to trust for depth calibration?* Paper presented at SEG Postconvention Workshop W-20: DAS-Validating Measurements, Developing Processing Methods, *and Integrating to Optimize Velocity Models for Improving Subsurface Imaging*. Anaheim, CA, USA.

Duckworth, G. L., & Ku, E. M. (2013). *OptaSense distributed acoustic and sesismic sensing using COTS fiber optic cables for infrastructure protection and counter terrorism*. Sensors, and Command, Control, Communications, and Intelligence (C3I) Technologies for Homeland Security and Homeland Defense XII, SPIE 8711, 87110G. https://doi.org/10.1117/12.2017712

Dy, T., Gou, W., & Meades, I. (2018). *DAS VSP processing and imaging—a marine case study in a highly deviated well*. Abstract. Paper presented at SEG Summer Research Workshop: Recent Advances and Applications in Borehole Geophysics. Galveston, TX, USA.

Eaid, M., & Innanen, K. (2018). *Modeling the sensitivity of shaped DAS fibre-optic cables to elastic wave data*. GeoConvention 2018, Expanded Abstracts.

Eaid, M., Li, J., & Innanen, K. A. (2018). *Modeling the response of shaped DAS fibres to microseismic moment tensor sources*. 88th SEG Annual International Meeting, *Expanded Abstracts* (pp. 4698–4702). https://doi.org/10.1190/segam2018-2998378.1

Edme, P., Paitz, P., Nap, A., Metraux, V., Martin, F., Dupuy, D., et al. (2020). Towards good practice of cable layout for surface Distributed Acoustic Sensing. Seismological Society of America Annual Meeting, *Abstract*. Albuquerque, NM, USA.

Effiom, O. (2016). *Achieving cost effective 4D monitoring in deep water fields*. SPE Nigeria Annual International Conference and Exhibition, *SPE-184375-MS*. https://doi.org/10.2118/184375-MS

Egan, M. S. (2019). Seismic. *Journal of Petroleum Technology*, *71*(3). *SPE-0319-0086-JPT*. https://doi.org/10.2118/0319-0086-JPT

Egorov, A., Bona, A., Pevzner, R., Glubokovskikh, S., & Puzyrev, V. (2018). *A feasibility study of time-lapse FWI on DAS VSP data acquired with permanent sources*. 80th EAGE Conference and Exhibition, Expended Abstracts, *We* P7 16. https://doi.org/10.3997/2214-4609.201801294

Eisler, B., & Lanan, G. A. (2012). *Fiber optic leak detection systems for subsea pipelines*. Offshore Technology Conference, *OTC-23070-MS*. https://doi.org/10.4043/23070-MS

Eisner, L., & Stanek, F. (2018). Microseismic data interpretation—what do we need to measure first? *First Break*, 36(2). 55–58. https://doi.org/10.3997/1365-2397.n0069

Elesztos, G., & Dookhee, L. (2013). Sensing system provides synchronized acoustic measurements. *Journal of Petroleum Technology*, 65(03), 38–41. https://doi.org/10.2118/0313-0038-JPT

Ellmauthaler, A., Willis, M., Barfoot, D., Wu, X., Erdemir, C., Barrios-Lopez, O., et al. (2016). *Depth calibration for DAS VSP: Lessons learned from two field trials*. 86th SEG Annual International Meeting, *Expanded Abstracts* (pp. 632–636). https://doi.org/10.1190/segam2016-13951487.1

Ellmauthaler, A., Willis, M., Wu, X., & Barfoot, D. (2016). *Factors affecting the quality of DAS VSP data*. Paper presented at SEG Postconvention workshop W-10: Fiber-optic Sensing for Exploration and Monitoring: Development, Applications, *and Challenges*. Dallas, TX, USA.

Ellmauthaler, A., Willis, M. E., Wu, X., & LeBlanc, M. (2017). *Noise sources in fiber-optic Distributed Acoustic Sensing VSP Data*. 79th EAGE Conference and Exhibition, Expanded Abstracts, Th A3 14. https://doi.org/10.3997/2214-4609.201700515

Ellmauthaler, A. (2019). *Topside DAS interrogation of subsea wells*. Paper presented at SEG Postconvention Workshop W-1: DAS—Part 1: Recent Advances in Subsurface Characterization using Distributed Acoustic Sensing and the Road Ahead. San Antonio, TX, USA.

Ellmauthaler, A., Palacios, W., LeBlanc, M., Willis, M., & Knapo, G. (2019). *Vertical seismic profiling via coiled tubing-conveyed Distributed Acoustic Sensing*. SPE/ICoTA Well Intervention Conference and Exhibition, *SPE-194244-MS*. https://doi.org/10.2118/194244-MS

Ellmauthaler, A., LeBlanc, M., Willis, M., *Maida*, J., & Wilson, G. (2020). *Real-time DAS VSP acquisition and processing*. First EAGE Workshop on Fibre Optic Sensing, Expended Abstract. https://doi.org/10.3997/2214-4609.202030013

Ellmauthaler, A., Maida, J., Wilson, G., Bush, J., & Willis, M. (2020). *Achieving dry-tree DAS bandwidth and SNR performance on Subsea Wells*. First EAGE Workshop on Fibre Optic Sensing, Expended Abstract. https://doi.org/10.3997/2214-4609.202030014

Ellmauthaler, A., Willis, M., Palacios, W., LeBlanc, M., *Knapo*, G., & Wilson, G. (2020). *DAS VSP via Coiled Tubing Fiber Conveyance*. First EAGE Workshop on Fibre Optic Sensing, Expended Abstract. https://doi.org/10.3997/2214-4609.202030012

Ellsworth, W. L., Karrenbach, M. H., & Zumberge, M. A. (2017). *Full wave field recording of the vertical strain at SAFOD from local, regional and teleseismic earthquakes. AGU Fall Meeting Abstract S33B-2378*.

Eriksrud, M., Langhammer, J., & Nakstad, H. (2009). *Towards the optical oil field*. 79th SEG Annual Meeting, *Expanded Abstracts* (pp. 3400–3404). https://doi.org/10.1190/1.3255568

Eriksrud, M. (2010). Towards the optical seismic era in reservoir monitoring. *First Break*, 28(6), 105–111.

Eriksrud, M., & Kringlebotn, J. T. (2013). *Fiber optic sensor technology for oil and gas applications. In Photonics for Safety and Security* (pp. 309–333). https://doi.org/10.1142/9789814412971_0014

Evans, S., Holley, E., Dawson, K., Garrison, N., Montes, M., Preston, G., & Hudson, S. (2016). *Eagle Ford case history: Evaluation of diversion techniques to increase stimulation effectiveness*. SPE/AAPG/SEG Unconventional Resources Technology Conference, *URTEC-2459883-MS*. https://doi.org/10.15530/URTEC-2016-2459883

Eyal, A., Gabai, H., & Shpatz, I. (2017). *Distributed acoustic sensing: how to make the best out of the Rayleigh-backscattered energy?* Proceedings of SPIE 10323, 25th International Conference on Optical Fiber Sensors, 103230I. https://doi.org/10.1117/12.2272458

Fagbami, D., Echem, C., Okoli, A., Mondanos, M., Bain, A., Carbonneau, P., & Martey, A. (2017). *A practical application of pipeline surveillance and intrusion monitoring system in the Niger Delta: The Umugini case study*. SPE Nigeria Annual International Conference and Exhibition, *SPE-189056-MS*. https://doi.org/10.2118/189056-MS

Fang, G., Li, Y. E., Du, Y., Ma, J. H. Y., & Yu, D. (2018). *Near-surface monitoring enabled by distributed acoustic sensing: An example of the Stanford Array Data*. 88th SEG Annual International Meeting, *Expanded Abstracts* (pp. 2677–2681). https://doi.org/10.1190/segam2018-2998119.1

Fang, G., Li, Y. E., Zhao, Y., & Martin, E. R. (2020). Urban near-surface seismic monitoring using Distributed Acoustic Sensing. *Geophysical Research Letters*, 47(6). https://doi.org/10.1029/2019GL086115

Farhadiroushan, M. (2016). *Versatile distributed fiber optic sensing for seismic and microseismic surveillance*. Paper presented at SEG Postconvention workshop W-10: Fiber-optic Sensing for Exploration and Monitoring: Development, Applications, *and Challenges*. Dallas, TX, USA.

Farhadiroushan, M., Parker, T., Clarke, A., Miller, D., Gillies, A., Shatalin, S., et al. (2017). *High definition seismic and* *microseismic data acquisition using distributed and engineered fiber optic acoustic sensors*. *AGU Fall Meeting Abstract S33F-07*.

Farhadiroushan, M. (2018a). *Principles and recent advances in Distributed Acoustic Sensing*. Paper presented at AGU Workshop: Distributed Acoustic Sensing-Principles and Case Studies. Washington, D.C., *USA*.

Farhadiroushan, M. (2018b). *Fiber optic distributed and engineered acoustic sensors for new seismic and microseismic applications*. Paper presented at SEG Postconvention Workshop W-20: DAS-Validating Measurements, Developing Processing Methods, *and Integrating to Optimize Velocity Models for Improving Subsurface Imaging*. Anaheim, CA, USA.

Farhadiroushan, M. (2018c). *Seismic and microseismic detection using a wide dynamic-range distributed an engineered fiber optic acoustic sensor*. 80th EAGE Conference and Exhibition, Expended Abstracts, *WS08*. https://doi.org/10.3997/2214-4609.201801921

Farhadiroushan, M. (2019). *Advanced geophysical applications using precision engineered distributed acoustic sensor*. Paper presented at SEG Postconvention Workshop W-1: DAS—Part 1: Recent Advances in Subsurface Characterization using Distributed Acoustic Sensing and the Road Ahead. San Antonio, TX, USA.

Farhadiroushan, M., Parker, T., Shatalin, S., Gillies, A., Chen, Z., Clarke, A., & Naldrett, G. (2019a). *Practical reservoir monitoring using distributed acoustic sensor with engineered fiber*. Second EAGE Workshop Practical Reservoir Monitoring, Expanded Abstracts, *Th PRM05*. https://doi.org/10.3997/2214-4609.201900006

Farhadiroushan, M., Parker, T., Shatalin, S., Gillies, A., Chen, Z., Clarke, A., & Naldrett, G. (2019b). *Advanced geophysical measurement methods using engineered fiber optic acoustic sensor*. 81st EAGE Conference and Exhibition, Expanded Abstracts, *We_R09_11*. https://doi.org/10.3997/2214-4609.201901247

Feder, J. (2020). Distributed fiber-optic sensors characterize flow-control-device performance. *Journal of Petroleum Technology*, 72(04), 64–65. https://doi.org/10.2118/0420-0064-JPT

Feigl, K. L., & PoroTomo Team (2017). *Overview and preliminary results from the PoroTomo Project at Brady Hot Springs, Nevada: Poroelastic Tomography by Adjoint Inverse Modeling of Data from Seismology, Geodesy, and Hydrology*. 42nd Workshop on Geothermal Reservoir Engineering. Proceedings (pp. 1000–1014). *SGP-TR-212*.

Feigl, K. L., Patterson1, J., Parker, L., Reinisch, E. C., Zeng, X., Cardiff, M. A., et al. (2017). *Characterization of material properties at Brady Hot Springs, Nevada by Inverse Modeling of Data from Seismology, Geodesy, and Hydrology*. *AGU Fall Meeting Abstract H41O-01*.

Feigl, K. L. & The PoroTomo Team. (2018). *Overview and preliminary results from the PoroTomo project at Brady Hot Springs, Nevada: Poroelastic Tomography by Adjoint Inverse Modeling of Data from Seismology, Geodesy, and Hydrology*. 43rd Workshop on Geothermal Reservoir Engineering, PROCEEDINGS (pp. 1–13). SGP-TR-213.

Feo, G., Sharma, J., Williams, W., KortuKov, D., & Toba, O. (2019). *Application of distributed fiber optics sensing technology for real-time gas kick detection*. SPE Annual Technical Conference and Exhibition, *SPE-196113-MS*. https://doi.org/10.2118/196113-MS

Ferla, M., Miranda, F., Nutricato, G., Galli, G., Moriggi, S., Malossi, A., et al. (2018). *Efficiency and innovation for borehole seismic acquisition in a well completed with permanent fiber: DAS technology for saving time and minimizing risk*. Abu Dhabi International Petroleum Exhibition & Conference, *SPE-192616-MS*. https://doi.org/10.2118/192616-MS

Ferla, M., Miranda, F., Malossi, A., Nutricato, G., Moriggi, S., Galli, G., et al. (2019). *Processing of pseudo 3D VSP acquired using permanent fibre optic technology deployed in an exploration well*. 81st EAGE Conference and Exhibition, Expanded Abstracts, *We_R09_14*. https://doi.org/10.3997/2214-4609.201901250

Fernández-Ruiz, M. R., Soto, M. A., Williams, E. F., Martin-Lopez, S., Zhan, Z., Gonzalez-Herraez, M., & Martins, H. F. (2020). *Distributed acoustic sensing for seismic activity monitoring*. *APL Photonics*, 5, 030901. https://doi.org/10.1063/1.5139602

Fidaner, O. (2017). *Downhole multiphase flow monitoring using fiber optics*. SPE Annual Technical Conference and Exhibition, *SPE-187415-MS*. https://doi.org/10.2118/187415-MS

Finfer, D. C., Mahue, V., Shatalin, S. V., Parker, T. R., & Farhadiroushan, M. (2014). *Borehole flow monitoring using a non-intrusive passive Distributed Acoustic Sensing (DAS)*. SPE Annual Technical Conference and Exhibition, *SPE-170844-MS*. https://doi.org/10.2118/170844-MS

Finfer, D., Parker, T. R., Mahue, V., Amir, M., Farhadiroushan, M., & Shatalin, S. (2015). *Non-intrusive multiple zone distributed acoustic sensor flow metering*. SPE Annual Technical Conference and Exhibition, *SPE-174916-MS*. https://doi.org/10.2118/174916-MS

Fitzel, S., Sekar, B. K., Alvarez, D., & Gulewicz, D. (2015). *Gas injection EOR optimization using fiber-optic logging with DTS and DAS for remedial work*. SPE/CSUR Unconventional Resources Conference, *SPE-175891-MS*. https://doi.org/10.2118/175891-MS

Fonseca, E. (2014). *Emerging technologies and the future of hydraulic fracturing design in unconventional gas and tight oil*. International Petroleum Technology Conference, *IPTC-17439-MS*. https://doi.org/10.2523/IPTC-17439-MS

Ford, S. R., Mellors, R. J., & Gok, R. (2020). *Explosion yield estimation by distributed acoustic sensing: Insights from the source physics experiments*. Seismological Society of America Annual Meeting, *Abstract*. Albuquerque, NM, USA.

Forster, L., & Dria, D. E. (2013). *Real-time subsea fiber-optic monitoring*. Offshore Technology Conference, *OTC-23930-MS*. https://doi.org/10.4043/23930-MS

Franquet, J. (2020). *Advances of Straddle Packer Microfrac stress measurements for reservoir development—the pursuit of subsurface tectonic strain behavior*. International Petroleum Technology Conference, *IPTC-20257-MS*. https://doi.org/10.2523/IPTC-20257-MS

Fratta, D., Lancelle, C., Ak, E., Lord, N. E., Wang, H. F., & Porotomo Team. (2017). *Distributed Acoustic Sensing (DAS) array near a highway for traffic monitoring and near-surface shear-wave velocity profiles*. *AGU Fall Meeting Abstract S33B-2380*.

Fratta, D. (2018). *Traffic monitoring with DAS*. Paper presented at AGU Workshop: Distributed Acoustic Sensing-Principles and Case Studies. Washington, D.C., *USA*.

Freifeld, B. M., Pevzner, R., Dou, S., Correa, J., Daley, T M., Robertson, M., et al. (2016). *The CO2CRC Otway Project deployment of a Distributed Acoustic Sensing Network Coupled with Permanent Rotary Sources*. 78th EAGE Conference and Exhibition, Extended Abstract. *Tu LHR2* 06. https://doi.org/10.3997/2214-4609.201600577

Freifeld, B. M., Dou, S., Ajo-Franklin, J. B., Robertson, M., Wood, T., Daley, T. M., et al. (2017). *Using DAS for reflection seismology—lessons learned from three field studies*. *AGU Fall Meeting Abstract S33F-01*.

Frignet, B. G., & Hartog, A. H. (2014). *Optical vertical seismic profile on wireline cable*. SPWLA 55th Annual Logging Symposium, Abu Dhabi. *SPWLA-2014-FFFF*

Frings, J., & Walk, T. (2011). Distributed fiber optic sensing enhances pipeline safety and security. *Oil Gas European Magazine*, 37(3), 132–136.

Gabai, H., & Eyal, A. (2016a). *SNR characterization in distributed acoustic sensing*. Proceedings of SPIE 9916, 6th European Workshop on Optical Fibre Sensors, 99162W. https://doi.org/10.1117/12.2236640

Gabai, H., & Eyal, A. (2016b). On the sensitivity of distributed acoustic sensing. *Optics Letters*, 41(24), 5648–5651. https://doi.org/10.1364/OL.41.005648

Gabai, H., & Eyal, A. (2017). *How to specify and measure sensitivity in distributed acoustic sensing (DAS)? 25th Optical Fiber Sensors Conference (OFS)*, Jeju, South Korea. https://doi.org/10.1117/12.2265527

Garcia-Hernandez, A., & Bennett, J. (2016). *Leak detectability in an off-shore multiphase production system*. Pipeline Simulation Interest Group (PSIG) Annual Meeting, *PSIG-1601*.

Gardner, N., Hveding, F., & Sambrook, R. (2015). Technology update: Distributed fiber-optic technologies drive new intervention applications. *Journal of Petroleum Technology*, 67 (01), 36–40. https://doi.org/10.2118/0115-0036-JPT

Garofoli, L., Moriggi, S., & Galli, G. (2019). *Maximization of downhole tracer profiling evaluation through the integration of different technologies in challenging environments*. 14th Offshore Mediterranean Conference and Exhibition, *OMC-2019-0976*.

Gaston, G., & Bostick. T. (2011). Practical downhole production and reservoir monitoring with optical sensors. *First Break*, 29 (7), 86–88. https://doi.org/0.3997/1365-2397.29.7.51917

Gaston, G., & Bostick. T. (2012). Permanent downhole optical sensing continues to deliver value—well into the 4th dimension. 74th EAGE Conference and Exhibition, Expanded Abstracts, Y007. https://doi.org/10.3997/2214-4609.20148802

Gerritsen, S., Ernst, F., Field, C., Abdullah, Y., Daud, D. N. PH., & Nizkous, I. (2016a). *Velocity model building challenges and solutions in a SE Asian basin*. EAGE Workshop on Velocities: Reducing Uncertainties in Depth. Extended Abstracts, *D1S1O3*. https://doi.org/10.3997/2214-4609.201600065

Gerritsen, S., Ernst, F., Field, C., Abdullah, Y., Daud, D. N. PH., & Nizkous, I. (2016b). Velocity model building challenges and solutions in a SE Asian basin: Beyond reflection tomography. *First Break*, 34(10), 91–97. https://doi.org/0.3997/1365-2397.34.10.86978

Ghazali, D. R., Mad Sahad, S., & Alimat, M. R. U. (2017). *Solving the seismic detectability issue of emulsion formation for chemical EOR*. 79th EAGE Conference and Exhibition, Extended Abstracts, *We* B1 04. https://doi.org/10.3997/2214-4609.201701207

Ghazali, A. R., ElKady, N., Abd Rahim, M. F., Hardy, R. J. J., Dzukelfi, F. S., Chandola, S., et al. (2018). Reservoir delineation beneath a heterogeneous shallow gas overburden using "True-3D" seismic imaging approaches. *First Break*, 36(11), 89–96. https://doi.org/10.3997/1365-2397.n0137

Ghazali, A. R., Abdul Rahim, M. F., Mad Zahir, M. H., Muhammad, M. D. D., Mohammad, M. A., & A. Aziz, K. M. A. (2019). *Ears on wells: Reservoir delineation and monitoring using true 3D imaging approaches*. SPE Annual Technical Conference and Exhibition, SPE-195954-MS. https://doi.org/10.2118/195954-MS

Giunta, G., Dionigi, F., Bassan, A., Veneziani, M., Bernasconi, G., Giudice, S. D., et al. (2011). *Third party interference and leak detection on buried pipelines for reliable transportation of fluids*. Offshore Mediterranean Conference and Exhibition, *OMC-2011-114*. https://doi.org/10.13140/RG.2.1.3447.1440

Glaser, D. R., Costley, R. D., Hathaway, K. K., Boitnott, G. L., & Weale, J. (2019). *Snow coupled distributed acoustic sensing for intrusion detection of Polar Bears in Arctic Camps*. *AGU Fall Meeting Abstract NS11B-0634*.

Glisic, B., & Yao, Y. (2012). Fiber optic method for health assessment of pipelines subjected to earthquake-induced ground movement. *Structural Health Monitoring*, 11(6), 696–711. https://doi.org/10.1177/1475921712455683

Gohari, K., Jutila, H., Kshirsagar, A., Chattopadhyay, A., Mascagnini, C., Gryaznov, A., et al. (2016). *DAS/DTS/DSS/DPS/DxS—do we measure what adds value?* SPE Europec featured at 78th EAGE Conference and Exhibition, *SPE-180165-MS*. https://doi.org/10.2118/180165-MS

Gok, R., & Mellors, R. J. (2020). *Coda amplitude measurements using Distributed Acoustic Sensing (DAS) data*. Seismological Society of America Annual Meeting, *Abstract*.

Gonzalez, L. E., Chokshi, R. N., & Lane, W. (2015a). *Importance of downhole measurements, visualization and analysis in producing unconventional wells*. Unconventional Resources Technology Conference, *URTEC-2164102-MS*. https://doi.org/10.15530/URTEC-2015-2164102

Gonzalez, L. E., Chokshi, R. N., & Lane, W. (2015b). *Real-time surface and downhole measurements and analysis for optimizing production*. SPE/IATMI Asia Pacific Oil & Gas Conference and Exhibition, *SPE-176233-MS*. https://doi.org/10.2118/176233-MS

Gordon, A., & Lawton, D. (2018). *VSP processing in Distributed Acoustic Sensing and Geophone data at CaMI field Research Station, Newell County, Alberta*. GeoConvention 2018, Expanded Abstracts.

Gordon, A., Lawton, D., Hall, K., Freifeld, B., Daley, T., & Cook, P. (2018). *Depth registration of VSP DAS fiber*. 88th SEG Annual International Meeting, *Expanded Abstracts* (pp. 5427–5431). https://doi.org/10.1190/segam2018-2998408.1

Gorham, T., Sims, J., Buell, R. S., Miller, R., Fermaniuk, B., & Heukelman, H. (2019). *Horizontal steam injection liner deployed flow control device design development and testing*. SPE Thermal Well Integrity and Design Symposium, *SPE-198698-MS*. https://doi.org/10.2118/198698-MS

Götz, J., Lüth, S., Henninges, J., & Reinsch, T. (2015). *Using a fibre optic cable as distributed acoustic sensor for vertical seismic profiling at the Ketzin CO2 storage site*. 77th EAGE Conference and Exhibition. Expanded Abstracts, Th P2 13. https://doi.org/10.3997/2214-4609.201413363

Götz, J., Lüth, S., Henninges, J., & Reinsch, T. (2018). *Vertical seismic profiling using a daisy-chained deployment of fibre-optic cables in four wells simultaneously—case study at the Ketzin carbon dioxide storage site*. *Geophysical Prospecting*, 66(6), 1201–1214. https://doi.org/10.1111/1365-2478.12638

Grandi, S. K., Webster, P., Hornman, K., Lumens, P. G. E., Franzen, A., Kindy, F., et al. (2013). Microseismic applications using DAS. 4th EAGE Passive Seismic Workshop, Expanded Abstracts, PS02. https://doi.org/10.3997/2214-4609.20142338

Grandi, S. K., Cox, B., Mateeva, A., & Lopez, J. (2017). *DAS enables cost-effective reservoir monitoring onshore and offshore. EAGE/DGG Workshop on Fibre Optic Technology in Geophysics*, Expended Abstracts, Fr SR 08. https://doi.org/10.3997/2214-4609.201700157

Grindei, L., Kelley, M., Modroo, A., Mondanos, M., Farhadiroushan, M., & Coleman, T. (2019). *Distributed Acoustic Sensing (DAS) for monitoring CO2 injected into a Pinnacle-Reef Reservoir. 2nd EAGE Workshop Practical Reservoir Monitoring*, Expanded Abstracts, Th PRM 04. https://doi.org/10.3997/2214-4609.201900005

Gustavo, A., Ugueto, C., Huckabee, P. T., Reynolds, A., Somanchi, K., Wojtaszek, M., et al. (2018). *Hydraulic fracture placement assessment in a fiber optic compatible coiled tubing activated cemented single point entry system*. SPE Hydraulic Fracturing Technology Conference and Exhibition, *SPE-189842-MS*. https://doi.org/10.2118/189842-MS

Gutscher, M. A., Roye, J. Y., Graindorge, D., Murphy, S., Klingelhoefer, F., Cattaneo, A., et al. (2017). *A novel approach for studying submarine faults: the FOCUS project (FOCUS = Fiber Optic Cable Use for Seafloor studies of earthquake hazard and deformation). AGU Fall Meeting Abstract S33F-08*.

Gutscher, M.-A., Royer, J.-Y., Graindorge, D., Murphy, S., Klingelhoefer, F., Aiken, C., et al. (2019). Fiber optic monitoring of active faults at the seafloor: The FOCUS project. *Photoniques*, *Special EOS (3)*, 32–37. https://doi.org/10.1051/photon/2019S432

Haberer, S., Pfrang, D., Schölderle, F., Meinecke, M., Lipus, M., *Reinsch*, T., & Zosseder, K. (2020). *Permanent fiber-optic installation in the reservoir section of a deep geothermal well*. First EAGE Workshop on Fibre Optic Sensing, Expended Abstract. https://doi.org/10.3997/2214-4609.202030042

Haldorsen, J. B. U., & Hilton, T. (2018). *HybridVSP: An optimal combination of fiber-optical and three-component antennas*. Abstract. *Paper presented at SEG Summer Research Workshop: Recent Advances and Applications in Borehole Geophysics*. Galveston, TX, USA.

Haldorsen, J. B. U., Jahren, L., Milenkovic, M., & Hilton, T. (2018a). *Vertical seismic profiling combining three-component geophones with single-axis DAS sensors*. 80th EAGE Conference and Exhibition, Expended Abstracts, *WS08*. https://doi.org/10.3997/2214-4609.201801919

Haldorsen, J. B. U., Jahren, L., Milenkovic, M., & Hilton, T. (2018b). *Vertical-seismic profiling using a hybrid tool, combining three-component geophones with DAS sensors*. 80th EAGE Conference and Exhibition, Expended Abstracts, Th H 09. https://doi.org/10.3997/2214-4609.201801498

Hall, K. W., Lawton, D. C., Daley, T. M., Freifeld, B. M., & Cook, P. (2018). *Effect of source effort and source distance on optical-fibre data at CaMI.FRS, Newell County, Alberta*. 88th SEG Annual International Meeting, *Expanded Abstracts* (pp. 206–210). https://doi.org/10.1190/segam2018-2996243.1

Hall, K. W., Bertram, K. L., Bertram, M., Innanen, K., & Lawton, D. C. (2019). *Simultaneous accelerometer and optical fibre multi-azimuth walk-away VSP experiment: Newell County, Alberta, Canada*. 89th SEG Annual International Meeting, *Expanded Abstracts* (pp. 5340–5344). https://doi.org/10.1190/segam2019-3216606.1

Halladay, A., O'Brien, S., Tucker, O., & Duer, J. (2018). *Three years of safe operations at the quest CCS facility, Fort Saskatchewan, Alberta, Canada*. 5th CO2 Geological Storage Workshop, Expended Abstracts, *Fr CO2* 12. https://doi.org/10.3997/2214-4609.201803000

Halladay, A., Orpeza Bacci, V., O'Brien, S., & Hindriks, K. (2018). *Results from the second monitor DAS VSP at quest CCS*. 5th CO2 Geological Storage Workshop, Expended Abstracts, *Th CO2* 13. https://doi.org/10.3997/2214-4609.201802981

Hance, T., Jiang, T., Zhan, G., Kjos, E., Geetan, R., Soulas, S., & Thomas, I. (2016). *Learnings from Distributed Acoustic Sensing data processing for seismic applications—a case study from the North Sea*. 78th EAGE Conference and Exhibition, Extended Abstract. *Th STZ2* 04. https://doi.org/10.3997/2214-4609.201601601

Harris, K., White, D., Melanson, D., Samson, C., & Daley, T. M. (2016). Feasibility of time-lapse VSP monitoring at the Aquistore CO2 storage site using a distributed acoustic sensing system. *International Journal of Greenhouse Gas Control*, 50, 248–260. https://doi.org/10.1016/j.ijggc.2016.04.016

Harris, K., & White, D. (2018). *CO2 monitoring results from Aquistore using Distributed Acoustic Sensing 3D VSPs: Results from 1st and 2nd monitor surveys*. Abstract. *Paper presented at SEG Summer Research Workshop: Recent Advances and Applications in Borehole Geophysics*. Galveston, TX, USA.

Hartog, A. H., & Gold, M. P. (1984). On the theory of backscattering in single-mode optical fibers. *Journal of Lightwave Technology*, 2(2), 76–82. https://doi.org/10.1109/JLT.1984.1073598

Hartog, A. H., Kotov, O. I., & Liokumovich, L. B. (2013). *The optics of distributed vibration sensing*. 2nd EAGE Workshop on Permanent Reservoir Monitoring, Expanded Abstracts, *Th–01–04*. https://doi.org/10.3997/2214-4609.20131301

Hartog, A., Frignet, B., Mackie, D., & Allard, W. (2014). *Multi-offset vertical seismic profile acquisition with hybrid* *optical-electrical wireline cable*. 76th EAGE Conference and Exhibition, Expanded Abstract, *Tu* P09 09. https://doi.org/10.3997/2214-4609.20140613

Hartog, A., Frignet, B., Mackie, D., & Clark, M. (2014). Vertical seismic optical profiling on wireline logging cable. *Geophysical Prospecting*, 62(4), 693–701. https://doi.org/10.1111/1365-2478.12141

Hartog, A., Frignet, B., Mackie, D., Clarke, M., Constantinou, A., Allard, W., & Lees, G. (2014). Wireline deployment of optical VSP in vertical and deviated wells. 76th EAGE Conference and Exhibition—Workshops, Extended Abstracts, *WS15-B03*. https://doi.org/10.3997/2214-4609.20140613

Hartog, A., Liokumovich, L. B., Ushakov, N. A., Kotov, O. I., Dean, T., Cuny, T., & Constantinou, A. (2016). *The use of multi-frequency acquisition to significantly improve the quality of fibre-optic distributed vibration sensing*. 78th EAGE Conference and Exhibition, Expended Abstracts, *Tu* P4 08. https://doi.org/10.3997/2214-4609.201600685

Hartog, A. H. (2017). *An introduction to distributed optical fibre sensors*. Boca Raton, FL: CRC Press.

Hartog, A., Liokumovich, L. B., Ushakov, N. A., Kotov, O. I., Dean, T., Cuny, T., et al. (2018). The use of multi-frequency acquisition to significantly improve the quality of fibre-optic distributed vibration sensing. *Geophysical Prospecting*, 66 (S1), 192–202. https://doi.org/10.1111/1365-2478.12612

Hartog, A. H., Belal, M., & Clare, M. A. (2018). Advances in distributed fiber-optic sensing for monitoring marine infrastructure, measuring the deep ocean, and quantifying the risks posed by seafloor hazards. *Marine Technology Society Journal*, 52(5), 58–73. http://nora.nerc.ac.uk/id/eprint/521128

Haustveit, K., Dahlgren, K., Greenwood, H., Peryam, T., Kennedy, B., & Dawson, M. (2017). *New age fracture mapping diagnostic tools-A STACK case study*. SPE Hydraulic Fracturing Technology Conference and Exhibition, *SPE-184862-MS*. https://doi.org/10.2118/184862-MS

Haustveit, K., Elliott, B., Haffener, J., Ketter, C., O'Brien, J., Almasoodi, M., et al. (2020). *Monitoring the pulse of a well through sealed wellbore pressure monitoring, a breakthrough diagnostic with a multi-basin case study*. SPE Hydraulic Fracturing Technology Conference and Exhibition, *SPE-199731-MS*. https://doi.org/10.2118/199731-MS

He, X., Zhang, M., Gu, L., Xie, S., Liu, F., & Lu, H. (2020). Performance improvement of dual-pulse heterodyne distributed acoustic sensor for sound detection. *Sensors*, 20(4), 999. https://doi.org/10.3390/s20040999

Healey, P. (1985). Statistics of Rayleigh backscatter from a single-mode optical fibre. *Electronics Letters*, 21(6), 226–228. http://dx.doi.org/10.1049/el:19850161

Heigl, W. M., Diller, D. E., Fish, B., Shuck, T., & Wilson, S. (2018). *The Enigma of dip-slip and aligned strike-slip events within the same event cloud*. Seventh EAGE Workshop on Passive Seismic, Extended Abstracts. https://doi.org/10.3997/2214-4609.201800070

Heigl, W. M., Diller, D. E., Gibson, R. L., & Pete Richter, P. (2019). *New insights into hydraulic fracture mechanics from next generation distributed acoustic data*. Paper presented at SEG Postconvention Workshop W-14: DAS Part2: What is next for DAS? *Operator needs versus Technology Suppliers' vision*. San Antonio, TX, USA.

Hemink, G., Groen, L., Deitrick, G., van der Horst, J., Kechichian, J., & Bakker, G. (2016). *Fiber optic based reservoir surveillance for injection conformance monitoring and production profiling in EOR fields*. SPE EOR Conference at Oil and Gas West Asia, *SPE-179813-MS*. https://doi.org/10.2118/179813-MS

Hemink, G., & van der Horst, J. (2018). On the use of distributed temperature sensing and distributed acoustic sensing for the application of gas lift surveillance. *SPE Production & Operations*, 33(04), 896–912. https://doi.org/10.2118/191130-PA

Henninges, J., Götz, J., Jousset, P., Lüth, S., & Reinsch, T. (2017). *New methods in geophysical exploration and monitoring with DTS and DAS. EAGE/DGG Workshop on Fibre Optic Technology in Geophysics*, Expended Abstracts, Fr SR 07. https://doi.org/10.3997/2214-4609.201700156

Higginson, P., Purkis, D., & Webster, M. (2017). *Advancing the application of downhole fibre optics with a novel low-cost disposable deployment method*. SPE Offshore Europe Conference & Exhibition, *SPE-186124-MS*. https://doi.org/10.2118/186124-MS

Hill, D. J. (2013). *Distributed Acoustic Sensing for permanent downhole monitoring*. 2nd EAGE Workshop on Permanent Reservoir Monitoring, Expanded Abstracts, *Th-01-05*. https://doi.org/10.3997/2214-4609.20131302

Hill, D. J. (2014). *Case study of a multi-well 4D DAS-VSP*. 76th EAGE Conference and Exhibition—Workshops, Extended Abstracts, *WS15-B02*. https://doi.org/10.3997/2214-4609.20140612

Hill, D. (2015). *Distributed Acoustic Sensing (DAS): Theory and applications*. In Frontiers in Optics, *OSA Technical Digest (Optical Society of America), paper FTh4E*.1. https://doi.org/10.1364/FIO.2015.FTh4E.1

Hill, D. (2019). *Next generation Distributed Fiber Sensing*. Paper presented at SEG Postconvention Workshop W-14: DAS Part2: What is next for DAS? *Operator needs versus Technology Suppliers' vision*. San Antonio, TX, USA.

Hill, K. O., Fujii, Y., Johnson, D. C., & Kawasaki, B. S. (1978). Photosensitivity in optical fiber waveguides: Application to reflection filter fabrication. *Applied Physics Letters*, 32(10), 647–649. https://doi.org/10.1063/1.89881

Holland, A. A., Preston, L., Larmat, C., & Morton, E. A. (2019). Microseismicity associated with the DAG-2 chemical explosion. Seismological Society of America Annual Meeting, *Abstract*. Seattle, WA, USA.

Holley, E. H., Jones, T. A., Dodson, J., & Salazar, J. (2014). Using distributed optical sensing to constrain fracture models and confirm reservoir coverage in the Permian Basin. SPE Hydraulic Fracturing Technology Conference, *SPE-168610-MS*. https://doi.org/10.2118/168610-MS

Holley, E. H., & Kalia, N. (2015). *Fiber-optic monitoring: Stimulation results from unconventional reservoirs*. Unconventional Resources Technology Conference, *URTEC-2151906-MS*. https://doi.org/10.15530/URTEC-2015-2151906

Holley, E., Martysevich, V., Cook, K., & Gale, S. (2020). *Using automation while pumping to improve stimulation uniformity and consistency: A series of case studies*. SPE Hydraulic

Fracturing Technology Conference and Exhibition, *SPE-199742-MS*. https://doi.org/10.2118/199742-MS

Hopp, C., Schoenball, M., Rodríguez Tribaldos, V., Ajo-Franklin, J. B., & Guglielmi, Y. (2020). *Fracture stimulation as seen through picoseismicity, borehole displacement probes and distributed fiber-optic sensing: The EGS collab experiment*. Seismological Society of America Annual Meeting, *Abstract*. Albuquerque, NM, USA.

Hornby, B. E., Williams, B. A., Lewis, K. A., Garossino, P. G., & Bostick, F. X. (2003). *Field test of a permanent in-well fiber optic seismic system*. 73rd SEG Annual International Meeting, *Expanded Abstract* (pp. 2219–2222). https://doi.org/10.1190/1.1817788

Hornby, B. E., Bostick, F. X., Williams, B., Lewis, K., & Garossino, P. (2005). Field test of a permanent in-well fiber-optic seismic system. *Geophysics*, 70(4), E11–E19. https://doi.org/10.1190/1.1993709

Hornby, B. E., Barkved, O. I., Askim, O. J., Knudsen, S., Bostick, F. X., & Williams, B. A. (2006). *Reservoir monitoring using permanent in-well seismic*. 68th EAGE Conference and Exhibition, *Expanded Abstracts*, A02. https://doi.org/10.3997/2214-4609.201402556

Hornby, B., Barkved, O., Askim, O., Bostick, F. X., & Williams, B. (2007). *Permanent fiber-optic borehole seismic installation and imaging at Valhall*. 69th EAGE Conference and Exhibition, *Expanded Abstracts* (pp. 1–5). https://doi.org/10.3997/2214-4609.201401872

Hornby, B., Barkved, O. I., Williams, B., & Bostick, T. (2007). *Reservoir monitoring using permanent in-well seismic*. International Petroleum Technology Conference, *IPTC11789*. https://doi.org/10.3997/2214-4609-pdb.147.iptc11789

Hornby, B., & Burch, T. (2008). *Passive "drive by" imaging in a deepwater production well using permanent borehole seismic sensors*. 78th SEG Annual International Meeting, *Expanded Abstracts* (pp. 349–352). https://doi.org/10.1190/1.3054820

Hornby, B., Barkved, O., Sugianto, H., & Nahm, J. (2012*). 4D monitoring with permanent borehole seismic sensors: progress, challenges, and the road ahead*. 82nd SEG Annual International Meeting, Expanded Abstracts. https://doi.org/10.1190/segam2012-1519.1

Hornby, B. E., Li, Q., Konkler, J., & Soulas, S. (2014). *A permanent borehole seismic field trial comparing fiber-optic distributed acoustic sensing with dedicated geophones and hydrophones*. 76th EAGE Conference and Exhibition—Workshops, Extended Abstracts, *WS15-D02*. https://doi.org/10.3997/2214-4609.20140618

Hornby, B. (2017). *Achieving business value using high-end borehole geophysics: Are we there yet?* 87th SEG Annual International Meeting, *Expanded Abstracts* (pp. 5255–5260). https://doi.org/10.1190/segam2017-17589064.1

Horne, S., Baird, A., Stork, A., & Naldrett, G. (2019). *Machine learning for DAS microseismic event detection*. 81st EAGE Conference and Exhibition, Expanded Abstracts, *WS10_13*. https://doi.org/10.3997/2214-4609.201901972

Hornman, K., & Forgues, E. (2013). *Permanent reservoir monitoring with onshore surface seismic*. 2nd EAGE Workshop on Permanent Reservoir Monitoring, Expanded Abstracts, *We-01-04*. https://doi.org/10.3997/2214-4609.20131292

Hornman, K., Kuvshinov, B., Zwartjes, P., & Franzen, A. (2013). *Field trial of a broadside-sensitive distributed acoustic sensing cable for surface seismic*. 75th EAGE Conference & Exhibition, Expanded Abstracts, Tu 04 08. https://doi.org/10.3997/2214-4609.20130383

Hornman, J. C., Mateeva, A., Potters, J. H. H. M., & Lopez, J. L. (2015). *New concepts for lowering the cost of frequent seismic reservoir monitoring onshore*. 85th SEG Annual International Meeting, *Expanded Abstracts* (pp. 5518–5522). https://doi.org/10.1190/segam2015-5826463.1

Hornman, J. C. (2017). Field trial of seismic recording using distributed acoustic sensing with broadside sensitive fibre-optic cables. *Geophysical Prospecting*, 65(1), 35–46. https://doi.org/10.1111/1365-2478.12358

Huckabee, P., Ellis, D., Keable, B., Gouthaman, V., Ugueto, G., Nasse, D., & Sawyer, J. (2017). *Evaluation and management of stimulation placement control in cemented sleeve completions*. SPE Annual Technical Conference and Exhibition, SPE Annual Technical Conference and Exhibition, *SPE-187080-MS*. https://doi.org/10.2118/187080-MS

Hull, R., Meek, R., Bello, H., & Miller, D. (2017). *Case history of DAS fiber-based microseismic and strain data, monitoring horizontal hydraulic stimulations using various tools to highlight physical deformation processes (Part A)*. SPE/AAPG/SEG Unconventional Resources Technology Conference, *URTEC-2695282-MS*. https://doi.org/10.15530/URTEC-2017-2695282

Hull, R., Meek, R., Bello, H., Woller, K., & Wagner, J. (2019). *Monitoring horizontal well hydraulic stimulations and geomechanical deformation processes in the unconventional shales of the Midland Basin using fiber-based time-lapse VSPs, microseismic, and strain data. The Leading Edge*, 38, 130–137. https://doi.org/10.1190/tle38020130.1

Humphries, M., Vidal, J. A. M., & de Dios, J. C. (2015). *VSP monitoring for CO2 migration tracking in fractured rock massifs*. 77th EAGE Conference and Exhibition, Expanded Abstracts, Tu N112 02. https://doi.org/10.3997/2214-4609.201412672

Humphries, M., Marin Vidal, J. A., & de Dios, J. C. (2016). *VSP monitoring for CO2 migration tracking in fractured rock massifs*. 78th EAGE Conference and Exhibition, Expended Abstracts, *WS05* A03. https://doi.org/10.3997/2214-4609.201601642

Huot, F., Ma, Y., Cieplicki, R., Martin, E., & Biondi, B. (2017). *Automatic noise exploration in urban areas*. 87th SEG Annual International Meeting, *Expanded Abstracts* (pp. 5027–5032). https://doi.org/10.1190/segam2017-17774369.1

Huot, F., & Biondi, B. (2018). Machine learning algorithms for automated seismic ambient noise processing applied to DAS acquisition. 88th SEG Annual International Meeting, *Expanded Abstracts* (pp. 5501–5505). https://doi.org/10.1190/segam2018-w20-03.1

Huot, F., Biondi, B., & Beroza, G. (2018). *Jump-starting neural network training for seismic problems*. 88th SEG Annual International Meeting, *Expanded Abstracts* (pp. 2191–2195). https://doi.org/10.1190/segam2018-2998567.1

Huot, F., Martin, E. R., & Biondi, B. (2018). *Automated ambient-noise processing applied to fiber-optic seismic acquisition (DAS)*. 88th SEG Annual International Meeting, *Expanded Abstracts* (pp. 4688–4692). https://doi.org/10.1190/segam2018-2997880.1

Hveding, F., & Porturas, F. (2015). *Integrated applications of fiber-optic distributed acoustic and temperature sensing*. SPE Latin American and Caribbean Petroleum Engineering, *SPE-177222-MS*. https://doi.org/10.2118/177222-MS

Hveding, F., & Bukhamsin, A. (2018). *Distributed Fiber Optic Sensing—a technology review for upstream oil and gas applications*. SPE Kingdom of Saudi Arabia Annual Technical Symposium and Exhibition, *SPE-192323-MS*. https://doi.org/10.2118/192323-MS

Hveding, F. (2020). *Best practice for fiber optic leak detection, injection and production profiling*. First EAGE Workshop on Fibre Optic Sensing, Expended Abstract. https://doi.org/10.3997/2214-4609.202030020

Ichikawa, M., Kurosawa, I., Uchida, S., Kato, A., Ito, Y., Takagi, S., et al. (2019). *Case study of hydraulic fracture monitoring using low-frequency components of DAS data*. 89th SEG Annual International Meeting, *Expanded Abstracts* (pp. 948–952). https://doi.org/10.1190/segam2019-3214251.1

Idachaba, F., Wokoma, E., Okuns, G., Brown, C., & Walker, I. (2013). *Fiber optic based pipeline oil and gas leak and intruder detection system with security intervention plan*. SPE Nigeria Annual International Conference and Exhibition, *SPE-167537-MS*. https://doi.org/10.2118/167537-MS

In 't Panhuis, P., den Boer, H., van der Horst, J., Paleja, R., Randell, D., Joinson, D., et al. (2014). Flow monitoring and production profiling using DAS. SPE Annual Technical Conference and Exhibition, SPE-170917-MS. https://doi.org/10.2118/170917-MS

Innanen, K. A. (2017a). *Parameterization of a helical DAS fibre wound about an arbitrarily curved cable axis*. 79th EAGE Conference and Exhibition, Expanded Abstracts, We A5 15. https://doi.org/10.3997/2214-4609.201701202

Innanen, K. A. (2017b). *Determination of seismic-tensor strain from Helical Wound Cable-Distributed Acoustic Sensing cable with arbitrary and nested-helix winds*. 87th SEG Annual International Meeting, *Expanded Abstracts* (pp. 926–930). https://doi.org/10.1190/segam2017-17664060.1

Innanen, K., & Eaid, M. (2018). *Towards discrimination of elastic wave modes with shaped DAS Fibre-optic cables*. 80th EAGE Conference and Exhibition, Expended Abstracts, *Th* P7 14. https://doi.org/10.3997/2214-4609.201801628

Innanen, K. A., Lawton, D., Hall, K., Bertram, K. L., Bertram, M. B., & Bland, H. C. (2019). Design and deployment of a prototype multicomponent Distributed Acoustic Sensing loop array. 89th SEG Annual International Meeting, *Expanded Abstracts* (pp. 953–957). https://doi.org/10.1190/segam2019-3216304.1

Irvine-Fortescue, J., Battashi, F., & Rubalcava, D. (2016). *Application of fiber optics in EOR trials*. SPE EOR Conference at Oil and Gas West Asia, *SPE-179777-MS*. https://doi.org/10.2118/179777-MS

Jacobs, T. (2014). Downhole fiber-optic monitoring: An evolving technology. *Journal of Petroleum Technology*, 66(08), 44–53. https://doi.org/10.2118/0814-0044-JPT

James, S. R., Knox, H. A., Preston, L., Knox, J. M., Grubelich, M. C., King, D. K., et al. (2017). Fracture detection and imaging through relative seismic velocity changes using distributed acoustic sensing and ambient seismic noise. *The Leading Edge*, 36, 1009–1017. https://doi.org/10.1190/tle36121009.1

Jaroszewicz, L. R., Kurzych, A., Krajewski, Z., Marć, P., Kowalski, J. K., Bobra, P., et al. (2016). Review of the usefulness of various rotational seismometers with laboratory results of fibre-optic ones tested for engineering applications. *Sensors (Basel, Switzerland)*, 16(12), 2161. https://doi.org/10.3390/s16122161

Jayaram, V., Hull, R., Wagner, J., & Zhang, S. (2019). *Hydraulic fracturing stimulation monitoring with distributed fiber optic sensing and microseismic in the Permian Wolfcamp Shale Play*. SPE/AAPG/SEG Unconventional Resources Technology Conference, *URTEC-2019-291-MS*. https://doi.org/10.15530/urtec-2019-291

Jestin, C., Lanticq, V., Clément, P., Calbris, G., Villar, M., & Maurer, V. (2020). *Combination of DTS, DAS and pressure measurements using fibre optics in the geothermal site of Soultz-sous-Forêts*. First EAGE Workshop on Fibre Optic Sensing, Expended Abstract. https://doi.org/10.3997/2214-4609.202030024

Jiang, T., Zhan, G., Hance, T., Sugianto, S., Soulas, S., & Kjos, E. (2016). *Valhall dual-well 3D DAS VSP field trial and imaging for active wells*. 86th SEG Annual International Meeting, *Expanded Abstracts* (pp. 5582–5586). https://doi.org/10.1190/segam2016-13871754.1

Jin, G., & Roy, B. (2017). Hydraulic-fracture geometry characterization using low-frequency DAS signal. *The Leading Edge*, 36, 975–980. https://doi.org/10.1190/tle36120975.1

Jin, G. (2019). *DAS: A broadband strain-rate sensor and its applications. Paper presented at SEG Postconvention Workshop W-1: DAS—Part* 1: Recent Advances in Subsurface Characterization using Distributed Acoustic Sensing and the Road Ahead. San Antonio, TX, USA.

Jin, G., Friehauf, K., Roy, B., Constantine, J. J., Swan, H. W., Krueger, K. R., & Raterman, K. T. (2019). *Fiber optic sensing-based production logging methods for low-rate oil producers*. SPE/AAPG/SEG Unconventional Resources Technology Conference, *URTEC-2019-943-MS*. https://doi.org/10.15530/urtec-2019-943

Joe, H.-E., Yun, H., Jo, S.-H., Jun, M. B. G., & Min, B.-K. (2018). A review on optical fiber sensors for environmental monitoring. *International Journal of Precision Engineering and Manufacturing-Green Technology*, 5(1), 173–191. https://doi.org/10.1007/s40684-018-0017-6

Johannessen, K., Drakeley, B., & Farhadiroushan, M. (2012). *Distributed Acoustic Sensing—a new way of listening to your well/reservoir*. SPE Intelligent Energy International, Expended Abstracts, *SPE* 149602. https://doi.org/10.2118/149602-MS

Jousset, P., Reinsch, T., Henninges, J., Blanck, H., & Ryberg, T. (2016). *Strain and ground-motion monitoring at magmatic areas: ultra-long and ultra-dense networks using fibre optic sensing systems*. General Assembly European Geosciences Union, Geophysical Research Abstracts 18, *EGU2016-15707*.

Jousset, P., Reinsch, T., Henninges, J., Blanck, H., & Ryberg, T. (2017). *Crustal exploration and monitoring seismic events with a fibre-optic cable deployed at the ground surface in Iceland.*

79th EAGE Conference and Exhibition, Expanded Abstracts. *Fr SR* P09. https://doi.org/10.3997/2214-4609.201700169

Jousset, P., Reinsch, T., Ryberg, T., Blanck, H., Clarke, A., Aghayev, R., et al. (2018). Dynamic strain determination using fibre-optic cables allows imaging of seismological and structural features. *Nature Communications*, 9, 2509. https://doi.org/10.1038/s41467-018-04860-y

Jreij, S., Trainor-Guitton, W., & Miller, D. (2017). *Field data comparison of 3D horizontal distributed acoustic sensing and geophones*. 87th SEG Annual International Meeting, *Expanded Abstracts* (pp. 1–6). https://doi.org/10.1190/segam2017-17793499.1

Jreij, S. F., Trainor-Guitton, W. J., & Simmons, J. L. (2018). *Determining the added value of surface-distributed acoustic sensors in sparse geophone arrays using transfer learning with a convolutional neural network*. 88th SEG Annual International Meeting, *Expanded Abstracts* (pp. 4693–4697). https://doi.org/10.1190/segam2018-2997965.1

Jreij, S. F., Trainor-Guitton, W. J., Simmons, J. L., & PoroTomo Team. (2018). *Improving point-sensor image resolution with Distributed Acoustic Sensing at Brady's enhanced geothermal system*. 43rd Workshop on Geothermal Reservoir Engineering, PROCEEDINGS (pp. 1–12). *SGP-TR-213*.

Juskaitis, R., Mamedov, A. M., Potapov, V. T., & Shatalin, S. V. (1994). Interferometry with Rayleigh backscattering in a single-mode optical fiber. *Optics Letters*, 19(3), 225–227. https://doi.org/10.1364/OL.19.000225

Kahn, D., & Fish, B. (2017). *A comparison of DAS, surface patch, and surface 3C microseismic data: A case study from the Eagle Ford*. GeoConvention 2017, Expanded Abstracts.

Kahn, D., Karrenbach, M. H., Cole, S., Boone, K., Ridge, A., Rich, J., et al. (2017). *DAS microseismic and strain monitoring during hydraulic fracturing*. *AGU Fall Meeting Abstract S33F-04*.

Kamal, S. Z. (2014). *Fiber optic sensing: Evolution to value*. SPE Intelligent Energy Conference & Exhibition, *SPE-167907-MS*. https://doi.org/10.2118/167907-MS

Kammerer, C. G., & MacLaughlin, M. M. (2017). *Performance of fiber optic sensing technologies for distributed monitoring of ground deformation and temperature in an underground facility*. 51st U.S. Rock Mechanics/Geomechanics Symposium, *ARMA-2017-0944*.

Karrenbach, M., Ridge, A., Cole, S., Boone, K., Kahn, D., Rich, J., et al. (2017). *DAS microseismic monitoring and integration with strain measurements in hydraulic fracture profiling*. SPE/AAPG/SEG Unconventional Resources Technology Conference, *URTEC-2670716-MS*. https://doi.org/10.15530/URTEC-2017-2670716

Karrenbach, M. H., Cole, S., Williams, J. J., Biondi, B. L., McMurtry, T., Martin, E. R., & Yuan, S. (2017). *Detection and mapping of the September 2017 Mexico Earthquakes using DAS fiber-optic infrastructure arrays*. *AGU Fall Meeting Abstract S33G-2374*.

Karrenbach, M., Kahn, D., Cole, S., Ridge, A., Boone, K., Rich, J., et al. (2017). Hydraulic-fracturing-induced strain and microseismic using in situ distributed fiber-optic sensing. *The Leading Edge*, 36, 837–844. https://doi.org/10.1190/tle36100837.1

Karrenbach, M. (2018a). OptaSense update. Paper presented at AGU Workshop: Distributed Acoustic Sensing-Principles and Case Studies. Washington, D.C., *USA*.

Karrenbach, M. (2018b). *Hydrocarbon reservoir monitoring*. Paper presented at AGU Workshop: Distributed Acoustic Sensing-Principles and Case Studies. Washington, D.C., *USA*.

Karrenbach, M., Kahn, D., Cole, S., & Langton, D. (2018). *Analyzing hydraulic fracturing operations using Distributed Fiber-optic Sensing*. Abstract. *Paper presented at SEG Summer Research Workshop: Recent Advances and Applications in Borehole Geophysics*. Galveston, TX, USA.

Karrenbach, M., Kahn, D., Cole, S., Langton, D., Boone, K., & Chavarria, A. (2018). *DAS as a tool for monitoring hydraulic fracturing operations*. Paper presented at SEG Postconvention Workshop W-20: DAS-Validating Measurements, Developing Processing Methods, *and Integrating to Optimize Velocity Models for Improving Subsurface Imaging*. Anaheim, CA, USA.

Karrenbach, M. (2019a). *Keynote—Fibre-optic distributed sensing for infrastructure objects and near-surface monitoring*. EAGE Near Surface Geoscience Conference & Exhibition, Expended Abstracts, *Tu_INFRA_14*. https://doi.org/10.3997/2214-4609.201902548

Karrenbach, M. (2019b). *Opportunities with multi-fiber DAS installation in hydraulic fracture monitoring. Paper presented at SEG Postconvention Workshop W-1: DAS—Part* 1: Recent Advances in Subsurface Characterization using Distributed Acoustic Sensing and the Road Ahead. San Antonio, TX, USA.

Karrenbach, M., & Cole, S. (2019). *DAS microseismic source mechanism estimation by forward-modeling*. 89th SEG Annual International Meeting, *Expanded Abstracts* (pp. 1004–1008). https://doi.org/10.1190/segam2019-3216570.1

Karrenbach, M., Cole, S., *Minto*, C., & Godfrey, A. (2019). *Distributed fiber-optic sensing on infrastructure installations*. Seismological Society of America Annual Meeting, Abstract. Seattle, WA, USA.

Karrenbach, M., Cole, S., Ridge, A., Boone, K., Kahn, D., Rich, J., et al. (2019). Fiber-optic distributed acoustic sensing of microseismicity, strain and temperature during hydraulic fracturing. *Geophysics*, 84(1), D11–D23. https://doi.org/10.1190/geo2017-0396.1

Karrenbach, M., & Laing, C. (2020). *Towards long-range distributed acoustic sensing in subsea applications*. Seismological Society of America Annual Meeting, *Abstract*. Albuquerque, NM, USA.

Kasahara, J., Hasada, Y., & Yamaguchi, T. (2018). *Seismic time-lapse approach to image the oil, gas and geothermal reservoirs and CO2 storage zones*. Abstract. *Paper presented at SEG Summer Research Workshop: Recent Advances and Applications in Borehole Geophysics*. Galveston, TX, USA.

Kasahara, J., Hasada, Y., Kawashima, H., Sugimoto, Y., Yamauchi, Y., Yamaguchi, T., & Yamaguchi, K. (2018). *Comparison of DAS (distributed acoustic sensor) and seismometer measurements to evaluate physical quantities in the field*. 88th SEG Annual International Meeting, *Expanded Abstracts* (pp. 191–195). https://doi.org/10.1190/segam2018-2989627.1

Kasahara, J., Hasada, Y., Sugimoto, Y., Kawashima, H., Yamauchi, Y., Yamaguchi, T., & Kubota, K. (2018a). *Distinct temporal change of waveforms due to precipitation suggesting the near-surface effect revealed by a Dense-But-Sh*. 80th EAGE Conference and Exhibition, Expended Abstracts, *Th* P1 04. https://doi.org/10.3997/2214-4609.201801532

Kasahara, J., Hasada, Y., Sugimoto, Y., Kawashima, H., Yamauchi, Y., Yamaguchi, T., & Kubota, K. (2018b). *Evaluation of time lapse of the near-surface layer due to precipitation*. 88th SEG Annual International Meeting, *Expanded Abstracts* (pp. 5348–5351). https://doi.org/10.1190/segam2018-2990865.1

Kasahara, J. (2019). *Seismic approach characterizing geothermal reservoirs using DAS and FWI*. EAGE/BVG/FKPE Joint Workshop on Borehole Geophysics and Geothermal Energy, Expended Abstracts. https://doi.org/10.3997/2214-4609.201903335

Kasahara, J., Hasada, Y., & Yamaguchi, T. (2019). *Seismic imaging of supercritical geothermal reservoir using full-waveform inversion method*. 44th Workshop on Geothermal Reservoir Engineering, Proceedings (pp. 1–5). *SGP-TR-214*.

Kasahara, J., Hasada, Y., Kuzume, H., Fujise, Y., & Yamaguchi, T. (2019). *Seismic feasibility study to identify supercritical geothermal reservoirs in a geothermal borehole using DTS and DAS*. 81st EAGE Conference and Exhibition, Expended Abstracts, *We_R10_11*. https://doi.org/10.3997/2214-4609.201901263

Kasahara, J., Hasada, Y., & Kuzume, H. (2019). *A possible geothermal source at around 4 km depth estimated by the seismic observation in Ibusuki geothermal area*. Japan Geoscience Union (JPGU) annual meeting abstract, ACV39-03. Makuhari, Chiba, Japan.

Kasahara, J., Hasada, Y., Kuzume, H., Mikada, H., & Fujise, Y. (2020). *The second seismic study at the geothermal field in Southern Kyushu, Japan using an optical fiber system and surface geophones*. 45th Workshop on Geothermal Reservoir Engineering, PROCEEDINGS, *SGP-TR-216*. 1–5.

Kavousi Ghahfarokhi, P., Carr, T., Wilson, T., Amini, S., Wilson, C., Thomas, M., et al. (2017). *Correlating distributed acoustic sensing (DAS) to natural fracture intensity for the Marcellus Shale*. 87th SEG Annual International Meeting, *Expanded Abstracts* (pp. 5386–5390). https://doi.org/10.1190/segam2017-17675576.1

Kavousi Ghahfarokhi, P., Carr, T., & Mellors, R. J. (2017). *Improved interpretation of Distributed Acoustic Sensing (DAS) fiber optic data in stimulated wells using seismic attributes. AGU Fall Meeting Abstract S33B-2379*.

Kavousi Ghahfarokhi, P., Carr, T., Bhattacharya, S., Elliott, J., Shahkarami, A., & Martin, K. (2018). *A fiber-optic assisted multilayer perceptron reservoir production modeling: A machine learning approach in prediction of gas production from the Marcellus Shale*. SPE/AAPG/SEG Unconventional Resources Technology Conference, *URTEC-2902641-MS*. https://doi.org/10.15530/URTEC-2018-2902641

Kavousi Ghahfarokhi, P., Carr, T., Song, L., Shukla, P., & Pankaj, P. (2018). *Seismic attributes application for the distributed acoustic sensing data for the Marcellus Shale: New insights to cross-stage flow communication*. SPE Hydraulic Fracturing Technology Conference and Exhibition, *SPE-189888-MS*. https://doi.org/10.2118/189888-MS

Kavousi Ghahfarokhi, P., Wilson, T., Carr, T., Kummar, A., Hammack, R., & Di, H. (2018). *Integrating Distributed Acoustic Sensing (DAS) and Borehole 3C Geophone array data to identify long-period long-duration seismic events during stimulation of a Marcellus Shale Gas Reservoir*. Paper presented at SEG Postconvention Workshop W-20: DAS-Validating Measurements, Developing Processing Methods, *and Integrating to Optimize Velocity Models for Improving Subsurface Imaging*. Anaheim, CA, USA.

Kavousi Ghahfarokhi, P., Wilson, T. H., Carr, T. R., Kumar, A., Hammack, R., & Di, H. (2019). Integrating distributed acoustic sensing, borehole 3C geophone array, and surface seismic array data to identify long-period long-duration seismic events during stimulation of a Marcellus Shale gas reservoir. *Interpretation*, *7*(1), *SA1–SA10*. https://doi.org/10.1190/INT-2018-0078.1

Kelley, M. (2018). *CO2 sequestration monitoring*. Paper presented at AGU Workshop: Distributed Acoustic Sensing-Principles and Case Studies. Washington, D.C., *USA*.

Kelley, M., Miller, D., Grindei, L., Modroo, A., & Gupta, N. (2018). *Distributed Acoustic Sensing (DAS) based Vertical Seismic Profiling (VSP) for monitoring CO2 injected into a Pinnacle-Reef Reservoir*. *14th International Conference on Greenhouse Gas Control Technologies GHGT-14*, Melbourne, Australia.

Kendall, R. (2014a). *A comparison of trenched Distributed Acoustic Sensing (DAS) to trenched and surface 3C geophones—Daly, Manitoba, Canada*. 76th EAGE Conference and Exhibition, Extended Abstracts, *Th ELI2* 10. https://doi.org/10.3997/2214-4609.20141464

Kendall, R. (2014b). A comparison of trenched Distributed Acoustic Sensing (DAS) to trenched and surface 3C geophones—Daly, Manitoba, Canada. 84th SEG Annual International Meeting, *Expanded Abstract* (pp. 36–40). https://doi.org/10.1190/segam2014-1539.1

Kersey, A. D. (2000). Optical Fiber Sensors for Permanent Downwell Monitoring Applications in the Oil and Gas Industry. *IEICE Transactions on Electronics, E83-C*(3), 400–404.

Keul, P. R., Mastin, E., Blanco, J., Maguérez, M., Bostick, F., & Knudsen, S. (2005). Using a fiber-optic seismic array for well monitoring. *The Leading Edge*, 24(1), 68–70, http://dx.doi.org/10.1190/1.1859704

Khalifeh, M., Gardner, D., & Haddad, M. Y. (2017). Technology trends in cement job evaluation using logging tools. Abu Dhabi International Petroleum Exhibition & Conference, *SPE-188274-MS*. https://doi.org/10.2118/188274-MS

Kimura, T., Lees, G., & Hartog, A. (2016). *Optical fiber vertical seismic profile using DAS (Distributed Acoustic Sensing) technology*. *20th International Symposium on Recent Advances in Exploration Geophysics* (RAEG), Extended Abstracts. https://doi.org/10.3997/2352-8265.20140207

Kimura, T., & Galybin, K. (2017). *Borehole seismic while sampling using FO technology*. 79th EAGE Conference and Exhibition, Extended Abstracts, *Th* A3 16. https://doi.org/10.3997/2214-4609.201700517

Kimura, T., Martinez, A., Cuny, T., Santivanez, R., Gmach, H., & Eliuk, N. (2017). *Borehole seismic acquisition using* *fiber-optic technology: Zero rig-time operation*. 87th SEG Annual International Meeting, *Expanded Abstracts* (pp. 936–940). https://doi.org/10.1190/segam2017-17678368.1

Kimura, T., Suzuki, K., Ali, S., Breninger, J., Tessman, J., Mahmoud, I. Z., & Hajjaj, S. (2018). *Hybrid 3D VSP using fiber-optic technology and a conventional borehole seismic array tool. 80th EAGE Conference and Exhibition*, Expended Abstracts, Th H 10. https://doi.org/10.3997/2214-4609.201801499

Kiyashchenko, D., Lopez, J., Berlang, W., Birch, B., Zwaan, M., Adawi, R., et al. (2013). Steam injection monitoring in a field of South Oman with borehole seismic—from single pattern to field scale surveillance with DAS. *The Leading Edge*, 32, 1246–1256. https://doi.org/10.1190/tle32101246.1

Kiyashchenko, D., Duan, Y., Mateeva, A., Johnson, D., Pugh, J., Geisslinger, A., & Lopez, J. (2019). *Maturing 4D DAS VSP for on-demand seismic monitoring in deepwater*. 89th SEG Annual International Meeting, *Expanded Abstracts* (pp. 5285–5289). https://doi.org/10.1190/segam2019-3216625.1

Knudsen, S., Havsgard, G. B., Berg, A., Nakstad, H., & Bostick, T. (2003). Permanently installed high-resolution fiber optic 3C/4D seismic sensor systems for in-well imaging and monitoring applications. SPIE Sixth Pacific Northwest Fiber Optic Sensor Workshop, *SPIE Proceedings*, 5278, 51–55. https://doi.org/10.1117/12.544383

Knudsen, S., Havsgård, G. B., Berg, A., & Bostick, F. (2006). *Flow-induced noise in fiber-optic 3-C seismic sensors for permanent tubing-conveyed installations*. 68th EAGE Conference and Exhibition, *Expanded Abstracts*. https://doi.org/10.3997/2214-4609.201402113

Kobayashi, Y., Uematsu, Y., Mochiji, S., & Xue, Z. (2020). A field experiment of walkaway distributed acoustic sensing vertical seismic profile in a deep and deviated onshore well in Japan using a fibre optic cable deployed inside coiled tubing. *Geophysical Prospecting*, 68(2), 501–520. https://doi.org/10.1111/1365-2478.12863

Koelman, J. V. (2011). Fiber-optic sensing technology providing well, reservoir information—anyplace, anytime. *Journal of Petroleum Technology*, 63(7), 22–23. https://doi.org/10.2118/0711-0022-JPT

Koelman, J. V., Lopez, J. L., & Potters, H. (2012a). *Fiber optic technology for reservoir surveillance*. International Petroleum Technology Conference, *IPTC-14629-MS*. https://doi.org/10.2523/IPTC-14629-MS

Koelman, J. V., Lopez, J. L., & Potters, H. (2012b). *Optical fibers: The neurons for future intelligent wells*. SPE Intelligent Energy International, *SPE* 150203. https://doi.org/10.2118/150203-MS

Koivisto, E., Malinowski, M., Heinonen, S., Cosma, C., Wojdyla, M., Vaittinen, K., et al. (2018). *From regional seismics to high-resolution resource delineation: Example from the Outokumpu Ore district, Eastern Finland*. 2nd Conference on Geophysics for Mineral Exploration and Mining, Expanded Abstracts, Tu 2MIN P04. https://doi.org/10.3997/2214-4609.201802716

Koller, A., Stewart, R. R., & Palmer, G. (2016). *Signal-to-noise, velocities, and elastic effects in a multi-offset DAS VSP from West Texas*. Paper presented at SEG Postconvention workshop W-10: Fiber-optic Sensing for Exploration and Monitoring: Development, Applications, *and Challenges*. Dallas, TX, USA.

Kortukov, D., & Williams, M. (2019). Fast-loop quantitative analysis of proppant distribution among perforation clusters. SPE Oklahoma City Oil and Gas Symposium, *SPE-195219-MS*. https://doi.org/10.2118/195219-MS

Kragas, T. K., Williams, B., & Myers, G. A. (2001). *The optic oil field: Deployment and application of permanent in-well fiber optic sensing systems for production and reservoir monitoring*. SPE Annual Technical Conference and Exhibition, *SPE-71529-MS*. https://doi.org/10.2118/71529-MS

Kragas, T. K., Pruett, E., & Williams, B. (2002). *Installation of in-well fiber-optic monitoring systems*. SPE Annual Technical Conference and Exhibition. Extended Abstracts, *SPE-77710-MS*. https://doi.org/10.2118/77710-MS

Krawczyk, C., Jousset, P., & Reinsch, T. (2019). *Fibre-optic strain sensing: Game changer for (urban) seismic surveying?* EAGE Near Surface Geoscience Conference & Exhibition, 1st Conference on Geophysics for Infrastructure Planning Monitoring and BIM. *Expanded Abstracts*, https://doi.org/10.3997/2214-4609.201902547

Krietsch, H., Gischig, V., Jalali, M. R., Doetsch, J., Valley, B., & Amann, F. (2018). *A comparison of FBG- and Brillouin-strain sensing in the framework of a decameter-scale hydraulic stimulation experiment*. 52nd U.S. Rock Mechanics/Geomechanics Symposium, *ARMA-2018-800*.

Kruiver, P., Obando-Hernández, E., Pefkos, M., Karaoulis, M., Bakx, W., Doornenbal, P., et al. (2020). *Fibre optic monitoring of groundwater flow in a drinking water extraction well field*. First EAGE Workshop on Fibre Optic Sensing, Expended Abstract. https://doi.org/10.3997/2214-4609.202030010

Kuvshinov, B. N. (2016). Interaction of helically wound fibre-optic cables with plane seismic waves. *Geophysical Prospecting*, 64(3), 671–688. https://doi.org/10.1111/1365-2478.12303

La Follett, J., Wyker, B., Hemink, G., Hornman, K., Lumens, P., & Franzen, A. (2014). *Evaluation of fiber-optic cables for use in distributed acoustic sensing: Commercially available cables and novel cable designs*. 84th SEG Annual International Meeting, *Expanded Abstract* (pp. 5009–5013). https://doi.org/10.1190/segam2014-0297.1

La Follett, J. R., Yang, Z., Lopez, J., Grandi, S., & Hornman, K. (2016*). Maturing the buried cross-spread concept for land seismic monitoring: Borehole source tests*. 86th SEG Annual International Meeting, *Expanded Abstracts* (pp. 5446–5450). https://doi.org/10.1190/segam2016-13961501.1

Lancelle, C., Lord, N. E., Wang, H. F., Fratta, D., Nigbor, R. L., Chalari, A., et al. (2014). *Directivity and sensitivity of fiber-optic cable measuring ground motion using a distributed acoustic sensing array*. Paper presented at the 2014 AGU Fall Meeting, San Francisco, CA, USA. *Abstract NS31C-3935*.

Langhammer, J., Nakstad, H., Eriksrud, M., Berg, A., Rønnekleiv, E., Henrik, O., & Thompson, M. (2008). *Fibre optic reservoir monitoring: Field trials and results*. Offshore Technology Conference, OTC 19391, https://doi.org/10.4043/19391-MS

Langhammer, J., Eriksrud, M., Nakstad, H., & Berg, C. (2009a). *Measuring the seismic wave with photons: Realization* *of the optical oil field*. International Petroleum Technology Conference, *IPTC-13945-MS*, https://doi.org/10.2523/IPTC-13945-MS

Langhammer, J., Eriksrud, M., Nakstad, H., & Berg, C. (2009b). Fiber optic permanent seismic system for increased hydrocarbon recovery. 11th International Congress of the Brazilian Geophysical Society & EXPOGEF 2009SEG Global Meeting Abstracts (pp. 1955–1958). https://doi.org/10.1190/sbgf2009-412

Langton, D., Kahn, D., & Fuller, B. (2019). Seismic reflection imaging with active sources and microseismic events recorded on horizontal DAS cables. SPE/AAPG/SEG Unconventional Resources Technology Conference, URTEC-2019-1144-MS. https://doi.org/10.15530/urtec-2019-1144

Lawton, D., Hall, K., & Gordon, A. (2018). *Advances in DAS seismic monitoring for CO2 storage*. 88th SEG Annual International Meeting, *Expanded Abstracts* (pp. 5500–5500). https://doi.org/10.1190/segam2018-w20-02.1

Lawton, D., Saeedfar, A., Hall, K., & Gordon, A. (2018). Advances in permanent borehole geophysical monitoring for CO2 storage. Abstract. *Paper presented at SEG Summer Research Workshop: Recent Advances and Applications in Borehole Geophysics*. Galveston, TX, USA.

Lay, V., Buske, S., Bodenburg, S. B., Townend, J., Kellett, R., Savage, M. K., et al. (2020). Seismic P wave velocity model from 3-D surface and borehole seismic data at the Alpine Fault DFDP-2 drill site (Whataroa, New Zealand). *Journal of Geophysical Research: Solid Earth*, 125(4). e2019JB018519. https://doi.org/10.1029/2019JB018519

Leaney, S., Mizuno, T., Velez, E., Cuny, T., & Perez, M. (2019). *Anisotropic model building, DAS simulation and imaging*. 89th SEG Annual International Meeting, *Expanded Abstracts* (pp. 999–1003). https://doi.org/10.1190/segam2019-3215957.1

LeBlanc, M., Ellmauthaler, A., Willis, M., & Wu, X. (2018). Use of long gauge length distributed acoustic sensing for improved spatial resolution of first break detection in vertic. 80th EAGE Conference and Exhibition, Expanded Abstracts, Th H 12. https://doi.org/10.3997/2214-4609.201801501

Leclercq, M., Hubans, C., & Suaudeau, E. (2016). Metrology of a dataset acquired with an optical fiber in a horizontal well. Abu Dhabi International Petroleum Exhibition & Conference, SPE-183170-MS. https://doi.org/10.2118/183170-MS

Lee, E., Yang, L., Mascagnini, C., Kshirsagar, A., Gohari, K., Jutila, H., et al. (2016). Production logging—a fiber optics way. 78th EAGE Conference and Exhibition, Expanded Abstracts, WS05 A04. https://doi.org/10.3997/2214-4609.201601643

Lellouch, A., Biondi, B., Horne, S., Meadows, M. A., & Nemeth, T. (2019). DAS observation of guided waves in a shale reservoir generated by perforation shots. 89th SEG Annual International Meeting, Expanded Abstracts (pp. 943–947). https://doi.org/10.1190/segam2019-3212667.1

Lellouch, A., Horne, S., Meadows, M. A., Farris, S., Nemeth, T., & Biondi, B. (2019). DAS observations and modeling of perforation-induced guided waves in a shale reservoir. *The Leading Edge*, 38, 858–864. https://doi.org/10.1190/tle38110858.1

Lellouch, A., Spica, Z., Biondi, B., & Ellsworth, W. L. (2019). Using vertical DAS arrays for continuous monitoring of induced seismicity. 81st EAGE Conference and Exhibition, Extended Abstracts, WS16_06. https://doi.org/10.3997/2214-4609.201902004

Lellouch, A., Yuan, S., Spica, Z., Biondi, B., & Ellsworth, W. L. (2019a). Moveout-based method for the detection of weak seismic events using downhole DAS arrays. 81st EAGE Conference and Exhibition, Extended Abstracts, We_R09_06. https://doi.org/10.3997/2214-4609.201901242

Lellouch, A., Yuan, S., Spica, Z., Biondi, B., & Ellsworth, W. L. (2019b). Seismic velocity estimation using passive downhole distributed acoustic sensing records: Examples from the San Andreas Fault Observatory at Depth. *Journal of Geophysical Research: Solid Earth*, 124, 6931–6948. https://doi.org/10.1029/2019JB017533

Lellouch, A., Yuan, S., Spica, Z., Biondi, B., & Ellsworth, W. L. (2019c). *Velocity analysis and moveout-based event detection using downhole DAS records*. 89th SEG Annual International Meeting, *Expanded Abstracts* (pp. 989–993). https://doi.org/10.1190/segam2019-3214849.1

Lellouch, A., Yuan, S., Spica, Z., Biondi, B., Ellsworth, W. (2019d*). A velocity-based earthquake detection system using downhole DAS arrays—examples from SAFOD*. Seismological Society of America Annual Meeting, *Abstract*. Seattle, WA, USA.

Lellouch, A., Yuan, S., Spica, Z., Biondi, B., & Ellsworth, W. (2019e). A velocity-based earthquake detection system using downhole DAS arrays—examples from SAFOD. 2019 EGU General Assembly, Geophysical Research Abstracts Vol. 21, EGU2019-6163.

Lellouch, A., Yuan, S., & Ellsworth, W., & Biondi, B. (2019). Velocity-based earthquake detection using downhole distributed acoustic sensing—examples from the San Andreas fault observatory at depth. *Bulletin of the Seismological Society of America*, 109(6), 2491–2500. https://doi.org/10.1785/0120190176

Lellouch, A., Meadows, M., *Nemeth*, T., & Biondi, B. (2020). Fracture properties estimation in unconventional reservoirs using seismic DAS records. First EAGE Workshop on Fibre Optic Sensing, Expended Abstract. https://doi.org/10.3997/2214-4609.202030005

Lescanne, M., Hy-Billiot, J., Aimard, N., & Prinet, C. (2011). The site monitoring of the Lacq industrial CCS reference project. *Energy Procedia*, 4, 3518–3525. https://doi.org/10.1016/j.egypro.2011.02.279

Lesnikov, V., & Allanic, C. (2014). DAS VSP acquisition–perspectives and challenges. 76th EAGE Conference and Exhibition—Workshops, Extended Abstracts, WS15-D01. https://doi.org/10.3997/2214-4609.20140617

Li, D., Huang, L., Chi, B., Ajo-Franklin, J., Tribaldos, V. R., Schoenball, M., et al. (2020a). Distributed Acoustic Sensing monitoring at the First EGS collab testbeds. 45th Workshop on Geothermal Reservoir Engineering, PROCEEDINGS (pp. 1–11). SGP-TR-216.

Li, D., Huang, L., Chi, B., Ajo-Franklin, J. B., Tribaldos, V. R., Schoenball, M., et al. (2020b). *Distributed acoustic sensing monitoring at the first EGS collab testbed*. Seismological Society of America Annual Meeting, *Abstract*. Albuquerque, NM, USA.

Li, L., Luo, Q., & Xiong, Q. (2019). *A new strategy for developing horizontal well inner potential based on fiber optic distributed acoustic sensing monitoring*. SPE Annual Technical Conference and Exhibition, *SPE-196219-MS*. https://doi.org/10.2118/196219-MS

Li, M., Wang, H., & Tao, G. (2015). Current and future applications of distributed acoustic sensing as a new reservoir geophysics tool. *The Open Petroleum Engineering Journal*, 8, 272–281. https://doi.org/10.2174/1874834101508010272

Li, Q., Hornby, B., & Konkler, J. (2013). *A permanent borehole fiber-optic distributed acoustic sensing experiment*. 83rd SEG Annual International Meeting, *Expanded Abstracts* (pp. 5057–5061). https://doi.org/10.1190/segam2013-0698.1

Li, X., Zhang, J., Grubert, M., Laing, C., Chavarria, A., Cole, S., & Oukaci, Y. (2020). *Distributed acoustic and temperature sensing applications for hydraulic fracture diagnostics*. SPE Hydraulic Fracturing Technology Conference and Exhibition, *SPE-199759-MS*. https://doi.org/10.2118/199759-MS

Li, Y., Chang, G., Hewett, B., Beal, E., & Yang, Z. (2015). *Detect water velocity variations with direct arrivals and water bottom multiples from 3D subsurface seismic OBN/DAS-VSP*. 3rd EAGE Workshop on Borehole Geophysics. Expanded Abstracts, *BG27*. https://doi.org/10.3997/2214-4609.201412205

Li, Y., Wu, H., Wong, W., Hewett, B., Liu, Z., Mateeva, A., & Lopez, J. (2015). *Velocity analysis and update with 3D DAS-VSP to improve borehole/surface seismic images*. 85th SEG Annual International Meeting, *Expanded Abstracts* (pp. 5285–5289). https://doi.org/10.1190/segam2015-5864923.1

Li, Y., King, K., Wong, W., Chen, T., & Wu, H. (2018). *Diagnosing Azimuthal variations of velocity model uncertainties using 3D DAS-VSP in GOM*. 88th SEG Annual International Meeting, *Expanded Abstracts* (pp. 5511–5515). https://doi.org/10.1190/segam2018-w20-05.1

Li, Y., Duan, Y., Chen, T., & Johnson, D. (2019). *Delineating salt boundaries using 3D DAS-VSP acquired inside salt in the Gulf of Mexico*. 89th SEG Annual International Meeting, *Expanded Abstracts* (pp. 5355–5359). https://doi.org/10.1190/segam2019-w1-02.1

Li, Z. (2018). *Earthquake detection with DAS arrays*. Paper presented at AGU Workshop: Distributed Acoustic Sensing-Principles and Case Studies. Washington, D.C., *USA*.

Li, Z., & Zhan, Z. (2018). Pushing the limit of earthquake detection with distributed acoustic sensing and template matching: a case study at the Brady geothermal field. *Geophysical Journal International*, 215, 1583–1593. https://doi.org/10.1093/gji/ggy359

Li, Z., Zhan, Z., Kohler, M. D., & Hauksson, E. (2019). *Quantitative assessment of earthquake detection capability of DAS, MEMS and broadband networks in Pasadena, CA*. Seismological Society of America Annual Meeting, *Abstract*. Seattle, WA, USA.

Liang, X., Mei, J., Zhang, C., Xu, J., An, S., Yu, G., et al. (2020). *Fluid production profile monitoring of marine shale reservoir using fiber sensing within the coiled tubing*. First EAGE Workshop on Fibre Optic Sensing, Expended Abstract. https://doi.org/10.3997/2214-4609.202030037

Lim Chen Ning, Ning, I., & Sava, P. (2016). *Multicomponent distributed acoustic sensing*, 86th SEG Annual International Meeting, *Expanded Abstracts* (pp. 5597–5602). https://doi.org/10.1190/segam2016-13952981.1

Lim Chen Ning, I., & Sava, P. (2017). *High-resolution multicomponent distributed acoustic sensing*. 87th SEG Annual International Meeting, *Expanded Abstracts* (pp. 941–946). https://doi.org/10.1190/segam2017-17679990.1

Lim Chen Ning, I., & Sava, P. (2018a). High-resolution multicomponent distributed acoustic sensing. *Geophysical Prospecting*, 66(6), 1111–1122. https://doi.org/10.1111/1365-2478.12634

Lim Chen Ning, I., & Sava, P. (2018b). Multicomponent distributed acoustic sensing: Concept and theory. *Geophysics*, 83(2), P1–P8. https://doi.org/10.1190/GEO2017-0327.1

Lim Chen Ning, I., & Sava, P. (2018c). *Multicomponent imaging with distributed acoustic sensing*. 88th SEG Annual International Meeting, *Expanded Abstracts* (pp. 4683–4687). https://doi.org/10.1190/segam2018-2997182.1

Lim Chen Ning, I., & Sava, P. (2019). *Seismic imaging with optimal source wavefield reconstruction*. 89th SEG Annual International Meeting, *Expanded Abstracts* (pp. 4156–4160). https://doi.org/10.1190/segam2019-3215813.1

Lim Chen Ning, I., Sava, P., Schultz, W., & Simmons, J. (2019). *Distributed acoustic sensing elastic least-squares reverse time migration*. 89th SEG Annual International Meeting, *Expanded Abstracts* (pp. 994–998). https://doi.org/10.1190/segam2019-3215816.1

Lindsey, N. J., Martin, E. R., Dreger, D. S., Freifeld, B., Cole, S., James, S. R., et al. (2017). Fiber-optic network observations of earthquake wavefields. *Geophysical Research Letters*, 44(23), 11792–11799. https://doi.org/10.1002/2017GL075722

Lindsey, N. J., Dou, S., Martin, E. R., Wagner, A. M., & Ajo-Franklin, J. B. (2017). *4-D permafrost thaw observations from ambient road traffic noise and a very dense distributed fiber optic sensing array*. AGU Fall Meeting abstract, S31A-0804.

Lindsey, N. J. (2018a). *Signals before subsidence: seismic waves slow down during permafrost thaw*. Paper presented at 5th European Conference on Permafrost, Chamonix-Mont Blanc, France, 23th June–1st July 2018.

Lindsey, N. (2018b). *How broadband is DAS? An empirical evaluation of instrument response using teleseismic surface waves*. Presented at AGU Workshop: Distributed Acoustic Sensing-Principles and Case Studies. Washington, D.C., *USA*.

Lindsey, N. J., Rademacher, H., Dreger, D. S., Titov, A., & Ajo-franklin, J. B. (2019). *How broadband is DAS? Two empirical evaluations of instrument response*. Seismological Society of America Annual Meeting, *Abstract*. Seattle, WA, USA.

Lindsey, N. J., Rademacher, H., & Ajo-franklin, J. B. (2019). *On the broadband instrument response of fiber-optic DAS*. AGU Fall Meeting Abstract, *S23B-05L*.

Lindsey, N. J., Dawe, T. C., & Ajo-franklin, J. B. (2019). Illuminating seafloor faults and ocean dynamics with dark fiber distributed acoustic sensing. *Science*, 366(6469), 1103–1107. https://doi.org/10.1126/science.aay5881

Lindsey, N. J., Rademacher, H., & Ajo-Franklin, J. B. (2020). On the broadband instrument response of fiber-optic DAS arrays. *Journal of Geophysics Research: Solid Earth*, 125(2), 1–16. https://doi.org/10.1029/2019JB018145

Lindsey, N. J., Ajo-Franklin, J. B., Dawe, C., Retailleau, L. M., *Gualtieri*, L., & Biondi, B. (2020). *Seafloor seismology with Distributed Acoustic Sensing in Monterey Bay*. Seismological Society of America Annual Meeting, Abstract. Albuquerque, NM, USA.

Liu, X., Wang, C., Shang, Y., Wang, C., Zhao, W., Peng, G., & Wang, H. (2017). Distributed Acoustic Sensing with Michelson interferometer demodulation. *Photonic Sensors*, 7(3), 193–198. https://doi.org/10.1007/s13320-017-0363-y

Longton, M. (2015). *The potential of utilizing intelligent Distributed Acoustic Sensor and existing single-mode and multimode optical fibers for monitoring the reservoir characteristics*. GeoConvention 2015, Extended Abstracts.

Longton, M., Strudley, A., White, D., Daley, T. M., & Miller, D. E. (2015). *Simultaneous acquisition of distributed acoustic seismic surveys with single-mode and multi-mode fiber optic cables at Aquistore CO2 storage site and a comparison with 3C Geophones. 3rd EAGE Workshop on Permanent Reservoir Monitoring*, Expanded Abstracts, Th A04. https://doi.org/10.3997/2214-4609.201411962

Lopez, J. L., Kiyashchenko, D., Mateeva, A., Mestayer, J., Berlang, W., Wills, P., et al. (2012). *3D VSP for affordable permanent reservoir monitoring onshore and offshore*. 82nd SEG Annual International Meeting, Expanded Abstracts (pp. 1–3). https://doi.org/10.1190/segam2012-1609.1

Lopez, J. L., Przybysz-Jarnut, J. K., Hornman, J. C., Mateeva, A., Zwaan, M., & Potters, H. (2015). *IOR/EOR monitoring onshore with frequent time-lapse seismic*. SPE Kuwait Oil and Gas Show and Conference, *SPE-175232-MS*. https://doi.org/10.2118/175232-MS

Lopez, J. L., Wills, P. B., La Follett, J. R., Hornman, J. C., Potters, J. H. H. M., van Lokven, M., et al. (2015). *Permanent seismic reservoir monitoring for real-time surveillance of thermal EOR at Peace River. 3rd EAGE Workshop on Permanent Reservoir Monitoring*, Expanded Abstracts, Th A03. https://doi.org/10.3997/2214-4609.201411961

Lopez, J., Mateeva, A., Chalenski, D., & Przybysz-Jarnut, J. (2017). *Valuation of distributed acoustic sensing VSP for frequent monitoring in deepwater*. 87th SEG Annual International Meeting, *Expanded Abstracts* (pp. 6044–6048). https://doi.org/10.1190/segam2017-17685577.1

Lopez, J. L., Chalenski, D. A., & Grandi, S. (2018). *Developing a fully autonomous marine seismic acquisition system for low-cost on-demand reservoir monitoring. EAGE Marine Acquisition Workshop*, Expended Abstracts, Th MA 07. https://doi.org/10.3997/2214-4609.201802098

Loranger, S., Gagné, M., Lambin-Iezzi, V., & Kashyap, R. (2015). Rayleigh scatter-based order of magnitude increase in distributed temperature and strain sensing by simple UV exposure of optical fibre. *Scientific Reports*, 5, 11177. https://doi.org/10.1038/srep11177

Lord, N. E., Zeng, X., Fratta, D., Feigl, K. L., Wang, H. F., & PoroTomo Team (2016). *Multispectral Analysis of Surface Wave (MASW) analysis of near-surface structure at brady hot springs from active source and ambient noise using a 8700-meter Distributed Acoustic Sensing (DAS) array. AGU Fall Meeting Abstract S13B-2559*. https://agu.confex.com/agu/fm16/meetingapp.cgi/Paper/190705

Lowe, T., Potts, M., & Wood, D. (2013). *A case history of comprehensive hydraulic fracturing monitoring in the Cana Woodford*. SPE Annual Technical Conference and Exhibition, *SPE-166295-MS*. https://doi.org/10.2118/166295-MS

Lu, P., Wright, R. F., Ziomek-Moroz, M., Buric, M. P., Zandhuis, P., & Ohodnicki, P. R. (2018). *A multifunctional fiber optic sensor for internal corrosion monitoring in natural gas transmission pipelines*. NACE International CORROSION, *NACE-2018-11492*.

Lumens, P., Franzen, A., Hornman, K., Karam, G. S., Hemink, G., Kuvshinov, B., et al. (2013). *Cable development for distributed geophysical sensing, with a field trial in surface seismic*. 5th European Workshop on Optical Fibre Sensors, *Proceedings of SPIE* 8794. https://doi.org/10.1117/12.2025693

MacDougall, T. W., & Sanders, P. E. (2004). *Large-diameter waveguide Bragg grating components and their application in downhole oil and gas sensing*. Proceedings of SPIE 5589, *Fiber Optic Sensor Technology and Applications* III. https://doi.org/10.1117/12.579165

MacPhail, W. F. P., Lisoway, B., & Banks, K. (2012). *Fiber optic distributed acoustic sensing of multiple fractures in a horizontal well*. SPE Hydraulic Fracturing Technology Conference, *SPE-152422-MS*. https://doi.org/10.2118/152422-MS

MacPhail, W., Kirkpatrick, J., Banack, B., Rapati, B., & Asfouri, A. A. (2016). *SAGD production observations using fiber optic distributed acoustic and temperature sensing: "SAGD DAS—listening to wells to improve understanding of inflow*." SPE Canada Heavy Oil Technical Conference, Expanded Abstracts, *SPE-180726-MS*. https://doi.org/10.2118/180726-MS

Mad Zahir, M. H., Abdul Aziz, K. M., Ghazali, A. R., Abdul Rahim, M. F., & Mohamed, M. D. D. (2019). *Permanent Distributed Fiber Optic Sensors DFOS for pro-active abandonment subsurface monitoring*. SPE Symposium: Decommissioning and Abandonment, *SPE-199186-MS*. https://doi.org/10.2118/199186-MS

Madsen, K. N., Parker, T., & Gaston, G. (2012). *A VSP field trial using Distributed Acoustic Sensing in a producing well in the North Sea*. 74th EAGE Conference and Exhibition, *Expanded Abstracts*, Y006. https://doi.org/10.3997/2214-4609.20148801

Madsen, K. N., Dümmong, S., Parker, T., Finfer, D., Travis, P. N., Bostick, T., & Thompson, M. (2013). *Simultaneous multiwell VSP using Distributed Acoustic Sensing*. 2nd EAGE Borehole Geophysics Workshop, Extended Abstracts, *BG07*. https://doi.org/10.3997/2214-4609.20142555.

Madsen, K. N., Dümmong, S., Kritski, A., Pedersen, A. S., Finfer, D., Gillies, A., & Travis, P. (2013). *Simultaneous multiwell VSP in the North Sea using Distributed Acoustic Sensing*. 75th EAGE Conference & Exhibition, Expanded Abstracts, Tu 08 08. https://doi.org/10.3997/2214-4609.20130431

Madsen, K. N., Thompson, M., Parker, T., & Finfer, D. (2013). A VSP field trial using distributed acoustic sensing in a producing well in the North Sea. *First Break*, 31(11), 51–56. https://doi.org/10.3997/1365-2397.2013027

Madsen, K. N., Thompson, M., Dümmong, S., Kritski, A., Petersen, Å. S., Finfer, D., & Parker, T. (2014). *Distributed* *acoustic borehole seismic in producing offshore wells*. 76th EAGE Conference and Exhibition—Workshops, Extended Abstracts, *WS15-C01*. https://doi.org/10.3997/2214-4609.20140614

Madsen, K. N., Tondell, R., & Kva, O. (2016). *Data-driven depth calibration for distributed acoustic sensing*. *The Leading Edge*, 35(7), 610–614. https://doi.org/10.1190/tle35070610.1

Mali, G. A., Clark, R. R., Kenyon, S. B., Young, A. W., & Paulk, D. H. (2019). *Field deployment of fiber optic technology to monitor overburden deformation*. SPE Annual Technical Conference and Exhibition, *SPE-196209-MS*. https://doi.org/10.2118/196209-MS

Mallat, S. G., & Zhang, Z. (1993). Matching pursuits with time-frequency dictionaries. *IEEE Transactions on Signal Processing*, 41(12), 3397–3415. https://doi.org/10.1109/78.258082

Marra, G., Clivatti, C., Luckett, R., Tampellini, A., Kronjager, J., Wright, L., et al. (2018). Ultrastable laser interferometry for earthquake detection with terrestrial and submarine cables. *Science*, 361(6401), 486–490. https://doi.org/10.1126/science.aat4458

Martin, E. R., Ajo-Franklin, J., Dou, S., Lindsey, N., Daley, T. M., Freifeld, B., et al. (2015). *Interferometry of ambient noise from a trenched distributed acoustic sensing array*. 85th SEG Annual International Meeting, *Expanded Abstracts* (pp. 2445–2450). https://doi.org/10.1190/segam2015-5902207.1

Martin, E., Lindsey, N., Dou, S., Ajo-Franklin, J., Daley, T., Freifeld, B., et al. (2016). *Interferometry of a roadside DAS array in Fairbanks, AK*. 86th SEG Annual International Meeting, *Expanded Abstracts* (pp. 2725–2729). https://doi.org/10.1190/segam2016-13963708.1

Martin, E. R., & Biondi, B. L. (2017). Ambient noise interferometry across two-dimensional DAS arrays. 87th SEG Annual International Meeting, *Expanded Abstracts* (pp. 2642–2646). https://doi.org/10.1190/segam2017-17677759.1

Martin, E. R., Biondi, B., Karrenbach, M., & Cole, S. (2017). *Ambient noise interferometry from DAS array in underground telecommunications conduits*. 79th EAGE Conference and Exhibition, Extended Abstracts, *Th* P6 05. https://doi.org/10.3997/2214-4609.201700743

Martin, E. R., Biondi, B. L., Yuan, S., Cole, S., & Kurtenbach, M. H. (2017). *Earthquake recording at the Stanford DAS Array with fibers in existing telecom conduits*. *AGU Fall Meeting Abstract S33F-02*.

Martin, E. R., Castillo, C. M., Cole, S., Sawasdee, P. S., Yuan, S., Clapp, R., et al. (2017). *Seismic monitoring leveraging existing telecom infrastructure at the SDASA: Active, passive, and ambient-noise analysis*. *The Leading Edge*, 36, 1025–1031. https://doi.org/10.1190/tle36121025.1

Martin, E. R., Chang, J., Huot, F., Ma, Y., & Biondi, B. (2017). *Urban ambient noise: From dense nodes to DAS*. 79th EAGE Conference and Exhibition, Extended Abstracts, *WS05* D01. https://doi.org/10.3997/2214-4609.201701688

Martin, E. (2018). *Stanford Telecomm Array*. Paper presented at AGU Workshop: Distributed Acoustic Sensing-Principles and Case Studies. Washington, D.C., *USA*.

Martin, E. R., & Biondi, B. L. (2018). *Eighteen months of continuous near-surface monitoring with DAS data collected under Stanford University*. 88th SEG Annual International Meeting, *Expanded Abstracts* (pp. 4958–4962). https://doi.org/10.1190/segam2018-2997853.1

Martin, E., Biondi, B., Cole, S., & Yuan, S. (2018). *Lessons learned from two years of continuous monitoring with DAS under Stanford*. Paper presented at SEG Postconvention Workshop W-20: DAS-Validating Measurements, Developing Processing Methods, *and Integrating to Optimize Velocity Models for Improving Subsurface Imaging*. Anaheim, CA, USA.

Martin, E. R., Lindsey, N. J., Ajo-Franklin, J. B., & Biondi, B. (2018). *Beyond Cosine-squared: Understanding trends in passive DAS field data*. Paper presented at SEG Postconvention Workshop W-20: DAS-Validating Measurements, Developing Processing Methods, *and Integrating to Optimize Velocity Models for Improving Subsurface Imaging*. Anaheim, CA, USA.

Martin, E. R., Huot, F., Ma, Y., Cieplicki, R., Cole, S., Karrenbach, M., & Biondi, B. L. (2018). A seismic shift in scalable acquisition demands new processing: Fiber-optic seismic signal retrieval in urban areas with unsupervised learning for coherent noise removal. *IEEE Signal Processing Magazine*, 35, 31–40. https://doi.org/10.1109/MSP.2017.2783381

Martin, E. R. (2019). *A scalable algorithm for cross-correlations of compressed ambient seismic noise*. 89th SEG Annual International Meeting, *Expanded Abstracts*, 3006–3010. https://doi.org/10.1190/segam2019-3216637.1

Martinez, A., Useche, M., & Guerra, R. (2020). *Use of fiber optic acoustics to improve drilling efficiency and well placement*. Offshore Technology Conference, *OTC-30866-MS*. https://doi.org/10.4043/30866-MS

Martinez, R., Chen, K., Santos, R., Hill, A. D., & Zhu, D. (2014). *Laboratory investigation of acoustic behavior for flow from fracture to a wellbore*. SPE Annual Technical Conference and Exhibition, *SPE-170788-MS*. https://doi.org/10.2118/170788-MS

Martinez, R., Hill, A. D., & Zhu, D. (2014). *Diagnosis of fracture flow conditions with acoustic sensing*. SPE Hydraulic Fracturing Technology Conference, *SPE-168601-MS*. https://doi.org/10.2118/168601-MS

Martins, W. A., de Campos, M. L. R., Chaves, R., Lordelo, C., Ellmauthaler, A., Nunes, L. O., & Barfoot, D. (2017). Communication models for distributed acoustic sensing for telemetry. *IEEE Sensors Journal*, 17(15), 4677–4688. https://doi.org/10.1109/JSEN.2017.2714023

Martuganova, E., Henninges, J., Stiller, M., Bauer, K., Norden, B., Krawczyk, C., & Huenges, E. (2019). *DAS-VSP measurements using wireline logging cable at the Groß Schönebeck geothermal research site, NE German Basin*. 81st EAGE Conference and Exhibition, Expended Abstracts, *We_R09_10*. https://doi.org/10.3997/2214-4609.201901246

Masoudi, A., & Newson, T. P. (2016). Contributed Review: Distributed optical fibre dynamic strain sensing. *Review of Scientific Instruments*, 87, 011501. https://doi.org/10.1063/1.4939482

Mast, M., Hoffman, B., Cox, C., & Byrd, D. (2020). *A structured approach to solving completion challenges with downhole fiber optic monitoring*. SPE Hydraulic Fracturing Technology Conference and Exhibition, *SPE-199702-MS*. https://doi.org/10.2118/199702-MS

Mateeva, A., Mestayer, J., Cox, B., Kiyashchenko, D., Wills, P., Lopez, J., et al. (2012). *Advances in Distributed Acoustic Sensing (DAS) for VSP*. 82nd SEG Annual International Meeting, *Expanded Abstracts* (pp. 1–5). https://doi.org/10.1190/segam2012-0739.1

Mateeva, A., Lopez, J., Mestayer, J., Wills, P., Cox, B., Kiyashchenko, D., et al. (2013). Distributed acoustic sensing for reservoir monitoring with VSP. *The Leading Edge*, 32(10), 1177–1300. https://doi.org/10.1190/tle32101278.1

Mateeva, A., Mestayer, J., Cox, B., Kiyashchenko, D., Wills, P., Grandi, S., et al. (2013). *Distributed acoustic sensing (DAS) for reservoir monitoring with VSP*. 2nd EAGE Borehole Geophysics Workshop, Extended Abstracts, *BG08*. https://doi.org/10.3997/2214-4609.20142556

Mateeva, A., Mestayer, J., Yang, Z., Lopez, J., Wills, P., Roy, J., & Bown, T. (2013). *Dual-well 3D VSP in deepwater made possible by DAS*. 83rd SEG Annual International Meeting, *Expanded Abstracts* (pp. 5062–5066). https://doi.org/10.1190/segam2013-0667.1

Mateeva, A., Lopez, L., Detomo, R., Potters, H., Berlang, W., Grandi, S., et al. (2014). *Distributed Acoustic Sensing (DAS) for reservoir monitoring with VSP*. 76th EAGE Conference and Exhibition—Workshops, Extended Abstracts, *WS15-C02*. https://doi.org/10.3997/2214-4609.20140615

Mateeva, A., Lopez, J., Hornman, K., Wills, P., Cox, B., Kiyashchenko, D., et al. (2014). *Recent advances in seismic monitoring of thermal EOR*. International Petroleum Technology Conference, *IPTC-17407-MS*. https://doi.org/10.2523/IPTC-17407-MS

Mateeva, A., Lopez, J., Potters, H., Mestayer, J., Cox, B., Kiyashchenko, D., et al. (2014). Distributed acoustic sensing for reservoir monitoring with vertical seismic profiling. *Geophysical Prospecting*, 62(4), 679–692. https://doi.org/10.1111/1365-2478.12116|

Mateeva, A., Hornman, J. C., Hatchell, P., Potters, H., & Lopez, J. (2015). *Frequent seismic monitoring for pro-active reservoir management*. 85th SEG Annual International Meeting, *Expanded Abstracts* (pp. 4817–4821). https://doi.org/10.1190/segam2015-5899850.1

Mateeva, A., Hornman, K., Grandi, S., Potters, H., Lopez, J., & La Follett, J. (2016). *Monitoring IOR/EOR onshore with frequent time-lapse seismic—status and survey adaptations for the Middle East*. SPE EOR Conference at Oil and Gas West Asia, *SPE-179824-MS*. https://doi.org/10.2118/179824-MS

Mateeva, A., & Zwartjes, P. (2017). *Depth calibration of DAS VSP channels: A new data-driven method*. 79th EAGE Conference and Exhibition, Extended Abstracts. *We* A5 14. https://doi.org/10.3997/2214-4609.201701201

Mateeva, A., Lopez, J., Chalenski, D., Tatanova, M., Zwartjes, P., Yang, Z., et al. (2017). 4D DAS VSP as a tool for frequent seismic monitoring in deep water. *The Leading Edge*, 36(12), 995–1000. https://doi.org/10.1190/tle36120995.1

Mateeva, A., Chalenski, D., Kiyashchenko, D., Duan, Y., Lopez, J., & Zwartjes, P. (2018). *Maturing* 4D *DAS VSP for frequent monitoring in deepwater*. Abstract. Paper presented at SEG Summer Research Workshop: Recent Advances and Applications in Borehole Geophysics. Galveston, TX, USA.

Mateeva, A. (2019). *Status of 4D DAS VSP for on-demand monitoring in Deepwater. Paper presented at SEG Postconvention Workshop W-1: DAS—Part* 1: Recent Advances in Subsurface Characterization using Distributed Acoustic Sensing and the Road Ahead. San Antonio, TX, USA.

McCarthy, C., Williams, T., & Butz, S. (2020). *High accuracy leak detection performed on entire live wellbore in real time using fiber-optic diagnostic-capable coiled tubing*. International Petroleum Technology Conference, *IPTC-19576-MS*. https://doi.org/10.2523/IPTC-19576-MS

Meek, R., Woller, K., George, M., Hull, R., Bello, H., & Wagner, J. (2017). *Time-lapse imaging of a hydraulic stimulation using 4D vertical seismic profiles and fiber optics in the midland basin (Part B)*. SPE/AAPG/SEG Unconventional Resources Technology Conference, *URTEC-2695394-MS*. https://doi.org/10.15530/URTEC-2017-2695394

Meek, R., Hull, R., Woller, K. Van Dok, R., & Tamimi, N. (2018). Direct arrival travel time tomography for time-lapse hydraulic fracture monitoring using a walk-above DAS VSP. Abstract. Paper presented at SEG Summer Research Workshop: Recent Advances and Applications in Borehole Geophysics. Galveston, TX, USA.

Meek, R., Hull, R., Woller, K., Wright, B., Martin, M., Bello, H., & Bailey, J. (2019). *Estimation of hydraulic fracture height and pressure deflation using a pulsed vertical seismic profile and a DAS Fiber in the Midland Basin*. SPE/AAPG/SEG Unconventional Resources Technology Conference, *URTEC-2019-585-MS*. https://doi.org/10.15530/urtec-2019-585

Mellors, R. J., Pitarka, A., Kuhn, M., Stinson, B., Ford, S. R., Snelson, C., & Drachenberg, D. (2014). Fiber Optic Acoustic Sensing (FOAS) far-field observations of SPE 3. 2014 Annual Meeting, SSA, Anchorage, Alaska. *Seismological Research Letters*, 85, 450.

Mellors, R. J., Sherman, C. S., Ryerson, F. J., Morris, J., Allen, G. S., Messerly, M. J., et al. (2017). *Modeling borehole microseismic and strain signals measured by a distributed fiber optic sensor*. *AGU Fall Meeting Abstract S33B-2383*.

Mellors, R. (2018). *Simulating distributed fiber optic sensing in the subsurface: Potential for improvements*. Paper presented at AGU Workshop: Distributed Acoustic Sensing-Principles and Case Studies. Washington, D.C., *USA*.

Mellors, R. J., Sherman, C., Messerly, M., Morris, J., Pax, P., Yu, C., et al. (2018). *Simulating distributed fiber optic sensing in the subsurface*. Abstract. *Presented at SEG Summer Research Workshop: Recent Advances and Applications in Borehole Geophysics*. Galveston, TX, USA.

Mellors, R. J., Sherman, C., Ryerson, R., Morris, J., Messerly, M., Yu, C., & Allen, G. (2018). *Modeling potential EGS signals from a distributed fiber optic sensor deployed in a borehole*. 43rd Workshop on Geothermal Reservoir Engineering, Proceedings (pp. 1–6). *SGP-TR-213*.

Mellors, R. J., Yu, C., Mart, C., Sherman, C., Pax, P., Fisher, K., et al. (2018). Understanding distributed fiber-optic sensing response for modeling of signals. 88th SEG Annual International Meeting, *Expanded Abstracts* (pp. 4679–4682). https://doi.org/10.1190/segam2018-2997008.1

Mellors, R. J., Gok, R., Messerly, M., Pax, P., Yu, C., Mart, C., et al. (2019). *Fiber optic sensing of local and regional* *earthquakes*. Seismological Society of America Annual Meeting, *Abstract*. Seattle, WA, USA.

Mellors, R. J., Sherman, C., Fu, P., McLennan, J., Morris, J., Ryerson, F., & Morency, C. (2019). Potential use of distributed acoustic sensors to monitor fractures and microseismicity at the FORGE EGS site. 44th Workshop on Geothermal Reservoir Engineering, PROCEEDINGS (pp. 1–6). *SGP-TR-214*.

Mellors, R. J., *Pitarka*, A., & Abbott, R. (2020). *Modeling distributed acoustic sensing signals from an explosion*. Seismological Society of America Annual Meeting, Abstract. Albuquerque, NM, USA.

Mestayer, J., Cox, B., Wills, P., Kiyashchenko, D., Lopez, J., Costello, M., et al. (2011). Field trials of distributed acoustic sensing for geophysical monitoring. 81st SEG Annual International Meeting, *Expanded Abstracts* (pp. 4253–4257). https://doi.org/10.1190/1.3628095

Mestayer, J., Grandi, S. K., Cox, B., Wills, P., Mateeva, A., Lopez, J., et al. (2012). *Distributed acoustic sensing for geophysical monitoring*. 74th EAGE Annual Conference and Exhibition, *Expanded Abstracts*, Y005. https://doi.org/10.3997/2214-4609.20148800

Miah, K., & Potter, D. K. (2017). A review of hybrid fiber-optic distributed simultaneous vibration and temperature sensing technology and its geophysical applications. *Sensors (Basel)*,17(11), 2511. https://doi.org/10.3390/s17112511

Miah, K. (2018). *OTDR DAS development*. Paper presented at AGU Workshop: Distributed Acoustic Sensing-Principles and Case Studies. Washington, D.C., *USA*.

Miah, K., & Ha, N. (2018). *Fiber-optic phase-OTDR based distributed acoustic sensing (DAS) system for ground vibration measurements: a step-by-step 'how to' tutorial on system implementation and testing*. Paper presented at SEG Postconvention Workshop W-20: DAS-Validating Measurements, Developing Processing Methods, *and Integrating to Optimize Velocity Models for Improving Subsurface Imaging*. Anaheim, CA, USA.

Michelin, F., Lacaze, P., & Lamour, V. (2017). *Shape monitoring of subsea pipelines through optical fiber sensors: S-Lay process case study*. The Society of Naval Architects and Marine Engineers (SNAME) 22nd Offshore Symposium, *SNAME-TOS-2017-014*.

Miklashevskiy, D., Shako, V., Borodin, I., Wilson, C., Kortukov, D., Tarelko, N., & Zozulya, O. (2020). *Approach for wellbore production monitoring using distributed acoustic noise measurements*. International Petroleum Technology Conference, *IPTC-20125-Abstract*. https://doi.org/10.2523/IPTC-20125-Abstract

Miller, D., Parker, T., Kashikar, S., Todorov, M., & Bostick, T. (2012). *Vertical seismic profiling using a fiber-optic cable as a distributed acoustic sensor*. 74th EAGE Conference and Exhibition, *Expanded Abstracts*, Y004. https://doi.org/10.3997/2214-4609.20148799

Miller, D. E., Daley, T. M., White, D., Freifeld, B. M., Robertson, M., Cocker, J., & Craven, M. (2016). Simultaneous acquisition of distributed acoustic sensing VSP with multi-mode and single-mode fibre-optic cables and 3C-geophones at the Aquistore CO2 storage site. *CSEG Recorder*, 41(6), 28–33.

Miller, D. (2018). *Borehole DAS results at Brady Hot springs*. Paper presented at AGU Workshop: Distributed Acoustic Sensing-Principles and Case Studies. Washington, D.C., *USA*.

Miller, D. E., Coleman, T., Zeng, X., Patterson, J., Reinisch, E., Cardiff, M. A., et al. (2018). *DAS and DTS at Brady Hot Springs: Observations about coupling and coupled interpretations*. 43rd Workshop on Geothermal Reservoir Engineering, PROCEEDINGS (pp. 1–13). *SGP-TR-213*.

Mizuno, T., LeCalvez, J., & Raymer, D. (2017). *Revision of an automated microseismic location algorithm for DAS—3C geophone hybrid array*. *AGU Fall Meeting Abstract S33B-238*.

Mizuno, T., Le Calvez, J., & Raymer, D. (2018). *Microseismic monitoring using a focused automated location algorithm with a DAS–3C geophone hybrid array*. Abstract. *Paper presented at SEG Summer Research Workshop: Recent Advances and Applications in Borehole Geophysics*. Galveston, TX, USA.

Mizuno, T., Leaney, S., Le Calvez, J., Naseer, F., & Khaitan, M. L. (2019). *The significance of gauge length in particle velocity estimation from DAS data: VSP and microseismic cases*. 89th SEG Annual International Meeting, *Expanded Abstracts* (pp. 4869–4873). https://doi.org/10.1190/segam2019-3215250.1

Molenaar, M., Hill, D., & Koelman, V. (2011). Downhole tests show benefits of distributed acoustic sensing. *Oil and Gas Journal*, 109(1), 82–85.

Molenaar, M. M., Hill, D. J., Webster, P., Fidan, E., & Birch, B. (2011). *First downhole application of Distributed Acoustic Sensing (DAS) for hydraulic fracturing monitoring and diagnostics*. SPE Hydraulic Fracturing Technology Conference, *SPE* 140561. https://doi.org/10.2118/140561-MS

Molenaar, M. M., Fidan, E., & Hill, D. J. (2012). *Real-time downhole monitoring of hydraulic fracturing treatments using fibre optic distributed temperature and acoustic sensing*. SPE/EAGE European Unconventional Resources Conference and Exhibition, *SPE* 152981. https://doi.org/10.2118/152981-MS

Molenaar, M. M., Hill, D. J., Webster, P., Fidan, E., & Birch, B. (2012). *First downhole application of Distributed Acoustic Sensing (DAS) for hydraulic fracturing monitoring and diagnostics*. SPE Drilling & Completion, *SPE-140561-PA*. https://doi.org/10.2118/140561-PA

Molenaar, M. M., & Cox, B. E. (2013). *Field cases of hydraulic fracture stimulation diagnostics using fiber optic distributed acoustic sensing (DAS) measurements and analyses*. SPE Unconventional Gas Conference and Exhibition, *SPE-164030-MS*. https://doi.org/10.2118/164030-MS

Molteni, D., Hopperstad, J-F., & Hartog, A. (2016). Use of distributed fibre-optic sensing for marine seismic measurements. *First Break*, 34(12), 53–60.

Molteni, D., Williams, M., & Wilson, C. (2016). *Comparison of microseismic events concurrently acquired with geophones and hDVS*. 78th EAGE Conference and Exhibition, Expended Abstracts, *We STZ2* 10. https://doi.org/10.3997/2214-4609.201601260

Molteni, D., Williams, M. J., & Wilson, C. (2017). Detecting microseismicity using distributed vibration. *First Break*, 35 (4), 51–55.

Mondal, S., Ugueto, G., Huckabee, P., Wojtaszek, M., Daredia, T., Vitthal, S., et al. (2019). *Uncertainties in Step-down test* *interpretation for evaluating completions effectiveness and near wellbore complexities*. SPE/AAPG/SEG Unconventional Resources Technology Conference, *URTEC-2019-1141-MS*. https://doi.org/10.15530/urtec-2019-1141

Mondanos, M., & Coleman, T. (2019). Application of distributed fibre-optic sensing to geothermal reservoir characterization and monitoring. *First Break*, 37(7), 51–56. https://doi.org/10.3997/1365-2397.n0040

Morshed, A. H. E., & El-Sayed, I. M. (2016). *Monitoring of vibrations using multimode optical fiber sensors. 33rd National Radio Science Conference* (NRSC), Expanded Abstracts. https://doi.org/10.1109/NRSC.2016.7450863

Morton, A., Andersen, M., & Thompson, M. (2009). *Field trial of focused seismic monitoring on the Snorre field*. 71st EAGE Conference and Exhibition, *Extended Abstracts*, X026. https://doi.org/10.3997/2214-4609.201400511

Muhammed, M. D. D., Rahim, M. F. A., Bourdon, L. M., Hardy, R. J. J., Ghazali, A. R., Chavarria, J. A., et al. (2017). *Imaging beneath shallow gas using DAS 3D VSP within active dual string producing wells*. Asia Petroleum Geoscience Conference and Exhibition, Expanded Abstracts, 43552. https://doi.org/10.3997/2214-4609.201802850

Muhammed, M. D. D., Rahim, M. F. A., & Ghazali, A. R. (2019). *Integrated shallow gas imaging using fiber optics DAS VSP and OBN*. 81st EAGE Conference and Exhibition, Expended Abstracts, *We_R09_15*. https://doi.org/10.3997/2214-4609.201901251

Muir, J. B., & Zhan, Z. (2017). *Reconstructing the seismic wavefield using curvelets and distributed acoustic sensing*. *AGU Fall Meeting Abstract S33B-2381*.

Mullens, S., Lees, G., & Duvivier, G. (2010). *Fiber-optic distributed vibration sensing provides technique for detecting sand production*. Offshore Technology Conference, *OTC-20429-MS*. https://doi.org/10.4043/20429-MS

Munn, J. D., Coleman, T. I., Parker, B. L., Mondanos, M. J., & Chalari, A. (2017). *Novel cable coupling technique for improved shallow distributed acoustic sensor VSPs*. *Journal of Applied Geophysics*, 138, 72–79. https://doi.org/10.1016/j.jappgeo.2017.01.007

Nakatsukasa, M., Ban, H., Kato, A., Shimoda, N., White, D., & Nickel, E. (2018a). *VSP acquisition with combined fiber-optic DAS and permanent seismic source ACROSS for permanent reservoir monitoring at the Aquistore site*. 88th SEG Annual International Meeting, *Expanded Abstracts* (pp. 5273–5277). https://doi.org/10.1190/segam2018-2995929.1

Nakatsukasa, M., Ban, H., Kato, A., Shimoda, N., White, D., Nickel, E., & Daley, T. (2018b). *Combined use of optical-fiber DAS and a permanent seismic source for vertical seismic profiling demonstrated at the Aquistore CO2 Storage Site*. Abu Dhabi International Petroleum Exhibition & Conference, *SPE-193268-MS*. https://doi.org/10.2118/193268-MS

Nakatsukasa, M., Ban, H., Kato, A., Shimoda, N., White, D., Nickel, E., et al. (2018c). *Assessment of quality and repeatability of VSP data acquired by combining DAS and permanent rotary source at the Aquistore field. EAGE Workshop on* 4D Seismic and Reservoir Monitoring, Expended Abstracts. https://doi.org/10.3997/2214-4609.201900244

Nakstad, H., Langhammer, J., & Eriksrud, M. (2011). *Permanent reservoir monitoring technology breakthrough in the North Sea*. 73rd EAGE Conference and Exhibition, *Extended Abstracts*, I044, https://doi.org/10.3997/2214-4609.20149315

Naldrett, G., Cerrahoglu, C., & Mahue, V. (2018). Production monitoring using next-generation distributed sensing systems. *PETROPHYSICS*, 59(4). 496–510. https://doi.org/10.30632/PJV59V4-2018a5

Naldrett, G., Parker, T., Shatalin, S., Mondanos, M., & Farhadiroushan, M. (2020). *High-resolution Carina distributed acoustic fibreoptic sensor for permanent reservoir monitoring and extending the reach into subsea fields*. *First Break*, 38(2), 71–76. https://doi.org/10.3997/1365-2397.fb2020012

Naldrett, G., Soulas, S., van Gestel, J.-P., & Parker, T. (2020). *First Subsea das installation for deep water reservoir monitoring*. First EAGE Workshop on Fibre Optic Sensing, Expended Abstract. https://doi.org/10.3997/2214-4609.202030034

Naruse, R., Kobayashi, Y., Morishima, Y., & Xue, Z. (2018). *Inside CT-DAS-VSP acquisition using a highly deviated deep well, onshore Japan*. 88th SEG Annual International Meeting, *Expanded Abstracts*, 5407–5411. https://doi.org/10.1190/segam2018-2986135.1

Nelson, A., & Konopczynski, M. (2019). *Challenges in implementing the digital oil field a real-world look at data retrieval, storage and efficient utilization*. Offshore Mediterranean Conference and Exhibition, *OMC-2019-1221*.

Neri, P., & Philo, R. (2020). *Efficiency improvements for distributed acoustic sensing data exchange streamline operations and opens access to new uses*. First EAGE Workshop on Fibre Optic Sensing, Expended Abstract. https://doi.org/10.3997/2214-4609.202030003

Nesladek, N. J., Kammerer, C., Speece, M. A., Maclaughlin, M., Wang, H. F., & Lord, N. E. (2017). *Comparison of Distributed Acoustic Sensing (DAS) from fiber-optic cable to three component geophones in an underground mine*. *AGU Fall Meeting Abstract S33B-2382*.

Nishiguchi, K. (2016). *Phase unwrapping for fiber-optic distributed acoustic sensing*. The 47th ISCIE International Symposium on Stochastic Systems Theory and Its Applications. *Proceeding* 2016 (pp. 81–87). https://doi.org/10.5687/sss.2016.81

Nizkous, I., Gerritsen, S., Kiyashchenko, D., & Joinson, D. (2015). *Distributed Acoustic Sensing (DAS) VSP for imaging and velocity model building*. International Petroleum Technology Conference, *IPTC-18483-MS*. https://doi.org/10.2523/IPTC-18483-MS

Nöther, N. (2017). *Distributed fiber-optic measurements in geotechnical applications—capabilities and challenges of Brillouin sensing. EAGE/DGG Workshop on Fibre Optic Technology in Geophysics*, Expended Abstracts, Fr SR 10. https://doi.org/10.10.3997/2214-4609.201700159

Olofsson, B., & Martinez, A. (2017). Validation of DAS data integrity against standard geophones—DAS field test at Aquistore site. *The Leading Edge*, 36, 981–986. https://doi.org/10.1190/tle36120981.1

Oropeza Bacci, V., Halladay, A., O'Brien, S., Anderson, M., & Henderson, N. (2017). *Results from the first monitor VSP* *survey at the Quest CCS operation*. EAGE/SEG Research Workshop, Extended Abstracts, *We CO2* 02. https://doi.org/10.3997/2214-4609.201701949

Oropeza Bacci, V., Halladay, A., O'Brien, S., Henderson, N., & Anderson, M. (2017). *Time-lapse seismic as a component of the quest CCS MMV plan*. EAGE/SEG Research Workshop, Extended Abstracts, *Tu CO2* 01. https://doi.org/10.3997/2214-4609.201701937

Oropeza Bacci, V., O'Brien, S., Frank, J., & Anderson, M. (2017). Using a walk-away DAS time-lapse VSP for CO2 plume monitoring at the quest CCS project. *CSEG Recorder*, 42(3), 18–21.

Paap, B., Verdel, A., *Vandeweijer*, V., & Carpentier, S. (2020). *Potential of using DAS within a traffic light system at a geothermal site*. First EAGE Workshop on Fibre Optic Sensing, Expended Abstract. https://doi.org/10.3997/2214-4609.202030006

Paitz, P., & Fichtner, A. (2017). *Towards noise tomography and passive monitoring using distributed acoustic sensing*. *AGU Fall Meeting Abstract S33B-2385*.

Paitz, P., Sager, K., & Fichtner, A. (2018). *Ambient noise interferometry for distributed acoustic sensing and rotational seismology*. Paper presented at SEG Postconvention Workshop W-20: DAS-Validating Measurements, Developing Processing Methods, *and Integrating to Optimize Velocity Models for Improving Subsurface Imaging*. Anaheim, CA, USA.

Paitz, P., Sager, K., Schmelzbach, C., Doetsch, J., Chalari, A., & Fichtner, A. (2019a). *Towards multi-observational full-waveform inversion*. 2019 EGU General Assembly, Geophysical Research Abstracts Vol. 21, *EGU2019-8802*.

Paitz, P., Sager, K., Schmelzbach, C., Doetsch, J., *Chalari*, A., & Fichtner, A. (2019b). *Towards multi-observational full-waveform inversion*. Seismological Society of America Annual Meeting, Abstract. Seattle, WA, USA.

Paitz, P., Edme, P., Schmelzbach, C., Doetsch, J., Gräff, D., Walter, F., et al. (2020a). *Distributed Acoustic Sensing from mHz to kHz: Empirical investigations of DAS instrument response*. EGU General Assembly Abstract, *EGU2020-7343*. https://doi.org/10.5194/egusphere-egu2020-7343

Paitz, P., Edme, P., Schmelzbach, C., Doetsch, J., Gräff, D., Walter, F., et al. (2020b). *Distributed acoustic sensing from hours to milliseconds: Empirical investigations of DAS instrument response*. Seismological Society of America Annual Meeting, *Abstract*. Albuquerque, NM, USA.

Pakhotina, J., Zhu, D., Hill, A. D., & Santos, R. (2017). *Characterization of production through a fracture cell using acoustic data*. SPE Annual Technical Conference and Exhibition, *SPE-187357-MS*. https://doi.org/10.2118/187357-MS

Pakhotina, I., Sakaida, S., Zhu, D., & Hill, A. D. (2020). *Diagnosing multistage fracture treatments with distributed fiber-optic sensors*. SPE Hydraulic Fracturing Technology Conference and Exhibition, *SPE-199723-MS*. https://doi.org/10.2118/199723-MS

Paleja, R., Mustafina, D., in 't Panhuis, P., Park, T., Randell, D., Van der Horst, J., & Crickmore, R. (2015). *Velocity tracking for flow monitoring and production profiling using distributed acoustic sensing*. SPE Annual Technical Conference and Exhibition, SPE-174823-MS. https://doi.org/10.2118/174823-MS

Palmieri, L., & Schenato, L. (2013). Distributed optical fiber sensing based on Rayleigh scattering. *The Open Optics Journal*, 7(Suppl-1, M7), 104–127. https://doi.org/10.2174/1874328501307010104

Papp, B., Donno, D., Martin, J. E., & Hartog, A. H. (2014). *Fundamentals of vibration sensing with distributed fibre optic sensors through downscaled experiments*. 76th EAGE Conference and Exhibition, Extended Abstracts, *Th ELI2* 09. https://doi.org/10.3997/2214-4609.20141463

Papp, B., Donno, D., Martin, J. E., & Hartog, A. H. (2017). A study of the geophysical response of distributed fibre optic acoustic sensors through laboratory-scale experiments. *Geophysical Prospecting*, 65(5). 1186–1204. https://doi.org/10.1111/1365-2478.12471

Parikh, N. K., Flynn, G. S., *Casleton*, E., & Ray, W. (2019). *Monitoring a Nuclear Research Reactor with traditional and non-traditional vibration measurements*. Seismological Society of America Annual Meeting, Abstract. Seattle, WA, USA.

Park, T., Paleja, R., & Wojtaszek, M. (2018). *Robust regression and band switching to improve DAS flow estimates*. SPE Annual Technical Conference and Exhibition, *SPE-191721-MS*. https://doi.org/10.2118/191721-MS

Parker, L. M., Thurber, C. H., Zeng, X., Lord, N. E., Fratta, D., Wang, H. F., et al. (2018). Active-source seismic tomography at the Brady Geothermal Field, Nevada, with dense nodal and fibre-optic seismic arrays. *Seismological Research Letters*, 89 (5), 1629–1640. https://doi.org/10.1785/0220180085

Parker, T., Shatalin, S. V., Farhadiroushan, M., Kamil, Y. I., Gillies, A., Finfer, D., & Estathopoulos, G. (2012). *Distributed acoustic sensing—a new tool for seismic applications*. 74th EAGE Conference and Exhibition, *Expanded Abstracts*, Y002. https://doi.org/10.3997/2214-4609.20148797

Parker, T. R., Shatalin, S. V., Farhadiroushan, M., & Miller, D., (2013). *Distributed acoustic sensing: Recent field data and performance validation*. 2nd EAGE Workshop on Permanent Reservoir Monitoring, Expanded Abstracts, *Th-01-06*. https://doi.org/10.3997/2214-4609.20131303

Parker, T. R. (2014). *Distributed acoustic sensing for borehole seismic applications*. 76th EAGE Conference and Exhibition—Workshops, Extended Abstracts, *WS15-B01*. https://doi.org/10.3997/2214-4609.20140611

Parker, T. R., Gillies, A., Shatalin, V. S., & Farhadiroushan, M. (2014). *The intelligent distributed acoustic sensing*. 23rd International Conference on Optical Fibre Sensors, *Proceedings of SPIE* 9157, 91573Q. https://doi.org/10.1117/12.2064889

Parker, T., Shatalin, S., & Farhadiroushan, M. (2014). Distributed Acoustic Sensing—a new tool for seismic applications. *First Break*, 32(2), 61–69. https://doi.org/10.3997/2214-4609.20148797

Parkhonyuk, S., Nikolaev, M., Fedorov, A., Konchenko, A., & Vik, T. (2018). *Cloud-based solution for advanced real-time fracturing evaluation*. SPE Annual Technical Conference and Exhibition, *SPE-191680-MS*. https://doi.org/10.2118/191680-MS

Paulsson, B. N. P., Toko, J. L., Thornburg, J. A., & He, R. (2014). *Fiber optic vector sensors*. 76th EAGE Conference and Exhibition, *Expanded Abstracts* (pp. 415–416). https://doi.org/10.3997/2214-4609.20140610

Paulsson, B. N. P., Thornburg, J. A., & He, R. (2015). *A fiber-optic borehole seismic vector and acoustic sensor system for geothermal site characterization and monitoring*. Proceedings World Geothermal Congress 2015, *Melbourne (Australia)*, 19–25 Apr 2015.

Paulsson, B., He, R., Thornburg, J., Hardiman, H., & Wylie, M. (2016). *Fiber optic seismic vector sensors (FOSS)*. Paper presented at SEG Postconvention workshop W-10: Fiber-optic Sensing for Exploration and Monitoring: Development, Applications, *and Challenges*. Dallas, TX, USA.

Paulsson, B. (2017). *Fiber optic sensors for vector seismic, acoustic, strain and temperature measurements. Paper presented at SEG Postconvention workshop* W12: DAS: A vision of the future? Houston, TX, USA.

Paulsson, B., Wylie, M., Thornburg, J., He, R., Hardiman, H., & Patel, D. (2019). A fiber optic single well seismic system for geothermal reservoir imaging & monitoring. 44th Workshop on Geothermal Reservoir Engineering, Proceedings (pp. 1–8). *SGP-TR-214*..

Pellegrini, I. (2020). *DAS energy calibration applied to multi-rate injection profiling in a horizontal water injector*. First EAGE Workshop on Fibre Optic Sensing, Expended Abstract. https://doi.org/10.3997/2214-4609.202030026

Percher, F., & Valishin, O. (2018). *Overview of technologies for downhole seismic for geothermal industry. 1st EAGE/IGA/DGMK Joint Workshop on Deep Geothermal Energy*, Expended Abstracts, DGE 04, https://doi.org/10.3997/2214-4609.201802933

Pevzner, R., Urosevic, M., Popik, D., Shulakova, V., Tertyshnikov, K., Caspari, E., et al. (2017). 4D surface seismic tracks small supercritical CO2 injection into the subsurface: CO2CRC Otway Project. *International Journal of Greenhouse Gas Control*, *63*, 150–157. https://doi.org/10.1016/j.ijggc.2017.05.008

Pevzner, R., Urosevic, M., Popik, D., Tertyshnikov, K., Correa, J., Kepic, A., et al. (2017). *Seismic monitoring of CO2 geosequestration: Preliminary results from Stage 2C of the CO2CRC Otway Project one-year post injection*. 87th SEG Annual International Meeting, *Expanded Abstracts* (pp. 5895–5900). https://doi.org/10.1190/segam2017-17670937.1

Pevzner, R., Urosevic, M., Tertyshnikov, K., Gurevich, B., Shulakova, V., Glubokovskikh, S., et al. (2017). *Seismic monitoring of a small-scale supercritical CO2/CH4 injection—CO2CRC Otway Stage 2C case study*. EAGE/SEG Research Workshop, Extended Abstracts, *Tu CO2* 02. https://doi.org/10.3997/2214-4609.201701938

Pevzner, R., Bona, A., Correa, J., Tertyshnikov, K., Palmer, G., & Valishin, O. (2018). *Optimising DAS VSP data acquisition parameters: Theory and experiments at Curtin training well facility*. 80th EAGE Conference and Exhibition, Expended Abstracts, *WS08*. https://doi.org/10.3997/2214-4609.201801923

Pevzner, R., Gurevich, B., Tertyshnikov, K., Pirogova, A., & Glubokovskikh, S. (2018). *Repeat logging using distributed acoustic sensors and earthquakes*. EAGE Conference on Reservoir Geoscience, Expended Abstracts, 47. https://doi.org/10.3997/2214-4609.201803222

Pevzner, R., Tertyshnikov, K., &. Bona, A. (2018). Feasibility of passive vertical seismic profiling using distributed acoustic sensing for monitoring applications. 80th EAGE Conference and Exhibition, Expended Abstracts, Th F 16. https://doi.org/10.3997/2214-4609.201801473

Pevzner, R., Tertyshnikov, K., Bona, A. Correa, J., Gurevich, B., Palmer, G., et al. (2018). Distributed acoustic sensing for active and passive VSP acquisition: theory and experiments at Curtin training well facility. Paper presented at SEG Postconvention Workshop W-20: DAS-Validating Measurements, Developing Processing Methods, and Integrating to Optimize Velocity Models for Improving Subsurface Imaging. Anaheim, CA, USA.

Pevzner, R., Glubokovskikh, S., Tertyshnikov, K., Yavuz, S., Egorov, A., Sidenko, E., et al. (2019). *Permanent downhole seismic monitoring of CO2 geosequestration: Stage 3 of the CO2CRC Otway project*. Asia Petroleum Geoscience Conference and Exhibition, *Expended Abstracts*. https://doi.org/10.3997/2214-4609.201903366

Pevzner, R., Tertyshnikov, K., Sidenko, E., & Ricard, L. (2020). *Monitoring drilling and completion operations using distributed acoustic sensing: CO2CRC Stage 3 project case study*. First EAGE Workshop on Fibre Optic Sensing, Expended Abstract. https://doi.org/10.3997/2214-4609.202030004

Pierre, B., & Le Calvez, J. (2020). *From geophone to DAS: Evolution of Q estimation*. International Petroleum Technology Conference, *IPTC-19788-Abstract*. https://doi.org/10.2523/IPTC-19788-Abstract

Pimentel-Niño, M. A. (2017). *DAS: Pipeline monitoring and the blue colour of the sky*. Expended Abstract (pp. 1–11). *Paper presented at 12th Pipeline Technology Conference*, Berlin, Germany.

Podgornova, O., Leaney, S., Zeroug, S., & Liang, L. (2017). *On full-waveform modeling and inversion of fiber-optic VSP data*. 87th SEG Annual International Meeting, *Expanded Abstracts* (pp. 6039–6043). https://doi.org/10.1190/segam2017-17652912.1

Poletto, F., Clarke, A., Schleifer, A., Finfer, D., & Corubolo, P. (2014). *Seismic calibration of distributed acoustic sensors (DAS) in a joint borehole-surface experiment*. 76th EAGE Conference and Exhibition, Extended Abstracts, *Tu* D201 09. https://doi.org/10.3997/2214-4609.20140629

Poletto, F., Corubolo, P., Farina, B., & Finfer, D. (2014). *Dual seismic fields from distributed acoustic sensors*. 84th SEG Annual International Meeting, *Expanded Abstract* (pp. 1899–1903). https://doi.org/10.1190/segam2014-1055.1

Poletto, F., Finfer, D., & Corubolo, P. (2015). *Broadside wavefields in horizontal helically wound optical fiber and hydrophone streamer*. 85th SEG Annual International Meeting, *Expanded Abstracts* (pp. 95–99). https://doi.org/10.1190/segam2015-5896445.1

Prinet, C., Thibeau, S., Lescanne, M., & Jacques Monne, J. (2013). Lacq-Rousse CO2 capture and storage demonstration pilot: Lessons learnt from two and a half years monitoring. *Energy Procedia*, 37, 3610–3620. https://doi.org/10.1016/j.egypro.2013.06.254

Przybysz-Jarnut, J. K., Hornman, J. C., Potters, H., & Lopez, J. L. (2015). *IOR/EOR monitoring onshore with frequent time-lapse *seismic*. International Petroleum Technology Conference, *IPTC-18426-MS*. https://doi.org/10.2523/IPTC-18426-MS

Raab, T., Reinsch, T., Jousset, P., & Krawczyk, C. M. (2017). *Multi-station analysis of surface wave dispersion using distributed acoustic fiber optic sensing. EAGE/DGG Workshop on Fibre Optic Technology in Geophysics*, Expended Abstracts, Fr SR P04. https://doi.org/10.3997/2214-4609.201700164

Raab, T., Reinsch, T., Aldaz, C., Santaigo, R., & Henninges, J. (2019). Real-time well-integrity monitoring using fiber-optic distributed acoustic sensing. *SPE Journal,* 24(05), 1997–2009. SPE-195678-PA. https://doi.org/10.2118/195678-PA

Rachapudi, R. V., Alshehhi, S., Saadwai, O., Ayidinoglu, G., Dodan, C., Khaled, M. F., et al. (2018). *Smart hybrid technology for water injector wells: Installation, commissioning and data interpretation challenges—case study from a Middle Eastern field*. Abu Dhabi International Petroleum Exhibition & Conference, *SPE-192816-MS*. https://doi.org/10.2118/192816-MS

Ramurthy, M., Richardson, J., Brown, M., Sahdev, N., Wiener, J., & Garcia, M., (2016). *Fiber-optics results from an intra-stage diversion design completions study in the Niobrara formation of DJ basin*. SPE Hydraulic Fracturing Technology Conference, *SPE-179106-MS*. https://doi.org/10.2118/179106-MS

Rassenfoss, S. (2014). In search of better reservoir imaging using fiber optic receivers downhole. *Journal of Petroleum Technology*, 66(06), 58–65. https://doi.org/10.2118/0614-0058-JPT

Rassenfoss, S. (2019). *Fracturing creates hundreds of fractures—only a few matter*. *Journal of Petroleum Technology*, 71(12), 24–29. https://doi.org/10.2118/1219-0024-JPT

Raterman, K. T., Farrell, H. E., Mora, O. S., Janssen, A. L., Gomez, G. A., Busetti, S., et al. (2017). *Sampling a stimulated rock volume: An Eagle Ford example*. SPE/AAPG/SEG Unconventional Resources Technology Conference, *URTEC-2670034-MS*. https://doi.org/10.15530/URTEC-2017-2670034

Raterman, K. T., Farrell, H. E., Mora, O. S., Janssen, A. L., Gomez, G. A., Busetti, S., et al. (2018). Sampling a stimulated rock volume: An Eagle Ford example. *Source. SPE Reservoir Evaluation & Engineering*, 21(04). 927–941. https://doi.org/10.2118/191375-PA

Raterman, K., Liu, Y., & Warren, L. (2019). *Analysis of a drained rock volume: An Eagle Ford example*. SPE/AAPG/SEG Unconventional Resources Technology Conference, *URTEC-2019-263-MS*. https://doi.org/10.15530/urtec-2019-263

Rawahi, Z., Hemink, G., Freeman, F., & Groen, A. (2018). *Fibre optic surveillance for conformance monitoring in a polymer pilot by petroleum development Oman*. Abu Dhabi International Petroleum Exhibition & Conference, *SPE-192824-MS*. https://doi.org/10.2118/192824-MS

Ray, W. (2018). *Industrial monitoring with DAS*. Paper presented at AGU Workshop: Distributed Acoustic Sensing-Principles and Case Studies. Washington, D.C., *USA*.

Ray, W., Ramirez, C. A., & Poska, M. (2019). *Monitoring of industrial facilities with telecom fiber optics*. Seismological Society of America Annual Meeting, *Abstract*. Seattle, WA, USA.

Reinsch, T., Henninges, J., Götz, J., Jousset, P., Bruhn, D., & Lüth, S. (2015) . *Distributed acoustic sensing technology for seismic exploration in magmatic geothermal areas*. World Geothermal Congress 2015 Proceedings. https://gfzpublic.gfz-potsdam.de/pubman/item/item_1182900

Reinsch, T., Jousset, P., Henninges, J., & Blanck, H. (2016). *Distributed acoustic sensing technology in magmatic geothermal field—first results from a survey in Iceland*. General Assembly European Geosciences Union, Geophysical Research Abstracts, *18*, *EGU2016-16670*.

Reinsch, T., Thurley, T., & Jousset, P. (2017). On the mechanical coupling of a fiber optic cable used for distributed acoustic/vibration sensing applications—a theoretical consideration. *Measurement Science and Technology*, 28, 12, 127003. http://doi.org/10.1088/1361-6501/aa8ba4

Richards, J., Bartlett, R., Onen, D., Crowther, G., Molenaar, M. M., Reynolds, A., et al. (2015). *Cloud-based solution for permanent fiber-optic DAS flow monitoring*. SPE Digital Energy Conference and Exhibition, *SPE-173440-MS*. https://doi.org/10.2118/173440-MS

Richter, P., Parker, T., Woerpel, C., Wu, W., Rufino, R., & Farhadiroushan, M. (2019a). *High-resolution distributed acoustic sensor using engineered fiber for hydraulic fracture monitoring and optimization in unconventional completions*. 89th SEG Annual International Meeting, *Expanded Abstracts* (pp. 4874–4878). https://doi.org/10.1190/segam2019-3215860.1

Richter, P., Parker, T., Woerpel, C., Wu, Y., Rufino, R., & Farhadiroushan, M. (2019b). Hydraulic fracture monitoring and optimization in unconventional completions using a high-resolution engineered fibre-optic Distributed Acoustic Sensor. *First Break*, 37(4), 63–68.

Riedel, M., Cosma, C., Enescu, N., Koivisto, E., Komminaho, K., Vaittinen, K., & Malinowski, M. (2018a). *Distributed acoustic sensing versus conventional VSP imaging of the Kylylahti polymetallic deposit*. 2nd Conference on Geophysics for Mineral Exploration and Mining, Expended Abstracts, *We 2MIN* P12. https://doi.org/10.3997/2214-4609.201802744

Riedel, M., Cosma, C., Enescu, N., Koivisto, E., Komminaho, K., Vaittinen, K., & Malinowski, M. (2018b). Underground vertical seismic profiling with conventional and fiber-optic systems for exploration in the Kylylahti polymetallic mine, eastern Finland. *Minerals*, 8(11), 538. https://doi.org/10.3390/min8110538

Ringstad, C., Røed, M. H., Jestin, C., Calbris, G., Eliasson, P., Jordan, M., & Wüstefeld, A. (2020). *A multi-fibre optic sensing system for cross-well monitoring at the Svelvik CO2 field lab*. First EAGE Workshop on Fibre Optic Sensing, Expended Abstract. https://doi.org/10.3997/2214-4609.202030039

Rodríguez Tribaldos, V. (2018). *DAS for intermediate-scale near-surface imaging using seismic ambient noise*. Paper presented at AGU Workshop: Distributed Acoustic Sensing-Principles and Case Studies. Washington, D.C., *USA*.

Rodríguez Tribaldos, V. (2019). *DAS for continuous monitoring of hydrological properties using relative seismic velocity variations. Designing cross-well seismic for fiber optics: A case study for the Svelvik CO2 test site. Paper presented at SEG Postconvention Workshop W-1: DAS—Part* 1: Recent Advances in Subsurface Characterization using Distributed Acoustic Sensing and the Road Ahead. San Antonio, TX, USA.

Rodríguez Tribaldos, V., Dou, S., Lindsey, N. J., Ulrich, C., Robertson, M., et al. (2019). *Distributed Acoustic Sensing*

(DAS) for continuous monitoring of near-surface properties using coda wave interferometry. Seismological Society of America Annual Meeting, *Abstract*. Seattle, WA, USA.

Rodríguez Tribaldos, V., Lindsey, N. J., Monga, I., Tracy, C., & Ajo-Franklin, J. B. (2020). *Exploring the subsurface of urban areas with Distributed Acoustic Sensing (DAS) deployed on dark fiber networks*. Seismological Society of America Annual Meeting, *Abstract*. Albuquerque, NM, USA.

Sadigov, T., Thiruvenkatanathan, P., & Sheydayev, A. (2017). *Application of distributed acoustic sensing DAS technology in identification and remediation of sand producing zones in OHGP completion*. SPE Annual Caspian Technical Conference and Exhibition, *SPE-188991-MS*. https://doi.org/10.2118/188991-MS

Sahdev, N., & Cook, P. F. (2016). *Coiled tubing deployed fiber optics utilized in observing cross-well communication during stimulation*. SPE/AAPG/SEG Unconventional Resources Technology Conference, *URTEC-2430791-MS*. https://doi.org/10.15530/URTEC-2016-2430791

Sahdev, N., Doucette, J., Odegard, M., Ohlson, C., Bagherian, B., Stark, P., et al. (2018). *Prudent design of experiment with integrated diagnostics improves understanding of multiwell stimulation effects in a complex multibench reservoir*. SPE Hydraulic Fracturing Technology Conference and Exhibition, *SPE-189847-MS*. https://doi.org/10.2118/189847-MS

Sahin, O., Demircin, M. U., & Gevrekci, M. (2020). *Machine learning based automatic threat level assessment in fiber-optic Distributed Acoustic Sensing (DAS) intrusion detection system*. Proceedings Volume 11413, *Artificial Intelligence and Machine Learning for Multi-Domain Operations Applications* II; 1141322. https://doi.org/10.1117/12.2558400

Sanghvi, G., Le-Roch, J. F., Fernagu, J., Elazabi, S., Al-Naimi, A., Parker, T., et al. (2015). *DAS acquisition in a matured field during 4D: A challenging initiative with multiple objectives*. Abu Dhabi International Petroleum Exhibition and Conference, *SPE-177691-MS*, https://doi.org/10.2118/177691-MS

Sanni, M., Hveding, F., Kokal, S., & Zefzafy, I. (2018). *Lessons learned from in-well fiber-optic DAS/DTS deployment*. SPE Annual Technical Conference and Exhibition, *SPE-191470-MS*. https://doi.org/10.2118/191470-MS

Sarmah, B., Garrison, N., Bogle, E., Ross, K., & Noon, P. (2019). *Characterization and production influence of geological facies in the Eagle Ford*. SPWLA 60th Annual Logging Symposium, *SPWLA-2019-WW*. https://doi.org/10.30632/T60ALS-2019_WW

Sau, R., Kiyoumi, A., Amin, A., Correia, G., Barghouthi, A. K., Almheiri, A., et al. (2019). *Bullhead stimulation and first real-time fiber-optic surveillance in extended-reach horizontal laterals to maximize reservoir recovery in a giant offshore carbonate oil field Abu Dhabi*. Abu Dhabi International Petroleum Exhibition & Conference, *SPE-197752-MS*. https://doi.org/10.2118/197752-MS

Saxton, L. M., Ball, M., Soulas, S., Zhan, G., & Webster, M. (2018). *Results from a Clair DAS VSP pilot and lessons learned for DAS surveillance on Clair Ridge*. 80th EAGE Conference and Exhibition, Expended Abstracts, *WS08*. https://doi.org/10.3997/2214-4609.201801918

Schenato, L. (2017). A review of distributed fibre optic sensors for geo-hydrological applications. *Applied Sciences*, 7(9), 896. https://doi.org/10.3390/app7090896

Schilke, S., Donno, D., Chauris, H., Hartog, A., Farahani, A., & Pico, Y. (2016). *Numerical evaluation of sensor coupling of distributed acoustic sensing systems in vertical seismic profiling*. 86th SEG Annual International Meeting, *Expanded Abstracts* (pp. 677–681). https://doi.org/10.1190/segam2016-13527500.1

Schilke, S., Donno, D., Hartog, A. H., & Chauris, H. (2017). *DAS and its coupling for VSP applications using wireline cable. EAGE/DGG Workshop on Fibre Optic Technology in Geophysics*, Expended Abstracts, Fr SR 09. https://doi.org/10.3997/2214-4609.201700158

Schoenball, M., Ajo-Franklin, J. B., Wood, T., Robertson, M., Cook, P., Rodriguez-Tribaldos, V., et al. (2020). *Lessons learned from passive seismic monitoring of EGS Collab Experiment*. 45th Workshop on Geothermal Reservoir Engineering, PROCEEDINGS, *SGP-TR-216*. 1–7.

Schuberth, M. (2020). *Towards full integration of DAS/DTS data for continuous monitoring*. First EAGE Workshop on Fibre Optic Sensing, Expended Abstract. https://doi.org/10.3997/2214-4609.202030029

Scott, T. E., Gage, C., Martinez, R., & Dudley, J. W. (2017). *Monitoring the growth of hydraulic fractures with fiber optic strain technology*. 51st U.S. Rock Mechanics/Geomechanics Symposium, *ARMA-2017-0994*.

Seabrook, B. (2019). *Deployment of fiber optic sensors in an archetype subsea field development for DAS VSP and reservoir flow monitoring*. Paper presented at SEG Postconvention Workshop W-14: DAS Part2: What is next for DAS? *Operator needs versus Technology Suppliers' vision*. San Antonio, TX, USA.

Servette, V., & Lamour, V. (2016). *Optical fiber sensors for subsea and topside asset integrity monitoring applications*. The Society of Naval Architects and Marine Engineers (SNAME) 21st Offshore Symposium, *SNAME-TOS-2016-033*.

Shako, V., Miklashevskiy, D., Borodin, I., Kotlyar, L., Tarelko, N., Kortukov, D., et al. (2020). *Approach for wellbore production monitoring using distributed fiber optic measurements*. First EAGE Workshop on Fibre Optic Sensing, Expended Abstract. https://doi.org/10.3997/2214-4609.202030025

Shanafield, M., Banks, E. W., Arkwright, J. W., & Hausner, M. B. (2018). Fiber-optic sensing for environmental applications: Where we have come from and what is possible. *Water Resources Research*, 54(11), 8552–8557. https://doi.org/10.1029/2018WR022768

Shatalin, S. V., Treshikov, V. N., & Rogers, A. J. (1998). Interferometric optical time-domain reflectometry for distributed optical-fiber sensing. *Applied Optics*, 37(24), 5600–5604. https://doi.org/10.1364/AO.37.005600

Shen, J., Zhu, T., & Martin, E. R. (2020). *Noise characteristics of one year of DAS monitoring data from Penn State foresee array*. Seismological Society of America Annual Meeting, *Abstract*. Albuquerque, NM, USA.

Shen, Y., Holley, E., & Jaaskelainen, M. (2017). *Quantitative real-time DAS analysis for plug-and-perf completion operation*. SPE/AAPG/SEG Unconventional Resources Technology

Conference, *URTEC-2668525-MS*. https://doi.org/10.15530/URTEC-2017-2668525

Sherman, C., Morris, J., Mellors, R., & Ryerson, F. (2017). *Simulating fracture-induced strain signals measured by a distributed fiber-optic sensor*. 87th SEG Annual International Meeting, *Expanded Abstracts* (pp. 4113–4117). https://doi.org/10.1190/segam2017-17678887.1

Sherman, C. S., Mellors, R. J., Morris, J. P., & Ryerson, F. J. (2018). *Modeling distributed fiber optic sensor signals using computational rock mechanics*. SPE/AAPG/SEG Unconventional Resources Technology Conference, *URTEC-2900760-MS*. https://doi.org/10.15530/URTEC-2018-2900760

Sherman, C. (2019). *Modeling DAS data including subsurface models and fiber response. Paper presented at SEG Postconvention Workshop W-1: DAS—Part* 1: Recent Advances in Subsurface Characterization using Distributed Acoustic Sensing and the Road Ahead. San Antonio, TX, USA.

Sherman, C. S., Mellors, R. J., & Morris, J. P. (2019). *Subsurface monitoring via physics-informed deep neural network analysis of DAS*. 53rd U.S. Rock Mechanics/Geomechanics Symposium, *ARMA-2019-0433*.

Sheydayev, A., Atakishiyev, F., Zett, A., Schoepf, V., & Thiruvenkatanathan, P. (2018). ACG—20 years of downhole surveillance history. *Petrophysics*, 59(04). 511–527. https://doi.org/10.30632/PJV59V4-2018a6

Shiloh, L., Eyal, A., & Giryes, R. (2018). *Deep learning approach for processing fiber-optic DAS seismic data*. 26th International Conference on Optical Fiber Sensors, OSA Technical Digest (Optical Society of America), *paper ThE22*. https://doi.org/10.1364/OFS.2018.ThE22

Shirdel, M., Buell, R. S., Wells, M., Muharam, C., & Sims, J. (2016). *Horizontal steam injection flow profiling using fiber optics*. SPE Annual Technical Conference and Exhibition, *SPE-181431-MS*. https://doi.org/10.2118/181431-MS

Shirdel, M., Buell, R. S., & Wells, M. (2017). *Operational experience with fiber optic systems in horizontal steam injectors*. SPE Western Regional Meeting, *SPE-185667-MS*. https://doi.org/10.2118/185667-MS

Shirdel, M., Buell, R. S., Wells, M. J., Muharam, C., & Sims, J. C. (2019). Horizontal-steam-injection-flow profiling using fiber optics. SPE-181431-PA. *SPE Journal*, 24(02), 432–451. https://doi.org/10.2118/181431-PA

Shragge, J., Yang, J., Issa, N. A., Roelens, M., Dentith, M., & Schediwy, S. (2019). *Low-frequency ambient Distributed Acoustic Sensing (DAS): Useful for subsurface investigation?* 89th SEG Annual International Meeting, *Expanded Abstracts* (pp. 963–967). https://doi.org/10.1190/segam2019-3216479.1

Shultz, W., & Simmons, J. (2019). 3D DAS VSP in unconventionals: A case study. 89th SEG Annual International Meeting, Expanded Abstracts (pp. 979–983). https://doi.org/10.1190/segam2019-3214518.1

Shurunov, A., Iakovlev, A., Sheremeev, A., Kaeshkov, I., Rastegaeva, E., Suleymanov, A., et al. (2018). *Implementation of an integrated approach to develop low-productivity reservoirs of the Priobskoye Field (Russian)*. SPE Russian Petroleum Technology Conference, *SPE-191581-18RPTC-RU*. https://doi.org/10.2118/191581-18RPTC-RU

Shuvalov, A. (2018). Possibility of Distributed Acoustic Sensing (DAS) for geophysical problems solution. 24th European Meeting of Environmental and Engineering Geophysics, Extended Abstracts, Mo 24P1 04. https://doi.org/10.3997/2214-4609.201802456

Sidenko, E., Pevzner, R., Bona, A., & Tertyshnikov, K. (2019). *Seismic interferometry using walkaway DAS VSP Data: CO2CRC Otway Project Feasibility Study*. 81st EAGE Conference and Exhibition, Expended Abstracts, *Tu_P05_02*. https://doi.org/10.3997/2214-4609.201900694

Siebenaler, S., Krishnan, V. R., Lumens, P., Gesoff, G., & Salmatanis, N. (2015). *Evaluation of distributed acoustic sensing leak detection technology for offshore pipelines*. 25th International Ocean and Polar Engineering, *ISOPE-I-15-536*.

Siebenaler, S., Krishnan, V., Nielson, J., & Edlebeck, J. (2017). *Fiber-optic acoustic leak detection for multiphase pipelines*. The 27th International Ocean and Polar Engineering Conference, *ISOPE-I-17-679*.

Singer, J., Ibrahim, S., Karabacak, D., & Farnan, M. (2016). *FAZ I4: A high-performance FBG interrogator/seismic sensor system—how to qualify its performance relative to conventional seismic systems?* Paper presented at SEG Postconvention workshop W-10: Fiber-optic Sensing for Exploration and Monitoring: Development, Applications, *and Challenges*. Dallas, TX, USA.

Sladen, A., Rivet, D., Ampuero, J. P., De Barros, L., Hello, Y., Calbris, G., & Lamare, P. (2019). Distributed sensing of earthquakes and ocean-solid Earth interactions on seafloor telecom cables. *Nature Communications*, 10, 5777. https://doi.org/10.1038/s41467-019-13793-z

Smith, R., Bakulin, A., & Silvestrov, I. (2019). *Smart DAS uphole acquisition system for near-surface model building: Results from the first successful field tests*. SPE Middle East Oil and Gas Show and Conference, *SPE-195154-MS*. https://doi.org/10.2118/195154-MS

Smith, R., Bakulin, A., & Jervis, M. (2019). *Performance of a hybrid seismic monitoring system with buried receivers for an onshore carbonate reservoir: Current status and way forward*. 89th SEG Annual International Meeting, *Expanded Abstracts* (pp. 5234–5238). https://doi.org/10.1190/segam2019-3215586.1

Smolinski, K. T., Paitz, P., Bowden, D. C., Edme, P., *Kugler*, F., & Fichtner, A. (2020). *Urban distributed acoustic sensing using in-situ fibre beneath Bern, Switzerland*. Seismological Society of America Annual Meeting, Abstract. Albuquerque, NM, USA.

Somanchi, K., O'Brien, C., Huckabee, P., & Ugueto, G. (2016). *Insights and observations into limited entry perforation dynamics from fiber-optic diagnostics*. SPE/AAPG/SEG Unconventional Resources Technology Conference, *URTEC-2458389-MS*. https://doi.org/10.15530/URTEC-2016-2458389

Somanchi, K., Brewer, J., & Reynolds, A. (2017). Extreme limited entry design improves distribution efficiency in plug-n-perf completions: Insights from fiber-optic diagnostics. SPE Hydraulic Fracturing Technology Conference and Exhibition, *SPE-184834-MS*. https://doi.org/10.2118/184834-MS

Somanchi, K., Brewer, J., & Reynolds, A. (2018). Extreme limited-entry design improves distribution efficiency in plug-and-perforate completions: Insights from fiber-optic diagnostics.

SPE Drilling & Completion, 33(04). 298–306. https://doi.org/10.2118/184834-PA

Song, Z., Zeng, X., Thurber, C., Wang, H. F., & Fratta, D. (2018). Imaging shallow structure with active-source surface wave signal recorded by distributed acoustic sensing arrays. *Earthquake Science*, 31, 208–214. https://doi.org/10.29382/eqs-2018-0208-4

Song, Z., Zeng, X., & Thurber, C. H. (2020). *Surface-wave dispersion spectrum inversion method applied to love and Rayleigh waves recorded by DAS*. Seismological Society of America Annual Meeting, *Abstract*. Albuquerque, NM, USA.

Sookprasong, P. A., Hurt, R. S., & Gill, C. C. (2014a). *Lessons learned from DAS and DTS in multicluster, multistage horizontal well fracturing: Interpretation of hydraulic fracture initiation and propagation through diagnostics*. IADC/SPE Asia Pacific Drilling Technology Conference, *SPE-170512-MS*. https://doi.org/10.2118/170512-MS

Sookprasong, P. A., Hurt, R. S., & Gill, C. C. (2014b). *Downhole monitoring of multicluster, multistage horizontal well fracturing with fiber optic Distributed Acoustic Sensing (DAS) and Distributed Temperature Sensing (DTS)*. International Petroleum Technology Conference, *IPTC-17972-MS*. https://doi.org/10.2523/IPTC-17972-MS

Sookprasong, P. A., Hurt, R. S., Gill, C. C., & Lafollette, R. (2014). *Fiber optic DAS and DTS in multicluster, multistage horizontal well fracturing: Interpreting hydraulic fracture initiation and propagation through diagnostics*. SPE Annual Technical Conference and Exhibition, *SPE-170723-MS*. https://doi.org/10.2118/170723-MS

Soroush, M., Roostaei, M., Fattahpour, V., Mahmoudi, M., Keough, D., Cheng, L., & Moez, K. (2019). *Prognostics thermal well management: A review on wellbore monitoring and the application of Distributed Acoustic Sensing DAS for steam breakthrough detection*. SPE Thermal Well Integrity and Design Symposium, *SPE-198685-MS*. https://doi.org/10.2118/198685-MS

Spackman, T. W., & Lawton, D. C. (2018). *Analysis of distributed acoustic sensing and geophone VSP data for continuous seismic-source studies*. 88th SEG Annual International Meeting, *Expanded Abstracts* (pp. 4943–4947). https://doi.org/10.1190/segam2018-2996933.1

Spain, D. R., Gil, I. R., Sebastian, H. M., Smith, P., Wampler, J., Cadwallader, S., & Graff, M. (2015). *Geo-Engineered Completion Optimization: An integrated, multi-disciplinary approach to improve stimulation efficiency in unconventional shale reservoirs*. SPE Middle East Unconventional Resources Conference and Exhibition, *SPE-172921-MS*. https://doi.org/10.2118/172921-MS

Spica, Z. J., Perton, M., Martin, E. R., Beroza, G. C., & Biondi, B. (2020). Urban seismic site characterization by fiber-optic seismology. *Journal of Geophysics Research: Solid Earth, 125: e2019JB018656*. https://doi.org/10.1029/2019JB018656

Squires, C., Ramos, C., & Clay, M. (2020). *Perforating trends, technology and evaluation in North America*. SPE Hydraulic Fracturing Technology Conference and Exhibition, *SPE-199744-MS*. https://doi.org/10.2118/199744-MS

Staněk, F., Jechumtálová, Z., & Eisner, L. (2018). *Directivity of microseismic events as a tool for interpretation*. 88th SEG Annual International Meeting, *Expanded Abstracts* (pp. 2987–2991). https://doi.org/10.1190/segam2018-2997906.1

Stark, P. F., Bohrer, N. C., Kemner, T. T., Magness, J., Shea, A., & Ross, K. (2019). *Improved completion economics through real-time, fiber optic stimulation monitoring*. SPE Hydraulic Fracturing Technology Conference and Exhibition, *SPE-194314-MS*. https://doi.org/10.2118/194314-MS

Stark, P., Tran, J.-B., Mogck, D., & Mask, G. (2020). *Improving completions immediately: An applied methodology for real-time optimization*. SPE Hydraulic Fracturing Technology Conference and Exhibition, *SPE-199698-MS*. https://doi.org/10.2118/199698-MS

Starr, J. (2017). *Geophysics and its role in Appalachian Basin oil and gas exploration and development*. 87th SEG Annual International Meeting, *Expanded Abstracts* (pp. 4002–4006). https://doi.org/10.1190/segam2017-17642934.1

Starr, J., & Jacobi, R. (2017). *Simultaneous use of microseismic monitoring and DAS-strain measurements to analyze the anatomy of a hydraulic stimulation in the Marcellus Shale*. 87th SEG Annual International Meeting, *Expanded Abstracts* (pp. 2841–2845). https://doi.org/10.1190/segam2017-17559444.1

Staveley, C., Doyle, C., Coetzee, C., Franzen, A., Boer, H. Den, Rooyen, A. van, et al. (2017). *Development and field application of a permanent fiberoptic wellbore fluid level monitoring system*. Abu Dhabi International Petroleum Exhibition & Conference, *SPE-188868-MS*. https://doi.org/10.2118/188868-MS

Stiller, M., Bauer, K., Henninges, J., Norden, B., Krawczyk, C., & Huenges, E. (2018). 3D seismic survey at the geothermal research platform Groß Schönebeck/Germany. 80th EAGE Conference and Exhibition, Extended Abstracts, Th P7 13. https://doi.org/10.3997/2214-4609.201801627

Stokely, C. L. (2016). *Acoustics-based flow monitoring during hydraulic fracturing*. SPE Hydraulic Fracturing Technology Conference, *SPE-179151-MS*. https://doi.org/10.2118/179151-MS

Stork, A., Chalari, A., Mondanos, M., Coleman, T., & Farhadiroushan, M. (2019). *Seismic methods for geothermal reservoir characterization and monitoring using fiber optic distributed acoustic and temperature sensor*. EAGE/BVG/FKPE Joint Workshop on Borehole Geophysics and Geothermal Energy, Expanded Abstracts. https://doi.org/10.3997/2214-4609.201903162

Stork, A., Lund, B., David, A., Clarke, A., Nygren, C., *Johansson*, S., & Mondanos, M. (2020). *A comparison of the capabilities of DAS fibre-optic technologies and geophones for VSP surveys*. First EAGE Workshop on Fibre Optic Sensing, Expended Abstract. https://doi.org/10.3997/2214-4609.202030017

Sullivan, B. (2018). *DAS array on Colorado school of mines campus*. Paper presented at AGU Workshop: Distributed Acoustic Sensing-Principles and Case Studies. Washington, D.C., *USA*.

Sullivan, M., Zanganeh, B., Springer, A., & Clarkson, C. (2019). *Post-fracture pressure decay: A novel (and free) stage-level assessment method*. SPE/AAPG/SEG Unconventional Resources Technology Conference, *URTEC-2019-970-MS*. https://doi.org/10.15530/urtec-2019-970

Svelto, C., Pniov, A., Zhirnov, A., Nesterov, E., Stepanov, K., Karassik, V., Galzerano, G., & Laporta, P. (2019). *Online monitoring of gas & oil pipeline by distributed optical fiber sensors*. Offshore Mediterranean Conference and Exhibition, *OMC-2019-0830*.

Tamayo, D., Binder, G., Titov, A., Simmons, J., Tura, A., Byerley, G., et al. (2018). *Time lapse seismic monitoring of individual hydraulic frac stages using a downhole DAS array: initial field observations*. Abstract. *Paper presented at SEG Summer Research Workshop: Recent Advances and Applications in Borehole Geophysics*. Galveston, TX, USA.

Tanimola, F., & Hill, D. (2009). Distributed fibre optic sensors for pipeline protection. *Journal of Natural Gas Science and Engineering*, 1(4), 134–143. https://doi.org/10.1016/j.jngse.2009.08.002

Tatanova, M., Chalenski, D., Mateeva, A., Zwartjes, P., Wills, P., Du, Y., & Lopez, J. (2016). *Low-cost on-demand seismic monitoring with DAS VSP in Deepwater GoM*. Paper presented at SEG Postconvention workshop W-10: Fiber-optic Sensing for Exploration and Monitoring: Development, Applications, *and Challenges*. Dallas, TX, USA.

Tatanova, M., Chalenski, D., Mateeva, A., Zwartjes, P., Yang, Z., & Lopez, J. (2017). *DAS VSP in deepwater GoM for reservoir monitoring—lessons learned. First EAGE Workshop on Practical Reservoir Monitoring*, Expanded Abstracts, Th PRM 08. https://doi.org/10.3997/2214-4609.201700034

Teff, J., Silver, K., Langton, D., Kahn, D., Borell, J., & Chavarria, J. A. (2016). *A technical comparison of downhole methods through Fiber Optic VSP, in the Eagle Ford Formation*. SPE/AAPG/SEG Unconventional Resources Technology Conference, *URTEC-2462817-MS*. https://doi.org/10.15530/URTEC-2016-2462817

Tejedor, J., Macias-Guarasa, J., Martins, H. F., Pastor-Graells, J., Corredera, P., & Martin-Lopez, S. (2017). Machine learning methods for pipeline surveillance systems based on distributed acoustic sensing: A review. *Applied Sciences*, 7(8), 841, pp. 1–26. https://doi.org/10.3390/app7080841

Temizel, C., Irani, M., Ghannadi, S., Canbaz, C. H., Moreno, R., Bashtani, F., & Basri, M. A. (2019). *Optimization of steam-additive processes With DTS/DAS applications in heavy oil reservoirs*. SPE Annual Technical Conference and Exhibition, *SPE-196074-MS*. https://doi.org/10.2118/196074-MS

Tertyshnikov, K., & Pevzner, R. (2019). *Performance of different seismic sources for DAS VSP acquisitions: A case study at Curtin well site*. 81st EAGE Conference and Exhibition Expended Abstracts, *Tu_P05_01*. https://doi.org/10.3997/2214-4609.201900693

Tertyshnikov, K., Pevzner, R., Freifeld, B., Ricard, L., & Avijegon, A. (2019). *Watching the leakage: DAS seismic monitoring of the shallow CO2 controlled-release experiment at the South West Hub In-situ Laboratory*. 89th SEG Annual International Meeting, *Expanded Abstracts* (pp. 4888–4892). https://doi.org/10.1190/segam2019-3202377.1

Tertyshnikov, K., Pevzner, R., Freifeld, B., Ricard, L., Gillies, A., & Nikolov, S. (2019). *Downhole seismic methods for near surface characterisation: Otway Project SRD 3.3 case study*. 89th SEG Annual International Meeting, *Expanded Abstracts* (pp. 2974–2978). https://doi.org/10.1190/segam2019-3216096.1

Tertyshnikov, K., & Pevzner, R. (2020). 3C VSP with DAS—an obvious approach. First EAGE Workshop on Fibre Optic Sensing, Expended Abstract. https://doi.org/10.3997/2214-4609.202030016

Thiruvenkatanathan, P., Langnes, T., Beaumont, P., White, D., & Webster, M. (2016). *Downhole sand ingress detection using fibre-optic distributed acoustic sensors*. Abu Dhabi International Petroleum Exhibition & Conference, *SPE-183329-MS*. https://doi.org/10.2118/183329-MS

Thodi, P., Paulin, M., DeGeer, D., & Squires, M. (2015). *Real-time Arctic pipeline integrity and leak monitoring*. OTC Arctic Technology Conference, *OTC-25604-MS*. https://doi.org/10.4043/25604-MS

Thodi, P., Paulin, M., Forster, L., Burke, J., & Lanan, G. (2014). *Arctic pipeline leak detection using fiber optic cable distributed sensing systems*. OTC Arctic Technology Conference, *OTC-24589-MS*. https://doi.org/10.4043/24589-MS

Thomas, P., Kolltveit, E., Heggelund, Y., Wilks, M., Wuestefeld, A., Midttømme, K., & Landrø, M. (2018). *Exploring geophysical applications for Distributed Acoustic Sensing (DAS) using a flexible interrogator research platform*. 5th CO2 Geological Storage Workshop, Extended Abstracts, *Fr CO2* P01. https://doi.org/10.3997/2214-4609.201803001

Thompson, M., Amundsen, L., Karstad, P. I., Langhammer, J., Nakstad, H., & Eriksrud, M. (2006). *Field trial of fibre-optic multi-component sensor system for applications in ocean bottom seismic*. 76th SEG Annual Meeting, *Expanded Abstracts* (pp. 1148–1152). https://doi.org/10.1190/1.2369722

Thompson, M., Amundsen, L., Nakstad, H., Langhammer, J., & Eriksrud, M. (2007). *Field trial of a fibre optic ocean bottom seismic system*. 69th EAGE Conference & Exhibition, *Extended Abstracts*, P192. https://doi.org/10.3997/2214-4609.201401866

Thurber, C. H., Parker, L., Li, P., Fratta, D., Zeng, X., Feigl, K. L., et al. (2017). *Active-source seismic tomography at Bradys Geothermal Field, Nevada, with dense nodal and fiber-optic seismic arrays. AGU Fall Meeting Abstract S32A-04*.

Titov, A. (2018). *Understanding low-frequency and production DAS measurements via laboratory tests*. Paper presented at AGU Workshop: Distributed Acoustic Sensing-Principles and Case Studies. Washington, D.C., *USA*.

Titov, A., Binder, G., Lindsey, N., Ajo-Franklin, J., & Tura, A. (2018). *Understanding production and low-frequency DAS measurements via laboratory tests*. Paper presented at SEG Postconvention Workshop W-20: DAS-Validating Measurements, Developing Processing Methods, *and Integrating to Optimize Velocity Models for Improving Subsurface Imaging*. Anaheim, CA, USA.

Titov, A. (2019). *Multiphase flow monitoring with DAS: results of flow loop experiments. Paper presented at SEG Postconvention Workshop W-1: DAS—Part* 1: Recent Advances in Subsurface Characterization using Distributed Acoustic Sensing and the Road Ahead. San Antonio, TX, USA.

Titov, A., Binder, G., Liu, Y., Simmons, J., Tura, A., Byerley, G., & Monk, D. (2019). *Observations and modeling of scattered waves from hydraulic fractures in a DAS VSP experiment in the Permian Basin*. 89th SEG Annual International Meeting, *Expanded Abstracts* (pp. 4849–4853). https://doi.org/10.1190/segam2019-3203933.1

Titov, A., Jin, G., Fan, Y., Tura, A., Kutun, K., & Miskimins, J. (2020). *Distributed fiber-optic sensing based production logging investigation: Flowloop experiments*. First EAGE Workshop on Fibre Optic Sensing, Expended Abstract. https://doi.org/10.3997/2214-4609.202030035

Trainor-Guitton, W., Guitton, A., Jreij, S., Powers, H., Sullivan, C. B., Simmons, J., & PoroTomo Team (2018). 3D Imaging from vertical DAS fiber at Brady's Natural Laboratory. 43rd Workshop on Geothermal Reservoir Engineering, PROCEEDINGS (pp. 1–11). SGP-TR-213.

Trainor-Guitton, W., Jreij, S., Guitton, A., & Simmons, J. (2018). *Fault classification from 3D imaging of vertical DAS profile*. 88th SEG Annual International Meeting, *Expanded Abstracts* (pp. 4664–4668). https://doi.org/10.1190/segam2018-2989447.1

Trainor-Guitton, W., Guitton, A., Jreij, S., Powers, H., & Sullivan, B. (2019). 3D imaging of geothermal faults from a vertical DAS fiber at Brady Hot Spring, NV USA. *Energies*, 12, 1401. https://doi.org/10.3390/en12071401

Trainor-Guitton, W. J., Titov, A., LaFlame, L., Sullivan, B., Hannum, C., Huxel, Z., et al. (2019). *Preliminary analysis of distributed acoustic sensing at the Kafadar Commons Geophysical Laboratory*. Seismological Society of America Annual Meeting, *Abstract*. Seattle, WA, USA.

Trombin, G., Pirrone, M., Moriggi, S., Galli, G., Cicione, S., & Garofoli, L. (2019). *Downhole well monitoring: Innovative technologies in challenging environments*. Offshore Mediterranean Conference and Exhibition, *OMC-2019-0986*.

Trumble, M., Sinkey, M., & Meehleib, J. (2019). *Got diversion? Real time analysis to identify success or failure*. SPE Hydraulic Fracturing Technology Conference and Exhibition, *SPE-194336-MS*. https://doi.org/10.2118/194336-MS

Udd, E., Schulz, W. L., Seim, J. M., Haugse, E. D., Trego, A., Johnson, P. E., et al. (2000). Multidimensional strain field measurements using fiber optic grating sensors. *SPIE Proceedings*, Vol. 3986, 254–262, https://doi.org/10.1117/12.388113

Udd, E., Schulz, W. L., Seim, J. M., Nelson, D. V., & Makino, A. (1998). Transverse fiber grating strain sensors based on dual overlaid fiber gratings on polarization-preserving fibers. *SPIE Proceedings*, Vol. 3330, 253–263. https://doi.org/10.1117/12.316981

Ugueto, G. A., Ehiwario, M., Grae, A., Molenaar, M., Mccoy, K., Huckabee, P., & Barree, B. (2014). *Application of integrated advanced diagnostics and modeling to improve hydraulic fracture stimulation analysis and optimization*. SPE Hydraulic Fracturing Technology Conference, *SPE-168603-MS*. https://doi.org/10.2118/168603-MS

Ugueto, G. A., Huckabee, P. T., & Molenaar, M. M. (2015). *Challenging assumptions about fracture stimulation placement effectiveness using fiber optic distributed sensing diagnostics: Diversion, stage isolation and overflushing*. SPE Hydraulic Fracturing Technology Conference, *SPE-173348-MS*. https://doi.org/10.2118/173348-MS

Ugueto, C. G. A., Huckabee, P. T., Molenaar, M. M., Wyker, B., & Somanchi, K. (2016). *Perforation cluster efficiency of cemented plug and perf limited entry completions; Insights from fiber optics diagnostics*. SPE Hydraulic Fracturing Technology Conference, *SPE-179124-MS*. https://doi.org/10.2118/179124-MS

Ugueto, C. G. A., Wojtaszek, M., Huckabee, P. T., Reynolds, A., Brewer, J., & Acosta, L. (2018). *Accelerated stimulation optimization via permanent and continuous production monitoring using fiber optics*. SPE/AAPG/SEG Unconventional Resources Technology Conference, *URTEC-2901897-MS*. https://doi.org/10.15530/URTEC-2018-2901897

Ugueto, G. A., Huckabee, P., Wojtaszek, M., Daredia, T., & Reynolds, A. (2019). *New near-wellbore insights from fiber optics and downhole pressure gauge data*. SPE Hydraulic Fracturing Technology Conference and Exhibition, *SPE-194371-MS*. https://doi.org/10.2118/194371-MS

Ugueto, G. A., Todea, F., Daredia, T., Wojtaszek, M., Huckabee, P. T., Reynolds, A., et al. (2019). *Can you feel the strain? DAS Strain Fronts for Fracture Geometry in the BC Montney, Groundbirch*. SPE Annual Technical Conference and Exhibition, *SPE-195943-MS*. https://doi.org/10.2118/195943-MS

Ugueto, G., Huckabee, P., Nguyen, A., Daredia, T., Chavarria, J., Wojtaszek, M., et al. (2020). *A cost-effective evaluation of pods diversion effectiveness using fiber optics DAS and DTS*. SPE Hydraulic Fracturing Technology Conference and Exhibition, *SPE-199687-MS*. https://doi.org/10.2118/199687-MS

Urosevic, M., Bona, A., Ziramov, S., Martin, R., Dwyer, J., & Foley, A. (2018). *Reflection seismic with DAS, Why and Where?* 2nd Conference on Geophysics for Mineral Exploration and Mining, Extended Abstracts, *We 2MIN* 12. https://doi.org/10.3997/2214-4609.201802736

Urosevic, M., Bona, A., Ziramov, S., Pevzne, R., Tertyshnikov1, K., Martin, R., et al. (2019). *Seismic exploration of mineral resources in Western Australia with Distribute Acoustic Sensing*. EAGE Near Surface Geoscience Conference & Exhibition, *Expended Abstracts*. https://doi.org/10.3997/2214-4609.201902377

Valishin, O. (2017). *Alternative technologies. Paper presented at SEG Postconvention workshop* W12: DAS: A vision of the future? Houston, TX, USA.

Valishin, O. (2019a). *Simultaneous acquisition of borehole DAS and geophone data using a hybrid wireline cable. Paper presented at SEG Postconvention Workshop W-1: DAS—Part* 1: Recent Advances in Subsurface Characterization using Distributed Acoustic Sensing and the Road Ahead. San Antonio, TX, USA.

Valishin, O. (2019b). *Advances in DAS derived distributed temperature and strain sensing and use of engineered fibers*. Paper presented at SEG Postconvention Workshop W-14: DAS Part2: What is next for DAS? *Operator needs versus Technology Suppliers' vision*. San Antonio, TX, USA.

Van Der Horst, J., Den Boer, H., In 't Panhuis, P., Kusters, R., Roy, D., Ridge, A., & Godfrey, A. (2013). Fibre optic sensing for improved wellbore surveillance. International Petroleum Technology Conference, IPTC-16873-MS. https://doi.org/10.2523/IPTC-16873-MS

Van Der Horst, J., Lopez, J., Berlang, W., & Potters, H. (2013). In-well distributed fiber optic solutions for reservoir surveillance. Offshore Technology Conference, OTC-23949-MS. https://doi.org/10.4043/23949-MS

Van Der Horst, J., Den Boer, H., In 't Panhuis, P., Wyker, B., Kusters, R., Mustafina, D., et al. (2014). Fiber optic sensing for improved wellbore production surveillance. International Petroleum Technology Conference, IPTC-17528-MS. https://doi.org/10.2523/IPTC-17528-MS.

Van Der Horst, J. (2015). *Recent advances in fiber optic technology for in-well production and injection profiling*. International Petroleum Technology Conference, *IPTC-18563-MS*. https://doi.org/10.2523/IPTC-18563-MS

Van Der Horst, J., In 't Panhuis, P., Al-Bulushi, N., Deitrick, G., Mustafina, D., Hemink, G., et al. (2015). Latest developments using fiber optic based well surveillance such as Distributed Acoustic Sensing (DAS) for downhole production and injection profiling. SPE Kuwait Oil and Gas Show and Conference, SPE-175211-MS. https://doi.org/10.2118/175211-MS

Van der Horst, J. (2016). *Using fiber optics for in-well production/injection monitoring and reservoir compaction surveillance*. Paper presented at SEG Postconvention workshop W-10: Fiber-optic Sensing for Exploration and Monitoring: Development, Applications, *and Challenges*. Dallas, TX, USA.

Vandeweijer, V., Carpentier, S., Paap, B., Blacquiere, G., Jansen, R., & Reinsch, T. (2018). De-risking shallow geothermal energy storage in challenging urban environments. 24th European Meeting of Environmental and Engineering Geophysics, Extended Abstracts, We 24P1 07. https://doi.org/10.3997/2214-4609.201802604

Velarde, S. A. R., Hernandez, J. L. R., & Karande, D. (2020). *Fiber optics leak detection systems performance evaluation for detection of pinhole leaks in above-ground and buried pipelines under multiphase flow*. International Petroleum Technology Conference, *IPTC-20296-MS*. https://doi.org/10.2523/IPTC-20296-MS

Vera, V., Torres, C., Delgado, E., Pacheco, C., Higuera, J., & Torres, M. (2019a). *Real-time hybrid coiled tubing service redefines the concept of open architecture establishing a new generation of diagnostic and coiled tubing intervention*. Abu Dhabi International Petroleum Exhibition & Conference, *SPE-197872-MS*. https://doi.org/10.2118/197872-MS

Vera, V., Torres, C., Delgado, E., Pacheco, C., Higuera, J., Torres, M., & Lozano, R. (2019b). *Industry-first hybrid technology for coiled tubing services combining fiber-optic and electric line, enabling downhole power and real-time communication for the next-generation decision-making process with wider downhole insight*. Abu Dhabi International Petroleum Exhibition & Conference, *SPE-197177-MS*. https://doi.org/10.2118/197177-MS

Verdon, J. P., Horne, S. A., Clarke, A., Stork, A. L., Baird, A. F., & Kendall, J.-M. (2020). Microseismic monitoring using a fiber-optic distributed acoustic sensor (DAS) array. *Geophysics*, *85*(3), *KS89–KS99*. https://doi.org/10.1190/geo2019-0752.1

Verliac, M., Lesnikov, V., & Euriat, C. (2015). *The Rousse-1 DAS VSP experiment—observations and comparisons from various optical acquisition systems*. 85th SEG Annual International Meeting, *Expanded Abstracts* (pp. 5534–5538). https://doi.org/10.1190/segam2015-5886544.1

Walter, F., Gräff, D., Lindner, F., Paitz, P., Köpfli, M., Chmiel, M., & Fichtner, A. (2020). Distributed acoustic sensing of microseismic sources and wave propagation in glaciated terrain. *Nature Communications*, 11, 2436. https://doi.org/10.1038/s41467-020-15824-6

Wang, C. (2018). *Distributed surface seismic sensing based on interferometry of phase optical time-domain reflectometry*. 88th SEG Annual International Meeting, *Expanded Abstracts* (pp. 5495–5499). https://doi.org/10.1190/segam2018-w20-01.1

Wang, H. F., Lord, N. E., Chalari, A., Lancelle, C., Baldwin, J. A., Castongia, E., et al. (2014). *Field trial of distributed acoustic sensing using active sources at Garner Valley, California*. Paper presented at the 2014 AGU Fall Meeting, San Francisco, CA, USA. *Abstract NS41C-07*.

Wang, H. F., Zeng, X., Lord, N. E., Fratta, D., Coleman, T., & McLaughlin, M. (2017). *Field trial of distributed acoustic sensing in an active room-and-pillar mine*. *AGU Fall Meeting Abstract S33F-03*.

Wang, H. F., Fratta, D., Lord, N., & Coleman, T. (2018). *Distributed acoustic sensing (DAS) field trials for near-surface geotechnical properties, earthquake seismology, and mine monitoring*. 88th SEG Annual International Meeting, *Expanded Abstracts* (pp. 4953–4957). https://doi.org/10.1190/segam2018-2997833.1

Wang, H. F, Zeng, X., Fratta, D., & Lord, N. (2018). *Two DAS case studies: Ground Motion from a Regional Earthquake and Local Tomography from Blasts in a Room-and-Pillar Mine Reservoir*. Paper presented at SEG Postconvention Workshop W-20: DAS-Validating Measurements, Developing Processing Methods, *and Integrating to Optimize Velocity Models for Improving Subsurface Imaging*. Anaheim, CA, USA.

Wang, H. F., Zeng, X., Miller, D. E., Fratta, D., Feigl, K. L., Thurber, C. H., & Mellors, R. J. (2018). Ground motion response to an ML 4.3 earthquake using co-located distributed acoustic sensing and seismometer arrays. *Geophysical Journal International*, 213, 2020–2036. https://doi.org/10.1093/gji/ggy102

Wang, H., Comas, X., & Tyler, S. (2019). Fiber-optic networks find a new use as seismic sensor arrays. Eos Trans. AGU, 100. https://doi.org/10.1029/2019EO119897

Wang, K., Hatchell, P., Chalenski, D., & Lopez, J. (2017). *Advances in 4D seismic and geophysical monitoring of deepwater fields*. Offshore Technology Conference, *OTC-27828-MS*. https://doi.org/10.4043/27828-MS

Wang, K., Hatchell, P., Mateeva, A., Kiyashchenko, D., Duan, Y., & Lopez, J. (2019). *Practical frequent reservoir monitoring. 2nd EAGE Workshop Practical Reservoir Monitoring*, Expended Abstracts, Th PRM 06. https://doi.org/10.3997/2214-4609.201900007

Wang, X., Wang, Y., Zhang, L., & Cook, J. (2019). 3D Gaussian-beam migration on DAS VSP data. 89th SEG Annual International Meeting, Expanded Abstracts (pp. 984–988). https://doi.org/10.1190/segam2019-3214563.1

Wang, X., Williams, E. F., Karrenbach, M., González-Herráez, M., Martins, H. F., & Zhan, Z. (2020). Rose Parade seismology: Signatures of floats and bands on optical fiber. *Seismological Research Letters*, https://doi.org/10.1785/0220200091

Wang, Y., Yuan, H., Liu, X., Bai, Q., Zhang, H., Gao, Y., & Jin, B. (2019). A comprehensive study of optical fiber acoustic sensing. *IEEE Access*, 7, 85821–85837. https://doi.org/10.1109/ACCESS.2019.2924736

Warpinski, N. R. (2014). *A review of hydraulic-fracture induced microseismicity*. 48th U.S. Rock Mechanics/Geomechanics Symposium, *ARMA-2014-7774*.

Warpinski, N. R., Mayerhofer, M. J., Davis, E. J., & Holley, E. H. (2014). *Integrating fracture diagnostics for improved microseismic interpretation and stimulation modeling*. SPE/AAPG/SEG Unconventional Resources Technology Conference, *URTEC-1917906-MS*. https://doi.org/10.15530/URTEC-2014-1917906

Webster, P., Cox, B., & Molenaar, M. M. (2013). *Developments in diagnostic tools for hydraulic fracture geometry analysis*. SPE/AAPG/SEG Unconventional Resources Technology Conference, *URTEC-1619968-MS*, 218–224. https://doi.org/10.1190/urtec2013-025

Webster, P., Wall, J., Perkins, C., & Molenaar, M. (2013). *Micro-seismic detection using distributed acoustic sensing*. 83rd SEG Annual International Meeting, *Expanded Abstracts* (pp. 2459–2463). https://doi.org/10.1190/segam2013-0182.1

Webster, P. S., Cox, B. E., & Molenaar, M. M. (2014). Distributed acoustic sensing for cross-well frac monitoring. GeoConvention 2014, Extended Abstracts.

Webster, P. (2016). Introduction to June Focus: DAS/Borehole Geophysics. *CSEG Recorder*, 41(6), 17.

Webster, P., Molenaar, M., & Perkins, C. (2016). *DAS Microseismic*. *CSEG Recorder*, 41(6). 38–39.

Wheaton, B., Miskimins, J., Wood, D., Lowe, T., & Barree, R. (2014). *Integration of distributed temperature and distributed acoustic survey results with hydraulic fracture modeling: A case study in the Woodford Shale*. SPE/AAPG/SEG Unconventional Resources Technology Conference, *URTEC-1922140-MS*. https://doi.org/10.15530/URTEC-2014-1922140

Wheaton, B., Miskimins, J., Wood, D., Lowe, T., & Barree, R. (2015). *Integration of distributed temperature and distributed acoustic survey results with hydraulic fracture modeling: A case study in the Woodford Shale*. 85th SEG Annual International Meeting, *Expanded Abstracts* (pp. 4926–4927). http://dx.doi.org/10.1190/segam2015-5830237.1

Wheaton, B., Haustveit, K., Deeg, W., Miskimins, J., & Barree, R. (2016). *A case study of completion effectiveness in the eagle ford shale using DAS/DTS observations and hydraulic fracture modeling*. SPE Hydraulic Fracturing Technology Conference, *SPE-179149-MS*. https://doi.org/10.2118/179149-MS

White, D., Roach, L., Harris, K., Cheraghi, S., Samson, C., & Roberts, B. (2017). *Evolution of the aquistore deep CO2 plume from time-lapse seismics*. EAGE/SEG Research Workshop, Extended Abstracts, *Tu CO2* 03. https://doi.org/10.3997/2214-4609.201701939

White, D., Harris, K., Roach, L. A. N., & Robertson, M. (2019). 7 years of 4D seismic monitoring at the Aquistore CO2 storage site, Saskatchewan, Canada. 89th SEG Annual International Meeting, Expanded Abstracts (pp. 4918–4922). https://doi.org/10.1190/segam2019-3216776.1

Wilks, M., Wuestefeld, A., Thomas, P., Kolltveit, E., & Oye, V. (2017). *Initial results from the field on the use of DAS as a viable microseismic monitoring system of CCS sites*. EAGE/SEG Research Workshop, Extended Abstracts, *We CO2* P04. https://doi.org/10.3997/2214-4609.201701957

Wilks, M., Wuestefeld, A., Oye, V., Thomas, P., & Kolltveit, E. (2017). *Tailoring distributed acoustic sensing techniques for the microseismic monitoring of future CCS sites: Results from the field*. 87th SEG Annual International Meeting, *Expanded Abstracts* (pp. 2762–2766). https://doi.org/10.1190/segam2017-17153208.1

Wilks, M., & Wuestefeld, A. (2018). *Synthetic modelling of A DAS cable's sensitivity and performance in microseismic monitoring applications*. 7th EAGE Workshop on Passive Seismic, *Extended Abstracts*, P23. https://doi.org/10.3997/2214-4609.201800065

Williams, A., Kendall, J. M., Clarke, A., & Verdon, J. (2017). *Challenges in locating microseismic events using distributed acoustic sensors*. *AGU Fall Meeting Abstract S33B-2387*.

Williams, A., Kendall, J., Verdon, J., Clarke, A., & Stork, A. (2020). Applying conventional filtering and picking approaches to DAS microseismic data. First EAGE Workshop on Fibre Optic Sensing, Expended Abstract. https://doi.org/10.3997/2214-4609.202030011

Williams, E. (2019). Combining active- and passive-source surface waves for subsurface monitoring with DAS. Paper presented at SEG Postconvention Workshop W-1: DAS—Part 1: Recent Advances in Subsurface Characterization using Distributed Acoustic Sensing and the Road Ahead. San Antonio, TX, USA.

Williams, E. F., Zhan, Z., Karrenbach, M., Cole, S., & LaFlame, L. (2019). *High-resolution mapping and monitoring of shallow shear-wave velocity in urban Pasadena with distributed acoustic sensing*. Seattle, WA, *USA*.

Williams, E. F., Fernandez Ruiz, M. R., Fidalgo Martins, H., Zhan, Z., Gonzalez Herraez, M., *Vanthillo*, R., & Magalhaes, R. (2019). *Teleseisms and microseism generation observed by an ocean-bottom distributed acoustic sensing array offshore Belgium*. Seismological Society of America Annual Meeting, Abstract. Seattle, WA, USA.

Williams, E. F., Fernández-Ruiz, M. R., Magalhaes, R., Vanthillo, R., Zhan, Z., González-Herráez, M., & Martins, H. F. (2019). Distributed sensing of microseisms and teleseisms with submarine dark fibers. *Nature Communications*, 10, 5778. https://doi.org/10.1038/s41467-019-13262-7

Williams, J. (2012). Distributed acoustic sensing for pipeline monitoring. *Pipeline & Gas Journal*, 239(7). Available online: https://pgjonline.com/magazine/2012/july-2012-vol-239-no-7/features/distributed-acoustic-sensing-for-pipeline-monitoring

Williams, J. (2017). *The use of DAS in other industries. Paper presented at SEG Postconvention Workshop* W12: DAS: A vision of the future? Houston, TX, USA.

Williams, M. J., Le Calvez, J. H., Cuny, T., & Hartog, A. (2017). *An adaptive filtering approach to noise estimates for use in diversity stacks for DAS VSPs*. 79th EAGE Conference and Exhibition, Extended Abstracts, *Th* A3 15. https://doi.org/10.3997/2214-4609.201700516

Williams, M. J., Le Calvez, J., & Cuny, T. (2019). *A cloud approach to processing distributed vibration measurements*. 81st EAGE Conference and Exhibition, Expended Abstracts, *Tu_P10_09*. https://doi.org/10.3997/2214-4609.201900769

Williams, M. J., Le Calvez, J., Wilson, C., & Rodriguez-Herrera, A. (2019). *Integrated geomechanical interpretation of* *hydraulic stimulation operations using distributed vibration sensing*. SPE/AAPG/SEG Unconventional Resources Technology Conference, *URTEC-2019-184-MS*. https://doi.org/10.15530/urtec-2019-184

Williams, M. J., Cuny, T., Constantinou, A., & Armstrong, P. (2019). *Defining future DAS hardware and applications through use of a digital twin*. Paper presented at SEG Postconvention Workshop W-14: DAS Part2: What is next for DAS? *Operator needs versus Technology Suppliers' vision*. San Antonio, TX, USA.

Williams, T., Lee, E., Chen, J., Wang, X., Lerohl, D., Armstrong, G., & Hilts, Y. (2015). *Fluid ingress location determination using distributed temperature and acoustic sensing*. SPE Digital Energy Conference and Exhibition, *SPE-173446-MS*. https://doi.org/10.2118/173446-MS

Willis, M. E., Ellmauthaler, A., Wu, X., Barfoot, D., Erdemir, C., Barrios-Lopez, O. A., et al. (2016). *Calibration of Distributed Acoustic Sensing (DAS) VSP data*. 78th EAGE Conference and Exhibition, Expended Abstracts, *Th STZ2* 02. https://doi.org/10.3997/2214-4609.201601600

Willis, M. E., Erdemir, C., Ellmauthaler, A., Barrios, O., & Barfoot, D. (2016). Comparing DAS and Geophone Zero-Offset VSP data sets side-by-side. *CSEG Recorder*, 41(6), 22–26.

Willis, M., Ajo-Franklin, J., & Roy, B. (2017). Introduction to this special section: Geophysical applications of fiber-optic distributed sensing. *The Leading Edge*, 36, 973–974. https://doi.org/10.1190/tle36120973.1

Willis, M., Zhao, X., Wu, X., Ellmauthaler, A., Palacios, W., & Leblanc, M. (2017). *Effect of production flow and pump jack noise on a distributed acoustic sensing VSP data set*. 87th SEG Annual International Meeting, *Expanded Abstracts* (pp. 931–935). https://doi.org/10.1190/segam2017-17665036.1

Willis, M. E., Ellmauthaler, A., LeBlanc, M., Palacios, W., & Wu, X. (2018). *Comparing distributed acoustic sensing, vertical seismic profile data acquired with single- and multi-mode fiber optic cables*. 88th SEG Annual International Meeting, *Expanded Abstracts* (pp. 4674–4678). https://doi.org/10.1190/segam2018-2996212.1

Willis, M. E., Wu, X., Ellmauthaler, A., & LeBlanc, M. (2018). *Practical DAS acquisition and preprocessing*. Paper presented at SEG Postconvention Workshop W-20: DAS-Validating Measurements, Developing Processing Methods, *and Integrating to Optimize Velocity Models for Improving Subsurface Imaging*. Anaheim, CA, USA.

Willis, M. E., Wu, X., Padhi, A., Ellmauthaler, A., & LeBlanc, M. (2018a). *Effect of the angular response of a fiber-optic cable on DAS VSP recordings in lateral wells. 80th EAGE Conference and Exhibition*, Expended Abstracts, Th H 11. https://doi.org/10.3997/2214-4609.201801500

Willis, M. E., Wu, X., Padhi, A., Ellmauthaler, A., & LeBlanc, M. (2018b). *Effect of the angular response of a fiber-optic cable on DAS VSP recordings in lateral wells*. 80th EAGE Conference and Exhibition, Expended Abstracts, *WS08*. https://doi.org/10.3997/2214-4609.201801922

Willis, M. E., Wu, X., Palacios, W., & Ellmauthaler, A. (2019). *Understanding cable coupling artifacts in wireline-deployed DAS VSP data*. 89th SEG Annual International Meeting, *Expanded Abstracts* (pp. 5310–5314). https://doi.org/10.1190/segam2019-3208294.1

Wilson, J., & Verkhovtseva, N. (2019). *Applying multiple diagnostic technologies to understand well spacing*. SPE Liquids-Rich Basins Conference—North America, *SPE-197090-MS*. https://doi.org/10.2118/197090-MS

Wilson, R. E., Eckley, I. A., Nunes, M. A., & Park, T. (2019). Dynamic detection of anomalous regions within distributed acoustic sensing data streams using locally stationary wavelet time series. *Data Mining and Knowledge Discovery*, 33(3). 748–772. https://doi.org/10.1007/s10618-018-00608-w

Wong, W., Wu, H., Li, Y., Hewett, B., Liu, Z., Yang, Z., & Wills, P. (2015). *Experimental processing of dual-well 3D DASVSP simultaneously acquired with OBS in deep water environment in GOM*. 3rd EAGE Workshop on Borehole Geophysics. Expanded Abstracts, *BG18*. https://doi.org/10.3997/2214-4609.201412197

Worsley, J., Minto, C., Hill, D., Godfrey, A., & Ashdown, J. (2014). *Fibre optic four mode leak detection for gas, liquids and multiphase products*. Abu Dhabi International Petroleum Exhibition and Conference, *SPE-171824-MS*. https://doi.org/10.2118/171824-MS

Wu, C., Yi, S. S., & Sharma, M. M. (2017). *Proppant distribution among multiple perforation clusters in a horizontal wellbore*. SPE Hydraulic Fracturing Technology Conference and Exhibition, *SPE-184861-MS*. https://doi.org/10.2118/184861-MS

Wu, H., Kiyashchenko, D., & Lopez, J. (2011). Time-lapse 3D VSP using permanent receivers in a flowing well in the deepwater Gulf of Mexico. *The Leading Edge*, 30(9), 1052–1058. http://dx.doi.org/10.1190/1.3640529

Wu, H., Wills, P., Li, Y., Wong, W., Hewett, B., & Liu, Z. (2014). 3D DAS-VSP processing and learning—velocity diagnosis and update for seismic imaging improvement. 76th EAGE Conference and Exhibition—Workshops, Extended Abstracts, WS15-D04. https://doi.org/10.3997/2214-4609.20140620

Wu, H., Wong, W., Yang, Z., Wills, P., Lopez, J., Li, Y., et al. (2015). Dual-well 3D vertical seismic profile enabled by distributed acoustic sensing in deep water Gulf of Mexico. *Interpretation*, *3*, *SW11–SW25*. https://doi.org/10.1190/INT-2014-0248.1

Wu, J., Yu, G., Zhang, Q., Li, Y., Cai, D., Chen, Y., et al. (2017). *Walkaway-VSP survey using distributed optical fiber in China oilfield*. Proc. SPIE 10464, *AOPC 2017: Fiber Optic Sensing and Optical Communications*, 104642B; https://doi.org/10.1117/12.2282447

Wu, K., Anusarn, S., & Tang, J. (2016). Numerical study of flow rate distribution for simultaneous multiple fracture propagation in horizontal wells. 50th U.S. Rock Mechanics/Geomechanics Symposium, ARMA-2016-038.

Wu, Q., Nair, S., Shuck, M., van Oort, E., Guzik, A., & Kishida, K. (2016a). *Advanced distributed fiber optic sensors for monitoring poor zonal isolation with hydrocarbon migration in cemented annuli*. SPE Deepwater Drilling and Completions Conference, *SPE-180329-MS*. https://doi.org/10.2118/180329-MS

Wu, Q., Nair, S., Shuck, M., van Oort, E., Guzik, A., & Kishida, K. (2016b). *Advanced distributed fiber optic sensors to monitor cement hydration and detect annular hydrocarbon migration for enhanced zonal isolation*. SPE Annual Technical Conference and Exhibition, *SPE-181429-MS*. https://doi.org/10.2118/181429-MS

Wu, Q., Dininger, M., Nair, S., van Oort, E., Guzik, A., & Kishida, K. (2017). *Real time cement displacement tracking using distributed fiber optic sensors*. SPE Annual Technical Conference and Exhibition, *SPE-187409-MS*. https://doi.org/10.2118/187409-MS

Wu, Q., Nair, S., van Oort, E., Guzik, A., & Kishida, K. (2019). *Concurrent real-time distributed fiber optic sensing of casing deformation and cement integrity loss*. SPE/IADC International Drilling Conference and Exhibition, *SPE-194159-MS*. https://doi.org/10.2118/194159-MS

Wu, X., Willis, M., Palacios, W., Torres, L., Ellmauthaler, A., Barfoot, D., & Carrillo, J. D. (2016). *Combined use of P and S DAS VSP data*. Paper presented at SEG Postconvention workshop W-10: Fiber-optic Sensing for Exploration and Monitoring: Development, Applications, *and Challenges*. Dallas, TX, USA.

Wu, X., Willis, M. E., Palacios, W., Ellmauthaler, A., Barrios, O., Shaw, S., & Quinn, D. (2017). Compressional- and shear-wave studies of distributed acoustic sensing acquired vertical seismic profile data. *The Leading Edge*, 36(12), 987–993. https://doi.org/10.1190/tle36120987.1

Wu, Y., Richter, P., Hull, R., & Farhadiroushan, M. (2020). Hydraulic frac-hit corridor (FHC) monitoring and analysis with high-resolution distributed acoustic sensing (DAS) and far-field strain (FFS) measurements. *First Break*, 38(6), 65–70. https://doi.org/10.3997/1365-2397.fb2020045

Wuestefeld, A. (2019). *Designing cross-well seismic for Fiber Optics: A case study for the Svelvik CO2 test site. Paper presented at SEG Postconvention Workshop W-1: DAS—Part* 1: Recent Advances in Subsurface Characterization using Distributed Acoustic Sensing and the Road Ahead. San Antonio, TX, USA.

Wuestefeld, A., & Wilks, M. (2019). *Modelling microseismic event detection and location capabilities with DAS cables*. 81st EAGE Conference and Exhibition, Expended Abstracts, *We_R09_12*. https://doi.org/10.3997/2214-4609.201901248

Xiao, J., Farhadiroushan, M., Clarke, A., Khalifa, Q., A. Mulhem, A., Reyes, H. F., et al. (2013). *Inflow monitoring in intelligent wells using distributed acoustic sensor*. SPE Middle East Intelligent Energy Conference and Exhibition, SPE-167447-MS. https://doi.org/10.2118/167447-MS

Xiao, J., Farhadiroushan, M., Clarke, A., Abdalmohsen, R. A., Alyan, E., Parker, T. R., et al. (2014). Intelligent Distributed Acoustic Sensing for In-well Monitoring. SPE Saudi Arabia Section Technical Symposium and Exhibition, SPE-172197-MS. https://doi.org/10.2118/172197-MS

Xiao, J., Farhadiroushan, M., Clarke, A., Jacob, S., AlMulhem, A., Milne, H. C., et al. (2015). *Dynamic water injection profiling in intelligent wells using distributed acoustic sensor with multimode optical fibers*. SPE Annual Technical Conference and Exhibition, *SPE-174865-MS*. https://doi.org/10.2118/174865-MS

Yang, L., Bale, D. S., Yang, D., Raum, M., Bello, O., Failla, R., et al. (2018). *Enabling real-time asset analytics for a cloud-based fiber-optic data management system*. SPE Annual Technical Conference and Exhibition, *SPE-191592-MS*. https://doi.org/10.2118/191592-MS

Yang, X., Bello, O., Yang, L., Bale, D., & Failla, R. (2019). *Intelligent oilfield—cloud based big data service in upstream oil and gas*. International Petroleum Technology Conference, *IPTC-19418-MS*. https://doi.org/10.2523/IPTC-19418-MS

Yang, Y., *Williams*, E., & Zhan, Z. (2020). *Ambient noise tomography of the near surface using the Ridgecrest DAS array*. Seismological Society of America Annual Meeting, Abstract. Albuquerque, NM, USA.

Yavuz, S., Freifeld, B. M., Pevzner, P., Tertyshnikov, K., Dzunic, A., Ziramov, S., et al. (2016). *Subsurface imaging using buried DAS and geophone arrays—preliminary results from CO2CRC Otway project*. 78th EAGE Conference and Exhibition, Expanded Abstracts, Th SBT4 04. https://doi.org/10.3997/2214-4609.201601497

Yi, S. S., Wu, C.-H., & Sharma, M. M. (2018). *Proppant distribution among multiple perforation clusters in plug-and-perforate stages. SPE Production & Operations*, 33(04), 654–665. https://doi.org/10.2118/184861-PA

Yi, S. S., Wu, C.-H., & Sharma, M. (2019). *Optimization of plug-and-perf completions for balanced treatment distribution and improved reservoir contact*. SPE Hydraulic Fracturing Technology Conference and Exhibition, *SPE-194360-MS*. https://doi.org/10.2118/194360-MS

Young, B. A., Chojnicki, K. N., Knox, H. A., & Lowrey, J. D. (2020). *Comparison of distributed acoustic sensing and co-located geophones of a chemical explosion in a borehole at Blue Canyon Dome*. Seismological Society of America Annual Meeting, *Abstract*. Albuquerque, NM, USA.

Yu, C. (2018). *The potential of DAS in teleseismic studies: Insights from the Goldstone experiment*. Paper presented at AGU Workshop: Distributed Acoustic Sensing-Principles and Case Studies. Washington, D.C., *USA*.

Yu, C., Zhan, Z., Lindsey, N. J., Ajo-Franklin, J. B., & Robertson, M. (2019). The potential of DAS in Teleseismic studies: Insights from the Goldstone experiment. *Geophysical Research Letters*, 46(3), 1320–1328. https://doi.org/10.1029/2018GL081195

Yu, G., Chen, Y. Z., Wang, X. M., Zhang, Q. H., Li, Y. P., Zhao, B. Y., et al. (2016). *Walkaway VSP using multimode optical fibres in a hybrid wireline*. 78th EAGE Conference and Exhibition, Extended Abstracts, *Th STZ2* 05. https://doi.org/10.3997/2214-4609.201601602

Yu, G., Cai, Z., Chen, Y., Wang, X., Zhang, Q., Li, Y., et al. (2016a), Walkaway VSP using multimode optical fibers in a hybrid wireline. *The Leading Edge*, 35, 615–619. https://doi.org/10.1190/tle35070615.1

Yu, G., Cai, Z., Chen, Y., Wang, X., Zhang, Q., Li, Y., et al. (2016b). *Walkaway VSP using multimode optical fibers in a hybrid wireline*. Paper presented at SEG Postconvention workshop W-10: Fiber-optic Sensing for Exploration and Monitoring: Development, Applications, *and Challenges*. Dallas, TX, USA.

Yu, G., Sun, Q., Ai, F., Yan, Z., Li, H., & Li, F. (2018a). *Microstructured fiber distributed acoustic sensing system for borehole seismic survey*. 88th SEG Annual International Meeting, *Expanded Abstracts* (pp. 4669–4673). https://doi.org/10.1190/segam2018-2992410.1

Yu, G., Sun, Q., Ai, F., Yan, Z., Li, H., Li, F., & Zhang, Q. (2018b). *Micro-structured fiber distributed acoustic sensing system for borehole seismic survey*. Paper presented at SEG Postconvention Workshop W-20: DAS-Validating Measurements, Developing Processing Methods, *and Integrating to Optimize Velocity Models for Improving Subsurface Imaging*. Anaheim, CA, USA.

Yu, G. (2019). *The ultra-sensitive DAS (uDAS) system development and its applications. Paper presented at SEG Postconvention Workshop W-1: DAS—Part* 1: Recent Advances in Subsurface Characterization using Distributed Acoustic Sensing and the Road Ahead. San Antonio, TX, USA.

Yu, G., Chen, Y. Z., Wu, J., Li, Y. P., Li, F., Hu, G. M., et al. (2019). 3D-VSP survey using a DAS system and downhole geophone array in Southwest China. 81st EAGE Conference and Exhibition, Expended Abstracts, We_R09_16. https://doi.org/10.3997/2214-4609.201901252

Yu, G., Chen, Y., Wu, J., Li, Y., & Li, F. (2020). *DAS-VSP enhanced processing of simultaneous acquired surface seismic data*. First EAGE Workshop on Fibre Optic Sensing, Expended Abstract. https://doi.org/10.3997/2214-4609.202030032

Yu, G., Xiong, J. L., Wu, J. J., Chen, Y. Z., & Zhao, Y. S. (2020). Enhanced surface seismic data processing using simultaneous acquired DAS-VSP data. *First Break*, 38(6), 29–36. https://doi.org/10.3997/1365-2397.fb2020039

Yu, Z., Zhan, G., & Northall, J. (2017). *VSP and DAS data noise attenuation using complex wavelet transform*. 87th SEG Annual International Meeting, *Expanded Abstracts* (pp. 5999–6003). https://doi.org/10.1190/segam2017-17642809.1

Zaanen, L. V., Bona, A., Correa, J., Tertyshnikov, K., Dean, T., & Pevzner, R. (2017). *A comparison of borehole seismic receivers*. *SEG Technical Program Expanded Abstracts* (pp. 5974–5978). https://doi.org/10.1190/segam2017-17799478.1

Zdraveva, O. K., Ramirez, A., &. Chen, S. (2018). Joint inversion and cross-validation of bore-hole and surface seismic data for reducing the uncertainty of anisotropic models. 1st EAGE/PESGB Workshop on Velocities, Expended Abstracts, Fr MU02. https://doi.org/10.3997/2214-4609.201800015

Zeng, X., Thurber, C., Wang, H., Fratta, D., Matzel, E., & PoroTomo Team (2017). *High-resolution shallow structure revealed with ambient noise tomography on a dense array*. 42nd Workshop on Geothermal Reservoir Engineering, Proceedings (pp. 1122–1126). *SGP-TR-212*.

Zeng, X., Thurber, C. H., Wang, H. F., Fratta, D., & PoroTomo Team. (2017). *3D shear wave velocity structure revealed with ambient noise tomography on a DAS array*. AGU Fall Meeting Abstract S33F-06.

Zeng, X., Lancelle, C., Thurber, C., Fratta, D., Wang, H., Lord, N., et al. (2017). Properties of noise cross-correlation functions obtained from a distributed acoustic sensing array at Garner Valley, California. *Bulletin of the Seismological Society of America*, 107(2), 603–610. https://doi.org/10.1785/0120160168

Zeng, X., Wang, B., Li, X., Xu, W., Xu, S., & Song, Z. (2019). *Shallow Vs structure imaged with the ambient noise recorded by a telecommunication fiber-optic cable in urban area*. Seismological Society of America Annual Meeting, *Abstract*. Seattle, WA, USA.

Zeng, X., Yang, J., Zhang, Y., Song, Z., Li, X., Qin, M., & Wei, C. (2020). *Combining DAS and air-gun: A cost-effective medium change monitoring system*. Seismological Society of America Annual Meeting, *Abstract*. Albuquerque, NM, USA.

Zett, A., Webster, M., Ragbirsingh, F., Gysen, A., Limkar, P., & Johnson, J. (2014). *A case study of optical sensing applicability in reservoir surveillance—the non-unique solution dilemma*. SPWLA 55th Annual Logging Symposium, *SPWLA-2014-P*.

Zhan, G., Kommedal, J., & Nahm, J. (2015). *VSP field trials of distributed acoustic sensing in Trinidad and Gulf of Mexico*. 85th SEG Annual International Meeting, *Expanded Abstracts* (pp. 5539–5543). https://doi.org/10.1190/segam2015-5876420.1

Zhan, G., Li, Q., Nahm, J., Kommedal, J., & Konkler, J. (2016). Field trials of distributed acoustic sensing for reservoir delineation with VSP. *CSEG Recorder*, 41(6), 34–37.

Zhan, G., Ball, M., Saxton, L., Soulas, S., & Salt, M. (2018). *Lessons learned from a recent DAS VSP field trial in North Sea*. Paper presented at SEG Postconvention Workshop W-20: DAS-Validating Measurements, Developing Processing Methods, *and Integrating to Optimize Velocity Models for Improving Subsurface Imaging*. Anaheim, CA, USA.

Zhan, G., Li, Y., Tura, A., Willis, M., & Martin, E. (2019). Introduction to special section: Distributed acoustic sensing and its oilfield potential. *Interpretation*, *7*, *SAi–SAi*. https://doi.org/10.1190/INT-2019-0116-SPSEINTRO.1

Zhan, Z. (2018). *Distributed Acoustic Sensing as part of the next-generation Southern California Seismic Network*. Paper presented at SEG Postconvention Workshop W-20: DAS-Validating Measurements, Developing Processing Methods, *and Integrating to Optimize Velocity Models for Improving Subsurface Imaging*. Anaheim, CA, USA.

Zhan, Z. (2019). Distributed acoustic sensing turns fiber-optic cables into sensitive seismic antennas. *Seismological Research Letters*, 91(1), 1–15. https://doi.org/10.1785/0220190112

Zhang, J., Hoffman, A., Murphy, K., Lewis, J., & Twomey, M. (2013). *Review of pipeline leak detection technologies*. Pipeline Simulation Interest Group Annual Meeting, *PSIG-130*.

Zhang, S., Tang, H., Hurt, R., Jayaram, V., & Wagner, J. (2020). *Joint interpretation of fiber optics and downhole gauge data for near wellbore region characterization*. SPE Hydraulic Fracturing Technology Conference and Exhibition, *SPE-199715-MS*. https://doi.org/10.2118/199715-MS

Zhang, Y., & Xue, Z. (2019). Deformation-based monitoring of water migration in rocks using Distributed Fiber Optic Strain Sensing: A laboratory study. *Water Resources Research*, 55 (11), 8368–8383. https://doi.org/10.1029/2019WR024795

Zhang, Y., Xue, Z., Park, H., Shi, J., Kiyama, T., Lei, X., et al. (2019). Tracking CO2 plumes in clay-rich rock by Distributed Fiber Optic Strain Sensing (DFOSS): A laboratory demonstration. *Water Resources Research*, 55(1), 856–867. https://doi.org/10.1029/2018WR023415

Zhang, Z., Alajami, M., & Alkhalifah, T. (2019a). *Near-surface S-wave velocity estimation using ambient noise from fiber-optic* *acquisition*. 89th SEG Annual International Meeting, *Expanded Abstracts* (pp. 938–942). https://doi.org/10.1190/segam2019-3198045.1

Zhang, Z., Alajami, M., & Alkhalifah, T. (2019b). *Near-surface S-wave velocity estimation using ambient noise from fiber-optic acquisition*. 89th SEG Annual International Meeting, *Expanded Abstracts* (pp. 5403–5407). https://doi.org/10.1190/segam2019-w21-06.1

Zhao, H., Wu, D., Zeng, M., & Ling, J. (2018). Support conditions assessment of concrete pavement slab using distributed optical fiber sensor. *Transportmetrica A: Transport Science*, 15(1), 71–90. https://doi.org/10.1080/23249935.2018.1457733

Zhao, Y., Fang, G., & Li, Y. E. (2019). *Extracting subsurface information based on extremely short period of DAS recordings*. 89th SEG Annual International Meeting, *Expanded Abstracts* (pp. 958–962). https://doi.org/10.1190/segam2019-3216400.1

Zheng, J., Harris, J. M., Al-Rumaih, B., & Li, D. (2019). *Automatic phase picker for single component borehole seismic data with deep neural network*. 89th SEG Annual International Meeting, *Expanded Abstracts* (pp. 2217–2221). https://doi.org/10.1190/segam2019-3215226.1

Zhou, R., & Willis, M. (2017). *Characterization of a fractured reservoir using distributed acoustic sensing VSP: A model-based study*. 87th SEG Annual International Meeting, *Expanded Abstracts* (pp. 5979–5983). https://doi.org/10.1190/segam2017-17663170.1

Zhou, R., Willis, M. E., Cheng, D., & Green, K. (2017). *Characterization of a fractured reservoir using DAS VSP—a model-based reflection amplitude study*. 4th EAGE Borehole Geophysics Workshop, Extended Abstracts, *BGP03*. https://doi.org/10.3997/2214-4609.201702470

Zhou, R., & Pei, D. (2018). *Detecting effectiveness of hydraulic treatment using DAS VSP Traveltime Tomography*. Abstract. *Paper presented at SEG Summer Research Workshop: Recent Advances and Applications in Borehole Geophysics*. Galveston, TX, USA.

Zhou, R., Cheng, D., & Barrios, O. A. (2018). *Feasibility of local anisotropy estimation using DAS VSP*. 88th SEG Annual International Meeting, *Expanded Abstracts* (pp. 5417–5421). https://doi.org/10.1190/segam2018-2997243.1

Zhou, R., Cheng, D., Zhao, X., Barrios, O. A., Palacios, W., & George Knapo, G. (2018). *Extending lateral image coverage using DAS VSP*. Abstract. *Paper presented at SEG Summer Research Workshop: Recent Advances and Applications in Borehole Geophysics*. Galveston, TX, USA.

Zhou, R., Cheng, D., Zhao, X., Barrios, O. A., Palacios, W., & Knapo, G. (2018). *Application of Distributed Acoustic Sensing in model building and structural imaging*. Paper presented at SEG Postconvention Workshop W-20: DAS-Validating Measurements, Developing Processing Methods, *and Integrating to Optimize Velocity Models for Improving Subsurface Imaging*. Anaheim, CA, USA.

Zhou, R., Willis, M., & Palacios, W. (2019). *Detecting hydraulic fracture induced velocity change using rapid time-lapse DAS VSP. 89th Annual International Meeting*, SEG, Expanded Abstracts (pp. 4859–4863). https://doi.org/10.1190/segam2019-3214042.1

Zhu, T., & Stensrud, D. J. (2019). Characterizing thunder-induced ground motions using fiber-optic distributed acoustic sensing array. *Journal of Geophysics Research: Atmospheres*, 124(23), 12810–12823. https://doi.org/10.1029/2019JD031453

Zhu, T., & Stensrud, D. J. (2020). *Thunderquakes by fiber-optic distributed acoustic sensing array*. Seismological Society of America Annual Meeting, *Abstract*. Albuquerque, NM, USA.

Zhu, T., Martin, E. R., Shen, J., & Hone, S. (2020). *Fiber Optics for Environmental Sense-Ing (Foresee) at Pennsylvania State University*. Seismological Society of America Annual Meeting, *Abstract*. Albuquerque, NM, USA.

Zhu, T., Junzhu Shen, J., & Martin, E. R. (2020). *Sensing earth and environment dynamics by telecommunication fiber-optic sensors: An urban experiment in Pennsylvania USA*. Submitted to *Journal of Geophysics Research:* Solid Earth.

Zumberge, M. A., Hatfield, W., & Wyatt, F. K. (2018). Measuring seafloor strain with an optical fiber interferometer. *Earth and Space Science*, 5(8), 371–379. https://doi.org/10.1029/2018EA000418

Zwaan, M., Lopez, J., & Landman, A-J. (2015). *Thermal EOR field development and well and reservoir management*. SPE Kuwait Oil and Gas Show and Conference, *SPE-175306-MS*. https://doi.org/10.2118/175306-MS

Zwartjes, P., & Mateeva, A. (2015a). *Multi-fibre DAS walk-away VSP at Kapuni*. 3rd EAGE Workshop on Borehole Geophysics. Expanded Abstracts, *BG05*. https://doi.org/10.3997/2214-4609.201412184

Zwartjes, P. M., & Mateeva, A. (2015b). *High resolution walk-away VSP at Kapuni recorded on multi-fiber DAS and geophones*. 77th EAGE Conference and Exhibition. Expanded Abstracts, Tu N118 15. https://doi.org/10.3997/2214-4609.201412739

Zwartjes, P., Mateeva, A., Tatanova, M., Chalenski, D., Yang, Z., Lopez, J., et al. (2017). *4D DAS VSP in deepwater—Proof of concept and next steps*. 87th SEG Annual International Meeting, Expanded Abstracts (pp. 5802–5807). https://doi.org/10.1190/segam2017-17633006.1

Zwartjes, P., Mateeva, A., Chalenski, D., Duan, Y., Kiyashchenko, D., & Lopez, J. (2018). *Frequent, multi-well, stand-alone 3D DAS VSP for low-cost reservoir monitoring in Deepwater*. 88th SEG Annual International Meeting, *Expanded Abstracts* (pp. 4948–4952). https://doi.org/10.1190/segam2018-2997061.1

INDEX

Distributed Acoustic Sensing in Geophysics: Methods and Applications, Geophysical Monograph 268, First Edition.
Edited by Yingping Li, Martin Karrenbach, and Jonathan B. Ajo-Franklin.

DOI:10.1002/9781119521808.index